



# Relativistic outflows in X-ray binaries: simulations and observations



Jose López Miralles

Director:

**Manel Perucho Pla, Simone Migliari,  
Jose María Martí**

Doctorat en Física

Departament d'Astronomia i Astrofísica

Universitat de València

TESIS DOCTORAL

Junio 2023



VNIVERSITAT E VALÈNCIA

**Relativistic outflows in X-ray  
binaries: simulations and  
observations**

**Jose López Miralles**

Doctorat en Física  
Departament d'Astronomia i Astrofísica  
Universitat de València

TESIS DOCTORAL

Director:  
**Manel Perucho Pla, Simone Migliari,  
Jose María Martí**

Junio 2023

## DECLARACIÓN

Los Drs. MANEL PERUCHO PLA, Profesor Titular de Universidad de la Universitat de València, SIMONE MIGLIARI, Jefe de Operaciones de Aurora Technology BV y JOSE MARÍA MARTÍ PUIG, Catedrático de Universidad de la Universitat de València,

### CERTIFICAN:

Que la presente memoria, titulada **Relativistic outflows in X-ray binaries: simulations and observations**, ha sido realizada bajo su dirección en el Departament d'Astronomia i Astrofísica de la Universitat de València por Jose López Miralles y constituye su tesis doctoral para optar al título de Doctor por la Universitat de València una vez cursados los estudios en el Doctorado en Física.

Y para que así conste, en cumplimiento de la legislación vigente, firmamos el presente certificado en València, a 26 de junio de 2023.

Fdo: Manel Perucho Pla

Simone Migliari

Jose María Martí Puig



A mis padres y a mi hermano.

A Ana.



## Acknowledgements

*Hace casi cinco años, viajé a València para visitar por primera vez el Departamento de Astronomía y Astrofísica. Recuerdo haberme vestido como dicen que uno debe vestirse para las entrevistas de trabajo (algo que ahora me produce cierta vergüenza) y llegar en tranvía a las puertas de un edificio blanco circular rodeado de gatos. Allí me esperaba Simone Migliari, un astrónomo italiano experto en observaciones de binarias a quien había conocido algunas semanas antes, y Manel Perucho, un profesor de la Universitat de València que hacía simulaciones numéricas, con quien Simone había organizado aquella reunión. Algo nervioso, subí los cuatro pisos que separan la entrada del edificio del Departamento, y busqué el nombre de Manel en los despachos del pasillo. Recuerdo haberme fijado que el primer despacho era del profesor Jose María Martí, a quien conocía de haber leído alguno de sus trabajos sobre métodos numéricos. No había mucha gente aquel día –poco se parecía el Departamento a lo que es ahora–, y las voces de Manel y Simone –a quien pude reconocer por su marcado acento italiano– se escuchaban desde el pasillo, en lo que parecía una profunda discusión de trabajo. Esperé un poco porque no quería interrumpirlos, y antes de llamar a la puerta, repasé en mi cabeza todo lo que había leído aquellos días sobre chorros relativistas y sistemas binarios. Entré en el despacho, esperando encontrarme a dos investigadores escribiendo ecuaciones en la pizarra. Sin embargo, y mientras se giraban a la vez para saludarme, en la pantalla del ordenador de Manel sólo había una partitura de jazz para saxofón. Supe al momento que aquel era mi lugar.*

Primer, vull donar-li les gràcies a Manel, qui m'ha acompanyat i guiat dia a dia en aquesta aventura. Gràcies de tot cor per la teua ajuda i els teus consells, per respectar sempre el meu treball i les meues idees, per donar-me llibertat i per escoltar-me com a un company més. Gràcies, sobretot, per no ser un director de tesi usual. En realitat, crec que eres una de les persones més inusuals que he conegut. Mai oblidaré com m'has tractat durant aquest temps i de tot el que

has fet perquè pugues treballar de la forma més còmoda possible. Per això, sempre t'estaré agraït. T'estimo molt, Manel. I per favor, anota les teues contrasenyes...

Gracias también a Simone. Esta tesis empezó contigo, aquel día que como estudiante de máster, decidí escribirte un email que todavía me recuerdas a veces cuando nos vemos. Gracias por haberme introducido en el análisis de datos con observaciones de rayos X, por presentarme a algunos de tus colaboradores (que ahora son también los míos) y por invitarme a visitar ESAC en 2019, donde conocí por primera vez el Centro de Operaciones Científicas de XMM-Newton, que ahora también forma parte de mi vida. Gracias por confiar en mí desde el primer momento, por las oportunidades que me has dado y por la forma en la que siempre reconoces y defiendes mi trabajo ante cualquiera.

También, por supuesto, a Chema, con quien he compartido tantas horas de trabajo, revisando línea a línea los códigos que han hecho posible esta tesis. Nunca tendré forma de devolverte todo el tiempo que me has dedicado, ni todo lo que he podido aprender de ti y de tu forma tan especial –y precisa, tan precisa– de trabajar. De alguna manera, espero que esta tesis sea para ti una versión extendida de tu tercera libreta-diario de código. Aunque por encima de todo, siempre te voy a recordar como una de las mejores personas que he conocido, y con las que mejor me he podido entender para trabajar.

I also want to thank the referees of the thesis, Gianluigi Bodo, Oliver Porth, Sara Motta, Valentí Bosch-Ramon, Rob Fender and Sera Markoff for dedicating their time to review and comment the first version of the manuscript.

Gracias a mis compañeros y compañeras del Departamento de Astronomía y Astrofísica: Jens, Fabrizio, Sergio –con quien también pude compartir despacho y desayunos durante varios meses–, Miquel Llorens, Pancho, Tomek, Joan, Alejandro Cruz y Rebecca, quienes me acompañaron durante mi primer año en València, y a todos los que vinieron después, sobre todo a David y Miquel, mis inseparables compañeros de despacho, pero también a Raquel, Davide, Álex, Nico y Beatrice. También a Luca, quien nos visitó en varias ocasiones desde el Max Planck de Radio Astronomía en Bonn y con quien he podido colaborar en uno de sus trabajos sobre simulaciones numéricas. Gracias, también, a Martin, Pablo y Miguel Ángel, con quien compartí muchos desayunos durante mi primer año, y sobre todo a Vicent Quilis (nuestro querido Director), Susana y Joan Ferrando, per els esmorzars en Borbotó i els dinars fora del Departament. A Susana, también le agradezco especialmente su apoyo durante mi primer año de docencia en la universidad.

Se merecen una mención especial Maneel, Arancha y Ana Moya, quienes nos hacen la vida mucho más fácil en el Departamento con su gran trabajo y

---

profesionalidad; sin duda, tenemos mucha suerte de poder trabajar con ellos. También quiero acordarme de Feli, quien formó parte de la Secretaría durante mis primeros años en el Departamento y organizaba las mejores xocolataes durante la semana de Fallas.

Gracias también a Cuca, a quien saludábamos todos los días por la mañana y a la hora de comer; espero que te estén tratando bien y que te acuerdes un poco de nosotros.

I also want to thank two of my collaborators, Sara Motta and Valentí Bosch-Ramon. Sara, thank you very much for your time, your kindness and for your patient along all of these years. I have learnt with you a lot about data analysis, and I have always felt really comfortable working together. Thank you also for inviting me to the Osservatorio Astronomico di Brera in Merate, where together with Joe, we had a very nice week of work, Italian food and hail. Valentí, a tu et vaig conèixer en el meu primer Congrés com a estudiant de tesi en 2019, i hem pogut compartir també l'últim a Àustria aquest mateix any. Pel camí, hem pogut conversar en moltes ocasions sobre simulacions de jets en microquàsars, quasi sempre prenent unes cerveses, que és possiblement la mitllor manera de parlar sobre sistemes binaris. Per tot això, et tinc també un gran afecte.

I want to thank Matthias Kadler for inviting me to the Department of Astronomy at Wurzburg University, despite the visit was sadly affected by the Covid lockdown. Thank you also to Paul Burd, who gave me a very nice introduction to the analysis of radio data with VLBI. However, my residence in Wurzburg would not have been the same without Duccio, who shared with me the experience and was practically the only person I could see face to face during that month. Moreover, I am affectionately grateful to Dr. Stephan Schroder-Kohne for taking care of me during the residence in Wurzburg and for sharing with us exciting conversations during our daily coffee-break at the Life Sciences Graduate School.

I want to thank again my friend Jens for organizing my research residence in the Department of Astrophysical Sciences of Princeton University. Thank you also to Prof. Anatoly Spitkovsky for his hospitality, and Haik, Arnau and Benjamin for their kindness during my visit and some of the trips to New York. I am also grateful to Prof. James Stone, who kindly came to Peyton Hall to discuss my RMHD projects, and to Chris White, with whom I had an interesting conversation about GRMHD and numerical methods in general.

Thank you Herman Marshall, who was a great host at MIT Kavli Institute and showed me his amazing X-ray polarization laboratory (I will never forget the baseball team you support). During my visit at MIT, I am also grateful to

Melania Nynka, who showed me the beautiful city of Boston and took care of me during all the week. Thank you also to Prof. Erin Kara, who discussed with me my projects and kindly invited me to join her weekly group meeting, where I met all her PhD students.

Gracias a la Fundación La Caixa y al programa de becas pre-doctorales INPhINIT por haberme dado los recursos necesarios para llevar a cabo esta tesis, y a todos mis compañeros/as de promoción por los buenos momentos que pasamos en los días de Training en Girona y Barcelona.

También quiero agradecerles a mis compañeras y compañeros del SOC de XMM-Newton en ESAC que me hayan acogido tan bien durante este último año, y especialmente, que se hayan preocupado por el progreso de mi trabajo en la Universidad.

Finalmente, esta tesis no habría sido posible sin el apoyo y el cariño de mis amigos y mi familia. Por eso, estas últimas palabras van para ellos.

Querido Jens, tú eres el primer amigo de verdad que hice en Valencia; seguramente, la persona más buena y noble con la que me he encontrado en este camino científico. Contigo vi mis primeras Fallas, conocí el café Berlín, e incluso la Lonja de la Seda (aunque siempre te confundías de edificio). Y aunque te has ido de Valencia mucho antes de lo que me hubiera gustado, hemos podido disfrutar juntos de tu nueva vida en Estados Unidos; sin duda, uno de los viajes más emocionantes que he hecho hasta ahora. Sólo espero que hasta que nos volvamos a encontrar en la misma ciudad, nunca dejemos de tomar *telecafé*. Ich liebe dich so sehr.

Tampoco puedo hablar de David y Miquel como mis compañeros de despacho, porque tras estos últimos años se han convertido en dos amigos muy importantes para mí.

Querido David; sin duda, la persona más brillante que he conocido. Gracias por el Universo totalmente ajeno a la realidad que conocen el resto de personas que has creado conmigo (32°00'18" S 115°30'54" E), con el que tanto nos hemos reído –y también hecho reír– cada día. Gracias por hacerme sentir tan cómodo y tan libre, y por todo lo que he podido aprender de ti. Yo nunca recordaré los meses de pandemia por haberme sentido solo en la Universidad. Espero de verdad que puedas cumplir cada uno de los pasos que te propongas en tu camino científico, porque nadie lo merece más que tú. *Gràcies pel quokkisme, i avall la revolució!*

Miquel, querido Maiq; la persona con más carisma que conozco. Una persona buena y cariñosa envuelta en un papel de tremendo *maiqismo*. Tenerte en el despacho y compartir mi día a día contigo ha sido un regalo, y por eso te voy

a echar mucho de menos. Creo que ya nunca seré capaz de desprenderme de esa parte de tu personalidad que ahora también vive conmigo: *ostiaaaa...!* Eso sí, dentro de unos años, espero ser la primera persona a la que le enseñes los resultados de Lisa. Nos lo merecemos después de *tremendas turras* con esa cara de concentrado que pones en los meetings. Y si no, como dijo Juan Antonio Bayona en *Un monstruo viene a verme*, "a mí que me registren".

También quiero acordarme de vuestras parejas, Marina y Josep, a quien he tenido la suerte de conocer durante este tiempo; creo que no podíais haber elegido una compañía mejor. A los dos, Miquel y David, gracias por haberme acompañado día a día todo este tiempo. Me habéis hecho la vida y el trabajo mucho más fácil, y a mí mucho más feliz. Os quiero mucho. Viva el 3.02 (y viva Vigo también).

También a mis amigos de siempre, los que llevan acompañándome desde el colegio en cada uno de mis pasos. Gracias Rucho, Raul y Veiga. Nada me gusta más que juntarnos siempre que podemos, porque de alguna manera, significa volver a casa. Y a mis amigos de la carrera, Michael, Sergio y Dani, con quien compartí los primeros años de mi camino en la Universidad.

Por encima de todo, gracias a mis padres y a mi hermano Iván por su cariño y apoyo incondicional, por confiar siempre en mí desde pequeño y por darme todo para que pudiera llegar hasta aquí. Ninguno de los méritos que recoge esta tesis hubiera sido posible sin vosotros. Os quiero mucho. Gracias también a mis abuelas Elena y Pilar, y a mi abuelo Antonio, con quien siempre compartiré los momentos importantes de mi vida.

Grazas a Manuela e Daniel, quen dende hai moitos anos forman tamén parte da miña familia.

Y a ti, Ana, porque esta tesis es tan tuya como mía. Gracias por haberme ayudado tanto, por apoyarme y protegerme, y por intentar entenderme ciegamente, incluso cuando alguno de estos capítulos han pretendido desconectarme de mi mismo. Gracias por recorrer tu camino en el mundo a mi lado. Eres la mejor compañera de vida que existe en el Universo.

Gracias.



# Abstract

X-ray binaries are fascinating stellar binary systems that consist of a compact object as a neutron star or a stellar-mass black hole, in close orbital separation with a companion normal star. These systems are detected at all wavelengths across the electromagnetic spectrum, from radio in radio emitting binaries –also called microquasars–, to X-rays and  $\gamma$ -rays.

Accretion is a fundamental process in X-ray binaries, where the companion star transfers matter onto the compact object. As the material spirals towards the core, it releases gravitational potential energy, which is eventually converted into X-ray emission. This accretion-powered emission is a defining characteristic of X-ray binaries and provides remarkable insights into the powerful physical processes occurring in these systems. Moreover, most X-ray binaries fuel powerful bipolar relativistic outflows, where a significant fraction of the accreting matter is ejected with velocities close to the speed of light. These ejections, called relativistic jets, can propagate up to large distances and interact with the interstellar medium very far from the core of the binary. Thereby, jets are the main way by which these systems exert feedback on its environment.

This thesis presents a comprehensive study of the propagation of relativistic outflows in X-ray binaries, together with the accretion physics that powers them, by combining numerical simulations and X-ray data analysis to unravel the underlying fundamental mechanisms and physical properties of these fascinating high-energy phenomena.

The first part of this research focuses on the development of state-of-the-art numerical simulations to model relativistic outflows in these systems. By employing advanced computational techniques in high performance computing, we aim to accurately model the dynamics of the outflows and to reproduce their observed features. To this objective, we developed a new computational tool named LÓSTREGO, a code that solves the equations of special relativistic magnetohydrodynamics in Cartesian coordinates. The development of this code,

where we implemented the most advanced capabilities, physical modules and numerical methods in the field, is extensively validated in the thesis. Using this code, a bunch of simulations of a relativistic outflow interacting with the powerful stellar winds driven by the massive companion in a high-mass X-ray binary were performed, considering for the first time in the context of microquasars the dynamical evolution of magnetic fields. These type of simulations, including a more complex setup, were also performed to study the microquasar SS 433, one of the most powerful and exotic star system in the Galaxy.

In the second part of the thesis, we turn our attention to X-ray data analysis of observations from X-ray binaries. By employing timing and spectral data analysis techniques, we explored the characteristics of the X-ray emission and investigated the correlation between these properties with the underlying physical processes driving the outflows, which occur in the strong gravitational field of the compact object. Two systems were analysed in the thesis: the gamma-ray binary LS I+61 303, where we analysed the whole RXTE/PCA archival data of the source, and the neutron star X-ray binary Scorpius X-1, where we used the first observations of the source taken with the NICER observatory, a detector onboard the International Space Station.

The findings of this thesis enhance our understanding of relativistic outflows in microquasars. The synergistic approach of numerical simulations and X-ray data analysis provides a comprehensive framework for studying these enigmatic phenomena. Furthermore, the knowledge gained from this research has implications for a range of astrophysical phenomena involving compact objects, including active galactic nuclei –as also shown in the appendix of the thesis–, pulsar wind nebulae and gamma-ray bursts.

# Resumen

## Introducción

Las estrellas binarias de rayos X (XRBs, por sus siglas en inglés) son sistemas binarios estelares que albergan un objeto compacto (una estrella de neutrones o un agujero negro de masa estelar) en órbita con una estrella compañera no degenerada alrededor de un centro de masa común, que son luminosas –pero no exclusivamente– en el rango de energía de rayos X. La estrella compañera (es decir, la estrella donante o secundaria) suministra materia al objeto compacto (es decir, la estrella acreedora o primaria), un proceso físico impulsado a través del desbordamiento del lóbulo de Roche o por el impacto directo del viento estelar. Dado el gran momento angular de la materia transferida hacia el objeto, ésta no cae radialmente, sino que orbita a su alrededor, donde mediante procesos disipativos se forma un disco de acreción. Los mecanismos que gobiernan la física de los discos de acreción, la cual está directamente relacionada con los episodios más energéticos del Universo, dependen de la masa y el estado evolutivo de la compañera, de la masa relativa de las estrellas del sistema y también de su separación orbital.

La mayoría de XRBs son objetos transitorios, y en determinados estados espectrales de su evolución, estos sistemas producen potentes chorros relativistas bipolares, en los que una fracción significativa de la materia de acreción es expulsada con velocidades cercanas a la velocidad de la luz. Estos chorros, también denominados jets relativistas, son eyectados de forma colimada extrayendo energía del agujero negro [Blandford and Znajek 1977] o por fuerzas magnetocentrífugas desde el disco de acreción interno [Blandford and Payne 1982], y emiten radiación sincrotrón no térmica en la banda de radio. Debido a este hecho, las XRBs que también emiten en radio, en las que además se puede establecer el origen de un chorro relativista, se denominan microcuásares [véase, por ejemplo, Paredes and Martí 2003], por analogía con los chorros extragalácticos observados

en los cuásares y otros núcleos galácticos activos (AGN, por sus siglas en inglés). Aunque estos chorros se emiten desde una región muy cercana al objeto compacto sometida a los efectos de la relatividad general, pueden propagarse hasta grandes distancias e interactuar con el medio interestelar muy lejos del núcleo de la binaria. Por tanto, los chorros relativistas constituyen uno de los canales de salida de energía más importantes en este tipo de sistemas, y son la principal vía por la que el objeto compacto, ya sea un agujero negro o una estrella de neutrones, se comunica con su entorno.

De este modo, los microcuásares imitan los procesos dinámicos que rigen la física de los núcleos galácticos, pero en escalas espacio-temporales extraordinariamente pequeñas. Esto permite observar y monitorizar la evolución del sistema, ya que los tiempos característicos de la dinámica de acreción son accesibles para el ser humano, al contrario de lo que ocurre en el estudio de los chorros extragalácticos a gran escala. Debido a este hecho, las XRBS son escenarios excelentes para investigar muchas de las principales incógnitas que rodean los procesos físicos en este tipo de sistemas, por ejemplo, el vínculo entre la formación del chorro y los distintos estados de acreción. Además, constituyen un laboratorio natural para probar teorías de la gravedad en condiciones físicas extremas, o incluso permiten estudiar la materia exótica ultra-densa en las estrellas de neutrones, imposible de reproducir en los laboratorios terrestres.

En el contexto de esta tesis doctoral, el estudio de los chorros relativistas, así como los procesos de acreción que los producen, constituye uno de los objetivos principales. En los microcuásares, éstos se manifiestan como estructuras persistentes o como una secuencia aparente de estructuras discretas [véase, por ejemplo, Fender 2006], aunque también se han deducido otros tipos de eyecciones que no es posible catalogar en ninguna de estas dos categorías. Estos son, por ejemplo, los potentes vientos expulsados por el disco de acreción [Díaz Trigo et al. 2013], o los denominados flujos ultrarrelativistas (URFs, por sus siglas en inglés) descubiertos en algunos sistemas que contienen estrellas de neutrones.

- **Fuentes persistentes.** A diferencia de los chorros relativistas que existen en las galaxias activas, en los microcuásares estos chorros no se observan como estructuras extendidas, sino que se deducen principalmente de un espectro plano (o ligeramente invertido) en radio y el infrarrojo. Únicamente en dos XRBS, a saber, Cygnus X-1 [Gallo et al. 2005] y GRS 1915+105 [Dhawan, Mirabel, and Rodríguez 2000], se han podido resolver espacialmente estas estructuras con tamaños de unas pocas decenas de Unidades Astronómicas. El espectro del chorro se caracteriza por una *transición de chorro*, en la que la emisión pasa de ser ópticamente gruesa en la base

a ópticamente delgada, y a frecuencias más bajas por un continuo, que resulta de la superposición de radiación sincrotrón autoabsorbida emitida desde diferentes regiones del flujo del chorro. Sin embargo, a medida que el plasma se propaga desde el centro de la binaria, el campo magnético decae y las partículas pierden energía, por lo que cabría esperar un espectro electromagnético invertido, y no fundamentalmente plano, tal y como es observado. Tradicionalmente, esto se ha explicado por la existencia de un mecanismo de reposición de energía del plasma relativista que compensa las pérdidas adiabáticas debidas a la expansión del chorro [Blandford and Königl 1979, véase también Marino et al. 2020]. Por otro lado, aunque en los microcuásares no hay una forma directa de determinar la velocidad de un chorro estacionario compacto ya que el contra-chorro no está resuelto [véase, sin embargo, Saikia et al. 2019, Tetarenko et al. 2021, donde se intenta determinar el factor de Lorentz de un jet compacto], se puede suponer razonablemente una velocidad ligeramente relativista, con factores de Lorentz  $\Gamma < 2$ .

- **Eyecciones discretas/transitorias.** Este tipo de eyecciones se observan como estructuras nodulares resueltas en la banda de radio, con altas velocidades relativistas que pueden viajar a varios miles de UA del núcleo de la binaria, mostrando flujos que decaen rápidamente. Aunque este tipo de eyecciones se interpretaron tradicionalmente como plasmoides transitorios [en la llamada interpretación de van der Laan van der Laan 1966], este modelo muestra varias debilidades [Klein-Wolt et al. 2002, Fender et al. 2023, aunque véase también Tetarenko et al. 2017, donde los autores aplican una variación del modelo de Van der Laan en el contexto de la binaria V404 Cyg]. Esto favorece en su lugar la interpretación por choques [Kaiser, Sunyaev, and Spruit 2000], donde la aparente morfología discreta es producida por choques internos en el jet.

Por otro lado, Mirabel and Rodríguez 1994 demostraron por primera vez la existencia de movimientos superlumínicos aparentes en la emisión de radio de la fuente galáctica GRS 1915+105. Bajo este resultado, considerado uno de los principales avances en el campo de los sistemas binarios, se pudo concluir que los microcuásares pueden mostrar el mismo tipo de flujos relativistas observados en los potentes chorros de las galaxias activas.

- **Fluidos Ultrarelativistas** Aunque no es habitual encontrar este tipo de eyecciones en los sistemas binarios, se trata de una fenomenología relevante para los propósitos de esta tesis doctoral. Los URFs no se observan

directamente en los datos de radio o rayos X, sino que se deducen de la correlación entre las erupciones en el núcleo y en los radio-lóbulos, a mayor distancia del objeto compacto. Fomalont, Geldzahler, and Bradshaw 2001a y Fomalont, Geldzahler, and Bradshaw 2001b dedujeron la presencia de URFs en la binaria Sco X-1 correlacionando la variación de densidad de flujo de los lóbulos y el núcleo, asumiendo un flujo subyacente que se mueve a velocidades relativistas. Fender et al. 2004 también sugirió la existencia de un evento de este tipo en la fuente Cir X-1, mientras que Migliari et al. 2005 propuso la existencia de URFs en el microcuásar SS 433 para explicar la rápida variabilidad temporal de los chorros de rayos X extendidos, inferidos a partir de observaciones de Chandra.

## Objetivos

El estudio de los chorros relativistas puede llevarse a cabo desde diversos puntos de vista. En particular, destacan dos aproximaciones: desde un punto de vista observacional, mediante análisis de datos de observaciones a distintas longitudes de onda de estos objetos, o desde un punto de vista numérico, mediante complejas simulaciones numéricas realizadas en superordenadores capaces de manejar los enormes costes computacionales requeridos en este tipo de cálculos.

Por un lado, el objetivo principal de la tesis doctoral es, por tanto, el desarrollo de una herramienta de cálculo capaz de resolver las ecuaciones que rigen la dinámica de los chorros relativistas. Estas ecuaciones definen el sistema de la magnetohidrodinámica relativista (RMHD, por sus siglas en inglés), donde además, se tiene en cuenta el rol dinámico de los campos magnéticos en la evolución del fluido. Sin embargo, a pesar de la capacidad actual de las arquitecturas de alto rendimiento, las simulaciones numéricas de chorros en microcuásares apenas se han abordado en la literatura. Bajo nuestro punto de vista, esto se debe a que, en los sistemas binarios, los chorros no suelen observarse como estructuras espacialmente extendidas (salvo en unas pocas excepciones, como ya se ha mencionado), sino que se infieren a partir del espectro plano en radio y en el infrarrojo, por lo que la comparación directa entre las simulaciones numéricas y las observaciones es más difícil de abordar. Sin embargo, comprender los principios básicos que rigen la dinámica de los chorros en estas fuentes también es esencial para caracterizar el comportamiento general del sistema y su interacción con el medio, aunque los chorros de la fuente no se hayan podido resolver espacialmente. Para ello, las simulaciones numéricas son particularmente

necesarias. Así, siguiendo este razonamiento, esta tesis doctoral plantea los siguientes objetivos:

- En primer lugar, extender la línea de trabajo iniciada por una serie de trabajos hace más de una década [Perucho and Bosch-Ramon 2008, Perucho, Bosch-Ramon, and Khangulyan 2010, Perucho and Bosch-Ramon 2012], donde se desarrollaron simulaciones de interacción de un jet con el viento de la estrella compañera en el límite hidrodinámico relativista. Sin embargo, ninguno de dichos trabajos consideró el efecto dinámico de los campos magnéticos en la evolución del chorro, asumiendo que éstos últimos están dominados por la energía cinética en la escala de la binaria. Esta hipótesis resulta razonable, ya que aunque se estima que los chorros están dominados magnéticamente cerca del objeto compacto, son acelerados hasta velocidades (moderadamente) relativistas mediante procesos magnetohidrodinámicos y/o térmicos (es decir, proceso de Bernoulli), donde también pueden ser cargados con partículas a partir de la interacción con el disco de acreción y/o el viento de la estrella compañera. Por consiguiente, a pesar de que esperamos que la energía cinética domine la potencia total del chorro a escala de la binaria, debemos entender hasta qué punto incluso un campo magnético relativamente débil –desde el punto de vista de la potencia total del jet– puede afectar a la evolución dinámica del fluido, ya sea favoreciendo su colimación, o bien desencadenando más inestabilidades [véase, por ejemplo, Massaglia et al. 2022, para el caso de chorros de tipo Fanaroff-Riley I]. Además, incluso los campos magnéticos moderadamente débiles pueden reforzarse localmente y desempeñar un papel importante en la conformación de la emisión no térmica del chorro mediante la aceleración de partículas, enfriamiento y/o desencadenando emisión de radiación sincrotrón. Por otro lado, también es posible que la disipación magnética no sea tan eficiente como generalmente se espera y, por tanto, los chorros aún pueden estar cerca de equipartición en la escala de la binaria. Estas dos posibilidades, junto con los efectos de los campos magnéticos sobre la dinámica del chorro y la estabilidad a largo plazo, se abordarán por primera vez mediante simulaciones RMHD tridimensionales en esta tesis doctoral.
- Seguidamente, ayudar a la comprensión de los chorros relativistas en el microcuásar SS 433, especialmente la configuración del campo magnético en los chorros, así como su propia morfología global. De hecho, todavía no existe consenso acerca de la naturaleza continua o discreta del fluido

en los chorros de la fuente [véase, por ejemplo, Stirling et al. 2004, Miller-Jones et al. 2008, Marshall et al. 2013]. En particular, en esta tesis pretendemos abordar, precisamente, el efecto que dicha morfología tiene sobre la estructura del campo magnético a la escala del sub-parsec, donde un análisis de polarización de la emisión radio sugiere que el campo se alinea con la dirección local del vector velocidad tras un periodo de precesión completo. Además, mediante complejas simulaciones RMHD adaptadas a las particularidades de esta fuente, buscamos entender de qué manera las colisiones internas entre estructuras discretas afectan a la morfología global del sistema, procesos de disipación y deceleración efectiva de los chorros. Esta información puede ser especialmente relevante a la hora de establecer conexiones entre las pequeñas escalas en las que se concentran las simulaciones con los procesos dinámicos globales de la fuente, donde se plantea que los chorros relativistas de la binaria conforman una cavidad en la nebulosa W50 [véase, por ejemplo, Safi-Harb et al. 2022].

Por otro lado, desde un punto de vista puramente observacional, se plantean los siguientes objetivos:

- Discernir la naturaleza del objeto compacto y el comportamiento global del sistema en la binaria de rayos gamma LS I +61 303, una fuente compleja que muestra propiedades únicas entre todas las binarias conocidas. A lo largo de las últimas décadas se han establecido diferentes modelos para explicar dichas propiedades, especialmente los procesos de emisión no térmica. Por un lado, se plantea que dicha emisión puede provenir de la interacción de un chorro relativista con los potentes vientos de la estrella compañera (tal y como planteamos en nuestro primer trabajo de simulaciones), mientras que otros autores utilizan la interacción de vientos en un pulsar. Los resultados publicados recientemente por Weng et al. 2022, donde se detectan rápidos pulsos de radio que provienen de la localización de la binaria, sugieren la existencia de una estrella de neutrones, pero esto no aporta nueva información acerca de la configuración global del sistema, puesto que los chorros relativistas también pueden ser eyectados por estos objetos compactos.

El objetivo principal del análisis consiste en presentar un estudio completo de la variabilidad espectral y temporal de la fuente a lo largo de varios años de exposición, para lo que utilizaremos el archivo histórico de datos del detector Rossi X-ray Timing Explorer (RXTE). A pesar de que el reducido número de fotones detectados por unidad de tiempo dificulta el análisis

planteado, un estudio de estas características puede aportar información relevante que, de otra manera, se perdería en el ruido de la señal.

- Presentar y analizar los primeros datos de la binaria Scorpius X-1 (Sco X-1) medidos con el detector The Neutron Star Interior Composition Explorer (NICER), a bordo de la Estación Espacial Internacional. En este caso, el objetivo principal del estudio consiste en aplicar técnicas de análisis temporal para detectar, medir y clasificar la rápida variabilidad temporal de la fuente. En concreto, buscamos seguir la evolución de las llamadas oscilaciones cuasi-periódicas (QPOs, por sus siglas en inglés) de baja frecuencia, ya que estas pueden aportar información muy valiosa acerca de los procesos de acreción muy cerca del objeto compacto, así como de la conexión entre estos procesos y la formación de chorros relativistas. Es de especial interés para los objetivos de la tesis la comparación del análisis que presentamos con los resultados publicados en Motta and Fender 2019, ya que en este artículo, los autores plantean que la existencia de URFs asociados a Sco X-1 puede relacionarse con un determinado estado de acreción gracias a la detección simultánea de un patrón concreto de QPOs de baja frecuencia. Por tanto, este estudio pretende confirmar la existencia de dichos patrones también en los datos de NICER, ya que estos datos serán utilizados posteriormente para establecer la existencia de URFs a través de la correlación con observaciones simultáneas que se han realizado en la banda de radio durante la misma campaña de monitorización.

## Metodología

La metodología desarrollada en esta tesis doctoral se basa en tres aspectos fundamentales: la construcción de un entorno computacional en el que desarrollar simulaciones numéricas en el campo de la RMHD, la implementación de entornos específicos en el código para el desarrollo de dichas simulaciones en el contexto de la propagación de chorros en microcuásars y el desarrollo e implementación de algoritmos para el análisis de datos de observaciones de rayos X, especialmente aplicado a los instrumentos RXTE y NICER, puesto que son los detectores empleados en el análisis.

## Herramienta computacional

El código LÓSTREGO es una nueva herramienta computacional que permite simular plasmas astrofísicos relativistas en coordenadas cartesianas, desarrollado

en el contexto de esta tesis. El algoritmo está escrito íntegramente en FORTRAN, y resuelve las ecuaciones conservativas de la RMHD especial con volúmenes finitos. LÓSTREGO ha sido especialmente diseñado para ejecutarse en múltiples núcleos (*cores*), pudiendo explotar la capacidad de las arquitecturas paralelas modernas mediante un esquema de paralelización híbrido con descomposición paralela del dominio (message passing interface, MPI) e hilos (*threads*) paralelos (OpenMP, OMP). Las técnicas numéricas del algoritmo se basan en los métodos de captura de choque de alta resolución, los cuales a lo largo de las últimas décadas han demostrado ser robustos y precisos en múltiples aplicaciones, extendiendo las técnicas implementadas en Martí 2015b a tres dimensiones espaciales. De forma genérica, el algoritmo implementado en el programa se basa en el siguiente flujo de tareas: primero, las variables primitivas promedio de cada celda se reconstruyen sobre las interfaces, donde se resuelve numéricamente un problema de Riemann empleando un resolvidor de Riemann aproximado. Una vez resueltos los flujos en cada interfaz, las variables conservadas evolucionan en el tiempo explícitamente mediante algoritmos Runge-Kutta de variación total decreciente (TVD, por sus siglas en inglés), mientras que los campos magnéticos se actualizan mediante el método de transporte restringido (CT, por sus siglas en inglés). Después de cada iteración temporal, se aplica un esquema de inversión para recuperar las variables primitivas.

Además, también hemos desarrollado en el entorno del código un módulo de transporte radiativo, mediante el cual se tienen en cuenta los efectos dinámicos de acople entre la materia y un campo de radiación externo. Mediante este módulo, hemos implementado y testeado, por primera vez en este contexto, una nueva familia de resolvidores de Riemann que permiten mejorar los métodos existentes en cualquiera de los dos regímenes de radiación (medio ópticamente grueso vs. ópticamente delgado), los llamados *resolvidores de Riemann no jacobianos*. Este módulo, junto a las técnicas requeridas para su implementación en LÓSTREGO, supone un importante avance en los procesos físicos descritos por el código, y establece las bases para el desarrollo de simulaciones más complejas en diversos campos, como los procesos de acreción supercrítica (importantes para el estudio, también, del microcuásar SS 433) o la formación y propagación de chorros en los brotes de rayos gamma (GRBs, por sus siglas en inglés).

## Simulaciones numéricas

Para estudiar la propagación de jets en sistemas binarios, desarrollamos complejas simulaciones numéricas empleando nuestro código LÓSTREGO. Dichas

---

simulaciones se llevan a cabo en superordenadores, lo que permite explotar la paralelización híbrida basada tanto en procesos con memoria compartida en un mismo nodo, como procesos con distribución de memoria entre nodos distintos. Por otro lado, los métodos de volúmenes finitos en los que se basa el código permiten resolver las ecuaciones en una malla numérica, formada por un conjunto de elementos discretos donde se promedian las distintas variables del sistema.

En el caso de las simulaciones de interacción jet-viento con campo magnético, utilizamos una malla rectangular uniforme, donde el viento de la estrella llena toda la extensión de la malla. Consideramos, además, un viento inhomogéneo, al que caracterizamos con una estructura fractal. El jet, por el contrario, se inyecta como una condición de contorno, cargado con un campo magnético puramente toroidal, de forma que la interacción se produce desde el principio de la simulación. Este estudio requiere, además, el desarrollo de programas de post-proceso para poder analizar la distribución de energía a lo largo de las distintas fases de evolución del chorro.

La simulación de los chorros con movimiento de precesión en SS 433 es mucho más compleja que la anterior, donde empleamos una arquitectura de malla especialmente diseñada para realizar esta simulación. En este caso, la condición de contorno se extiende dentro de la malla, en la cual disponemos un inyector cilíndrico precesando a la frecuencia determinada por los chorros de la fuente. El objetivo principal de este trabajo consiste en estudiar la dinámica de estructuras discretas con velocidades relativas no uniformes, para lo que planteamos una estrategia basada en una serie de simulaciones sucesivas. En primer lugar, inyectamos un chorro de forma continua para crear una cavidad chocada y un entorno más adecuado para llevar a cabo la propagación de nuestras estructuras discretas. Seguidamente, éstas se inyectan también en la malla con una determinada dispersión de velocidades. Como el objetivo del estudio es estudiar la colisión de estas estructuras, hemos diseñado una malla numérica no uniforme en la que se concentra un mayor número de celdas de cálculo (es decir, una mayor resolución), en la región interior de la caja, donde esperamos que se produzcan dichas interacciones, a la vez que evitamos que la inyección anterior alcance las fronteras del sistema. Finalmente, hemos desarrollado un conjunto de algoritmos para poder extraer, a partir de los resultados de las simulaciones, observables específicos que puedan ser comparados directamente con los datos observacionales de la fuente real. Debido al elevado coste de estas simulaciones, éstas han sido desarrolladas a través de un proyecto de cálculo de alto rendimiento dentro de la Red Española de Supercomputación, para lo cual hemos empleado un total de 4 millones de horas de tiempo computacional.

## Procesado de datos

Para llevar a cabo el análisis de datos planteado en los objetivos de la tesis, hemos desarrollado una serie de algoritmos que, de forma automática, permiten extraer una gran cantidad de información a partir de una serie de datos de rayos X. Estos algoritmos se basan, fundamentalmente, en la aplicación de técnicas de análisis espectral (incluyendo el denominado análisis de color) y análisis temporal.

**Análisis espectral** El análisis espectral de XRBs consiste en calcular e interpretar espectros de energía para obtener información cuantitativa sobre sus diferentes componentes: emisión térmica del disco de acreción, emisión no térmica de la corona, emisión sincrotrón de un chorro relativista, etc. El espectro electromagnético suele ajustarse con modelos teóricos siguiendo estadísticos de prueba  $\chi^2$  [Arnaud 1996], lo que permite deducir magnitudes físicas como la temperatura del disco, la energía y opacidad de los electrones Comptonizantes en la corona, o la presencia de líneas de emisión procedentes del disco, entre otras.

**Análisis de color** Como alternativa a los espectros de energía tradicionales, el análisis de color puede proporcionar información importante sobre las propiedades espectrales de la fuente. Los colores de rayos X son, por definición, relaciones de dureza que cuantifican la diferencia de brillo entre dos bandas determinadas de energía. En otras palabras, un color es una relación entre los recuentos, flujos o luminosidades de la fuente en diferentes intervalos de energía, que deben definirse en cada caso según las características del sistema y la respuesta del instrumento. Las bandas de baja energía se denominan *suaves*, mientras que las bandas de alta energía se denominan *duras*.

En el campo de las XRBs, hay dos representaciones estándar que implican colores de rayos X: el diagrama color-color (CD, por sus siglas en inglés), en el que un color se representa frente a otro, y el diagrama dureza-intensidad (HID, por sus siglas en inglés), en el que un color (o la relación de dureza) se representa frente a la intensidad de la emisión. Ésta última se define como la tasa de recuento, flujo o luminosidad de la fuente en el rango de energía que cubre las sub-bandas utilizadas para definir los colores o, en su defecto, todo el rango de energía del instrumento. En esta tesis, utilizaré estas técnicas para estudiar las propiedades espectrales de la binaria Sco X-1. Además, los XRBs suelen trazar un patrón característico en este tipo de representaciones, que suele interpretarse como una consecuencia del régimen de acreción subyacente. De

esta manera, el análisis del color es una poderosa herramienta que debe utilizarse junto con el análisis espectral de banda ancha y las técnicas de análisis temporal, ya que, como se ha mencionado anteriormente, se ha demostrado que muchas de las propiedades espectrales de una fuente de rayos X están conectadas con los diagramas CD y HID.

**Análisis temporal** El análisis temporal es el principal objetivo de la segunda parte de la tesis [véase por ejemplo, Belloni, Psaltis, and van der Klis 2002, van der Klis 2006, Motta et al. 2017, Ingram and Motta 2019]. Consiste en un conjunto de técnicas para evaluar la rápida variabilidad en la emisión de rayos X de los XRBs, que es el principal trazador de los procesos dinámicos en el flujo de acreción interno, dentro del fuerte campo gravitatorio del objeto compacto.

Este tipo de análisis se realiza mediante técnicas de Transformada de Fourier (en concreto, algoritmos de Transformada Rápida de Fourier), que nos permiten convertir los datos desde el dominio temporal al dominio de la frecuencia. En particular, el espectro de densidad de potencia (PDS, por sus siglas en inglés) es en general el principal resultado del proceso, proporcionando una densidad de potencia en función de la frecuencia de Fourier, donde la primera es proporcional a la amplitud de variabilidad en la curva de luz en una escala de tiempo corta [van der Klis 1989].

Típicamente, el espectro de potencia refleja tres características fundamentales [véase, por ejemplo, Belloni, Psaltis, and van der Klis 2002, para una revisión profunda del tema]: (I) pulsaciones coherentes, que aparecen como picos de frecuencia única no resueltos originados principalmente por pulsaciones de espín en púlsares, (II) estructuras aperiódicas amplias, normalmente denominadas ruido, y (III) picos estrechos resueltos, las denominadas QPOs. Los componentes de ruido suelen representar señales reales de la fuente, ya que el ruido asociado a las estadísticas de recuento (es decir, el ruido de Poisson) suele eliminarse de la PDS durante el análisis. El potencial de los QPO como herramienta de diagnóstico para entender las regiones internas del disco de acreción se comprendió desde su descubrimiento hace más de 50 años, y se han observado en binarias de estrellas de neutrones y agujeros negros, así como en otros tipos de fuentes, como los AGN.

Sin embargo, al contrario de lo que ocurre con el análisis espectral, no existe un modelo físico particular para describir estos componentes temporales, que se caracterizan principalmente por la frecuencia central, su anchura y el estado espectral. El procedimiento estándar consiste en ajustar el espectro de potencia con un modelo multilorentziano, donde una función lorentziana representa la

transformada de Fourier de una senoide amortiguada exponencialmente. Para ello, emplearemos el software GHATS, un programa de análisis temporal, junto a las funciones de ajuste proporcionadas por el software XSPEC.

## Conclusiones

En esta tesis doctoral, hemos desarrollado una nueva herramienta para realizar simulaciones numéricas en el campo de la astrofísica relativista, en la que hemos implementado una gran cantidad de técnicas numéricas, algoritmos y procesos físicos, incluyendo un módulo de transporte radiativo. Utilizando este código, al que hemos bautizado como LÓSTREGO, hemos desarrollado las primeras simulaciones con campo magnético de chorros relativistas propagándose en un sistema binario. En concreto, hemos simulado la interacción de un jet con el viento emitido por su estrella compañera, centrándonos en los efectos dinámicos que la existencia de campos magnéticos tienen en este proceso. Además, hemos diseñado un setup para simular los jets de un sistema en particular, el microcuásar SS 433, donde la principal particularidad de estos chorros es su constante movimiento de precesión. Por otro lado, en el bloque observacional de la tesis, hemos estudiado las propiedades espectrales y temporales de dos binarias de rayos X específicas: el sistema LS I +61 303, uno de los objetos más misteriosos de la Galaxia, y la binaria de estrella de neutrones Sco X-1, ampliamente estudiada desde su descubrimiento en la década de los 60. Para ello, hemos utilizado, respectivamente, datos de los observatorios RXTE y NICER, y hemos empleado técnicas de análisis temporal para analizar la gran cantidad de datos proporcionados por dichos instrumentos. A continuación, expongo las conclusiones principales de nuestro estudio en estos bloques:

- Hemos realizado tres simulaciones numéricas diferentes de chorros de microcuásares propagándose a través de un viento estelar no homogéneo utilizando el nuevo código LÓSTREGO, creado en esta tesis para realizar cálculos en astrofísica relativista. Nuestra configuración numérica se basó en el espacio de parámetros descrito en simulaciones hidrodinámicas tridimensionales previas, incluyendo un campo magnético toroidal en equilibrio transversal con el gas para analizar su papel en la dinámica del chorro y su estabilidad a largo plazo. Presentamos la evolución del chorro a lo largo de los minutos iniciales tras la inyección, lo que nos permitió mantener un punto de inyección estable en la malla y despreciar el movimiento orbital de la binaria. Nuestras simulaciones muestran

que el campo magnético podría desempeñar un papel estabilizador en la evolución del chorro siempre que el flujo de energía magnética sea inferior al flujo de energía cinética. Este efecto estabilizador confiere a los chorros magnetizados simulados una colimación adicional, en comparación con chorros similares no magnetizados. Por el contrario, un flujo de energía magnética no despreciable se traduce en una desestabilización del fluido, con la consecuencia de una mayor disipación de energía y una velocidad de propagación de la cabeza del chorro más lenta. De esta manera, concluimos que la evaluación de la probabilidad de propagación del chorro más allá de la región de la binaria debe revisarse en presencia de campos magnéticos. En Perucho and Bosch-Ramon 2008, Perucho, Bosch-Ramon, and Khangulyan 2010 se llegó a la conclusión de que esto dependía básicamente de la potencia del chorro, mientras que en este trabajo vemos que los chorros de baja potencia con campos relativamente débiles podrían propagarse distancias más largas sin desestabilizarse. Sin embargo, los chorros más potentes, por el contrario, podrían verse perturbados por inestabilidades impulsadas por corrientes si el campo magnético es dinámicamente relevante a las escalas de la binaria. Por tanto, concluimos que es necesaria una caracterización más exhaustiva del papel del campo magnético en los chorros de microcuásares a estas escalas para poder establecer un límite adecuado del flujo de energía mínimo que permita la propagación del chorro más allá del sistema progenitor.

- Tras nuestro análisis preliminar, encontramos dos argumentos relevantes que apoyan la existencia de componentes discretos en los jets del microcuásar SS 433: en primer lugar, si las estructuras discretas tienen una dispersión de velocidad –lo que parece razonable según los datos observacionales– la interacción entre ellas da lugar a estructuras alargadas compactas que son menos propensas al desarrollo de inestabilidades que el flujo continuo. Estas estructuras más grandes, que no sufren deceleraciones importantes en las escalas simuladas, pueden por tanto propagarse con mayor facilidad a distancias mayores. En segundo lugar, mediante algoritmos de post-procesado, demostramos estadísticamente que la existencia de colisiones internas entre este tipo de estructuras discretas produce una componente del campo magnético que se alinea con la dirección del vector velocidad, al contrario que en los chorros continuous donde el campo toroidal es advechado siguiendo la traza cinemática extraída de la simulación. Además, también hemos intentado abordar la existencia de URFs

en el sistema, pero el espacio de parámetros de esta simulación no fue apropiado para reproducir el resultado observacional esperado.

- En cuanto a la binaria de rayos gamma LS I +61 303, hemos analizado todos los datos de rayos X del archivo de RXTE de la fuente, tomados entre 1996 y 2011, con el fin de investigar la variabilidad temporal rápida de rayos X en el sistema, utilizando el software GHATS.

En primer lugar, hemos calculado el periodo intrínseco de la emisión de rayos X medida por RXTE utilizando tres técnicas independientes. Los tres métodos arrojaron un periodo estadísticamente compatible tanto con el periodo orbital de la binaria como con el atribuido a los movimientos de precesión del jet (asumiendo en este caso que el sistema es un microcuásar), de modo que los datos de RXTE no permiten distinguir entre ellos.

Por otro lado, las PDS promediadas en fase no muestran ninguna señal periódica o aperiódica estadísticamente significativa, aparte de un débil componente de ruido rojo a bajas frecuencias, posiblemente atribuido al sistema. La amplitud de dicho componente muestra una dependencia de fase moderada, aunque no se pudo encontrar una correlación fuerte a lo largo de todas las fases. Nuestros resultados también muestran que la variabilidad tiende a disminuir cuando aumenta el flujo, algo típico de los sistemas binarios con procesos de acreción. En conclusión, nuestro análisis temporal no arroja luz sobre la naturaleza del sistema ni sobre el tipo de objeto compacto que alimenta la binaria. Por lo tanto, se requieren nuevas observaciones de esta fuente en el rango de energía de los rayos X para investigar su comportamiento con más detalle.

- El análisis de datos de Sco X-1 a partir de observaciones de NICER es el primero de estas características, el cual fue llevado a cabo en el año 2019 como parte de una gran campaña para estudiar la actividad de la fuente en distintas longitudes de onda. Gracias a la gran área colectora del instrumento y a la posibilidad de procesar las altas tasas de recuento de la fuente, NICER proporciona los datos de mayor calidad entre todos los instrumentos de rayos X involucrados en la campaña de observación. Utilizando el paquete de software GHATS, extrajimos una curva de luz y un HID para caracterizar los estados espectrales de la fuente durante estas observaciones. A continuación, empleamos técnicas de análisis temporal para obtener una amplia colección de PDS donde detectamos las QPOs del sistema, y seguimos la evolución de sus características en el tiempo y a lo largo de los diferentes estados espectrales que Sco X-1 traza en el HID.

Los resultados del ajuste muestran una rica variedad de QPOs de baja frecuencia en las observaciones de NICER: aproximadamente la mitad de las PDS que inspeccionamos muestran algún tipo de estructura cuasi-periódica, mientras que el resto están dominadas por componentes de ruido de banda ancha. También observamos dos tipos distintos de QPO más difíciles de clasificar según las categorías anteriores, que son eventos poco frecuentes que aparecen en estados activos de la fuente, similares a otras QPOs observadas en binarias de agujero negro. Por otro lado, hemos podido probar la existencia de un tipo particular de QPO conocida como HBO aislada, la cual no se había observado previamente en los datos de RXTE, aunque se tiene constancia de su existencia. Además, nuestros PDS muestran, de forma ocasional, el mismo tipo de patrón que aquél planteado por Motta and Fender 2019 en relación a la eyección de fluidos relativistas en la fuente. Aunque la discusión de este trabajo se encuentra todavía en una fase preliminar, los resultados que hemos presentado en esta tesis son prometedores para entender el comportamiento de la binaria. El estudio de los datos en la banda de radio permitirá determinar con mayor precisión la relación, en caso de existir, entre los dos fenómenos referidos anteriormente.

En conclusión, los resultados de esta tesis ayudan a comprender con mayor precisión los chorros relativistas en sistemas binarios, así como los procesos de acreción que los alimentan. El enfoque sinérgico de simulaciones numéricas y análisis de datos de rayos X proporciona un marco completo para estudiar estos enigmáticos fenómenos. Los conocimientos adquiridos en esta investigación tienen implicaciones para una serie de fenómenos astrofísicos en los que intervienen objetos compactos, incluidos los AGN –como también se muestra en la tesis, pero también muchos otros, como las nebulosas de viento de púlsar o los poderosos GRBs.



# Publications

- [1] **Testing jet geometries and disc-jet coupling in the neutron star LMXB 4U 0614+091 with the internal shocks model.** A. Marino, J. Malzac, M. Del Santo, S. Migliari, R. Belmont, T. Di salvo, D. M. Russell, **J. López-Miralles**, M. Perucho, A. D’Ai, R. Iaria, L. Burderi. *Monthly Notices of the Royal Astronomical Society*. Volume 498, Issue 3, November 2020. DOI: 10.1093/mnras/staa2570.
- [2] **Jet propagation through inhomogenous media and shock ionisation.** M. Perucho, **J. López-Miralles**, V. Reynaldi and A. Labiano. *Astronomische Nachrichten*, Volume 342, Issue 1171, pp. 1171-1175. November 2021. DOI: 10.1002/asna.20210051.
- [3] **3D RMHD simulations of jet-wind interaction in High-Mass X-ray Binaries.** **J. López-Miralles**, M. Perucho, J.M. Martí, S. Migliari and V. Bosch-Ramon. *Astronomy&Astrophysics*. Volume 661, id.A117, 28 pp. February 2022. DOI: 10.1051/0004-6361/202142968.
- [4] **On the application of Jacobian-free Riemann solvers for relativistic radiation magnetohydrodynamics under M1 closure.** **J. López-Miralles**, J.M. Martí and M. Perucho. *Computer Physics Communications*, Volume 284, article id. 108630. March 2023. DOI: 10.1016/j.cpc.2022.108630.
- [5] **RadioAstron discovery of a mini-cocoon around the restarted parsec-scale jet in 3C 84.** T. Savolainen, G. Giovannini, Y. Y. Kovalev, M. Perucho, J. M. Anderson, G. Bruni, P. G. Edwards, A. Fuentes, M. Giroletti, J. L. Gómez, K. Hada, S.-S. Lee, M. M. Lisakov, A. P. Lobanov, **J. López-Miralles**, M. Orienti, L. Petrov, A. V. Plavin, B. W. Sohn, K. V. Sokolovsky, P. A. Voitsik, and J. A. Zensus. *Astronomy&Astrophysics*. Volume 676, A114. August 2023. DOI: 10.1051/0004-6361/202142594.

- [6] **Rapid X-ray variability of the gamma-ray binary LS I +61°303.** J. López Miralles, Sara E. Motta, S. Migliari, F. Jaron. Monthly Notices of the Royal Astronomical Society, Volume 523, Issue 3, August 2023. DOI: 10.1093/mnras/stad1658.
- [7] **Numerical simulations of relativistic jets.** Manel Perucho, J. López-Miralles. Journal of Plasma Physics. Volume 89, Issue 5, October 2023. DOI: 10.1017/S0022377823000892.
- [8] **On the large scale morphology of Hercules A: destabilised hot jets?.** Manel Perucho, J. López-Miralles, Nectaria A. B. Gizani, José María Martí, Bia Boccardi. Monthly Notices of the Royal Astronomical Society, Volume 523, Issue 3, pp.3583-3594, August 2023. DOI: 10.1093/mnras/stad1640 .
- [9] **Jet acceleration in radio galaxies: an application to NGC 315.** L. Ricci, M. Perucho, J. López-Miralles, J.M-Martí, B. Boccardi. Submitted to Astronomy&Astrophysics, April 2023.
- [10] **Unravelling the relativistic magnetised jet dynamics of the microquasar SS 433: the scale of the subparsec.** J. López-Miralles et al. To be submitted to Nature Astronomy, September 2023.
- [11] **Timing analysis of Scorpius X-1 with NICER data.** J. López-Miralles et al. To be submitted to Monthly Notices of the Royal Astronomical Society, September 2023.
- [12] **Discovery of a possible third body in the X-ray binary system GRS 1747-312.** C. Painter, R. di Stefano, V. Kashyap, R. Soria, J. López-Miralles, R. Urquhart, J. Steiner, S. Motta, D. Ragozzine, H. Mori. To be submitted. September 2023.

# Contents

<b>1</b>	<b>Introduction</b>	<b>1</b>
1.1	Introduction . . . . .	1
1.2	Constituents and classification . . . . .	2
1.2.1	Compact object and companion star . . . . .	3
1.2.2	Accretion disc and corona . . . . .	6
1.2.3	Relativistic jets and outflows . . . . .	8
1.2.3.1	Mechanisms of jet formation . . . . .	8
1.2.3.2	Jet composition . . . . .	9
1.2.3.3	Jet emission and ISM interaction . . . . .	10
1.2.3.4	Types of outflows in X-ray binaries . . . . .	13
1.3	X-ray observations of XRBs/microquasars . . . . .	17
1.3.1	A historical note . . . . .	17
1.3.2	X-ray observatories . . . . .	18
1.3.3	Data analysis . . . . .	21
1.3.3.1	Spectral analysis . . . . .	21
1.3.3.2	Colour analysis . . . . .	21
1.3.3.3	Timing analysis . . . . .	23
1.4	Spectral states and disc-jet coupling . . . . .	26
1.4.1	Black Hole XRBs . . . . .	26
1.4.2	Neutron Star XRBs . . . . .	30
1.5	Numerical simulations of XRBs/microquasar outflows: an overview	33
1.5.1	Microquasar jets: the binary and beyond . . . . .	34
1.5.2	A special source: the microquasar SS 433 . . . . .	36
1.5.3	Pulsars and colliding winds . . . . .	37
1.6	X-ray binary/microquasar population . . . . .	40

1.6.1	BH X-ray binaries . . . . .	41
1.6.2	NS X-ray binaries . . . . .	45
1.7	Outline . . . . .	47
<b>I</b>	<b>Numerical methods and code development</b>	<b>49</b>
<b>2</b>	<b>Relativistic magnetohydrodynamics</b>	<b>51</b>
2.1	Basic equations . . . . .	52
2.2	Numerical methods . . . . .	53
2.2.1	Spatial and temporal discretization . . . . .	53
2.2.2	Spatial cell reconstruction . . . . .	54
2.2.3	Numerical fluxes and the Riemann problem . . . . .	55
2.2.4	Time integration . . . . .	58
2.2.5	Divergence-free constraint . . . . .	59
2.2.6	Recovery of primitive variables . . . . .	63
2.2.7	Correction of conserved variables . . . . .	64
2.3	Parallelisation . . . . .	65
2.4	Testing benchmark . . . . .	66
2.4.1	One dimension . . . . .	66
2.4.2	Two dimensions . . . . .	71
2.4.3	Three dimensions . . . . .	77
2.5	Relativistic Alfvén wave collisions . . . . .	82
2.5.1	Introduction . . . . .	82
2.5.2	Numerical setup . . . . .	82
2.5.3	Results . . . . .	84
<b>3</b>	<b>Relativistic radiation magnetohydrodynamics</b>	<b>89</b>
3.1	Introduction . . . . .	89
3.1.1	Radiation transport in high-energy astrophysics . . . . .	89
3.1.2	Review of numerical methods for radiation transport . . . . .	90
3.1.3	Objectives and organization . . . . .	93
3.2	Governing equations . . . . .	93
3.2.1	Radiation RMHD . . . . .	93
3.2.2	Radiation closure . . . . .	96
3.3	Numerical methods . . . . .	97
3.3.1	Numerical scheme . . . . .	97
3.3.2	Explicit step: the Riemann problem . . . . .	98
3.3.2.1	Radiative HLL . . . . .	99

3.3.2.2	Polynomial Viscosity Matrix Riemann solver . . .	101
3.3.3	Implicit step . . . . .	103
3.4	Testing benchmark . . . . .	104
3.4.1	One dimensional tests . . . . .	105
3.4.1.1	Circularly-polarised Alfvén wave . . . . .	105
3.4.1.2	Riemann problem for the optically-thin radiation transport . . . . .	109
3.4.1.3	Shock tubes . . . . .	110
3.4.1.4	Optically-thick radiation pulse . . . . .	114
3.4.2	Two and three dimensional tests . . . . .	115
3.4.2.1	Cylindrical/spherical magnetised blast wave . . .	115
3.4.2.2	The shadow problem . . . . .	117
3.5	Discussion and conclusions . . . . .	121
<b>4</b>	<b>Summary and future work</b>	<b>125</b>
4.1	Code repository: in a road for public release . . . . .	127
4.2	Code performance and GPU extension . . . . .	127
4.3	Implementing and improving physical processes . . . . .	129
4.4	Numerical methods for jet simulations . . . . .	132
<b>II</b>	<b>Numerical simulations</b>	<b>135</b>
<b>5</b>	<b>RMHD simulations of jet-wind interactions in high-mass X-ray binaries</b>	<b>137</b>
5.1	Introduction . . . . .	137
5.1.1	Relativistic jets in X-ray binaries/microquasars . . . . .	138
5.1.2	Numerical simulations of microquasar jets . . . . .	139
5.1.3	Objectives and organization . . . . .	142
5.2	Simulations . . . . .	142
5.2.1	Physical scenario . . . . .	143
5.2.2	Numerical setup . . . . .	143
5.3	Results . . . . .	149
5.3.1	Jet A . . . . .	150
5.3.2	Jet B . . . . .	152
5.3.3	Jet C . . . . .	154
5.4	Discussion . . . . .	157
5.4.1	Jet power and jet morphology . . . . .	157
5.4.2	Energy channels . . . . .	160

5.4.3	Radiative processes in the magnetised jet . . . . .	165
5.5	Conclusions . . . . .	168
<b>6</b>	<b>Unravelling the relativistic magnetized jet dynamics of the microquasar SS 433: the scale of the sub-parsec</b>	<b>171</b>
6.1	Introduction . . . . .	171
6.1.1	Multi-wavelength outflows . . . . .	172
6.1.2	Numerical simulations . . . . .	175
6.1.3	Overview . . . . .	177
6.2	Methods . . . . .	177
6.2.1	Numerical methods . . . . .	177
6.2.2	Physical scenario and numerical setup . . . . .	178
6.2.3	Simulations . . . . .	179
6.2.4	Projections and trace finder algorithm . . . . .	181
6.3	Results and preliminary discussion . . . . .	182
6.3.1	RUN I: Continuous injection . . . . .	182
6.3.2	RUN II: Discrete injection and blob-blob interactions . . . . .	184
6.3.3	RUN III: Ultra Relativistic Flows . . . . .	189
6.3.4	Jet magnetic fields . . . . .	191
6.4	Conclusions . . . . .	194
<b>7</b>	<b>Summary and future work</b>	<b>197</b>
7.1	The binary scale . . . . .	199
7.2	Beyond the binary scale . . . . .	200
7.3	Kink instabilities and non-thermal emission . . . . .	201
7.3.1	Improving magnetic field visualisation . . . . .	201
7.3.2	Magnetic dissipation in ideal RMHD simulations . . . . .	202
7.4	SS 433 jet simulations . . . . .	205
7.5	Beyond microquasars: AGN jet simulations . . . . .	207
<b>III</b>	<b>Observations and data analysis</b>	<b>209</b>
<b>8</b>	<b>Rapid X-ray variability of the <math>\gamma</math>-ray binary LS I +61°303</b>	<b>211</b>
8.1	Introduction . . . . .	211
8.1.1	High-energy emission models . . . . .	212
8.1.1.1	Microquasar model . . . . .	213
8.1.1.2	Pulsar wind model . . . . .	213
8.1.2	Source periodicities . . . . .	213

8.1.3	Objectives and organisation . . . . .	214
8.2	Observations and data analysis . . . . .	215
8.2.1	RXTE/PCA periodicity . . . . .	215
8.2.2	Data analysis . . . . .	216
8.2.2.1	Light curves . . . . .	218
8.2.2.2	Power density spectra . . . . .	219
8.2.2.3	Spectral fitting . . . . .	222
8.2.3	Results . . . . .	222
8.3	Discussion . . . . .	226
8.4	Summary and conclusions . . . . .	233
<b>9</b>	<b>Timing analysis of Scorpius X-1 with NICER data</b>	<b>235</b>
9.1	Introduction . . . . .	235
9.2	Observations and data analysis . . . . .	238
9.2.1	MAXI . . . . .	238
9.2.2	NICER . . . . .	239
9.2.2.1	Light-curve and Hardness-Intensity diagram . . . . .	240
9.2.2.2	Power Density Spectra . . . . .	240
9.3	Results . . . . .	242
9.3.1	Obs 1 (110803010) . . . . .	243
9.3.2	Obs 2 (110803011) . . . . .	248
9.3.3	Obs 3 (110803012) . . . . .	254
9.4	Discussion and ongoing work . . . . .	259
<b>10</b>	<b>Summary and future work</b>	<b>263</b>
10.1	Multi-wavelength campaign of Sco X-1 . . . . .	264
10.2	Chandra proposals . . . . .	265
10.3	GRS 1747-312: a third body system? . . . . .	267
<b>IV</b>	<b>Appendices</b>	<b>269</b>
<b>A</b>	<b>AGN jet simulations</b>	<b>273</b>
A.1	Jet propagation through inhomogeneous media and shock ionisation	273
A.1.1	Introduction . . . . .	273
A.1.2	First simulations with ionisation . . . . .	274
A.1.3	Preliminary results and first conclusions . . . . .	276
A.1.4	Improving the first simulations . . . . .	277
A.1.5	A particular scenario: the restarted jet in 3C 84 . . . . .	280

A.1.5.1	Numerical simulations . . . . .	281
A.1.5.2	Jet feedback . . . . .	283
A.2	The large scale morphology of Hercules A . . . . .	287
A.2.1	Introduction . . . . .	287
A.2.2	Numerical simulations . . . . .	291
A.2.2.1	The ambient medium . . . . .	291
A.2.2.2	Kinetically dominated jets . . . . .	292
A.2.2.3	Internal energy dominated jet . . . . .	293
A.2.3	Results . . . . .	294
A.2.3.1	Kinetically dominated jets . . . . .	294
A.2.3.2	Internal energy dominated jet . . . . .	296
A.2.4	Discussion . . . . .	301
A.2.4.1	Global morphology . . . . .	301
A.2.4.2	A hot jet . . . . .	304
A.2.4.3	A HEG to LEG transition? . . . . .	305
A.2.5	Conclusions . . . . .	306
<b>B</b>	<b>X-ray timing</b>	<b>309</b>
B.1	Testing jet geometries and disc-jet coupling in LMXB 4U 0614+091	309
B.1.1	Introduction . . . . .	310
B.1.2	Contribution . . . . .	311
B.1.3	Results and conclusions . . . . .	312

# Chapter 1

## Introduction

### 1.1 Introduction

X-ray binaries (XRBs) are stellar binary systems hosting a compact object (CO; a neutron star (NS) or a stellar-mass black hole (BH)) in orbit with a companion non-degenerate star around a common centre of mass, which are luminous –but not exclusively– in the X-ray energy range (Fig. 1.1). The star (i.e, the donor or secondary star) supplies matter to the CO (i.e, the accretor or primary star), a physical process driven through Roche-lobe overflow or by the direct impact of the stellar wind (see Sec. 1.2.2). Given the large angular momentum of the fallen matter, the latter does not fall radially towards the CO, but spirals around it, where by dissipative processes an accretion disc is formed (see below). The mechanisms that govern the accretion physics, which is directly connected to the most powerful events in the Universe, depend on the mass and evolution stage of the companion, the mass ratio of the stars in the system and also their orbital separation.

Most XRBs are transient objects, and in some specific states, these systems produce powerful bipolar relativistic outflows, where a fraction of the accreting matter is ejected with velocities close to the speed of light. These collimated ejections, called relativistic jets, may be launched by extracting energy from the BH [Blandford and Znajek 1977] or by magnetocentrifugal forces from the inner accretion disc [Blandford and Payne 1982], and emit non-thermal synchrotron radiation in the radio band. Due to this fact, radio emitting XRBs are also called microquasars [see e.g., Paredes and Marti 2003], in analogy with the large-scale extragalactic jets observed in quasars and other Active Galactic Nuclei (AGN).

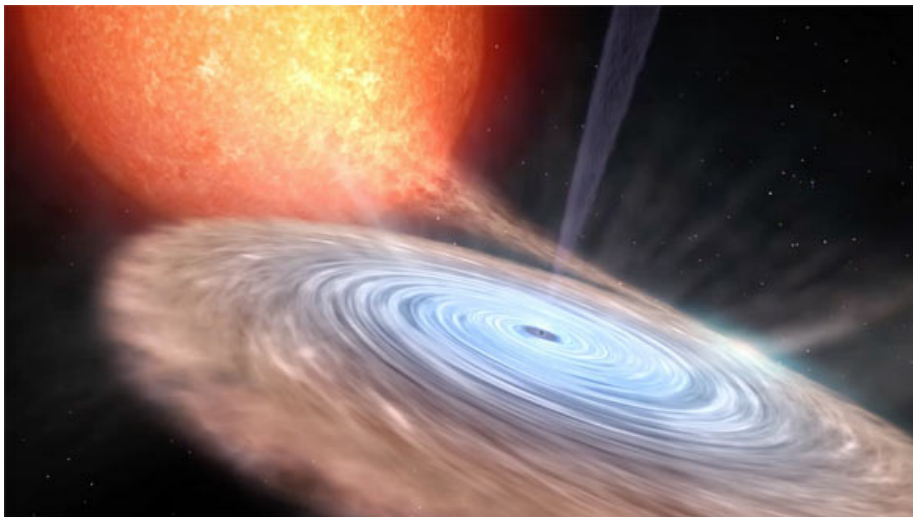


Figure 1.1 An artist's impression of a black hole X-ray binary. In this picture, accretion is driven by Roche-lobe overflow and the formation of relativistic jets and winds is also represented. Image credit: Instituto de Astrofísica de Canarias.

Although these jets are emitted from a region very close to the CO, they can propagate up to large distances and interact with the interstellar medium (ISM) very far from the core of the binary. Therefore, relativistic jets are one of the most important energy output channels and the main way by which the CO provides feedback with the environment.

In such a way, microquasars mimic the dynamical processes that govern the physics of AGN, but in extraordinarily small spatial and temporal scales. This allows us to observe and follow the evolution of the system, because the characteristic times of the accretion dynamics is humanly accessible, contrary to what happens in AGN. Due to this fact, XRBs are excellent systems to investigate the link between the jet formation and the different accretion states, and they also constitute a natural laboratory to test theories of gravity under extreme physical conditions, or even the exotic physics of ultra-dense matter in NSs, unfeasible to reproduce in Earth-based facilities.

## 1.2 Constituents and classification

The most relevant elements of XRBs/microquasars are: the **CO** (primary star), which accretes matter from the **companion star** (secondary star); the **accretion disc**, formed by the accreting material and responsible for the X-ray

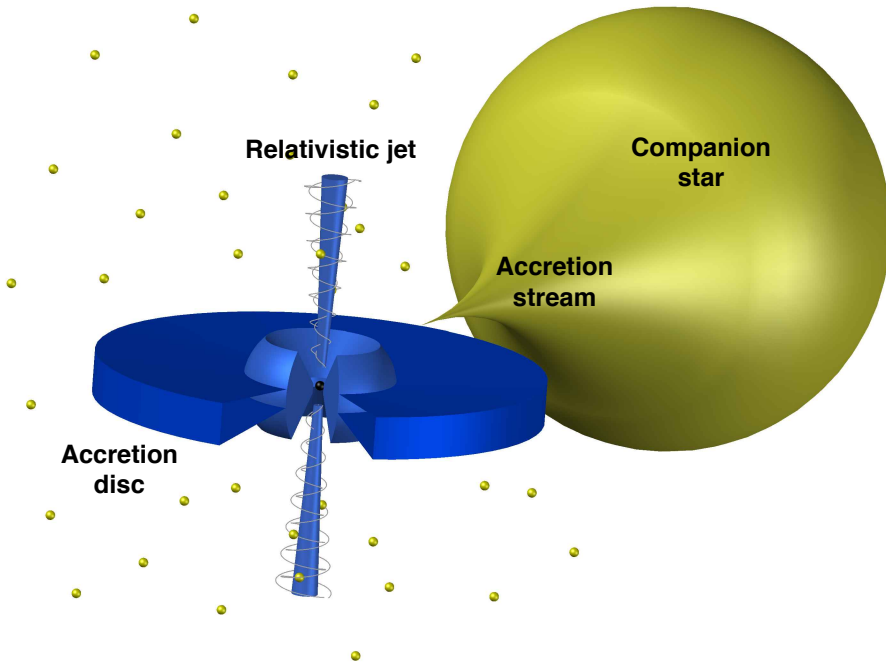


Figure 1.2 An schematic illustration of a BH microquasar, where accretion is governed by Roche-lobe overflow. The star and the disc are not to scale.

emission; and the **relativistic outflows**, ejected from the inner disc in the strong gravitational field of the CO. A simplistic sketch of these constituents (not to scale) is shown in Fig. 1.2. This section provides a brief but comprehensive description of their main physical properties.

### 1.2.1 Compact object and companion star

According to the type of CO, XRBs are mainly classified in three categories: **BH X-ray binaries** (BHXBs), which host a stellar-mass BH, **NS X-ray binaries** (NSXBs), which host a NS, and Cataclismic Variables (CVs), that host a white dwarf. In this chapter, I will focus on the first two types of systems, since CVs are less luminous in X-rays and thus are sometimes disregarded from this category [see e.g., Giovannelli 2008, for a review].

Generally speaking, NS and BHXBs show similar properties, and for many years they tended to be explained with the same physical models. However, there are also noteworthy differences in their emission and underlying physical behaviour. For example, relativistic jets are observed in both systems, but the

wealth of studies in BH binaries is unmatched when it comes to NSs, mainly because the latter usually have weaker radio emission (a factor  $\sim 30$  less for the same X-ray luminosity) that often lies below the instrumental detection capabilities. Jets are common in NSXBs that host NSs with weak magnetic fields ( $B \leq 10^9$  G), but recently they have also been associated with at least one highly magnetized HMXB [van den Eijnden et al. 2018]. Moreover, jets are not quenched in the so-called soft state of NSs [Migliari et al. 2004] with only a few exceptions [see e.g., Miller-Jones et al. 2010], while their emission is always suppressed in the case of BHs in this state [Coriat et al. 2011].

Their spectral and timing properties are very similar, defining in both cases three fundamental accretion states (see details in Sec. 1.4). The transition between them seems to be determined by the accretion rate itself, and barely affected by the nature of the CO. There are, however, slight distinctions. BHXBs usually have harder spectra, and NS systems show faster transitions between spectral states [see e.g., Muñoz-Darias et al. 2014]. There are also some timing features that are exclusive of NS systems (for example, the so-called hectohertz quasi-periodic oscillations (QPOs), see Sec. 1.3.3), while BHs tend to show less power at higher frequencies. In the so-called radio-X-ray luminosity diagram (see Sec. 1.3.3), these systems present a distribution in two separate branches, one corresponding to radio loud XRBs and other to radio quiet systems. However, the distribution appears more scattered for NSs than for BHs and it is thus more difficult to interpret in the former case.

In conclusion, the existence of a solid surface in the case of NSs, together with a magnetic field anchored to the surface could play a role in determining the physical behaviour of the binary, its emission and the properties of the outflow. Regarding the latter, even the mechanisms of jet formation can be different for these two types of systems, since among the two traditional mechanisms of jet formation (i.e., Blandford-Znajek vs. Blandford-Payne), only the latter can operate in the case of NSXBs. A brief discussion about the mechanisms of jet formation that operate on XRBs is provided below (see Sec. 1.2.3).

A special type of NS that deserves more attention is the **pulsar** [see e.g., Caballero and Wilms 2012, for a review], a rapidly rotating NS with a strong magnetic field that produce periodic multi-wavelength emission, mostly in the radio band, but also in X-rays and  $\gamma$ -rays. Pulsars may be divided in two main categories: isolated rotation-powered pulsars and accretion powered pulsars. In **rotation powered pulsars**, or isolated radio pulsars, the magnetic field of the star, which ranges from  $10^8$  to  $10^{15}$  G (the strongest magnetised pulsars with  $10^{13} - 10^{15}$  G are called magnetars), is misaligned with respect to the rotation

axis, and particles are accelerated towards the magnetic poles of the star, where they eventually produce powerful beams of radiation. As the pulsar rotates, these beams sweep across space like a lighthouse beam, and can be detected as a perfectly regular pulse in the radio emission of the system when crossing the line of sight of the observer. In **accretion powered pulsars**, or XRB pulsars, pulses are generated by the accretion flow striking the NS. Instead of falling uniformly onto the NS, the accreting matter from the companion star is channeled by the pulsar's magnetic field onto the magnetic poles of the CO, resulting in a pair of *hot spots* on the pulsar surface. As the pulsar spins, these hot spots are brighter in X-rays than the rest of the star, giving rise to X-ray pulsations at the spin rate. An interesting sub-class of these objects are the so-called **millisecond pulsars** [Patruno and Watts 2021], which are older stars characterised by faster spin periods (on the order of several milliseconds), and weaker magnetic fields. In the last years, magnetars have also been proposed to be at the origin of the mysterious Fast Radio Bursts, which are transient and intense bursts of radio emission that last for a very short time, but whose nature is still largely debated [see e.g., Mahlmann et al. 2022, and references therein].

Contrary to BH systems, NSs can also exhibit thermonuclear X-ray bursts [also called type-I X-ray bursts; Galloway et al. 2008], which are sudden increases of the X-ray luminosity followed by an exponential decay. These phenomena are typically related with a thermonuclear flash as accreted hydrogen and helium from the donor star piles up on the star surface. Since the presence of a solid surface is required for the existence of X-ray bursts, its detection is a good marker to disentangle the type of CO in a binary system.

According to the mass of the companion star, XRBs are classified as **low-mass X-ray binaries** (LMXBs), hosting solar or sub-solar mass companions, and **high-mass X-ray binaries** (HMXBs), which host secondary stars of O or B spectral class. The main difference between them is the way by which the donor star transfers matter to the CO, which depends on the mass and evolution stage of the companion and on the mass ratio of the stars in the system. These processes are: (1) **Roche-lobe overflow**, which can occur in both systems, and (2) **wind accretion**, which is particular of HMXBs with strong stellar winds.

**Low mass X-ray binaries** In this type of binary, the companion star is a main sequence star ( $\leq 2M_{\odot}$ ) and shows short orbital periods. Mass transfer occurs through Roche lobe overflow, where the Roche lobe is the region around a star in a binary system within which orbiting material is gravitationally bound to that star. This can be triggered by the evolution of the binary, where the

orbital separation can shrink, or by the stellar evolution of the companion, such that the donor can increase its size until the accretor remove its outer layers. Essentially, when the star fills its Roche lobe, matter flows freely through the first Lagrangian point ( $L_1$ ) into the gravitational well of the companion. Apart from a few exceptions, BH LMXBs are typically transient, while NS systems are generally –but not uniquely– persistent sources.

**High mass X-ray binaries** This type of binary involves a high-mass companion (typically  $> 10M_\odot$ ), a blue supergiant –a massive O or B-type star, as it is the case of Cygnus X-1 (Cyg X-1)–, or in some cases, a red supergiant or a Wolf–Rayet (WR) star –as it is the case of Cygnus X-3 (Cyg X-3). A further subdivision exists depending on whether the system contains a Be-type star (Be class) or an O-B star (SG class). In these objects, mass transfer is mainly driven by the direct impact of the powerful stellar winds that the massive companion ejects in the vicinity of the CO, leading to high accretion rates, X-ray luminosities and time variability. NSs in HMXBs have stronger magnetic fields and usually show X-ray pulsations, while only a minority of LMXBs are X-ray pulsars. The discovery of the microquasar LS 5039 [Paredes et al. 2000], which was later associated with the  $\gamma$ -ray source 3EG J1824-1514 [Hartman et al. 1999], and especially the detection of a transient event at very high-energy (VHE) from Cyg X-1 [Albert et al. 2007], showed that microquasars are sources of VHE radiation. This established the definition of the  $\gamma$ -ray emitting binaries (see Sec. 1.2.1) as a sub-class of HMXBs [see Dubus 2013, for a review]. The high-energy (HE; 0.1-100 GeV) and very high-energy (VHE;  $> 100$  GeV) emission detected from these sources, which in some cases seems to be correlated with the orbital phase of the binary [see e.g., Albert et al. 2006, for the case of LS I +61 303], can be explained by the interaction of a relativistic jet with the stellar wind of the companion in a microquasar, or by wind-wind interactions in a pulsar system.

## 1.2.2 Accretion disc and corona

Accretion discs are ubiquitous in the Universe and represent a major topic of research in a wide variety of astrophysical systems. They are present around stellar-mass BH and NS binaries and supermassive BHs in AGN, but also in Young Stellar Objects as protoplanetary discs, where planet formation takes place.

In XRBs, the accretion disc is formed by the in-falling plasma pulled from the donor star, which is accreted onto the CO. Due to its large angular momentum,

the transferred matter does not fall radially towards the CO, but orbits almost circularly at a certain radius from the core. Since the total angular momentum of the system must be preserved, it is transported from the central regions (in this case, the CO) outwards, a process mainly driven by the so-called magnetorotational instability [Balbus and Hawley 1991], which induces viscosity. Viscous dissipation heats the disc material, converting kinetic energy into thermal energy and allowing angular momentum to be transported outwards. The bulk of this gravitational potential energy is released in the inner regions of the disc, where plasma emits X-ray radiation (implying  $T > 10^7$  K). For an accreting body of mass  $M$  and radius  $R$ , the gravitational potential energy released by the accretion of a test-mass  $m$  is given by:

$$\Delta E = \frac{GMm}{R}. \quad (1.1)$$

From time derivation, the accretion luminosity  $L_{\text{acc}}$  becomes:

$$L_{\text{acc}} = \frac{GM\dot{m}}{R}, \quad (1.2)$$

where  $\dot{m}$  is the mass accretion rate.

The study of X-ray emission in XRBs is essential to understand the accretion physics very close to the CO, where physical processes and fluid (magneto)dynamics are subject to general relativistic effects (see also Sec. 1.3.3).

There is also strong observational evidence for the existence of a region of ultra-hot plasma that surrounds the CO, which manifests as a non-thermal component in the energy spectrum (see also Sec. 1.4). This is traditionally explained with a particular accretion disc configuration, where a geometrically thin, optically thick standard accretion disc [i.e., Shakura-Shun'yaev disc, Shakura and Sunyaev 1973] produces the black-body thermal components of the spectrum and an optically thin region close to the CO, known as the disc corona, produces a non-thermal hard power law. This region is composed by a cloud of very hot electrons that Compton-scatter the photons emitted from the Shakura-Shun'yaev disc, producing the hard power-law in the spectrum. The corona might also irradiate the disc and originate a reflection component [Fabian et al. 1989]. However, there is still no consensus about the nature and exact geometry of this region, although different models exist in the literature [see also Sec. 1.4.1, Ferreira et al. 2006].

**The Eddington limit and Ultra Luminous X-ray sources** The Eddington limit is a critical threshold that defines the maximum luminosity that an accreting object can achieve without being disrupted by its own radiation pressure.

Assuming purely ionised hydrogen, the Eddington luminosity follows:

$$L_{\text{Edd}} = \frac{4\pi GMm_p c}{\sigma_T} \sim 1.3 \times 10^{38} \frac{M}{M_\odot} \text{ erg/s}, \quad (1.3)$$

where  $M$  is the mass of the CO and  $\sigma_T$  is the Thomson scattering cross-section of the electron. This means that, for NSs and stellar-mass BHs in XRBs, the observed X-ray luminosity cannot be larger than  $10^{38} - 10^{39}$  ergs/s. However, several sources have been detected above this limit, as in the case of the BHXB GRS 1915+105 or the NS Circinus X-1 (Cir X-1; see Sec. 1.6 for a brief description of these two sources), as well as the so-called **Ultra Luminous X-ray (ULXs) sources**, which are extragalactic systems that show luminosities well above the Eddington limit ( $10^{39} - 10^{42}$  erg/s). Although in the past the existence of ULXs was explained in terms of intermediate mass BHs accreting at Eddington or sub-Eddington rates, the discovery of pulsations in some of these objects made this interpretation unsuitable. Then, King et al. 2001 suggested that ULXs in nearby galaxies are linked to microquasars with the assumption that their X-ray emission is restricted to a small cone angle aligned to the line of sight in ULXs, but away from the line of sight in microquasars. The system SS 433, which is a HMXB that shows persistent super-critical accretion, has been thus proposed as a galactic ULX candidate.

## 1.2.3 Relativistic jets and outflows

As previously mentioned, the formation of collimated outflows carrying ionised matter (i.e., plasma) with relativistic bulk velocities is the most powerful consequence of accretion onto COs, and it is one of the main ways of energy output, by which a vast amount of the accretion energy –and angular momentum– is transported from the central regions (i.e., deep in the strong gravity field) to large distances.

### 1.2.3.1 Mechanisms of jet formation

Following the physics behind powerful extragalactic jets, the formation of relativistic outflows in XRBs is traditionally related with the extraction of rotational energy from the central BH [Blandford and Znajek 1977] or by magnetocentrifugal forces from the inner accretion disc [Blandford and Payne 1982, Punsly and Coroniti 1990, Meier 2001, Fig. 1.6]. The first of these mechanisms can only operate in case of binaries hosting a BH, but even in this case Livio, Ogilvie, and Pringle 1999 suggested that the strength of the magnetic field threading the central object will not differ significantly from the inner accretion disc, and thus

the energy extracted from the BH will not exceed the electromagnetic output from the inner disc regions. In the case of NSs, Migliari, Miller-Jones, and Russell 2011 found a tentative correlation between the jet power and the spin frequency of the CO, suggesting that the rotation of the NS could play a role in the jet formation, but the results were subject to high statistical uncertainties (see also Appendix B of this thesis, where we found similar conclusions by the spectral modelling of LMXB 4U 0614+091). Indeed, it is also possible that both mechanisms operate at the same time, producing a two-flow ejection; a central leptonic relativistic spine surrounded by a mildly relativistic hadronic sheath launched from the accretion disc [Sol, Pelletier, and Asseo 1989].

Meier, Koide, and Uchida 2001 also suggested that the existence of compact jets in the hard state, coincident with geometrically thick discs, and their suppression in the soft state, which is dominated by geometrically thin accretion (see Sec. 1.4.1), support the idea that in XRBs jets are indeed powered from the inner accretion discs [see also Meier 2001]. This is the so-called disc-jet coupling paradigm [see e.g., Fender, Belloni, and Gallo 2004], which I will summarise in the next section. Furthermore, the discovery of a hadronic component in the relativistic outflows of two microquasars (i.e., SS 433 and 4U1630-47) also support this formation scheme. Alternatively to magnetic acceleration, radiation powered jets are not expected to be as efficient in achieving the expected plasma Lorentz factors, although this will be revisited later in the thesis to explain jet formation in the microquasar SS 433 (see Chapter 7).

### 1.2.3.2 Jet composition

The composition of the jet can be tightly correlated with the launching mechanism and is still not well understood, with some models favouring an electron-positron plasma composition (i.e., leptonic jets, which would imply that the bulk of the accretion matter never escapes from the binary system), while others suggest the presence of baryons, or a combination of baryons and leptons [Romero 2008], which can mass-load the jet directly from the accretion disc or during different phases of its propagation (for example, in the interaction with the stellar wind in a HMXB). Indeed, proving the existence of baryons in the jet may be important to understand the overall jet dynamics, since jet composition can impact the large-scale morphology given the larger relative inertia of protons with respect to leptons [see e.g., Perucho et al. 2014b, for the case of AGN jets].

The microquasars SS 433, which shows extended X-ray emission [Margon 1984, Marshall, Canizares, and Schulz 2002, Migliari, Fender, and Méndez 2002], or 4U1630-47 [Díaz Trigo et al. 2013], have both revealed the presence

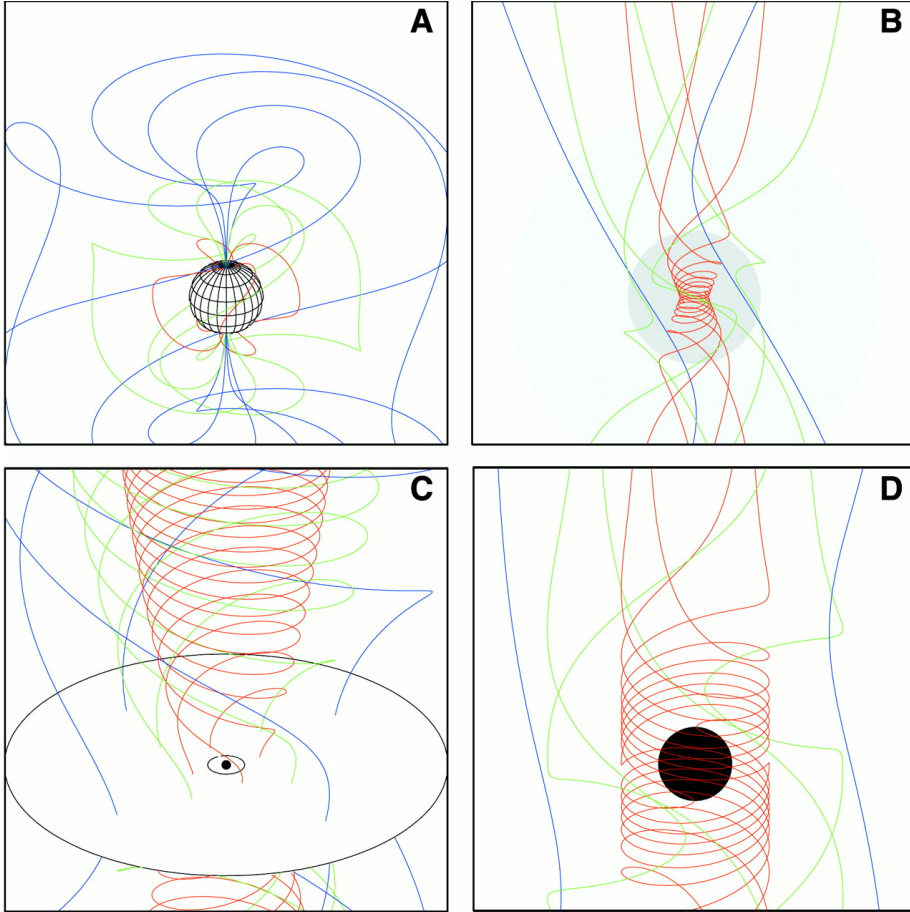


Figure 1.3 Four ways to make jets with magnetic fields. A: dipole field of a rotating neutron star. B: a collapsing object drawing and winding up an initially uniform field. C: Poloidal magnetic field from a magnetised accretion disc. D: frame-dragging near a rotating BH. Mechanisms C and D are relevant in the context of microquasars. From Meier, Koide, and Uchida 2001 (Fig. 4). Reprinted with permission from AAAS.

of baryons in the jets through Doppler shifted emission lines. By contrast, the LMXB XTE J1550-564 (that shows similar extended X-ray emission as SS 433), reveals a featureless continuum consistent with the extrapolation of the synchrotron spectrum from the radio band, suggesting in this case a purely leptonic composition [Kaaret et al. 2003], or a small amount of protons. Energetic considerations and circular polarisation measurements have instead provided conflicting evidence for the presence or absence of baryons in the outflows.

### 1.2.3.3 Jet emission and ISM interaction

Microquasars' jet radiation extends from low energy radio emission to VHE  $\gamma$ -rays, revealing multiple non-thermal processes that operate in the outflow at different temporal and spatial scales. An extensive review of the processes behind the bulk of the non-thermal emission in microquasars is given by Bosch-Ramon and Khangulyan 2009.

The most common way to study relativistic jets is by radio observations, where emission is characterised by non-thermal spectra, high brightness temperatures and, in some cases, a high degree of linear polarisation. This suggests a synchrotron origin from a population of relativistic electrons spiralling in the jet magnetic fields. If jets reveal an optically thin spectrum above some frequency (for example, during a particular X-ray state), the underlying electron population can be derived, showing a spectral index ( $-0.4 \geq \alpha \geq -0.8$ , for  $N(E)dE \sim E^{-(1-2\alpha)}dE$ ) which is compatible with the majority of AGN jets and other synchrotron emitting processes in the Universe.

When studying jets in XRB systems, one should consider three different spatial scales: (i) **the inner scale**, where the jet is launched, collimated and accelerated by the magnetic field and/or the Bernoulli process up to relativistic velocities, (ii) **the binary scale**, where the jet might interact with outflows emitted from the disc or, in the case of HMXBs, with the strong winds driven by the massive companion, and (iii) **the large scale**, where the jet propagates away from the binary and interacts with the ISM. The physical processes inside the jet and the subsequent emission mechanisms should be addressed in the strict context of this division.

Close to the CO, jets are expected to be magnetically dominated (i.e., a Poynting flux), so particles can be accelerated by ideal and non-ideal magnetohydrodynamical (MHD) processes: dissipation by MHD instabilities, magnetic reconnection in the surrounding corona [e.g., de Gouveia Dal Pino, Piovezan, and Kadowaki 2010] or the magnetocentrifugal mechanism. Markoff, Falcke, and Fender 2001 also suggested that, for reasonable assumptions about the jet physical parameters, the synchrotron emission could be extended up to the X-ray energy band to also explain the X-ray power-law [see also Falcke and Biermann 1996, Corbel and Fender 2002, Markoff et al. 2003], as opposed to thermal Comptonization models in the corona. Other leptonic processes that could be relevant at this scale are relativistic bremsstrahlung from electrons interacting with ions in the jet and Inverse Compton (IC) with coronal and/or disc photons, while proton-proton collisions and/or interactions between protons

with photons from the disc can produce high energy radiation in the form of  $\gamma$ -rays or neutrino emission [Torres, Romero, and Mirabel 2005, Adrián-Martínez et al. 2014].

At the scale of the binary, relativistic particles can be triggered by the Fermi process (shock diffusive/Fermi I, due to internal shocks in the jet, random scattering/Fermi II, if magnetic turbulence is strong enough, shear acceleration in the expanding jet), or by strong recollimation shocks due to the interaction of the jet with the stellar winds [see e.g., Bosch-Ramon, Khangulyan, and Aharonian 2008, Perucho and Bosch-Ramon 2008, Perucho, Bosch-Ramon, and Khangulyan 2010], where proton-proton collisions can be the most relevant hadronic process. Leptonic processes would possibly involve synchrotron emission, synchrotron-self Compton and external IC.

If the jet survives the binary scale without critical disruption [Perucho, Bosch-Ramon, and Khangulyan 2010], and there are no further instabilities that disrupt the flow afterwards [Heinz and Sunyaev 2002, Barkov and Bosch-Ramon 2022], jets can propagate up to large distances and interact with the ISM, where the characteristics of the external medium will play an important dynamical role on the jet evolution. Jets will produce a moving forward shock in the medium (i.e., the bow shock) and a reverse shock that moves backwards into the jet (in the jet reference frame). In these regions, Fermi I processes are a plausible mechanism to trigger particle acceleration. Radiation can be produced by synchrotron, Bremsstrahlung and IC. In particular, these type of interactions can also provide valuable information about unknown physical properties such as the total power of the jet, using the jet-driven structures in the ISM as astrophysical calorimeters [see e.g., Gallo et al. 2005, for the case of Cyg X-1].

Up to date, the most relevant examples of jet-ISM interactions are Cyg X-1 [Fig. 1.4, Gallo et al. 2005], which shows a jet-inflated bubble surrounding the source, and SS 433 [Fig. 1.5, Safi-Harb et al. 2022], where jets seem to be carving the supernova remnant (SNR) W50. These are not the only examples found in the literature [see Bordas et al. 2009, and references therein], but in the case of microquasars the evidence of jet-ISM interactions is not extensive if one compares it, for example, with jets in AGN.

#### 1.2.3.4 Types of outflows in X-ray binaries

In microquasars, relativistic jets manifest either as **persistent** radio structures or as a sequence of **discrete ejections**, although other types of outflows have also been inferred from multi-wavelength observations. These are, for example, the powerful **winds** launched from the accretion disc or the **underlying ultra**

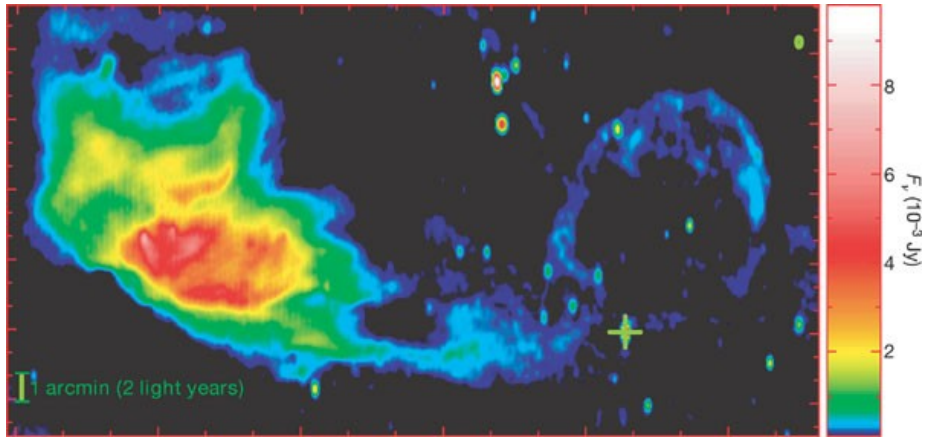


Figure 1.4 The field of view of the black hole in Cygnus X-1 (marked by a cross) observed by the Westerbork Synthesis Radio Telescope for 60 hours at 1.4 GHz. The ring appears to draw an edge between the tail of Sh2-101, the nearby HII nebula on the left hand side, and the direction of the inner radio jet. Reproduced with permission from Gallo et al. 2005 (Fig. 1).

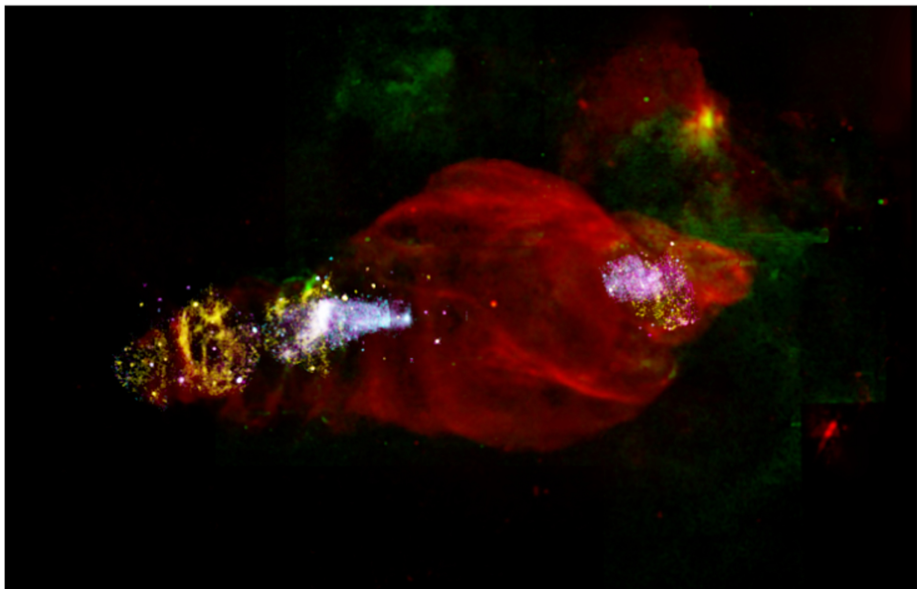


Figure 1.5 Multiwavelength image of the W50 nebula. Red: radio; green: optical; yellow: soft X-rays (0.5–1 keV); magenta: medium energy X-rays (1–2 keV); cyan: hard X-ray emission (2–12 keV). Reproduced with permission from Safi-Harb et al. 2022 (Fig. 1).

**relativistic flows** (URFs) discovered in some NS systems [Fomalont, Geldzahler, and Bradshaw 2001a, Fomalont, Geldzahler, and Bradshaw 2001b, Motta and Fender 2019]. I devote the rest of the section to summarise the main properties of the different type of ejections. A comprehensive revision of the observational properties of jets in XRBs can be found, for example, in Fender 2006.

**Persistent radio sources.** In contrast to relativistic jets in active galaxies, outflows are not observed as extended structures in binary systems, but mostly inferred from a radio-to-mid-infrared (IR) flat (or slightly inverted) spectrum. Steady jets have been spatially resolved in two XRBs, namely Cyg X-1 (Fig. 1.6, left panel) and GRS 1915+105 [Dhawan, Mirabel, and Rodríguez 2000], with sizes of a few tens of Astronomical Units (AU). The jet spectrum is characterised by a jet break [Corbel and Fender 2002], where emission goes from optically thick at the jet base to optically thin, and at lower frequencies by a continuum, which results from the superposition of self-absorbed synchrotron radiation emitted from different regions in the jet flow. However, as plasma propagates from the binary center, the magnetic field decays and particles lose energy, so one would expect to observe an effective inverted radio spectrum, and not a flat –or slightly inverted– one. This has been explained by the existence of a mechanism of energy replenishment of the relativistic plasma that compensates the adiabatic losses due to jet expansion [Blandford and Königl 1979, see also Appendix B of the thesis]. Although in microquasars there is no direct way of determining the speed of a steady jet because the counter-jet is not resolved [but see also Saikia et al. 2019, Tetarenko et al. 2021, who attempted to constraint the Lorentz factor of the compact jet in some BHXBs], it is reasonably assumed that jets might be mildly relativistic, with Lorentz factors  $\Gamma < 2$ .

**Discrete/transient ejections.** Transient ejections are observed as resolved radio emitting components with high relativistic velocities that can travel to several thousands of AU from the binary core, showing rapidly decaying fluxes (see Fig. 1.6, right panel, where transients ejections are observed in the XRB Cyg X-3). Although these type of ejections have been traditionally interpreted as radio emitting plasmons [the so-called van der Laan interpretation; van der Laan 1966], this model has been proven to show several caveats [see e.g., Klein-Wolt et al. 2002, Fender et al. 2023, but see also Tetarenko et al. 2017, who applied a modified van der Laan model to a mm-cm flaring period in the XRB V404 Cyg]. This favours instead the shock interpretation [Kaiser, Sunyaev, and Spruit 2000],

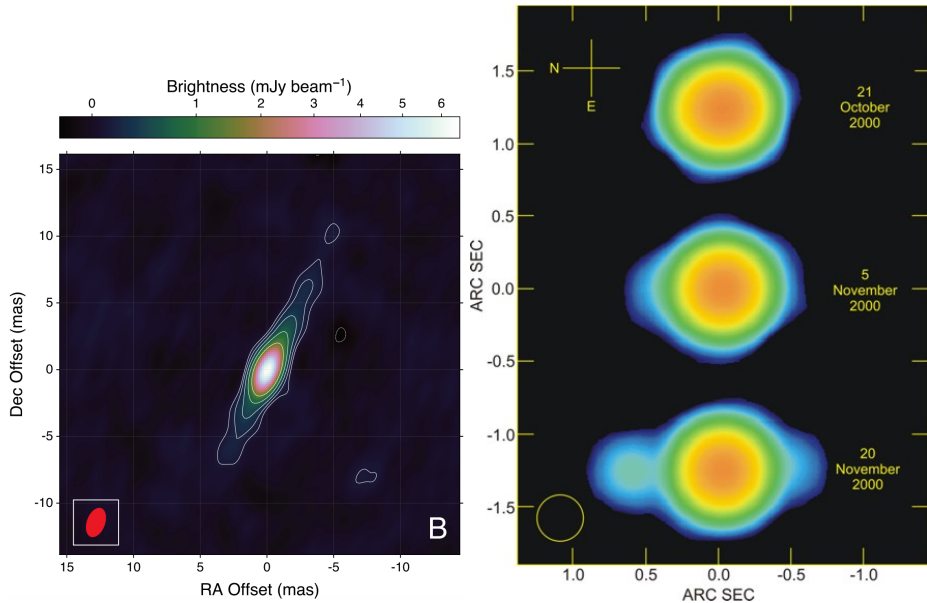


Figure 1.6 Left: Stacked radio image of the Cygnus X-1 jet in colour, with white contours every  $\pm\sqrt{2}$  times the rms noise level of  $23 \mu\text{Jy}$  per beam. From Miller-Jones et al. 2021 (Fig. 1), reprinted with permission from AAAS. Right: Transient extended radio jet in Cygnus X-3. Reproduced with permission from Martí, Paredes, and Peracaula 2001 (Fig. 6), ©ESO.

where the apparent discrete morphology is expected to be produced by internal shocks in the jet flow.

Mirabel and Rodríguez 1994 first reported apparent superluminal motions in the radio emission of the galactic source GRS 1915+105. The apparent velocity of the ejecta can be related with the intrinsic velocity by the following relativistic relation:

$$\beta_{\text{obs}} = \frac{\beta_{\text{int}} \sin \theta}{1 \pm \beta_{\text{int}} \cos \theta}, \quad (1.4)$$

which indicates that apparent superluminal velocities ( $\beta_{\text{obs}} > 1$ ) require at least  $\beta_{\text{int}} = 0.7$ , although Fender et al. 1999 later showed that the real Lorentz factor of the jet was possibly higher. This provided evidence, for the first time, that microquasars can exhibit the same type of relativistic outflows observed in the powerful jets of active galaxies. As I will show below, these type of discrete ejections are not unusual for BHXBs and are typically associated to a spectral transition during the XRB outburst hysteresis.

**Ultra relativistic flows (URFs).** URFs are not directly imaged in the radio or X-ray data, but inferred from the correlation between flares in the core and

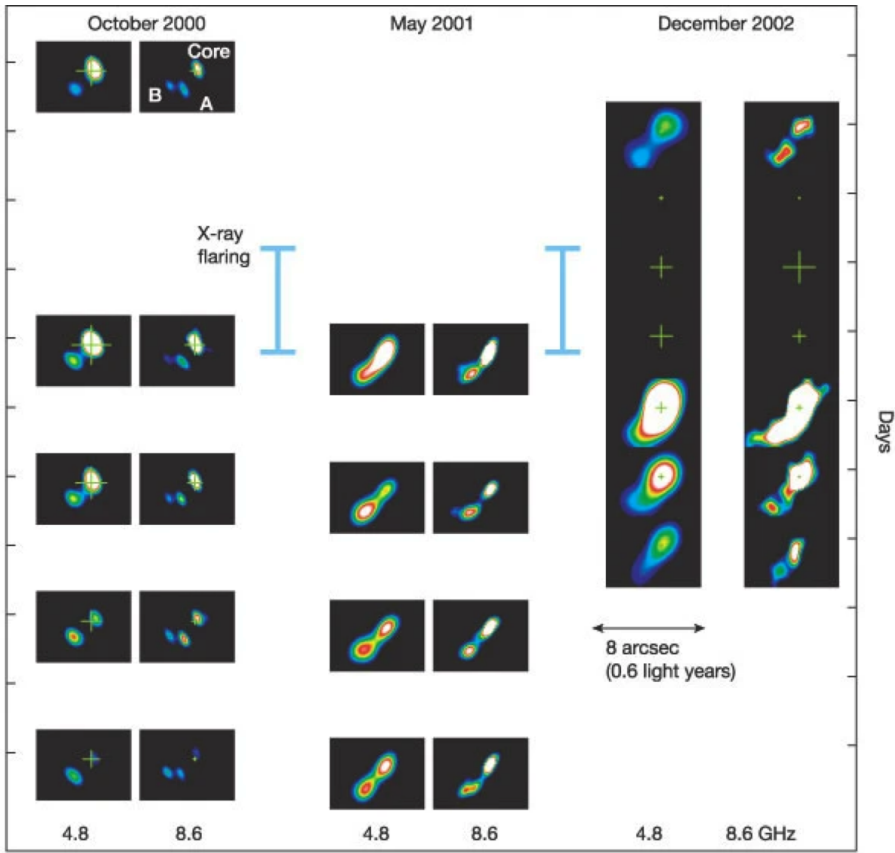


Figure 1.7 An ultrarelativistic outflow: sequences of radio observations of Circinus X-1 in October 2000, May 2001 and December 2002. Reproduced with permission from Fender et al. 2004 (Fig. 1).

in the radio lobes. Fomalont, Geldzahler, and Bradshaw 2001a and Fomalont, Geldzahler, and Bradshaw 2001b inferred the presence of URFs in the NSXB Scorpius X-1 (Sco X-1) by correlating the flux density variation in the lobes and in the core, assuming an underlying flow that moves at  $v \approx 0.95 c$ . Fender et al. 2004 also reported an URF-like event in the NSXB Cir X-1, while Migliari et al. 2005 suggested the existence of URFs in the microquasar SS 433 to explain the rapid time variability of the extended X-ray jets inferred from Chandra observations. Recently, Motta and Fender 2019 also proposed that the ejection of URFs in the NSXB Sco X-1 is related with two particular types of QPOs (see Sec. 1.3.3).

**Accretion disc winds.** Accretion disc winds are dense outflows of highly ionised plasma ejected from the accretion disc, which have a wider opening angle as compared to relativistic jets, also carrying a greater matter content [see e.g., Díaz Trigo and Boirin 2016, for a review, and references therein]. Winds can be driven by thermal [e.g., Begelman, McKee, and Shields 1983], radiative [e.g., Proga and Kallman 2002] and/or magnetic pressure [e.g., Chakravorty et al. 2016], although the thermal mechanism is possibly dominant.

Since winds might carry a significant fraction of the mass supplied to the disc, these type of outflows could play an important role in the geometry of the inner accretion flow and in the accretion changes along the binary life cycle. Moreover, the role of binary winds in the feedback of the system with the ISM is still under debate, as it is the case, for example, for the powerful accretion winds observed in AGN [see e.g., Faucher-Giguère and Quataert 2012, and references therein].

Accretion winds are multi-wavelength emitters (from IR to X-rays), and due to their persistent nature, they are detected all over the binary spectral cycle, in both BH and NS systems [Ponti, Muñoz-Darias, and Fender 2014]. Observationally, winds are detected as narrow absorption lines from highly ionised plasma in a local absorber. The shift of these lines with respect to the theoretical wavelengths of the ions indicates an outflowing plasma. Highly ionised plasmas were first detected by the Advanced Satellite for Cosmology and Astrophysics (ASCA) in two systems, GRO J1655-40 [Ueda et al. 1998] and GRS 1915+105 [Kotani et al. 2000], but photo-ionised absorbers were then reported in many other LMXBs. In HMXBs, however, the winds in the system are mainly dominated by the contribution of the companion star.

## 1.3 X-ray observations of XRBs/microquasars

### 1.3.1 A historical note

The history of XRBs is necessarily connected to the history of X-ray astronomy, which began in 1962 with the discovery of the first extra-solar X-ray source by a rocket-borne instrument [Giacconi et al. 1962]. This source, which was later identified as an accreting NS [Shklovsky 1967], is nowadays called Sco X-1, and it is the strongest source of X-ray emission in the sky (aside from the Sun). Although X-ray astronomy progressed from 1962 to the next decade mainly based on rocket-borne instruments, detectors attached to satellites from other primary missions, and high-flying balloons, the launch of Uhuru in 1970,

the first dedicated X-ray satellite, allowed to overcome all the limitations of previous surveys and began the era of space-based X-ray missions. This mission allowed to increase the number of known X-ray sources by a factor  $\sim 10$  and to unravel the nature of their emission, which started to be associated with accretion processes in binary objects. At the same time, the source Cyg X-1 was first discovered with a sounding rocket [Bowyer et al. 1965, Kristian et al. 1971] and later identified as a BH persistent source [Shipman 1975]. The first BH transient was also discovered in 1975 by the Ariel V satellite [A0620-00; Elvis et al. 1975], and confirmed as a BH source in 1986 [McClintock and Remillard 1986].

Following the launch of Uhuru, the field of X-ray astronomy experienced an astonishing progress, mainly guided by the development and deployment of dozens of high-energy space missions. The Japanese satellite Ginga, equipped with a large area detector, discovered new BH transients, but it was not until the second half of the 90's when X-ray astronomy experienced a major revolution. The deployment of the Rossi X-ray Timing Explorer (RXTE) satellite started a new era in the timing analysis and variability studies of XRBs thanks to its astonishing time resolution, and the progress in the field culminated some years later with the launch of two space telescopes carrying high-resolution spectral instruments; XMM-Newton and Chandra (1999).

Following the discovery of luminous X-ray sources in the 1960's and 1970's, the counter-part in the radio range was explored in the brightest ones, namely Sco X-1 [Hjellming and Wade 1971b], Cyg X-1 [Hjellming and Wade 1971a], and Cyg X-3 [Gregory et al. 1972]. The relation between the X-ray and radio emission became clearer with the observations of a resolved strong radio source associated with the binary SS 433 (see also Sec. 1.6), beginning the field of XRB jets [Spencer 1979, Margon et al. 1979]. However, the relation between the outflows in SS 433 with the powerful jets observed in active galaxies was not entirely clear, since in SS 433 the velocity of the jets is only  $\sim 25\%$  of the speed of light. Then, the second milestone in the field arrived some years later with the discovery of apparent superluminal motions in the radio knots from the BHBs GRS 1915+105 [Mirabel and Rodríguez 1994, Mirabel and Rodríguez 1999] and GRO J1655-40 [Tingay et al. 1995]. This was essential to prove, for the first time, that microquasars can also show the same kind of significant relativistic motions as observed in AGN jets.

Although microquasars are multi-wavelength emitters, for the purpose of this thesis I will concentrate on X-ray observations. The rest of the section is

devoted to describe some of the most relevant X-ray instruments as well as the main techniques used to analyse X-ray data in the context of XRBs.

### 1.3.2 X-ray observatories

Some of the most important X-ray missions that are currently in scientific operations are **X-ray telescopes**. These devices are able to focus the incident radiation in the detector plane, where a collection of Charge-Couple Devices (CCD) cameras measure the collected photons. In this type of instruments, one of the most critical design elements is the telescope optics. Since photons can only be reflected at very low incident angles, focusing is achieved by reflecting photons with grazing incidence mirrors; a parabolic mirror followed by a hyperbolic mirror, a special configuration known as Wolter type I [Wolter 1952]. The long-lived X-ray missions XMM-Newton and Chandra are based on this type of technology.

Other X-ray detectors, for example RXTE, are based on **proportional counters**, which are chambers filled by an inert gas that is ionised by the incident radiation. Although this type of instruments do not provide spatial information about the incident photons, they are usually characterised by a large collecting area and high time resolution, making them specially convenient for X-ray timing studies.

**XMM-Newton** XMM-Newton [Jansen et al. 2001] is an X-ray space observatory launched by the European Space Agency (ESA) on 10th December 1999, and it is the second cornerstone satellite of the four missions defined in ESA's Horizon 2000 program. The spacecraft is aimed at investigating X-ray sources, allowing narrow- and broad-range spectroscopy, and performing the first simultaneous imaging of objects in both X-ray and optical –visible and ultraviolet(UV)– wavelengths. Thus, the observational scope of XMM-Newton includes the detection of X-ray emission from astronomical objects, detailed studies of star-forming regions, investigation of the formation and evolution of galaxy clusters, and the environment of (supermassive) BHs and NSs, among many others. XMM-Newton satellite carries three different types of scientific instruments: (1) the European Photon Imaging Camera (EPIC), 3 CCD (two MOS and one PN) cameras for X-ray imaging, moderate resolution spectroscopy and X-ray photometry, (2) two Reflection Grating Spectrometer (RGS) for high resolution spectroscopy and (3) the Optical Monitor (OM), for optical/UV imaging and grism spectroscopy. All scientific instruments onboard the XMM-Newton satellite can operate simultaneously, and, altogether, provide the instrument

with high sensitivity (with the largest effective area of a focusing telescope), good angular resolution (full width at half maximum (FWHM) of the order of  $6''$ ), moderate (EPIC) and high (RGS) spectral resolution and long continuous target visibility, thanks to its highly elliptical orbit. This thesis does not contain any analysis of XMM-Newton data and the instrument is only presented for future work purposes.

**Chandra** The Chandra X-ray Observatory [Weisskopf et al. 2000], which together with the Hubble Space Telescope and the Spitzer Space Telescope is one of the NASA Great Observatories, is a space based X-ray telescope launched on July 23, 1999. Chandra uses four pairs of nested mirrors (together with their support structure) in a Wolter type I configuration, called the High Resolution Mirror Assembly (HRMA). This assembly yields an effective angular resolution of  $\sim 0.5$  arcsec, which is by far the best angular resolution of any X-ray telescope up to date. The telescope focal plane holds two different type of detectors: the Advanced CCD Imaging Spectrometer (ACIS), which consists on ten CCD chips arranged in two arrays (ACIS-I and ACIS-S), and the High Resolution Camera (HRC), which provides a time resolution up to  $16 \mu\text{s}$ . In addition, transmission diffraction gratings provide Chandra with high resolution spectroscopy. These spectrometers are the High Energy Transmission Grating Spectrometer (HETGS), which operates in the energy range 0.4-10 keV, and the Low Energy Transmission Grating Spectrometer (LETGS), which instead has a range of 0.09-3 keV. As in the case of the XMM-Newton satellite, this thesis does not contain any analysis of Chandra data and the instrument is only presented for future work purposes.

**Rossi X-ray Timing Explorer** RXTE was a space-based observatory dedicated to studying the timing properties of X-ray sources in the Universe, launched by NASA on December 30, 1995 [Bradt, Rothschild, and Swank 1993]. The mission was decommissioned in 2012 after 16 years of continuous operations, where RXTE provided unprecedented information about the timing properties of BHs and NSs in binary systems, established the existence of highly magnetised NSs (aka magnetars), discovered the first accreting millisecond pulsars or established observational evidence for the existence of the relativistic frame-dragging effect, among many other groundbreaking findings.

The three instruments carried by the satellite were: (1) the Proportional Counter Array (PCA), aimed to cover the lower part of the energy band (2 – 60 keV), (2) the High Energy X-ray Timing Experiment (HEXTE), aimed to

collect hard X-rays (20 – 200 keV), and (3) the All-Sky Monitor (ASM), aimed at monitoring  $\sim 80\%$  of the X-ray sky every  $\sim 90$  min in the 2 – 10 keV energy range.

For the purposes of this thesis, I will only briefly describe the characteristics of the PCA [Jahoda et al. 2006], which is the instrument used for the timing analysis presented in Chapter 8 to study the  $\gamma$ -ray binary LS I +61 303. This instrument consists of a collection of five different proportional counters filled with Xenon with a large collecting area, named as Proportional Counter Units (PCUs, labelled from 0 to 4), although only PCU-2 has been kept on during the whole extent of the mission. Collectively, the instrument is characterised by an approximately circular field of view of  $\sim 2^\circ$  (spatial resolution  $\sim 1^\circ$  at FWHM), moderate energy resolution ( $< 18\%$  at 6 keV) and extraordinary high time resolution of only a few microseconds.

**NICER** The Neutron Star Interior Composition Explorer [NICER; Gendreau et al. 2016] is an International Space Station (ISS) payload devoted to the study of NSs with unprecedented sensitivity through simultaneous soft (0.2-12 keV) X-ray fast timing and spectroscopy, which was launched on June 3, 2017. With respect to RXTE, NICER works on a softer energy passband but provides a remarkable increase in energy and timing resolution (85 eV at 1keV,  $< 300$  ns). The primary science instrument of NICER is the X-ray Timing Instrument (XTI), which is an aligned array of 56 X-ray detectors based on X-ray concentrator optics and silicon drift detector pairs collecting X-rays over a large geometric area (30 arcmin<sup>2</sup>). These instrument properties make NICER an ideal detector to study not only X-ray pulsars, but also a wide variety of astrophysical scenarios in X-ray astrophysics. In this thesis, I will make use of NICER data to perform a timing analysis of the NS LMXB Sco X-1 (Chapter 9).

### 1.3.3 Data analysis

#### 1.3.3.1 Spectral analysis

The spectral analysis of XRBs consists of calculating and interpreting broad-band energy spectra in order to obtain quantitative information about their X-ray emitting components: thermal emission from the *standard* accretion disc, non-thermal emission from the corona, synchrotron emission from a relativistic jet, etc. (Fig. 1.8). The broad-band energy spectrum is usually fitted with theoretical models following  $\chi^2$ -test statistics [Arnaud 1996], which allows us to deduce physical quantities like the disc temperature, energy and opacity of

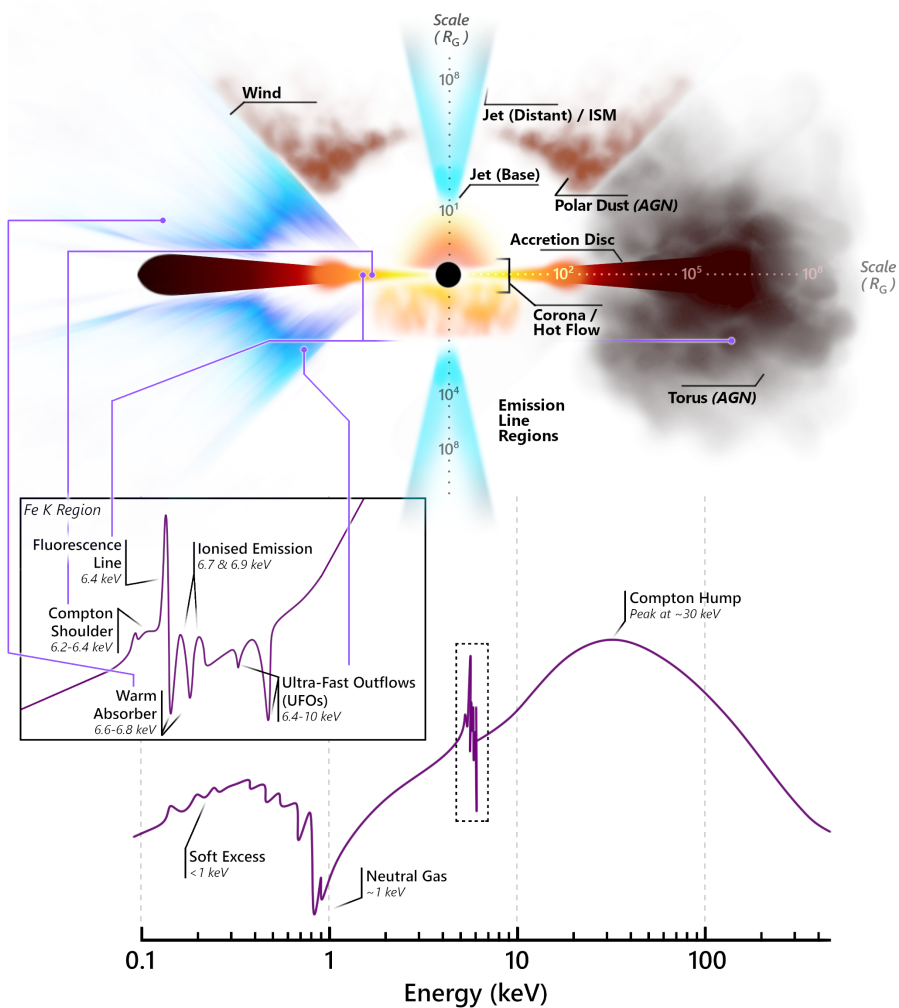


Figure 1.8 Schematic overview of the environment of accreting compact objects and their X-ray spectra. Reproduced with permission from Gandhi et al. 2022 (Fig. 1).

Comptonising electrons in the corona or the presence of emission lines from the disc, among others. The integral of the best-fit model specific flux over a particular energy band gives an estimate of the total flux in that energy band.

An example of an energy spectrum showing several fitting model components is displayed in Fig. 1.9 for the NS LMXB 4U 0614+091. Without loss of generality, X-ray energy spectra of XRBs can be fitted using the following multi-component statistical model: (1) a multi-temperature black-body model for the accretion

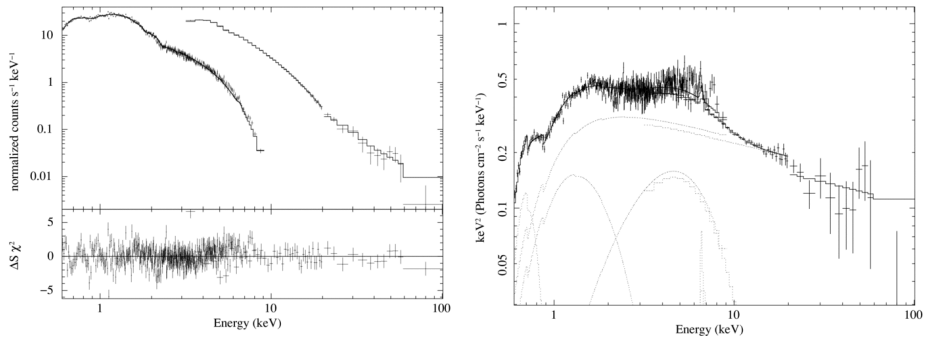


Figure 1.9 Left: Swift (XRT) and RXTE (PCA and HEXTE) energy spectrum of the NSXB 4U 0614+091 in the range 0.6–100 keV. The fitting model consists of two black bodies, an iron Gaussian emission line and a power law, corrected for photoelectric absorption. A Gaussian emission line around 0.62 keV (possibly an oxygen line) is also needed. Right: unfolded energy spectrum showing the spectral components. Reproduced with permission from Migliari et al. 2010 (Fig. 2), ©AAS.

disc emission, (2) a gaussian function to fit highly-ionised emission lines from the disc and (3) a power law or a Comptonization model to fit the hard non-thermal emission from the hot plasma in the corona. Moreover, if the CO is a NS, an additional black-body component to account for the star surface emission is also needed.

### 1.3.3.2 Colour analysis

Alternatively to the standard broad-band energy spectra, colour analysis can provide insightful information about the spectral properties of the source. X-ray colours are, by definition, hardness ratios that quantify the difference in brightness between two broad energy bands. In other words, a colour is the ratio between source counts, fluxes or luminosities measured in different energy intervals, which need to be defined in each case according to the source characteristics and the instrument response. Low-energy bands are referred to as *soft*, while high energy bands are referred to as *hard*.

In the field of XRBs, there are two fiducial representations that involve X-ray colours: the colour-colour diagram (CD), where a colour is plotted against another colour, and the hardness-intensity diagram (HID), in which a colour (or the hardness ratio) is plotted against the intensity. The latter is defined as the source count rate, flux or luminosity measured in a broad energy range covering the sub-bands used to define the colours, or, otherwise, the entire energy range

of the instrument. In this thesis, I will use these techniques in Chapter 9 to study the spectral properties of the NS LMXB Sco X-1.

XRBs often trace a characteristic pattern in this type of representations, which is usually interpreted as a consequence of the underlying accretion regime of the source. Thus, colour analysis is a powerful tool to be used in conjunction with broad-band spectral analysis and the timing techniques that I will describe in the next section.

### 1.3.3.3 Timing analysis

Timing analysis is the main focus of the second part of the thesis (see Part II). It consists on a set of techniques to assess the rapid variability in the X-ray emission from XRBs, which is the principal tracer of the dynamical processes in the inner accretion flow, deep in the strong gravity field of the CO.

In this section, I will briefly summarise the main concepts of timing analysis, the basis of the techniques involved and the most important timing signals for both BH and NSXBs. Extensive reviews on these topics can be found in the literature from several authors [see e.g., Belloni, Psaltis, and van der Klis 2002, van der Klis 2006, Motta et al. 2017, Ingram and Motta 2019], and this section is mainly based on their work.

This type of analysis is performed by means of Fourier Transform techniques (specifically, Fast Fourier Transform algorithms), which allow us to convert the data from the time domain (i.e., count rate vs. time) to the frequency domain. In particular, the power density spectrum (PDS) is in general the main output of the process, which gives a power density,  $P_\nu$ , as a function of the Fourier frequency,  $\nu$ , where  $P_\nu$  is proportional to the variability amplitude in the light-curve in a short time scale [van der Klis 1989].

Typically, the power spectrum reflects three fundamental features [see e.g., Belloni, Psaltis, and van der Klis 2002, for a review]: (I) **coherent pulsations**, which appear as unresolved single-frequency spikes mainly originated by spin pulsations in pulsars, (II) broad aperiodic structures, usually called **noise**, and (III) narrow-peaked resolved features, the so-called **QPOs**. Noise components usually represent real signals from the source, since the noise associated to counting statistics (i.e., Poisson noise) appears as a flat broad-frequency components in the PDS, which is usually removed. QPOs can also manifest as a series of harmonically related peaks, which together with the finite width of the QPO, means that the oscillation in the time domain is more complex than purely sinusoidal. Thus, the potential of QPOs as a diagnosis tool to understand the inner regions of the accretion disc was understood since its discovery 50 years

ago, and they have been observed in NS and BH binaries, CVs, ULXs and even AGN sources.

However, contrary to what happens with the spectral analysis, there is not a particular physical model to describe these timing components, which are mainly characterised by the central frequency, their width and the spectral state of the system. The standard procedure consists on fitting the power spectrum with a multi-Lorentzian model, where a Lorentzian function represents the Fourier transform of an exponentially damped sinusoid:

$$L(\nu) = \frac{a_0^2}{\pi/2 + \arctan(\nu_0/\Delta)} \frac{\Delta}{\Delta^2 + (\nu - \nu_0)^2}, \quad (1.5)$$

where  $\nu$  is the Fourier frequency,  $\nu_0$  is the Lorentzian central frequency,  $\Delta$  is the half width at half maximum and  $a_0^2$  represents the integral of  $L(\nu)$  from  $\nu = 0$  to  $\nu = \infty$ . The sharpness of the peak can be quantified by a quality factor,  $Q = \nu_0/\Delta\nu$ . This allows us to identify the different features in the power spectrum with enough accuracy, and to follow their evolution. The time evolution can also be addressed with a dynamical PDS (see Chapter 9 for details), which represents power  $P_\nu$  in the time – frequency plane.

Depending on the central frequency, QPOs are typically classified as **low-frequency** (LF) QPOs and **high-frequency** (HF) QPOs.

**Low-frequency QPOs** In BH systems, LF QPOs are typically found below 30 Hz. Based on their specific frequency range, shape and spectral state, they are sub-classified as type C, type B and type A QPOs (see Fig. 1.10, left panel). These LF QPOs were originally identified in the PDS of the BH system XTE J1550-564 [Wijnands, Homan, and van der Klis 1999].

- **Type C QPOs.** These represent the most common type of QPO in BH systems, appearing in all accretion states. Type-C QPOs are characterised by a high-amplitude (up to 20% root mean square, rms) and narrow ( $Q > 8$ ) peak in the PDS, coincident with flat-top noise. The centroid frequency rises from a few mHz at low luminosities to  $\sim 10$  Hz, showing occasionally up to  $\sim 30$  Hz. A series of (sub)harmonics are also generally detected together with the fundamental oscillation.

- **Type B QPOs.** They are characterised by a relatively high amplitude (up to  $\sim 5\%$  rms) and narrow ( $Q > 6$ ) peak, with a centroid frequency that ranges in 5-6 Hz. As in type-C QPOs, a weak second harmonic and a subharmonic

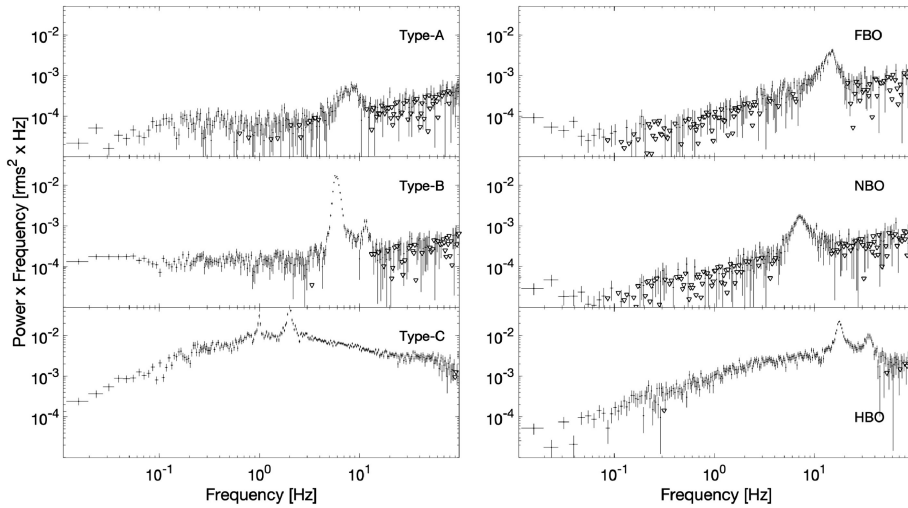


Figure 1.10 Examples of LF QPOs from BHXBs (left) and from NSXBs (right). Reproduced with permission from Ingram and Motta 2019 (Fig. 1).

peak are often observed. Since type B QPOs usually appear at the same time as transient jets (see below), the possibility that both phenomena are causally connected has been a matter of speculation. Rapid transitions in which type B QPOs appear and disappear are often observed.

- **Type A QPOs.** These represent the less common type of QPO, characterised by a weak and broad peak ( $Q \leq 3$ ) in the PDS, with centroid frequency in the range 6 – 8 Hz. Type-A QPOs are also associated with a very low amplitude red noise, and neither subharmonics nor a second harmonic are usually detected.

**High-frequency QPOs** HF QPOs ( $> 60$  Hz) are very rare in BHXBs, with only a few detections performed up to date with RXTE. The majority of these examples have a central frequency at a few hundred Hz, with only one exception at  $\sim 60$  Hz in the binary GRS 1915+105 [Morgan, Remillard, and Greiner 1997], for which dozens of HF QPOs have also been detected [Belloni and Altamirano 2013]. They appear at high-flux/accretion rates, and as single or double peaks in the PDS, but only GRS 1915+105 shows two simultaneous peaks [Motta et al. 2014]. In NSXBs, HF QPOs are called kHz QPOs (200 – 1300 Hz) and are much more common than in BH systems, showing also a larger amplitude and quality factor. The first two sources in which kHz QPOs were resolved are Sco X-1 [van der Klis et al. 1996] and 4U 1728-34 [Méndez and van der Klis 1999].

Usually, kHz QPOs manifest in pairs of two peaks separated by 200 – 400 Hz (the so-called twin-peak QPOs) and are typically related with the Keplerian frequency at the inner edge of the accretion disc.

NS systems also display QPOs that do not have a BH equivalent [Ingram and Motta 2019]. Some examples of these types are: (1)  $\sim 1$  Hz QPOs sometimes seen in dipping sources [Jonker, van der Klis, and Wijnands 1999], (2) hectohertz QPOs [Altamirano et al. 2008], (3) a  $\sim 26$  Hz QPO only seen in the dipping flaring state of the NSXB Cyg X-2 [Kuulkers and van der Klis 1995].

Despite the rich phenomenology of QPOs in both BH and NS systems, their origin and physical nature is still under debate. There is a large variety of theoretical models that aim to explain the origin of this quasiperiodic emission, most of them relying on disc instabilities and general relativistic effects [e.g., the relativistic precession model Stella and Vietri 1998]. For an extensive overview on the topic (mainly focusing on LF QPOs), I refer the reader to Belloni, Psaltis, and van der Klis 2002 or Motta et al. 2017.

## 1.4 Spectral states and disc-jet coupling

### 1.4.1 Black Hole XRBs

As already mentioned, the spectrum of BH LMXBs can be considered as the sum of two different components: the thermal contribution from an optically thick, geometrically thin standard disc, and non-thermal Comptonization from a hot accretion flow (i.e., the corona). Although XRBs show in general a rich variety of states and complex transitions between them, the relative weight of these two components in the spectrum can be used to characterise the spectral states of the system. A broad dichotomy exists between a **hard state**, interpreted by thermal Comptonization models, and a **soft state**, dominated by the thermal contribution of a standard accretion disc in the soft X-ray band (0.1-10 keV), which extends all the way to the inner-most stable circular orbit (ISCO). The transitions between hard and soft states define the so-called **intermediate spectral states**. In the literature, this dichotomy is usually described in the context of the **truncated disc model** [e.g., Esin, McClintock, and Narayan 1997], which proposes that in the hard state a standard geometrically thin optically thick disc (i.e., Shakura-Sunyaev) is truncated at some particular variable radius from the CO, coexisting with a hot optically thin geometrically thick corona that extends from the truncation radius to the ISCO. During a transition from the hard state to the soft state, the standard disc expands towards

the central object, reducing the space occupied by the hot corona. Recently, Méndez et al. 2022 also suggested that, at least in GRS 1915+105, the X-ray corona could indeed morph into the relativistic jets during this transition [see also Markoff, Nowak, and Wilms 2005].

Apart from the well-known system Cyg X-1 (a persistent luminous source), all BHXBs are transient objects that experience recurrent outbursts, with a recurrence period that ranges from some months to several decades (although still humanly accessible) and outburst characteristic times from days to several months, and more rarely years (e.g., GRS 1915+105).

BHXBs spend most of their life in the so-called **quiescent state**, showing a faint X-ray luminosity ( $< 10^{33}$  erg/s in BHs). However, due to instabilities in the accretion disc, the mass supplied to the central object (i.e., the accretion rate) can sporadically increase, making the binary to enter the outburst phase. The outburst evolution is typically represented in a HID, where strong regularities emerge among outbursts of different sources.

Figure 1.11 shows the HID for 4 RXTE/PCA observations of the source GX 339-4 [see e.g., Muñoz-Darias et al. 2014], where a particular q-shaped pattern (followed counter-clockwise) is traced. The two main spectral states (hard vs. soft) are clearly identified by vertical branches, while horizontal branches in the central part of the diagram identify the transition between them. The whole outburst follows a **hysteresis cycle** that moves through the following spectral states [Miyamoto et al. 1995]: (i) **the low-hard state** (LHS), which defines the start and the end of the outburst and is characterised by large variability (in the form of a broad-band noise) and hard spectrum; (ii) **the hard-intermediate state** (HIMS), which covers part of the region after the LHS and when the sources comes back from the soft state. Flux from the thermal disc appears in the optical range while the hard component steepens and the PDS shows type C QPOs. The centroid frequency of the QPO is tightly correlated with the spectral state, rising from a few mHz in the LHS to  $\sim 10$  Hz in the intermediate state, showing occasionally up to  $\sim 30$  Hz in the soft state; (iii) **the soft intermediate state** (SIMS), characterised by the replacement of the broad-band noise component by a weaker power law (with lower fractional rms), together with a switch from type C to type B QPOs; and (iv) **the high soft state** (HSS), with a soft spectrum from an optically thick disc that shows low variability. The transition from HIMS to SIMS is historically known as the **jet-line** because jets suffer important morphological changes. This was traditionally associated to the launching of ballistic ejections as the source

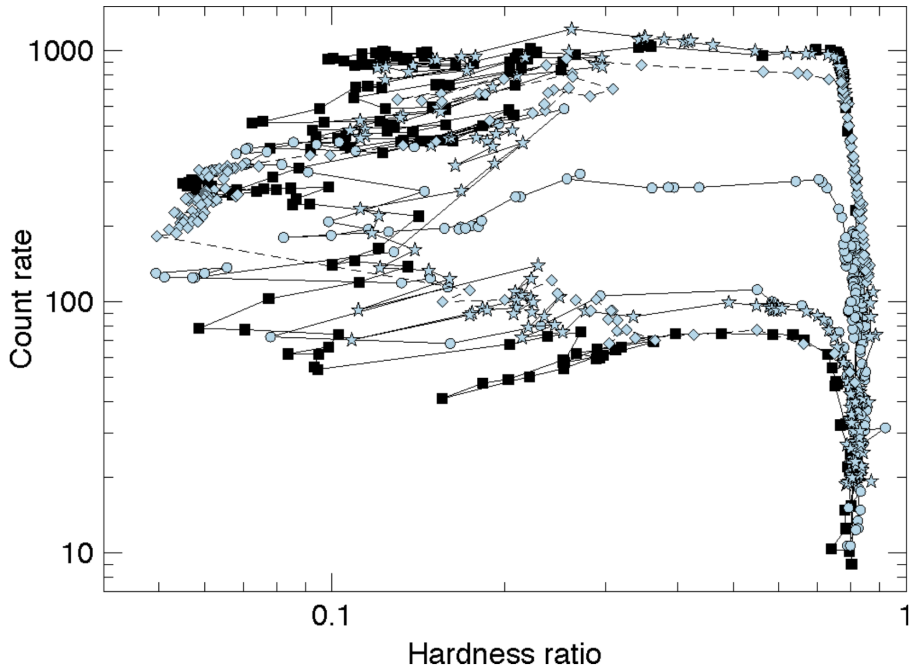


Figure 1.11 Hardness-Intensity diagram for four outbursts of GX 339-4 observed with RXTE, showing a q-shape pattern. From Belloni 2018 (Fig. 1.6).

transits from a steady jet scenario to jet quenching in the HSS. Type-A QPOs also appear in this state, after the spectral transition.

**Disc-jet coupling** Coordinated radio and X-ray observations of BH binaries in the hard state have revealed that radio and X-ray luminosities are correlated over three orders of magnitude in X-ray power [Corbel et al. 2003], from quiescent up to the transition to the soft state. Indeed, a fundamental plane has been identified [Merloni, Heinz, and di Matteo 2003] in the radio-X-ray luminosity diagram ( $L_R - L_X$ ), on which a single non-linear relation (i.e., a power law  $L_R \propto L_x^\beta$ ) can describe the dependences between BH mass, X-ray and radio luminosity, considering all BHs (including also supermassive BHs in AGN) for which these three quantities can be measured. This relation, which is also scale invariant over more than five orders of magnitude in the BH mass, suggests a strong physical connection between the accretion flow, responsible for the X-ray emission, and the relativistic jets. This is usually referred as the **disc-jet coupling**.

The situation becomes more complicated when considering a group of BHXBs (with high fluxes) that seem to follow a different correlation in the  $L_R - L_X$  plane. This established a dichotomy between two different branches [Gallo, Miller, and Fender 2012, Bassi et al. 2019, but see also Gallo et al. 2014]: a radio-quiet branch and a radio-loud branch, although the distinction is not as clear as originally thought, with sources moving from one branch to the other [Coriat et al. 2011] or following a significantly steeper path [Russell et al. 2015]. In the case of NSs, the distribution in the  $L_R - L_X$  plane appears more scattered than in BHs and it is more difficult to interpret [Tetarenko et al. 2016], although Gallo, Degenaar, and van den Eijnden 2018 also proposed a single-track population for both systems with different coefficients of the power law.

A unified model for BHXBs was established by Fender, Belloni, and Gallo 2004, where radio emission correlates with the position in the q-diagram in the following way (Fig. 1.12):

- In the quiescent state, where binaries spent most of their life, only a weak flat spectrum has been detected. When the outburst starts and the source climbs in the HID towards higher luminosities, the radio flux also increases (with a strong positive non-linear correlation, as previously mentioned), showing a flat spectrum compatible with self-absorbed synchrotron emission. This can be interpreted as a compact jet propagating outwards with mildly relativistic speeds ( $\Gamma < 2$ ).

- After peaking in luminosity, the motion in the HID becomes more horizontal as the source enters the HIMS. The hardness ratio decreases, but the steady jet persists with a similar coupling as in the hard state.

- As the source approaches the jet line, the radio flux peaks and the physical properties of the compact jet change dramatically. During the transition from HIMS to SIMS, the emission is no longer steady, but shows either resolved radio knots or bright radio flares, and the Lorentz factor increases ( $\Gamma > 2$ ). Radio flares occur in most sources for extended periods of time and are also associated with strong X-ray flaring activity. As introduced before, it is still unclear if this transition is related with a jet that undergoes a real physical transition from a continuous outflow to discrete ejecta [van der Laan 1966, Tetarenko et al. 2017], or if faster material creates internal shocks through the slower-moving jet [Klein-Wolt et al. 2002, Kaiser, Sunyaev, and Spruit 2000, Fender et al. 2023].

- The HSS is characterised by the absence of radio emission, which suggests that the jet is quenched during the spectral transition [Coriat et al. 2011], or less likely, turns radiatively dark. Multiple transitions between the SIMS/HIMS in which the jet appears and disappears are observed in some sources.

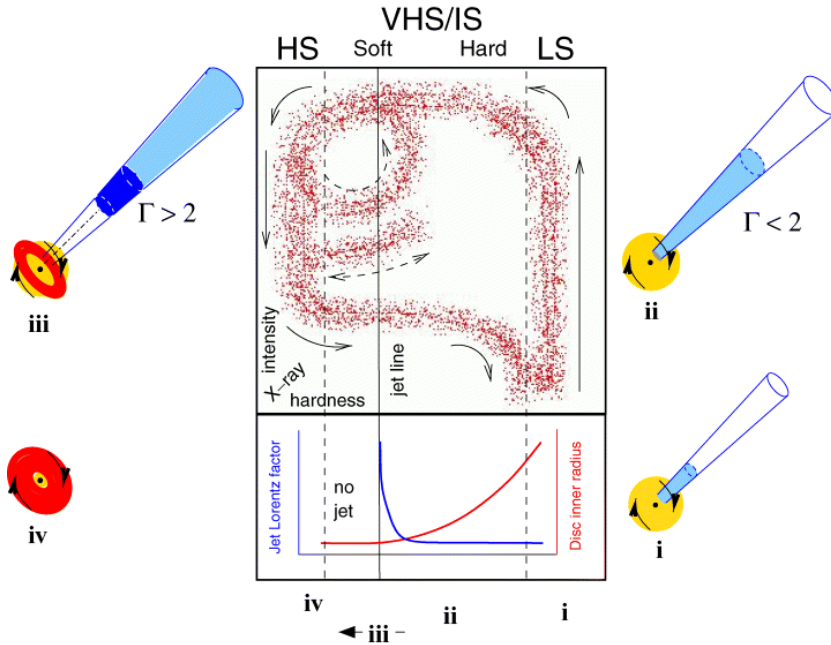


Figure 1.12 A schematic representation of the simplified model for the jet-disc coupling in black hole binaries. Reproduced with permission from Fender, Belloni, and Gallo 2004 (Fig. 7).

- Although Fender, Belloni, and Gallo 2004 propose that the jet is reactivated as the source crosses the jet line from the soft to the hard state, Kalemci et al. 2013, Kalemci et al. 2014 suggest that the jet reappearance is not coincident with the transition, but it happens when the system has reached the LHS.

## 1.4.2 Neutron Star XRBs

From the point of view of their spectral properties, NSXBs can be classified in three different groups: Z-type NSXBs, atoll-type NSXBs and weak low-mass NSXBs [Hasinger and van der Klis 1989].

**Z-type NSXBs** Z-type NSXBs are the most luminous, with accretion rates that represent a significant fraction of the Eddington limit ( $0.5L_{Edd} < L < L_{Edd}$ ), similar to bright BH transients. The name of these type of NSXBs is related with the particular 'Z' shape that they trace in the CD diagram on time-scales that can be as short as hours to days. The three branches of the trace are called, from top to bottom, Horizontal Branch (HB), Normal Branch (NB) and Flaring Branch (FB; see right panel of Fig. 1.13), where the transitions among them

are physically related with specific spectral changes and the mass accretion rate, which increases from the HB to FB. A hard apex separates the HB and NB, and a soft apex separates the NB and the FB. Z sources are rapidly variable in X-rays, tracing the whole Z track on time scales from hours to days in an apparent random, but continuous way. The number of known Z-type XRBs is small, where Sco X-1, GX 17+2, GX 349+2, Cyg X-2, GX 5-1, GX 340+0 are the only confirmed sources of this kind [plus Cir X-1 which also shows some Z-like properties Shirey, Bradt, and Levine 1999]. Z sources also show rapid variability in the radio band, where optically thin flares are frequently observed. Moreover, Sco X-1 [Fomalont, Geldzahler, and Bradshaw 2001a] and Cir X-1 [Fender et al. 2004] show extended radio lobes, where underlying URFs have also been inferred (see Sec. 1.2.3.4). Penninx et al. 1988 first identified in GX 17+2 that the radio emission varies as the source changes its position in the CD, decreasing while increasing the mass accretion rate from HB to FB. A similar behaviour was found in other sources, for example Cyg X-2 [Hjellming et al. 1990b] or Sco X-1 [Hjellming et al. 1990a]. Migliari and Fender 2006 showed that while a Z-source is moving through the HB towards the NB, the radio power increases, where radio emission can be related with a compact radio jet similar to BHXBs in the LH state. As the source moves from the HB to NB, the radio power decreases and a transient jet is launched. Finally, in the FB, jets are typically quenched [Bradshaw, Geldzahler, and Fomalont 2003], establishing a connection with the soft state of BH transients.

**Atoll-type NSXBs** These type of NS binaries are less luminous than the Z-type sources, with luminosities that can range from a few percent of the Eddington limit ( $\sim 0.01L_{Edd}$ ) to a considerably, but moderate, fraction ( $\sim 0.5L_{Edd}$ ). The shape traced in the CD diagram is also distinctive (Fig. 1.13, left panel), with a harder island state (IS; hard state) and a softer banana state (BS; soft state). The number of known atoll sources is much higher than the Z class. They share many spectral and timing properties with BHXBs, although only a few have been detected at radio wavelengths. A significant fraction of atoll sources spend most of their life in quiescent state and only occasionally go into outburst activity. Hysteresis cycles have also been resolved in these systems [Maccarone and Coppi 2003, Muñoz-Darias et al. 2014].

**Weak low-mass NSXBs** This group is formed by millisecond pulsars, faint bursters and faint transients, although many of these sources can also exhibit properties compatible with low-luminosity atoll-type NSs. They show very low

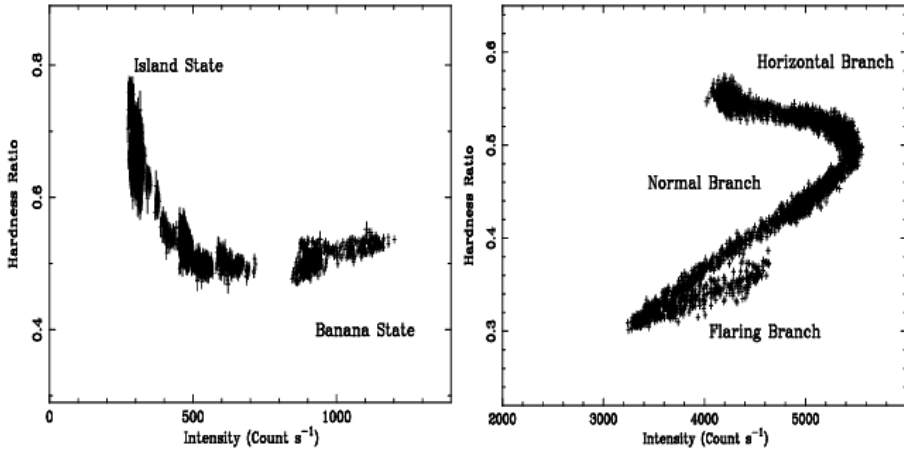


Figure 1.13 Typical hardness-intensity diagrams. Left: an atoll source 4U 0614+091 showing the island and banana states and right: a Z-track source GX 340+0 showing the Horizontal, Normal and Flaring Branches. Reproduced with permission from Church, Gibiec, and Bałucińska-Church 2014 (Fig. 1).

X-ray luminosities, far below the Eddington rate ( $L < 0.01L_{Edd}$ ).

In NS systems, spectral and timing analysis of Z and atoll sources revealed a tight relation between the timing properties of the source and the position in the CD, suggesting that both are determined by the same physical parameters and/or have a common origin.

In Z-type sources, the division is similar to that of BH systems (although the phenomenology is more complex), but the nomenclature of QPOs is related with the spectral state of the binary in the CD: flaring branch oscillations (FBOs), normal branch oscillations (NBOs) and horizontal branch oscillations (HBOs). These have been suggested to be the NS equivalent of the aforementioned type A, type B and type C QPOs found in BH binaries, respectively (see Fig. 1.10, right panel). The characteristic frequency of the QPO varies smoothly along the CD [Psaltis, Belloni, and van der Klis 1999], increasing from the HB to FB (Fig. 1.14).

The classification in atoll sources is similar, although as shown by Motta et al. 2017, the equivalent of NBOs is not present. In the hard state of both BH and NS atoll sources, a flat-top noise component is also present in the PDS, which eventually decreases in amplitude as the source moves from the hard to the soft state and the LF QPOs shifts to higher frequencies. As in the case of Z sources, the characteristic frequency of QPOs increases smoothly from the IS to BS.

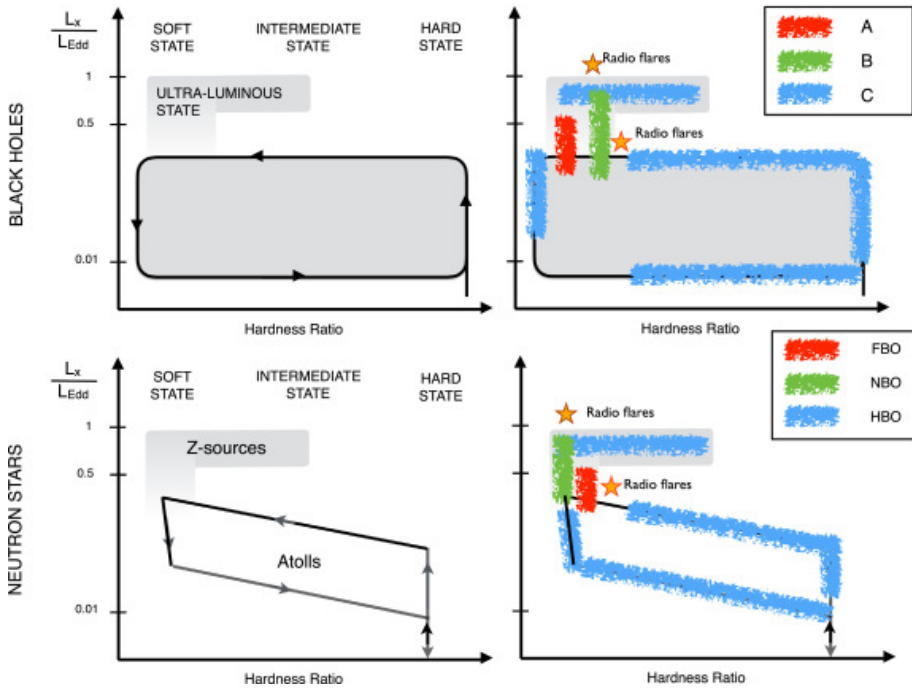


Figure 1.14 Schematic description of the behavior of BH (upper) and NS (lower) systems in a HID, showing the characteristic location of LF QPOs. Reproduced with permission from Ingram and Motta 2019 (Fig. 2).

In summary, as already mentioned, regardless of the nature of the CO in the binary, each spectral state is characterised (and thus can be distinguished) by a particular subspace of timing features. For example, in the previous section I stated that type B QPOs appear in the SIMS, while type C QPOs are present in the hard or HIMS. In NSs, the characteristic frequency of the QPO varies smoothly when the source moves along the different branches in the CD, increasing from the HB to the FB in Z-sources and from the IS to the BS in atoll sources.

## 1.5 Numerical simulations of XRBs/microquasar outflows: an overview

Despite the current capability of high-performance computing (HPC) architectures, numerical simulations of jets in XRBs/microquasars have been barely addressed. This is probably because, in binary systems, jets are not typically ob-

served as extended structures (with only a few exceptions, as mentioned before), but inferred from radio-to-mid-IR flat spectrum, so the direct comparison with observables is more challenging. However, understanding the basic principles that govern the jet dynamics in these sources is also essential to characterise the system behaviour and its interaction with the medium, even though jets are not spatially resolved. To this aim, numerical simulations are strongly needed.

Beyond the field of XRBs, numerical simulations have been typically devoted to study extragalactic relativistic outflows, from the formation by MHD mechanisms in general relativity [see e.g., McKinney and Blandford 2009, Tchekhovskoy, Narayan, and McKinney 2011, McKinney, Tchekhovskoy, and Blandford 2012, Porth 2013, Cruz-Ororio et al. 2021, Liska et al. 2022] to the morphological characterisation at kilo-parsec scales, both of powerful Fanaroff-Riley (FR) II jets [e.g., Martí et al. 1997, Komissarov and Falle 1998, Aloy et al. 1999, Scheck et al. 2002, Mignone et al. 2010, Massaglia et al. 2016, English, Hardcastle, and Krause 2016, Mukherjee et al. 2020, Seo, Kang, and Ryu 2021, Perucho, Quilis, and Martí 2011, Perucho et al. 2014a, Perucho, Martí, and Quilis 2019, Perucho, Martí, and Quilis 2022], low-power, FRI jets [e.g. Perucho and Martí 2007, Rossi et al. 2008, Perucho et al. 2014a, Massaglia et al. 2016, Massaglia et al. 2019, Massaglia et al. 2022], or Hercules A-like sources, showing ambiguous classification [Nakamura et al. 2008, Saxton, Bicknell, and Sutherland 2002, Perucho et al. 2023]. An extensive review on numerical simulations of jets from AGN is provided by Martí 2019. Some of these simulations also consider the dynamical role of magnetic fields on jet propagation [Komissarov 1999b, Leismann et al. 2005, Mignone, Massaglia, and Bodo 2005, Keppens et al. 2008, Komissarov, Porth, and Lyutikov 2015, Martí 2015b, Moya-Torregrosa et al. 2021, Mignone et al. 2010, Massaglia et al. 2022, Guan, Li, and Li 2014, Mizuno, Hardee, and Nishikawa 2007] .

At large scales, relativistic plasmas are well described by the equations of relativistic (magneto)hydrodynamics (R(M)HD), a collection of partial differential equations that can be formulated as a system of hyperbolic conservation laws. In the absence of analytic solutions, these equations are solved in a numerical grid employing finite difference or finite volumes approaches. The former are based on the differential form of the conservation equations and evolve point values of the state vectors in time, while the latter employ the integral form of the conservation laws and cell average values. In particular, the development of the so-called high-resolution shock capturing methods initiated a revolution on the field of numerical R(M)HD simulations, given its extraordinary properties of accuracy and convergence, and the ability to handle discontinuous solutions

such as shock waves. On Chapter 2 of the thesis, I will provide a deep revision of the state-of-the-art numerical methods to solve the equations of RMHD.

In the rest of the section, I will review past work on XRB simulations, from the propagation of relativistic jets in microquasars to the interaction of the stellar wind with the pulsar wind in a non-accreting pulsar system.

### 1.5.1 Microquasar jets: the binary and beyond

The most relevant line of work on microquasar jets consists of a series of papers that studied jet-wind interactions in HMXBs by means of RHD simulations, which were originally published more than one decade ago [Perucho and Bosch-Ramon 2008, Perucho, Bosch-Ramon, and Khangulyan 2010, Perucho and Bosch-Ramon 2012]. Perucho and Bosch-Ramon 2008 performed two-dimensional numerical simulations of jets crossing the stellar wind of the massive companion, showing the formation of strong recollimation shocks that can accelerate particles and produce non-thermal emission. Similar results, but with three-dimensional (3D) hydrodynamical simulations, were found by Perucho, Bosch-Ramon, and Khangulyan 2010. In this work, the authors confirmed that jets with total power  $L_j < 10^{36}$  erg s<sup>-1</sup> can be disrupted by the impact of the stellar wind (with the imposed wind conditions), impeding the radio-band detection of this particular population of XRBs at large scales. Later, Perucho and Bosch-Ramon 2012 analysed the effect of the wind clumpiness on the steady jet dynamics and found significant differences in the flow stability and disruption degree when inhomogeneities were considered, even in jets with luminosities  $L_j \sim 10^{37}$  erg s<sup>-1</sup>.

Numerical calculations of the high-energy emission from one clump-jet interaction were also performed by de la Cita et al. 2017, who predicted that these interactions may collectively dominate the non-thermal radiation. Yoon and Heinz 2015 developed non-relativistic simulations to derive an analytic formula for the asymptotic jet bending and applied it to two well-known systems, Cyg X-1 and Cyg X-3. This work was then extended by Yoon, Zdziarski, and Heinz 2016 and Bosch-Ramon and Barkov 2016.

More recently, Charlet et al. 2022 analysed the dynamical and structural effects of radiative losses in those two fiducial binaries. They performed large-scale 3D RHD simulations using the PLUTO code [Mignone et al. 2007], focusing on jet outbreak and early propagation, and found that radiative cooling effects are more relevant for the parameters space of Cyg X-3 than of Cyg X-1.

In a different line of work, Barkov and Bosch-Ramon 2022 used 3D hydrodynamical simulations to study the combined effect of stellar winds and orbital

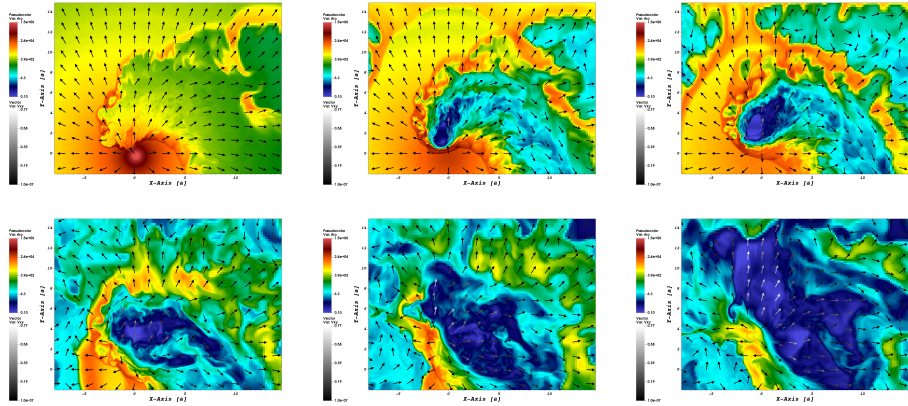


Figure 1.15 Coloured density maps and velocity vector distribution for relativistic jet simulations considering the binary orbital motion. Reproduced with permission from Barkov and Bosch-Ramon 2022 (Fig. 7).

motion on the scales of the binary and beyond, showing that even jets with power  $L_j \sim 10^{37}$  erg s $^{-1}$ , which were barely affected by the stellar wind impact [Perucho, Bosch-Ramon, and Khangulyan 2010], can be disrupted on scales  $\sim 1$  AU (Fig. 1.15).

Nevertheless, all the numerical simulations mentioned above neglect the dynamical effect of the magnetic fields on the flow evolution, thus assuming that jets are kinetically dominated on the scale of the binary and beyond. Jets are thought to be magnetically dominated close to the CO (i.e., a Poynting flux), and accelerated up to (mildly) relativistic speeds by MHD and/or thermal processes (e.g., L. Ricci et al, submitted, 2023, for the case of AGN jet simulations), where jets can also be mass-loaded from the disc or the stellar wind. Therefore, we expect the kinetic energy to dominate the total jet power at the scale of the binary, but it is still unclear to which extent even a relatively weak magnetic field can affect the jet dynamical evolution, either by favouring jet collimation or triggering more instabilities [see e.g., Massaglia et al. 2022, for the case of FRI radio sources]. Moreover, even moderately weak magnetic fields can be locally reinforced and thus play an important role in shaping the non-thermal emission of the jet by casting particle acceleration, cooling, and/or triggering synchrotron radiation. On the other hand, it is also possible that magnetic dissipation might not be as efficient as generally expected, and thus jets can still be near equipartition on the scale of the binary. These two possibilities, together with the effects of magnetic fields on the jet dynamics and the long-term stability,

will be addressed for the first time by means of dedicated 3D RMHD simulations in Chapter 5 of this thesis (originally published in López-Miralles et al. 2022).

### 1.5.2 A special source: the microquasar SS 433

Another set of studies –that can be considered a self-contained line of research– are devoted to reproducing the dynamics and jet-ISM interactions of the exotic microquasar SS 433 (a brief introduction to this source is provided on Sec. 1.6). This system shows powerful bipolar precessing mildly relativistic jets with dynamical properties that are unique among other galactic binaries.

Even more than twenty years ago, Muller and Brinkmann 2000 performed the first low-resolution, non-relativistic, time-dependent 3D hydrodynamical simulations of the SS 433 precessing jets, showing the development of highly complex structures and instabilities and the deceleration of the jet head.

More than one decade later, Monceau-Baroux et al. 2014 performed 3D RHD simulations of SS 433 sub-parsec jets to show that the best match with the existing radio images was achieved by using the canonical propagation speed,  $v = 0.26 c$ , and a precession angle of  $20^\circ$ , in good agreement with the observed parameters of the source. The apparent discrepancy between sub-parsec and parsec scales was also addressed by means of long-term hydrodynamical simulations in Monceau-Baroux et al. 2015, considering that jets interact with the SNR W50 (Fig. 1.16). In this work, the authors showed that precessing jets with an angle of  $20^\circ$  can naturally recollimate into a continuous non-precessing hollow flow due to pure hydrodynamical processes, providing a tentative explanation for the system morphology at large distances. Some years later, Bowler and Keppens 2018 deduced fundamental scaling relations to extend the computations in Monceau-Baroux et al. 2014 and Monceau-Baroux et al. 2015 to lower densities and pressures of the ambient medium, finding that SS 433 jets could be responsible for the large scale morphology of the system. Indeed, other authors focused on reproducing the W50 elongated shell morphology, relying either on the jet interaction with the SNR [Velázquez and Raga 2000, Zavala et al. 2008, Goodall, Alouani-Bibi, and Blundell 2011] or on the jet MHD processes [Ohmura et al. 2021].

The formation of relativistic jets under super-Eddington accretion rates, as suggested for SS 433, was also addressed by means of general relativistic radiation magnetohydrodynamics (Rad-RMHD) simulations. For example, in Sądowski and Narayan 2015 the authors performed a set of simulations of super-critical accretion onto a supermassive non-rotating BH, where accretion takes the form

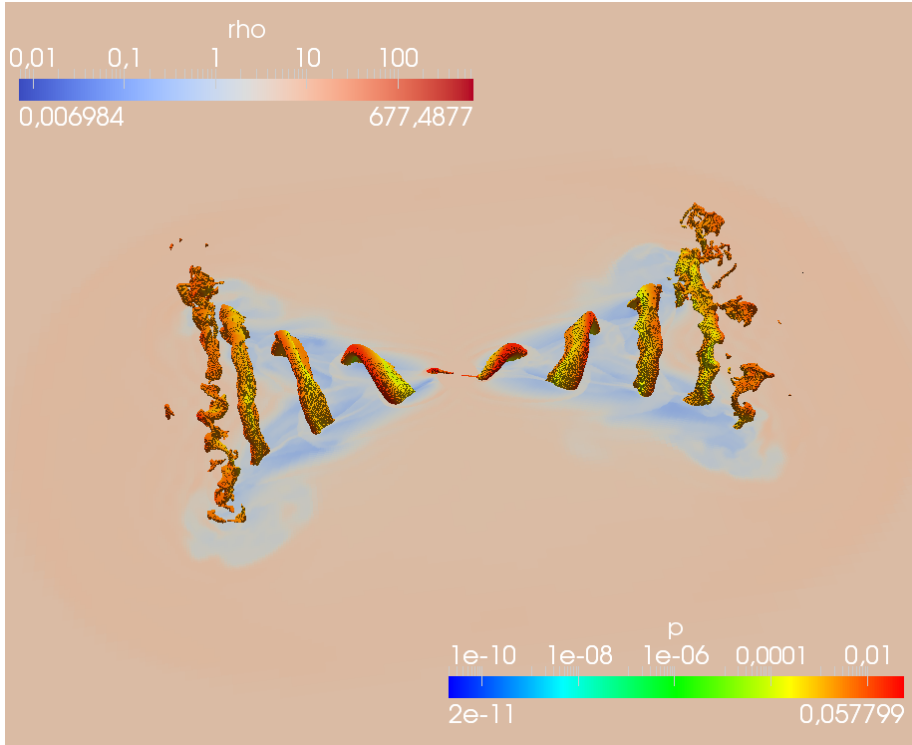


Figure 1.16 Overall view of the large simulation of SS433 zoomed to the scale reached at  $t = 6.5$  years, i.e.  $0.1$  pc. The jet volume is rendered using the tracer to locate the jet. The jet volume is coloured with the pressure. The two-dimensional cut shows the proper density. Reproduced with permission from Monceau-Baroux et al. 2015 (Fig. 1), ©ESO.

of a geometrically thick disc dominated by the radiation pressure. The results show that photons from the disc can flow into the funnel (which is optically thick) and accelerate the plasma up to  $v \sim 0.3 c$ , compatible with the jet velocity observed in the source. The radiation-driven jet obtained in the simulation is, however, characterised by an opening angle ( $\theta \sim 15^\circ$ ) that differs significantly from the highly collimated outflows (i.e.  $\theta < 5^\circ$ ) observed in SS 433 (Fig. 1.17). This fact reveals that either an additional collimating agent is not operating in the simulation (possibly related with the magnetic field configuration), or that the precessing jet launching mechanism differs from the assumed radiatively driven outflow.

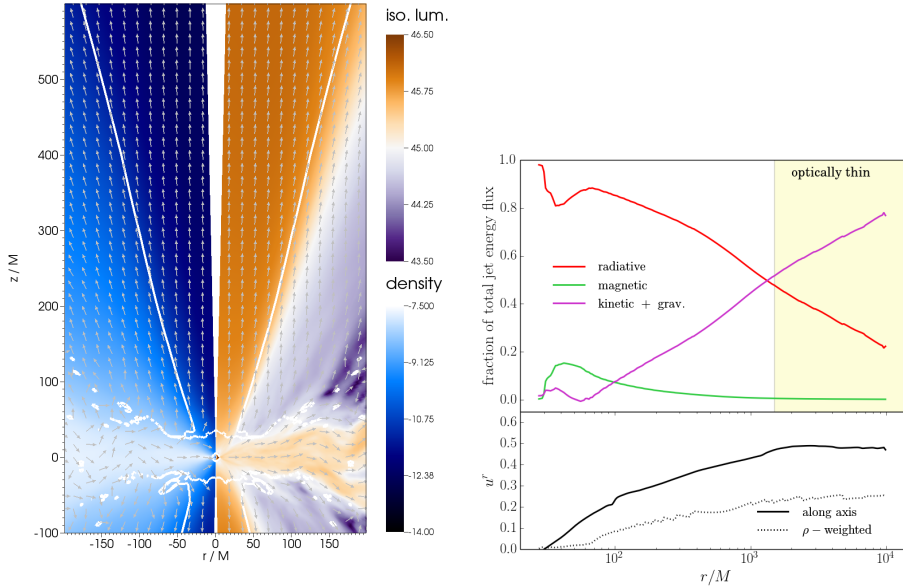


Figure 1.17 Left: logarithmic density+velocity field (arrows) and logarithmic isotropic equivalent luminosity of total energy+energy flux (arrows). Right: fractional contribution of different energy channels (radiative, kinetic+gravitational, magnetic) in the jet flow, showing the conversion of radiation energy into kinetic energy. The bottom panel shows the radial gas velocity in the jet axis. Reproduced with permission from Sądowski and Narayan 2015 (Fig. 2 and Fig. 3).

### 1.5.3 Pulsars and colliding winds

Another scenario that received attention from the simulation community in the last years is the interaction of the stellar wind of a massive star with the wind of a non-accreting pulsar (Fig. 1.18), since it has been proposed to explain, together with accretion and jet ejection, the origin of high-energy emission in  $\gamma$ -ray emitting binaries. The relativistic pulsar wind and the non-relativistic stellar outflows interact all along the orbit, producing ultrarelativistic particles that radiate from radio to  $\gamma$ -rays.

During the last decades, this scenario has been widely accepted as a plausible model to explain most of the observables in  $\gamma$ -ray binaries, such as the orbital dependency of X-ray and  $\gamma$ -ray emission, or the flaring activity observed at particular orbital phases. However, the interaction of winds is a complex phenomenon that depends on several variables, such as the physical properties of the pulsar, and the characteristics of the stellar wind, just to name some examples. Thus, 3D numerical simulations are essential to understand these

physical processes. In the following, I summarise the main contributions to the field.

Romero et al. 2007 performed non-relativistic smoothed particle hydrodynamics simulations (including the effects of orbital motion) for both pulsar wind-stellar wind collision and accretion jet models, and confronted them in the context of the  $\gamma$ -ray binary LS I +61 303, concluding that the microquasar model seemed to be more appropriate. The same type of simulations, but for the system PSRB1259-63/LS 2883 were performed by Okazaki et al. 2011. Bogovalov et al. 2008 and Bogovalov et al. 2012 performed, respectively, HD and MHD axisymmetric simulations of colliding winds, taking into account relativistic effects, but neglecting orbital motions. The latter aspect was addressed some years later in Bosch-Ramon et al. 2012 and Bosch-Ramon, Barkov, and Perucho 2015, where by means of RHD simulations along one single orbit, the authors showed that shocks, instabilities and mass-loading yield to efficient mass, momentum and energy exchange between both winds in the interaction region (Fig. 1.18). In Bosch-Ramon et al. 2012, in addition to the pulsar-wind shock facing the star, the simulations revealed additional sites of non-thermal activity, as the strong shocks *behind* the pulsar [see also Bosch-Ramon and Barkov 2011]. These same type of simulations were later applied by Bosch-Ramon et al. 2017 to explain the non-thermal orbital phenomenology of the system HESS J0632+057. The role of the eccentricity on the evolution of colliding winds was addressed by Barkov and Bosch-Ramon 2021 by means of quasi-3D numerical simulations in spherical coordinates (i.e., 2.5D), showing that low eccentricity systems were more favorable for wind mixing. The impact of the high pulsar wind magnetisation on the geometrical structure of the shocked flow was addressed by Bogovalov et al. 2019. Recently, Barkov, Kalinin, and Lyutikov 2022 presented new RMHD simulations taking into account various possible pulsar geometries [Barkov, Lyutikov, and Khangulyan 2019] and wind trust ratios. The feedback of pulsars on their environment on large scales has also been addressed by several numerical studies [Vigelius et al. 2007, Porth 2013, Barkov, Lyutikov, and Khangulyan 2019, Barkov and Lyutikov 2019].

## 1.6 X-ray binary/microquasar population

There are approximately  $\sim 500$  XRBs detected in the Galaxy, distributed according to the mass of the companion star [Liu, van Paradijs, and van den Heuvel 2005, Liu, van Paradijs, and van den Heuvel 2006, Liu, van Paradijs, and van den Heuvel 2007]; in the case of HMXBs, due to the short lifetime of the

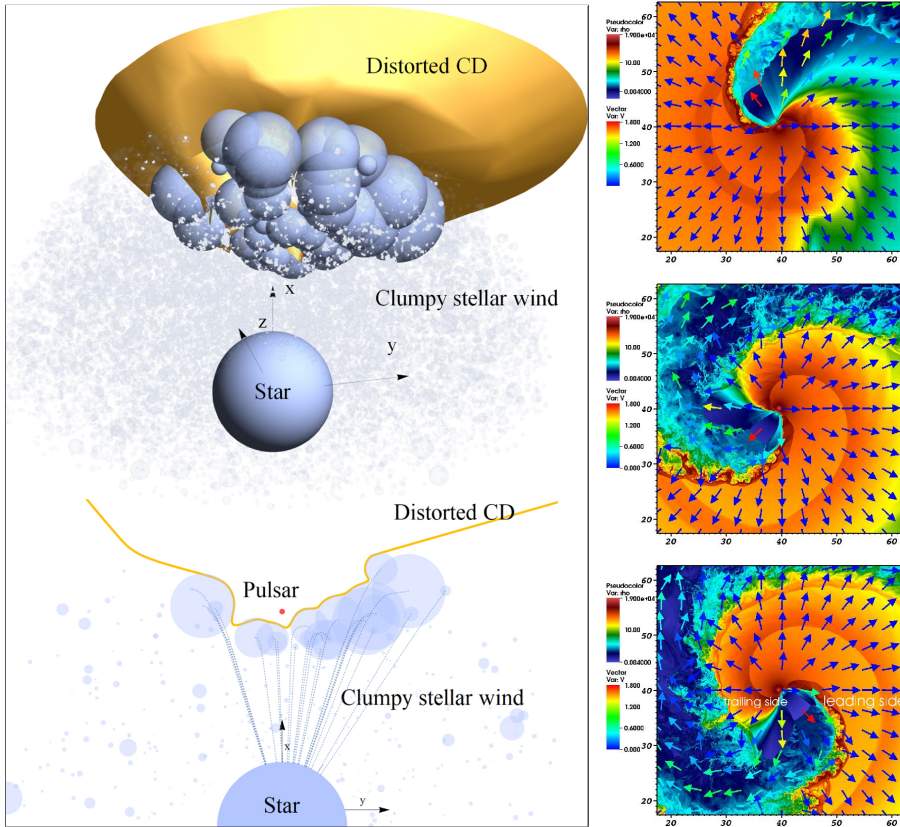


Figure 1.18 Left: Three-dimensional schematic (top) and two-dimensional cut (bottom) of the physical scenario comprising a massive star with a clumpy stellar wind and a pulsar. Reproduced with permission from Kefala and Bosch-Ramon 2023 (Fig. 1). Right: Density distribution at different times in a simulations of stellar/pulsar-wind interaction along one full orbit. Reproduced with permission from Bosch-Ramon et al. 2012 (Fig. 4), ©ESO.

donor star, the systems appear associated with young stellar populations and are mainly placed in the star-forming regions of the galactic disc, while LMXBs appear associated with an older stellar population in the galactic bulge and in globular clusters. The Magellanic Clouds contain very few LMXBs, but have a rich population of HMXBs. The most up to date catalogues for both HMXBs and LMXBs are given in Neumann et al. 2023 and Avakyan et al. 2023, showing respectively 168 and 348 sources (Fig. 1.19).

In this last section of the Introduction, I present a brief description of a small selection of BH and NSXBs that are relevant for the purposes of this thesis, either directly or indirectly.

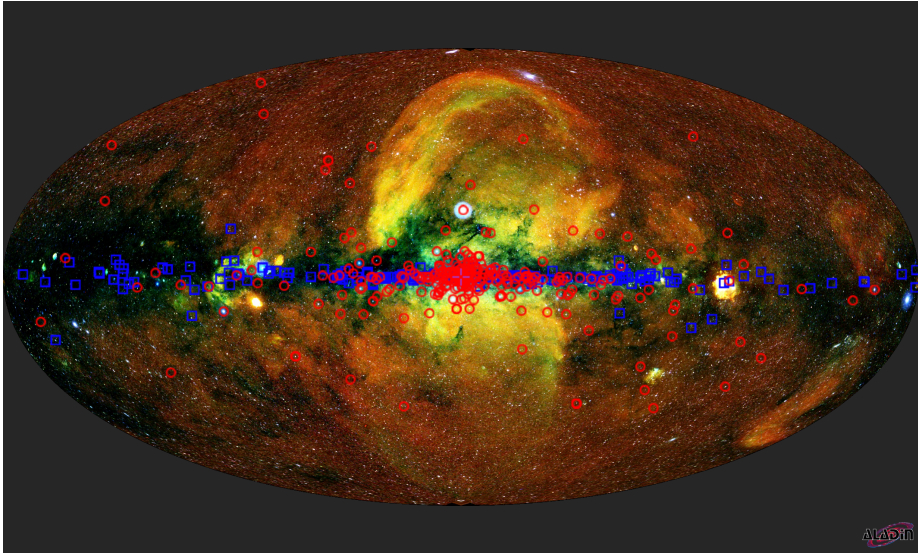


Figure 1.19 HMXBs [blue squares; Neumann et al. 2023] and LMXB [red circles; Avakyan et al. 2023] catalogue sources overlaid on the eRosita sky map. From <http://astro.uni-tuebingen.de/xrbcat/>.

### 1.6.1 BH X-ray binaries

**Cyg X-1** The source Cyg X-1 is one of the most studied microquasars in the Galaxy and was the first system widely accepted to host a stellar-mass BH [Shipman 1975] accreting matter from an O-type supergiant star [Gies and Bolton 1986]. In a recent publication [Miller-Jones et al. 2021], the mass of the BH was constrained to be  $21.2 \pm 2.2 M_{\odot}$ , higher than previous estimates and well above other galactic BHXBs. The system is located at a distance  $\sim 2.22$  kpc [Miller-Jones et al. 2021], has an almost circular orbit with period of 5.6 days and reaches luminosities  $L > 10^{37}$  erg/s. Moreover, contrary to other BHXBs, it usually appears in a canonical LH state [e.g., Ling et al. 1983, Fender et al. 2000], showing a flat radio spectrum compatible with a steady compact jet [Stirling et al. 2001], while only occasional transitions to the soft state (with no compact jet) have been detected [Grinberg et al. 2011, Grinberg et al. 2015]. While radio emission remains rather stable with only occasional flaring episodes [20–30% of the average flux density; Fender 2006], fast episodes of X-ray flux variation by a factor  $\sim 3 - 30$  have been detected at different timescales [Gierliński and Zdziarski 2003]. In 2006 [Albert et al. 2007], Cyg X-1 became the first stellar-mass BH found to display evidence of  $\gamma$ -ray emission in the VHE (above 100 GeV). The powerful jets from the source are thought to

inflate a bubble in the surrounding medium [Gallo et al. 2005, Russell et al. 2007], where the shocked heated ISM is observed through thermal Bremsstrahlung radiation from radio to optical wavelengths. The study of this interaction (for example, in Gallo et al. 2005) revealed a larger jet power than that inferred from direct observations of the compact jet, which could reveal the presence of large amounts of cold protons in the jet, or that the power driving the ISM shell is related with other type of outflows in the system such as winds [Heinz 2006].

**Cyg X-3** The microquasar Cyg X-3 is also a persistent, bright radio and X-ray source, but contrary to Cyg X-1, it hosts a WR companion that confers the system with unique behaviour [van Kerkwijk et al. 1996]. Occasionally, Cyg X-3 undergoes giant radio outbursts, when it becomes the brightest galactic radio source [Waltman et al. 1996]. These outburst are seen when the source moves from the soft state to the hard state, something unusual in this kind of systems [Koljonen et al. 2010]. During the outburst, a one-sided relativistic jet with multiple knots has been resolved by Very Long Baseline Interferometry (VLBI) observations [Mioduszewski et al. 2001]. Interestingly, outbursts are preceded by the so-called hyper-soft state, a radio quiet period [Koljonen et al. 2018]. This binary is also a  $\gamma$ -ray source [Fermi LAT Collaboration et al. 2009], mainly on the transition from/to the hyper-soft state. All these properties are expected to be connected with the short orbital separation and the powerful winds driven by the WR star in which the CO is embedded.

**V404 Cyg** The source V404 Cyg is a variable BHXB located in the constellation of Cygnus that shows strong variability. It first jumped to prominence during a moderately fast nova explosion in 1938. Approximately 50 years later, the Japanese X-ray satellite Ginga (together with high-energy instruments on board the MIR Space station) detected a new eruption [Kitamoto et al. 1989]. Further inspection of the historical data revealed two other possible outbursts that were previously unnoticed, in 1956 and 1979 [Richter 1989]. More recently, when the Swift satellite detected signs of renewed activity on June 2015, the source caught again the attention of the scientific community. The INTEGRAL  $\gamma$ -ray observatory monitored the outburst two days later, detecting repeated extraordinary bright flares [Rodriguez et al. 2015]. During the peak of the outburst, Miller-Jones et al. 2019 also conducted a high-angular resolution radio monitoring of V404 Cyg with the Very Long Baseline Array (VLBA). In this paper, the authors reported on a rapidly changing jet orientation on timescales shorter than an hour which can be interpreted as Lense-Thirring precession

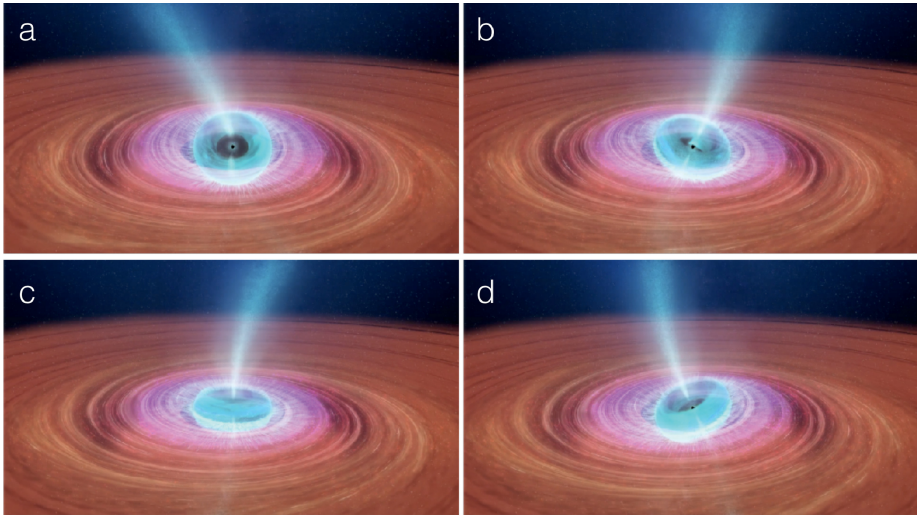


Figure 1.20 Schematic illustration of the precessing inner flow model. Reproduced with permission from Ingram and Motta 2019 (Fig. 14) and adapted from an animation made by ICRAR in association with Miller-Jones et al. 2019.

(Fig. 1.20), as supported by numerical simulations of tilted accretion discs [Liska et al. 2018].

**SS 433** The system SS 433 is one of the most powerful and exotic star systems in our Galaxy. It is an eclipsing HMXB located at a distance of  $\sim 5.5$  kpc [Blundell and Bowler 2004, line of sight  $\sim 78^\circ$ ] formed by a CO (a stellar-mass BH or a NS) orbiting a companion supergiant ( $\sim 30 M_\odot$ ). The main property that characterises SS 433 with respect to other binaries is the presence of a continuous regime of supercritical accretion [see e.g., Fabrika 2004, for a review] that exceeds by far the Eddington limit. This accretion power also feeds bipolar, narrow ( $< 5^\circ$ ), regular precessing ( $\theta \sim 20^\circ$ ,  $P \sim 162$  days,  $P_{nut} \sim 6$  days), mildly-relativistic jets ( $v \sim 0.26c$ ), as inferred from Doppler-shifted optical emission lines. The system is also the first galactic binary to reveal the presence of baryonic matter in the relativistic outflows by Doppler-shifted iron emission lines from spatially resolved regions [Migliari, Fender, and Méndez 2002]. These outflows are resolved in a wide range of spatial scales at all wavelengths, from X-rays near the binary core ( $\sim 10^{10-13}$  cm) to radio emission ( $\sim 10^{15-17}$  cm), where the projection of the jets in the plane of the sky shows a characteristic twisted trace (see Fig. 1.21). Extended X-ray emission has also been inferred by Chandra observations at sub-parsec scales ( $\sim 10^{17}$  cm). I address the characterisation of the jet dynamics and the magnetic field structure in these

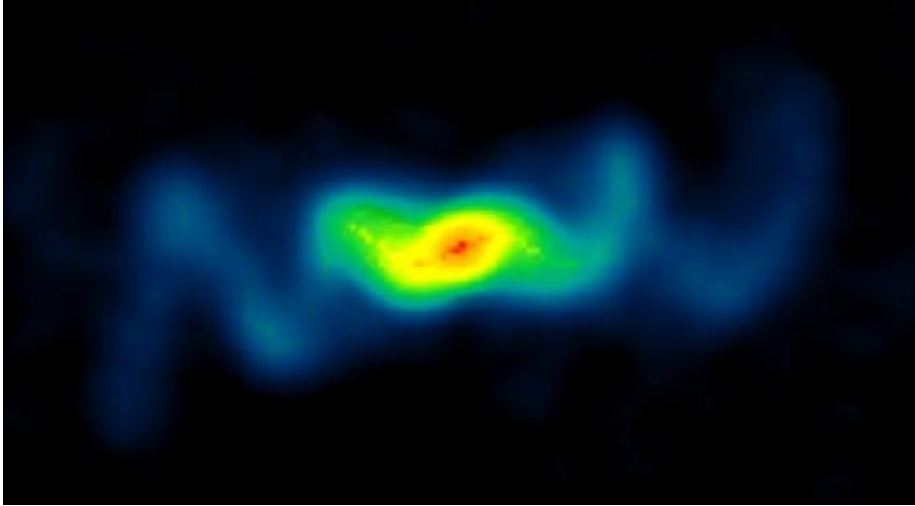


Figure 1.21 VLA Image of the microquasar SS433. Credit: Blundell&Bowler, NRAO/AUI/NSF.

regions by means of large-scale numerical simulations in Chapter 6 of the thesis. Further out from the binary core, jets are not detected until distances of tens of parsecs where termination shocks are observed, presumably while the outflows deform the W50 nebula (see Fig. 1.5).

**GRS 1915+105** GRS 1915+105 (also known as V1487 Aquilae) is a well-known XRB star system hosting a BH, which, together with Cyg X-1, is one of the heaviest stellar-mass BHs known in the Galaxy [ $\sim 12.4 M_{\odot}$ , Reid et al. 2014]. The system was discovered on 1992 by the WATCH all-sky monitor aboard GRANAT [Castro-Tirado et al. 1994], and in 1994, a campaign of Very Large Array (VLA) observations resolved superluminal motions in unusually bright bipolar discrete plasma clouds, ejected after a violent burst in X-rays and  $\gamma$ -rays [Mirabel and Rodríguez 1994]. GRS 1915+105 then became the first known galactic source that ejects material with apparent superluminal velocities, a phenomenon that was previously exclusive for quasar jets. Mirabel and Rodríguez 1999 showed that the apparent asymmetries in the brightness and the displacement of two plasma clouds could be naturally explained in terms of the relativistic effect known as relativistic aberration, as long as plasma bullets are ejected in an antisymmetric way with  $v \sim 0.98 c$ . These apparent superluminal motions were later observed with higher angular resolution with the MERLIN array [Fender et al. 1999].

**GRS 1758-258** The system GRS 1758-258 is a LMXB and is one of the brightest objects in hard X-rays in the vicinity of the Galactic centre. It was first detected by GRANAT/SIGMA [Sunyaev et al. 1991] and over many decades the source has captured the attention of many other instruments at different wavelengths. In particular, observations in the radio band show two clearly extended lobes [Rodríguez, Mirabel, and Martí 1992]. Martí et al. 2015 also showed that the large scale radio jets of GRS 1758-258 displayed significant morphological changes (in a time scale of years), which were related with instabilities in the jet and interaction with the ISM [Luque-Escamilla, Martí, and Martínez-Aroza 2020]. This source was also the first microquasar to resolve a cocoon-like shell around the jet [Martí et al. 2015], establishing a new similarity between microquasars and radio galaxies that had not been observed before [Martí et al. 2017].

### 1.6.2 NS X-ray binaries

**Scorpius X-1** The XRB Sco X-1 is one of the most studied XRBs since its discovery in 1962 [Giacconi et al. 1962], and the brightest extrasolar X-ray source in the sky, located at a distance of  $2.8 \pm 0.3$  kpc [Bradshaw, Fomalont, and Geldzahler 1999] in the constellation of Scorpius. It is classified as a LMXB with an orbital period of 18.9 h [Gottlieb, Wright, and Liller 1975], containing a later than K4 spectral type companion star ( $0.28M_{\odot} < M < 0.70M_{\odot}$ ) and a weakly magnetised NS with mass  $< 1.73 M_{\odot}$  [Steeghs and Casares 2002, Mata Sanchez et al. 2015]. Regarding the spectral properties of the binary, it is one of the clearest examples of Z-type sources, showing extended radio emission, spatially resolved at sub-milliarcsecond scales [Fomalont, Geldzahler, and Bradshaw 2001b]. Correlations of flares in the core and in the lobes revealed the existence of an underlying burst of energy that propagates in the jet with  $v > 0.95 c$  [Fomalont, Geldzahler, and Bradshaw 2001a, Fomalont, Geldzahler, and Bradshaw 2001b], which has recently been associated with the simultaneous appearance of two particular types of QPOs in the X-ray PDS [Motta and Fender 2019].

**4U 0614+091** This system, which was discovered by the Uhuru survey [Forman et al. 1978], is classified as a NS LMXB, and it is located at a distance of 3.2 kpc [Kuulkers et al. 2010]. Given the ultra-short orbital period of the binary [ $\sim 50$  min Shahbaz et al. 2008], it is also classified as an Ultra Compact XRB [Juett, Psaltis, and Chakrabarty 2001], possibly hosting an out-of-main sequence companion star [Kuulkers et al. 2010]. From the point of view of its spectral behaviour, it is a persistent atoll source that spends most of the time in

the hard state, only showing sporadic transitions to softer states [Muñoz-Darias et al. 2014]. Spectral modelling of 4U 0614+091 also shows the so-called hard-tail component [Piraino et al. 1999], whose origin is controversial, but can be modelled either by thermal Comptonization of low-energy photons on electrons having a very high temperature, or as a non-thermal power-law. The existence of a compact jet was proposed by Migliari et al. 2010 based on the derived flat radio-to-mid-IR spectrum.

**Circinus X-1** Cir X-1 is a NS LMXB that shows regular 16.6 day radio and X-ray flares [Whelan et al. 1977]. The spectral properties of the source are very peculiar, since, at different epochs, Cir X-1 approaches the behaviour of an atoll source, a Z source, or none of the above [Oosterbroek et al. 1995, Shirey et al. 1998, Soleri et al. 2009], although Shirey, Bradt, and Levine 1999 found time segments on RXTE observations that clearly demonstrated evolution along the HB, NB and FB of a Z-type NS LMXB. Thus, Cir X-1 can be classified as a peculiar Z-type source. This erratic behaviour is related with the fact that Cir X-1 is one of the youngest NS LMXB [Heinz et al. 2013]. Relativistic outflows have also been detected at different wavelengths and temporal scales [Fender et al. 1998, Heinz et al. 2007], where underlying unseen URFs (similar to Sco X-1) have been inferred between the time delay of radio core flaring and re-brightening of the downstream plasma [Fender et al. 2004, Tudose et al. 2008, but see also Miller-Jones et al. 2012].

**LS I +61 303** The HMXB LS I +61 303 consists of a CO with an eccentric orbit ( $e \approx 0.7$ ) around a rapidly rotating B0 Ve type star [Casares et al. 2005], whose orbital period is  $P_1 = 26.496 \pm 0.0028$  days [Gregory 2002]. The nature of the CO in LS I +61 303 is still unclear, although the recent discovery of radio pulsations by Weng et al. 2022 suggests that the system is powered by a NS. LS I +61 303 has been detected in a wide range of wavelengths, from radio [i.e., non-thermal synchrotron, see e.g., Gregory and Taylor 1978] to X-rays [see e.g., Bignami et al. 1981], as well as at HE, at GeV [Abdo et al. 2009], and VHE, at TeV [Albert et al. 2006]. It is therefore one of the very few  $\gamma$ -ray emitting binaries [see e.g., Mirabel 2007, Chernyakova and Malyshev 2020, and references therein], together with other few canonical systems such as LS 5039, HESS J0632+057 or 1FGL J1018.6-5856. Two main competing scenarios have been proposed to explain the multi-wavelength observations of the source, with a special focus on the origin of the non-thermal emission: accretion onto a CO and jet ejection (i.e., a NS or BH microquasar, as first proposed by Taylor and

Gregory 1982), or the interaction of a non-accreting pulsar with the wind of the companion star [first proposed by Maraschi and Treves 1981].

## 1.7 Outline

This thesis is organised as follows:

**PART I.- Numerical methods and code development** (Chapters 2, 3, 4). In this first block, I present the numerical codes that I have developed during the thesis to be run in HPC facilities (*Servei d'Informàtica de la Universitat de València, Red Española de Supercomputación*). Our tool, named LÓSTREGO, has two main implementations: (1) a RMHD module (Chapter 2) and (2) a Rad-RMHD module (Chapter 3). In the first two chapters, I describe the system of equations solved with the code, the numerical methods I have implemented and the testing benchmark I performed to validate the algorithms. Finally, in Chapter 4, I summarise the main conclusions of Part I and I present open projects, future work and new implementations to upgrade the current numerical methods and the overall code capabilities.

**PART II.- Numerical simulations of XRBs** (Chapters 5, 6, 7). This second block can be considered the main part of the thesis, as it contains the first numerical simulations performed with our new code LÓSTREGO in supercomputing facilities to study relativistic outflows in XRBs/microquasars. In Chapter 5, I study the interaction of jets with the powerful stellar winds driven by the companion in a HMXB, focusing on the role of magnetic fields in the jet dynamics and the long-term stability. In Chapter 6, I present the results of a large project performed within the Spanish Supercomputer Network to simulate the sub-parsec dynamics of the precessing jets in the microquasar SS 433, including for the first time the dynamical evolution of magnetic fields and the role of discrete blob collisions in the overall dynamics of the source. Finally, in Chapter 7, I summarise the main conclusions of Part II and I present ongoing projects and future applications of our code.

**PART III.- Timing analysis of XRBs** (Chapters 8, 9, 10). In this last block, I present the results of two projects I performed during the thesis in the field of X-ray data analysis, with a special focus on timing techniques. In Chapter 8, I analyse the whole RXTE archive of the  $\gamma$ -ray binary LS I +61 303, employing a phase-folding approach to enhance the statistics of the original data. In Chapter

9, I study the NS LMXB Sco X-1 using NICER observations, which provides high quality data for timing analysis. Finally, in Chapter 10, I summarise the main conclusions of Part III and I present ongoing projects and future work.

**APPENDIX.-** (Appendix A, B) In the appendices, I present a collection of research articles that I have co-authored during the development of this thesis. In Appendix A, I present my contribution to the field of AGN jet hydrodynamical simulations, while in Appendix B, I summarise an article where we applied X-ray timing techniques in the context of multi-wavelength spectral modelling of a NS LMXB.

## Part I

# Numerical methods and code development



# Chapter 2

## Relativistic magnetohydrodynamics

---

This chapter was originally published in the appendix of *J. López-Miralles, M. Perucho, J.M-Martí, S. Migliari and V. Bosch-Ramon. 3D-RMHD simulations of jet-wind interactions in high-mass X-ray binaries. Astronomy&Astrophysics, Volume 661, id.A117, 28 pp. May 2022. DOI:10.1051/0004-6361/202142968. Reproduced with permission, ©ESO.*

---

In this chapter, I present LÓSTREGO, a new computational tool for simulating astrophysical relativistic plasmas in one (1D), two (2D), and three dimensional (3D) Cartesian coordinates. The code is entirely written in the FORTRAN programming language and solves the conservative equations of special relativistic magnetohydrodynamics (RMHD) in finite volumes (FV). It is especially designed to run in multiple cores to exploit the capacity of modern parallel architectures. LÓSTREGO is based on the high-resolution shock-capturing (HRSC) methods that have been probed to be robust and accurate in other similar codes [see, e.g., Martí and Müller 2015, and references therein], extending the techniques implemented in Martí 2015b to three spatial dimensions. Essentially, the algorithm follows the reconstruct-solve-average strategy: first, cell-average primitive variables are reconstructed to the cell interfaces, where a Riemann problem is then solved

numerically by any approximate Riemann solver. Once fluxes are known at each cell face, the conserved variables are evolved explicitly in time using total variation diminishing (TVD) Runge-Kutta algorithms. Finally, an inversion scheme is applied to recover the primitive variables from the time-evolved solution. Several one-dimensional and multidimensional tests are presented at the end of the chapter to prove the ability of the new code to solve classical problems in the field of RMHD.

## 2.1 Basic equations

The RMHD system of partial differential equations in the Minkowski metric<sup>1</sup> and Cartesian coordinates can be written as a system of conservation laws [Komissarov 1999a],

$$\partial_t \mathbf{U} + \partial_i \mathbf{F}^i = 0, \quad (2.1)$$

where  $\mathbf{U} = \{D, S^j, \tau, B^j\}$  is a vector of conserved variables, and  $\mathbf{F}^i$  are the vector of fluxes for each spatial direction. Both the vector of conserved variables  $\mathbf{U}$  and the vector of fluxes  $\mathbf{F}^i$  can be expressed in terms of a set of primitive variables  $\mathbf{V} = \{\rho, v^j, p, B^j\}$  using the following relations:

$$\mathbf{U} = \begin{pmatrix} D \\ S^j \\ \tau \\ B^j \end{pmatrix} = \begin{pmatrix} \rho W \\ \rho h^* W^2 v^j - b^0 b^j \\ \rho h^* W^2 - p^* - b^0 b^0 - \rho W \\ B^j \end{pmatrix}, \quad (2.2)$$

$$\mathbf{F}^i = \begin{pmatrix} \rho W v^i \\ \rho h^* W^2 v^i v^j + p^* \delta^{ij} - b^i b^j \\ \rho h^* W^2 v^i - b^0 b^i - \rho W v^i \\ v^i B^j - B^i v^j \end{pmatrix}, \quad (2.3)$$

where  $D$  is the relativistic rest mass density,  $S^j$  is the momentum density of the magnetised fluid,  $\tau$  is the energy density measured in the Eulerian frame,  $\delta^{ij}$  is the Kronecker delta and  $W = 1/\sqrt{1 - \mathbf{v}^2}$  is the Lorentz factor. The set of primitive variables are the fluid rest-mass density  $\rho$ , fluid three-velocity  $v_j$ , and gas pressure  $p$ . The magnetic field vector  $B^j$  is at the same time primitive and conserved variable, so the conversion from one set to the other is trivial. In Eqs.

<sup>1</sup>We assume a metric signature  $(-, +, +, +)$ . Greek subscripts in 4-vectors run from 0 to 3. Latin indices run from 1 to 3. In the following, we use a system of units where  $c = 1$  and a factor of  $1/\sqrt{4\pi}$  is absorbed in the definition of the magnetic field.

2.2 and 2.3 we introduced the hydromagnetic specific enthalpy  $h^*$ ,

$$h^* = h + \frac{b^\alpha b_\alpha}{\rho} = 1 + \epsilon + \frac{p}{\rho} + \frac{|b|^2}{\rho}, \quad (2.4)$$

where  $\epsilon$  is the specific internal energy. The total pressure  $p^*$  of the magnetic fluid is given by

$$p^* = p_g + p_{\text{mag}} = p + \frac{|b|^2}{2}. \quad (2.5)$$

In terms of the vectors  $\mathbf{v}$  and  $\mathbf{B}$  in the laboratory frame, the four-velocity  $u^\alpha$  and magnetic field  $b^\alpha$  covariant vectors are

$$u^\alpha = W(1, \mathbf{v}), \quad (2.6)$$

$$b^0 = W(\mathbf{v} \cdot \mathbf{B}), \quad (2.7)$$

$$b^i = \frac{B^i}{W} + v^i b^0, \quad (2.8)$$

with the normalizations

$$u^\alpha u_\alpha = -1, \quad u^\alpha b_\alpha = 0, \quad (2.9)$$

$$|b|^2 = b_\alpha b^\alpha = \frac{B^2}{W^2} + (\mathbf{v} \cdot \mathbf{B})^2, \quad (2.10)$$

where summation over repeated indices is assumed. The time evolution of the system of equations of classical and relativistic MHD must also preserve the magnetic field divergence-free constraint,

$$\nabla \cdot \mathbf{B} = 0. \quad (2.11)$$

Finally, the system of RMHD equations is closed with an equation of state (EoS) of the form

$$p = p(\rho, \epsilon), \quad (2.12)$$

which relates the thermodynamic primitive variables with each other. For the particular case of ideal gases, this relation becomes

$$p = (\Gamma - 1)\rho\epsilon, \quad (2.13)$$

where  $\Gamma$  is the adiabatic index. This index should be set as  $\Gamma = 5/3$  for non-relativistic or mildly relativistic flows and as  $\Gamma = 4/3$  in the ultra-relativistic limit.

## 2.2 Numerical methods

### 2.2.1 Spatial and temporal discretization

We have implemented multidimensional HRSC methods following the FV strategy and dimensional splitting, taking the integral form of the conservation laws (Eq. 2.1) and cell-averaged values. This means that operators that involve spatial derivatives are applied dimension by dimension, permuting the spatial coordinates cyclically. Eq. 2.1 admits a conservative semi-discretization in a rectangular grid of size  $L_x \times L_y \times L_z$  and resolution  $N_x \times N_y \times N_z$ ,

$$\begin{aligned} \frac{dU_{i,j,k}}{dt} = & -\frac{1}{\Delta x} \left( \hat{\mathbf{F}}_{i+1/2,j,k}^x - \hat{\mathbf{F}}_{i-1/2,j,k}^x \right) \\ & -\frac{1}{\Delta y} \left( \hat{\mathbf{F}}_{i,j+1/2,k}^y - \hat{\mathbf{F}}_{i,j-1/2,k}^y \right) \\ & -\frac{1}{\Delta z} \left( \hat{\mathbf{F}}_{i,j,k+1/2}^z - \hat{\mathbf{F}}_{i,j,k-1/2}^z \right), \end{aligned} \quad (2.14)$$

where  $\{i, j, k\}$  is the position of each cell center, and  $\{i \pm 1/2, j \pm 1/2, k \pm 1/2\}$  is the position of the right and left cell interface, respectively. The elements  $\Delta x = L_x/N_x, \Delta y = L_y/N_y, \Delta z = L_z/N_z$  are the cell sizes for each spatial dimension. As mentioned before, in the FV formalism, the conserved variables represent an approximation to the average over the cell volume,

$$U_{i,j,k}^n = \frac{1}{\Delta x \Delta y \Delta z} \int_{z_{k-1/2}}^{z_{k+1/2}} \int_{y_{j-1/2}}^{y_{j+1/2}} \int_{x_{i-1/2}}^{x_{i+1/2}} U(x, y, z, t) dx dy dz, \quad (2.15)$$

while the numerical fluxes represent an approximation to the space-time average in the surface of the cell,

$$\hat{\mathbf{F}}_{i+1/2,j,k}^x = \frac{1}{\Delta y \Delta z \Delta t} \int_{z_{k-1/2}}^{z_{k+1/2}} \int_{y_{j-1/2}}^{y_{j+1/2}} \int_{t^n}^{t^{n+1}} \mathbf{F}^x(x_{i+1/2}, y, z, t) dy dz dt, \quad (2.16)$$

$$\hat{\mathbf{F}}_{i,j+1/2,k}^y = \frac{1}{\Delta x \Delta z \Delta t} \int_{z_{k-1/2}}^{z_{k+1/2}} \int_{x_{i-1/2}}^{x_{i+1/2}} \int_{t^n}^{t^{n+1}} \mathbf{F}^y(x, y_{j+1/2}, z, t) dx dz dt, \quad (2.17)$$

$$\hat{\mathbf{F}}_{i,j,k+1/2}^z = \frac{1}{\Delta y \Delta x \Delta t} \int_{x_{i-1/2}}^{x_{i+1/2}} \int_{y_{j-1/2}}^{y_{j+1/2}} \int_{t^n}^{t^{n+1}} \mathbf{F}^z(x, y, z_{k+1/2}, t) dy dx dt. \quad (2.18)$$

### 2.2.2 Spatial cell reconstruction

To advance the set of conserved variables in time, numerical fluxes must be known at cell interfaces, where the latter are functions of the primitive variables. These

are reconstructed from cell-centred values by means of interpolation routines that are designed to reconstruct a piece-wise polynomial approximation inside each cell preserving the monotonicity and Total Variation (TV)-stability properties of the algorithm. Consistently with our dimensional splitting, reconstruction is performed in one dimension following each spatial coordinate. The current version of LÓSTREGO admits either Godunov (zero-th order) or linear (first order) spatial reconstruction. The piece-wise linear method (PLM) in the  $x$ -direction follows

$$\mathbf{V}(x, t^n) = \mathbf{V}_i^n + s_i^n(x - x_i), \quad (2.19)$$

where  $s_i^n$  is the linear slope at cell  $i$ . Similar expressions hold for the  $y, z$  spatial directions. The most popular slope limiters are MinMod [Fig. 2.1, left; Roe 1986a], MC [monotonised central difference limiter, Fig. 2.1, right; van Leer 1977], and VanLeer [Leer 1974]. The slope  $s_i^n$  is given by:

- MINMOD:

$$s_i^n = \frac{1}{\Delta x} \text{minmod}(\mathbf{V}_i^n - \mathbf{V}_{i-1}^n, \mathbf{V}_{i+1}^n - \mathbf{V}_i^n) \quad (2.20)$$

where the minmod function picks the argument that has a smaller modulus if all of them have the same sign, or is otherwise zero. This means that MinMod reconstruction takes the least steep among the two slopes provided by the backward and forward finite differences.

- MC (monotonised central difference limiter):

$$s_i^n = \frac{1}{\Delta x} \text{minmod} \left[ \frac{\mathbf{V}_{i+1}^n - \mathbf{V}_{i-1}^n}{2}, 2(\mathbf{V}_i^n - \mathbf{V}_{i-1}^n), 2(\mathbf{V}_{i+1}^n - \mathbf{V}_i^n) \right] \quad (2.21)$$

- VANLEER:

$$s_i^n = \frac{2}{\Delta x} \frac{\max(0, (\mathbf{V}_i^n - \mathbf{V}_{i-1}^n)(\mathbf{V}_{i+1}^n - \mathbf{V}_i^n))}{\mathbf{V}_{i+1}^n - \mathbf{V}_{i-1}^n} \quad (2.22)$$

These limiters avoid the generation of spurious extrema at cell interfaces and reduce the accuracy of the method to first order at extrema with a vanishing slope. Although conserved variables can be directly reconstructed to cell interfaces, we interpolate the primitive variables since experience has shown that this is more robust than the former approach. If the PLM reconstruction leads to nonphysical situations in which  $\mathbf{v}^2 > 1$ , we reduce the method to first order (i.e., Godunov reconstruction). High-order schemes like the Monotonicity Preserving (MP) reconstruction [Suresh and Huynh 1997] are also available in the code, and have been tested in the context of RMHD on Chapter 3 of the thesis.

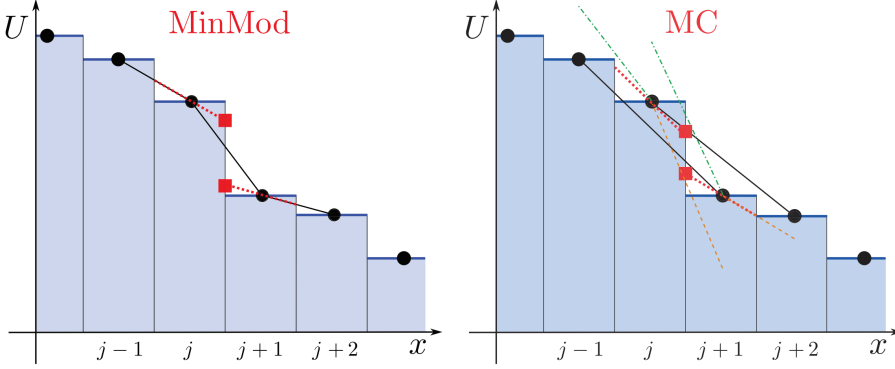


Figure 2.1 Schematic representation of the MinMod (left panel) and the MC (right panel) slope limiter. Reproduced from Rezzolla and Zanotti 2013 with permission of The Licensor through PLSclear (Fig. 9.4, page 429).

### 2.2.3 Numerical fluxes and the Riemann problem

When the cell-centred primitive variables are spatially reconstructed to obtain  $\mathbf{V}_{i+1/2}^L, \mathbf{V}_{i+1/2}^R$  (i.e., the values of  $\mathbf{V}$  at the left and right sides of the interface  $i + 1/2$ ), computation of numerical fluxes requires solving a Riemann problem at each zone edge:

$$\mathbf{U}(\mathbf{V}(x, 0)) = \begin{cases} \mathbf{U}(\mathbf{V}^L)_{i+1/2} & \text{if } x < x_{i+1/2} \\ \mathbf{U}(\mathbf{V}^R)_{i+1/2} & \text{if } x > x_{i+1/2}. \end{cases} \quad (2.23)$$

Although exact Riemann solvers exist in the literature for RMHD [Giacomazzo and Rezzolla 2006], this step usually involves upwind strategies based on approximate solutions. The current version of LÓSTREGO includes three different approximate solvers of the Harten-Lax-van Leer (HLL) family: HLL [Harten, Lax, and Leer 1983], HLLC [Mignone and Bodo 2006], and HLLD [Mignone, Ugliano, and Bodo 2009]. Jacobian-free Riemann solvers based on internal approximations to the Polynomial Viscosity Matrix are also included in the code and will be tested on Chapter 3 of the thesis against the HLL family.

In the collection of nonlinear solvers pertaining to the HLL class, the solution is approximated by  $N < 7$  waves that travel with characteristic speeds  $\lambda_{k+1} > \lambda_k, k = 1, \dots, N - 1$ , separated by  $N + 1$  intermediate states. To obtain the characteristic speed of the outermost waves in the Riemann fan (i.e., the fast magnetosonic waves), which are the maximum and minimum eigenvalues of the Jacobian matrix of the left and right states, we need to find the roots of a quartic equation employing a root-finder numerical method [see, e.g., Anile 1989, Antón

et al. 2010]:

$$C_4\lambda^4 + C_3\lambda^3 + C_2\lambda^2 + C_1\lambda + C_0 = 0, \quad (2.24)$$

where coefficients  $C$  are given by:

$$\begin{aligned} C_0 &= (v^x)^4(1 - \Omega^2) - \frac{(v^x)^2\Omega^2}{W^2} + \frac{(b^x)^2c_s^2}{(\rho h + |b|^2)W^4}, \\ C_1 &= -4(v^x)^3(1 - \Omega^2) + \frac{2v^x\Omega^2}{W^2} - \frac{2b^0b^xc_s^2}{(\rho h + |b|^2)W^4}, \\ C_2 &= 6(v^x)^2(1 - \Omega^2) - \frac{(1 - (v^x)^2)\Omega^2}{W^2} + \frac{((b^0)^2 - (b^x)^2)c_s^2}{(\rho h + |b|^2)W^4}, \\ C_3 &= -4v^x(1 - \Omega^2) - \frac{2v^v\Omega^2}{W^2} + 2\frac{2b^0b^xc_s^2}{(\rho h + |b|^2)W^4}, \\ C_4 &= 1 - \Omega^2|v|^2 - \frac{(b^0)^2c_s^2}{(\rho h + |b|^2)W^4}, \end{aligned} \quad (2.25)$$

where  $\Omega^2 = c_s^2 + c_a^2 - c_s^2c_a^2$  and  $c_a^2 = |b|^2/(\rho h + |b|^2)$  is the Alfvén speed.

As the number of waves and intermediate states increases, the diffusion of the method is reduced, and thus we can obtain more accurate representations of the real solution.

Figure 2.2 shows a typical Riemann fan representing all different states in the three approximate solvers of the HLL family. In HLL ( $N = 2$ ), which is the simplest method, the initial discontinuity is decomposed in two fast magnetosonic waves with characteristic speeds  $\lambda_L, \lambda_R$ :

$$\hat{\mathbf{F}}_{i+1/2} = \begin{cases} \mathbf{F}_L, & \text{if } \lambda_L > 0, \\ \mathbf{F}_{i+1/2}^{\text{hll}}, & \text{if } \lambda_L \leq 0 \leq \lambda_R, \\ \mathbf{F}_R, & \text{if } \lambda_R < 0. \end{cases} \quad (2.26)$$

such that the internal flux in the fan,  $\mathbf{F}_{i+1/2}^{\text{hll}}$ , can be derived from the Rankine-Hugoniot jump conditions across the magnetosonic waves:

$$\begin{aligned} \mathbf{F}_L^{\text{hll}} &= \mathbf{F}_L + \lambda_L(\mathbf{U}^{\text{hll}} - \mathbf{U}_L) \\ \mathbf{F}_R^{\text{hll}} &= \mathbf{F}_R + \lambda_R(\mathbf{U}^{\text{hll}} - \mathbf{U}_R), \end{aligned} \quad (2.27)$$

where  $\mathbf{U}^{\text{hll}}$  is given by:

$$\mathbf{U}^{\text{hll}} = \frac{\lambda_R\mathbf{U}_R - \lambda_L\mathbf{U}_L + \mathbf{F}_L - \mathbf{F}_R}{\lambda_R - \lambda_L}. \quad (2.28)$$

By substituting Eq. 2.28 into Eq. 2.27, the HLL flux becomes:

$$\mathbf{F}_{i+1/2}^{\text{hll}} = \frac{\lambda_R\mathbf{F}_L - \lambda_L\mathbf{F}_R + \lambda_R\lambda_L(\mathbf{U}_R - \mathbf{U}_L)}{\lambda_R - \lambda_L}, \quad (2.29)$$



### 2.2.4 Time integration

When numerical fluxes are resolved at cell interfaces, conserved variables can be advanced one time step following Eq. 2.14 and predictor-corrector methods. In our scheme, numerical time integration is based on second and third-order TVD Runge-Kutta (RK) time integrators described by Shu and Osher 1989. The second-order method (RK2) follows

$$\begin{aligned} U^{(1)} &= U^{(0)} + \Delta t L(U^{(0)}) \\ U^{(2)} &= U^{(0)} + \frac{1}{2} \Delta t L(U^{(0)}) + \frac{1}{2} \Delta t L(U^{(1)}), \end{aligned} \quad (2.30)$$

while the third-order method (RK3) is given by

$$\begin{aligned} U^{(1)} &= U^{(0)} + \Delta t L(U^{(0)}) \\ U^{(2)} &= U^{(0)} + \frac{1}{4} \Delta t L(U^{(0)}) + \frac{1}{4} \Delta t L(U^{(1)}) \\ U^{(3)} &= U^{(0)} + \frac{1}{6} \Delta t L(U^{(0)}) + \frac{1}{6} \Delta t L(U^{(1)}) + \frac{2}{3} \Delta t L(U^{(2)}), \end{aligned} \quad (2.31)$$

where in both cases  $L(U^{(n)})$  is the upwind differencing operator,

$$\begin{aligned} L(U^{(n)}) &= -\frac{1}{\Delta x} \left( \hat{\mathbf{F}}_{i+1/2,j,k}^x - \hat{\mathbf{F}}_{i-1/2,j,k}^x \right) \\ &\quad -\frac{1}{\Delta y} \left( \hat{\mathbf{F}}_{i,j+1/2,k}^y - \hat{\mathbf{F}}_{i,j-1/2,k}^y \right) \\ &\quad -\frac{1}{\Delta z} \left( \hat{\mathbf{F}}_{i,j,k+1/2}^z - \hat{\mathbf{F}}_{i,j,k-1/2}^z \right). \end{aligned} \quad (2.32)$$

### 2.2.5 Divergence-free constraint

In general, HRSC methods do not preserve the divergence-free condition given by Eq. 2.11. This can produce numerical artificial forces that can lead to incorrect solutions and the eventual failure of the code. Thus, different approaches exist to control the solenoidal condition in RMHD codes [see e.g., Tóth 2000, Martí and Müller 2015, and references therein]. The most popular approaches are the eight-wave method [Powell 1994], the hyperbolic-parabolic divergence cleaning [Dedner et al. 2002], the projection scheme [Brackbill and Barnes 1980], and the constrained transport method [CT; Evans and Hawley 1988, Ryu et al. 1998, Balsara and Spicer 1999]. The latter has been proved to be robust and accurate because it guarantees that the divergence-free constraint is fulfilled up to machine round-off errors by definition, preserving the divergence of the initial setup during the simulation. Thus, it is the only scheme we have implemented in LÓSTREGO. The method was originally proposed by Evans and Hawley 1988

and adapted to Godunov-type Riemann solvers by Ryu et al. 1998, Balsara and Spicer 1999. The main characteristic of this approach is that it requires the introduction of a staggered representation of the magnetic field at cell interfaces, which is evolved according to a semi-discrete version of the induction equation,

$$\frac{dB_{i+1/2,j,k}^x}{dt} = \frac{\hat{\Omega}_{i+1/2,j+1/2,k}^z - \hat{\Omega}_{i+1/2,j-1/2,k}^z}{\Delta y} - \frac{\hat{\Omega}_{i+1/2,j,k+1/2}^y - \hat{\Omega}_{i+1/2,j,k-1/2}^y}{\Delta z}, \quad (2.33)$$

$$\frac{dB_{i,j+1/2,k}^y}{dt} = \frac{\hat{\Omega}_{i,j+1/2,k+1/2}^x - \hat{\Omega}_{i,j+1/2,k-1/2}^x}{\Delta z} - \frac{\hat{\Omega}_{i+1/2,j+1/2,k}^z - \hat{\Omega}_{i-1/2,j+1/2,k}^z}{\Delta x}, \quad (2.34)$$

$$\frac{dB_{i,j,k+1/2}^z}{dt} = \frac{\hat{\Omega}_{i+1/2,j,k+1/2}^y - \hat{\Omega}_{i-1/2,j,k+1/2}^y}{\Delta x} - \frac{\hat{\Omega}_{i,j+1/2,k+1/2}^x - \hat{\Omega}_{i,j-1/2,k+1/2}^x}{\Delta y}, \quad (2.35)$$

where  $B_{i+1/2,j,k}^x$ ,  $B_{i,j+1/2,k}^y$ ,  $B_{i,j,k+1/2}^z$  are the staggered field components, which represent an average of the magnetic field at the cell surface,

$$B_{i+1/2,j,k}^x = \frac{1}{\Delta S_{i+1/2,j,k}} \int_{S_x} \mathbf{B} \cdot d\mathbf{S}_x, \quad (2.36)$$

$$B_{i,j+1/2,k}^y = \frac{1}{\Delta S_{i,j+1/2,k}} \int_{S_y} \mathbf{B} \cdot d\mathbf{S}_y, \quad (2.37)$$

$$B_{i,j,k+1/2}^z = \frac{1}{\Delta S_{i,j,k+1/2}} \int_{S_z} \mathbf{B} \cdot d\mathbf{S}_z. \quad (2.38)$$

The electromotive forces (emf)  $\Omega^i$  are discrete representations of the components of  $\boldsymbol{\Omega} = \mathbf{v} \times \mathbf{B}$  defined at cell corners (see Fig. 2.3). To compute them, we can follow the flux-CT formalism [Balsara and Spicer 1999, Giacomazzo and Rezzolla 2007], taking the average of the neighbouring upwind numerical fluxes,

$$\bar{\Omega}_{i,j+1/2,k+1/2}^x = \frac{1}{4} (\hat{F}_{i,j+1/2,k}^{yz} + \hat{F}_{i,j+1/2,k+1}^{yz} - \hat{F}_{i,j,k+1/2}^{zy} - \hat{F}_{i,j+1,k+1/2}^{zy}), \quad (2.39)$$

$$\bar{\Omega}_{i+1/2,j,k+1/2}^y = \frac{1}{4} (\hat{F}_{i,j,k+1/2}^{zx} + \hat{F}_{i+1/2,j,k+1/2}^{zx} - \hat{F}_{i+1/2,j,k+1/2}^{xz} - \hat{F}_{i+1/2,j,k+1}^{xz}), \quad (2.40)$$



approximation, the average electromotive forces are modified according to

$$\begin{aligned} \hat{\Omega}_{i+1/2,j+1/2,k}^z &= \bar{\Omega}_{i+1/2,j+1/2,k}^z \\ &+ \frac{\delta y}{8} \left( \left( \frac{\partial \Omega^z}{\partial y} \right)_{i+1/2,j+1/4} - \left( \frac{\partial \Omega^z}{\partial y} \right)_{i+1/2,j+3/4} \right) \\ &+ \frac{\delta x}{8} \left( \left( \frac{\partial \Omega^z}{\partial x} \right)_{i+1/4,j+1/2} - \left( \frac{\partial \Omega^z}{\partial x} \right)_{i+3/4,j+1/2} \right), \end{aligned} \quad (2.42)$$

where similar expressions hold for  $\Omega^x, \Omega^y$  by cyclic permutation of the spatial indices. Gardiner and Stone 2005 proposed several ways to compute the derivatives of Eq. 2.42. Here, we follow the  $\epsilon_z^c$ -CT algorithm, where derivatives are selected in an upwind way according to the sign of the velocity of the contact mode,

$$\left( \frac{\partial \Omega^z}{\partial y} \right)_{i+1/2,j+1/4} = \begin{cases} (\partial \Omega^z / \partial y)_{i,j+1/4}, & \text{if } v_{x,i+1/2,j} > 0, \\ (\partial \Omega^z / \partial y)_{i+1,j+1/4}, & \text{if } v_{x,i+1/2,j} < 0, \\ \frac{1}{2}((\partial \Omega^z / \partial y)_{i,j+1/4} + (\partial \Omega^z / \partial y)_{i+1,j+1/4}), & \text{otherwise.} \end{cases} \quad (2.43)$$

To obtain the derivatives that appear in Eq. 2.43, Gardiner and Stone 2005 proposed to subtract the face centred emf  $\Omega_{i,j+1/2}^z$  computed with the upwind fluxes and the emf  $\Omega_{i,j}^z$  evaluated at the cell centre,

$$\left( \frac{\partial \Omega^z}{\partial y} \right)_{i,j+1/4} = \frac{2}{\delta y} \left( \Omega_{i,j+1/2}^z - \Omega_{i,j}^z \right). \quad (2.44)$$

The cell-center magnetic field can be recovered from the staggered representation using a simple linear interpolation at the end of the CT step,

$$B_{i,j,k}^x = \frac{1}{2}(B_{i-1/2,j,k}^x + B_{i+1/2,j,k}^x), \quad (2.45)$$

$$B_{i,j,k}^y = \frac{1}{2}(B_{i,j-1/2,k}^y + B_{i,j+1/2,k}^y), \quad (2.46)$$

$$B_{i,j,k}^z = \frac{1}{2}(B_{i,j,k-1/2}^z + B_{i,j,k+1/2}^z). \quad (2.47)$$

The interpolations performed to obtain the required fluxes at cell edges in the CT-contact formalism, and to recover the cell-centred magnetic field from the staggered solution, limit the accuracy of the algorithm to second order. Other strategies such as the UCT-HLL(D) method of Mignone and Del Zanna 2021 may be followed to increase the order of the CT method.

### 2.2.6 Recovery of primitive variables

Finally, in order to start a new time iteration, we must recover the primitive variables from the evolved conserved solution. In relativistic hydrodynamics (RHD) and RMHD codes, this task requires solving a highly nonlinear algebraic system of equations, which constitutes one of the most challenging tasks from the point of view of computational efficiency. The recovery of primitive variables is usually considered as one of the bottlenecks for the speed-up of the code [Wright and Hawke 2019].

Among the different strategies that exist in the literature [see e.g. Martí and Müller 2015, and references therein], we chose to recover the set of primitive variables following the inversion scheme of Mignone and McKinney 2007. This algorithm can be extended to general EoS, and it has been proved to avoid numerical problems due to loss of precision in the non-relativistic and ultra-relativistic limit. For example, this might be relevant for microquasar jet simulations, where we showed that other inversion schemes such as the one used by Leismann et al. 2005 or Martí 2015b failed to recover the low pressure of the non-relativistic stellar wind with acceptable accuracy. The relevant equations of this inversion scheme are

$$E' = Z' - p + \frac{|\mathbf{B}|^2}{2} + \frac{|\mathbf{B}|^2|\mathbf{S}|^2 - S_B^2}{2(|\mathbf{B}|^2 + Z' + D)^2}, \quad (2.48)$$

$$|\mathbf{S}|^2 = (Z + |\mathbf{B}|^2)^2 \frac{|\mathbf{u}|^2}{1 + |\mathbf{u}|^2} - \frac{S_B^2}{Z^2} (2Z + |\mathbf{B}|^2), \quad (2.49)$$

where  $E' = E - D$ ,  $Z' = Z - D$ ,  $Z = DhW$ ,  $S_B = \mathbf{S} \cdot \mathbf{B}$  and  $|\mathbf{u}|^2 = W^2|\mathbf{v}|^2$ . Equation 2.48 can be solved for  $Z'$  by means of a one-dimensional Newton-Raphson iterative method using Eq. 2.49 to express  $|\mathbf{u}|^2$  as a function of  $Z'$ . The method involves the computation of the derivative

$$\frac{dE}{dZ'} = 1 - \frac{dp}{dZ'} - \frac{|\mathbf{B}|^2|\mathbf{S}|^2 - S_B^2}{(|\mathbf{B}|^2 + Z' + D)^3}, \quad (2.50)$$

where  $dp/dZ'$  depends on the EoS of the code. To avoid catastrophic losses of accuracy in the non-relativistic and ultra-relativistic limits, Mignone and McKinney 2007 chose  $p = p(\chi, \rho)$  with  $\chi = \rho\epsilon + p$  to obtain

$$\frac{dp}{dZ'} = \left. \frac{\partial p}{\partial \chi} \right|_{\rho} \frac{d\chi}{dZ'} + \left. \frac{\partial p}{\partial \rho} \right|_{\chi} \frac{d\rho}{dZ'}. \quad (2.51)$$

For ideal gases,  $\partial p/\partial \chi$  and  $\partial p/\partial \rho$  become

$$\frac{\partial p}{\partial \chi} = \frac{\Gamma - 1}{\Gamma} \chi; \quad \frac{\partial p}{\partial \rho} = 0. \quad (2.52)$$

Moreover, on the one hand, the variable  $\chi$  can be written as a function of  $Z'$  as

$$\chi = \frac{Z'}{W^2} - \frac{D|\mathbf{u}|^2}{(1+W)W^2}, \quad (2.53)$$

and its derivative with respect to  $Z'$  as

$$\frac{d\chi}{dZ'} = \frac{1}{W^2} - \frac{W}{2}(D + 2W\chi)\frac{d|\mathbf{v}|^2}{dZ'}, \quad (2.54)$$

where

$$\frac{d|\mathbf{v}|^2}{dZ'} = \frac{-2S_B^2[3Z(Z + |B|^2) + |B|^4] + |S|^2Z^3}{Z^3(Z + |B|^2)^3}. \quad (2.55)$$

On the other hand,

$$\frac{d\rho}{dZ'} = -\frac{DW}{2}\frac{d|\mathbf{v}|^2}{dZ'}. \quad (2.56)$$

When  $Z'$  and  $p$  are found with some desirable degree of accuracy, the inversion scheme is completed by recovering the three-velocity and the density of the gas through

$$v^j = \frac{1}{Z + |B|^2} \left( S^j + \frac{S_B}{W} B^j \right), \quad (2.57)$$

$$\rho = \frac{D}{W}. \quad (2.58)$$

We refer to Mignone and McKinney 2007 for further details of the full algorithm. If the inversion step fails to recover a proper physical solution (i.e.,  $p < 0$ ), we follow the same strategy as in the PLUTO code fixing the pressure to a positive threshold before solving for  $|v|^2$  using a bisections root finder with the following function:

$$|v|^2 - \frac{S_B^2(2Z + |B|^2) + |S|^2Z^2}{(Z + |B|^2)^2Z^2} = 0. \quad (2.59)$$

Using this approach,  $Z$  has to be recomputed after each iteration using Eqs. 2.48 to 2.55. Then, the total energy has to be corrected according to the new solution.

### 2.2.7 Correction of conserved variables

The RMHD codes based on constrained transport algorithms are subject to several pathologies that may lead to nonphysical solutions, especially for highly magnetised flows under the influence of strong shocks. The decoupled evolution of the staggered and cell-centred magnetic field makes the algorithm inconsistent because the conserved variables are evolved according to the fluxes computed from the cell-centred field, while the staggered solution is computed with the

CT method. This inconsistency is the main motivation to develop correction algorithms of the conserved variables, which may be especially important when the magnetic pressure dominates over the gas pressure by more than two orders of magnitude [Martí 2015a]. LÓSTREGO admits both the non-relativistic energy correction of Mignone and Bodo 2006

$$E_{\text{stag}} = E_{\text{cell}} - \frac{B_{\text{cell}}^2 - B_{\text{stag}}^2}{2} \quad (2.60)$$

and the fully relativistic correction of both energy and momentum of Martí 2015a. In this last approach, the non-relativistic correction of the energy, now  $E_{\text{stag}}^{(1)}$ , is used to obtain a first approximation of the primitive variables and then use the new flow velocity  $\mathbf{v}^{(1)}$  to complete the relativistic correction of the momentum and energy,

$$S_{\text{stag}}^{i(2)} = S^i - (B_{\text{cell}}^2 - B_{\text{stag}}^2)v^{i(1)} + \mathbf{v}^{(1)} \cdot (B_{\text{cell}}^i \mathbf{B}_{\text{cell}} - B_{\text{stag}}^i \mathbf{B}_{\text{stag}}), \quad (2.61)$$

$$E_{\text{stag}}^{(2)} = E_{\text{stag}}^{(1)} - \frac{(v^{(1)})^2}{2}(B_{\text{cell}}^2 - B_{\text{stag}}^2) + \frac{(\mathbf{v}^{(1)} \cdot \mathbf{B}_{\text{cell}})^2 - (\mathbf{v}^{(1)} \cdot \mathbf{B}_{\text{stag}})^2}{2}. \quad (2.62)$$

Although these algorithms can be applied before or after recovering the primitive variables, in LÓSTREGO, we decided to perform the correction before. Following the notation of Martí 2015a, these algorithms are called CA1 (Eq. 2.60) and CA2 (Eq. 2.61 and Eq. 2.62), respectively.

## 2.3 Parallelisation

LÓSTREGO is parallelised with an hybrid scheme using OpenMP (OMP) and Message Passing Interface (MPI) library instructions in order to exploit the computational power of both distributed and shared memory. This parallelisation configuration is based on the parallel architecture of the code RATPENAT [Perucho et al. 2010]. The hybrid scheme is only available in the code for fully 3D simulations, while 2D computations like the tests described in the next section might benefit from shared memory parallelisation with OMP directives. For the large 3D simulations for which the hybrid scheme is available, the computational box is initially decomposed into several subdomains such that each one is assigned to an MPI node that performs all the calculations independently using shared-memory OMP threads. At the beginning of each time step, all MPI blocks that share internal boundaries must interchange a collection of *ghost* cells with the neighbours in the three spatial directions. These cells are used as boundary conditions for the blocks that are not physical boundaries of the grid. The latter are imposed according to the physical conditions on the box

boundaries, which are particular for each numerical simulation. Moreover, the implementation of the CT-contact algorithm (see Sec. 2.2) requires one more MPI communication step before the time evolution of the staggered components of the magnetic field. This CT algorithm requires not only the direction-wise boundaries in the three spatial directions, but also the corners of each sub-box. Nevertheless, this information can be also transmitted direction-wise because the corners are already available in the neighbouring boundaries after the first MPI communication.

## 2.4 Testing benchmark

We provide an extensive collection of one-dimensional and multidimensional numerical tests to probe the performance of the new LÓSTREGO code. Unless otherwise stated, all tests shown in this section were performed with the HLLD Riemann solver and the second-order PLM with the VanLeer slope limiter for cell reconstruction. A weak form of flattening is introduced that degrades the slope limiter to MinMod whenever a strong shock is detected [Mignone and Bodo 2006], but no degradation of the HLLD Riemann solver is applied in the tests. We used a third-order TVD-preserving Runge-Kutta algorithm for time integration with CFL=0.3. The magnetic field divergence-free constraint is preserved with the CT method, where electromotive forces were averaged according to the CT-contact formalism. The relativistic correction scheme CA2 was used to correct the conserved variables after each time integration.

### 2.4.1 One dimension

**Sinusoidal perturbation** As a first 1D application, we show the purely hydrodynamical problem initially formulated by Dolezal and Wong 1995 with a nuclear EoS and adapted to ideal gases in Del Zanna and Bucciantini 2002. A 1D unitary shock tube with a resolution of 2000 computational zones is perturbed in the right zone ( $0.5 < x < 1.0$ ) with a density sinusoidal profile such that  $\mathbf{V}_L = (\rho, v, p) = (5, 0, 50)$  and  $\mathbf{V}_R = (\rho, v, p) = (2 + 0.3 \sin(50x), 0, 5)$ . Figure 2.4 shows the solution of the problem at  $t = 0.35$ . The original jump in pressure generates a blast wave that interacts with the density perturbation. Qualitatively, our results are similar to those presented in Del Zanna and Bucciantini 2002.

**RMHD shock tubes** A collection of 1D RMHD test problems were initially proposed by Dubal 1991, van Putten 1993 and extended in Komissarov 1999a,

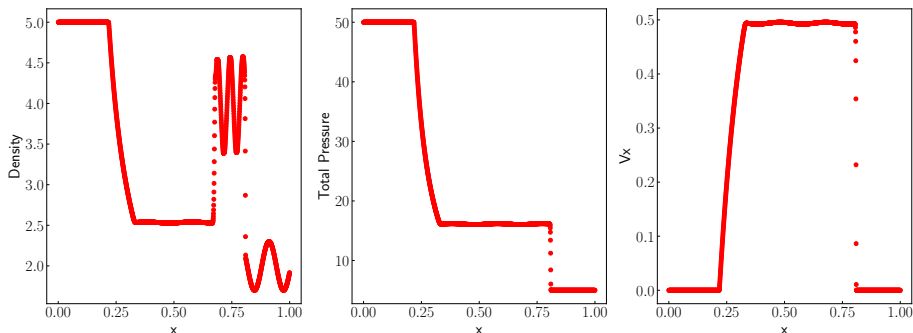


Figure 2.4 Gas density (left), pressure (middle), and  $x$ -velocity (right) at  $t = 0.35$  for the hydrodynamical sinusoidal perturbation test. The shock tube contains 2000 grid points in the  $x$ -direction.

Balsara 2001. These tests constitute a set of Riemann problems that have been established as a benchmark to test the robustness, accuracy, stability, and diffusion of any RMHD code. We consider the five shock tube problems of Balsara 2001 (hereinafter, BA1-5). The initial conditions of these five tests can be found in the aforementioned reference, so I do not reproduce them in the thesis. For all of these tests, we considered a 1D unit grid with a resolution of 1600 cells. The adiabatic coefficient was set to  $\Gamma = 5/3$  for all tests except for BA1, where  $\Gamma = 2$ .

The BA1 problem, which was originally proposed by Brio and Wu 1988 and extended to relativistic MHD by van Putten 1993, describes the formation of a left-going fast rarefaction wave, a left-going compound wave (that only appears in the numerical solution), a contact discontinuity, a right-going slow shock, and a right-going fast rarefaction wave in a moderate relativistic flow. The right part of the shock tube is magnetically dominated. The solution of the BA1 test at  $t = 0.4$  (red dots) and the analytical solution provided by Giacomazzo and Rezzolla 2006 (blue line) is shown in Fig. 2.5.

BA2 and BA3 tests are both blast wave problems, although the initial pressure jump is moderate for BA2 and strong for BA3. The BA2 problem is well-resolved with our code, and we clearly identify a left-going fast rarefaction wave, a left-going slow rarefaction, a contact discontinuity, a right-going slow shock, and a right-going fast shock (Fig. 2.6).

Figure 2.7 shows the solution of the BA3 test at  $t = 0.4$  (red dots) and the analytical solution provided by Giacomazzo and Rezzolla 2006 (blue line). The collection of waves that develops as a consequence of the initial pressure discontinuity is similar to those obtained in BA2, but due to the jump in pressure

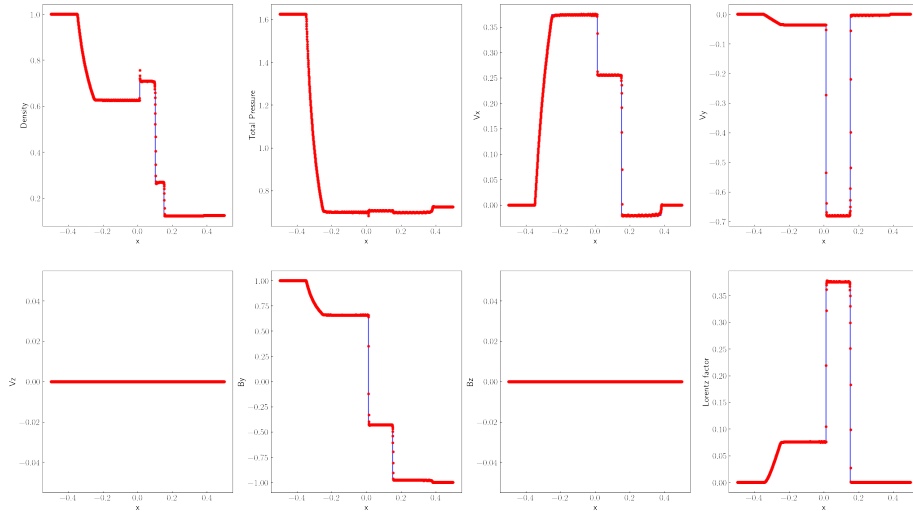


Figure 2.5 From left to right (top): Density, total pressure,  $x$ -velocity and  $y$ -velocity. From left to right (bottom):  $z$ -velocity,  $B_y$ ,  $B_z$  and logarithmic Lorentz factor at  $t = 0.4$  for the test BA1 (red dots). The analytic solution of the Riemann problem is over-plotted (blue solid line). The shock tube contains 1600 grid points in the  $x$ -direction.

of several orders of magnitude, it develops a strong relativistic flow. As a direct consequence of the large Lorentz factors achieved, the contact discontinuity and the right-going shocks are under-resolved, even with the less diffusive HLLD Riemann solver. This was not the case of BA2, where a weaker blast wave leads to lower Lorentz factors and thus to mildly relativistic flows.

The solution of the BA4 test at  $t = 0.4$  is shown in Fig. 2.8 (red dots), overplotted with the analytical solution provided by Giacomazzo and Rezzolla 2006 (blue line) for this test. This problem was originally proposed in Noh 1987, and it describes the interaction of two streams moving in opposite direction with high Lorentz factor, so the problem is strongly relativistic. As a byproduct of this collision, four shocks are generated: two strong external fast shocks and two internal slow shocks, one of each left-going and right-going, respectively.

Finally, BA5 is the only generic RMHD Riemann problem that allows all seven waves to appear after the decay of the initial discontinuity: a left-going fast shock, a left-going Alfvén wave, a left-going slow rarefaction, a contact discontinuity, a right-going slow shock, a right-going Alfvén wave, and a right-going fast shock. The initial setup includes transverse components of the velocity and magnetic field vectors. The results of this test, shown in Fig. 2.9, demonstrate that the code is able to capture the whole set of waves predicted by the analytical solution.

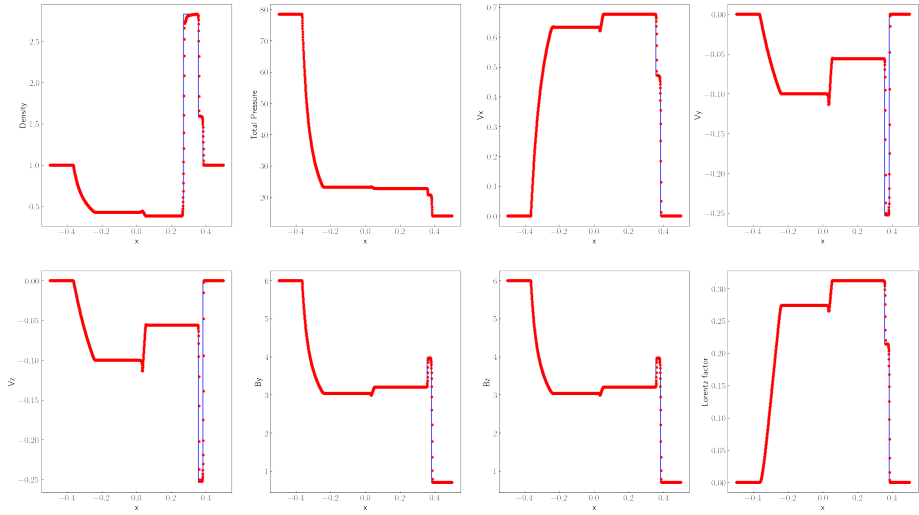


Figure 2.6 From left to right (top): Density, total pressure,  $x$ -velocity and  $y$ -velocity. From left to right (bottom):  $z$ -velocity,  $B_y$ ,  $B_z$  and logarithmic Lorentz factor at  $t = 0.4$  for the test BA2 (red dots). The analytic solution of the Riemann problem is over-plotted (blue solid line). The shock tube contains 1600 grid points in the  $x$ -direction.

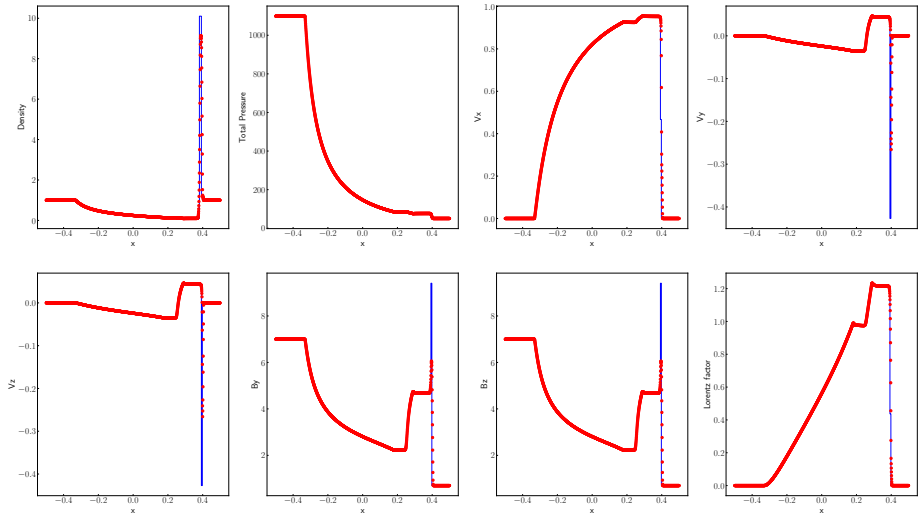


Figure 2.7 From left to right (top): Density, total pressure,  $x$ -velocity, and  $y$ -velocity. From left to right (bottom):  $z$ -velocity,  $B_y$ ,  $B_z$ , and logarithmic Lorentz factor at  $t = 0.4$  for the test BA3 (red dots). The analytic solution of the Riemann problem is overplotted (solid blue line). The shock tube contains 1600 grid points in the  $x$ -direction.

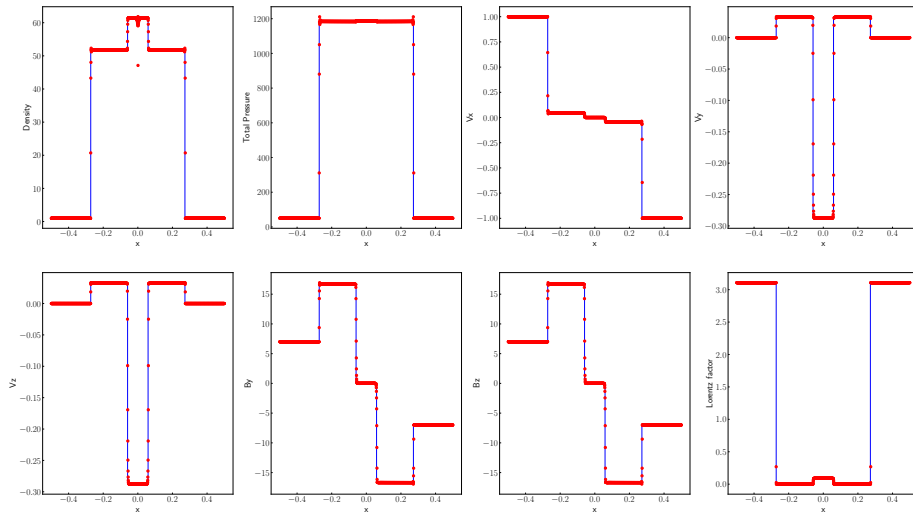


Figure 2.8 From left to right (top): Density, total pressure,  $x$ -velocity, and  $y$ -velocity. From left to right (bottom):  $z$ -velocity,  $B_y$ ,  $B_z$ , and logarithmic Lorentz factor at  $t = 0.4$  for the test BA4 (red dots). The analytic solution of the Riemann problem is overplotted (solid blue line). The shock tube contains 1600 grid points in the  $x$ -direction.

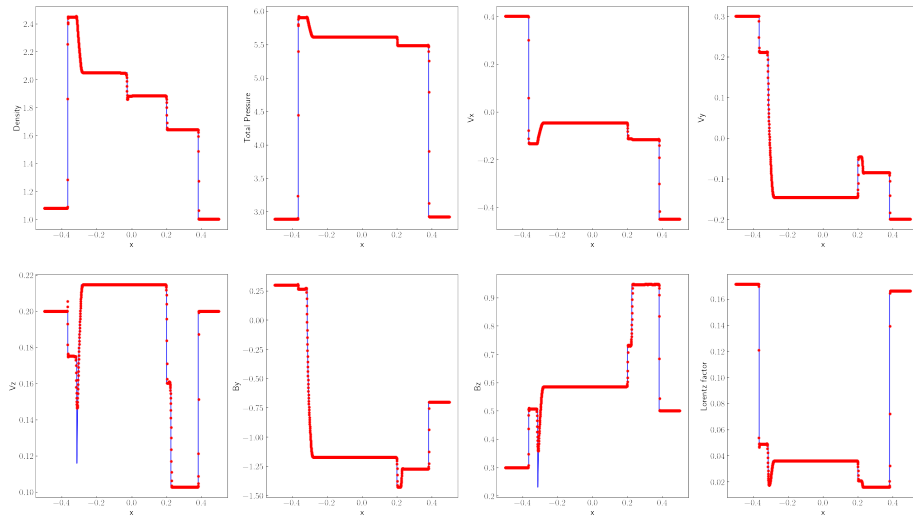


Figure 2.9 From left to right (top): Density, total pressure,  $x$ -velocity and  $y$ -velocity. From left to right (bottom):  $z$ -velocity,  $B_y$ ,  $B_z$  and logarithmic Lorentz factor (from left to right, bottom) at  $t = 0.55$  for the test BA5 (red dots). The analytic solution of the Riemann problem is over-plotted (blue solid line). The shock tube contains 1600 grid points in the  $x$ -direction.

## 2.4.2 Two dimensions

**Cylindrical magnetised blast wave** The cylindrical magnetised blast wave is a classical problem in RMHD to test the performance of the code handling MHD wave degeneracies parallel and perpendicular to the field orientation [see e.g., Martí and Müller 2015, and references therein]. Our initial setup follows the version proposed by Beckwith and Stone 2011 and adapted from Leismann et al. 2005. We considered the domain  $[-6, 6] \times [-6, 6]$  with  $1024^2$  cells and free-flow boundaries everywhere. An overpressured ( $p_s = 1$ ) and overdense ( $\rho_s = 10^{-2}$ ) cylinder of radius  $r = 0.8$  was placed at the centre of the grid, filled with a homogeneous ambient medium of density  $\rho_a = 10^{-4}$  and pressure  $p_a = 5 \times 10^{-3}$ . A transition layer between  $r = 0.8$  and  $r = 1$  was established to smooth the initial jump and avoid numerical problems when the flow starts to propagate outward. All velocities were initially set to zero, and the magnetic field was aligned with the x-axis in the whole grid. For this test, we considered two degrees of magnetisation: moderate ( $B = 0.1$ ) and strong ( $B = 1$ ). The adiabatic coefficient was set to the relativistic value,  $\Gamma = 4/3$ . The solution of the problem at  $t = 4.0$  is shown in Fig. 2.10 and Fig. 2.11. The difference in pressure between the cylindrical region and the ambient medium produces the expansion of the central region, which is delimited by a strong forward shock propagating radially near the speed of light. When we increase the magnetisation of the medium ( $B = 1$ ), the strong sideways magnetic confinement produced an elongated flow structure. The test preserves the symmetry with good accuracy, and no numerical artifacts or instabilities appear in our simulation.

**Rotor** We consider the relativistic rotor problem of Del Zanna, Bucciantini, and Londrillo 2003 in a unitary Cartesian 2D grid with a resolution of  $1024^2$  cells and free-flow boundary conditions in all directions. The initial setup consisted of a disc with radius  $r = 0.1$  rotating with an angular relativistic velocity  $\omega = 0.95$ . The disc was ten times denser than the ambient medium ( $\rho_r = 10$ ,  $\rho_a = 1$ ) and the entire system was in pressure equilibrium with  $p = 1$ . The background was initially at rest ( $\mathbf{v} = 0$ ), and the magnetic field was aligned with the  $x$  direction in the whole grid,  $B_x = 1, B_y = 0, B_z = 0$ . An adiabatic coefficient of  $\Gamma = 5/3$  was used for this test. The solution of the problem at  $t = 0.4$  is shown in Fig. 2.12. The results show complex wave patterns and torsional Alfvén waves that are generated due to the rotation of the disc. At the end of the simulation, the magnetic field lines inside the rotor are almost perpendicular with respect to the background field. The entire system is embedded in a fast rarefaction. The

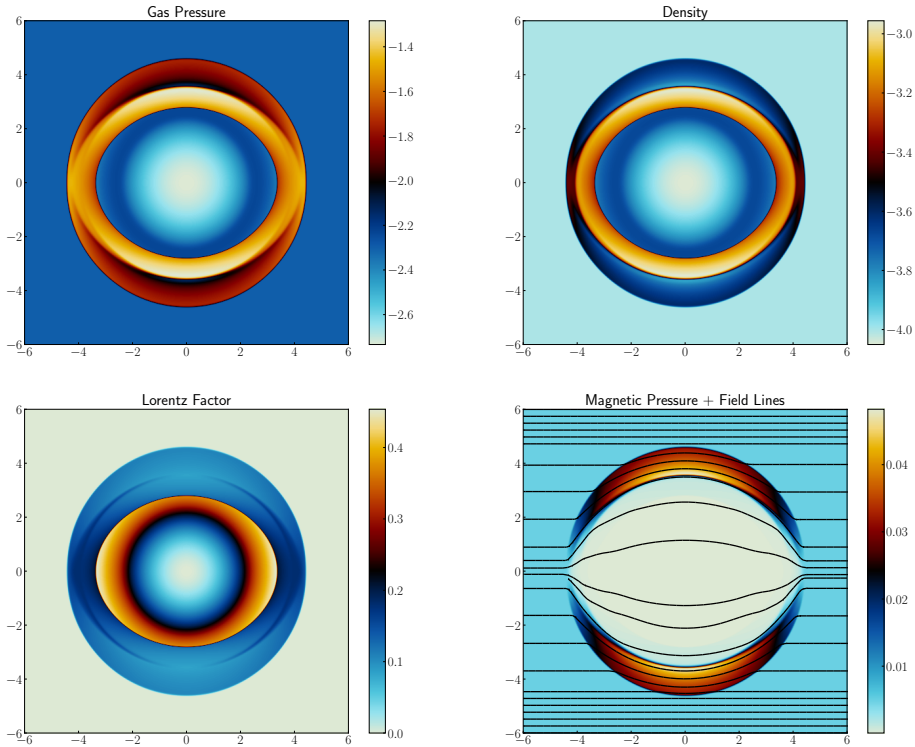


Figure 2.10 Logarithmic gas pressure (top left), logarithmic density (top right), logarithmic Lorentz factor (bottom left), and logarithmic magnetic pressure (bottom right) at  $t = 0.4$  for the 2D cylindrical magnetised blast wave with moderate magnetisation. Magnetic field lines are superposed on the magnetic pressure. We consider the Cartesian grid  $[-6, 6] \times [-6, 6]$  with 1024 cells per spatial dimension.

initial overdensity was swept away by the torsional waves and distributed in a thin oblique shell.

**Shock-cloud interaction** A multidimensional test with relevance in astrophysical applications is the interaction of a strong shock wave with a density clump. We considered the relativistic version of the problem proposed by Mignone and Bodo 2006, where the magnetic field is orthogonal to the plane and carries a rotational discontinuity. We set a Cartesian 2D grid with dimensions  $[0, 1] \times [-0.5, 0.5]$  and a resolution of  $1024^2$  cells, with outflow boundaries in all directions. The shock wave was initially located at  $x = 0.6$  such that the pre-shocked values (i.e.,  $x > 0.6$ ) are  $(\rho, W_x, p_g, B_z) = (1.0, 10, 10^{-3}, 0.5)$  (with the flow propagating to the left) and the shocked gas at  $x < 0.6$  is given by  $(\rho, W_x, p_g, B_z) = (42.5942, 1.0, 127.9483, -2.12917)$ , where  $\rho$  is the density,  $W_x$

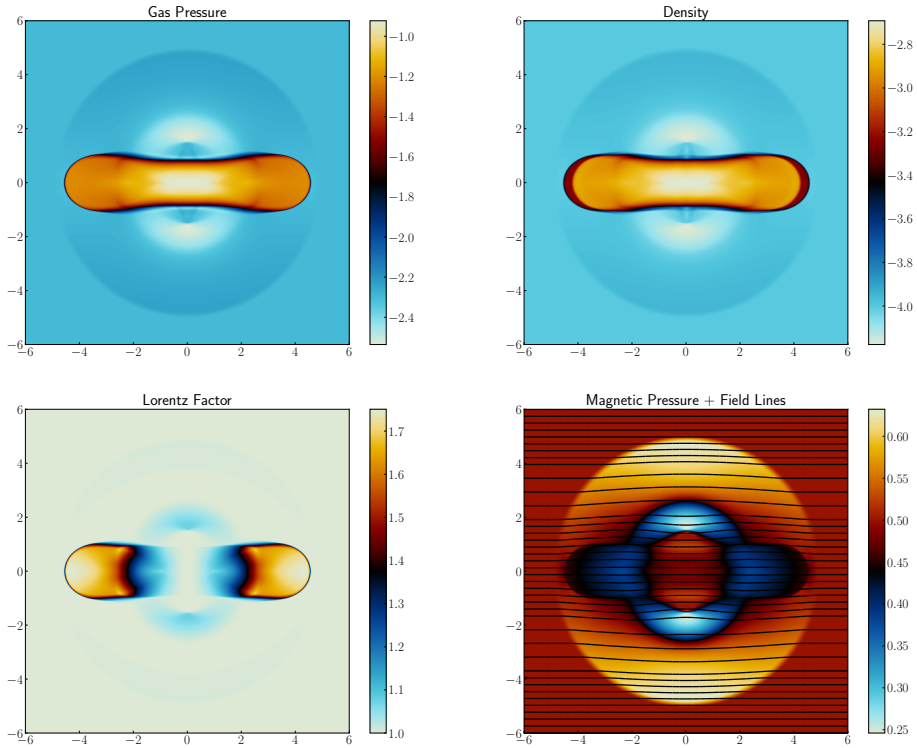


Figure 2.11 Logarithmic gas pressure (top left), logarithmic density (top right), logarithmic Lorentz factor (bottom left), and logarithmic magnetic pressure (bottom right) at  $t = 0.4$  for the 2D cylindrical magnetised blast wave with strong magnetisation. Magnetic field lines are superposed on the magnetic pressure. We consider the Cartesian grid  $[-6, 6] \times [-6, 6]$  with 1024 cells per spatial dimension.

is the Lorentz factor,  $p_g$  is the gas pressure, and  $B_z$  is the  $z$ -component of the magnetic field. The transverse components of the velocity  $v_y$  and  $v_z$  and the components of the magnetic field  $B_x$  and  $B_y$  were initially equal to zero in the whole domain. The cloud was characterised as a cylinder with radius  $r = 0.15$  and density  $\rho = 10.0$ , centred at  $x = 0.8$  in pressure equilibrium with the pre-shocked material. An adiabatic coefficient of  $\Gamma = 4/3$  was used for this test. The solution of the problem at  $t = 1.0$  is shown in Fig. 2.13. Immediately after the impact between the cloud and the shock wave, the sphere experiences a strong compression that increases the density of the clump significantly. As a byproduct of this collision, a bow shock propagates to the left in the shocked material and a reverse shock is transmitted to the right, penetrating the cloud and producing a mushroom-shaped structure. The overall evolution of the cloud after the impact of the shocked wave and the development of a mushroom-shaped

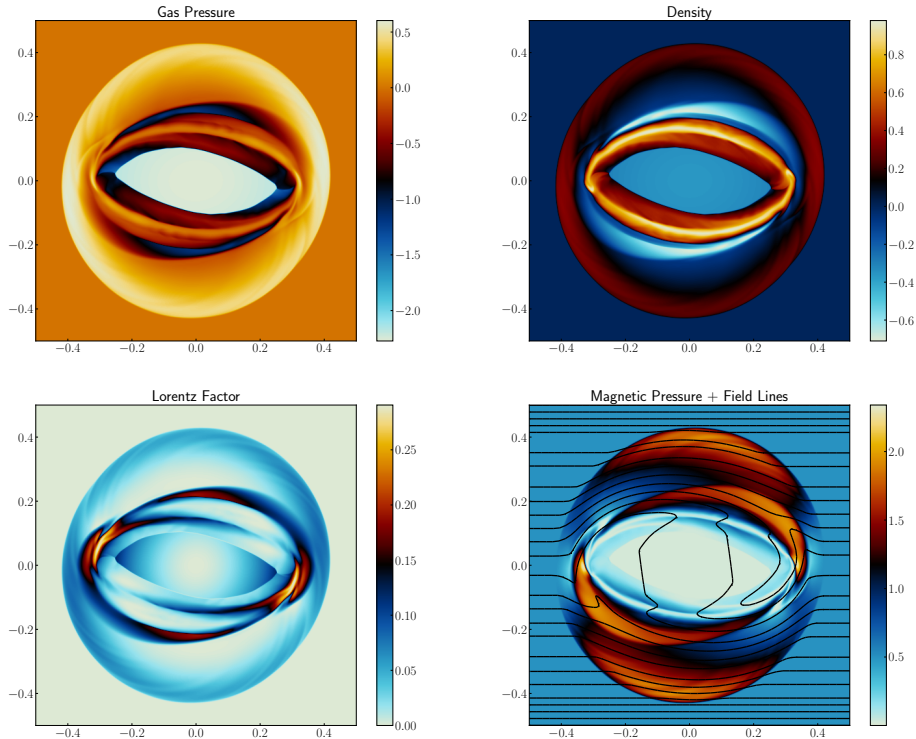


Figure 2.12 Logarithmic gas pressure (top left), logarithmic density (top right), logarithmic Lorentz factor (bottom left), and logarithmic magnetic pressure (bottom right) at  $t = 0.4$  for the 2D relativistic rotor problem. Magnetic field lines are superposed on the magnetic pressure. We consider the unit square  $[-0.5, 0.5] \times [-0.5, 0.5]$  with 1024 cells per spatial dimension.

shell agrees well with Mignone and Bodo 2006. However, the higher resolution employed in our work and the use of the HLLD Riemann solver produce a less diffusive result where several complex wave patterns and eddies are noticeable in the arms of the shell.

**Relativistic Orszag-Tang vortex** The Orszag-Tang vortex problem was originally proposed in Orszag and Tang 1979, and it has become a classical test for Newtonian MHD applications [Ryu et al. 1998, Londrillo and Del Zanna 2000]. We adapted the relativistic version of the test proposed by Castro, Gallardo, and Marquina 2017 into a 2D Cartesian grid with dimensions  $[0, 6] \times [0, 6]$  and a resolution of  $1024^2$  cells, with periodic boundary conditions in all directions. Initially, density ( $\rho$ ) and pressure ( $p$ ) were set to 1.0 with an adiabatic index of  $\Gamma = 4/3$ . The velocity field in the laboratory frame was given by

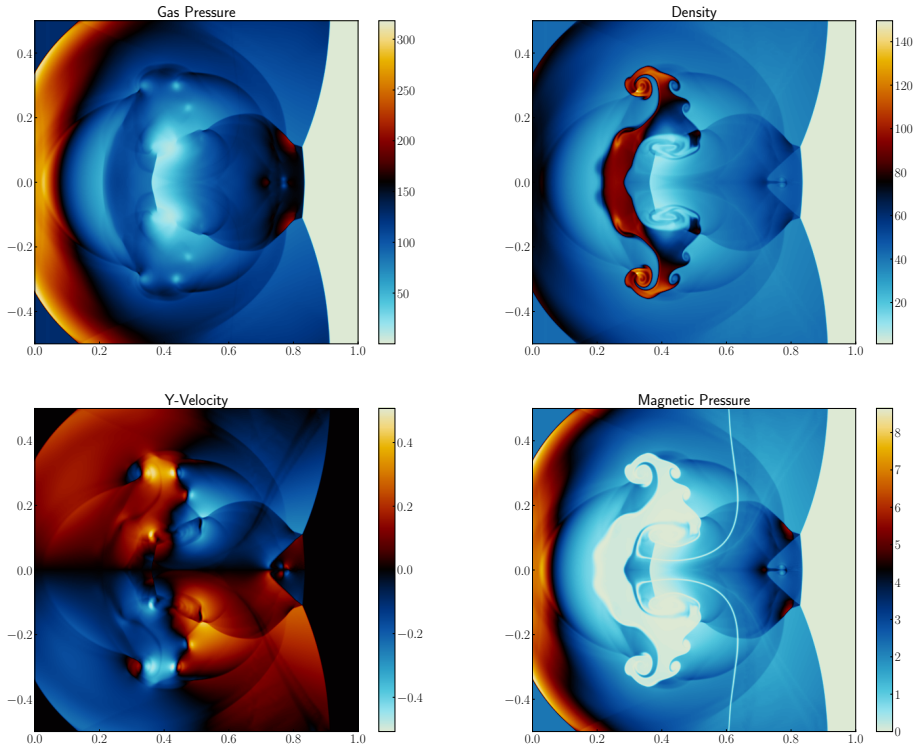


Figure 2.13 Gas pressure (top left), density (top right),  $y$ -velocity (bottom left), and magnetic pressure (bottom right) at  $t = 1.0$  for the 2D shock-cloud interaction test. We consider the unit square  $[0, 1] \times [-0.5, 0.5]$  with 1024 cells per spatial dimension.

$$\mathbf{v} = \left( -\frac{0.75}{\sqrt{2}} \sin y, \frac{0.75}{\sqrt{2}} \sin x, 0 \right), \quad (2.63)$$

while the proposed magnetic field configuration was

$$\mathbf{B}_0 = (-\sin y, \sin 2x, 0). \quad (2.64)$$

Figure 2.14 shows the solution to the problem at  $t = 4.0$ . Our results agree well with those obtained in Castro, Gallardo, and Marquina 2017. This test validates the performance of the code describing the transition to supersonic MHD turbulence and its ability to handle the formation of shocks and shock-shock interactions in the relativistic domain.

**Relativistic Kelvin-Helmholtz instability** The last 2D test that we propose is the linear growth phase of the relativistic Kelvin-Helmholtz instability

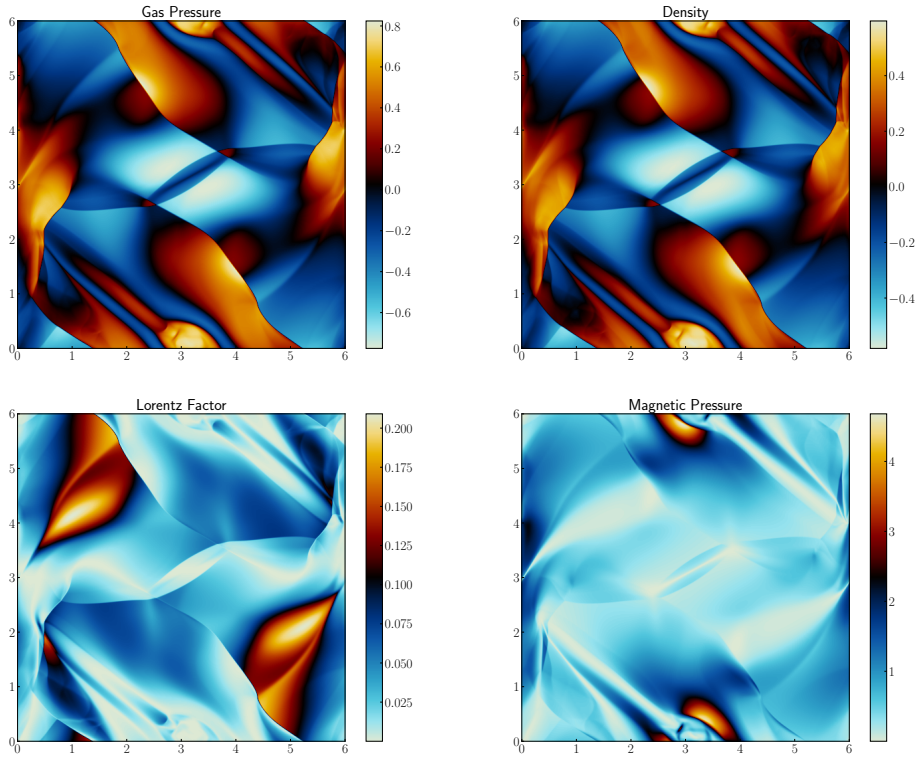


Figure 2.14 Logarithmic pressure (top left), logarithmic density (top right), logarithmic Lorentz factor (bottom left), and magnetic pressure (bottom right) at  $t=4.0$  for the relativistic Orszag-Tang vortex test. We consider the 2D Cartesian grid  $[0, 6] \times [0, 6]$  with 1024 cells per spatial dimension.

(KHI). Like the shock-cloud interaction problem, this test is also relevant for astrophysical application since KHIs are commonly present in nature. In particular, this test may be useful to probe the performance of the code describing turbulence zones and the description of the growth of small-scale perturbations. KHIs develops when there is a velocity shear in a continuous flow or when there is a velocity difference across two separated flow states. Thus, it is a useful setup to test the response of the code when unstable initial conditions are provided. We considered a 2D Cartesian grid with dimensions  $[-0.5, 0.5] \times [-1.0, 1.0]$  and resolution  $512 \times 1024$  cells, with periodic boundaries. We followed the initial configuration given by Beckwith and Stone 2011, which in turn was adapted from Mignone, Ugliano, and Bodo 2009 and exploited by other authors [Castro, Gallardo, and Marquina 2017]. The shear velocity and density profiles are given by

$$V^x = \begin{cases} V_{\text{shear}} \tanh\left(\frac{y-0.5}{a}\right) & \text{if } y > 0 \\ -V_{\text{shear}} \tanh\left(\frac{y+0.5}{a}\right) & \text{if } y < 0 \end{cases}, \quad (2.65)$$

$$\rho = \begin{cases} \rho_0 + \rho_1 \tanh\left(\frac{y-0.5}{a}\right) & \text{if } y > 0 \\ \rho_0 - \rho_1 \tanh\left(\frac{y+0.5}{a}\right) & \text{if } y < 0 \end{cases}, \quad (2.66)$$

where  $a = 0.01$  is the characteristic thickness of the shear layer and  $V_{\text{shear}} = 0.5$  determines the velocity profile. The characteristic densities are  $\rho_0 = 0.505$ , and  $\rho_1 = 0.495$ . The instability was triggered by a perturbation in the transverse velocity  $V_y$  of the form

$$V^y = \begin{cases} A_0 V_{\text{shear}} \sin(2\pi x) \exp[-((y-0.5)/\sigma)^2] & \text{if } y > 0 \\ -A_0 V_{\text{shear}} \sin(2\pi x) \exp[-((y+0.5)/\sigma)^2] & \text{if } y < 0 \end{cases}, \quad (2.67)$$

where  $A_0 = 0.1$  is the amplitude of the perturbation and  $\sigma = 0.1$  the characteristic length scale. The gas pressure was constant everywhere,  $p = 1$ , and we considered an ideal EoS with  $\Gamma = 4/3$ . The magnetic field was aligned with the  $x$ -axis,  $\mathbf{B} = (10^{-3}, 0, 0)$ . Figure 2.15 shows the solution of the problem at  $t = 3.0$ , which is qualitatively similar to the one presented in the aforementioned papers. In our simulation, we also resolved the secondary vortex near  $x = 0.1$ , although Beckwith and Stone 2011 showed that it can be annihilated by using more diffusive Riemann solvers such as HLL. As pointed out by Castro, Gallardo, and Marquina 2017, these secondary instabilities may be nonphysical, and their appearance depends on the Riemann solver and on the resolution employed in the simulation.

### 2.4.3 Three dimensions

**Spherical magnetised blast wave** The spherical magnetised blast wave allows us to test the ability of the code to handle parallel and perpendicular strong 3D shocks in magnetised plasma. The initial setup is similar to the one described in the cylindrical blast wave problem in 2D (see Sec. 2.4.2). We considered the domain  $[-6 \times 6]^3$  with  $256^3$  cells and free boundaries everywhere. An overpressured and overdense sphere of radius  $r = 0.8$ , density  $\rho_s = 10^{-2}$ ,

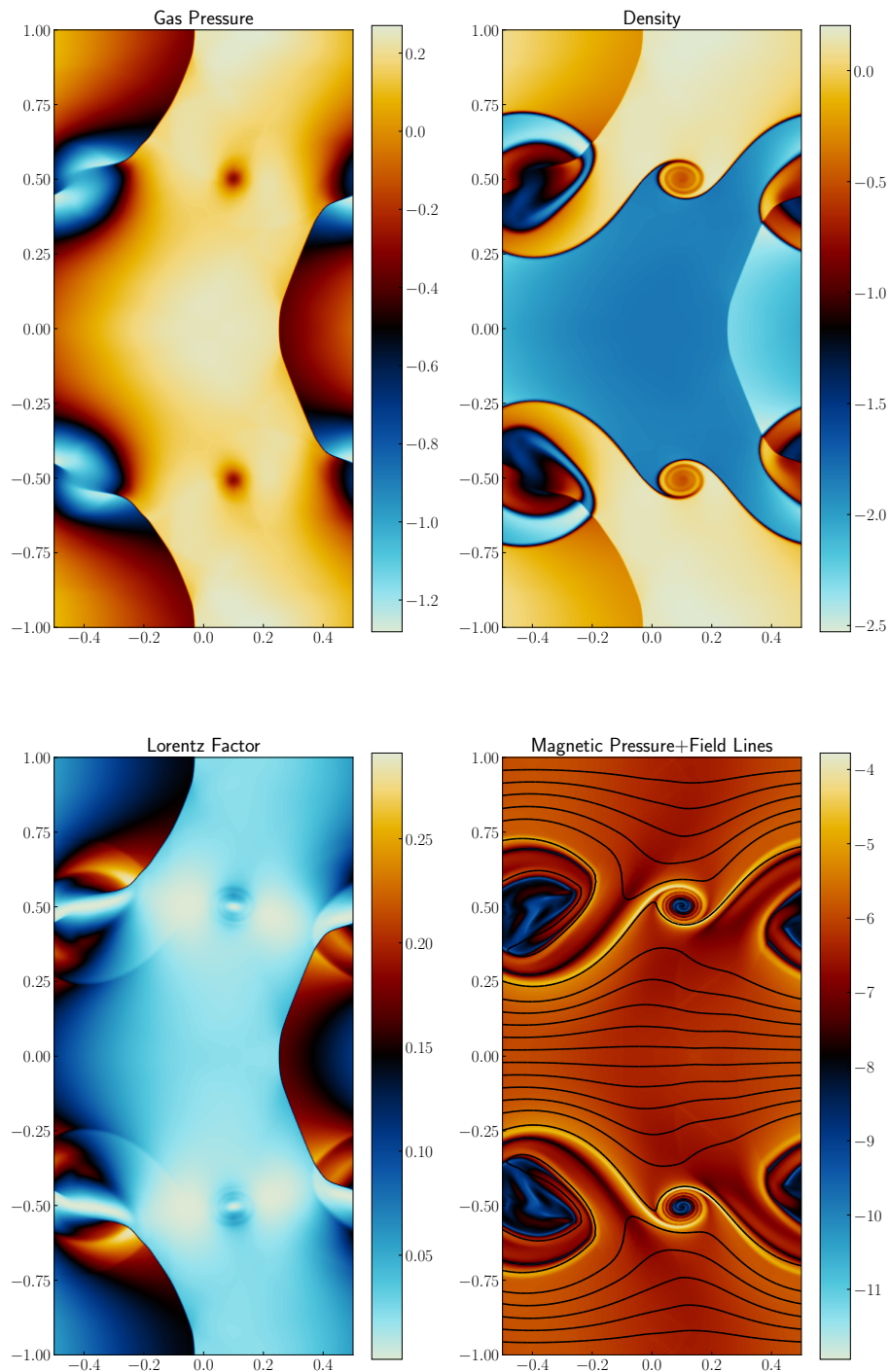


Figure 2.15 Logarithmic pressure (top left), logarithmic density (top right), logarithmic Lorentz factor (bottom left), and magnetic pressure (bottom right) at  $t=3.0$  for the relativistic Kelvin-Helmholtz test. Magnetic field lines are superposed on the magnetic pressure. We consider the 2D Cartesian grid  $[-0.5, 0.5] \times [-1.0, 1.0]$  with  $512 \times 1024$  cells.

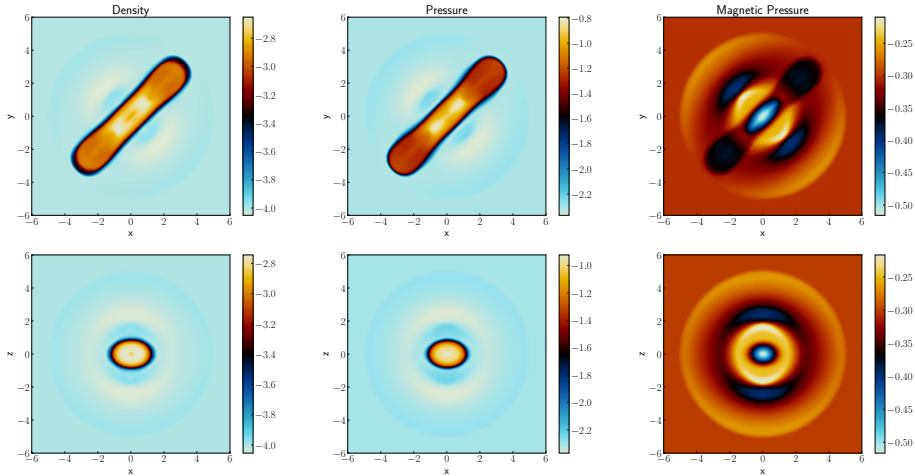


Figure 2.16 Logarithmic density (left), logarithmic pressure (middle), and logarithmic magnetic pressure (right) at  $t = 4.0$  for the spherical magnetised blast wave in the  $xy$  plane at  $z = 0$  (top) and  $xz$  plane at  $y = 0$  (bottom). We consider the 3D Cartesian grid  $[-6, 6] \times [-6, 6] \times [-6, 6]$  with 256 cells per spatial dimension.

and pressure  $p_s = 1$  was placed in the centre of the grid, where  $\rho_a = 10^{-4}$ ,  $p_a = 5 \times 10^{-3}$  are the density and pressure of the ambient medium, respectively. A transition layer between  $r = 0.8$  and  $r = 1$  was established to smooth the initial jump and to avoid numerical problems when the flow starts to propagate. All velocities were initially set to zero. The adiabatic coefficient was set to the relativistic value,  $\Gamma = 4/3$ . In this test, we chose a magnetic field oblique to the grid as in Castro, Gallardo, and Marquina 2017,

$$\mathbf{B} = B_0(\sin \theta \cos \phi, \sin \theta \sin \phi, \cos \theta), \quad (2.68)$$

where  $B_0 = 1$  (high magnetisation). The solution of the problem at  $t = 4.0$  is shown in Fig. 2.16. Due to the high magnetisation of the test, the blast wave propagates outward, following the oblique field lines. The test preserves the symmetry with good accuracy, and no numerical artifacts or undesired instabilities appear in our simulation.

**3D rotor problem** A 3D version of the relativistic rotor problem was considered [Mignone, Ugliano, and Bodo 2009]. The computational box covered the domain  $[-0.5, 0.5]^3$ , with  $256^3$  cells and free boundary conditions everywhere. The initial configuration consisted of a sphere of density  $\rho_s = 10$  and radius  $r_s = 0.1$  that rotated around the  $z$ -axis with relativistic velocity components

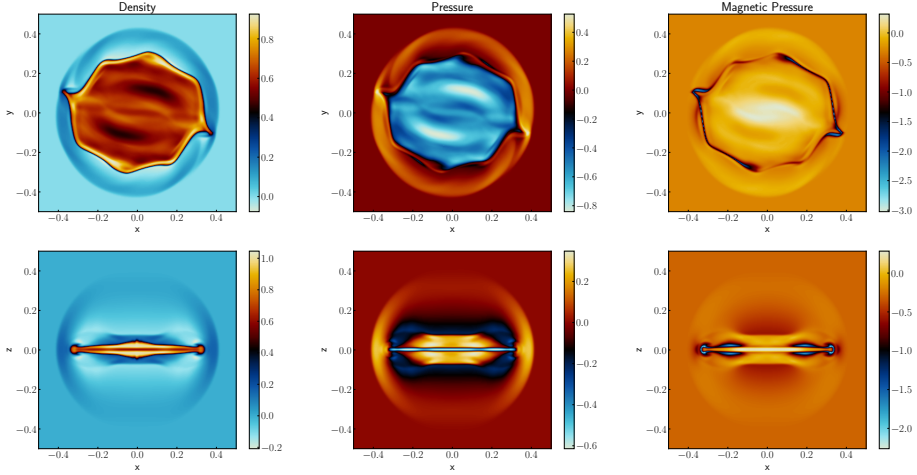


Figure 2.17 Logarithmic density (left), logarithmic pressure (middle), and logarithmic magnetic pressure (right) at  $t = 0.4$  for the 3D relativistic rotor problem in the  $xy$  plane at  $z = 0$  (top) and  $xz$  plane at  $y = 0$  (bottom). We consider the 3D Cartesian grid  $[-0.5, 0.5] \times [-0.5, 0.5] \times [-0.5, 0.5]$  with 256 cells per spatial dimension.

$(v_x, v_y, v_z) = \omega(-y, x, 0)$ , where  $\omega = 9.95$  is the angular velocity. The sphere was in pressure equilibrium with the ambient medium, whose pressure and density were  $p_a = 1$  and  $\rho_a = 1$ , respectively. The magnetic field was aligned with the  $x$ -direction in the whole domain,  $\mathbf{B} = (1, 0, 0)$ , and we used the non-relativistic adiabatic index,  $\Gamma = 5/3$ . The solution of the problem at  $t = 0.4$  is shown in Fig. 2.17. When the sphere starts to spin, complex torsional waves and shocks propagate outward, carrying angular momentum from the sphere to the medium, producing an octagon-like disc in the  $xy$  plane ( $z = 0$ ) surrounded by a shell of higher density and lower magnetic pressure, all embedded in a spherical fast rarefaction. The overall shape and the internal distribution of the flow agree well with the results presented in Mignone, Ugliano, and Bodo 2009 using the HLLD Riemann solver. The test also shows the same flow distortions in the  $xy$  plane along the  $x$ -axis, which are 3D numerical pathologies that do not manifest in the 2D version of the problem. This demonstrates that our version of HLLD works similar to the version in PLUTO for 3D applications.

**3D shock-cloud interaction** Finally, we considered a 3D version of the shock-cloud collision problem of Mignone and Bodo 2006, following the method described in Mignone et al. 2012. We performed the simulation in the computational box  $[0, 1] \times [-0.5, 0.5] \times [-0.5, 0.5]$ , with  $256^3$  cells and free boundary conditions in the whole domain. A shock-wave was initially located at  $x = 0.6$ .

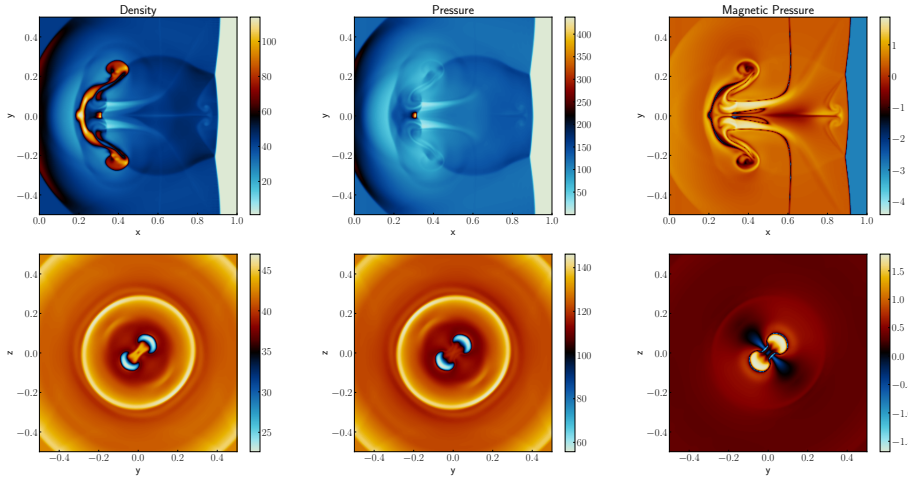


Figure 2.18 Density (left), pressure (middle), and logarithmic magnetic pressure (right) at  $t = 1.0$  for the 3D relativistic shock-cloud interaction in the  $xy$  plane at  $z = 0$  (top) and  $xz$  plane at  $y = 0$  (bottom). We consider the 3D Cartesian grid  $[0, 1.0] \times [-0.5, 0.5] \times [-0.5, 0.5]$  with 256 cells per spatial dimension.

Upstream ( $x > 0.6$ ), the pre-shocked material was defined by  $\rho = 1$ ,  $p_g = 10^{-3}$ ,  $W_x = 10$  ( $v_x = -0.995$ ),  $B_z = 0.5$ , while downstream, the medium was given by  $\rho = 42.5942$ ,  $p_g = 127.9483$ ,  $W_x = 1$ ,  $B_z = -2.12971$ . In this version, we reduced the magnitude of the  $z$ -component of the magnetic field with respect to the 2D test by  $B_z = B_z^{2D} / \sqrt{2}$ , and we set  $B_y = B_z$ . Transversal velocities  $v_y, v_z$  and the component of the magnetic field parallel to the  $x$ -axis,  $B_x$ , were initially set to zero everywhere. At  $x = 0.8$ , an overdense sphere of radius  $r = 0.15$  and density  $\rho = 10$  was set in pressure equilibrium with the preshocked material and was advected with the flow. For the ideal EoS, we considered the relativistic adiabatic factor,  $\Gamma = 4/3$ . The solution of the problem at  $t = 1.0$  is shown in Fig. 2.18. As in the 2D simulation, immediately after the impact between the cloud and the shock wave, the sphere experiments a strong compression that increases the density of the clump significantly. As a byproduct of this collision, a bow shock propagates to the left in the shocked material, and a reverse shock is transmitted to the right, penetrating the cloud and producing a mushroom-shaped structure like in the 2D shock-cloud interaction test. However, due to the lower resolution employed in this case, the pattern of waves that appear at the end of the test is more diffusive.

## 2.5 Relativistic Alfvén wave collisions

### 2.5.1 Introduction

In this last section of the chapter, I present the results of a project I performed during a research residence in the Department of Astrophysical Sciences of Princeton University (April-May 2022), in collaboration with Dr. Jens Mahlmann.

We study a scenario intended to test the ability of our new code LÓSTREGO to accurately model the energy transfer expected in weak Alfvénic turbulence for strongly magnetised plasma. The building block of MHD turbulence in these conditions are the counter-propagating Alfvén waves [see e.g., Howes and Nielson 2013, and references therein], which are excited in a broad range of astrophysical systems, as accretion discs around black holes and neutron star magnetospheres. In these systems, non-linear wave-wave interactions can provide a channel for the magnetic energy budget to be converted into kinetic and thermal energy by a weak turbulent cascade. In particular, three-wave collisions have been proposed as a key element in the development of weak Alfvénic turbulence and in the efficient transport of energy to smaller scales in both relativistic and non-relativistic plasmas, where it is eventually dissipated.

Two recent papers studied the regime of weak Alfvénic turbulence in relativistic plasmas by means of theory and numerical simulations. First, TenBarge et al. 2021 derived reduced RMHD equations of weak Alfvénic turbulence focusing on three-wave interactions and compared numerical and analytical solutions to show the similarities and discrepancies of both relativistic and non-relativistic regimes. In Ripperda et al. 2021, the authors used the same numerical scenario to show that the counter-propagating Alfvén wave collisions lead to the formation of currents sheets that act as local spots for magnetic energy dissipation.

### 2.5.2 Numerical setup

Our setup is based on the numerical simulations originally presented by TenBarge et al. 2021 and Ripperda et al. 2021. We consider the non-linear interaction between two overlapping, perpendicularly polarised Alfvén waves that counter-propagate in a periodic 3D domain along a uniform guide field  $\mathbf{B}_0 = B_0 \hat{z}$ , where we fix  $B_0 = 1$ . An explicatory 3D visualisation of the setup, but for the case of two counter-propagating Alfvén wave packets collision, is shown in Fig. 2.19.

The box dimensions are  $L_\perp = L_\parallel = L_x = L_y = L_z = 2\pi$  and we employ a resolution of  $N = 64^3$ . The medium is initially characterised by  $p_g = 0.01$  and  $\rho_0 = B_0^2/\sigma_{\text{cold}} = 0.1$ , such that  $\sigma_{\text{cold}} = 10$  (i.e., highly magnetised plasma).

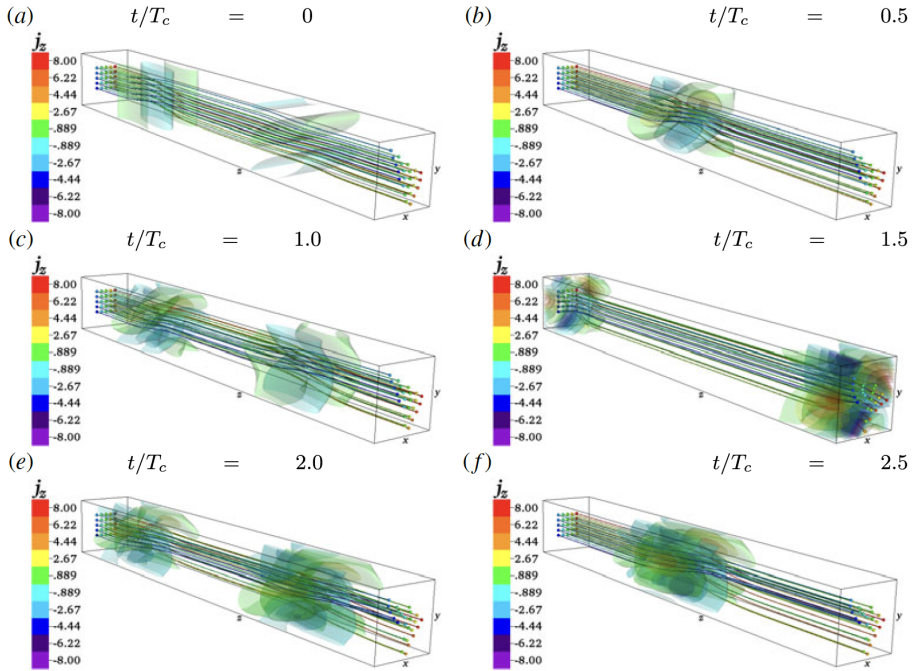


Figure 2.19 Three-dimensional isocontours of the normalised parallel current density between Alfvén wave packet collisions at six time frames. Reproduced with permission from Verniero, Howes, and Klein 2018 (Fig. 2).

This results in a pressure ratio  $\beta = 2p_g/B_0^2 = 0.02$ . The wave-vectors of the two Alfvén waves are  $\mathbf{k}_1^+ = k_\perp \hat{\mathbf{x}} + k_\parallel \hat{\mathbf{z}}$  and  $\mathbf{k}_1^- = k_\perp \hat{\mathbf{y}} - k_\parallel \hat{\mathbf{z}}$ , where  $k_\perp = k_\parallel = 1$ . The initial magnetic field is given by:

$$\begin{aligned} B_x &= k_\perp \chi B_0 \cos(k_\perp y - k_\parallel z), \\ B_y &= -k_\perp \chi B_0 \cos(k_\perp x + k_\parallel z), \\ B_z &= B_0, \end{aligned} \quad (2.69)$$

where the parameter  $\chi$  characterises the strength of the non-linearity as  $\chi = k_\perp \delta B_\perp / k_\parallel B_0$ . For this simulation, we consider  $\chi = 0.1$ , as in Ripperda et al. 2021.

From ideal MHD, the electric field follows:

$$\begin{aligned} E_x &= v_a B_y, \\ E_y &= v_a B_x, \\ E_z &= 0, \end{aligned} \quad (2.70)$$

where  $v_a$  is the Alfvén speed that is given by:

$$v_a = \sqrt{\frac{\sigma_{\text{hot}}}{1 + \sigma_{\text{hot}}}}. \quad (2.71)$$

In the latter equation,  $\sigma_{\text{hot}} = B_0^2/(h_0\rho_0)$ , and  $h_0$  is the specific enthalpy,  $h_0 = 1 + 4p/\rho_0$ , assuming an ideal equation of state with an adiabatic index  $\Gamma = 4/3$ . The initial velocity field is equal to the drift velocity,  $\mathbf{v} = \mathbf{E} \times \mathbf{B}/|B|^2$ :

$$\begin{aligned} v_x &= (E_x B_z - E_z B_y)/|B|^2, \\ v_y &= (E_z B_x - E_x B_z)/|B|^2, \\ v_z &= (E_x B_y - E_y B_x)/|B|^2. \end{aligned} \quad (2.72)$$

### 2.5.3 Results

Figure 2.20 shows the solution of the test until  $t = 5\omega_0/2\pi$ , where we represent perpendicular ( $B_\perp$ ) and parallel ( $B_\parallel$ ) mode amplitude as a function of the crossing time. This figure can be directly compared with the results presented in the third panel of Fig. 1 and Fig. 2 ( $\sigma_{\text{cold}} = 10$ ) of TenBarge et al. 2021.

As shown in the left panel of Fig. 2.20, the two initial perpendicularly polarised Alfvén waves (red lines) interact to produce a secondary mode (green line), represented by wave-vector (1,1,0), meaning that  $k_\parallel = 0$ . This mode is a non-linear magnetic shear mode which is purely oscillatory in time (i.e., there is no secularly mode growth) with  $\omega = 2\omega_0$ . This secondary mode interacts with the two initial waves to produce two higher order Alfvén waves (blue line), represented by wave-vectors (1,2,-1) and (2,1,1). The high order modes grow secularly in time following  $B_\perp \propto t$  (see black solid line, which is scaled by the mode amplitude). The evolution of the  $B_\parallel$  modes (right panel) can be used as a proxy for the development of fast mode fluctuations, since Alfvén waves have always  $k_\parallel = 0$ . Although the  $B_\parallel$  modes have zero amplitude at the beginning, they quickly develop finite amplitude, mixing at least two frequencies. In the parallel direction, the amplitude of the tertiary modes is similar to the initial waves, and the amplitude of the secondary mode (which is also composed of at least two frequencies) is the highest of the triad.

One important characteristic of this energy cascade in both weak and strong Alfvénic turbulence is that the energy transfer to smaller scales is anisotropic [Shebalin, Matthaeus, and Montgomery 1983], meaning that regardless of the strength of turbulence and isotropy at large scales, it eventually satisfies  $k_\parallel < k_\perp$ . This effect is clearly shown in Fig. 2.21, where we represent the binned spectral energy in the Fourier space ( $k_\perp$  vs.  $k_\parallel$ ). The energy cascade to smaller scales is

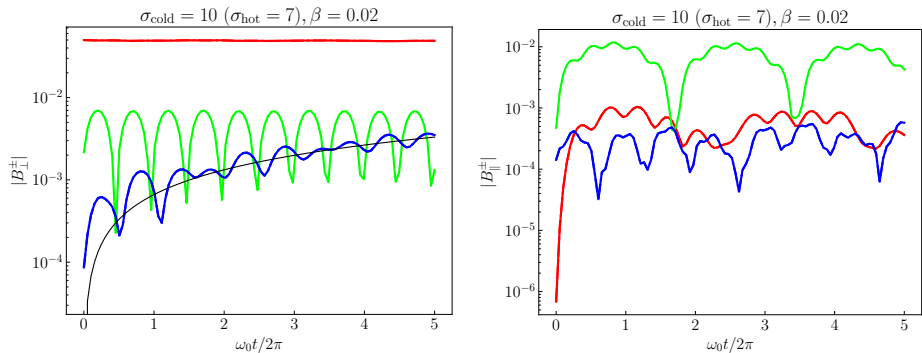


Figure 2.20 Mode evolution of  $B_{\perp}$  (left) and  $B_{\parallel}$  (right) for the Alfvén wave collision problem. Red lines correspond to the initial modes, green lines represent the second order non-linear mode and blue lines the third order modes. The black line corresponds to a secular growth linearly proportional to  $t$  and scaled by the wave amplitude. This figure can be directly compared with the results presented in the third panel of Fig. 1 and Fig. 2 of TenBarge et al. 2021 for  $\sigma_{\text{cold}} = 10$ .

also shown pictorially in Fig. 2.22, where we represent the spectral energy for 9 bins in the perpendicular plane ( $k_x$  vs.  $k_y$ ) for a set of 20 time frames. Primary, secondary and tertiary modes are represented with red, green and blue boxes, respectively. The figure shows the pulsating nature of the secondary wave and the smooth increase in energy of the secularly growing modes.

By solving this problem, we have demonstrated that LÓSTREGO is able to capture, even at low resolution, the energy cascade in relativistic, strongly magnetised, weak Alfvénic turbulence, driven by the interaction of three Alfvén waves; the building block of this type of process. Comparing our results with those presented in TenBarge et al. 2021, we conclude that we correctly solved the linear growing regime of high-frequency modes, as well as the anisotropic cascade predicted by weak Alfvénic turbulence theory. This means that our code shows good dissipation properties, allowing to capture the growth of little perturbations.

This will also allow us to explore the regime dominated by non-linear effects, which must be addressed at larger time scales than the ones presented in this section. In this way, the study of the magnetic and kinetic energy evolution, and especially the comparison between them, will enable to prove the existence of residual energy driven by the interaction of counter propagating Alfvén modes, as it has been proposed in the literature by different authors [Boldyrev, Perez, and Zhdankin 2012, Dorfman et al. 2021]. This analysis will be essential to

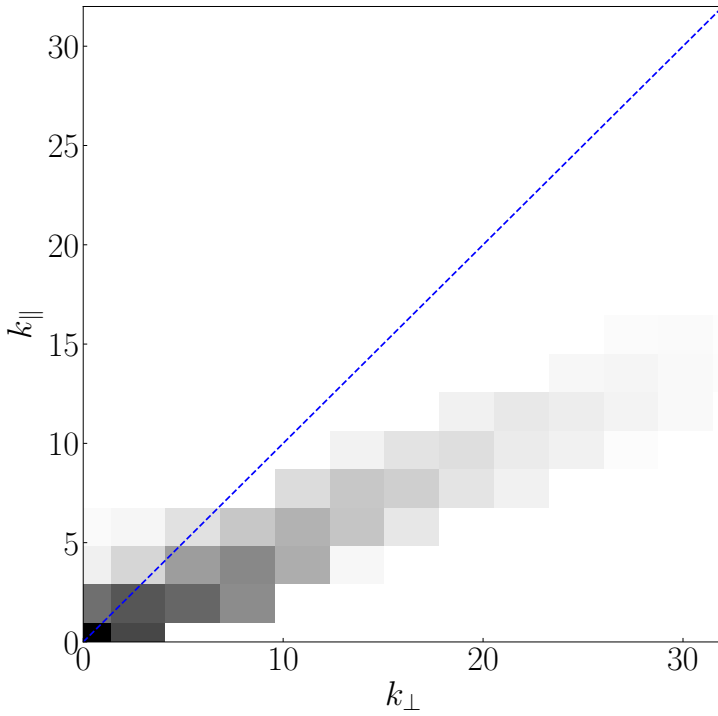


Figure 2.21 Energy spectra in the  $k_{\perp}$  vs.  $k_{\parallel}$  Fourier space, showing the anisotropic energy cascade to smaller wave amplitudes. Colour scale goes from white (lower energy) to black (higher energy).

understand, for example, the results obtained from observations of the solar wind [Chen et al. 2013, Bowen et al. 2018].

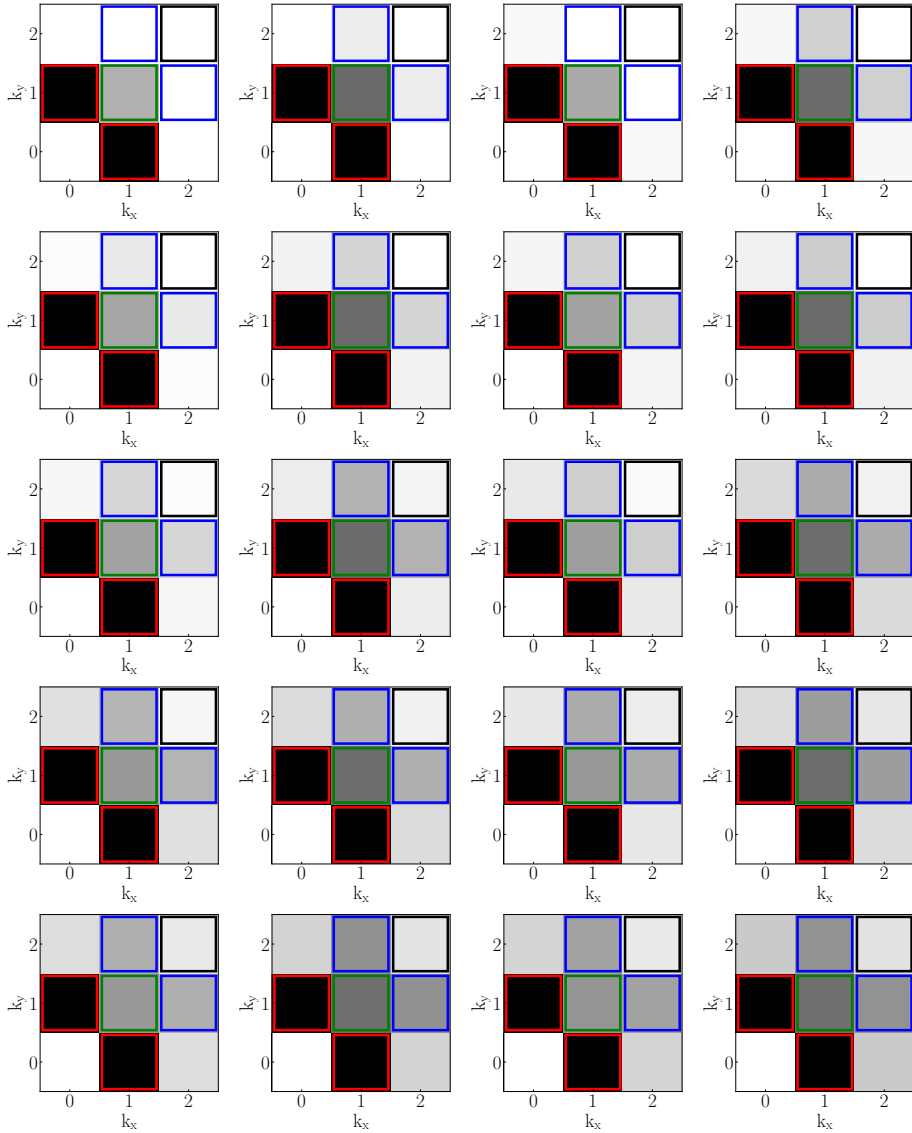


Figure 2.22 Energy spectra in the  $k_x$  vs.  $k_y$  Fourier space for 20 time frames, where colour scale ranges from white (lower energy) to black (higher energy). Red boxes show the two initial waves, while green and blue boxes show the second and third order modes represented in Fig. 2.20, respectively. Time goes from left to right and from top to bottom.



# Chapter 3

## Relativistic radiation magnetohydrodynamics

---

This chapter was originally published in *J. López-Miralles, J.M-Martí and M. Perucho. On the application of Jacobian-free Riemann solvers for relativistic radiation magnetohydrodynamics under M1 closure. Computer Physics Communications, 284, 108630. March 2023. DOI: 10.1016/j.cpc.2022.108630. Reproduced with permission.*

---

### 3.1 Introduction

#### 3.1.1 Radiation transport in high-energy astrophysics

Among the wide and complex variety of physical processes that govern high-energy astrophysics, radiative transfer plays a fundamental role in a broad range of energy scales. For example, the existence of a radiation field that coexists with plasma and (strong) electromagnetic fields is of great importance for modelling core-collapse supernovae [Obergaullinger, Just, and Aloy 2018, Burrows, Radice, and Vartanyan 2019], gamma-ray bursts [Aloy and Rezzolla 2006, Mészáros 2006, Rivera-Paleo and Guzmán 2016, Rivera-Paleo et al. 2017, Rivera-Paleo and Guzmán 2018], tidal disruption events [see e.g., Krolik et al. 2020], the extreme

environment around magnetars, pulsars [Becker et al. 2009] or accretion discs around black holes [Thorne 1974, Zanotti et al. 2011]. It is also essential for understanding the dynamical evolution of black hole and neutron star mergers [Hayashi et al. 2022, Radice et al. 2022], as well as the post-merger state [Foucart et al. 2015, Shibata, Fujibayashi, and Sekiguchi 2021]. In many of these systems, matter and radiation are strongly coupled and thus their feedback effects may be dynamically relevant.

For accretion discs around black holes, matter and photons can interact when the mass accretion rate is near or over the Eddington limit (i.e., supercritical accretion flows). This is the case of Seyfert galaxies [Ramos Almeida and Ricci 2017], but also for some microquasars in the high-luminous state, which have also been proposed to be at the origin of the emission of extragalactic Ultra Luminous X-ray Sources [King et al. 2001, Mineshige and Ohsuga 2011]. The high-mass X-ray binary SS433 is a fiducial example of this type of accretion [Begelman, King, and Pringle 2006, Khabibullin and Sazonov 2016]. In this scenario, geometrically thick discs are supported by radiation pressure. On the other hand, the dominance of radiation pressure in optically thick, geometrically thin (i.e., standard) accretion discs could be unstable to thermal and viscous instabilities [Shakura and Sunyaev 1976, Takahashi and Masada 2011]. Moreover, radiation pressure force could play a role in the acceleration of relativistic jets and/or winds [Sikora et al. 1996, Ohsuga et al. 2005, Okuda et al. 2005, Ohsuga et al. 2009, Okuda, Lipunova, and Molteni 2009, Takeuchi, Ohsuga, and Mineshige 2010, Ohsuga and Mineshige 2011, Sądowski and Narayan 2015, Raychaudhuri, Vyas, and Chattopadhyay 2021, see also Fig. 3.1], while radiation drag could act against it [Beskin, Zakamska, and Sol 2004].

Due to all of these reasons, radiative transfer plays a major role in high-energy astrophysics, and it is essential for understanding the interplay between theory, observations and numerical simulations. However, solving the full Boltzmann radiative transfer equation is in general a very computationally expensive task, so full three-dimensional (3D) global solutions are prohibited even for modern parallel architectures.

### 3.1.2 Review of numerical methods for radiation transport

In numerical simulations, the most common approach to assess the problem of radiative transfer is by radiative post-processing with ray-tracing algorithms [see e.g., Fromm et al. 2017, Fuentes et al. 2018, Fromm et al. 2019, Fuentes et al. 2021], specially for those scenarios where the interaction between matter and the

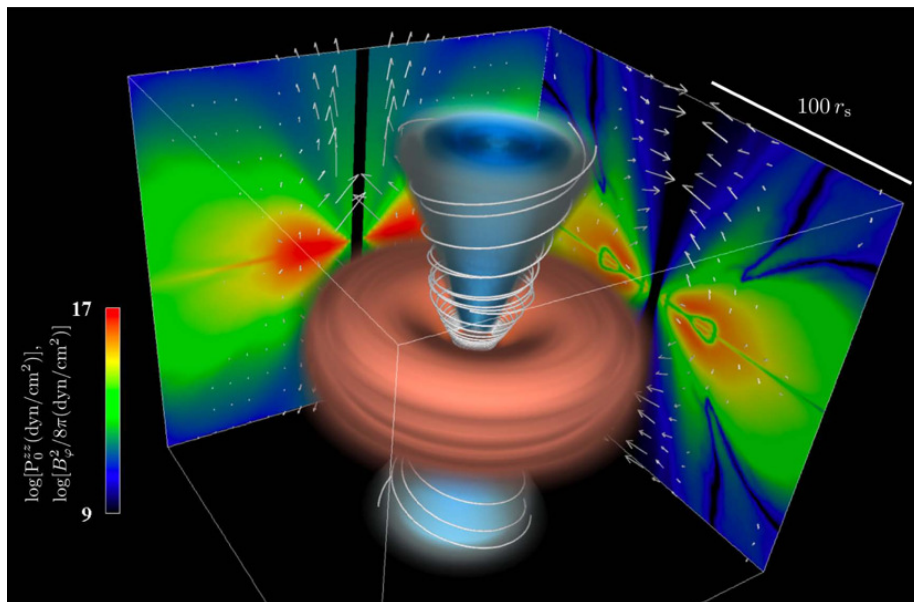


Figure 3.1 3D render of a relativistic jet accelerated by the radiation pressure force and collimated by the effect of magnetic fields. Reproduced with permission from Takeuchi, Ohsuga, and Mineshige 2010 (Fig. 1).

photon field can be neglected. This means that the radiative output is calculated once the hydrodynamical simulation has finished, avoiding the complexity of the coupling problem. In this kind of methods, the photon field is modelled as a large number of narrow beams (i.e., rays) that propagate through the computational grid. Although these strategies are generally accurate for a large range of scenarios, they are also computationally expensive and do not account for the back-reaction of radiation in the plasma dynamics. One alternative approach (followed in this chapter) consists on taking successive moments of the Boltzmann radiative transfer equation. These methods are usually faster and accurate and account for the photon-matter coupling, but they can suffer for high levels of numerical diffusion in some particular situations.

For example, the Flux-Limited Diffusion (FLD) approximation [Levermore and Pomraning 1981] takes a zeroth-order momentum of the Boltzmann equation to evaluate the radiation energy density. Then, radiation fluxes are evaluated as the gradient of the radiation energy density without solving the first moment equation. Although some authors reported appropriate results for the radiation field using the FLD approximation in the optically-thick regime, it might lead to wrong solutions when the optical depth is close to or lower than unity [Ohsuga

and Mineshige 2011]. Therefore, in order to have a robust method for both optically-thin and optically-thick regimes, both zero-th and first-order moments of the transport equation need to be considered. However, when solving more than one moment equation, a closure identity that relates the second moment of radiation (i.e., the radiation pressure tensor) with one of the lower order moments (e.g., the radiation energy density) is required, in the same way as the equation of state (EoS) relates the primitive thermal variables of the hydrodynamical system. This equation has the form,  $\tilde{P}_r^{ij} = \tilde{D}_r^{ij} \tilde{E}_r$ , where  $\tilde{E}_r$  is the radiation energy,  $\tilde{P}_r^{ij}$  is the radiation pressure tensor and  $\tilde{D}_r^{ij}$  is the Eddington tensor<sup>1</sup>. To select the particular form of the Eddington tensor, there are two main strategies. The first one, which is also the simplest, consists on assuming that the radiation field is isotropic in the comoving frame, taking  $\tilde{D}_r^{ij} = \delta^{ij}/3$  [Mihalas and Mihalas 1984]. This strategy, called the Eddington approximation, is only accurate for optically thick radiation transport. Other possibility, which is the one included in our code, is the M1 closure [Minerbo 1978, Levermore 1984]. This method takes into account the possible spatial anisotropies of the photon field and gives accurate results for both optically-thin and optically-thick regimes. With all of these considerations, the equations of relativistic radiation magnetohydrodynamics (Rad-RMHD) can be written as a system of conservations laws, where radiation-matter coupling appears as source terms in the equations. The main drawback of this approach is that, specially in the optically thick regime when matter and radiation interact more frequently, the equations of Rad-RMHD might become *stiff*, meaning that the time scales of radiation processes (i.e., heating/cooling and scattering) might be too short compared to the dynamical scales of the plasma. We overcome this issue by using an implicit-explicit (IMEX) Runge-Kutta (RK) time integration method [Takahashi et al. 2013], where the spatial derivatives on the Rad-RMHD equations are treated explicitly (i.e., with the same methods used for non-radiation RMHD), while interaction terms that account for the exchange of energy and momentum between matter and radiation are integrated implicitly.

In the context of relativistic radiation hydrodynamics (Rad-RHD) and Rad-RMHD, other authors have followed similar approaches. Takahashi et al. 2013 proposed an IMEX scheme for solving the equations of Rad-RHD taking zeroth and first moment equations of the radiative transfer equation. A similar approach was followed by Takahashi and Ohsuga 2013 to solve special relativistic, resistive

---

<sup>1</sup>In this expression, tildes indicate that all quantities are defined in a frame of reference moving with the radiation field (i.e., the comoving frame), which is the notation adopted for the rest of the chapter.

radiation magnetohydrodynamics equations, consistently updated using the M1 closure. This same closure was included in the codes R-CAFE [Rivera-Paleo and Guzmán 2019] and HARMRAD [McKinney et al. 2014] in the context of special Rad-RHD and general relativistic radiation magnetohydrodynamics, respectively. Weih, Olivares, and Rezzolla 2020 also followed a two-moment approach within an IMEX scheme under the M1 closure for general-relativistic radiation hydrodynamics. Melon Fuksman and Mignone 2019 included an independent module of radiation transport in the freely available PLUTO code, using an IMEX approach under the M1 closure relation. Other authors, for example Miniati and Colella 2007 or Sekora and Stone 2009, considered a slightly different method. They follow a higher order modified Godunov scheme that directly couples *stiff* source term effects to the hyperbolic structure of the system of conservation laws. This method is composed of a predictor step based on Duhamel’s principle and a corrector step based on Picard iterations.

### 3.1.3 Objectives and organization

In this chapter, I present a new scheme for treating radiation transport within the code LÓSTREGO, by which we solve the Rad-RMHD equations using an IMEX RK time integration method under the M1 closure for the radiation field. However, what makes this approach unique among others is the introduction of a new family of Jacobian-free approximate Riemann solvers based on Polynomial Viscosity Matrix (PVM) methods [Castro, Gallardo, and Marquina 2017, and references therein], which has never been applied before in the context of Rad-RMHD. For the sake of completeness, I have also introduced in LÓSTREGO a new family of high-order reconstruction methods [Monotonicity Preserving, MP; Suresh and Huynh 1997] and a five-step RK integration algorithm [Balsara 2001]. These high-order methods are properly tested in the numerical benchmark section (see Sec. 3.4) with a classical test problem in RMHD.

The chapter is organised as follows: in Sec. 3.2 I briefly describe the theoretical basis of radiative transfer and the system of equations of Rad-RMHD. In Sec. 3.3 I describe our scheme and the new methods and algorithms included in LÓSTREGO. In Sec. 3.4 I provide a benchmark of one-dimensional and multi-dimensional test problems to demonstrate that the scheme is robust and stable in different radiative scenarios. Finally, in Sec. 3.5 I discuss the results of the benchmark and I summarise the main conclusions of the chapter.

## 3.2 Governing equations

### 3.2.1 Radiation RMHD

The Rad-RMHD system of partial differential equations in the Minkowski metric<sup>2</sup> and Cartesian coordinates can be written as a system of conservation laws [see e.g., Melon Fuksman and Mignone 2019]:

$$\partial_t \mathbf{U} + \partial_i \mathbf{F}^i = \mathbf{S}, \quad (3.1)$$

where  $\mathbf{U} = \{D, S^j, \tau_e, B^j, E_r, F_r^j\}$  is a vector of conserved variables,  $D$  is the relativistic rest mass density,  $S^j$  is the momentum density of the magnetised fluid,  $\tau_e$  is the energy density (all of them measured in the Eulerian frame), and  $\mathbf{F}^i$  are the vector of fluxes for each spatial direction. These two vectors can be expressed as a function of a set of primitives  $\mathbf{V} = \{\rho, v^j, p, B^j, E_r, F_r^j\}$  through the following relations:

$$\mathbf{U} = \begin{pmatrix} D \\ S^j \\ \tau_e \\ B^j \\ E_r \\ F_r^j \end{pmatrix} = \begin{pmatrix} \rho W \\ \rho h^* W^2 v^j - b^0 b^j \\ \rho h^* W^2 - p^* - b^0 b^0 - \rho W \\ B^j \\ E_r \\ F_r^j \end{pmatrix}, \quad (3.2)$$

$$\mathbf{F}^i = \begin{pmatrix} \rho W v^i \\ \rho h^* W^2 v^i v^j + p^* \delta^{ij} - b^i b^j \\ \rho h^* W^2 v^i - b^0 b^i - \rho W v^i \\ v^i B^j - B^i v^j \\ F_r^j \\ P_r^{ij} \end{pmatrix}. \quad (3.3)$$

The set of primitive variables are the fluid rest-mass density  $\rho$ , fluid three-velocity  $v_j$ , and gas pressure  $p$ . In Eqs. 3.2 and 3.3,  $p^* = p + |b|^2/2$  is the total pressure,  $h^* = 1 + \epsilon + p/\rho + |b|^2/\rho$  is the total specific enthalpy and  $W = \sqrt{1 + u_i u^i}$  is the Lorentz factor of the fluid, where  $u^\mu = W(1, v^i)$  is the relativistic four-velocity and  $b^\mu$  is the relativistic magnetic field four-vector:

$$b^0 = W(\mathbf{v} \cdot \mathbf{B}), \quad (3.4)$$

$$b^i = \frac{B^i}{W} + v^i b^0. \quad (3.5)$$

<sup>2</sup>We assume a metric signature  $(-, +, +, +)$ . Greek subscripts in 4-vectors run from 0 to 3. Latin indices run from 1 to 3. In the following, we use a system of units where  $c = 1$  and a factor of  $1/\sqrt{4\pi}$  is absorbed in the definition of the magnetic field.

As in the case of RMHD, the magnetic field also obeys the divergence-free constraint:

$$\nabla \cdot \mathbf{B} = 0. \quad (3.6)$$

We shall consider a classical ideal gas with adiabatic exponent  $\Gamma$  which verifies the  $\Gamma$ -law EoS:

$$p = (\Gamma - 1)\rho\epsilon, \quad (3.7)$$

where  $\epsilon$  is the specific internal energy.

The magnetic field three-vector  $B^j$ , radiation energy density,  $E_r$ , and radiation flux,  $F_r^j$ , are both primitive and conserved variables.  $P_r^{ij}$  is the radiation pressure tensor, which is related with the radiation fields by means of a specific closure relation, as described in Sec. 3.2.2. The three radiation variables represent the first three moments of the radiation field and conform the radiation energy tensor in the laboratory frame [see e.g., Mihalas and Mihalas 1984, Takahashi et al. 2013]:

$$T_r^{\mu\nu} = \begin{pmatrix} E_r & F_r^i \\ F_r^j & P_r^{ij} \end{pmatrix}, \quad (3.8)$$

which satisfies:

$$\nabla_\mu T_r^{\mu\nu} = -\nabla_\mu (T_g^{\mu\nu} + T_{em}^{\mu\nu}) = -G^\nu, \quad (3.9)$$

where  $G^\nu$  is the radiation four-force and  $T_g^{\mu\nu}$ ,  $T_{em}^{\mu\nu}$  and  $T_r^{\mu\nu}$  are respectively the gas, electromagnetic and radiation components of the total energy-momentum tensor. The radiation four-force,  $G^\nu$ , represents the exchange of energy and momentum of matter and photons through absorption/emission and scattering processes, so the source terms in Eq. 3.1 are given by:

$$\mathbf{S} = \begin{pmatrix} 0 \\ G^j \\ G^0 \\ 0 \\ -G^0 \\ -G^j \end{pmatrix}, \quad (3.10)$$

which implies that the equations of evolution of relativistic density,  $D$ , and magnetic fields,  $B^j$ , are not affected by the photon field. The radiation four-force is explicitly given in the laboratory frame by [Takahashi et al. 2013]:

$$G^0 = -\rho\kappa (4\pi\mathcal{B}W - W E_r + u_i F_r^i) - \rho\sigma_s [W(W^2 - 1)E_r + W u_i u_j P_r^{ij} - (2W^2 - 1) u_i F_r^i], \quad (3.11)$$

$$G^i = -4\pi\rho\kappa\mathcal{B}u^i + \rho(\kappa + \sigma_s)(WF_r^i - u_j P_r^{ij}) - \rho\sigma_s u^i (W^2 E_r - 2W u_j F_r^j + u_j u_k P_r^{jk}), \quad (3.12)$$

where  $\kappa$  and  $\sigma_s$  are respectively the frequency-averaged absorption and scattering coefficients measured in the comoving frame (i.e., the grey-body approximation). This means that Eq. 3.9 is also a mixed-frame energy-momentum equation.

The variable  $\mathcal{B}$  represents the fluid blackbody intensity, which is related with the comoving emissivity  $\varepsilon$  through the Kirchhoff-Planck relation,  $\varepsilon = \kappa\mathcal{B}$ , which is valid for emission and absorption processes in matter in thermal equilibrium. Using the gas temperature,  $\mathcal{B}$  can be determined as:

$$\mathcal{B} = \frac{a_R T^4}{4\pi}, \quad (3.13)$$

where  $a_R$  is a radiation constant (that is related with the Stefan-Boltzmann constant by  $a_R = 4\sigma_{\text{SB}}$ ), and the gas temperature  $T$  is given by the ideal gas EoS:

$$T = \frac{p\mu m_p}{\rho k_B}, \quad (3.14)$$

where  $\mu$  is the mean molecular weight,  $m_p$  is the proton mass and  $k_B$  is the Boltzmann constant.

### 3.2.2 Radiation closure

Equation 3.7 provides a relation between the thermodynamic variables that closes the system of RMHD equations. For the Rad-RMHD system, an extra closure is needed to relate the radiation fields. This equation has the form:

$$P_r^{ij} = D_r^{ij} E_r, \quad (3.15)$$

where  $D_r^{ij}$  is the Eddington tensor. Among the different types of closure relations proposed in the literature, the simplest approach is the Eddington approximation, where the Eddington tensor in the comoving frame takes the form  $\tilde{D}_r^{ij} = \delta^{ij}/3$  [Mihalas and Mihalas 1984]. However, this method is only valid for the optically-thick radiation regime and it requires Lorentz transformations to calculate the radiation pressure tensor in the laboratory frame. Therefore, we have implemented the M1 closure [Minerbo 1978, Levermore 1984], which is valid in any reference frame and in both optical depth regimes, so it provides a better approximation to the radiation field than the Eddington approximation. Under this approach, the Eddington tensor is given by:

$$D_r^{ij} = \frac{1-\xi}{2}\delta^{ij} + \frac{3\xi-1}{2}n^i n^j, \quad (3.16)$$

where  $n^i = F_r^i/|\mathbf{F}_r|$  and  $\xi$  is the Eddington factor:

$$\xi = \frac{3 + 4f^2}{5 + 2\sqrt{4 - 3f^2}}, \quad (3.17)$$

where  $f = |\mathbf{F}_r|/E_r$  is the reduced radiative flux. In the optically-thick regime,  $|\mathbf{F}_r| \ll E_r$  and thus  $f \rightarrow 0$  which describes the diffusion limit, where  $P_r^{ij} \approx (\delta^{ij}/3) E_r$  (i.e., the Eddington approximation). In the optically-thin regime,  $|\mathbf{F}_r| \approx E_r$  and thus  $f \rightarrow 1$ , which is associated to the free-streaming limit of the Rad-RMHD equations.

### 3.3 Numerical methods

Our new radiation scheme is implemented in LÓSTREGO. Since the coupling between matter and radiation is represented by a collection of source terms (Eq. 3.10), the general structure of the RMHD code can be preserved, making the extension to Rad-RMHD more natural. This means that all methods described in Chapter 2, as well as the code parallelisation strategy, are still valid so I do not reproduce the techniques again. Instead, in this section I will concentrate on the methods and algorithms that are specific to solve the system of equations of Rad-RMHD.

#### 3.3.1 Numerical scheme

As described in Chapter 2, LÓSTREGO is based on multidimensional High Resolution Shock-Capturing (HRSC) methods where we follow the finite volumes (FV) scheme and dimensional splitting, taking the integral form of the conservation laws and cell-averaged values. A conservative one-dimensional discretisation of Eq. 3.1 yields:

$$\mathbf{U}_i^{n+1} = \mathbf{U}_i^n - \frac{\Delta t}{\Delta x} \left( \hat{\mathbf{F}}_{i+1/2} - \hat{\mathbf{F}}_{i-1/2} \right) + \Delta t \mathbf{S}_i^n, \quad (3.18)$$

where  $\mathbf{U}_i^n$  and  $\mathbf{S}_i^n$  are respectively the conserved variables and the source terms at  $t = n \Delta t$ , and  $\hat{\mathbf{F}}_{i\pm 1/2}$  are the numerical fluxes. In Eq. 3.18,  $x = x_i$  represents the position of the cell centre and  $x = x_{i\pm 1/2}$  the position of the right and left cell interfaces, respectively. The element  $\Delta x$  is the cell size and  $\Delta t$ , the time step. In the FV formalism,  $\mathbf{U}_i^n$  and  $\mathbf{S}_i^n$  represent an approximation to the averages of the corresponding quantities over the cell volume, while numerical fluxes  $\hat{\mathbf{F}}_{i+1/2}$  represent an approximation to the average of fluxes between  $t = n \Delta t$  and  $t = (n + 1) \Delta t$  at cell interfaces, obtained by solving Riemann problems with initial data at  $t = n \Delta t$ .

In our implementation of the IMEX scheme, we follow an extension of the total-variation-diminishing (TVD) RK schemes of Shu and Osher 1989 that we implemented in LÓSTREGO to integrate the equations of RMHD (see Chapter 2). In this case, the one-dimensional version of Eq. 3.1 is solved in two steps. First, the explicit step of the algorithm consists on solving the hyperbolic part of the equation:

$$\mathbf{U}_i^* = \mathbf{U}_i^n - \frac{1}{\Delta x} \left( \hat{\mathbf{F}}_{i+1/2} - \hat{\mathbf{F}}_{i-1/2} \right), \quad (3.19)$$

where  $\mathbf{U}_i^*$  are the conserved variables after the explicit step. The new Riemann solvers, which are the central element of the explicit step, are described in Sec. 3.3.2. Secondly, after every flux integration, the equation that gives the solution at  $t = (n + 1) \Delta t$ ,

$$\mathbf{U}_i^{n+1} = \mathbf{U}_i^* + \Delta t \mathbf{S}_i^n, \quad (3.20)$$

is solved implicitly as described in Sec. 3.3.3. For example, the third-order RK method (RK3) of Shu and Osher 1989 is adapted to this purpose as:

$$\begin{aligned} \mathbf{U}_i^* &= \mathbf{U}_i^{(0)} + \Delta t L \left( \mathbf{U}_i^{(0)} \right) \\ \mathbf{U}_i^{(1)} &= \mathbf{U}_i^* + \Delta t \mathbf{S}_i^{(0)} \\ \mathbf{U}_i^* &= \frac{3}{4} \mathbf{U}_i^{(0)} + \frac{1}{4} \mathbf{U}_i^{(1)} + \frac{1}{4} \Delta t L \left( \mathbf{U}_i^{(1)} \right) \\ \mathbf{U}_i^{(2)} &= \mathbf{U}_i^* + \frac{1}{4} \Delta t \mathbf{S}_i^{(1)} \\ \mathbf{U}_i^* &= \frac{1}{3} \mathbf{U}_i^{(0)} + \frac{2}{3} \mathbf{U}_i^{(2)} + \frac{2}{3} \Delta t L \left( \mathbf{U}_i^{(2)} \right) \\ \mathbf{U}_i^{(3)} &= \mathbf{U}_i^* + \frac{2}{3} \Delta t \mathbf{S}_i^{(2)}, \end{aligned} \quad (3.21)$$

where  $L \left( \mathbf{U}_i^{(n)} \right)$  is the upwind differencing operator:

$$L \left( \mathbf{U}_i^{(n)} \right) = -\frac{1}{\Delta x} \left( \hat{\mathbf{F}}_{i+1/2} - \hat{\mathbf{F}}_{i-1/2} \right). \quad (3.22)$$

### 3.3.2 Explicit step: the Riemann problem

The explicit step of the algorithm is based on the reconstruct-solve-update strategy. First, cell-average primitive variables are reconstructed to the cell interfaces by means of one of the following piecewise linear methods (PLM): MinMod [Roe 1986b], MC [van Leer 1977] or VanLeer [van Leer 1974]. The slope limiters implemented in these methods are essential to preserve the monotonicity and TV-stability of the algorithm. For the sake of completeness, we have also included the high-order MP reconstruction of Suresh and Huynh 1997, although

for the purposes of this work we restrict its applicability to problems with no radiative transport. In RMHD, we reduce the reconstruction to zero-th order (i.e., Godunov reconstruction) when the algorithm lead to non-physical solutions, as it is the case for superluminal velocities,  $|\mathbf{v}|^2 > 1$ . In Rad-RMHD, we also need to provide an upper limit for the radiation flux, such that:

$$|\mathbf{F}_r| \leq E_r. \quad (3.23)$$

After reconstructing the primitives at the cell boundaries, we solve an initial value problem by using an approximate Riemann solver to obtain the numerical fluxes at each cell interface. Finally, once fluxes are known at each cell face, the conserved variables are evolved explicitly in time according to Eq. 3.19. Although the HLL-family of Riemann solvers can be naturally extended to Rad-RMHD, matter and radiation usually have different maximum/minimum characteristic velocities. We devote the rest of this section to describe the Rad-RMHD version of the HLL Riemann solver, what type of limitations one can expect and a different approach based on a new family of algorithms.

### 3.3.2.1 Radiative HLL

A radiative version of the HLL Riemann solver was proposed, for instance, by González, Audit, and Huynh 2007 and Melon Fuksman and Mignone 2019. In classical fluid dynamics [Harten, Lax, and Leer 1983, Toro 2013], the initial discontinuity is decomposed into two fast magnetosonic waves with characteristic speeds  $\lambda_L, \lambda_R$ , such that the internal fluxes are derived from the Rankine-Hugoniot jump conditions across the two magnetosonic waves. The numerical fluxes at  $x = x_{i+1/2}$  are then given by:

$$\hat{\mathbf{F}}_{i+1/2} = \begin{cases} \mathbf{F}_L, & \text{if } \lambda_L > 0, \\ \mathbf{F}_{i+1/2}^{\text{hll}}, & \text{if } \lambda_L \leq 0 \leq \lambda_R, \\ \mathbf{F}_R, & \text{if } \lambda_R < 0. \end{cases} \quad (3.24)$$

where:

$$\mathbf{F}_{i+1/2}^{\text{hll}} = \frac{\lambda_R \mathbf{F}_L - \lambda_L \mathbf{F}_R + \lambda_R \lambda_L (\mathbf{U}_R - \mathbf{U}_L)}{\lambda_R - \lambda_L}, \quad (3.25)$$

with  $\mathbf{U}_{L,R} = \mathbf{U}_{i,i+1}^n$  and  $\mathbf{F}_{L,R} = \mathbf{F}(\mathbf{U}_{L,R})$ . The new version of HLL is based on the fact that the Jacobian matrix for the radiation part of Eq. 3.1,  $J_{\text{rad}}^i$ , is only a function of the radiation energy density  $E_r$  and the radiation flux  $\mathbf{F}_r$ :

$$J_{\text{rad}}^i = \begin{pmatrix} \partial F_r^i / \partial E_r & \partial F_r^i / \partial F_r^j \\ \partial P_r^{ij} / \partial E_r & \partial P_r^{ij} / \partial F_r^j \end{pmatrix}, \quad (3.26)$$

so the Jacobian of the system of Rad-RMD equations can be decomposed in two different blocks: one submatrix for the magnetofluid and other submatrix for the radiation field. This means that the wave speeds  $\lambda_L, \lambda_R$  can be calculated independently for each of these blocks, avoiding the excessive numerical diffusion that appears when employing the same velocities for both subsystems. On the one hand, for the RMHD block, these characteristic speeds (which are the maximum and minimum eigenvalues of the Jacobian matrix of the reconstructed states) are the solution of a quartic equation, for which we employ a root-finding method [Anile 1989, Antón et al. 2010]. On the other hand, for the radiation block, the full set of eigenvalues are given by the following analytical expressions [Audit et al. 2002, Skinner and Ostriker 2013, Melon Fuksman and Mignone 2019]:

$$\lambda_{r1} = \frac{f \cos \theta - \zeta(f, \theta)}{\sqrt{4 - 3f^2}}, \quad (3.27)$$

$$\lambda_{r2} = \cos \theta \frac{3\xi(f) - 1}{2f}, \quad (3.28)$$

$$\lambda_{r3} = \frac{f \cos \theta + \zeta(f, \theta)}{\sqrt{4 - 3f^2}}, \quad (3.29)$$

where  $\xi(f)$  is given by Eq. 3.17 and  $\zeta(f, \theta)$  by:

$$\zeta(f, \theta) = \left[ \frac{2}{3} \left( 4 - 3f^2 - \sqrt{4 - 3f^2} \right) + 2 \cos \theta^2 \left( 2 - f^2 - \sqrt{4 - 3f^2} \right) \right]^{1/2}, \quad (3.30)$$

where  $\theta$  represents the angle between  $\mathbf{F}_r$  and the upwind direction  $\hat{\mathbf{e}}_d$ , adopting the same notation as in Melon Fuksman and Mignone 2019. A different approach is followed by Takahashi et al. 2013, where the wave velocities were computed from the Jacobian matrix and tabulated before time integration. In the free-streaming limit (i.e.,  $f \rightarrow 1$ ), the three eigenvalues are degenerate and become  $\lambda_{r1} = \lambda_{r2} = \lambda_{r3} \rightarrow \cos \theta$ , such that in the parallel direction to  $\mathbf{F}_r$  the speed of light is recovered. In the same way, in the perpendicular direction, there is no transport of radiation. On the other hand, in the diffusion limit (i.e.,  $f \rightarrow 0$ ), the three characteristic speeds are  $\lambda_{r2} \rightarrow 0$  and  $\lambda_{r1,r3} \rightarrow \pm 1/\sqrt{3}$ . However, for optically thick media, these speeds can overestimate the correct speeds, leading to excessive numerical diffusion. To avoid it, Sądowski et al. 2013 suggests to

locally limit the maximum and minimum speeds by means of:

$$\lambda_{r,L} = \max\left(\lambda_{r1}, -\frac{4}{3\tau}\right); \lambda_{r,R} = \min\left(\lambda_{r3}, +\frac{4}{3\tau}\right), \quad (3.31)$$

where  $\tau = \rho W(\kappa + \sigma_s)\Delta x$  is the optical depth along one single cell.

Although HLL is usually a robust solver, it can be rather diffusive for some specific applications. Thus, to improve the accuracy of the solutions, Melon Fuksman and Mignone 2019 presented a novel version of the three-wave HLLC Riemann solver of Mignone, Massaglia, and Bodo 2005 and Mignone and Bodo 2006 for the radiation transport. However, since the outermost velocities must be limited in optically thick cells, their scheme is no longer valid and the algorithm must be switched to the standard HLL when this occurs. This means that the radiative HLLC solver of Melon Fuksman and Mignone 2019 can only improve the accuracy of Rad-HLL in optically thin media. Furthermore, the five-wave HLLD scheme of Mignone, Ugliano, and Bodo 2009, which is also included in LÓSTREGO, cannot be adapted for radiation transport since the radiation block has only three non-degenerate characteristic waves.

### 3.3.2.2 Polynomial Viscosity Matrix Riemann solver

As discussed in the previous section, one fundamental obstacle to solve the system of Rad-RMHD equations is that the characteristic speeds of the two individual blocks can be, in general, very different. This means that using the same signals for both systems could lead to unacceptable levels of numerical diffusion. Moreover, in the optically thick regime, the maximum and minimum characteristic speeds have to be limited by Eq. 3.31, what makes that Rad-HLLC only improves the accuracy of the standard HLL Riemann solver in the optically thin limit. Thus, Jacobian-free low dissipative solvers are desirable for these reasons.

The Polynomial Viscosity Matrix (PVM) methods were introduced by Castro Díaz and Fernández-Nieto 2012 for hyperbolic systems. These solvers are defined in terms of viscosity matrices that are based on polynomial evaluations of a Roe matrix [see e.g., Cargo and Gallice 1997, Toro 2013] or the Jacobian of the flux at some average value. Castro, Gallardo, and Marquina 2014 further extended the idea to the case of Rational Viscosity Matrix functions (RVM), while Castro, Gallardo, and Marquina 2016 applied the technique to the Dumber-Osher-Toro (DOT) schemes, which are a simpler approximation of the classical Osher-Solomon method [Osher and Solomon 1982, Castro, Gallardo, and Marquina 2016]. Later, Castro, Gallardo, and Marquina 2017 investigated two Jacobian-

free implementations of the PVM/RVM methods in the context of the special RMHD equations, one based on Chebyshev polynomials and other built using internal approximations to the absolute value function. All together, these methods form a new family of approximate Riemann solvers.

In the rest of this section, I will concentrate on PVM solvers based on internal approximations of  $n$ -degree (hereinafter, PVM-int- $n$ ). The main advantage of these techniques is that they guarantee the stability conditions needed to ensure the robustness and convergence of the algorithm. Moreover, the underlying polynomials allows a Jacobian-free formulation of the scheme, where only evaluations of the flux and vector operations are involved. This is particularly relevant to solve the system of Rad-RMHD equations, where the eigenvalues of the radiation Jacobian matrix have to be calculated independently of the magnetofluid subsystem.

In general, the numerical fluxes of any hyperbolic system of conserved equations have the following form:

$$\hat{\mathbf{F}}_{i+1/2} = \frac{\mathbf{F}_L + \mathbf{F}_R}{2} - \frac{1}{2} Q_{i+1/2} (\mathbf{U}_R - \mathbf{U}_L), \quad (3.32)$$

where  $Q_{i+1/2}$  is the numerical viscosity matrix, and  $\mathbf{U}_{L,R} = \mathbf{U}_{i,i+1}^n$ ,  $\mathbf{F}_{L,R} = \mathbf{F}(\mathbf{U}_{L,R})$ . In the Roe's method, the viscosity matrix can be written as  $Q_{i+1/2} = |A_{i+1/2}|$ , where  $A_{i+1/2}$  is a Roe matrix of the system [Torrilhon 2012, Cordier, Degond, and Kumbaro 2014]. The PVM method allows to approximate the viscosity matrix by:

$$Q_{i+1/2} = |\lambda_{i+1/2,\max}| p(|\lambda_{i+1/2,\max}|^{-1} A_{i+1/2}), \quad (3.33)$$

where  $p(x)$  is a polynomial approximation of  $|x|$  in the interval  $[-1, 1]$  and  $\lambda_{i+1/2,\max}$  is an upper bound to the maximum eigenvalue of the Roe matrix. In the internal polynomial approximation,  $p(x)$  is iteratively constructed as:

$$p_0(x) = 1, p_k(x) = \frac{1}{2} (2p_{k-1}(x) - p_{k-1}(x)^2 + x^2), \quad (3.34)$$

where  $k = 1, 2, \dots$  determines the degree of the approximation as  $\deg(p_k) = 2^k$ . Following Castro, Gallardo, and Marquina 2017, we consider  $k = 3$  ( $\deg(p_3) = 8$ ) and we assume  $\lambda_{i+1/2,\max} = 1$ , which is a reasonable upper bound for radiation transport. Using the explicit form, Eq. 3.34 becomes:

$$p_3(x) = x^2(x^2(x^2(\alpha_0 x^2 + \alpha_1) + \alpha_2) + \alpha_3) + \alpha_4, \quad (3.35)$$

with coefficients  $\alpha_0 = -1/128$ ,  $\alpha_1 = 3/32$ ,  $\alpha_2 = -23/64$ ,  $\alpha_3 = 31/32$ ,  $\alpha_4 = 39/128$  [Castro, Gallardo, and Marquina 2017]. With all of these ingredients, the term  $Q_{i+1/2} (\mathbf{U}_R - \mathbf{U}_L)$  in Eq. 3.32 can be computed for each cell interface

using the Horner's algorithm [Horner 1819]. Our implementation is summarised as follows for a polynomial of  $\deg(p_k) = 2^k$ :

1. Starting from the reconstructed primitive variables  $\mathbf{V}_L, \mathbf{V}_R$ , calculate  $\mathbf{U}_L, \mathbf{U}_R$  with Eq. 3.2 and  $\mathbf{F}_L, \mathbf{F}_R$  with Eq. 3.3. Define  $\mathbf{U}_0 = \mathbf{U}_R - \mathbf{U}_L$ .
2. Take  $\mathbf{U}_m = (\mathbf{U}_L + \mathbf{U}_R)/2$  as an arbitrary state and evaluate the Jacobian matrix,  $A \equiv A(\mathbf{U}_m)$ , on this state. Recover the primitive variables for the arbitrary state,  $\mathbf{V}_m$ , by the inversion algorithm presented on Chapter 2.
3. Define a new set of variables  $\mathbf{U}_\epsilon = \mathbf{U}_m + \epsilon \mathbf{U}_0$ , where  $\epsilon = 10^{-8}$ , and recover  $\mathbf{V}_\epsilon$ . Calculate  $\mathbf{F}(\mathbf{U}_m(\mathbf{V}_m))$  and  $\mathbf{F}(\mathbf{U}_\epsilon(\mathbf{V}_\epsilon))$  with Eq. 3.3.
4. Define a new set of variables  $\tilde{\mathbf{U}}_\epsilon = \mathbf{U}_m + \mathbf{F}(\mathbf{U}_\epsilon) - \mathbf{F}(\mathbf{U}_m)$  and recover  $\tilde{\mathbf{V}}_\epsilon$ .
5. Calculate  $\mathbf{U}_1 = \alpha_0 \tilde{\mathbf{U}}_0 + \alpha_1 \mathbf{U}_0$ , where:

$$\tilde{\mathbf{U}}_0 = A^2 \mathbf{U}_0 \equiv \Phi_\epsilon(\mathbf{U}_m(\mathbf{V}_m); \mathbf{U}_0(\mathbf{V}_0)) \approx \frac{\mathbf{F}(\tilde{\mathbf{U}}_\epsilon(\tilde{\mathbf{V}}_\epsilon)) - \mathbf{F}(\mathbf{U}_m(\mathbf{V}_m))}{\epsilon}. \quad (3.36)$$

6. For  $l = 1, 2, \dots, k$ , repeat steps 3 and 4 for  $\epsilon \mathbf{U}_0 \rightarrow \epsilon \mathbf{U}_l$ . Calculate  $\mathbf{U}_{l+1} = \tilde{\mathbf{U}}_l + \alpha_{l+1} \mathbf{U}_0$ , where  $\tilde{\mathbf{U}}_l \equiv \Phi_\epsilon(\mathbf{U}_m(\mathbf{V}_m); \mathbf{U}_l(\mathbf{V}_l))$  is given by Eq. 3.36.
7. Finally,  $|A(\mathbf{U}_m)|\mathbf{U}_0 \equiv Q_{i+1/2}(\mathbf{U}_R - \mathbf{U}_L) \approx \mathbf{U}_{k+1}$ .

Nevertheless, we must stress the fact that in the optically-thick regime, this scheme might introduce undesirable levels of numerical diffusion (see details on Sec. 3.4.1.4). This pathology has been also identified with other types of Riemann solvers [see e.g., González, Audit, and Huynh 2007]. Intuitively, one might be tempted to suppress the viscosity matrix when the opacity is larger than 1.

However, since this yields oscillatory solutions, we propose to reduce the numerical viscosity,  $Q_{i+1/2}(\mathbf{U}_R - \mathbf{U}_L)$ , in optically-thick media in a smooth

way inversely proportional to the cell local opacity,  $\tau$ , such that:

$$\hat{\mathbf{F}}_{i+1/2} \approx \frac{\mathbf{F}_L + \mathbf{F}_R}{2} - \beta \frac{\mathbf{U}_{k+1}}{2}, \quad (3.37)$$

with

$$\beta = \min \{1/\tau_L, 1/\tau_R, 1\} \quad (3.38)$$

( $\tau_{L,R}$  stand for the cell optical depth at the left and right, respectively, of interface  $i + 1/2$ ). This particular choice of the coefficient  $\beta$  is based on the adimensional nature of the cell opacity and the robustness of the algorithm in the optically-thick regime.

### 3.3.3 Implicit step

The implicit step of the algorithm consists of a series of steps to integrate Eq. 3.20 in time. Due to the particular form of the source terms (Eq. 3.10), we only need to deal with the following reduced subsystem:

$$\mathbf{U}_r^{n+1} = \mathbf{U}_r^* + \Delta t \mathbf{S}_r^n, \quad (3.39)$$

where  $\mathbf{U}_r = (E_r, \mathbf{F}_r)$ , while  $\mathbf{S}_r = (-G^0, -G^i)$  is given by Eqs. 3.11 and Eq. 3.12. This is because the total energy and the total momentum of the system:

$$\tau_{e,t} = \tau_e^* + E_r^*, \quad (3.40)$$

$$\mathbf{S}_t = \mathbf{S}^* + \mathbf{F}_r^*, \quad (3.41)$$

must be conserved during the implicit step, such that the energy density and momentum of the magnetofluid can be finally updated as  $\tau_e^{n+1} = \tau_{e,t} - E_r^{n+1}$  and  $\mathbf{S}^{n+1} = \mathbf{S}_t - \mathbf{F}_r^{n+1}$ . This implicit step is based on an iterative process which comprises the following substeps:

1. Starting from the output of the explicit step  $\mathbf{U}^*$ , calculate the total energy and total momentum of the magnetofluid with Eq. 3.40 and Eq. 3.41.
2. Construct the matrix  $\mathbf{C}^{(m)}$ , whose elements are [see e.g., Takahashi and Ohsuga 2013]:

$$\begin{aligned} C_{11}^{(m)} &= 1 - \Delta t \rho W [-\kappa + \sigma_s (W^2 - 1 + u_i u_j D_r^{ij})] \\ C_{1j+1}^{(m)} &= -\Delta t \rho u_j [\kappa - \sigma_s (2W^2 - 1)] \\ C_{i+11}^{(m)} &= -\Delta t \rho [(\kappa + \sigma_s) u_j D^{ij} + \sigma_s u^i (W^2 + u_k u_l D_r^{kl})] \\ C_{i+1j+1}^{(m)} &= \delta_j^i - \Delta t \rho W [(\kappa + \sigma_s) \delta_j^i + 2\sigma_s u^i u_j]. \end{aligned} \quad (3.42)$$

3. Solve the system:

$$\mathbf{C}^{(m)} \begin{pmatrix} E_r^{(m+1)} \\ F_r^{i,(m+1)} \end{pmatrix} = \begin{pmatrix} E_r^* + (4\pi\rho W\kappa B)^{(m)} \Delta t \\ F_r^{i,*} + (4\pi\rho u^i\kappa B)^{(m)} \Delta t \end{pmatrix} \quad (3.43)$$

using an inversion method, for example, the LU-decomposition [Takahashi et al. 2013]. For the first iteration, we take  $E_r^0 = E_r^*$  and  $\mathbf{F}_r^0 = \mathbf{F}_r^*$ .

4. Update the fluid energy density,  $\tau_e^{(m+1)} = \tau_{e,t} - E_r^{(m+1)}$ , and momentum,  $\mathbf{S}^{(m+1)} = \mathbf{S}_t - \mathbf{F}_r^{(m+1)}$ . For the relativistic rest-mass density and magnetic fields, we already have  $D^{(n+1)} = D^*$  and  $\mathbf{B}^{(n+1)} = \mathbf{B}^*$ .

5. Recover primitive variables with the inversion scheme.

6. Check if the relative error of the radiation fields falls below a specified threshold; if not, update radiation fields and start a new iteration (substep 2).

## 3.4 Testing benchmark

In this section, I provide a collection of one dimensional and multidimensional numerical problems. Unless otherwise stated, all tests were performed using the PVM-int-8 Riemann solver and the second-order accurate PLM VanLeer reconstruction algorithm. In multidimensional problems, the VanLeer reconstruction algorithm is degraded to the more diffusive MinMod slope limiter around strong shocks [Mignone, Massaglia, and Bodo 2005]. For time integration, we used the IMEX third-order TVD RK algorithm [Shu and Osher 1989] with CFL=0.3. Magnetic field divergence free constraint is preserved by using the CT method, where electromotive forces were averaged according to the CT-contact formalism [Gardiner and Stone 2005]. In high magnetization regimes, the relativistic correction scheme of Martí 2015a was used to correct the conserved variables after each time integration.

### 3.4.1 One dimensional tests

We propose a collection of 1D problems to test the performance of the new methods in the context of RMHD and Rad-RMHD. First, we solve a large-amplitude circularly-polarised Alfvén wave without radiation to demonstrate

that the code achieves third order and fifth order of accuracy using high-order spatial reconstruction together with third order and fourth order RK, respectively. Secondly, we test the explicit part of the new radiation module with a Riemann problem for the optically-thin radiation transport, neglecting any interaction between matter and radiation. Finally, we implement a collection of shock problems and the diffusion of a radiation pulse without neglecting the interaction terms, in order to test the performance of the new IMEX scheme.

### 3.4.1.1 Circularly-polarised Alfvén wave

We considered a smooth RMHD test problem that consists on the propagation of a large-amplitude, circularly polarised Alfvén wave along a uniform background magnetic field  $B_0$ . This test was previously used by Del Zanna et al. 2007 and Beckwith and Stone 2011 to test the accuracy of their codes ECHO and ATHENA, respectively. Martí and Müller 2015 also reported second-order accuracy for their code with this test. The transverse components of the velocity field were initialised as:

$$v_y = -A \cos\left(\frac{2\pi}{\lambda}(x - v_a t)\right), v_z = -A \sin\left(\frac{2\pi}{\lambda}(x - v_a t)\right), \quad (3.44)$$

where  $A$  is the amplitude of the wave, and  $\lambda$  its wavelength, and

$$B_x = B_0, B_y = -B_0 v_y / v_a, B_z = -B_0 v_z / v_a. \quad (3.45)$$

In the previous expressions, the speed of the Alfvén wave,  $v_a$ , is given by:

$$v_a = \pm \sqrt{\frac{B_0^2 (1 - A^2)}{\rho_0 h_0 + B_0^2 (1 - A^2)}}, \quad (3.46)$$

where  $\rho_0$  and  $h_0$  are the density and the specific enthalpy of the background uniform medium. For this, we choose  $\rho_0 = 1$ ,  $h_0 = 5$  ( $\Gamma = 4/3$ ) and  $B_0 = 1$ . The amplitude of the wave is taken as:

$$A = \sqrt{\frac{2}{7 + 3\sqrt{5}}}. \quad (3.47)$$

To test the order of our code with this problem, we run a collection of simulations in the domain  $[0, 2\pi]$  for different spatial resolutions (i.e, from  $N=16$  to  $N=512$  zones) and we measured the L1-errors in one of the transverse components of the velocity field (i.e.,  $v_z$ ) after one entire wave period ( $T = \lambda/v_a$ ), comparing with the initial conditions. This process was repeated for all the Riemann solvers (HLL, HLLC, HLLD) and all the PLM limiters (MinMod, MC, VanLeer) available in LÓSTREGO. Additionally, we also tested the MP reconstruction of

Suresh and Huynh 1997 together with HLLD and the new PVM-int-8 Riemann solver. To highlight the performance of the solver, we have also run the test with the first-order version of the code (i.e, Godunov spatial reconstruction).

The results of our analysis are shown in Tables 3.1-3.5 and in Fig. 3.2. We demonstrated that our code achieves first-order accuracy in the case of Godunov reconstruction and second-order accuracy for all the PLM methods, although in the latter case MinMod generally yields higher errors than the other slope limiters. In the case of HLLC (Tab. 3.2), our results are the same as those obtained in Martí and Müller 2015. HLLD (Tab. 3.3) shows similar performance than HLLC, as it is expected for smooth solutions. Using MP3 reconstruction together with HLLD and RK3, we achieved third order of accuracy, but we were not able to increase the order of the code using fifth-order spatial reconstruction (i.e., MP5).

This means that, for smooth RMHD problems, RK3 limits the accuracy of the code to third order, even should we employ higher-order spatial reconstructions. This is not the case, however, if we use a five-step RK4 algorithm [Balsara 2017, and references therein], with which the code achieves the nominal fifth order of accuracy (MP5+RK4 in Tab. 3.5). Finally, the results of the PVM-int-8 solver shown in Tab. 3.4 are very similar to those found with HLLC (see also Fig. 3.2). We also proved third order of accuracy with the new Riemann solver together with the MP3 reconstruction and the RK3 algorithm.

Table 3.1 Code accuracy for the large-amplitude circularly polarized Alfvén wave test employing the HLL Riemann solver and zero-th/first-order reconstruction. RK3 was used in all the calculations. For each reconstruction algorithm, the first row displays the L1-norm errors for the  $v_z$  component of the velocity after one period of time. The second row compiles the corresponding order of accuracy from contiguous spatial resolutions.

<b>HLL</b>	N=8	N=16	N=32	N=64	N=128	N=256	N=512
Godunov	0.242793	0.209234	0.157907	0.105586	0.063334	0.035223	0.018672
	-	0.214612	0.406045	0.580648	0.737373	0.846470	0.915669
MinMod	0.200698	0.100186	0.029124	0.006919	0.001937	0.000533	0.000139
	-	1.002341	1.782403	2.073510	1.836458	1.861338	1.937243
MC	0.148572	0.033643	0.006466	0.001386	0.000326	$7.927 \times 10^{-5}$	$1.948 \times 10^{-5}$
	-	2.142766	2.379298	2.221720	2.086197	2.042077	2.024194
VanLeer	0.169355	0.050479	0.010169	0.001901	0.000398	$9.017 \times 10^{-5}$	$2.112 \times 10^{-5}$
	-	1.746282	2.311483	2.418651	2.254662	2.143970	2.093994

Table 3.2 Same as Table 3.1 but employing the HLLC Riemann solver.

<b>HLLC</b>	N=8	N=16	N=32	N=64	N=128	N=256	N=512
Godunov	0.237358	0.192402	0.137008	0.087538	0.050748	0.027606	0.014446
	-	0.302943	0.489863	0.646273	0.786574	0.878347	0.934353
MinMod	0.182472	0.081609	0.021935	0.005471	0.001513	0.000404	0.000104
	-	1.160869	1.895440	2.003176	1.854302	1.902286	1.948340
MC	0.126914	0.027667	0.005486	0.001279	0.000313	$7.749 \times 10^{-5}$	$1.926 \times 10^{-5}$
	-	2.197577	2.334295	2.100195	2.030285	2.015140	2.007810
VanLeer	0.148915	0.039794	0.007867	0.001579	0.000355	$8.357 \times 10^{-5}$	$2.013 \times 10^{-5}$
	-	1.903846	2.338629	2.316817	2.151387	2.088442	2.053370

Table 3.3 Same as Table 3.1 but employing the HLLD Riemann solver, including the MP3 reconstruction.

<b>HLLD</b>	N=8	N=16	N=32	N=64	N=128	N=256	N=512
Godunov	0.231373	0.182843	0.126489	0.078187	0.044176	0.023622	0.012235
	-	0.339613	0.531601	0.694016	0.823657	0.903157	0.949035
MinMod	0.171364	0.073171	0.019213	0.004800	0.001308	0.000348	$8.994 \times 10^{-5}$
	-	1.227719	1.929134	2.000842	1.875652	1.909334	1.953022
MC	0.113706	0.025652	0.005504	0.001301	0.000316	$7.790 \times 10^{-5}$	$1.932 \times 10^{-5}$
	-	2.148129	2.220420	2.080788	2.040914	2.020979	2.011657
VanLeer	0.136352	0.036726	0.007871	0.001612	0.000360	$8.445 \times 10^{-5}$	$2.026 \times 10^{-5}$
	-	1.892460	2.222038	2.287145	2.161129	2.094082	2.059075
MP3	0.061922	0.009593	0.001285	0.000163	$2.055 \times 10^{-5}$	$2.576 \times 10^{-6}$	$3.224 \times 10^{-7}$
	-	2.690331	2.899875	2.974505	2.991875	2.996154	2.998231

Table 3.4 Same as Table 3.1 but employing the PVM-int-8 Jacobian-free Riemann solver, including the MP3 reconstruction.

<b>PVM</b>	N=8	N=16	N=32	N=64	N=128	N=256	N=512
Godunov	0.236296	0.192590	0.136829	0.086507	0.049650	0.026810	0.013965
	-	0.295066	0.493159	0.661477	0.801016	0.889058	0.940912
MinMod	0.181923	0.080879	0.021910	0.005388	0.001481	0.000401	0.000103
	-	1.169493	1.884117	2.023693	1.863015	1.882146	1.950976
MC	0.125110	0.028691	0.005910	0.001349	0.000322	$7.873 \times 10^{-5}$	$1.942 \times 10^{-5}$
	-	2.124491	2.279383	2.130461	2.065503	2.034027	2.019233
VanLeer	0.147824	0.040515	0.008698	0.001720	0.000375	$8.675 \times 10^{-5}$	$2.061 \times 10^{-5}$
	-	1.867340	2.219613	2.337903	2.197052	2.112699	2.073304
MP3	0.069036	0.011010	0.001475	0.000187	$2.358 \times 10^{-5}$	$2.954 \times 10^{-6}$	$3.696 \times 10^{-7}$
	-	2.648510	2.899967	2.974409	2.992596	2.996515	2.998835

Table 3.5 Same as Table 3.1 but employing the HLLD Riemann solver and high-order spatial and temporal methods. Resolution is restricted to  $N \geq 64$ .

HLLD	N=64	N=128	N=256	N=512
MP5	$2.456 \times 10^{-6}$	$2.813 \times 10^{-7}$	$3.440 \times 10^{-8}$	$4.284 \times 10^{-9}$
	3.432235	3.126066	3.031713	3.005290
MP5+RK4	$3.086 \times 10^{-7}$	$9.634 \times 10^{-9}$	$2.977 \times 10^{-10}$	$9.006 \times 10^{-12}$
	4.982834	5.001730	5.016265	5.046792

### 3.4.1.2 Riemann problem for the optically-thin radiation transport

The second step in the validation of the new scheme consists in testing the explicit part of the radiation module, but neglecting any interaction between the fluid and the radiation field. For this purpose, we considered two Riemann problems proposed by Melon Fuksman and Mignone 2019 in the optically-thin regime.

The tests are initialised in a one-dimensional Cartesian grid that cover the space  $[-20, 20]$ , where a discontinuity at  $x = 0$  separates two different radiation states. For Test 1, the radiation field is given by  $(E_r, F_r^x, F_r^y)_L = (1, 0, 1/2)$  and  $(E_r, F_r^x, F_r^y)_R = (1, 0, 0)$ , while for Test 2,  $(E_r, F_r^x, F_r^y)_L = (1/10, 1/10, 0)$  and  $(E_r, F_r^x, F_r^y)_R = (1, 0, 1)$ . In both cases, we run the test two times: first, we calculate an approximation to the analytic solution using high resolution ( $2^{14}$  cells) and second-order accurate reconstruction techniques (PLM-VanLeer). Then, we employed  $2^8$  zones and zero-th order spatial reconstruction to solve the test with our two Riemann solvers: Rad-HLL and PVM-int-8. We considered outflow boundary conditions. Figure 3.3 shows the solution of these two problems at  $t = 20$ . The pseudo-analytic solution is represented with a black solid line, while the results with  $2^8$  zones and Rad-HLL/PVM-int-8 are shown in red and blue, respectively. The spatial reconstruction techniques are distinguished with a solid line (Godunov), dotted line (PLM-MinMod) and dash-dot line (PLM-VanLeer).

As it is expected for the Jacobian decomposition of the Rad-RMHD equations (see Eqs. 3.26-3.30), we obtained in both cases a three-wave pattern. In Test 1, we can distinguish a left-going shock, a right-going expansion wave and the analogous of a contact wave near  $x = -1$  (Fig. 3.3, left column). In Test 2, we found a left-going shock, a right-going shock and a contact wave (Fig. 3.3, right column). Specially for Test 1, our implementation of PVM-int-8 gives a sharper solution around the contact wave than Rad-HLL. In Test 2, this discrepancy is mitigated. The effect of the Riemann solver on the solution accuracy is also less

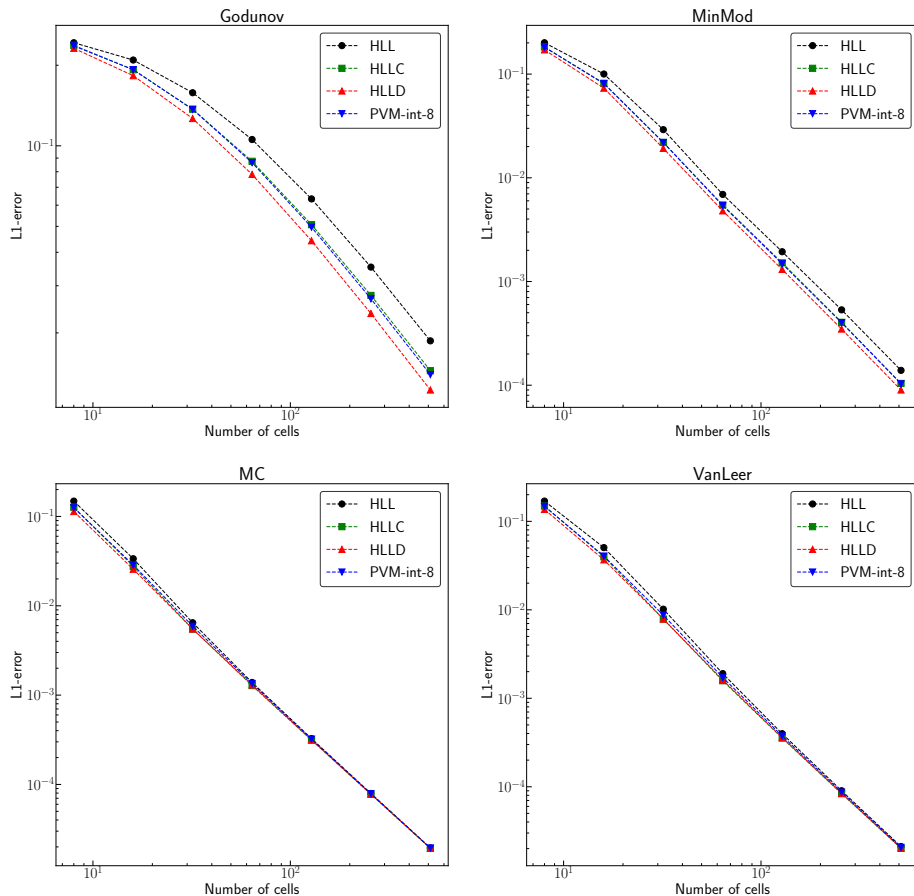


Figure 3.2 L1 errors of  $v_z$  as a function of the number of cells for different Riemann solvers and spatial zero-th and first order reconstruction techniques.

significant with the second order accurate reconstruction, as it was previously mentioned in Sec. 3.4.1.1.

### 3.4.1.3 Shock tubes

We consider a collection of four shock tube problems initially proposed in Farris et al. 2008. These tests were solved by several authors using the Eddington approximation [Zanotti et al. 2011, Fragile et al. 2012, Takahashi et al. 2013, Sądowski et al. 2013], and later solved by McKinney et al. 2014, Rivera-Paleo and Guzmán 2019, Melon Fuksman and Mignone 2019 for the M1 closure. These tests, which are similar to the Balsara shock tube problems of RMHD [Balsara 2001], consist of two different radiation and fluid states separated by

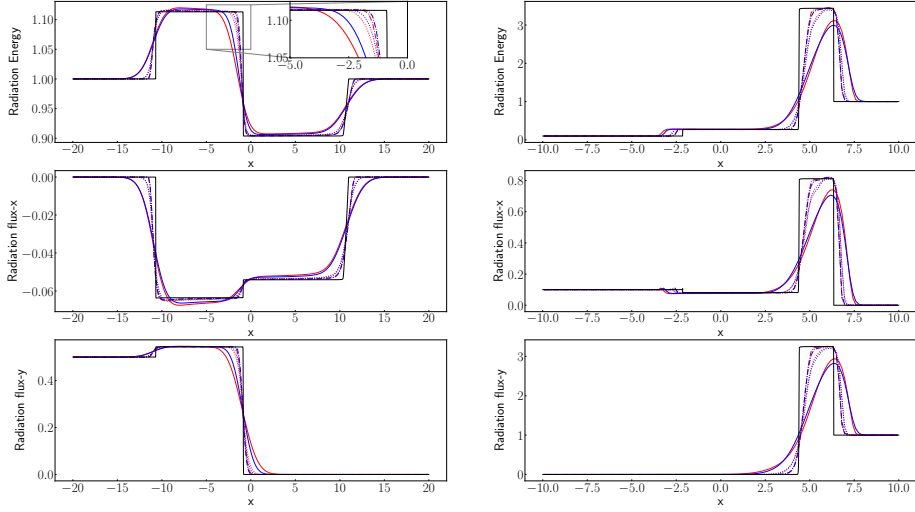


Figure 3.3 Radiation energy (top), radiation flux in the x-direction (middle) and radiation flux in the y-direction (bottom) for the optically-thin radiation transport problems Test 1 (left column) and Test 2 (right column). We show an approximation to the analytic solution at  $t = 20$  using  $2^{14}$  zones (black solid line). The solution of the problem, computed with  $2^8$  zones, is over-plotted for our two Riemann solvers: Rad-HLL (red) and PVM-int-8 (blue). We also compare the effect of different reconstructions: first-order (solid line), PLM-MinMod (dot line) and PLM-VanLeer (dash-dot line).

a discontinuity at  $x = 0$ . The initial conditions of the problems are shown in the aforementioned references, so we do not reproduce them here. In all of these papers, the radiation field is given in the comoving frame, so we start by applying a Lorentz boost to convert all radiation quantities to the laboratory frame. This transformation is given by the following relations [see e.g., Park 2006, Rivera-Paleo and Guzmán 2019]:

$$\tilde{E}_r = W^2 (E_r - 2v_i F_r^i + v_i v_j P^{ij}), \quad (3.48)$$

$$\begin{aligned} \tilde{F}_r^i = -W^2 v^i E + W \left[ \delta_j^i + \left( \frac{W-1}{v^2} + W \right) v^i v_j \right] F_r^j - \\ W v_j \left( \delta_k^i + \frac{W-1}{v^2} v^i v_k \right) P^{jk}, \end{aligned} \quad (3.49)$$

where replacing  $\mathbf{v}$  for  $-\mathbf{v}$  yields the inverse transformation.

The radiation constant for each problem, in the units of the code, is given in McKinney et al. 2014. We evolve the system until we achieve a final stationary state. For the first problem, the domain is the one-dimensional Cartesian grid  $[-20, 20]$  with a resolution of 800 zones. In all other cases, we consider the domain  $[-40, 40]$  with a resolution of 1600 zones to avoid that boundaries interfere in

the stationarity of the final solution [Rivera-Paleo and Guzmán 2019]. Outflow conditions are considered at both boundaries of the grid. We choose  $\Gamma = 5/3$  for each test except for the highly-relativistic shock, where we choose  $\Gamma = 2$ . As in Melon Fuksman and Mignone 2019, initial fluxes follow  $\tilde{F}_r^x = 0.01\tilde{E}_r$ .

**Non-relativistic strong shock.** The initial conditions for this test are set such that the gas energy density dominates over the radiation energy density and the initial velocities are non-relativistic. The solution of the problem at  $t = 5000$  is shown in the left column of Fig. 3.4. Due to the initial conditions, radiation is transported from right to left, in front of the shock ( $F_x < 0$ ). Although fluid quantities show a strong discontinuity at  $x = 0$ , the radiation field is continuous in the whole domain. With the M1 closure, the radiation field decays with  $e^{-\rho\kappa|x|}$  from the position of the shock [see e.g., Takahashi and Ohsuga 2013]. Our solution is consistent with the results presented in the literature by other authors (both with the Eddington approximation and with M1, since for this test the results are similar) and with the semi-analytic solution [Farris et al. 2008, Fragile et al. 2012, McKinney et al. 2014].

**Mildly-relativistic strong shock.** As in the non-relativistic strong shock, the gas energy density dominates over the radiation energy density, although in this case the initial velocities are higher ( $u_L = 0.25$ ). The solution of the problem at  $t = 500$  is shown in the right column of Fig. 3.4. Apart from the fact that the radiation energy profile is sharper near the shock, the solution is similar to the non-relativistic test. The M1 closure produces a smoothing of the numerical profiles at the shock position compared to the discontinuity found with the Eddington approximation [Farris et al. 2008, Takahashi et al. 2013, Tolstov et al. 2015].

**Highly-relativistic shock.** The initial conditions for this test are set such that the gas energy density dominates over the radiation energy density and the upstream Lorentz factor is highly relativistic,  $W \approx 10$  [Farris et al. 2008]. The solution of the problem at  $t = 500$  is shown in the left column of Fig. 3.5. In this case, both the fluid quantities and the radiation field are smooth and continuous. Although the shock front is stationary for the Eddington approximation, it drifts with a small velocity of  $\sim 1.6 \times 10^{-4}$  with the M1 closure [Takahashi and Ohsuga 2013, Rivera-Paleo and Guzmán 2019], which is not relevant for the time scales of the test. The maximum at  $\tilde{F}_r^x/\tilde{E}_r$  is  $\sim 0.31$ , consistent with the literature [see e.g., Takahashi and Ohsuga 2013].

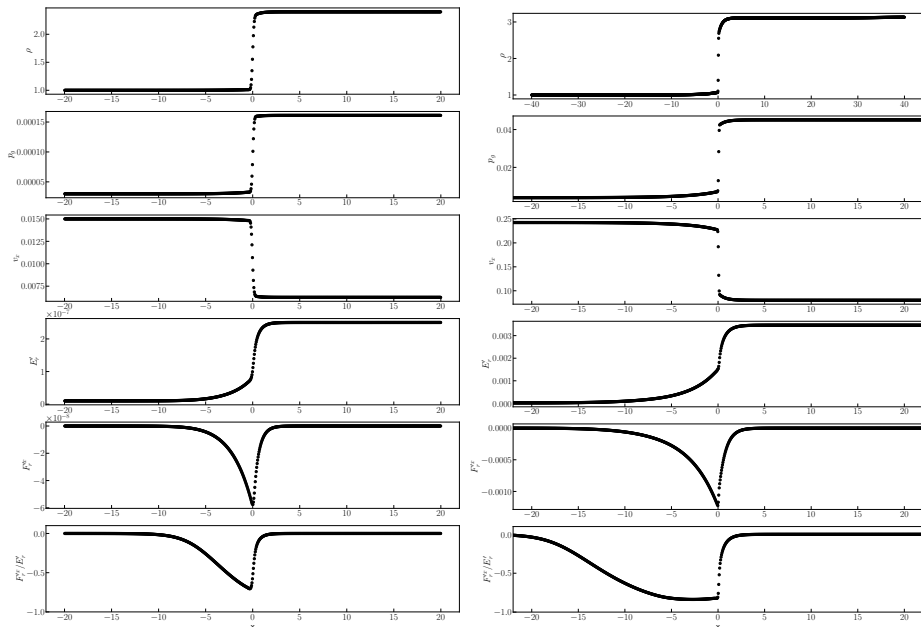


Figure 3.4 From top to bottom, density, gas pressure, x-velocity, radiation energy in the comoving frame, radiation energy flux in the x direction and in the comoving frame and reduced flux in the comoving frame for the non relativistic strong shock problem (left) at  $t = 5000$  (using 800 zones), and for the mildly relativistic strong shock (right) at  $t = 500$  (using 1600 zones). Only a zoom of the  $[-20, 20]$  central region is shown in the right column.

**Radiation-pressure-dominated shock.** In this problem, the initial conditions are set such that the radiation pressure dominates over the gas pressure and the upstream velocity is mildly relativistic. The solution of the problem at  $t = 500$  is shown in Fig. 3.5. After the initial discontinuity at  $x = 0$  breaks up, fluid and radiation achieve a steady state solution with a small drift velocity [Takahashi and Ohsuga 2013], where the shock front remains approximately at the origin. As in the previous tests, radiation is transported from the left to the right ( $\tilde{F}_r^x < 0$ ), penetrating up to  $x \sim -12$ , while the radiation flux is reduced by absorption. Since matter and radiation are strongly coupled, radiation force produces a decrease in the fluid velocity, while density is enhanced. This solution is smooth and continuous for both fluid and radiation quantities, and it can be compared with the results shown in the literature elsewhere [Takahashi and Ohsuga 2013, Melon Fuksman and Mignone 2019].

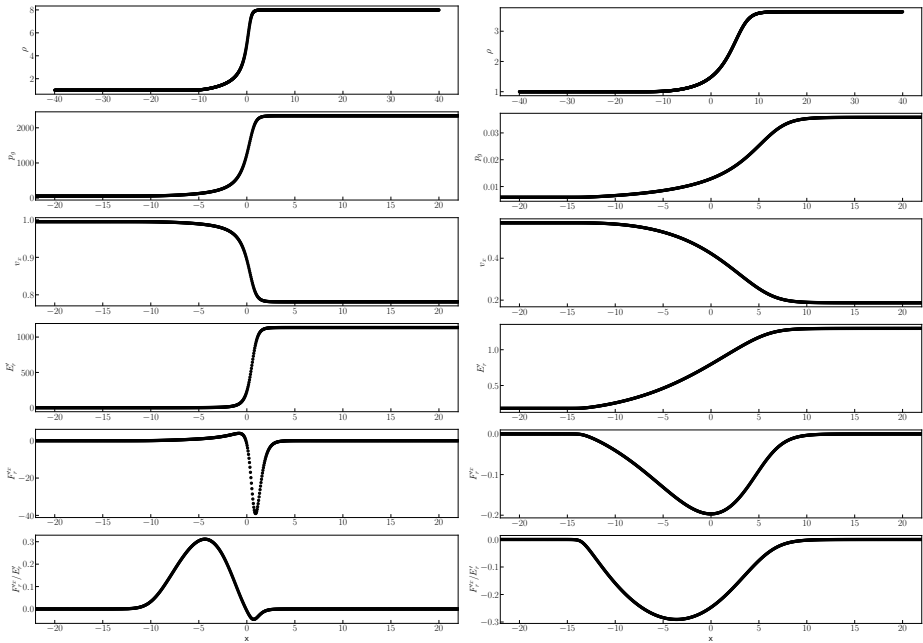


Figure 3.5 From top to bottom, density, gas pressure, x-velocity, radiation energy in the comoving frame, radiation energy flux in the x direction and in the comoving frame and reduced flux in the comoving frame for the highly relativistic strong shock problem (left) at  $t = 500$  (using 1600 zones) and for the radiation pressure dominated shock (right). Only a zoom of the  $[-20,20]$  central region is shown in the figure.

#### 3.4.1.4 Optically-thick radiation pulse

The last one-dimensional problem of this section consists on a radiative pulse propagating along one of the spatial Cartesian coordinates in an optically-thick medium [McKinney et al. 2014, Rivera-Paleo and Guzmán 2019, Melon Fuksman and Mignone 2019]. Assuming initial thermal equilibrium, the radiation energy profile is given by:

$$E_r = a_r \left[ T_0 \left( 1 + 100 e^{-x^2/\omega^2} \right) \right]^4, \quad (3.50)$$

where  $T_0 = 10^6$  and  $\omega = 5$ . We choose the value of the radiation constant in the code units as  $a_r = 6.24 \times 10^{-64}$  such that the ratio  $k = T\rho/p = 1$ . The background density is  $\rho = 1$  and the adiabatic exponent,  $\Gamma = 5/3$ . With these initial conditions, the evolution of the system follows [McKinney et al. 2014]:

$$E_r(t) = A \exp\left(\frac{-x^2}{4D(t+t_0)}\right) \left(\frac{t+t_0}{t_0}\right)^{-1/4}, \quad (3.51)$$

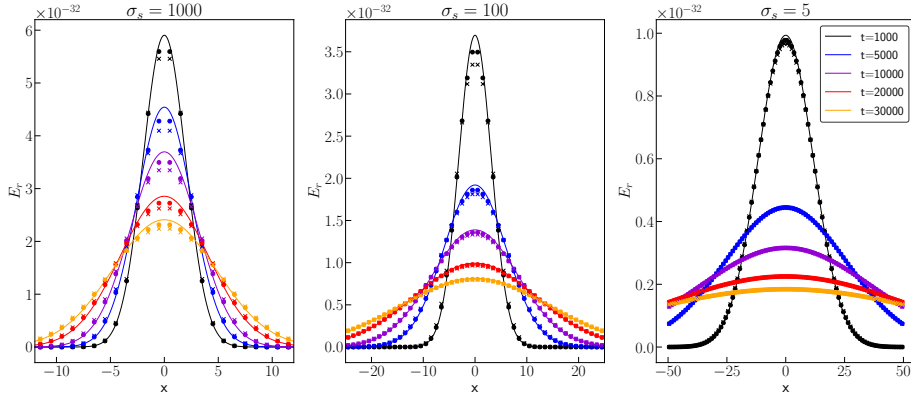


Figure 3.6 Radiation energy density for the optically-thick radiative pulse diffusion at  $\sigma_s = 1000$  (left),  $\sigma_s = 100$  (middle) and  $\sigma_s = 5$  (right). The analytic solution (solid lines) is over-plotted with the numerical results with the PVM-int-8 Riemann solver (dots) and the Rad-HLL Riemann solver (crosses) for different time frames.

where  $A \approx 6.49 \times 10^{-32}$ ,  $t_0 \approx 4800$ , and  $D = 1/(3(\kappa + \sigma_s))$ . For this test, the absorption opacity is set to zero while we run the pulse for three different values of the scattering coefficient, namely  $\sigma_s = 5, 100, 1000$ . The grid covers the domain  $[-50, 50]$  and we use 100 computation zones. With the chosen values of the grid size, the corresponding cell opacities for the runs are  $\tau = 5, 100, 1000$ . To avoid the effects of the grid boundaries, the analytic solution is imposed there. Figure 3.6 shows the solution of the problem at different times, compared to the analytic solution given by Eq. 3.51. Dots represent the solution with the PVM-int-8 Riemann solver and crosses show the results with Rad-HLL, where the maximum and minimum velocities were limited according to Eq. 3.31. As suggested by McKinney et al. 2014, the solution of the central points exhibits more diffusion at earlier times, while the effect is mitigated later in the evolution. The similarity of our results with respect to the analytic solution for different values of the scattering opacity demonstrates a good performance of our scheme in the optically thick regime, where PVM-int-8 improves slightly the accuracy of Rad-HLL. On the other hand, the solution of the problem with zero-th order reconstruction, PVM-int-8 with  $\beta = 1$  or Rad-HLL with no velocity limiting, results in catastrophic diffusive solutions (specially for  $\tau > 100$ ).

### 3.4.2 Two and three dimensional tests

We propose a collection of multidimensional problems to test the performance of the new implemented methods in more than one spatial dimension. In order

to avoid spurious oscillations, we introduced a shock flattening around strong shocks and sharp radiation gradients [Mignone, Massaglia, and Bodo 2005]. In particular, the VanLeer reconstruction algorithm is degraded to the more diffusive MinMod algorithm around strong shocks.

### 3.4.2.1 Cylindrical/spherical magnetised blast wave

The cylindrical/spherical magnetised blast wave is a classical problem in RMHD and has been extensively used to test the performance of the HRSC numerical methods handling MHD wave degeneracies parallel and perpendicular to the field orientation [see e.g., Martí and Müller 2015, and references therein]. In Chapter 2, we solved the test in RMHD for both weak and strong magnetisation regimes. The version that we consider in this thesis was first proposed in Melon Fuksman and Mignone 2019 and it is the first and only test that we solve considering both radiation and magnetic fields. However, unlike Melon Fuksman and Mignone 2019, we also consider the spherical version of the magnetised blast wave in 3D. The main particularity of this test in Rad-RMHD is that it can switch from the radiation-dominated to the magnetically dominated regime varying the medium's opacity; when the opacity is small, the flow is magnetically dominated, but radiation dominates the blast wave dynamics in the optically-thick regime. We consider the two-dimensional computational grid  $[-6, 6] \times [-6, 6]$  with  $360^2$  cells, such that the initial geometry is identical to the test presented in Sec. 2.4.2. The ambient density and pressure are  $\rho_0 = 10^{-4}$ ,  $p_0 = 3.49 \times 10^{-5}$ , while inside the cylinder/sphere of unit radius they become  $\rho_1 = 10^{-2}$ ,  $p_1 = 1.31 \times 10^{-2}$ . The adiabatic exponent is  $\Gamma = 4/3$ . The magnetic field is aligned with the  $x$ -direction,  $\mathbf{B} = (0.1, 0, 0)$ , and the fluid is initially at rest (i.e.,  $\mathbf{v} = 0$ ). For the radiation field, we assume thermal equilibrium with the plasma and  $\mathbf{F}_r = 0$ . The opacity of the medium is controlled with the absorption coefficient, which is  $\kappa = 1$  for the magnetically dominated problem and  $\kappa = 1000$  for the radiation dominated explosion, while the scattering opacity is  $\sigma_s = 0$  in the two cases. For  $\kappa = 1$ , the initial optical depth along the central sphere is  $\tau_1 = 2\rho_1\kappa = 0.02 \ll 1$  (optically thin case). For  $\kappa = 1000$ ,  $\tau_1 = 20$ . Figure 3.7 and Fig. 3.8 show the solution of the problem at  $t = 4$  for  $\kappa = 1$  and  $\kappa = 1000$ , respectively. In the optically-thin scenario, flow dynamics is barely affected by the presence of radiation and the evolution is dominated by the magnetic field. Thus, flow quantities like pressure or density develop an elongated horizontal structure, following the magnetic field lines, which are slightly deformed by the wave, as in the RMHD case. The maximum Lorentz factor that we get is  $W_{\max} \approx 1.7$ , which is similar to Melon Fuksman and Mignone 2019. Since photons can diffuse freely,

radiation energy density preserves the cylindrical symmetry. However, in the optically-thick problem ( $\kappa = 1000$ ), radiation pressure is dominant and matter is strongly coupled to the photon field. In this case, the flow recovers an oblate ring shape, with  $W_{\max} \approx 2.72$  along the x-axis. Magnetic field lines are highly deformed and the radiation energy density is no longer symmetric because of the interaction with the gas. Due to the exigent test conditions (source terms are very *stiff*), in this problem we used the Rad-HLL Riemann solver, the MinMod slope limiter and a CFL=0.01 to avoid the appearance of non-physical solutions during the simulation. Figure 3.9 shows the solution at  $t = 4$  of a 3D version of the optically-thin explosion (numerical resolution: 256 computational zones per spatial dimension). Since the symmetry of the radiation field is well preserved, we demonstrated the capability of our scheme to handle both radiation and magnetic fields in full three dimensional applications.

### 3.4.2.2 The shadow problem

**Single shadow.** The shadow test is one of the most common problems in Rad-RHD to test the performance of the M1 closure [Hayes and Norman 2003, González, Audit, and Huynh 2007, Sądowski et al. 2013, McKinney et al. 2014, Fragile, Olejar, and Anninos 2014, Rivera-Paleo and Guzmán 2019, Melon Fuksman and Mignone 2019, Weih, Olivares, and Rezzolla 2020]. This problem consists on a free-streaming radiation beam that impacts into a highly opaque region, producing a shadow behind it. Although there are multiple versions of the shadow problem, we follow the initial conditions given by González, Audit, and Huynh 2007, Fragile, Olejar, and Anninos 2014 or Melon Fuksman and Mignone 2019. We consider the two dimensional Cartesian grid  $[-0.5, 0.5] \times [-0.12, 0.12]$  cm, with a resolution of  $280 \times 80$  computational cells. The initial density distribution is given by:

$$\rho(x, y) = \rho_0 + \frac{\rho_1 - \rho_0}{1 + e^{\Delta}}, \quad (3.52)$$

$$\Delta = 10 \left[ \left( \frac{x}{x_0} \right)^2 + \left( \frac{y}{y_0} \right)^2 - 1 \right], \quad (3.53)$$

where  $\rho_0 = 1 \text{ g/cm}^3$ ,  $\rho_1 = 10^3 \text{ g/cm}^3$  and  $(x_0, y_0) = (0.10, 0.06) \text{ cm}$ . Matter and radiation are initially in thermal equilibrium with a temperature  $T = 290 \text{ K}$  and we consider constant absorption opacity  $\kappa = 0.1 \text{ cm}^2/\text{g}$ , while we neglect photon scattering. Fluxes are set to zero and matter is also initially at rest. From the left boundary (at  $x = -0.5 \text{ cm}$ ), we inject a radiation beam at temperature  $T = 1740 \text{ K}$  and flux  $\mathbf{F}_r = (cE_r, 0, 0)$  (i.e., radiation is in the free streaming

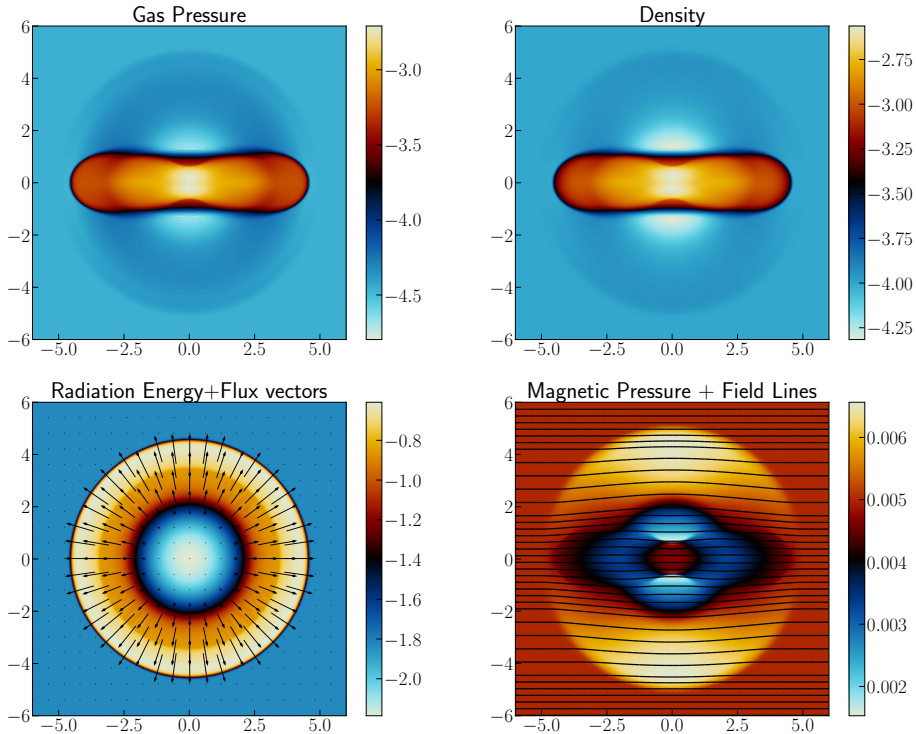


Figure 3.7 Logarithmic gas pressure (top left), logarithmic density (top right), logarithmic radiation energy density (bottom left) and logarithmic magnetic pressure (bottom right) at  $t = 4$  for the two-dimensional cylindrical magnetised blast wave. In the bottom left panel, the vector field represents the radiation flux, which propagates radially from the centre. Magnetic field lines are superposed to the magnetic pressure. We consider the Cartesian grid  $[-6,6] \times [-6,6]$  with 360 cells per spatial dimension. The absorption coefficient is  $\kappa = 1$ .

limit). In the rest of the boundaries, we impose outflow conditions. The adiabatic exponent is  $\Gamma = 5/3$ . Figure 3.10 shows the solution of the problem at  $t = 1.5 t_c$ , where  $t_c = 1 \text{ cm}/c$ . The highly opaque ellipsoid (represented with contours) produces a shadow behind it that can be compared with the aforementioned references. A 3D version of this problem, simulated with the same initial conditions, is shown in Fig. 3.11 at  $t = 1.5 t_c$ . For this favourable setup, the M1 closure yields a flux that remains parallel to the injection direction casting a shadow behind the 3D ellipsoid.

**Double shadow.** We consider an extension of the shadow problem that we described in the previous paragraph to the case of multiple sources of light, where the M1 closure is expected to be less accurate [Sądowski et al. 2013, McKinney et al. 2014, Rivera-Paleo and Guzmán 2016, Rivera-Paleo and Guzmán 2019].

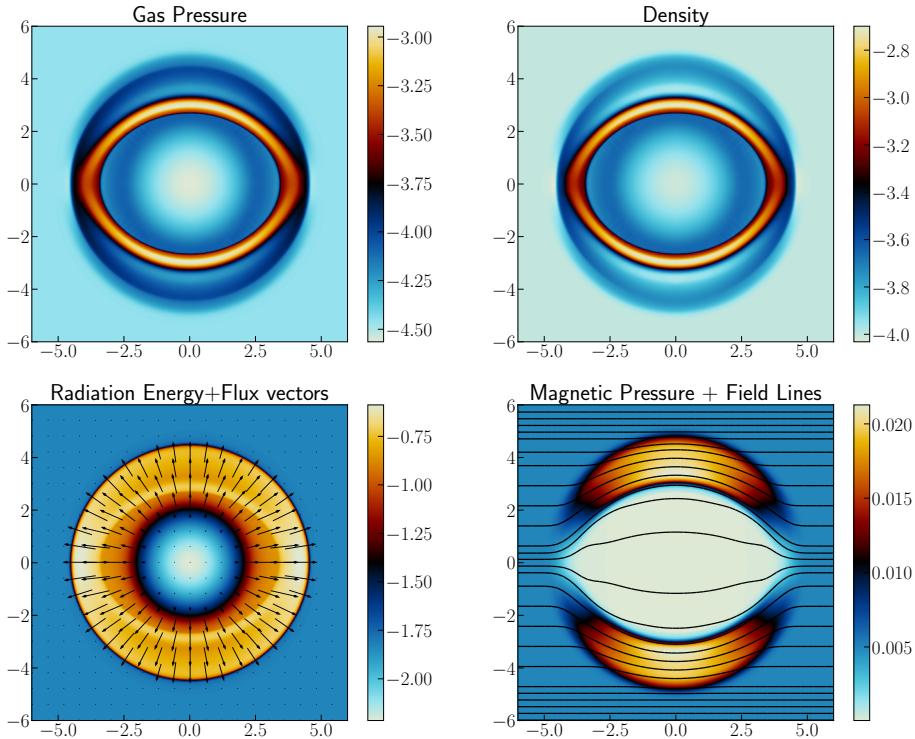


Figure 3.8 Same as Fig. 3.7 for an absorption coefficient  $\kappa = 1000$ .

The initial setup is the same as in the single shadow test, although in this case we consider a slightly larger domain:  $[-0.6, 0.6] \times [0, 0.15]$  cm, with the same cell size as before. For this problem, we only simulate the upper half of the grid since we establish reflecting symmetry boundary conditions at  $y = 0$ . In the left x-boundary (only where  $y > 0.03$  cm), we inject an inclined radiation beam with the same radiation energy than in the single shadow problem, but in this case the radiation flux is given by  $F_r^x = 0.93cE_r$  and  $F_r^y = -0.37cE_r$ . Due to the reflecting boundary at  $y = 0$ , the optically-thick ellipsoid is effectively illuminated by two self-crossing beams of light. In the remaining boundaries, we assume outflow conditions. In the bottom panel of Fig. 3.12, we show the solution of the problem at  $t = 4.5t_c$ . In the left x-boundary, we can distinguish a small triangular region which is not illuminated. After this region, approximately at  $x \approx -0.45$  cm, radiation overlaps and the radiative energy density increases as  $E_r = 2E_r^0$ , while the radiation flux aligns with the x-direction with  $F_r^x = 0.93cE_r$ . Therefore, since the radiation flux is no longer  $F_r^x \approx cE_r$  as in the single shadow problem, the implied distribution of specific intensity is not pointing along the

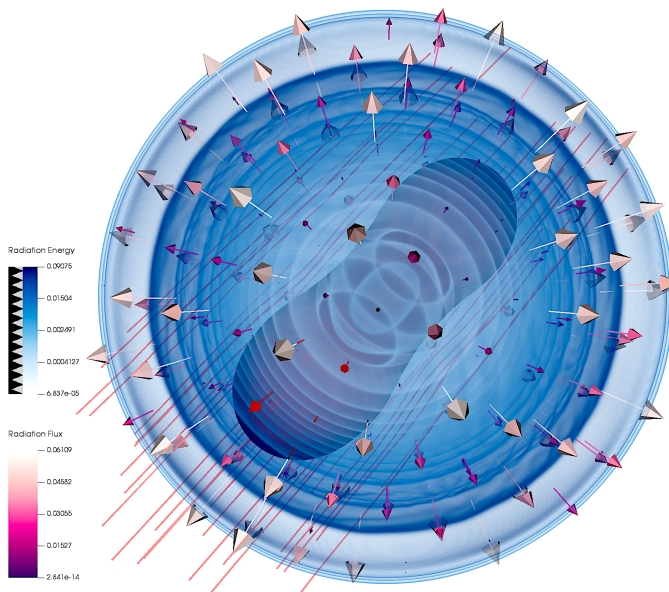


Figure 3.9 Radiation energy density for the optically-thin, spherical magnetised blast wave at  $t = 4$ . The vector field represents the radiation flux. Magnetic field lines (pink solid lines) are slightly deformed by the flow.

x-axis but spreads in other directions about this axis [see the discussion in Sądowski et al. 2013]. As a result, the radiation front is indeed an elongated ellipsoid pointing along the x-direction (Fig. 3.12, top panel).

Eventually, this has an effect on the shadow characteristics behind the clump, with a region of total shadow (umbra) limited by the edges of a wider region of partial shadow (penumbra). As it is evident from the bottom panel of Fig. 3.12, there is also a narrow horizontal shadow extended along the x-axis. This non-physical feature, which has been shown in the literature [see e.g., Sądowski et al. 2013, McKinney et al. 2014, Rivera-Paleo and Guzmán 2019, and references therein], is an artefact related with the M1 closure.

## 3.5 Discussion and conclusions

In this chapter, I have presented a novel scheme for treating radiation transport within our code LÓSTREGO.

In our approach, the equations of Rad-RMHD, which are formulated taking successive moments of the Boltzmann radiative transfer equation, are solved

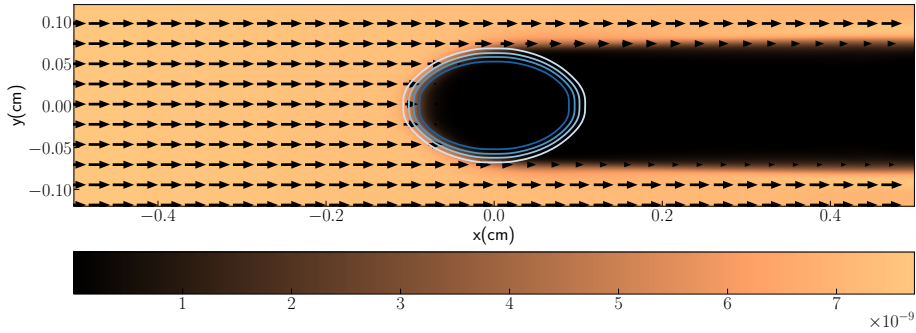


Figure 3.10 Radiation energy density for the single shadow problem at  $t = 1.50 t_c$ . The vector field represents the radiation flux. Contours show the position of the optically-thick blob.

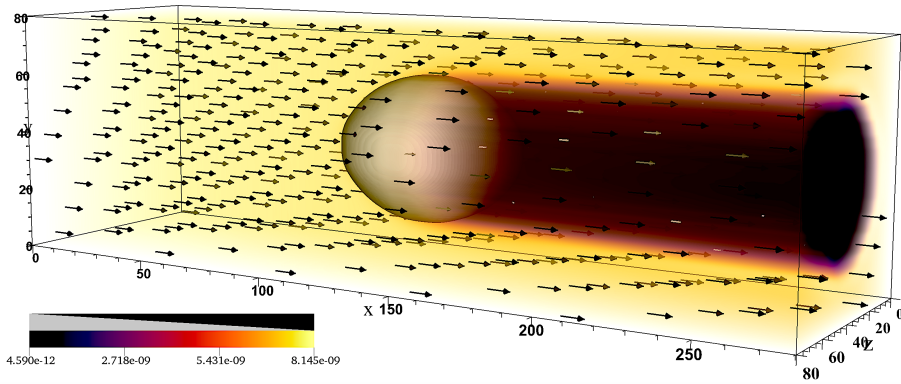


Figure 3.11 Radiation energy density for the single shadow problem in three dimensions at  $t = 1.50 t_c$ . The vector field represents the radiation flux. The 3D white contour shows the position of the optically-thick blob.

under the grey-body approximation and the M1 closure using an IMEX time integration scheme. This closure scheme allows to handle accurately both the free-streaming and diffusion radiation transport limits. We have introduced, for the first time in the context of Rad-RMHD, a new family of approximate Riemann solvers based on internal polynomial approximations to the viscosity matrix (PVM methods; see Sect. 3.3.2.2). The underlying polynomials of this group of solvers admit a Jacobian-free formulation of the scheme, where only evaluations of the conserved variables and flux vectors are required. In the context of Rad-RMHD, this is particularly useful because the characteristic speeds of the magnetofluid and the radiation subsystem of equations can be –in general– very different, and therefore these two blocks must be independently handled when using Riemann solvers based on characteristic wave decomposition

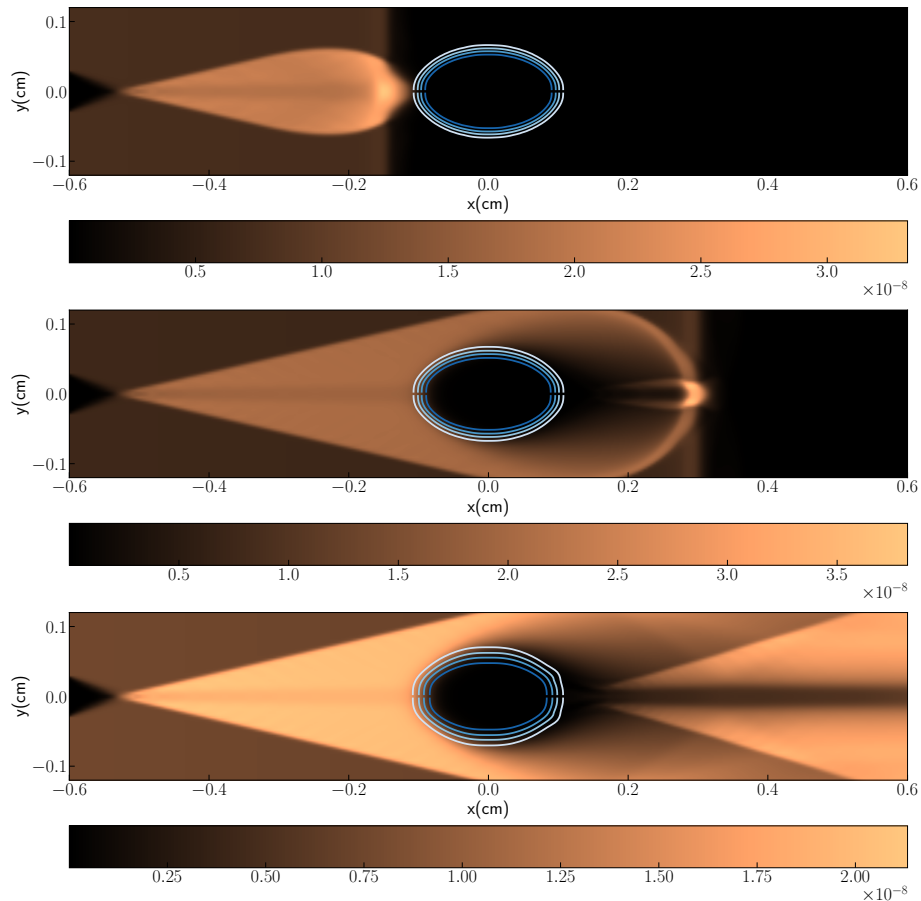


Figure 3.12 Radiation energy density for the double shadow problem at  $t = 0.50 t_c$  (top panel),  $t = 1.00 t_c$  (middle panel) and  $t = 4.50 t_c$  (bottom panel). Contours show the position of the optically-thick blob.

to avoid excessive diffusion. Moreover, the maximum and minimum characteristic speeds of the radiation block must be limited in the optically-thick regime for the same reason. As we described in this chapter, the PVM-int solver overcomes these issues in a very natural and elegant way. On the one hand, the same algorithm is used to compute the numerical fluxes of the full Rad-RMHD system of equations. On the other hand, the numerical viscosity of the original solver is reduced gradually as the opacity of the numerical cells around an interface increases.

We tested the new PVM-int Riemann solver in the context of RMHD, comparing its performance with the HLL family. For that purpose, we also introduced in

LÓSTREGO high-order methods both in space and time, although in this chapter we kept second-order nominal accuracy (PLM+RK3) to test the new radiation module. For the cell reconstruction step, we have introduced the MP scheme of Suresh and Huynh 1997, which yields from third to ninth spatial order of accuracy. The algorithm was tested with a smooth RMHD test problem that consists on the propagation of a large-amplitude, circularly polarised Alfvén wave along a uniform background magnetic field (see Sect. 3.4.1.1). We demonstrated that the third order MP reconstruction (i.e., MP3) together with RK3 (MP3+RK3), yields third order of accuracy for all of our Riemann solvers, including the new PVM-int-8. This extends the results of Martí 2015a, where the code was tested up to second order. Castro, Gallardo, and Marquina 2017 also showed third order of accuracy with the PVM family of Riemann solvers, but using the Piecewise Hyperbolic Method [Marquina 1994]. Nevertheless, when we increased the order of spatial reconstruction (using, e.g., MP5), the order of accuracy of the code was limited to the order of the RK (in this case, RK3), although the L1 errors were almost two orders of magnitude lower than with MP3+RK3 (see Table 3.3). Thus, MP5+RK3 is a good configuration for applications involving smooth solutions that required high degree of accuracy (for example, development of instabilities or perturbation analysis in RMHD). To achieve an order of accuracy higher than third order, we have implemented a fourth-order (RK4), strong-stability-preserving RK scheme, based on five integration steps [Balsara 2017]. Using this algorithm together with MP5 (MP5+RK4) we were able to achieve the nominal fifth order of accuracy, for which we used the HLLD Riemann solver because it was the least diffusive scheme in the benchmark. Let us note that Del Zanna et al. 2007 probed fifth order of accuracy by limiting *ad hoc* the integration time step, but this approach is unpractical for large-scale simulations. Indeed, the same applies to the RK4 algorithm of Balsara 2001, which is computationally expensive due to the large number of RK substeps. A specific benchmark of these high-order methods based on real multi-dimensional (Rad)-RMHD applications will be addressed in future work and presented elsewhere.

Focusing on Rad-RMHD, we have used a collection of one-dimensional and multi-dimensional test problems (see Sects. 3.4.1.2 - 3.4.1.4 and 3.4.2) to demonstrate that our scheme is robust and accurate for systems with different initial conditions, including both scattering and absorption opacity in the free-streaming and diffusion radiation transport limits. The convergence analysis presented on Tables 3.1-3.5 and displayed in Fig. 3.2 shows that our PVM-int-8 solver performs similar to HLLC, although all solvers behaved similar with first order linear reconstruction, as expected. In radiation magnetohydrodynamics, PVM-int-8

improves the accuracy of Rad-HLL, specially around strong discontinuities of the radiation field (see Fig. 3.3). Comparing with Melon Fuksman and Mignone 2019, the difference between these two solvers seems to be less prominent than the one reported for Rad-HLL and the radiation version of HLLC. However, in the optically-thick regime PVM-int-8 improves slightly the accuracy of Rad-HLL, specially in those regions that show more numerical diffusion (see central region of the gaussian pulse in Fig. 3.6), where Rad-HLLC is not valid. This is the first time to our knowledge that a Riemann solver improves the accuracy of Rad-HLL in the highly optically thick regime ( $\tau \gg 1$ ). Moreover, we want to stress out that our choice of the parameter  $\beta$  (Eq. 3.38), devised to reduce the numerical diffusion in the optically thick regime, is somehow arbitrary.

As previously mentioned, our definition of  $\beta$  relies on its simplicity and the results in 1D tests, but other functions should be explored in the future. Similarly, other schemes of the Jacobian-free family should be also adapted and tested for Rad-RMHD. For example, Castro, Gallardo, and Marquina 2017 found that the PVM-Cheb-12 [based on the Chebyshev approximation of degree 12; Castro, Gallardo, and Marquina 2016], or the DOT-Cheb-12 and DOT-int-8 approximate DOT solvers using the same polynomials but a Gauss-Legendre quadrature [Castro, Gallardo, and Marquina 2016], gave promising results in 1D RMHD applications. Indeed, PVM-Cheb-12 and DOT-Cheb-12 are slightly less diffusive than PVM-int-8, although the latter automatically satisfies the stability condition needed to ensure the robustness and convergence of the schemes. Moreover, Castro, Gallardo, and Marquina 2017 also showed that, at least for the 1D Brio-Wu test problem, PVM-based methods were a better option than DOT-based ones from the point of view of computational efficiency, and that using PVM-int-8 increases the total CPU time with respect to HLL by a factor  $\sim 2$ . This is mainly because PVM requires multiple calls to the recovery of primitive variables, whose algorithm is computationally expensive. Since the variables of the radiation field are at the same time primitive and conserved, the additional cost of our version of PVM with respect to Rad-HLL will not be affected by this, but only by the number of additional operations and flux evaluations, which will also increase for Rad-HLL. In two-dimensions, all schemes were similar, but DOT solvers are also computationally more expensive. We also tested in LÓSTREGO the PVM-int-16 solver, but the results were identical to PVM-int-8 at higher computational cost, so we did not reproduce the results in this thesis. In conclusion, the Jacobian-free character of this type of solvers (1) allows to solve the equations of Rad-RMHD with the same algorithm without decomposing the system in two independent blocks, (2) improves the accuracy

of Rad-HLL both in the optically thin and optically-thick radiation transport limits and (3) it is robust and accurate for several test problems in one and more than one spatial dimensions.

We have also shown that the M1 closure is also capable to reproduce shadows in two and three dimensions, although it is less accurate when multiple sources of light are involved in optically-thin regions, leading to numerical artefacts and non-physical solutions (as shown in the double-shadow test problem of Sec. 3.4.2.2). In order to treat accurately this scenario, other authors have proposed –in the context of Rad-RHD and Rad-RMHD– to compute a closure relation directly from the Eddington tensor [i.e., the variable Eddington tensor formalism, Stone, Mihalas, and Norman 1992, González, Audit, and Huynh 2007, Jiang, Stone, and Davis 2012]. However, a deep revision of the closure scheme is beyond the scope of this thesis and will be addressed in future work (see also Chapter 4).

# Chapter 4

## Summary and future work

On this first Part of the thesis, I have presented the code `LÓSTREGO`, a new computational tool to simulate relativistic astrophysical plasmas in Cartesian coordinates. The algorithm is entirely written in FORTRAN, and solves the conservative equations of special relativistic magnetohydrodynamics (RMHD) with finite volumes. `LÓSTREGO` has been designed to run in multiple cores to exploit the capacity of modern parallel architectures, using a hybrid parallelisation scheme with parallel domain decomposition (message passing interface, MPI) and parallel threads (OpenMP, OMP). The numerical techniques of the algorithm are based on the high-resolution shock capturing methods, which have been proved to be robust and accurate, extending the techniques implemented in Martí [2015b](#) to three spatial dimensions. In a nutshell, cell-average primitive variables are reconstructed to the cell interfaces, where a Riemann problem is solved numerically employing an approximate Riemann solver. Once fluxes are solved at each cell interface, the conserved variables are evolved in time explicitly using total variation diminishing (TVD) Runge-Kutta (RK) algorithms, while magnetic fields are updated by means of the Constrained Transport (CT) method. After each time iteration, an inversion scheme is applied to recover the primitive variables.

On **Chapter 2** (originally published in the appendix of López-Miralles et al. [2022](#)), I described the equations of RMHD, and the numerical methods implemented in `LÓSTREGO` to integrate these equations in time. This includes a version of the HLLD Riemann solver of Mignone, Ugliano, and Bodo [2009](#) and a new CT scheme adapted to parallel domain decomposition, based on the interpolations proposed by Gardiner and Stone [2005](#); these two algorithms were

not previously implemented by Martí 2015b. The last section of the chapter shows an extensive numerical benchmark of the code, where I have introduced several one-dimensional and multi-dimensional test problems to probe the performance of LÓSTREGO in the field of RMHD. This collection of test problems also includes a three-dimensional study of the collision of two counter-propagating circularly polarised Alfvén waves, the building block of energy transfer in weak Alfvénic turbulence. All these test problems show that the new code is robust and accurate in different relativistic and magnetisation regimes, handling accurately both strong shocks and smooth solutions.

On **Chapter 3** (originally published in López-Miralles, Martí, and Perucho 2023), I presented the extension of our code with a module of radiation transport. Radiative transfer plays a major role in high-energy astrophysics. In multiple scenarios and in a broad range of energy scales, the coupling between matter and radiation is essential to understand the interplay between theory, observations and numerical simulations. I have introduced the equations of relativistic radiation magnetohydrodynamics (Rad-RMHD), which are formulated taking successive moments of the Boltzmann radiative transfer equation. As in other similar codes, we solve these equations under the grey-body approximation and the M1 closure using an implicit-explicit (IMEX) time integration scheme. The main novelty of our method is that we have introduced – for the first time in the context of Rad-RMHD – a family of Jacobian-free Riemann solvers based on internal approximations to the Polynomial Viscosity Matrix (PVM), which had been only tested with non-radiation applications. The robustness and the limitations of the new algorithms have been tested by solving a collection of one-dimensional and multi-dimensional test problems (both in the free-streaming and in the diffusion radiation transport limits), where I have showed that the Jacobian-free methods improve the accuracy of the classical Rad-HLL solver in the optically thin and optically thick radiation regimes.

In conclusion, the development of LÓSTREGO constitutes a major milestone of this doctoral thesis. This tool will allow us –together with our collaborators– to perform a broad range of numerical simulation in high-energy astrophysics, covering different type of scenarios (beyond the scope of the simulations I am presenting for X-ray binaries/microquasars) that includes many types of physical processes, as the dynamical effects of radiation and magnetic fields, among many others.

In the following, I propose different lines of work that aim to improve the architecture of LÓSTREGO, upgrade its numerical methods and overcome some of the limitations I encountered in the context of this thesis.

## 4.1 Code repository: in a road for public release

LÓSTREGO is the byproduct of several years of code development that also include the extension of two existing numerical tools: RATPENAT, a 3D relativistic hydrodynamics (RHD) parallel code, and the code originally presented by Martí 2015b, a 2D axisymmetric RMHD algorithm. This means that the current version of LÓSTREGO is a giant collection of numerical algorithms, parallelisation routines and physics modules that make the tool unmanageable to be used outside our group, unless an extensive code documentation is created and distributed. Therefore, in the short term I will construct a documented repository including the current version of our code together with a set of self-contained specific instructions to perform numerical simulations exploiting its different capabilities. This will allow our collaborators to perform numerical simulations employing their own computational resources, maximising the scientific outcome from the code potential. A well-documented code repository is also an important legacy for future members of the group that aim to improve the code by upgrading the existing methods or by implementing new algorithms. Moreover, this is also a first step in the development of a public version of LÓSTREGO, that we also plan to release in a short-to-medium term. Consistent with this objective, I will also improve the code management of errors (i.e., non-physical solutions, non-zero magnetic field divergence, etc), such that at the end of a simulation the user can have access to a detailed report of potential issues faced during the code execution.

## 4.2 Code performance and GPU extension

LÓSTREGO inherited most of the parallelisation architecture implemented in the code RATPENAT, which was originally parallelised with the support of the Barcelona Supercomputing Center. This architecture was proved to be optimal for many years, showing good scaling up to 2048 cores. Nevertheless, in LÓSTREGO I have modified the original parallelisation scheme, as this was required to implement our version of the CT algorithm. Although the code showed robust performance up to 4096 cores, a dedicated study of the impact of these changes on the code parallel efficiency needs to be addressed in the future.

In the same line of work, I will consider the development of a portable version of the code that can be run in different machine architectures. LÓSTREGO is optimised to run in both distributed and shared memory architectures, which was the prevailing parallel programming paradigm for roughly two decades. This

is achieved with a hybrid OMP+MPI parallelisation scheme. However, it is questionable whether this generic approach will be capable of making efficient use of available hardware features such as parallel threads and vectorisation across different multiple-core architectures and between nodes. The field of high performance computing (HPC), on the way to the exascale era [Gagliardi et al. 2019], has moved towards the implementation of graphical processor units (GPU). Although GPUs were initially designed for graphics rendering, they have gained lot of attention in the scientific community due to their capability for massive thread parallelisation. For example, the codes ATHENA++ [K-ATHENA, Grete, Glines, and O’Shea 2021, based on KOKKOS] or H-AMR [Liska et al. 2022] have been efficiently ported to GPUs, just to name some representative examples. In the latter, the authors reported an acceleration of 2-5 orders of magnitude in computation time for a wide range of applications in general-relativistic magnetohydrodynamics (GRMHD) using multi-faceted optimisations. A GPU version of the PLUTO code is also currently under development<sup>1</sup>.

From the strict point of view of coding, porting an existing hybrid OMP+MPI parallelisation to GPUs is not particularly complex. The Compute Unified Device Architecture [CUDA; Nickolls et al. 2008] developed by NVIDIA, which is a general purpose parallel computing platform and programming model, is supported by many programming languages (including FORTRAN), and leverages the parallel compute engine in NVIDIA GPUs. In practice, the instructions needed by CUDA are similar to the OMP directives that we have already implemented in LÓSTREGO, which from version OpenMP 4.5, has also been extended to support the offloading of the compute intensive code to devices such as GPUs<sup>2</sup>. The most challenging part comes indeed from memory optimisation, since GPUs require a high level of parallelism and have relatively small caches and memory bandwidth compared to classical central processing units (CPUs).

Thus, a first step towards the implementation of a GPU-based parallelisation consists on extending an existing CPU parallelisation scheme without changing significantly the original code structure, keeping MPI for parallelism between nodes and focusing on on-node performance. This requires identifying the bottlenecks in the algorithm (i.e., the most computationally intensive tasks) and port these tasks to the GPUs in order to exploit its massive multi-thread parallelisation capabilities. For example, Wright and Hawke 2019 presented a proof of concept of CUDA-capable, resistive RMHD scheme based on IMEX time integration algorithms, similar to the scheme presented in Chapter 3 for

---

<sup>1</sup><https://hpc4ai.unito.it/pluto-gpu-gpu-enabled-astrophysical-gasdynamics/2175/>

<sup>2</sup><https://www.openmp.org/updates/openmp-accelerator-support-gpus/>

Rad-RMHD. In this case, the authors reported parallel speed-ups of over a factor  $\sim 21$  using double-precision floating-point accuracy, which encourages to follow this approach in other similar codes, as it is the case of LÓSTREGO [see also Subramanian et al. 2022, where the authors present a collection of techniques and algorithms for solving high order hyperbolic partial differential equations on GPUs].

### 4.3 Implementing and improving physical processes

**Radiation RMHD** I will improve the radiation module in LÓSTREGO with three main upgrades: (1) improving the characterisation of the opacity coefficients, (2) extending the Jacobian-free Riemann solvers with other approaches, and (3) revisiting the IMEX time integration scheme and the closure relation.

First, constant scattering and absorption coefficients should be replaced by specific functions that depend on the local properties of the fluid, in order to account for the physics involved in the photon-matter interactions. For example, considering only thermal bremsstrahlung and Thomson scattering the opacity coefficient follows [see e.g., Sądowski et al. 2013, Fragile, Olejar, and Anninos 2014]:

$$\chi = 1.7 \times 10^{-25} T^{-7/2} m_p^{-2} \rho \text{ cm}^{-1} + 0.4 \rho \text{ cm}^{-1}, \quad (4.1)$$

where  $\rho$  is the plasma density and  $T$  is the plasma temperature. Alternatively, a deep revision of several approaches found in the literature was presented by Rivera-Paleo and Guzmán 2018. For example, when plasma temperature is  $10^9$  K, the electron scattering opacity can be approximated by Buchler and Yueh 1976. Another useful approach is given by the so-called Kramer's formula, which approximates the opacity by free-free ( $ff$ ), bound-free ( $bf$ ) and bound-bound ( $bb$ ) emission as:

$$\begin{aligned} \kappa^{ff} &= 3.8 \times 10^{22} (1 + X)(X + Y + Z) \rho T^{-7/2} \text{ cm}^2/\text{g}, \\ \kappa^{bf} &= 4.3 \times 10^{25} Z(1 + X) \rho T^{-7/2} \text{ cm}^2/\text{g}, \\ \kappa^{bb} &= 10^{25} Z \rho T^{-7/2} \text{ cm}^2/\text{g}, \end{aligned} \quad (4.2)$$

where  $X, Y, Z$  represents the mass fraction of hydrogen, helium and heavier elements, respectively.

As already discussed in Chapter 3 [see also López-Miralles, Martí, and Perucho 2023], the Jacobian-free solver I have implemented in LÓSTREGO is based on internal approximations to the PVM (i.e., PVM-int-8 and PVM-int-16),

but this family of solvers admit other type of schemes that has not been tested in the context of Rad-RMHD. For example, Castro, Gallardo, and Marquina 2017 found that the PVM-Cheb-12 (based on the Chebyshev approximation of degree 12), or the DOT-Cheb-12 and DOT-int-8 approximate Dumber-Osher-Toro (DOT) solvers that employ the internal and Chebyshev polynomials but a Gauss-Legendre quadrature [Castro, Gallardo, and Marquina 2016], give promising results in one-dimensional RMHD applications, and therefore should also be implemented in LÓSTREGO with testing purposes. Moreover, I will also revisit the definition of the parameter that controls the solver diffusion in the optically thick regime (i.e.,  $\beta$ ), since the approach originally presented in López-Miralles, Martí, and Perucho 2023 was a simplistic definition that admits further investigation.

In the next version of LÓSTREGO, I will also revisit the IMEX integration scheme described in Chapter 3. As we presented in López-Miralles, Martí, and Perucho 2023, our IMEX algorithm includes an implicit step after each explicit step of the TVD second/third order RK of Shu and Osher 1989, propagating the same coefficients of the explicit part to the radiation source terms [McKinney et al. 2014, Melon Fuksman and Mignone 2019]. This yields an IMEX scheme which is first order in time, but that has been proved to be robust in the diffusion and free-streaming limits showing good stability and positivity-preserving properties. Although due to the good performance of the algorithm I consider that this is a non-priority task, the extension to higher order methods should be addressed in a future upgrade [see e.g., McKinney et al. 2014, for a review]. For example, Melon Fuksman and Mignone 2019 implemented a second-order scheme called SSP2(2,2,2) [Pareschi and Russo 2005], which however leads to stability problems when the source terms are very *stiff* and there are large differences in the orders of magnitude of matter and radiation fields [see also Bucciantini and Del Zanna 2013]. Another interesting approach has been recently published by Izquierdo et al. 2022 in the context of neutrino radiation MHD, who presented different IMEX schemes compatible with the RK3 of Shu and Osher 1989 which are at least second order in the implicit part preserving the CFL of the explicit step. These algorithms, together with the schemes mentioned before, could be tested in LÓSTREGO under the Jacobian-free approach.

Finally, in Chapter 3 I have also discussed the limitations of the M1 closure, which leads to numerical artifacts and non-physical solutions when treating multiple sources of light in optically thin regions. This happens because under the radiation fluid approximation the M1 closure can only distinguish a single direction of the radiation flux in each cell. Although other schemes overcome this issue by computing a closure relation directly from the Eddington tensor

[the variable Eddington tensor formalism, see e.g., Stone, Mihalas, and Norman 1992, González, Audit, and Huynh 2007, Jiang, Stone, and Davis 2012], this requires a space-angle discretisation of the intensity field in each cell [see also White et al. 2023], increasing the computational cost. A promising method that provides the correct solution for both free-streaming scenarios and the intermediate optical-depth regime is the relativistic lattice Boltzmann method of Weih et al. 2020. As shown by the authors, the method is based on the direct solution of the Boltzmann equation by an extension of the lattice Boltzmann equation and allows to model the evolution of the radiation field as it interacts with a background fluid, featuring smaller or comparable computational costs compared to the M1 scheme. I plan to test this method in a future code release, since the solution of crossed beams in optically thin plasmas could be relevant for the type of simulations that I plan for the future (see Chapter 7).

**Ionization module in RMHD** In Appendix A [see also Perucho et al. 2021], I presented a module of hydrogen ionization that we have recently implemented in the hydrodynamical code RATPENAT. Given the positive results that we have reported in our preliminar simulations including neutral hydrogen and shock ionisation, we also plan to implement this module in the next version of the LÓSTREGO code. Since the existence of magnetic fields do not affect the equation of state nor the evolution of hydrogen densities, the module extension from RATPENAT is straightforward. Furthermore, an important milestone in our code development roadmap will be the numerical treatment of ionisation physics together with radiation transport. This would allow to include, for the first time to our knowledge, the thermodynamical effects of photo-ionisation in numerical simulations of relativistic jets.

**Numerical resistivity and magnetic dissipation** As it will be discussed with more detail in Chapter 7, an interesting outcome of the post-processing stage of an RMHD simulation is the characterisation of magnetic dissipation regions, which can only be addressed by means of heuristic methods in ideal MHD. However, as a first step in this type of study, the correct characterisation of the numerical dissipation of the code (and specially its origin) can bring useful information about the limitations of the ideal limit with the numerical techniques employed in the simulation. This type of studies has not been done before with LÓSTREGO nor with any of its numerical predecessors.

I will use the methodology presented by Rembiasz et al. 2017, where the authors proposed a simple ansatz and a corresponding calibration method to

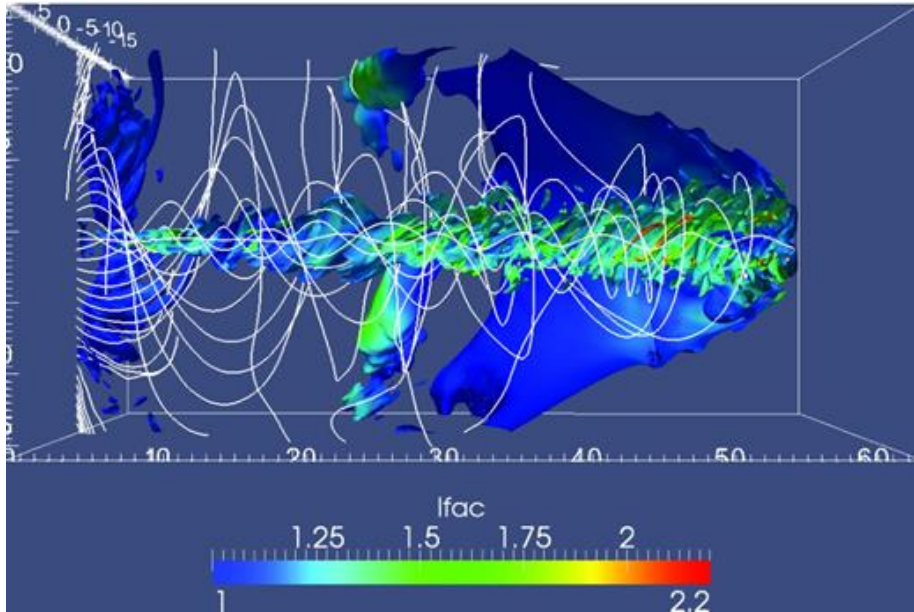


Figure 4.1 Rendering of the reference simulation, showing cut open pressure isocontour coloured according to Lorentz factor with magnetic field lines. Reproduced with permission from Porth 2013 (Fig. 2).

estimate the numerical resistivity and viscosity of an Eulerian MHD code by investigating the dependence of the numerical resistivity and viscosity on both the numerical (i.e., grid resolution, Riemann solver, reconstruction scheme, time integrator) and physical setup of a simulation. This method assumes that the amount of numerical dissipation depends on the characteristic length and velocity of the system under consideration, the numerical resolution, and some free parameters that have to be calibrated depending on the numerical scheme in use. The calibration of these parameters and the eventual determination of the magnitude of numerical resistivity and viscosity is performed by choosing a specific setup—for example, a one-dimensional wave damping test—and comparing the analytical solutions of the resistive MHD problem with the results of the simulations performed for different resolutions and code methods.

#### 4.4 Numerical methods for jet simulations

For progressing on the development of more complex jet simulations, two important questions should be addressed in the future: (1) the connection of GRMHD and RMHD scales and (2) the injection of non-toroidal magnetic fields.

**GRMHD-RMHD coupling** One of the most recurrent questions in the jet community is the multi-scaling problem. The formation of jets is studied by means of GRMHD simulations covering a small region around the central compact object, and propagate up to distances which are larger by several order of magnitude using RMHD codes. Due to this fact, these two disparate scales can hardly be addressed together even for modern parallel computers. Nevertheless, this would be essential to understand, for example, if a jet formed in a GRMHD simulation can survive to the interaction with the ambient medium without critical disruption.

To assess this problem, and as a preliminary approach, I will analyse if the output of a GRMHD simulation (i.e., a stationary slice near the box upper boundary) can be used as a boundary condition in LÓSTREGO. This type of approach was first used by Pavan et al. 2021, where the outcome of a previous binary neutron star merger simulation was imported to initialise a 3D RHD simulation of incipient gamma-ray burst jets propagating through a post-merger environment.

After a first inspection of the problem, I can spot two main obstacles in our context: (1) the scale of the GRMHD output as compared to the characteristic scale of jet propagation and interaction with the external medium, and (2) the magnetic field lines, which would lead to magnetic monopoles at the boundary when translating the field to the new numerical box. While the first issue can be possibly tackled degrading the resolution of the imported grid and employing stretched or logarithmic patterns, the second problem is more difficult to address on a first-thought and requires a dedicated study that is beyond the scope of this thesis.

**Injection of non-toroidal fields** The numerical simulations presented in this thesis are based on jets injected with a strictly toroidal magnetic field configuration, but in many circumstances, jets might also carry a poloidal field component. However, since we inject the outflow by placing a cylindrical nozzle at the boundary ghost zones, even by employing a potential vector to initialise the magnetic field, the existence of poloidal components would lead to magnetic monopoles (in other words, open field lines) at the boundary. Previously, other authors addressed this issue by imposing an internal boundary, i.e, extending the cylindrical nozzle within the numerical box [see e.g., Keppens et al. 2008, Guan, Li, and Li 2014]. Alternatively, in Porth 2013 [but see also Bromberg and Tchekhovskoy 2016, Tchekhovskoy and Bromberg 2016] the grid was threaded by an initial poloidal magnetic field with monopolar shape such that the jet

was launched from a rotating inlet resembling the corona of an accretion disk (see Fig. 4.1). However, the latter configurations require that the magnetic field fills all the grid from the beginning (which could not be desirable for certain simulation setups) and jets are injected as Poynting flux dominated flows. Thus, as a first step towards relaxing the toroidal field hypothesis, I will test the injection method proposed by Keppens et al. 2008, where the magnetic field is initialised within an inner cylindrical boundary through a potential vector. In this case, a proper study of the effects of the new boundary on the divergence-free condition in the context of the CT method should be performed as part of the new injection testing.

## Part II

# Numerical simulations



# Chapter 5

## RMHD simulations of jet-wind interactions in high-mass X-ray binaries

---

This chapter was originally published in **J. López-Miralles, M. Perucho, J.M-Martí, S. Migliari and V. Bosch-Ramon. 3D-RMHD simulations of jet-wind interactions in high-mass X-ray binaries. *Astronomy&Astrophysics*, Volume 661, id.A117, 28 pp. May 2022. DOI:10.1051/0004-6361/202142968. Reproduced with permission, ©ESO.**

---

### 5.1 Introduction

Jets are the most spectacular and powerful consequences of accretion onto compact objects (CO); they have been observed in systems containing white dwarfs, neutron stars (NSs), and black holes (BHs) of all mass scales, from stellar mass in X-ray binaries (XRBs) to supermassive in active galactic nuclei (AGN). These outflows are relativistic and extract a large and possibly dominant fraction of the total available accretion energy [Ghisellini et al. 2014], and they may even tap the power of the BH spin [Blandford and Znajek 1977]. Studies of

plasma dynamics and radiative processes in relativistic jets, and especially the comparison of different classes of compact objects [Migliari and Fender 2006], allows us to investigate the physics of strong-gravity and curved space-time; the presence of a stellar surface in NSs, or the existence of an event horizon in BHs; the role of magnetic fields in jet formation, collimation, and evolution; and the shock-acceleration mechanisms of plasma particles, to name some representative examples [see e.g., Event Horizon Telescope Collaboration et al. 2019, Kim et al. 2020, Janssen et al. 2021]. Moreover, powerful relativistic jets are one of the main ways in which accreting BHs provide kinetic feedback to their surroundings [see e.g., Bordas et al. 2009, McNamara and Nulsen 2007, in the case of microquasars and AGN, respectively]. However, most of the fundamental questions regarding jet formation mechanisms, composition, acceleration, collimation, and interaction with the interstellar medium (ISM) are still debated.

### 5.1.1 Relativistic jets in X-ray binaries/microquasars

XRBs, also called microquasars, are binary systems hosting a CO (i.e., a stellar mass BH or NS) and a companion star that has not collapsed and supplies matter to the CO through Roche-lobe overflow (in low-mass XRBs) or through the capture of stellar winds (in high-mass XRBs; HMXBs). This matter accumulates around the central object in the form of an accretion disc. Most XRBs are transient objects [Belloni and Motta 2016], but in some spectral states, these systems produce powerful bipolar relativistic jets launched by magnetocentrifugal forces [Blandford and Znajek 1977, Blandford and Payne 1982] that emit nonthermal synchrotron radiation [Mirabel and Rodríguez 1999]. On smaller scales, these processes mimic most of the phenomena observed in quasars and AGN, but in XRBs, accretion varies on much faster humanly accessible timescales than in supermassive BHs. This allows us to observe and follow the evolution of the system and to investigate the link between jet formation and the different accretion states. Therefore, numerical simulations that study the physical conditions that may reproduce existing observations are strongly needed.

In order to understand how XRBs produce relativistic ejections and how these jets affect the binary system and the surrounding ISM, we may distinguish three different regions of interest: (1) the innermost scale close to the CO, where the jet is launched by magnetocentrifugal forces from the inner accretion disc [Migliari et al. 2003, Migliari et al. 2004, Fender, Belloni, and Gallo 2004, Kylafis et al. 2012, Marino et al. 2020], (2) the binary scale, where the collimated outflow interacts with the wind of the companion star and may be disrupted [Perucho

and Bosch-Ramon 2008, Perucho, Bosch-Ramon, and Khangulyan 2010, Perucho and Bosch-Ramon 2012, Bosch-Ramon and Barkov 2016, de la Cita et al. 2017, Barkov and Bosch-Ramon 2022], and (3) the interaction of the jet with the ISM, where nonthermal particles could produce a significant amount of radiation at different wavelengths [Bordas et al. 2009, Bosch-Ramon, Perucho, and Bordas 2011, Yoon et al. 2011, Monceau-Baroux et al. 2014].

For HMXBs, jet-wind interactions are particularly relevant because of the strong winds that the massive and hot companion star injects in the vicinity of the CO. As mentioned above, this wind can have a strong impact on jet dynamics by jeopardising its stability and eventually preventing a detection of the jet [Perucho and Bosch-Ramon 2008, Perucho, Bosch-Ramon, and Khangulyan 2010]. Moreover, the one-sided impact of the wind on the relativistic flow may produce strong collisionless shocks and other dissipative processes that lead to efficient particle acceleration [Rieger, Bosch-Ramon, and Duffy 2007], resulting in significant nonthermal radiation from synchrotron, inverse Compton (IC), or even proton-proton collisions [see e.g., Romero et al. 2003, Molina, del Palacio, and Bosch-Ramon 2019]. Indeed, these processes may be at the origin of the  $\gamma$ -ray emission detected in some XRBs such as LS 5039 [e.g., Paredes et al. 2000, Aharonian et al. 2005], LS I +61 303 [e.g., Tavani et al. 1998, Albert et al. 2006] (if they really host accreting BHs), Cygnus X-1 [e.g., Albert et al. 2007, Zanin et al. 2016], and Cygnus X-3 [e.g., Albert et al. 2007, Zanin et al. 2016].

### 5.1.2 Numerical simulations of microquasar jets

Several attempts have been made in the past to describe jet-wind/star interactions from the point of view of theory and numerical simulations. Romero and Orellana 2005 studied the situation of a misaligned microquasar with its jet being periodically directed to the companion star, where the stellar wind can balance the jet pressure triggering a jet-wind collision region or, in the case of very powerful jets, nucleosynthesis in the stellar surface [as first suggested by Butt, Maccarone, and Prantzos 2003]. Perucho and Bosch-Ramon 2008 performed numerical two-dimensional (2D) simulations of jets crossing the stellar wind, reporting the formation of strong recollimation shocks that can accelerate particles efficiently and produce nonthermal radiation. Similar results, but with three-dimensional (3D) relativistic hydrodynamical (RHD) simulations, were found by Perucho, Bosch-Ramon, and Khangulyan 2010 (see Fig. 5.1). This work also confirmed that jets with total power  $L_j \lesssim 10^{36} \dot{M}_{w,-6} \text{ erg s}^{-1}$  ( $\dot{M}_{w,-6} \equiv \dot{M}_w / 10^{-6} M_\odot \text{ yr}^{-1}$ : the wind mass-loss rate) may be disrupted

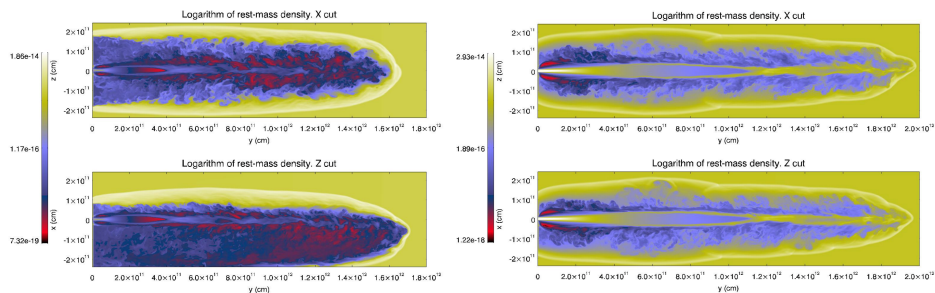


Figure 5.1 Cut of rest-mass density in the star-jet perpendicular plane of a numerical simulation representing a low-power (left) and high-power (right) jet interacting with the stellar wind in a HMXB. Reproduced with permission from Perucho, Bosch-Ramon, and Khangulyan 2010 (Fig. 1 and Fig. 3), ©ESO.

by the impact of the stellar wind, conditioning the radio-band detection of this population of XRBs. Perucho and Bosch-Ramon 2012 analysed the effect of the wind clumpiness on the jet dynamics and found significant differences in the flow stability and disruption degree even with jets with luminosities  $L_j \sim 10^{37} \dot{M}_{w,-6} \text{ erg s}^{-1}$  (see Fig. 5.2). Numerical calculations of the high-energy emission from one clump-jet interaction were performed by de la Cita et al. 2017, who predicted that these interactions may collectively dominate the nonthermal radiation. Yoon and Heinz 2015 developed numerical simulations to derive an analytic formula for the asymptotic jet bending and applied it to two well-known XRBs, Cygnus X-1 and Cygnus X-3. This work was then extended by Yoon, Zdziarski, and Heinz 2016 and Bosch-Ramon and Barkov 2016. More recently, Charlet et al. 2022 analysed the dynamical and structural effects of radiative losses in the same two fiducial cases. They performed large-scale 3D RHD simulations of jet outbreak and early propagation, finding that radiative cooling effects are more relevant for Cygnus X-3 than for Cygnus X-1. Furthermore, Barkov and Bosch-Ramon 2022 used 3D hydrodynamical simulations to study the combined effect of stellar winds and orbital motion on the scales of the binary and beyond, finding that jets with power  $L_j \sim 10^{37} \dot{M}_{w,-6} \text{ erg s}^{-1}$  can be disrupted on scales  $\sim 1 \text{ AU}$ .

However, all of these numerical works did not consider the dynamical effect of one fundamental ingredient: the existence of magnetic fields. For example, toroidal magnetic fields may have a relevant role in jet evolution by either favoring collimation through magnetic hoop-stress or by acting as a destabilising agent via the growth of current-driven instabilities [see e.g., Martí, Perucho, and Gómez 2016, Perucho 2019].

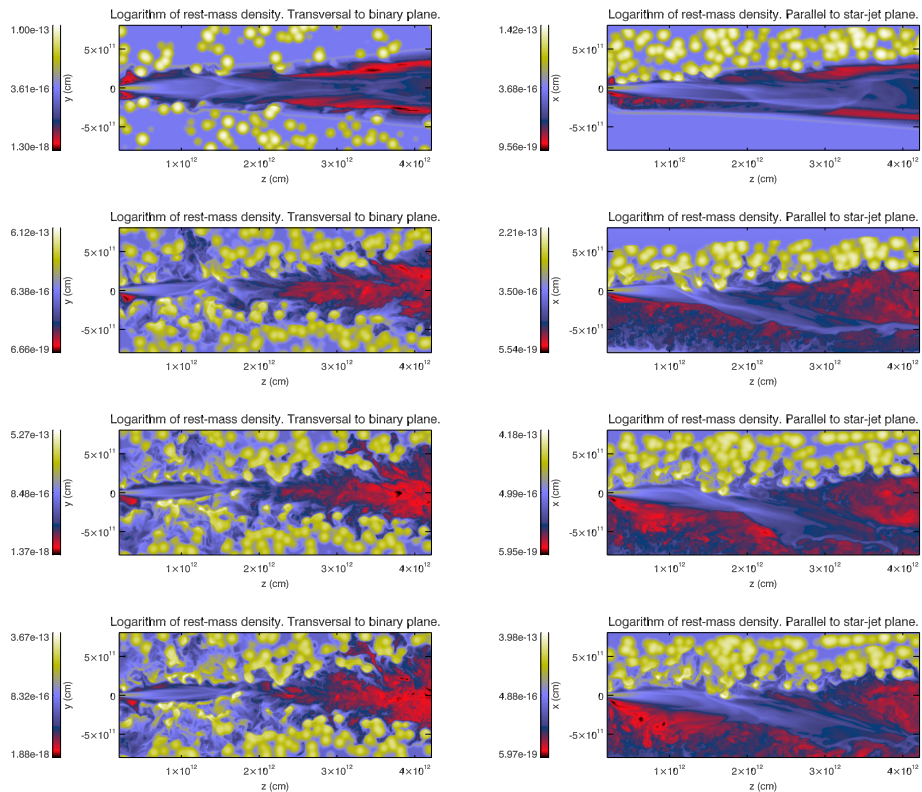


Figure 5.2 Axial cut of rest-mass density at different times for a jet interacting with a clumpy stellar wind. Reproduced with permission from Perucho and Bosch-Ramon 2012 (Fig. 5), ©ESO.

Jets are thought to be magnetically dominated close to the CO, but as the jet propagates away from the binary centre, different magnetohydrodynamical processes convert the magnetic energy into kinetic energy. This accelerates the flow, which may be also wind mass-loaded through mixing produced by small-scale instabilities. The scale of the binary is the main focus of this chapter. We expect the kinetic energy at this scale to dominate the total jet power, but it is still unclear to which extent even a relatively weak magnetic field can affect the jet dynamical evolution by favouring jet collimation or triggering more instabilities. Moreover, even moderately weak magnetic fields can be locally reinforced and thus play an important role in shaping the nonthermal emission of the jet by affecting particle acceleration, cooling, and synchrotron radiation. On the other hand, it is also possible that magnetic dissipation may not be as

efficient as generally expected, and thus jet magnetic and kinetic or thermal powers are still near equipartition on the scale of the binary.

Previously, relativistic magnetohydrodynamics (RMHD) simulations have concentrated on the formation of jets from MHD mechanisms [McKinney and Blandford 2009, Tchekhovskoy, Narayan, and McKinney 2011, McKinney, Tchekhovskoy, and Blandford 2012, Porth 2013, Cruz-Ororio et al. 2021] and the morphological characterisation of kilo-parsec scale magnetised jets [see e.g., Martí 2019, and references therein]. Different authors focused on the properties of stationary one-dimensional and 2D axisymmetric relativistic magnetised jet models [Komissarov 1999b, Leismann et al. 2005, Mignone, Massaglia, and Bodo 2005, Keppens et al. 2008, Komissarov, Porth, and Lyutikov 2015, Martí 2015b, Moya-Torregrosa et al. 2021]. Mizuno, Hardee, and Nishikawa 2007 studied the long-term stability of 3D magnetized spine-sheath relativistic jets. The first high-resolution numerical simulations of the propagation in 3D of an RMHD jet were performed by Mignone et al. 2010. Using similar methods, Guan, Li, and Li 2014 studied the propagation of Poynting-flux-driven jets in AGNs and provided a detailed analysis of energy conversion. Porth, Komissarov, and Keppens 2014 also performed the first 3D RMHD simulations of pulsar wind nebulae with parameters most suitable for the Crab nebula.

### 5.1.3 Objectives and organization

In this work, we have performed the first 3D RMHD numerical simulations of magnetised microquasar jets interacting with a moderate to strong stellar wind in an HMXB. Our main goal is to analyse the role of a toroidal magnetic field configuration in the dynamics of a collection of relativistic jets with different parameters. To do this, we compared the results with those obtained in Perucho, Bosch-Ramon, and Khangulyan 2010 and Perucho and Bosch-Ramon 2012. These simulations can be used as a numerical benchmark upon which to build new high-resolution simulations that can be directly compared with observations by radiative postprocess calculations.

The chapter is organised as follows: in Sec. 5.2 I describe the physical scenario that we consider in this work and the numerical setup of the collection of simulations we performed. In Sec. 5.3 I present the results of the simulations. In Sec. 5.4 I discuss the results by comparing our outcome with previous studies of HMXBs jet-wind interactions and analyse different mechanisms of energy conversion. Finally, in Sec. 5.5 I summarise the main conclusions of our work.

## 5.2 Simulations

For our numerical simulations, we developed a new proprietary code named LÓSTREGO, a program that solves the conservative equations of special RMHD in three dimensions using high-resolution shock-capturing methods in Cartesian coordinates. This code is fully parallelised with a hybrid scheme with parallel processes (message passing interface, MPI) and parallel threads (OpenMP, OMP), based on the same configuration as the hydro code RATPENAT [Perucho et al. 2010]. This hybrid MPI+OMP scheme exploits the architecture of modern supercomputers and keeps all the cores busy inside each node with OMP instructions. A description of the numerical methods we employed to solve the RMHD equations and the performance of the new code solving classical tests in RMHD were presented in Chapter 2 of the thesis. All simulations were performed in Tirant, the supercomputer at the Servei d'Informàtica de la Universitat de València, using up to 1024 cores.

### 5.2.1 Physical scenario

We studied the scenario of a relativistic magnetised jet propagating through the clumpy wind of the companion star in an HMXB, similar to the winds of typical XRBs such as Cygnus X-1 or LS 5039 (if it really hosts an accreting BH). For simplicity, we located the star in the plane perpendicular to the direction of propagation of the jet, at  $R_{\text{orb}} = 3 \times 10^{12}$  cm from the position of the CO, and no orbital motion was considered because the characteristic simulation time is much shorter than the typical orbital period of the system. The jet was injected with an initial radius  $R_j = 6 \times 10^9$  cm at a distance to the CO  $y_0 = 6 \times 10^{10}$  cm, propagating along the  $y$ -axis with an initially mildly relativistic velocity  $v_j = 0.55c$ . The distance between the injection point and the CO was enough to guarantee that general relativistic effects (e.g., the curvature of space-time) can be disregarded from these simulations. For the ambient medium, we considered an inhomogeneous stellar wind with radial velocity field  $v_0 = 2 \times 10^8$  cm s $^{-1}$ , mass-loss rate  $\sim 10^{-6} M_{\odot}$  yr $^{-1}$ , temperature  $T_w \sim 10^4$  K, thermal pressure  $p_w \sim 1,6 \times 10^{-3}$  erg cm $^{-3}$ , and mean density  $\rho_w \sim 3 \times 10^{-15}$  g cm $^{-3}$  (we made the assumption that the mean wind density is roughly constant within the binary, i.e.,  $y < R_{\text{orb}}$ ). These are typical values for a moderate to strong stellar wind from a primary OB-type star [see e.g., Perucho and Bosch-Ramon 2008, Muijres et al. 2012, Krtićka 2014]. The stellar wind parameters are based on a simplified model. For example, the wind may still be accelerating when it

interacts with the jets, but on the other hand, we did not take the beaming toward the CO due to the ionisation of the accelerating stellar wind close to the star into account [Molina, del Palacio, and Bosch-Ramon 2019, Vilhu et al. 2021]. The characterisation of these nontrivial effects, among other complexities of the wind structure, requires dedicated simulations that are beyond the scope of this work. The stellar wind filled the computational box from the beginning, and we did not account for radiation pressure from the star or other related physical effects. We also considered that the wind was dominated by the kinetic component at the scales of the binary, so we neglected the magnetisation of the ambient medium. We modelled the plasma as an ideal gas with  $\Gamma = 5/3$ , and we neglected both thermal and nonthermal cooling.

### 5.2.2 Numerical setup

We simulated three different magnetised jets in order to study the effect of the magnetic field in the jet evolution inside the binary. The physical parameters of each simulation are listed in Table 5.1. The total luminosities of jet A and jet B are  $\sim 10^{35}$  and  $\sim 10^{37}$  erg s $^{-1}$ , respectively, which are similar to the luminosities studied in Perucho, Bosch-Ramon, and Khangulyan 2010. Jet A and jet B are cold ( $h \approx 1$ ) and kinetically dominated, such that the internal and magnetic energy fluxes that are injected in the grid represent a small fraction of the total jet luminosity (i.e.,  $L_B \approx 0.004 \times L_h$ , where  $L_h$  is the sum of the kinetic and internal energy powers, and  $L_B$  is the magnetic power). The total luminosity of jet C is similar to that of jet B, but in this case, the jet is set in equipartition between kinetic/thermal and magnetic energy fluxes. For all of our models, the  $\beta$  ratio (i.e., the ratio of the average magnetic pressure,  $\bar{p}_m$ , to the average gas pressure,  $\bar{p}_g$ ), remains close to unity, although magnetic pressure dominates over gas pressure by a factor  $\sim 1.5$  in jet C. The initial densities at the jet base were  $\rho_A = 0.088 \rho_w$  for jet A,  $\rho_B = 8.8 \rho_w$  for jet B, and  $\rho_C = 0.88 \rho_w$  for jet C. Because jet C is more dilute and the total pressure (gas+magnetic) is higher than in jet B, the flow is also initially hotter ( $h \approx 1.66$ ).

We performed the simulations in a numerical grid box with physical dimensions of  $80 \times 240 \times 80 R_j$  (in units of the jet radius at the injection plane) with an initial resolution of 6 cells/ $R_j$ , so the box has  $480 \times 1440 \times 480$  cells. The resolution of the grid improves the resolution used in Perucho, Bosch-Ramon, and Khangulyan 2010 and Perucho and Bosch-Ramon 2012 by a factor  $\sim 1.5$ , but we only considered 75% of the longitudinal length in Perucho, Bosch-Ramon, and Khangulyan 2010 to keep the computational requirements within reasonable

Table 5.1 Summary of the main parameters of the three jets.  $L_h$  ( $\text{erg s}^{-1}$ ) is the sum of kinetic and internal power,  $L_B$  ( $\text{erg s}^{-1}$ ) is the magnetic power,  $\beta$  is the ratio between the average magnetic pressure,  $\bar{p}_m$ , and the average gas pressure,  $\bar{p}_g$ ,  $\rho$  ( $\rho_w$ ) is the jet density in units of the stellar-wind density,  $h$  ( $c^2$ ) is the jet specific enthalpy, and  $B_{j,m}^\phi$  ( $(4\pi\rho_0c^2)^{1/2}$ ) is the maximum value of the toroidal magnetic field within the jet.

Simulation	$L_h$	$L_B$	$\beta$	$\rho$	$h$	$B_{j,m}^\phi$
jet A	$10^{35}$	$5 \times 10^{32}$	1.03	0.088	1.00	0.011
jet B	$10^{37}$	$5 \times 10^{34}$	1.03	8.8	1.00	0.11
jet C	$5 \times 10^{36}$	$5 \times 10^{36}$	1.56	0.88	1.66	1.24

limits. No grid extensions or mesh refinement were employed in our simulations. As the jets expands in the numerical box, the effective resolution of the simulation is increased because the time growing transversal section of the jet involves more computational cells.

Time-resolved spectroscopic monitoring of hot star emission lines supports the idea that the stellar wind is formed by clumps. These clumps are density inhomogeneities that are created as a result of thermal instabilities during the wind acceleration phase [Runacres and Owocki 2002, Cassinelli et al. 2008, Moffat 2008]. Moreover, the similarity of the scaling laws between these clumps and the molecular clouds favours the interpretation that the clumpy structure of the wind is also a result of turbulence, with scaling laws similar to those of the fractalised ISM [Moffat 2008]. Thus, the initial inhomogeneous density distribution of the stellar wind was constructed using the publicly available PyFC code<sup>1</sup> [Wagner and Bicknell 2011], which is a Python package that is useful to represent a dense, inhomogeneous component embedded in a smooth background. This method is different from the approach adopted in Perucho and Bosch-Ramon 2012, where clouds were modelled as Gaussian-shape spheres that were randomly distributed in the computational box. The distribution of inhomogeneities was established by an iterative process following the original work on terrestrial cloud models by Lewis and Austin [2002]. The 3D density field followed a log-normal single-point statistics in real space, while the fractal structure of the system was achieved by first Fourier transforming and then multiplying the computational box by a power law with a Kolmogorov spectral index  $\alpha = -5/3$ . The mean ( $\mu$ ) of the log-normal parent distribution was  $\mu = 1.0$  and the variance  $\sigma^2 = 0.6$ , such that the minimum density of the wind is  $\rho_{\min} \approx 0.1 \rho_w$  and the maximum density is  $\rho_{\max} \approx 10 \rho_w$ . Based on the dimensions of the computational box, we set a minimum sampling wave-number  $k_{\min} = 3$ , so that the radius of the largest

<sup>1</sup><https://www2.ccs.tsukuba.ac.jp/Astro/Members/ayw/code/pyFC/index.html>

fractal structure in the cube (i.e., the maximum cloud size) was approximately  $R_{c,\max} = 6.5 R_j$  ( $R_{c,\max} < 2R_\odot$ ,  $\sim 20\%$  of the stellar radius).

In each simulation, the jet was injected into the  $y = y_0$  plane (in the system of coordinates with origin in the CO) as a cylindrical nozzle with  $r = \sqrt{x^2 + z^2} < 1$  (where length units are normalised to the jet injection radius). In this plane, density ( $\rho$ ) profile is given by:

$$\rho(r) = \begin{cases} \rho_{\text{jet}}, & 0 \leq r \leq 1, \\ \rho_{j=1}, & r > 1, \end{cases} \quad (5.1)$$

while velocity ( $\mathbf{v}$ ) components follow:

$$v^x(r) = \begin{cases} 0, & 0 \leq r \leq 1, \\ v_{j=1}^x, & r > 1 \text{ and } p_g > p_c, \\ -v_0 \cos \theta \cos \phi, & r > 1 \text{ and } p_g < p_c, \end{cases} \quad (5.2)$$

$$v^y(r) = \begin{cases} v_{\text{jet}}^y, & 0 \leq r \leq 1, \\ -v_{j=1}^y, & r > 1 \text{ and } p_g > p_c, \\ v_0 \cos \theta \sin \phi, & r > 1 \text{ and } p_g < p_c, \end{cases} \quad (5.3)$$

$$v^z(r) = \begin{cases} 0, & 0 \leq r \leq 1, \\ v_{j=1}^z, & r > 1 \text{ and } p_g > p_c, \\ v_0 \sin \theta, & r > 1 \text{ and } p_g < p_c, \end{cases} \quad (5.4)$$

where  $\theta, \phi$  are the characteristic angles of spherical coordinates,

$$\theta = \arctan \left( \frac{z}{\sqrt{(R_{\text{orb}} - x)^2 + (y + y_0)^2}} \right), \quad \phi = \arctan \left( \frac{y + y_0}{R_{\text{orb}} - x} \right), \quad (5.5)$$

and the subscript  $j = 1$  indicates that the values of density and velocity in the  $y$ -boundary cells outside the nozzle are a copy of the values in the  $y = y_0$  plane inside the box. Beyond the cylindrical nozzle (i.e.,  $r > 1$ ), we distinguish two different inlet boundary conditions: the jet cocoon, a dynamical region in which boundaries reflect to simulate the presence of a counter-jet, and the stellar wind, following the radial velocity field with origin in the location of the star (see Fig. 5.3). To distinguish between these two regions during the simulation, the jet cocoon was defined as the set of cells for which the gas pressure  $p_g > p_c$ , where we chose the threshold  $p_c = 10^{-8}$  (in units of  $\rho_0 c^2$ ). The azimuthal component of the jet axisymmetric magnetic field in the laboratory frame has the form [Lind et al. 1989, Komissarov 1999a, Leismann et al. 2005, Martí 2015b]

$$B^\phi(r) = \begin{cases} 2B_{j,m}^\phi(r/R_{B^\phi,m})/(1 + (r/R_{B^\phi,m})^2), & 0 \leq r \leq 1, \\ 0, & r > 1, \end{cases} \quad (5.6)$$

where  $R_{B^\phi, m}$  is the magnetisation radius normalised to the jet radius, and  $B_{j, m}^\phi$  is the maximum value of the magnetic field. Thus, the magnetic field grows linearly for  $r < R_{B^\phi, m}$ , reaches a maximum at  $r = R_{B^\phi, m}$ , and decreases as  $1/r$  for  $r > R_{B^\phi, m}$ . Hereinafter, we fixed  $R_{B^\phi, m} = 0.37$ , and we chose  $B_{j, m}^\phi$  for each simulation according to the magnetic power of the jet (see Table 5.1),

$$L_B = 2\pi \int_0^{R_j} (B_\phi)^2 v^y r dr. \quad (5.7)$$

In order to avoid the appearance of nonphysical magnetic monopoles, boundaries were always free with respect to the magnetic field vector components. For jets without rotation ( $v^\phi = 0$ ), the gas pressure profile can be derived from a single ordinary differential equation for the transversal equilibrium across the beam,

$$\frac{dp(r)}{dr} = -\frac{B_\phi^2}{rW^2} - \frac{B_\phi}{W^2} \frac{dB^\phi}{dr}, \quad (5.8)$$

where  $W$  is the Lorentz factor. When we integrate Eq. 5.8 by separation of variables, the gas pressure profile  $p(r)$  yields

$$p(r) = \begin{cases} 2 \left( \frac{B_{j, m}^\phi}{W(1+(r/R_{B^\phi, m})^2)} \right)^2 + C, & 0 \leq r \leq 1 \\ p_a, & r > 1, \end{cases} \quad (5.9)$$

where

$$C = p_a - \frac{(B_1^\phi)^2}{2W^2} (1 + (R_{B_{j, m}^\phi})^2). \quad (5.10)$$

In Eq. 5.10,  $B_1^\phi$  represents the value of the toroidal magnetic field evaluated at the jet radius, and we assumed that  $B^r = B^y = 0$ . This assumption is supported by two main arguments: (1) an axial component contained in the boundary zone would lead to open field lines and thus to violate the divergence-free condition, and (2) the injection scale likely exceeds the jet acceleration region, and so the magnetic field is expected to be mainly toroidal. The total pressure in  $r = R_j = 1$ ,  $p_a$ , can be derived from the hydrodynamic (kinetic+internal) jet luminosity equation,

$$L_h = 2\pi \int_0^{R_j} \rho W (h(r)W - 1) v^y r dr, \quad (5.11)$$

where  $h(r)$  is the specific enthalpy. The stellar wind enters the grid from the X-MAX boundary (see Fig. 5.3), while in all the remaining boundaries of the computational box (i.e., X-MIN, Y-MAX, Z-MIN, Z-MAX), we considered free-flow conditions.

The simulations presented in Sec. 5.3 were performed with LÓSTREGO, a new conservative, finite-volume 3D special RMHD code in Cartesian coordinates. The

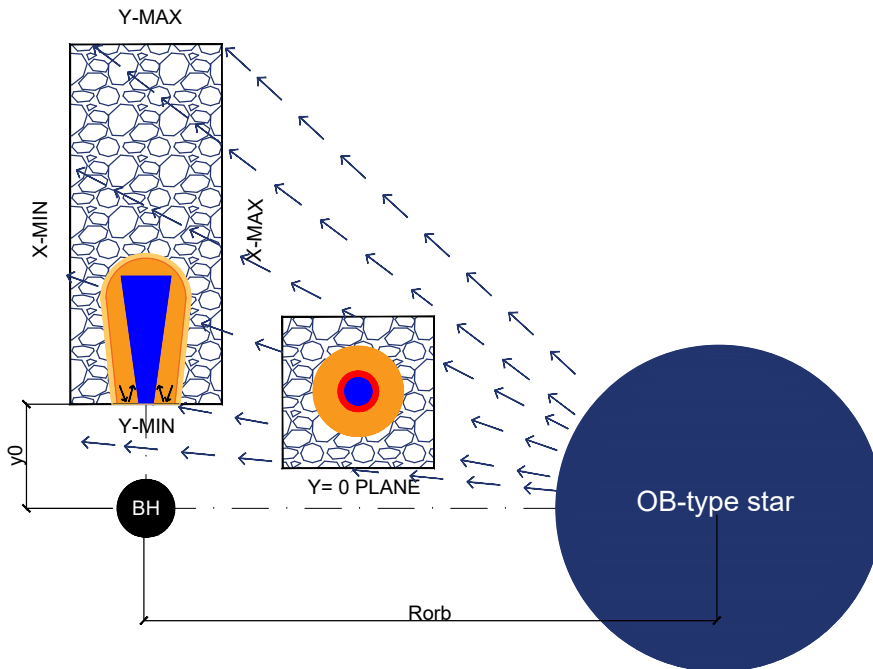


Figure 5.3 Scheme of the simulation setup in the  $XY$  plane. The radial velocity field that represents the stellar wind fills the box from the beginning. We also show a top view of the injection plane at  $Y=0$ , where we distinguish the cylindrical nozzle (blue), the shear layer (red), and the jet cocoon (orange), where boundaries are reflecting.

configuration of the code is based on our testing benchmark results (see Chapter 2). We employed a second-order Godunov-type scheme with the HLLD Riemann solver [Mignone, Ugliano, and Bodo 2009] and the piecewise linear method for cell reconstruction, with the VanLeer slope limiter [Leer 1974, Mignone and Bodo 2006]. The limiter was degraded to MinMod [Roe 1986a] when strong shocks are detected in order to avoid spurious numerical oscillations around shocks [Mignone and Bodo 2006]. When shock-flattening is applied to cell reconstruction, the HLLD Riemann solver is also degraded to the simpler and more diffusive HLL solver. The advance in time was performed using the third-order TVD-preserving Runge-Kutta [Shu and Osher 1989] with  $CFL = 0.2$ . The relativistic correction algorithm CA2 of Martí 2015a was used to correct the conserved variables after each time iteration. In our test simulations, this scheme was tested to be robust even when the magnetic pressure dominates over the gas pressure by more than two orders of magnitude. The magnetic field divergence-free constraint is preserved with the constrained transport method [Evans and Hawley 1988, Ryu

et al. 1998, Balsara and Spicer 1999], where electromotive forces at cell corners are interpolated following Gardiner and Stone 2005. An additional equation that describes the advection of a tracer function  $f$  was included in the system of equations to indicate the composition of the fluid in every cell of the box as a function of time. This tracer was used to distinguish between jet material ( $f = 1$ ), wind material ( $f = 0$ ), and the regions in which jet has been mixed with the environment ( $0 < f < 1$ ).

In RMHD jet simulations, the plane of injection is one of the most challenging regions of the grid and it is critical for the long-term survival of the whole simulation. This might become especially relevant when jets are injected as axisymmetric top-hat distributions with low numerical resolution in Cartesian coordinates. For example, we have found by analysing the first seconds of jet propagation that the axial velocity is slightly perturbed along the jet surface. This perturbation is translated into the toroidal magnetic field, which develops an axial component that grows with time and may lead to local nonphysical solutions. Porth 2013 also described the introduction of a significant amount of noise caused by the Cartesian discretisation and quadrantal symmetry of the grid, which led to the pump of multiples of the  $m = 4$  mode in all flow quantities [see Sec. 3.2 in Porth 2013]. These pathologies are controlled in our simulations first by using inhomogeneous stellar winds that naturally break the original Cartesian symmetry, and second, by smoothing the initial top-hat field distribution. In order to smooth the initial profile to avoid the growth of random perturbations at the jet base, we replaced the discontinuous functions that we described above by smooth functions of the form [Bodo et al. 1994]

$$v^y(r) = \frac{v_j}{\cosh(r^4)}, \quad B^\phi(r) = \frac{B^\phi(r)}{\cosh(r^4)}. \quad (5.12)$$

To guarantee that the injected toroidal field has zero divergence up to machine accuracy, we fixed one of the field components according to its analytical expression (smoothed with the shear layer of Eq. 5.12) and calculated the other component numerically using the solenoidal condition (i.e.,  $\nabla \cdot B = 0$ ), where spatial derivatives are approximated with finite differences. For the sake of completeness, a schematic representation of the whole setup is shown in Fig. 5.3.

Units are used in which the light speed ( $c$ ), the mean density of the stellar wind ( $\rho_w$ ), and the jet radius ( $R_j$ ) are set to unity. A factor of  $1/\sqrt{4\pi}$  is absorbed in the definition of the magnetic field, so that the actual field is smaller by  $1/\sqrt{4\pi}$ .

## 5.3 Results

To illustrate the early evolution of a fiducial jet model of our three simulations, Fig. 5.4 shows the rest-mass density distribution of jet B within a small computational box soon after injection (after the first  $20 R_j$  of propagation through the ambient medium). In the plot, we show a 3D cut of the logarithmic density of the ambient medium, a volume render of the tracer function and a gas pressure contour to show the position of the jet bow shock. When the jet starts to propagate, the highly supersonic gas generates a strong forward shock that pushes the ambient medium and a reverse shock that decelerates the jet gas at the terminal region (i.e., the hot spot), deflecting backward off the jet flow and forming a hot and light cavity surrounding the jet called cocoon. In the following, we refer equally to cocoon, shocked cavity, or jet cavity. Surrounding the cocoon, there is a dense shell of shocked gas that is separated from the cocoon by a contact discontinuity and is isolated from the unshocked ambient medium by the bow shock. In these simulations, the cocoon and the shear layer are both subject to the development of irregular structures through the interaction of the bow shock with the clumps of the stellar wind. In Fig. 5.5 we show that the toroidal magnetic field is advected following the jet gas through the clumps of the stellar wind, represented with gold isosurfaces at  $\rho = 3 \rho_w$ . Field vectors of Fig. 5.5 were integrated to represent a collection of magnetic field lines in the hot spot of Fig. 5.4 (solid black lines), where the density of the lines and the rest-mass density reach their maximum.

### 5.3.1 Jet A

Jet A propagates up to  $y \leq 220 R_j$  at  $t = 1020 (R_j/c)$ , which corresponds to  $y \leq 1.3 \times 10^{12}$  cm at  $t \approx 200$  s in physical units. This means that the propagation velocity of the jet head through the stellar wind is  $v_j \approx 0.21 c$ , slightly higher than the one-dimensional relativistic approximation of Martí et al. 1997. The relativistic velocity of the jet head can be estimated based on a one-dimensional hydrodynamical momentum balance throughout the working surface.,  $v_{1D} \approx 0.15 c$ . This small difference in the velocity of propagation can be explained by considering the ballistic nature of jet A, as described below.

In the vertical panels of Fig. 5.6, we show the logarithms of rest-mass density, gas pressure, and magnetic pressure at  $t = 1020 (R_j/c)$ . A collection of ten tracer contours is overplotted together with the logarithm of gas pressure to show the position of the jet core and the composition of the jet cavity. In the horizontal panels of this figure, we show the distribution of axial velocity at

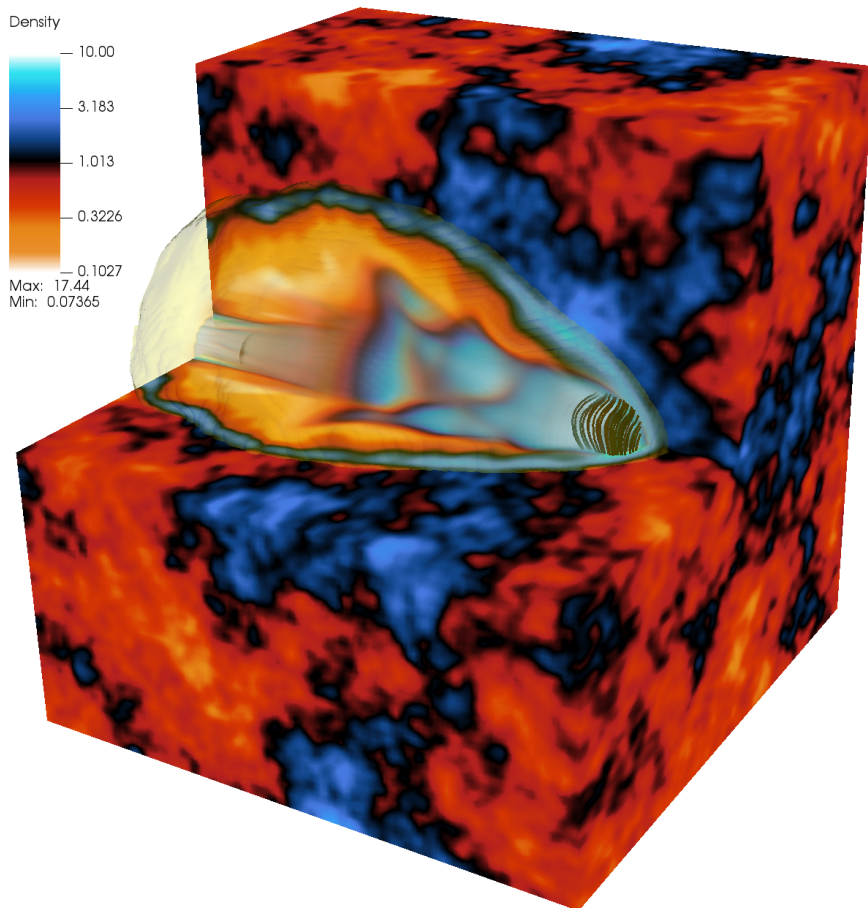


Figure 5.4 Propagation of a fiducial jet (jet B) during the first seconds after injection. The dimensions of the box are  $20 R_j^3$ , with an effective resolution of  $6 \text{ cells}/R_j$ . The density distribution of the ambient medium is represented in logarithmic scale, where we limited the maximum density to  $\rho_{\text{max}} = 10 \rho_w$  to highlight the wind clumps. Magnetic field lines are represented in the head of the jet, where the density is the highest. The 3D jet render is constructed using the jet tracer function and is coloured with the same colour scale as the density distribution (although we do not show the tracer legend to avoid redundancy), where jet particles ( $f = 1$ ) are represented in light blue and white and the ambient medium ( $f = 0$ ) in yellow and white. A gas pressure contour (faint yellow) is also included to show the position of the jet bow shock.

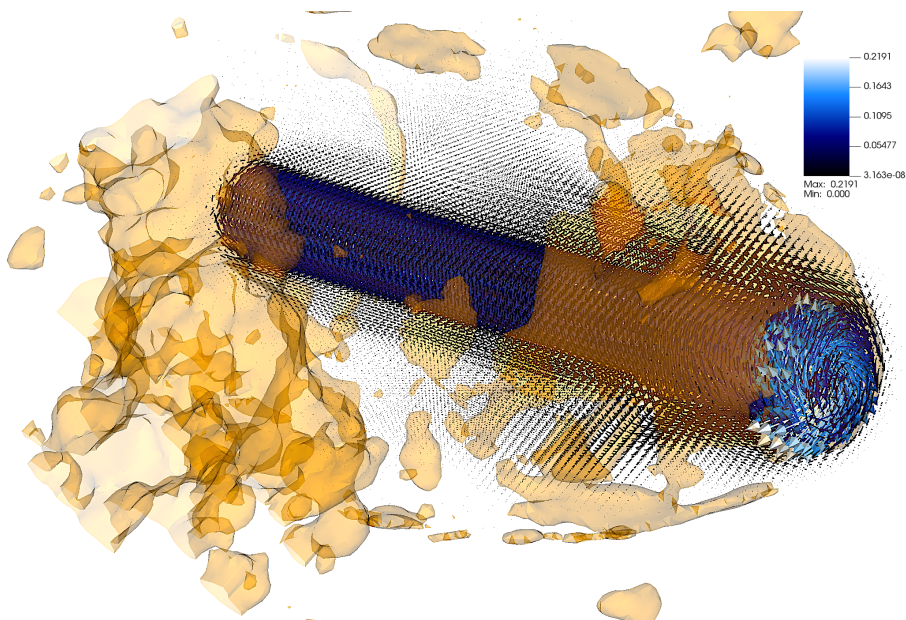


Figure 5.5 Toroidal magnetic field vectors in the same time frame as in Fig. 5.4. Stellar wind clumps are represented with gold isosurfaces at  $\rho = 3 \rho_w$ .

three different time frames:  $t = 310$ ,  $t = 610$ , and  $t = 1020 (R_j/c)$ . In the top panel of Fig. 5.7, we show a 3D render of the jet morphology and the clumpy wind distribution after jet propagation through the numerical domain, using the jet tracer and the rest-mass density, respectively. We also include a gas pressure contour (in faint yellow) to show the position of the jet bow shock at the last time frame. The overall structure of the jet is highly ballistic in the timescales of the simulation, but the interaction with the denser clumps of the stellar wind deforms the bow shock and produces an irregular shell. Near the base of the jet, the cavity seems to be inflated because of the effect of reflecting boundary conditions inside the shocked gas, producing a small equatorial bulge. The jet central spine shows several pinches due to weak reconfinement shocks, but jet collimation is preserved during the whole evolution. The jet bends slightly to the left (in the XY plane of Fig. 5.6) due to the lateral impact of the stellar wind and the subsequent difference in the total pressure on either side of the jet. Instabilities caused by this asymmetry trigger some degree of mixing between the jet material and the ambient gas at the jet boundaries close to the head. In this simulation, the jet spine maintains the injection velocity until the terminal region (i.e.,  $v_j \simeq 0.55 c$ ). In the bottom panel of Fig. 5.7, we show a collection of density isocontours that represent the jet cocoon ( $\rho = 0.1 \rho_w$ ,

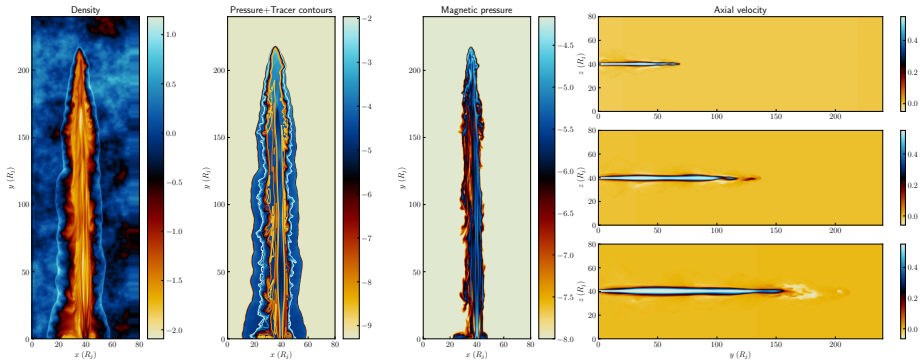


Figure 5.6 Axial cuts of jet A simulation. Vertical panels: Logarithmic rest-mass density, logarithmic gas pressure, and logarithmic magnetic pressure at  $t=1020 (R_j/c)$ . Ten tracer contours are overlotted together with the gas pressure, from  $f \approx 0$  (white to blue) to  $f = 1$  (yellow to white). Horizontal panels: evolution of the jet velocity at  $t=310$  (top),  $t=610$  (middle), and  $t=1020$  (bottom) ( $R_j/c$ ).

red), the unperturbed low-density clumps of the stellar wind ( $\rho = 2.5 \rho_w$ , gold), and the clumps compressed by the bow shock at two density levels:  $\rho = 5 \rho_w$  (dark blue) and  $\rho = 7.5 \rho_w$  (light blue). The toroidal magnetic field lines remain anchored to the jet central spine, whereas the gas that fills the cocoon drives a large-scale mildly entangled toroidal to helical field structure. At  $y \leq 80 R_j$ , magnetic field lines near the jet surface are subject to shear effects, which lead to the development of a poloidal component. This effect, which explains the melted appearance of the toroidal field in this model, might be produced by the combined effect of numerical and possibly nonphysical instabilities and the irregular structure of the poloidal velocity profile.

### 5.3.2 Jet B

The propagation of jet A and jet B is similar from a qualitative point of view, although important dynamical differences are triggered by the asymmetric impact of the stellar wind and the reconfinement shocks produced within the jet. Fig. 5.8 is similar to Fig. 5.6, but it shows the solution of jet B at  $t = 560 (R_j/c)$  and three frames of the jet axial velocity along its evolution, at  $t = 110$ ,  $t = 360$ , and  $t = 560 (R_j/c)$ . This jet propagates rather ballistically up to  $y \leq 220 R_j$  at  $t = 560 (R_j/c)$ , which corresponds to  $y \leq 1.3 \times 10^{12}$  cm at  $t \approx 110$  s, in physical units. This means that the propagation velocity of the jet head through the stellar wind is  $v_j \approx 0.39 c$ , which agrees well with the one-dimensional relativistic estimate,  $v_{1D} \approx 0.43 c$ .

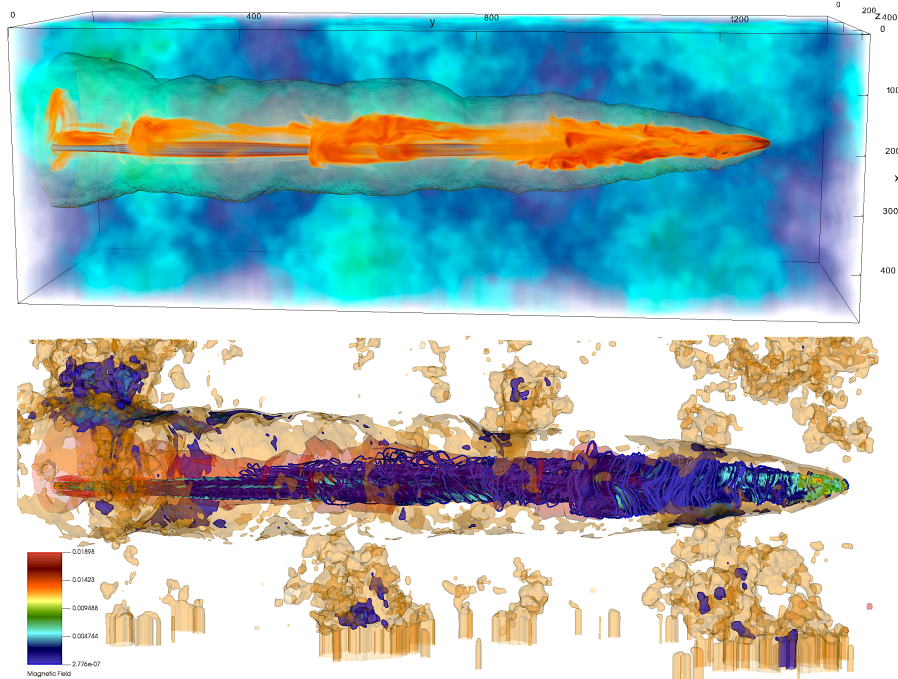


Figure 5.7 3D model of jet A simulation. Top panel: 3D render of tracer at  $t=1010 (R_j/c)$  and stellar wind clumps. A gas pressure contour (faint yellow) is included to show the position of the jet bow shock. Bottom panel: Density isocontours at  $\rho = 0.1 \rho_w$  (red),  $\rho = 2.5 \rho_w$  (gold),  $\rho = 5.0 \rho_w$  (dark blue), and  $\rho = 7.5 \rho_w$  (light blue) together with a collection of magnetic field lines.

Because the total power of jet B is two orders of magnitude larger than for jet A, the effect of the impact of the lateral wind on the long-term evolution of the jet is clearly smaller and the symmetry of the cocoon is almost preserved. The interaction of the backflow and the shocked ambient medium in the shear layer leads to the development of Kelvin-Helmholtz instabilities (KHI) and turbulence, but the jet core is unmixed ( $f \approx 1$ ) and maintains the velocity of the injection point with good accuracy until the end of the simulation (i.e.,  $v_j \simeq 0.55 c$ ). The cocoon is more elongated than in jet A because the jet head advances faster. In this case, the jet is initially denser than the average ambient medium (i.e.,  $\rho_j = 8.8 \rho_w$ ), and the total pressure is also higher. This produces an initial lateral expansion near the base with a corresponding drop in total pressure, which finally leads to underpressure with respect to the cocoon and to the generation of a recollimation shock far from the injection plane. The position of the shock changes from  $y \approx 120 R_j$  at  $t = 360 (R_j/c)$  to  $y \approx 160 R_j$  at  $t = 560 (R_j/c)$ , meaning that it moves with  $v_{\text{shock}} \approx 0.2 c$ . At the terminal shock,

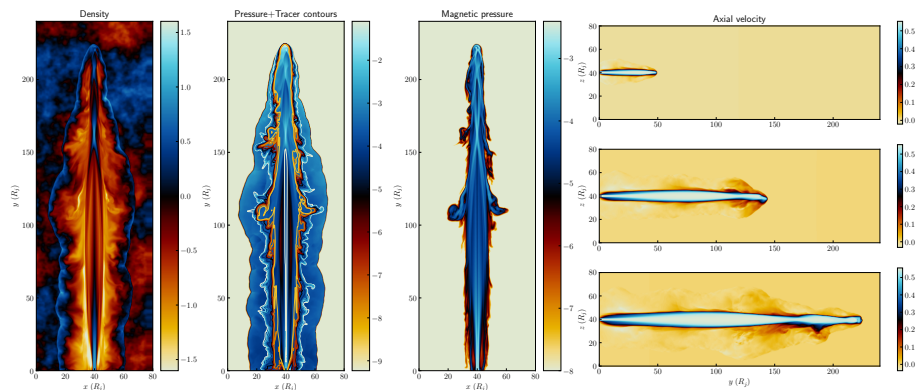


Figure 5.8 Axial cuts of jet B simulation. Vertical panels: Logarithmic rest-mass density, logarithmic gas pressure, and logarithmic magnetic pressure at  $t=560 (R_j/c)$ . Ten tracer contours are overlotted together with the gas pressure, from  $f \approx 0$  (white to blue) to  $f = 1$  (yellow to white). Horizontal panels: Evolution of the jet velocity at  $t=110$  (top),  $t=360$  (middle), and  $t=560 (R_j/c)$  (bottom).

the magnetic pressure also increases because the field lines are compressed. Near the reconfinement shock region, jet material cannot flow freely and accumulates in the head of the jet, leading to backflow blobs of jet gas that drag the magnetic field filling the cocoon (Fig. 5.8, bottom panel). As the shock moves downstream, the stretched nozzle deposits more plasma in the cocoon and creates a filamentous structure, where  $f < 1$  because of mixing with the ambient medium gas.

### 5.3.3 Jet C

Even though the total luminosity of jet C is the same as in jet B, the jet dynamics are vastly different, as are evolution and overall morphology. This is triggered by the moderate to strong magnetic fields within the jet. Figure 5.10 is similar to Figs. 5.6 and 5.8, but it shows the solution of jet C at  $t = 720 (R_j/c)$ , and three panels of the axial velocity distribution at times  $t = 210$ ,  $t = 490$ , and  $t = 720 (R_j/c)$  to illustrate the jet evolution. In this simulation, the jet propagates up to  $y \leq 200 R_j$  at  $t = 720 (R_j/c)$ , which corresponds to  $y \leq 1.2 \times 10^{12}$  cm at  $t \approx 142$  s, in physical units. This means that the propagation velocity of the jet head through the stellar wind is  $v_j \approx 0.26 c$ , which is lower than the one-dimensional relativistic estimate of Martí et al. 1997,  $v_{1D} \approx 0.33 c$ . It is important to note, however, that this simulation cannot be prolonged in time because the bow shock has touched the lateral walls of the grid at  $t < 720 (R_j/c)$ . Because the magnetic field is initially larger than in the two previous models (as it is required to achieve power equipartition with the energy flux associated

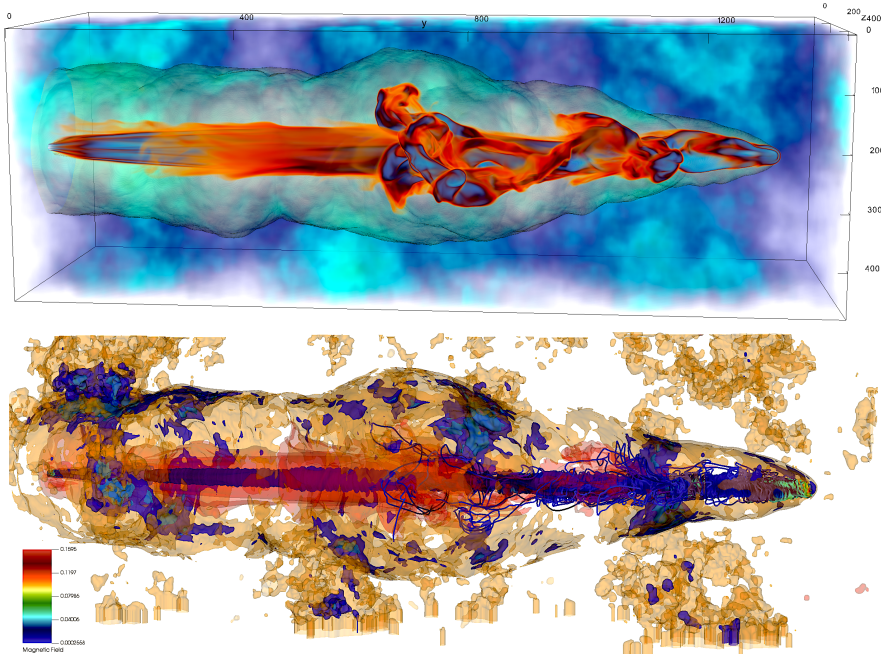


Figure 5.9 3D model of jet B simulation. Top panel: 3D render of tracer at  $t=560$  ( $R_j/c$ ) and stellar wind clumps. A gas pressure contour (faint yellow) is included to show the position of the jet bow-shock. Bottom panel: Density isosurfaces at  $\rho = 0.1 \rho_w$  (red),  $\rho = 2.5 \rho_w$  (gold),  $\rho = 5.0 \rho_w$  (dark blue), and  $\rho = 7.5 \rho_w$  (light blue) together with a collection of magnetic field lines.

with the particles), the initial overpressure of the jet nozzle with respect to the medium is even higher than in jet B, leading to a pronounced lateral expansion and a quick, strong recollimation. During this quick process, the jet flow increases its bulk velocity from the mildly relativistic value at injection (i.e.,  $v_j \simeq 0.55 c$ ) to a maximum of  $v_j \simeq 0.95 c$  at the jet core. The difference with respect to the one-dimensional estimate is even more evident if we calculate the velocity of propagation considering the maximum velocity after the first quick expansion (i.e.,  $v_j \simeq 0.95c$ ), yielding  $v_{1D} \approx 0.76 c$  (a factor  $\sim 3$  higher than the actual velocity of propagation).

The effect of the toroidal field on the jet dynamics is visible from the early jet evolution by the development of current-driven instabilities that destabilise the jet beyond the first reconfinement shock. The consequent increase in cross-section in which the head deposits its momentum slows down the velocity of propagation of the head with respect to jet B. The morphology and dynamics of the cocoon are also different than in the other two simulations (Fig. 5.11,

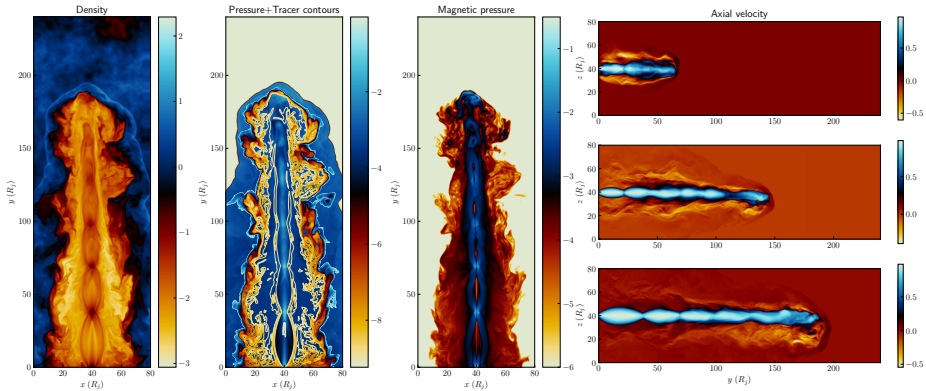


Figure 5.10 Axial cuts of jet C simulation. Vertical panels: Logarithmic rest-mass density, logarithmic gas pressure, and logarithmic magnetic pressure at  $t=720 (R_j/c)$ . Ten tracer contours are overlaid together with the gas pressure, from  $f \approx 0$  (white to blue) to  $f = 1$  (yellow to white). Horizontal panels: Evolution of the jet velocity at  $t=210$  (top),  $t=490$  (middle), and  $t=720$  (bottom) ( $R_j/c$ ).

top panel) for the same reason. The first reconfinement shock drives a chain of shocks that are evident throughout the entire jet spine, where magnetic pressure reaches its maximum within the jet due to the compression of toroidal field lines. At  $t = 720 (R_j/c)$ , at least four reconfinement shocks have appeared after jet evolution, at  $y \approx 35 R_j$ ,  $y \approx 70 R_j$ ,  $y \approx 100 R_j$ , and  $y \approx 130 R_j$ . This means that at the end of the simulation, there is a shock at approximately every  $y \approx 30 R_j$ . The backflow interacts strongly with the shocked ambient medium, developing KHI that lead to turbulence and mixing with the jet gas within the cocoon ( $f < 1$ ). The morphology of the magnetic field lines is also different in the lower body of the cocoon and in the jet head (Fig. 5.11, bottom panel): at  $y \leq 100 R_j$ , the magnetic field remains roughly ordered and the field lines preserve the toroidal morphology. At  $y > 100 R_j$ , the field lines are highly tousled, forming an entangled lobe structure around the head of the central axis. This structure of the magnetic field is translated into the morphology of the cocoon material, where gas exhibits toroidal filaments at  $y \leq 100 R_j$ , but it appears heavily disordered downstream from the chain of shocks (Fig. 5.11, top panel). However, we find that this representation of the field lines is not optimal, since the field of the cavity obscures the direct view of the jet core in the head. A better representation of the field lines, showing the internal field structure, is presented on Chapter 7 of this thesis.

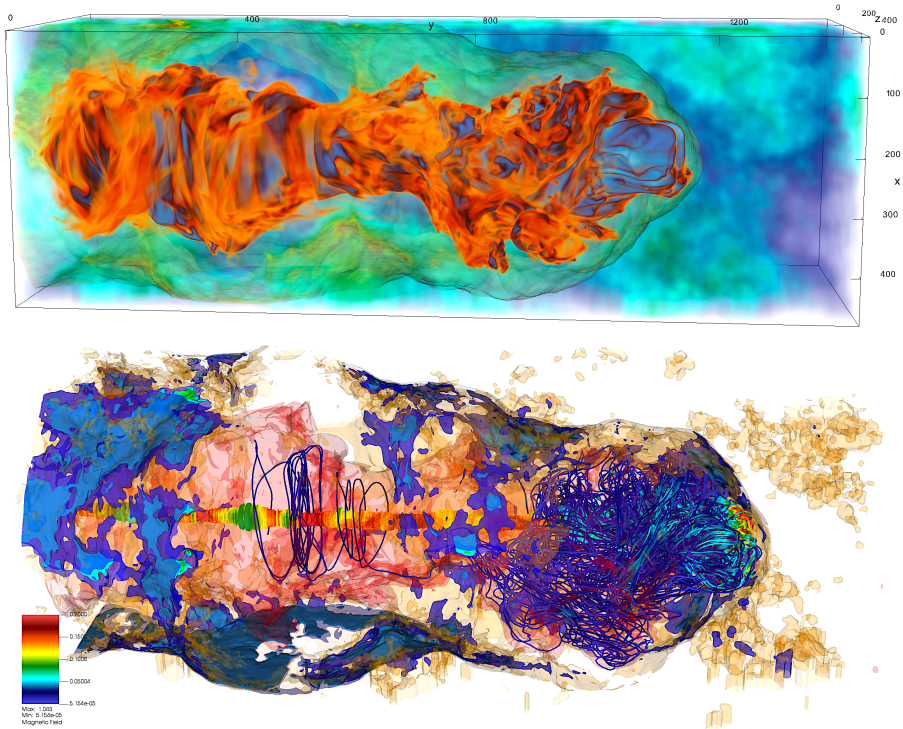


Figure 5.11 3D model of jet C simulation. Top panel: 3D render of tracer at  $t=720 (R_j/c)$  and stellar wind clumps. A gas pressure contour (faint yellow) is included to show the position of the jet bow shock. Bottom panel: Density isosurfaces at  $\rho = 0.1 \rho_w$  (red),  $\rho = 2.5 \rho_w$  (gold),  $\rho = 5.0 \rho_w$  (dark blue), and  $\rho = 7.5 \rho_w$  (light blue) together with a collection of magnetic field lines.

## 5.4 Discussion

### 5.4.1 Jet power and jet morphology

In our RMHD simulations, the total jet power was chosen to be comparable to those of the RHD simulations performed in Perucho, Bosch-Ramon, and Khangulyan [2010]. Jet A and jet B have a power similar to that of jet 1 and jet 2, respectively. We focus first on the case of jet A compared to jet 1. Although the magnetised jet propagates up to almost the same distance ( $y \simeq 1.3 \times 10^{12}$  vs.  $y \simeq 1.5 \times 10^{12}$  cm), there is a remarkable difference in the amount of time that these two models take to achieve this distance: whereas jet A needs approximately 200 s, jet 1 takes 1250 s (i.e., a difference of a factor  $\sim 6$ ). The reason for this difference is related to the destabilisation and disruption of jet 1 beyond a moderate to strong recollimation shock at  $y \simeq 5 \times 10^{11}$  cm. The

jet flow is strongly decelerated following that shock, and it is thus prone to the fast development of helical instabilities triggered by the impact of the stellar wind. In jet A, magnetic tension of the toroidal field acts against expansion (furthermore, the gas pressure profile is set up initially to ensure transversal equilibrium with the magnetic pressure), whereas in jet 1, the jet expands only as determined by the jet-to-cocoon total pressure ratio.

Although jet B is also slightly faster than jet 2 in Perucho, Bosch-Ramon, and Khangulyan [2010] (the first reaches  $y \simeq 1.3 \times 10^{12}$  cm in  $t \simeq 110$  s, and the second takes almost twice as long to reach  $y \simeq 2 \times 10^{12}$  cm), the difference is reduced precisely because jet 2 is more collimated and develops a very oblique recollimation shock, which does not decelerate the flow enough to favour its disruption, in contrast to jet 1. Both jets are fairly similar in their evolution, with the minor difference in both advance velocity and location of the first recollimation shock (which is slightly farther downstream in jet 2), probably due to the longer simulation time in the RHD run. Nevertheless, the hydrodynamical jet shows a lower degree of collimation than the RMHD one (see Fig. 5.9). Again, although in this case the magnetic tension does not seem to play such an obvious role as in the case of jet A, its effect can be crucial for jet evolution and long-term stability. Whether this difference is related to the development of a poloidal sheared component around the jet flow (see the bottom panel in Fig. 5.9) should be a matter of study, but it is beyond the scope of the work presented on this chapter.

Overall, we find that the presence of a toroidal field, as long as it is non-dominant from an energetic point of view, might contribute to stabilising the jet evolution in microquasars. Nevertheless, a stronger magnetic field (as is the case for jet C) causes the jet to become prone to the development of fast recollimation shocks and current-driven instabilities, which do not develop in the case of jet A and jet B. Therefore, future work should address the threshold from which the magnetic field can become a destabilising factor for the jet structure at the scales of the binary. This comment is of remarkable relevance in terms of the long-term stability of relativistic jets not only for microquasars, but also for AGN: a nondominant toroidal field, as is expected to be the case beyond collimation and acceleration scales in both microquasar and AGN jets, could have a stabilising role with respect to purely hydrodynamical jets. The reasons are magnetic tension to avoid rapid expansion and large-angle recollimation shocks with the consequent flow deceleration on the one hand, and the possible generation of a sheared poloidal component in the backflow that shields the

jet against the development of instabilities on the other hand (although KHI, mainly helical, can still develop).

Interestingly, jet C is more similar to jet 1 (which is two orders of magnitude less luminous) than to jet 2 in Perucho, Bosch-Ramon, and Khangulyan [2010] or jet B in this work, which stresses the relevance of the development (or lack) of instabilities in outflows in terms of energy dissipation and the subsequent kinematics and morphology. This jet resembles the structures observed in axisymmetric simulations [see e.g., Martí, Perucho, and Gómez 2016, Moya-Torregrosa et al. 2021] for the case of jets in which the Poynting flux is relevant or dominates the total energy flux. In this type of models, the presence of a chain of recollimation shocks forced by the toroidal field favours the dissipation of kinetic energy. However, it is important to note that this process takes place after the jet has reached higher velocities than are expected in microquasar jets, which is precisely a consequence of the acceleration provided by the presence of strong fields and high internal energies at injection. Jets with higher kinetic energies or inertia are expected to be less prone to developing disrupting instabilities, at least in the non magnetised case [Perucho, Martí, and Hanasz 2005]. Despite the large inertia achieved by the jet after acceleration, kinetic energy is efficiently dissipated at the series of recollimation shocks. These shocks therefore destabilise the flow not only by themselves, but also by making the jet sensitive to the effect of the lateral wind, as reported in Perucho, Bosch-Ramon, and Khangulyan 2010 for jet 1. Whether microquasar jets eventually reach such velocities and are later decelerated at larger distances (beyond the binary system) should be tested by comparison of the synthetic radiative output from simulations and observational features from known sources.

Finally, we highlight that jet 1 and jet 2 in Perucho, Bosch-Ramon, and Khangulyan 2010 faced a homogeneous medium, but this is not the case of jet A and jet B in this paper. However, our results show that the differences caused by clumps are likely minor at the timescales of our simulations. In contrast, in Perucho and Bosch-Ramon 2012 the authors adopted a setup in which the jet was established in equilibrium with the ambient medium, a simplified version of the clumpy stellar wind. The stage of direct wind-jet interaction is only plausible when the forward bow shock has propagated far enough from the simulated binary region, that is, at longer timescales than those studied here.

### 5.4.2 Energy channels

The analysis of the energy distribution and the evolution of the energy fluxes along the jet can shed light on the interplay among the different energy channels (i.e., kinetic, internal, and magnetic) and, in particular, the possibility of jet acceleration via extraction of magnetic and/or internal energies. Furthermore, it is well understood that the relativistic nature of jets favours the very efficient exchange of a good fraction of the kinetic and internal energy fluxes with the ambient medium, mediated by strong shocks. This effect was previously described based on 2D axisymmetric models [Perucho, Quilis, and Martí 2011, Perucho et al. 2014b] and was extended to long-term 3D hydrodynamical simulations in Perucho, Martí, and Quilis 2019 for AGN jet evolution. However, this effect has not been explored so far with magnetised jet models or in the particular context of microquasars.

The accumulated energies in each of the three channels described above can be computed numerically considering the relativistic version of the energy equations and summation over all cells in the 3D numerical box,

$$\begin{aligned}\tau_k(t) &\approx \sum_{\text{cells}} \xi \rho W (W - 1) \Delta x \Delta y \Delta z, \\ \tau_\epsilon(t) &\approx \sum_{\text{cells}} \xi \left[ \rho \left( \epsilon + \frac{p_g}{\rho} \right) W^2 - p_g \right] \Delta x \Delta y \Delta z, \\ \tau_B(t) &\approx \sum_{\text{cells}} \xi \left[ B^2 - \frac{B^2}{2W^2} - \frac{1}{2} (\vec{v} \cdot \vec{B})^2 \right] \Delta x \Delta y \Delta z,\end{aligned}\tag{5.13}$$

where  $\tau_k(t)$  is the kinetic energy,  $\tau_\epsilon(t)$  is the internal energy,  $\tau_B(t)$  is the magnetic energy (all expressed in the observer's reference frame), and  $\xi$  represents the jet tracer,  $\xi = f$ , to calculate the energy of jet particles, or  $\xi = 1 - f$ , to calculate the energy transferred to the ambient medium. Finally,  $\Delta x$ ,  $\Delta y$ , and  $\Delta z$  are the cell sizes for each spatial dimension. Considering that the wind is stationary and the bow shock has not crossed the outer boundaries of the numerical grid, the sum of the different energies should be equal to the total energy injected by the jet nozzle at a given time,  $t$  (plus the internal and kinetic energy of the stellar wind).

For the purposes of this section, we restrict our analysis to simulations of jet B and jet C because these two models have an equivalent total jet power, but the energy flux is distributed in a different way among the three energy channels; while in jet B the kinetic energy flux dominates over the internal energy flux and the magnetic energy flux by almost two orders of magnitude, in jet C the magnetic flux is initially in equipartition with the sum of internal

and kinetic energy fluxes (whereas the internal energy flux is also a factor  $\sim 5$  higher than the kinetic energy flux). Figure 5.12 shows the time evolution of the logarithm of the different types of energies for jet B (left panel) and jet C (right panel) at  $t = 110, 360, 560 (R_j/c)$  and  $t = 10, 110, 210, 490, 720 (R_j/c)$ , respectively. In the case of jet C, we included two additional time frames to those shown in Fig. 5.10 in order to analyse energy conversion during the early moments of jet propagation, because some of these processes occur very quickly after the injection of the jet. In Fig. 5.12 the solid lines (without marks) show the logarithm of the energy injected in the computational box as a function of time. We recall that the inclusion of a shear layer to smooth the initial top-hat axial velocity and magnetic field profiles as described in Sec. 5.2.2 implies that the eventually injected power is lower than the theoretical value given in Table 5.1. This is translated into a power reduction of  $\sim 20\%$  for the simulation of jet B and  $\sim 10\%$  for jet C. The difference in the percentages of the two models can be explained by the higher sensitivity of kinetic energy flux to our shear layer than the magnetic and internal energy fluxes.

As said before, the sum of the jet and ambient medium energies accumulated in the numerical grid must be equal to the injected energy plus the original internal and kinetic energies of the ambient medium. The small difference (a few percent; see the next paragraphs) comes from the use of a correction algorithm for the conserved variables and, more importantly, the low resolution of the numerical representation of the circular injection nozzle by a Cartesian grid. On the other hand, assuming that no energy conversion between the different channels (internal, magnetic, and kinetic) takes place within the jet, and that the only transfer of energy within each of those channels is that between the jet and the ambient medium, the sum of the jet and the ambient energies (solid lines with square marks) should be close to the theoretical injected energy (solid lines) for each energy channel. Thus, the difference between the numerical values for the total energy in each channel and the theoretical curves implies that different physical processes of energy conversion are operating during jet evolution. We describe these processes for the two jet simulations in the remaining paragraphs of the section.

**Jet B:** In the left panel of Fig. 5.12, we show that total energy (solid green line with squares) is roughly conserved during the evolution from  $t = 110$  to  $t = 560 (R_j/c)$  because the three points we considered for this analysis overlap (with an error smaller than 1%) with the total injected energy (solid green line without marks). Although the total kinetic energy (solid red line with squares),

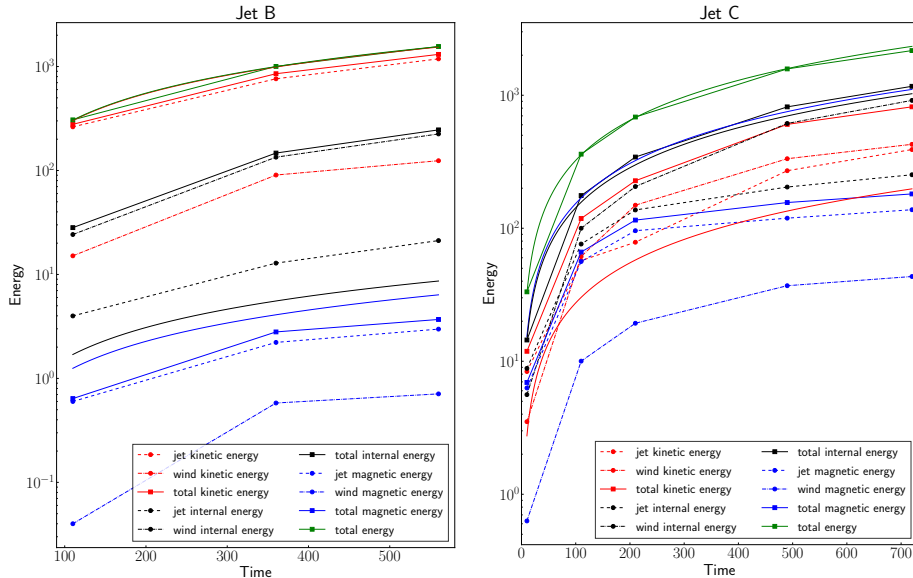


Figure 5.12 Time evolution of the logarithm of the energy in the simulation for jet B (left) and jet C (right) at the three time frames of Fig. 5.8 and Fig. 5.10, respectively. In the right panel (jet C), we have included two additional time frames at  $t = 10$  ( $R_j/c$ ) and  $t = 110$  ( $R_j/c$ ). Energy stored by the jet plasma ( $f \neq 0$ ) is represented with dots and dashed lines, ambient medium energies ( $f = 0$ ) with dots and dash-dotted lines, and total energies (jet+ambient medium) with squares and solid lines. Continuous solid lines (without marks) are the theoretical curves (i.e., the injected values) for each type of energy: kinetic (red), internal (black), magnetic (blue), and total (green). Energy units are  $\rho_w c^2 R_j^3$ .

total internal energy (solid black line with squares) and total magnetic energy (solid line with squares) do not coincide with their respective injected energies (because of effective energy conversion), the initial global energy distribution is preserved: kinetic energy dominates the whole evolution, and magnetic energy remains residual (below 1% of the total energy) even when the jet is fully developed. The jet magnetic energy (dashed blue line with dots) is lower than the injected value even at early  $t = 110$  ( $R_j/c$ ) (we also confirmed that this is true for earlier times).

A direct conversion of magnetic energy into kinetic energy seems unlikely, because the jet is highly dominated by the kinetic energy and the expansion profile is not parabolic. In that case, the origin of the difference between the total magnetic energy and the injected energy can be attributed to the numerical resistivity of the code, which can produce a continuous effective conversion of magnetic energy into internal energy.

On the other hand, the blue points connected with dash-dotted lines shown in the left panel of Fig. 5.12 represent the total magnetic energy accumulated in the ambient medium. Optimally, this energy would have to be zero because in ideal MHD, there is no physical mechanism to transfer magnetic energy from the jet fluid into the non magnetised ambient medium. However, it is important to note that the magnetic energy assigned to the ambient medium comes mainly from numerical cells with a mixture of jet and ambient fluids, where according to Eq. 5.13 the magnetic energy is distributed arbitrarily proportional to the corresponding mass fraction. Then, the amount of magnetic energy that is accumulated in the ambient medium ( $\sim 10\%$  of the injected magnetic energy at the end of the simulation) may be interpreted as an ample upper bound of the magnetic diffusion of our numerical code.

In this simulation, the main manifestation of energy transfer concerns the conversion of jet kinetic energy (dashed red line with dots) into kinetic and internal energy of the ambient medium (dash-dotted red and black lines with dots, respectively), mediated by the propagation of the bow shock, and into internal energy of jet plasma in the shocked cavity (dashed black line with dots). At the end of the simulation, the jet plasma preserves more than 70% of the injected kinetic energy. At the same time, the transferred portion ( $\sim 30\%$ ) has been used to accelerate ( $\sim 10\%$ ) and heat ( $\sim 20\%$ ) the shocked stellar wind, and to increase the total internal energy of the jet plasma by a factor  $\sim 2$ .

**Jet C:** In the right panel of Fig. 5.12, we show the energy distribution for jet C simulation between  $t = 10$  and  $t = 720$  ( $R_j/c$ ), where we included two additional time frames at  $t = 10$  and  $t = 110$  ( $R_j/c$ ) with respect to those shown in the horizontal panels of Fig. 5.10. The total energy is conserved during the evolution with an error smaller than 1%<sup>2</sup>, whereas the magnetic energy assigned to the ambient medium by the end of the simulation is lower than 5% of the total injected magnetic energy.

The evolution of the energy distribution in this simulation is strongly conditioned by the physical processes operating at very early times. At  $t = 10$  ( $R_j/c$ ), magnetic or internal and kinetic energies are already lower and higher than their injected values, respectively, with  $\tau_{B,jet}/\tau_{B,inj} \approx 0.40$ ,  $\tau_{\epsilon,jet}/\tau_{\epsilon,inj} \approx 0.60$  and  $\tau_{k,jet}/\tau_{k,inj} \approx 3$ , meaning that about 60% of the jet magnetic energy and 40% of the internal energy have been converted into jet kinetic energy by that time. Thermal acceleration occurs in hot, expanding flows by the Bernoulli

---

<sup>2</sup>This error increases up to 8% in the last time frame because some fraction of the shocked gas has left the box through the lateral boundaries.

process. Magnetic acceleration, in contrast, needs a particular expanding flow geometry [differential collimation; see e.g., Vlahakis 2004, Vlahakis and Königl 2004, Komissarov 2011, and references therein]. According to the results of Komissarov et al. 2007 for axisymmetric models, magnetic acceleration is very efficient with as much as  $\sim 75\%$  of the Poynting flux converted into kinetic energy at long enough spatial scales. The fast expansion experienced by jet C close to the injection nozzle (see Fig. 5.10) could provide the correct dynamical and geometric conditions to trigger the magnetic acceleration process, which would then have been observed in microquasar jet simulations for the first time and at much shorter spatial scales.

The plot of the evolution of the energy accumulated in the different channels, with the curves overtaking each other several times, reveals the complex nature of jet propagation in model C. As an example, we note that the internal energy of the jet dominates the magnetic and kinetic energies between  $t = 10 (R_j/c)$  and  $t = 210 (R_j/c)$ , but at  $t = 490 (R_j/c)$ , it has exchanged its position with the kinetic energy. Additionally, the figure shows that the magnetic channel loses energy steadily with time. The decrease of magnetic energy can take place within the jet at the magnetic acceleration sites after the reconfinement shocks (where the flow expansion could admit the differential collimation), but also at the magnetically dominated regions of the turbulent shocked cavity (see Fig. 5.13).

Finally, we observe a relevant difference between models B and C in terms of kinetic and internal energy distribution: in the case of jet B, most of the energy in the grid is hosted by the jet matter, whereas the opposite seems to be the case for jet C. It has been shown in a series of papers [Perucho, Quilis, and Martí 2011, Perucho et al. 2014b, Perucho, Martí, and Quilis 2019] that relativistic jets are very efficient in transferring energy to the ambient medium. In Perucho et al. 2017, the authors attributed this efficiency to the relativistic nature of jets and showed that massive, cold jets are less efficient in the process of energetic transfer because a large fraction of the energy flux is in the form of kinetic energy, dominated by the mass of the particles. This agrees with the results we derived here, where jet B is significantly denser and colder than jet C, which makes it highly inefficient with respect to jet C in terms of energy transfer to the ambient medium. As in the aforementioned paper, this shows the relevance of the relativistic nature of outflows in the feedback process.

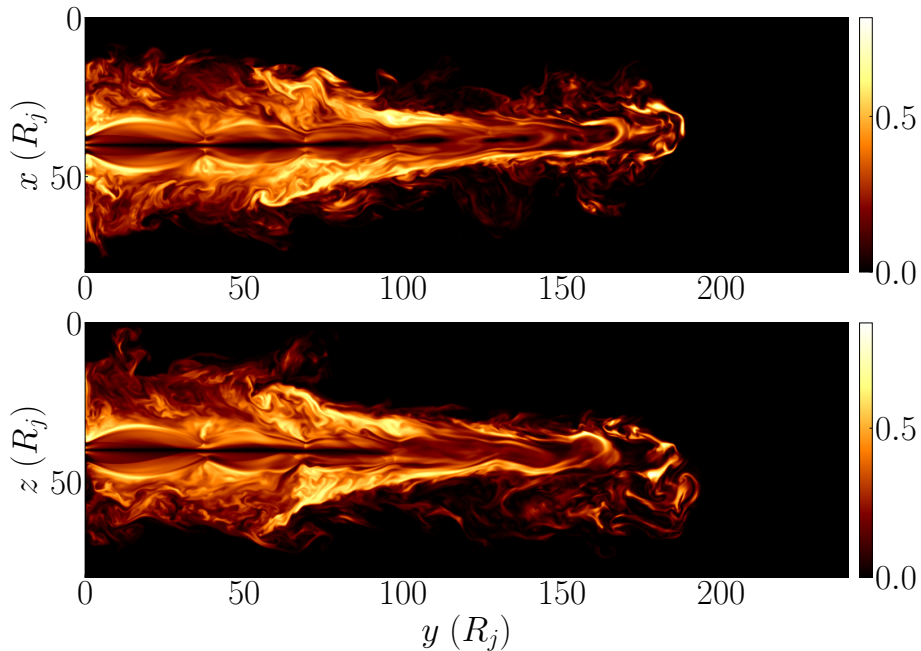


Figure 5.13 Fraction of magnetic energy density with respect to total energy density for jet C in the XY (top) and ZY (bottom) plane.

### 5.4.3 Radiative processes in the magnetised jet

As discussed, for instance, in Rieger, Bosch-Ramon, and Duffy 2007 and Bosch-Ramon and Rieger 2012, particle acceleration is expected to be more efficient in strong shocks in microquasar jets, with electrons and positrons typically cooling much more efficiently than protons and nuclei [see e.g., Bosch-Ramon and Khangulyan 2009]. In these systems, strong magnetic field dissipation through magnetic reconnection could also be relevant for particle acceleration [Bosch-Ramon 2012, Bosch-Ramon and Rieger 2012].

With respect to hydrodynamical shocks, the strong recollimation shock(s) in relativistic jets can be a perfect candidate for generating a significant nonthermal population of particles. The nonthermal emission related to the jet-wind interaction has been discussed in previous works [see e.g., Molina, del Palacio, and Bosch-Ramon 2019, and references therein], although in all but one case [i.e., de la Cita et al. 2017, where the one clump-jet interaction was simulated using relativistic hydrodynamics], the jet dynamics was semi-analytical. Nevertheless, in these works, the magnetic field was not informed using devoted RMHD simulations, but assuming either a fixed ratio of the magnetic to internal

energy density, or establishing frozen-in conditions in the hydrodynamical flow. Therefore, in this context, the simulations presented here provide with new insights into the nonthermal processes of HMXB jets.

The most straightforward conclusion that we can derive from the results of this work is that synchrotron emission and IC may be anti-correlated space-wise in the jet. Nonthermal electrons in highly magnetised regions may emit more synchrotron and less IC radiation, whereas in regions that are not strongly magnetised, it may be the opposite [see e.g., Khangulyan and Aharonian 2005, for subtle effects of synchrotron and IC losses on the radiation spectra]. All this applies in particular to electrons emitting synchrotron X-rays or very high energy IC photons, as they are more sensitive to radiative cooling versus advection in the jet.

On the other hand, our results for jet C show more shocks than in jet B. In these shocks, kinetic energy turns into internal energy, favouring plausible particle acceleration within the scales of the binary. Magnetic energy is also transferred to matter rather efficiently through magnetic acceleration at favourable expansions. Magnetic acceleration introduces greater complexity to radiation coming from the region where this occurs through a complex pattern of Doppler boosting. Another nonthermal process linked to the magnetic field, which is difficult to capture here but might be relevant in highly magnetised jets as well, is magnetic reconnection. Magnetic energy can be injected into particles by reconnecting magnetic lines, which can trigger (multiple) shocks in the region in which this occurs. These nonthermal processes and others that might be relevant (e.g., acceleration driven by turbulence or shear motion or gamma-ray reprocessing in the complex jet-wind environment), are very difficult to quantify unless specific detailed studies are carried out. Although this is beyond the scope of this work, I will briefly discuss the possibility to characterise the dissipation of magnetic energy by means of ideal RMHD simulations in Chapter 7.

As shown, jets might be more stable if they are moderately magnetised. If this were the case, they could reduce the amount of energy transferred to nonthermal particles within the binary system. However, as suggested in Bosch-Ramon and Barkov 2016 and shown by Barkov and Bosch-Ramon 2022, the impact of orbital motion in longer time-scales than simulated here can further destabilise the jet, and so most of the energy dissipation may not take place within the system, but farther out, where orbital motion strongly shapes the jet evolution [see Molina and Bosch-Ramon 2018, for an example of such a situation].

If the jet kinetic and magnetic powers are roughly similar, or if the latter dominates the former, the jet may become severely disrupted on the scales of

the binary. This may seem incompatible with milliarcsecond observations of the jet of Cygnus X-1 [Stirling et al. 2001], which show that the jet is still rather collimated on scales of tens of orbital separation distances. However, the combined effects of the stellar wind and orbital motion may cause the binary system to act as a nozzle for the highly magnetised, disordered jet, allowing the jet to reaccelerate and potentially recollimate on relatively short timescales given the fast drop in density and pressure outside this region. In addition, the magnetic field of the jet may act as a protective shield against mixing with the stellar wind, which would allow the jet to again reach relativistic speeds if the environment and/or the magnetic field were appropriate [e.g., Komissarov 2011]. No such effect is expected from a hydrodynamical jet, which could hardly become relativistic again due to heavy wind entrainment [Bosch-Ramon and Barkov 2016, Barkov and Bosch-Ramon 2022].

Depending on the magnetic field strength, the jet will present different emission properties. Specifying these differences for comparison with observations requires specific simulations covering regions that are larger than the orbital separation distance. Simulations of quasi-steady state jets would be also needed, as they are complementary to the present ones because the timescales involved in observations are often long enough to capture this jet regime. Moreover, the magnetic flux in the jet may be different depending on the particular accretion-ejection state of HMXBs. This different magnetisation in the ejections, which would be continuous or discrete depending on the state of the source, would be a major factor (in addition to the flow energetics) determining the properties of the nonthermal emission. This possibility requires a detailed analysis of the observed outflow properties and it is left for future work.

Nevertheless, recent large-scale 3D hydrodynamical simulations [Charlet et al. 2022] show that for two fiducial HMXBs (namely, Cygnus X-1 and Cygnus X-3), thermal cooling (i.e., free-free losses) could dominate the emission in the beam and inner cocoon (see e.g. Fig. 7 in Charlet et al. 2022). In particular, the authors analysed the jet outbreak and early propagation beyond the scale of the binary and concluded that these radiative losses do not play a dynamical or structural role for the space of parameters in Cygnus X-1, although they can be relevant for the evolution of Cygnus X-3 due to the denser stellar winds of the Wolf-Rayet primary. According to our models and the timescales of our simulations, we do not expect that (non)thermal cooling produces a significant effect on the relativistic jet dynamics, but the characterisation of the system emission would require a dedicated analysis. This is beyond the scope of the simulations we have performed.

## 5.5 Conclusions

We have performed three different numerical simulations of microquasar jets propagating through an inhomogeneous stellar wind using the new code LÓSTREGO for computations in relativistic astrophysics. Our numerical setup was based on the space of parameters described in previous 3D hydrodynamical jet-wind simulations, including a toroidal magnetic field in transversal equilibrium with the gas to analyse its role for jet dynamics and long-term stability. We present the jet evolution throughout the initial minutes after the trigger of jet formation, which allowed us to keep a steady injection point in the grid and neglect the orbital motion of the binary.

Our simulations show that the magnetic field could play a stabilising role in jet evolution as long as the flux of magnetic energy is lower than the kinetic energy flux. This stabilising effect provides the simulated, magnetised jets, with additional collimation along the grids, as compared to similar, non magnetised jets. In contrast, a non-negligible magnetic energy flux translates into a destabilisation of the flow, with the consequence of increased energy dissipation and a slower jet head propagation velocity. The study of the threshold at which the magnetic field changes its role should be addressed by future simulations.

The evaluation of the probability of jet propagation beyond the binary region has thus to be revisited in the presence of magnetic fields. In Perucho and Bosch-Ramon 2008, Perucho, Bosch-Ramon, and Khangulyan 2010 it was concluded that this depended basically on the jet power, whereas in this work, we see that low-power jets threaded by relatively weak fields could propagate longer distances without being destabilised. However, more powerful jets, in contrast, might be disrupted by current-driven instabilities if the magnetic field is dynamically relevant at the scales of the binary. Therefore, we conclude that a more thorough characterisation of the magnetic field role in microquasar jets at these scales is needed in order to set a proper limit on the minimum energy flux to allow for propagation beyond the progenitor system.

In RMHD jet simulations, the presence of recollimation shocks within the binary region is more probable than in the case of RHD jets due to the role of magnetic tension, which acts against expansion and contributes to jet collimation [Martí, Perucho, and Gómez 2016, Fuentes et al. 2018], independently of drops in the ambient pressure [in contrast to RHD flows, Perucho and Bosch-Ramon 2008, Perucho, Bosch-Ramon, and Khangulyan 2010], but the pressure jumps at these shocks and its consequent radiative properties still depend on the obliqueness with respect to the jet stream lines.

A detailed analysis of the energy distribution in the jet shows that magnetic and internal energies can both contribute very efficiently to jet acceleration in expansion regions. At shock waves (recollimation, standing, and terminal shocks), both magnetic and internal energies may grow at the expense of the kinetic energy budget. In the turbulent backflow, these magnetically dominated regions can convert magnetic energy into kinetic and internal energy of the flow (the latter by magnetic diffusion), while if the kinetic energy is dominant, this can be used as a reservoir to locally reinforce the magnetic field and to increase the internal energy. Moreover, we have also contributed further evidence to the relevant role of the relativistic nature of outflows in the study of jet energy transfer to the ambient medium, as predicted before by Perucho et al. 2017 for AGN, and as analysed here for the first time in the context of microquasar jet simulations.

# Chapter 6

## Unravelling the relativistic magnetized jet dynamics of the microquasar SS 433: the scale of the sub-parsec

### 6.1 Introduction

The microquasar SS 433 is one of the most powerful and exotic star systems in our Galaxy. It is a high-mass X-ray binary (HMXB) located at a distance of  $\sim 5.5$  kpc [Blundell and Bowler 2004, line of sight  $\sim 78^\circ$ ] formed by a compact object (CO; a stellar-mass black hole [Bowler 2018, Blundell, Bowler, and Schmidtobreick 2008, Cherepashchuk, Postnov, and Belinski 2018] or a neutron star [Fabian 1980, D’Odorico et al. 1991]) orbiting a companion supergiant [Hillwig et al. 2004], with  $P_{\text{orb}} \approx 13$  days.

The main characteristic that distinguishes SS 433 from other binary systems is the presence of a continuous regime of supercritical accretion [Fabrika 2004] ( $M_{\text{accr}} \sim 10^{-4} M_{\odot}/\text{yr}$ ) that exceeds by far the Eddington limit, which also powers bipolar, very narrow ( $< 5^\circ$ ), regular precessing ( $\theta \sim 20^\circ$ ,  $P \sim 162$  days,  $P_{\text{nut}} \sim 6$  days), mildly-relativistic jets ( $v \sim 0.26 c$ ), as inferred from Doppler-shifted optical emission lines [Margon et al. 1979, Abell and Margon 1979]. Moreover, it is the first galactic binary to reveal the presence of baryonic matter

in the relativistic outflows by Doppler-shifted iron emission lines from spatially resolved regions [Migliari, Fender, and Méndez 2002]. The projection of these jets on the plane of the sky reveals a corkscrew trace that can be explained by helical motions of gas flowing along ballistic trajectories [the so-called kinematic model; Abell and Margon 1979, Stirling et al. 2002].

The kinetic luminosity of the jets is  $L_k > 10^{39}$  erg/s [Marshall, Canizares, and Schulz 2002], while the observed X-ray luminosity is considerably lower,  $\sim 10^{36}$  erg/s [Brinkmann et al. 1991]. One possibility is that the powerful winds driven by the thick accretion flow obscures the direct view of the core, in analogy with Seyfert-2 galaxies. Indeed, King et al. 2001 proposed that Ultra Luminous X-ray sources (ULXs) in nearby galaxies are linked to microquasars with the supposition that the X-ray emission is restricted to a small cone angle aligned to the line of sight in ULXs, but away from the line of sight in microquasars. Under this assumption, it has been suggested that the effective X-ray luminosity would be  $L_k > 10^{39}$  erg/s if viewed along the axis. Thus, SS 433 is the most promising ULX candidate in the Galaxy [Begelman, King, and Pringle 2006, Khabibullin and Sazonov 2016, Middleton et al. 2021, Marshall 2022], possibly together with the HMXB Cygnus X-3 [see e.g., Veledina et al. 2023, and references therein].

### 6.1.1 Multi-wavelength outflows

SS 433 jets are resolved across the whole energy spectrum, depending on the distance to the core and, most importantly, the bulk plasma temperature. Close to the CO ( $\sim 10^{10-13}$  cm), the jet gas is hot (consistent with the temperatures of the inner accretion disc,  $T \sim 10^8$  K) and emits high-temperature continuum and Doppler-shifted lines in the soft X-ray band [see e.g., Marshall et al. 2013]. Farther out ( $> 10^{13}$  cm), the jet emission is approached by the adiabatic cooling expansion model. At  $\sim 10^{13-15}$  cm, jets manifest as shifted optical emission lines (mainly H and HeI,  $T \sim 10^4$  K) due to variations of the jet axis with respect to the line of sight [Murdin, Clark, and Martin 1980]. A continuous source of heating is expected to maintain the emission in the optical jets. The scale  $\sim 10^{15-17}$  cm is mainly characterized by non-thermal synchrotron radiation produced by relativistic electrons accelerated in the jet magnetic field [Hjellming and Johnston 1981, Stirling et al. 2004, Roberts et al. 2008, Miller-Jones et al. 2008]. Very Long Baseline Array (VLBA) continuous monitoring of the source [Paragi et al. 1999, Mioduszewski et al. 2004] reveals the presence of knotty emission regions (Fig. 6.1), which suggests that SS 433 radio jets are based on discrete blobs rather than a continuous outflow, as inferred from soft X-rays

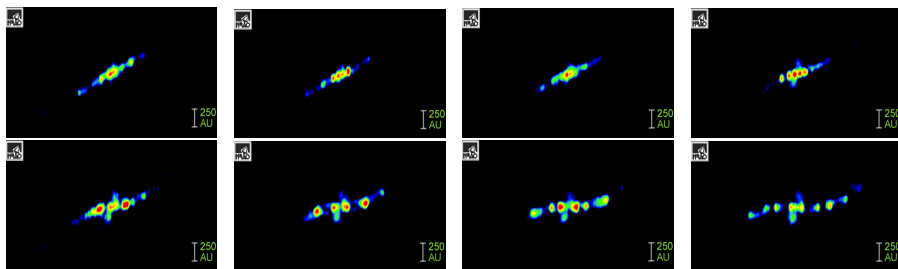


Figure 6.1 Different time frames of VLBA observations of SS 433 jets, where time goes from left to right and from top to bottom. From Mioduszewski et al. 2004.

close to the CO [Marshall et al. 2013]. Thus, it seems SS 433 outflows experience a transition from a continuous stream to regularly spaced clumps (or blobs), possibly as the result of thermal cooling instabilities.

At  $\sim 10^{17}$  cm, a collection of Chandra observations [Marshall, Canizares, and Schulz 2002, Migliari, Fender, and Méndez 2002, Migliari et al. 2005, Miller-Jones et al. 2008] revealed the presence of extended X-ray emission (Fig. 6.2), where according to the adiabatic cooling model, plasma should be too cool to emit X-ray radiation. The existence of these arc-sec X-ray jets suggests that local reheating of the atomic component takes place within the jet flow. Although the mechanisms of particle reheating remains unclear, (1) the existence of internal shocks formed by collisions of blobs ejected at almost the same precession phase but with different propagation velocity, (2) reflected radiation from the core or (3) the interaction of the jet with the powerful winds of the accretion disc seem plausible scenarios. Rapid X-ray variability has also been inferred from Chandra observations [Migliari et al. 2005], which could suggest that a second, faster underlying flow (which is not directly observed) might energise the jet material at this scale, similar to the Ultra Relativistic Flows (URFs) reported in other X-ray binaries [Fomalont, Geldzahler, and Bradshaw 2001a, Fomalont, Geldzahler, and Bradshaw 2001b, Fender, Belloni, and Gallo 2004, Motta and Fender 2019]. Nevertheless, later studies could not prove the existence of these outflows [Miller-Jones et al. 2008], meaning that if they really exist, they should be transient and/or short-lived events.

Polarization imaging of the arc-sec jets also shows that the magnetic field apparently aligns with the local velocity vector after one precession cycle (Fig. 6.3). As suggested by Miller-Jones et al. 2008, this could support the hypothesis that jets are composed of discrete bullets, rather than being a continuous flux tube. However, no strong evidence for this connection could be established so far in the literature. There is also evidence of regions of anomalous polarized emission

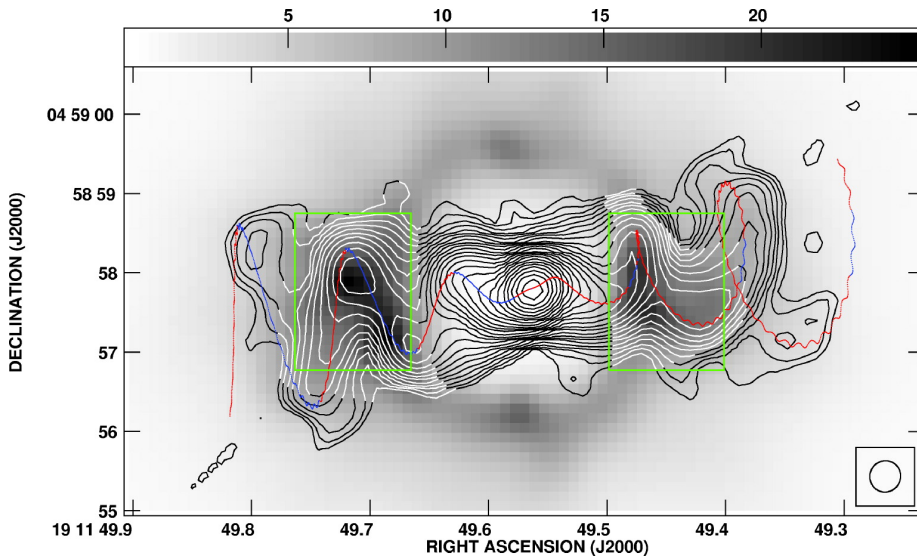


Figure 6.2 Chandra ACIS-S X-ray greyscale image of the 60-ks observation of 2003 July with radio contours superposed. The calculated jet kinematic model precession trace, including nodding, has been overlaid. Reproduced with permission from Miller-Jones et al. 2008 (Fig. 1). ©AAS.

away from the jet kinematic locus [Stirling et al. 2004, Miller-Jones et al. 2008], where the magnetic field is observed to be aligned perpendicular to the velocity vector away from the core.

At the large scale, jets are not detected until distances of  $\sim 10^{19-20}$  cm where termination shocks are observed, possibly due to the jet interaction with the W50 nebula [Safi-Harb and Ögelman 1997, Safi-Harb et al. 2022], as suggested by the elongation of W50 aligned with the axes of the jets' precession cone. W50, catalogued as a Galactic supernova remnant (SNR), is one of the largest SNR in the Galaxy, expanding over  $200 \times 100$  pc ( $\sim 2^\circ$  East-West x  $\sim 1^\circ$  North-South).

While the outermost region of W50 is dominated by thermal X-ray emission, Safi-Harb and Petre 1999 inferred a hard (non)-thermal component in the interior of the lobe, approximately at  $\sim 30$  pc from the location of SS 433. Using Chandra observations, Safi-Harb et al. 2022 also showed that this emission can be resolved into  $\sim 1'$ -scale knotty structures ( $\sim 1.6$  pc at  $d=5.5$  kpc, see Fig. 6.4), and suggested that this region could also be associated with the SS 433 arc-sec scale jets, where particles are possibly being re-accelerated through some unknown mechanism.

Emission of  $\gamma$ -rays has also been related with the SS 433/W50 system [Bordas et al. 2015]. Abeysekara et al. 2018 first discovered TeV emission with the High

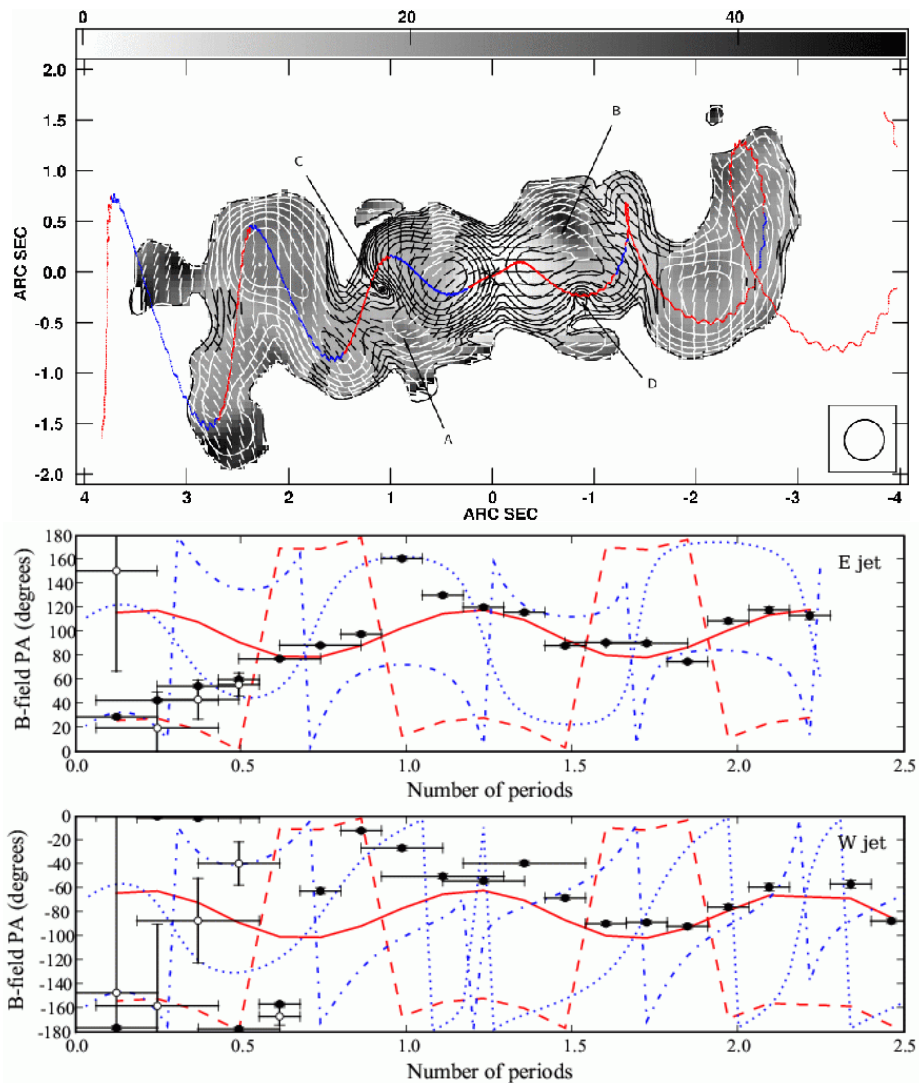


Figure 6.3 Top: Linear polarization contours superposed on fractional polarization greyscale with EVPA vectors overlaid. Bottom: Plots of the variation of the magnetic field direction with position away from the core along the kinematic model trace. Reproduced with permission from Miller-Jones et al. 2008 (Fig. 7 and Fig. 8). ©AAS.

Altitude Water Cherenkov (HAWC) Observatory, while more recently a joint Fermi-LAT and HAWC analysis found GeV-to-TeV  $\gamma$ -ray emission inside the lobes [Fang, Charles, and Blandford 2020]. Li et al. 2020 also reported the discovery of two new  $\gamma$ -ray sources in the field of view of SS433/W50; while one of them can be associated with the eastern SS 433 lobe, the second source

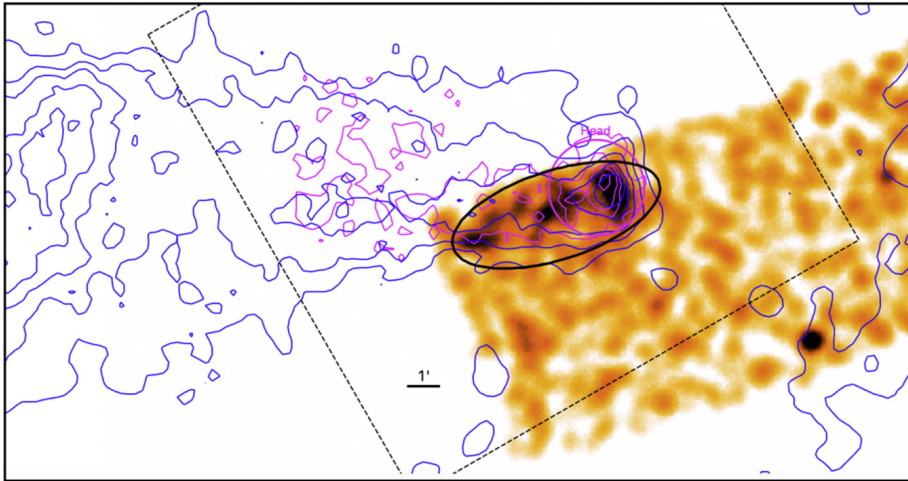


Figure 6.4 Serendipitous partial Chandra coverage of the inner part of the eastern lobe. Contours are NuSTAR (magenta) and XMM-Newton (blue). The dashed box is the NuSTAR FoV, and the ellipse (black) shows the Chandra spectral extraction region that partially overlaps the "Head" region. The image is bounded by SS 433 on the right (west) and the "lenticular" region on the left (east). Reproduced with permission from Safi-Harb et al. 2022.

displays variability compatible with the jet precession period of the binary, but apparently outside the jet propagation trace. Although some models are proposed by the authors (for example, a scenario based on illumination of dense gas clouds by relativistic protons accelerated at the interface of the accretion disc envelope), the connection of this source with the binary is still unclear.

### 6.1.2 Numerical simulations

Despite the large number of observational studies that exist in the literature [see e.g., Margon 1984, Fabrika 2004, Li 2007, for a review, and references above] and the current capability of high-performance computing (HPC) architectures, only a few simulations of the system have been performed so far.

Even more than twenty years ago, Muller and Brinkmann 2000 performed the first low-resolution non-relativistic time-dependent three-dimensional (3D) hydrodynamical simulations of the SS 433 precessing jets, showing the development of highly complex structures and instabilities and the deceleration of the jet head.

More than one decade later, Monceau-Baroux et al. 2014 performed 3D relativistic hydrodynamical simulations of SS 433 sub-parsec jets and showed that the best match with the existing radio images of the source was achieved

by using the canonical propagation speed of  $v = 0.26 c$  and a precession angle of  $20^\circ$ , in good agreement with the observed parameters. The apparent discrepancy between sub-parsec and parsec scales was also addressed by means of long-term hydrodynamical simulations in Monceau-Baroux et al. 2015, considering that jets interact with the supernova remnant W50. In that work, the authors showed that precessing jets with an angle of  $20^\circ$  can naturally recollimate into a continuous non-precessing hollow flow due to pure hydrodynamical processes, providing a tentative explanation for the system morphology at large distances. Some years later, Bowler and Keppens 2018 deduced a set of simple scaling relations to extend the computations in Monceau-Baroux et al. 2014 and Monceau-Baroux et al. 2015 to lower densities and pressures of the ambient medium, finding that SS 433 jets could be responsible for the large scale morphology of the system. Indeed, other authors focused on reproducing the W50 elongated shell morphology, either on the jet interaction with the SNR [Zavala et al. 2008, Goodall, Alouani-Bibi, and Blundell 2011] or on the own jet (magneto)hydrodynamics processes [Ohmura et al. 2021]. The formation of relativistic jets under super-Eddington accretion rates (as suggested for SS 433 and ULXs in general) was also addressed by means of general relativistic radiation magnetohydrodynamics simulations [see e.g. Sądowski and Narayan 2015].

### 6.1.3 Overview

In this chapter of the thesis, we present the most detailed large-scale 3D numerical simulations of the SS 433 precessing jets at the scale of the subparsec (i.e. arcsec projection), including for the first time the dynamical evolution of the jet magnetic fields. The physical processes governing the jet dynamics at this scale are essential not only for our understanding of optical, radio and X-ray observations of the source, but also for explaining the astonishing SS 433-W50 system morphology. We explore how a precessing jet based on the parameter space of SS 433 with an initial toroidal magnetic field configuration can develop a non-toroidal component during the first precession cycles, and specifically, the role of discrete plasmon collisions into this process. We also address the effect of these interactions on the overall jet morphology, deceleration pattern and long-term stability, which are essential to increase our understanding of particle acceleration and high-energy emission beyond the sub-parsec region, in the SS 433/W50 lobes. Due to the complexity of the post-processing analysis, in this chapter I overview the simulations performed and I present a preliminary discussion of the main results, but a deeper interpretation requires a more

detailed study which is still ongoing. This analysis will be presented elsewhere in the future.

## 6.2 Methods

This chapter gathers the results of a research project developed within the Spanish Supercomputing Network (*Red Española de Supercomputación*; AECT-2022-1-0022). Numerical simulations were performed in the Picasso supercomputer (The Supercomputing and Bioinnovation Center of the University of Malaga) using 4096 cores and a total of 4000 khrs of HPC computation.

### 6.2.1 Numerical methods

The simulations presented in this chapter were performed with LÓSTREGO [López-Miralles et al. 2022], a conservative, finite-volume 3D relativistic magnetohydrodynamics (RMHD) code based on high-resolution shock-capturing methods in Cartesian coordinates. This code is parallelized with a hybrid scheme with parallel domain decomposition (message passage interface, MPI) and parallel threads (OpenMP, OMP). An extensive review of the code and the implemented numerical methods was presented on Chapter 2 of the thesis.

We employed a second-order Godunov-type scheme with the HLLD Riemann solver [Mignone, Ugliano, and Bodo 2009] and the piecewise linear method reconstruction with VanLeer slope limiter [Leer 1974] to preserve monotonicity. The limiter is degraded to MinMod [Roe 1986a] when strong shocks are detected in order to avoid spurious numerical oscillations [Mignone and Bodo 2006]. HLLD is also degraded to the simpler and more diffusive HLL solver around shocks. The advance in time was performed using a third-order total variation diminishing preserving Runge-Kutta [Shu and Osher 1989] with CFL = 0.2. A relativistic correction algorithm was used to correct the conserved variables after each time iteration [Martí 2015a]. The magnetic field divergence-free constraint is preserved with the constrained transport method [Ryu et al. 1998] with electromotive force interpolation [Gardiner and Stone 2005]. We include an additional equation that describes the advection of a tracer function to track each cell composition, where  $f = 0$  represents the ambient medium and  $f = 1$ , the jet plasma. Plasma is modeled with a general equation of state (EoS) based on analytical expressions that closely reproduce the Sygne EoS for a multi-component relativistic gas [Perucho and Martí 2007, Choi and Wiita 2010].

Thermal cooling terms are also included following canonical approximations [Myasnikov, Zhekov, and Belov 1998, see also Appendix A].

## 6.2.2 Physical scenario and numerical setup

We study the scenario of a precessing mildly-relativistic jet that aims to reproduce the sub-parsec dynamics of the microquasar SS 433 outflows, which corresponds to the first cycles of the jet corkscrew kinematic trace in Fig. 6.2. The initial parameters of the ambient medium intend to reproduce the remnant of a SNR, with  $\rho_a = 0.5 \text{ m}_p/\text{cm}^3$  (with  $n_{e^-} = n_{p^+}$ ),  $p_a = 2 \times 10^{-10} \text{ erg cm}^{-3}$ ,  $T_a = 1.45 \times 10^6 \text{ K}$  [see e.g., Safi-Harb and Ögelman 1997, Thornton et al. 1998, Bowler and Keppens 2018].

We performed the simulations in a numerical grid box with total physical dimensions  $(0.2 \text{ pc})^3$ , which corresponds to  $(280 R_j)^3$  in units of the jet radius at injection (see below). The grid follows a stretched pattern in the three spatial directions: while the innermost  $(100 R_j)^3$  (i.e.,  $(0.07 \text{ pc})^3$ , in physical units) box has an uniform resolution of 10 cells/ $R_j$ , the cell size increases proportionally from the centre to the grid boundaries. The stretch factors are set to  $r_x = r_z = 1.019$ ,  $r_y = 1.017$  (i.e., we keep a resolution degradation  $< 2\%$  between two adjacent cells), such that the total number of computational zones is  $1300 \times 1200 \times 1300$ . This pattern allows us to maximize the grid resolution within the region of interest (i.e., during the first two precession cycles), confining the jet within the box during the whole evolution while keeping computational resources under acceptable limits. All grid boundaries are set to outflow, while injection is placed within an internal boundary. This internal boundary is set as a semi-sphere with  $R_s = 0.008 \text{ pc}$ , similar to Monceau-Baroux et al. 2014. Inside the sphere, a cylinder (i.e., the injector) with radius  $R_c \approx 0.0008 \text{ pc}$  precesses with period  $P = 162 \text{ days}$  and precession angle  $\theta = 20^\circ$  between the Y-axis and the cylinder axis. This radius corresponds to a jet opening angle of  $\sim 6^\circ$ . The angle is probably wider than expected for SS 433 jets [see e.g. Marshall et al. 2013], but this value should also average the jet nodding motions, that we neglect in the setup. Moreover, the cylinder is smoothed with an hyperbolic shear layer to avoid steep gradients at injection, which eventually yields an effective injection radius  $R_j \approx 0.0007 \text{ pc}$  ( $\alpha \approx 5^\circ$ ). Outside the injector, the semi-sphere is restarted to the initial values after each time iteration.

In the system of units of the code, the light speed ( $c$ ), the initial density of the ambient medium ( $\rho_a$ ), and the jet radius ( $R_j$ ) are set to unity. A factor of  $1/\sqrt{4\pi}$  is absorbed in the definition of the magnetic field.

### 6.2.3 Simulations

We run three different simulations, hereinafter RUN I, RUN II and RUN III, where RUN II and RUN III are two independent simulations that both restart from the output of RUN I. In such a way, the fundamental objective of RUN I is to create a shocked medium to propagate the ejecta in RUN II and RUN III simulations, which represent the main scientific target of the work.

**RUN I** RUN I comprises three full precession cycles with continuous injection ( $t \sim 480$  days). The magnetic field is purely toroidal with respect to the cylinder,  $B_\phi = 2B_j^\phi(r/R_{B\phi})/(1 + (r/R_{B\phi})^2)$ , where  $B_j^\phi$  is the maximum value of the magnetic field and  $R_{B\phi}$  is the magnetisation radius normalised to the jet radius, that we fixed as  $R_{B\phi} = 0.37$ . The magnetic field is initialised in the grid with a potential vector, and we used the finite difference approximation of the solenoidal equation to preserve zero divergence up to machine accuracy. Imposing transversal pressure equilibrium between the magnetic and the gas pressure [Martí and Müller 2015], the maximum toroidal field,  $B_j^\phi$ , is given by  $\beta = \bar{p}_m/\bar{p}_g = 1$ , which yields  $B_j^\phi \approx 90 \mu G$ . By definition, the average magnetic pressure,  $\bar{p}_m$ , and the average gas pressure,  $\bar{p}_g$ , follow:

$$\bar{p}_{m,g} := \int_0^1 p(r)rdr / \int_0^1 rdr. \quad (6.1)$$

The kinetic power of the jet is given by:

$$L_k = 2\pi \int_0^R \rho_j W(h(r)W - c^2)V_j r dr = 10^{39} \text{ erg/s}, \quad (6.2)$$

where the velocity field is parallel to the injector axis, with  $|V_j| = 0.26 c$ . From Eq. 6.2, the injector density is  $\rho_j = 312 \rho_a$  ( $T_j = 4.6 \cdot 10^3$  K). With this initial conditions, the jet is largely dominated by the kinetic energy flux ( $L_k$ ).

**RUN II** RUN II is the main simulation of the project. We performed three new precession cycles ( $t \sim 960$  days), restarted after RUN I. As previously mentioned, this strategy allows us to study the jet dynamics under the influence of previous ejections, since the observed sub-parsec dynamics should be barely affected by the interaction of the terminal region with the SNR. The main difference with respect to the previous RUN is that jet injection is switched from continuous to pulsated mode, in order to simulate a jet composed by discrete plasmons (we use the terminology plasmon, bullet or blob indistinctly throughout the chapter). The physical conditions within each bullet are the same as in RUN I for the injection cylinder. To perform blob injection, we modified the internal

boundary including a thin spherical layer,  $R_s < R < R_L$  ( $R_L$  is the radius of the new injection layer) where blobs are placed as discrete structures in a particular time step. Blobs are injected with a frequency  $\sim 1$  blob/4 days ( $\sim 40$  blobs/cycle), such that blobs emitted at almost the same precession phase can interact within the homogeneous box. The velocity of each blob is randomly chosen with a scatter of  $\sim 15\%$  around the canonical SS 433 jet velocity (i.e.,  $|V_j| = 0.26 \pm 0.04 c$ ) and their width ( $w_B$ ) is adapted to the velocity of the previous ejection in the cycle ( $0.7 R_j < w_B < 1.1 R_j$ ), so the initial separation between blobs is kept roughly constant,  $\Delta R \sim 0.4 R_j$ . When a new blob is injected, the spherical layer is also restarted to the initial conditions of the whole internal boundary. For numerical consistency, following RUN I the semi-sphere ( $R < R_S$ ) is also restarted to the initial parameters after each time iteration.

**RUN III** RUN III is a test simulation which is independent of RUN II. The main objective of this setup is to address the existence of URFs in SS 433 by studying their interaction with the jet plasmons. We divided this RUN in two time frames: RUN III-A and RUN III-B. RUN III-A is very similar to RUN II, but all blobs are injected for simplicity with the same axial velocity,  $|V_j| = 0.26 c$ . After almost three full precession cycles, in RUN III-B we interrupted the discrete injection and we continuously inject an outflow that aims to reproduce the physical conditions of an URF. We defined this outflows with a total power similar to the one in the jet/blobs ( $\sim 8 \times 10^{38}$  erg/s), but in equipartition between the kinetic and internal energy fluxes. In this case, we increased the velocity in a factor  $\times 3$  ( $|V_j| = 0.75 c$ ), density is much lower ( $\rho \sim 2\rho_a$ , with only leptons) and plasma is highly over-pressed with respect to the initial external medium ( $p = 2 \times 10^{-4}$  erg/cm<sup>3</sup>). For the sake of simplicity, we neglect the magnetization of the underlying flow. This outflow is injected during  $20 R_j/c$  (in time units of the code,  $\sim 10\%$  of precession cycle), so due to its wide opening angle it may interact with different blobs launched in the last ejection period. The results of this RUN are not satisfactory and are only presented in the chapter to introduce future improvements in the SS 433 simulations.

## 6.2.4 Projections and trace finder algorithm

**Projections.** Aiming to mock the observations of the source, we have computed the two-dimensional projections of the simulated jet along the line of sight, at an angle of  $\phi = 78^\circ$  with respect to the direction of the angular velocity of precession ( $\hat{\phi} \parallel \hat{u}_y$ ). That is to say, the images shown below correspond to an integration along the direction of the unit vector  $\hat{l} = \cos \phi \hat{u}_y + \sin \phi \hat{u}_z$ , where

we have arbitrarily chosen the north vector to be  $\hat{u}_N = \hat{u}_x$ , so that the jet propagates essentially along the west-east direction. Vector quantities, such as the velocity or magnetic field, are correspondingly rotated to match the projection reference frame, so that the east component of the vector quantity  $\vec{V}$  is  $V_E = V_y \cos \phi - V_z \sin \phi$ . To highlight the jet structure in the projections, all integrations are weighted by the function:

$$w(\vec{x}) = \begin{cases} f(\vec{x}), & \text{if } f(\vec{x}) > f^{\text{thr}} \equiv 0.65 \\ \varepsilon \equiv 10^{-6}, & \text{otherwise} \end{cases}. \quad (6.3)$$

where  $f$  is the tracer function and the parameter  $\text{thr}$ , albeit arbitrary, has been empirically tuned to visually highlight the kinematic trace, while  $\varepsilon$  is set to a negligible but non-zero value to prevent indeterminate forms arising along the integration rays which do not cross any jet material.

**Trace detection.** Here we describe the heuristics applied in order to characterise the trace of the jet and its tangent direction, which we use to compute the angle  $\theta_{\text{trace}}$ . Starting from the projected image of the tracer field, we downgraded the resolution to  $200 \times 200$  cells to suppress high-frequency noise. Since the trace does not present any apparent retrograde feature, it is possible to obtain the trace as a function  $y_{\text{im}} = y_{\text{trace}}(x_{\text{im}})$ , where  $x_{\text{im}}$  and  $y_{\text{im}}$  are, respectively, the horizontal [east, E] and vertical [north, N] directions in the image. Then, for each  $x_i$ , we compute  $y_{\text{trace}}(x_i)$  as a weighted mean over the corresponding column:

$$y_{\text{trace}}(x_i) = \frac{\sum_j y_j w_{ij}}{\sum_j w_{ij}}, \quad \text{where } w_{ij} = (f_{ij} - f^{\text{thr}})^\alpha. \quad (6.4)$$

Thus, the weight is essentially the (threshold-subtracted) projected value of the tracer, where the exponent  $\alpha > 1$  is introduced to prevent the integral to be dominated by extended diffuse regions. The resulting set of points  $\{(x_i, y_i)\}$  is smoothed with a cubic filter [Savitzky and Golay 1964] with a window length of 5 dots to damp small-scale noise. The angle of the trace with the south direction is finally computed as  $\theta_{\text{trace}} = \arctan(\dot{x}/\dot{y})$ , where the dot represents second-order centred finite differences. Likewise, the angle of the velocity and the magnetic fields with respect to the south direction are computed as  $\theta_{\text{vel}} = \arctan(v_E/v_N)$  and  $\theta_B = \arctan(B_E/B_N)$ .

In the case of RUN II, the discontinuous morphology of the trace limits the robustness of the identification procedure described above. For the sake of

comparison with the continuous simulation, in this case we use the same trace extracted for RUN I, which is properly re-scaled and displaced to visually match the trace in RUN II. Then, for each  $x_i$  we refine  $y_{\text{trace}}(x_i)$  by iteratively repeating the weighted average of Eq. 6.4 in a shrinking interval, starting with 20 image pixels and halving each iteration.

## 6.3 Results and preliminary discussion

### 6.3.1 RUN I: Continuous injection

In order to simulate an effective continuous injection, each time iteration the cylindrical injector inserts a plasma component (with  $R = R_0$ ) into the grid, following the expected precession path of the axis ( $P=162$  d,  $\theta = 20^\circ$ ). These quasi-discrete components, which are highly supersonic, create a shock on the ambient medium. As the injector precesses within the internal boundary, adjacent plasma components, together with the shocks they have triggered, converge to create a continuous stream surrounded by an homogeneous shocked cavity. Behind the jet stream, there is an under-pressured and under-dense region –emptied by the outflowing twisted jet– which is re-filled by the shocked plasma as the jet propagates away from the internal boundary surface.

After almost 1 precession cycle, the bow-shock of the first injection – which has already expanded and increased its size – collides with the bow-shock triggered by the new material, producing a strong transverse shock and a pinch in the jet helix, that breaks locally the homogeneity of the continuous stream. Figure 6.5 shows 3 time frames in RUN I simulation ( $t = 200, 380, 560 R_j/c$ , i.e. 1 frame per precession period) of a 3D render of density, that we limited from  $\rho_{\min} = \rho_0$  to  $\rho_{\max} = 10\rho_0$  to highlight the complex structure of these shocks within the jet cavity.

A 3D render of the tracer function  $f$  after almost 3 full precession cycles ( $t \sim 468$  days) is shown in the top panel of Fig. 6.6, where the jet has propagated up to  $y \sim 0.085$  pc from the core, meaning that the jet head is already on the extended stretched grid ( $y > 0.07$  pc). In this image, the 3D render has been mirrored to show at the same time two different perspectives of the helical jet. This representation shows that the jet helix is disrupted in the top part of the figure as a consequence of the first bow-shock collision, as already mentioned. After  $\sim 2$  precession periods, the working surface of the jet shows instabilities that lead to jet deceleration and mixing with the ambient medium, leaving behind a wake of mixed plasma that is swept afterwards by a younger stream.

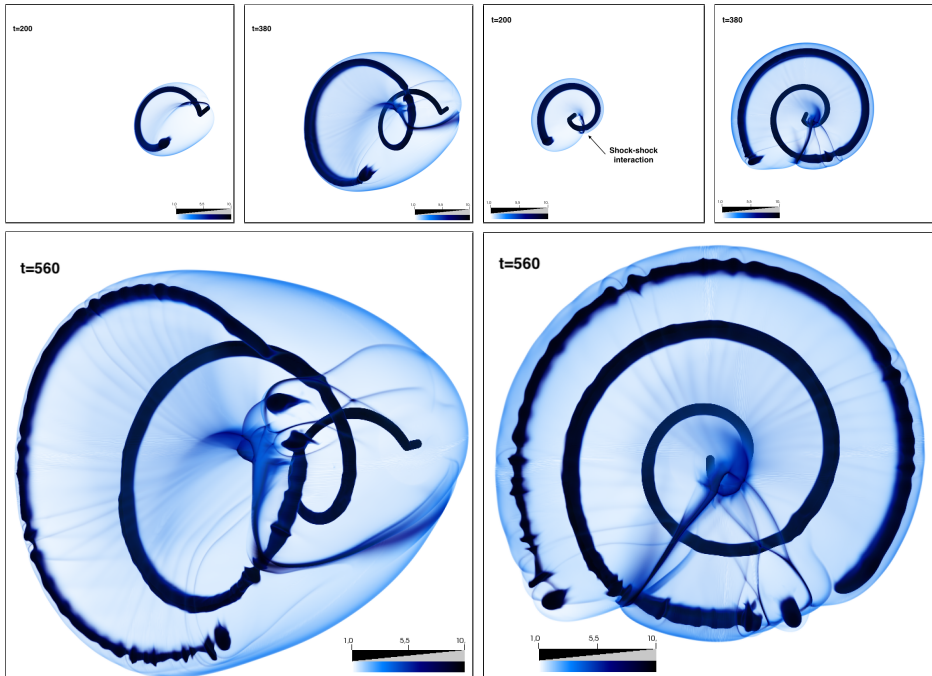
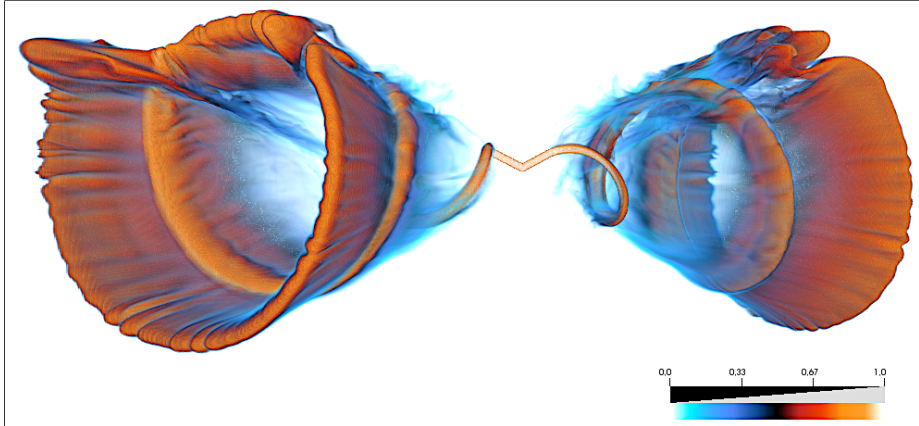


Figure 6.5 3D render of density for the continuous jet simulation (RUN 1) at three time frames ( $t = 200, 380, 560$  Rj/c) and two different perspectives: lateral (left) and top (right). To highlight shocks and discontinuities, density is limited from  $\rho_{\min} = \rho_0$  to  $\rho_{\max} = 10\rho_0$ . The interaction of bow-shocks created at different precession cycles creates strong shocks that destabilise the jet plasma in this region, as shown during the first interaction at  $t = 200$  Rj/c.

Although the main objective of this simulation is to create a shocked cavity that serves as initial condition to inject the discrete components (which is the principal aim of the work), at this early stage in the total jet evolution ( $t \sim 468$  days) the propagation reveals one interesting dynamical feature: after approximately two precession periods, the continuous stream is prone to the development of instabilities that corrugate the jet surface and favour its deceleration at  $y > 0.07$  pc. Although this would require further analysis (and possibly, a specific simulation following the conditions in RUN 1), we propose three possible origins for these instabilities: (1) Kelvin Helmholtz instabilities (KHI; as first proposed by Heavens, Ballard, and Kirk 1990), since the jet ballistic velocity has a tangential component with respect to the outflow/ambient contact discontinuity, while the shocked plasma in front of it is at rest; (2) centrifugal instabilities [Gourgouliatos and Komissarov 2018b, Gourgouliatos and Komissarov 2018a], since this tangential component rotates along the jet surface, and (3) corrugation instabilities [Stone and Edelman 1995, see also D’Yakov-Kontorovich instabilities

### Continuous injection



### Blob-blob interactions

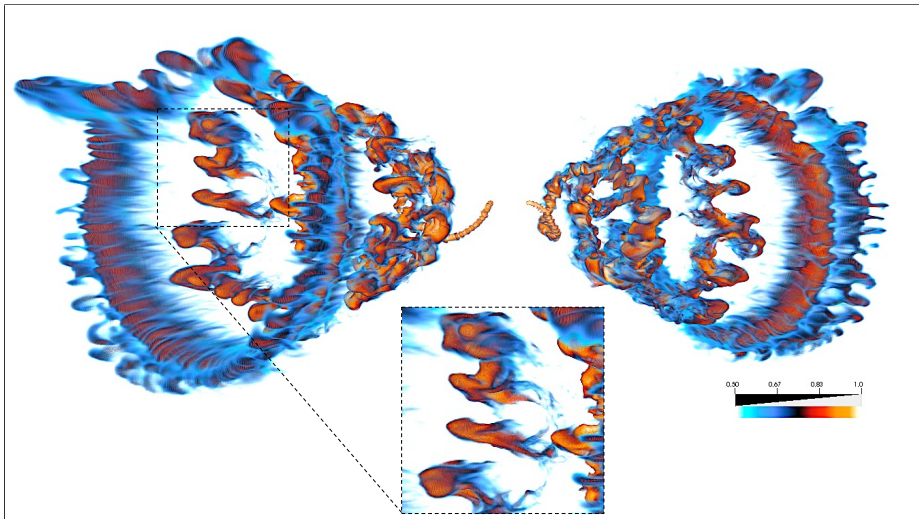


Figure 6.6 3D render of jet tracer  $f$  for continuous (RUN I, top) and discrete (RUN II, bottom) SS 433 jet simulations. The simulated jet has been mirrored for visualization purposes to show two different perspectives at the same time. The inset plot displays a zoom of a region of RUN II, showing that blobs interact in a coalescence process to form larger elongated structures.

Huete and Vera 2019, and references therein], which respond to perturbations to the shape and velocity of the shock front. For example, Heavens, Ballard, and Kirk 1990 predicted that KHI may arise at  $y > 0.035$  pc, but due to the large density ratio between the jet and its surroundings in our simulation, the instability growth rate could be smaller than this prediction [see e.g. Begelman, Blandford, and Rees 1984], which is indeed more compatible with the results in RUN I. A similar corrugation leading to jet disruption is observed in hydrodynamical simulations [Monceau-Baroux et al. 2014], so the magnetic field does not seem to play a role in the observed behaviour. We emphasise, however, that a proper description of the continuous injection would possibly require a larger number of precession periods [as performed by Monceau-Baroux et al. 2014, Monceau-Baroux et al. 2015], since a certain degree of stationarity should be required in the uniform grid.

### 6.3.2 RUN II: Discrete injection and blob-blob interactions

The bottom panel of Fig. 6.6 shows a 3D render of the tracer function  $f$  at  $t \sim 960$  days. A different visualisation, but showing a top (left) and front (top) view of the render, is displayed on Fig. 6.7, for the sake of completeness. Due to the intrinsic velocity scattering (following Eikenberry et al. 2001, Blundell and Bowler 2004), blobs interact within the uniform grid, as faster ejections catch up slower components injected at almost the same precession phase. These interactions create larger elongated coalescences (see inset plot in Fig. 6.6), which then propagate freely as no further collisions take place with other blobs. However, despite these collisions, the overall jet morphology and the twisted precession trace is well preserved, similar to the continuous jet in RUN I. In the stretched grid (i.e.  $> 0.07$  pc), we can follow the evolution of the continuous stream injected during RUN I, which at this time appear highly corrugated and shows that these cycles have merged in a ring-like structure. The jet material in front of the ring has been propelled when the second cycle collided with the first. However, we remind the reader that any interpretation about the jet dynamics within the stretched grid should be treated carefully, since in this region the dynamics is largely affected by numerical diffusion. Be that as it may, the formation of this terminal ring is interesting and should be analysed in the future, since ring-like features have been found observationally in the hypothetical interaction of the jet with the W50 SNR [see e.g., Safi-Harb et al. 2022].

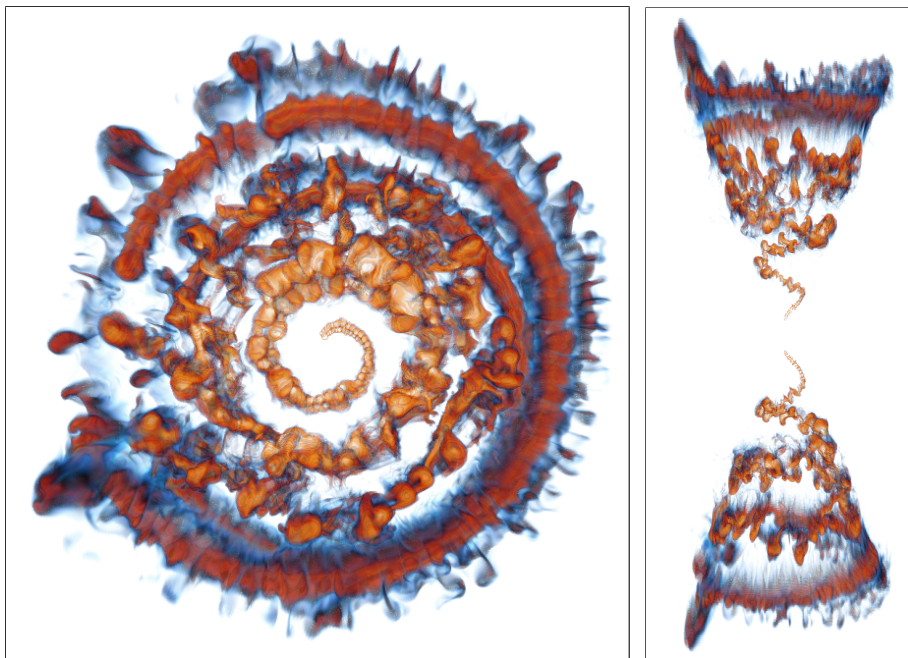


Figure 6.7 3D render of the tracer function of RUN II simulation showing a top (left) and front (right) view.

In Fig. 6.8, we show a 3D render of the magnetic field squared modulus (left), jet tracer (right, top) and jet velocity modulus (right, bottom). For visualisation purposes,  $|B|^2$  is limited to the range  $(10^{-13} - 10^{-8})$ , jet tracer to  $(0.25 - 1)$  and jet velocity to  $(0.1 - 0.25)$ , all in the code system of units. In the blobs, the field strength resembles the ring-like structure of the toroidal field at injection, which decreases as blobs merge and increase its size, and is only enhanced in the interaction spots, when field lines may be locally compressed. The collision of blobs can also lead to elongated structures outside the jet trace, as shown in the inset plot of left panel, which also require more analysis. The tracer function (right panel, top) shows that for  $f > 0.5$  the jet has an overall continuous morphology, as blob coalescence and mixing leads to an inhomogeneous plasma tube, where the jet material is concentrated on ballistic components. These bullets, however, preserve the injection velocity during the whole uniform grid, since as shown in the right bottom panel, the bulk velocity of these blobs is  $V \geq 0.25 c$  at  $y \sim 0.07 pc$ .

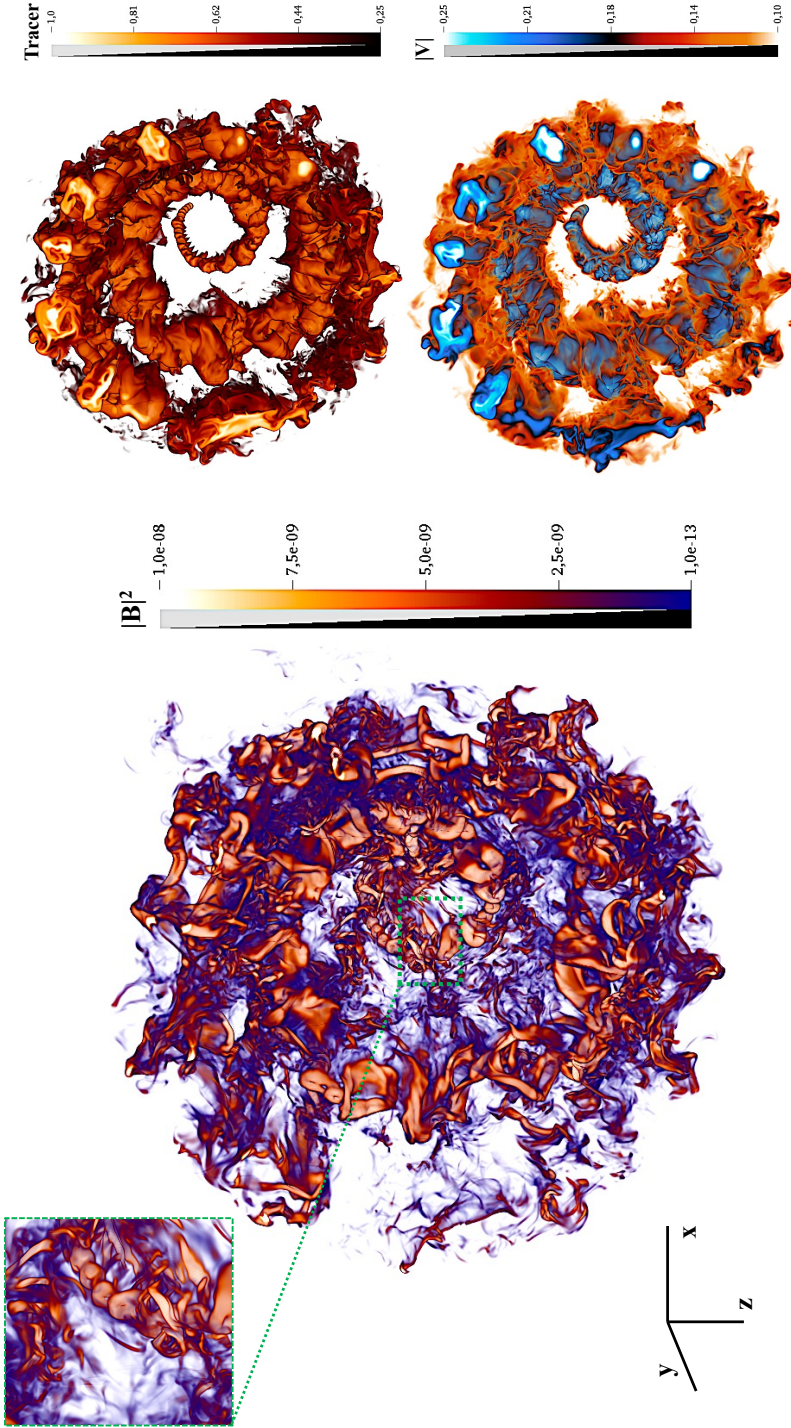


Figure 6.8 3D render of the magnetic field squared modulus (left), jet tracer (right, top) and jet velocity modulus (right, bottom) for RUN II simulation. The inset plot in the left panel shows a region in which magnetic field threads fill the cavity. For visualisation purposes,  $|B|^2$  is limited to  $[10^{-13} - 10^{-8}]$ , jet tracer to  $[0.25 - 1]$  and jet velocity to  $[0.1 - 0.25]$ . The jet propagates along the positive Y-axis.

The results of this RUN show two important dynamical effects. On the one hand, blob collisions do not result in losing the precession path, as this would be a critical point to disregard the model. These interactions produce larger elongated coalescences that then propagate without further collisions. On the other hand, the velocity of these blobs seem to be rather stable along the uniform grid (i.e.  $y < 0.07$  pc), which lose  $\sim 1\%$  of the injected velocity in the 2 first precession periods (see Fig. 6.8). This is also important for accepting the simulated morphology, since no relevant signs of deceleration are deduced from the radio imaging of the arcsec jets [Spencer 1984, Miller-Jones et al. 2008, but see also Stirling et al. 2004, where the authors considered a deceleration term of  $\sim 0.02$  c per period to reproduce accurately the source observations]. We expect, however, that these structures decelerate at larger distances as they collide with the material in the cavity, although we question whether the knotty features observed by Chandra at  $\sim 1.6$  pc could be connected with the simulated coalescences in the sub-parsec scale.

### 6.3.3 RUN III: Ultra Relativistic Flows

Figure 6.9 shows the result of RUN III, where after injecting a bunch of homogeneous blobs at  $V=0.26$  c during almost three full precession periods (i.e. RUN III-A), we injected a relativistic underlying flow at  $V=0.75$  c (i.e. RUN III-B). In the top panel of the figure, we display a 3D render of the simulation limited to the uniform grid, where we show the homogeneous non-interacting blobs and the URF, which fills the left part of the cavity. All these blobs have the same structure, with a ballistic head followed by a tail of material, as shear effects act in this case in all directions. In the bottom panel, we see that the magnetic field preserves the injected toroidal structure in the head of the blob, while it aligns with the propagation direction along the plasma tail. As we can also deduce from the figure, the relativistic flow is highly disrupted, has lost its coherence, and has not interacted with the blobs emitted in the previous period (located in the figure at  $\sim 0.07$  pc).

The existence of URFs in SS 433 was suggested by Migliari et al. 2005 based on the rapid variability observed by Chandra, where a knot in the east extended jet got brighter after another in a short time scale. The interpretation of this brightening as an URF that moves at  $> 0.5$  c is not unreasonable, since these type of outflows (even with higher velocities) have been proposed to exist in other X-ray binary systems (see Sec. 1.2.3). However, later observations of the source could not confirm their existence in the case of SS 433 [Miller-Jones

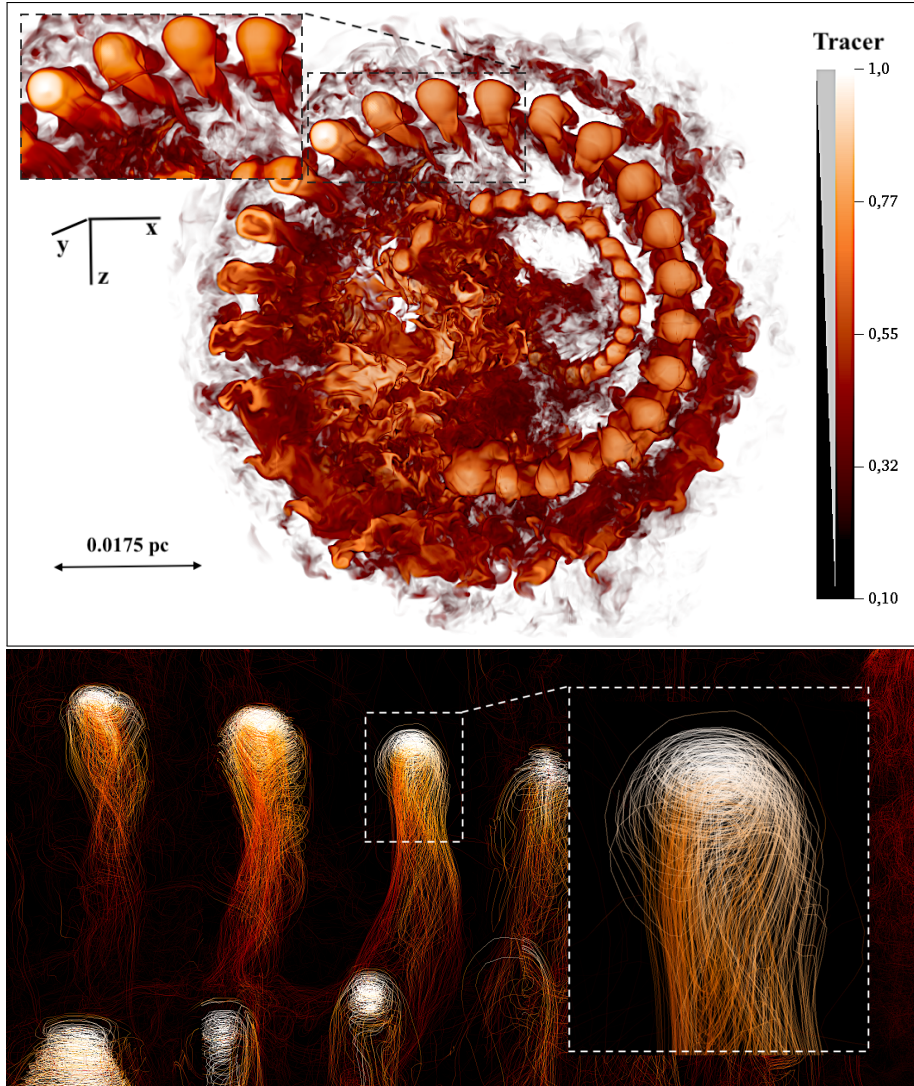


Figure 6.9 Top: 3D render of the tracer function of RUN III simulation, showing the underlying relativistic flow propagating through the cavity. The jet propagates along the positive Y-axis. Bottom: Integrated magnetic field lines in the homogeneous blobs. The toroidal field is preserved in the head of the blob, while shear creates an elongated tail behind it, where the field is aligned with the propagation direction.

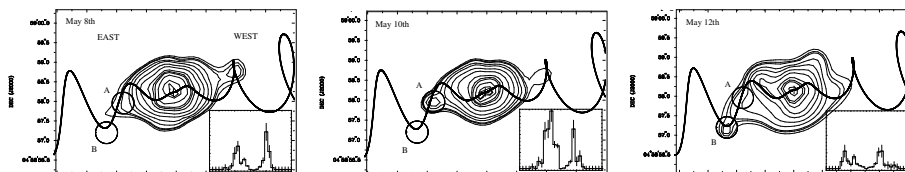


Figure 6.10 Three  $\sim 20$  ks zeroth order HETGS images of SS 433, taken every 2 days on 2001, May 8th (left), May 10th (middle), May 12th (right). Images are rebinned to one sixteenth of the original pixel size and smoothed. Contour levels are 2.7, 3, 3.2, 4, 5, 7, 10, 15, 18, 20, 25, 34, 37 counts per rebinned pixel for the May 12th observation and normalised to this for small changes in exposure times (less than 6%) in the other 2 observations. The twisted precession trace as predicted from Stirling et al. 2002 is superimposed to the images. The lower-right panels show the histograms of the three observations. These contour images indicate a brightening of the east jet and a rapid fading in the west jet. Reproduced with permission from Migliari et al. 2005 (Fig. 5).

et al. 2008], although Very Long Baseline Interferometry (VLBI) monitoring by Mioduszewski et al. 2004 shows hints for some knot re-energisation at smaller scales.

Our RUN III simulation does not reproduce the model dynamics, since as shown before, the outflow disrupts before colliding with the target blobs. This could be related with the properties of the URF, which is initially over-pressured with respect to the shocked cavity, leading to a rapid expansion and eventual lost of coherence. Moreover, since the fluid is also hotter, the growth of instabilities –of the same kind as before, due to the injection mechanism– could be also faster than in the continuous jet of RUN I.

### 6.3.4 Jet magnetic fields

In Sec. 6.3.2, I showed how the field strength is distributed in RUN II simulation, but no information about the field orientation was provided. Thus, Fig. 6.11 and Fig. 6.12 show the integrated field lines in RUN I and RUN II simulations, respectively. In these figures, the colour scale is coded according to the jet tracer function, although in the inset panels colours are inverted with respect to the main legend to highlight the jet trace.

In RUN I, the toroidal field is advected with each quasi-discrete component, thus following the path of the continuous stream (Fig. 6.11, inset b). Only when the tube is disrupted –as in the top part of the helix (Fig. 6.11, inset a)–, field lines display a poloidal component along the jet trace. Shear can act in the perpendicular direction to the trace, where very ordered poloidal field lines fill the whole cavity like a *magnetic curtain*. In RUN II, however, the interaction of blobs breaks the homogeneity of the toroidal field along the jet locus, which

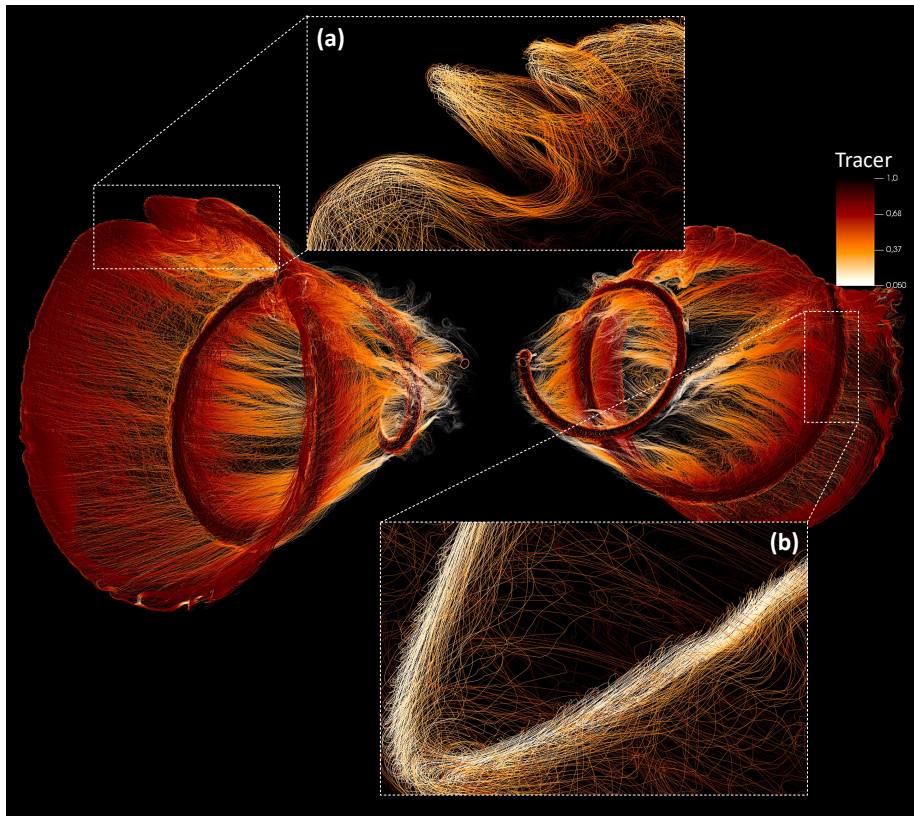


Figure 6.11 Integrated magnetic field lines for RUN I simulation, where the colour map represents the tracer function. Inset plots show that field lines align with the propagation direction when the flow is disrupted (a), while they follow the helix path if the jet is continuous (b). Colour map is inverted in the inset plots to highlight the jet trace. The cavity between two precession cycles is filled with a magnetic curtain of poloidal lines, which are formed by shear acting in the perpendicular direction to the jet path.

eventually tend to align with the velocity direction in the shocked blobs (see inset a and b in Fig. 6.12). Thus, we suggest that the field structure in the homogeneous blobs of Fig. 6.8 is an intermediate state, since shear can act in all directions, but the injected toroidal field is preserved in the core of the blob, as these propagate freely with no lateral collisions.

In order to quantify this effect, we followed the methodology described in Sec. 6.2.4 to integrate the velocity and magnetic field vectors along the line of sight, where the jet kinematic locus is derived from the projection of the tracer function. Figure 6.13 shows the jet projection in the uniform grid for RUN I (top) and RUN II (bottom) simulations, where red circles represent the extracted kinematic trace. The angle that this trace and the projected fields form with

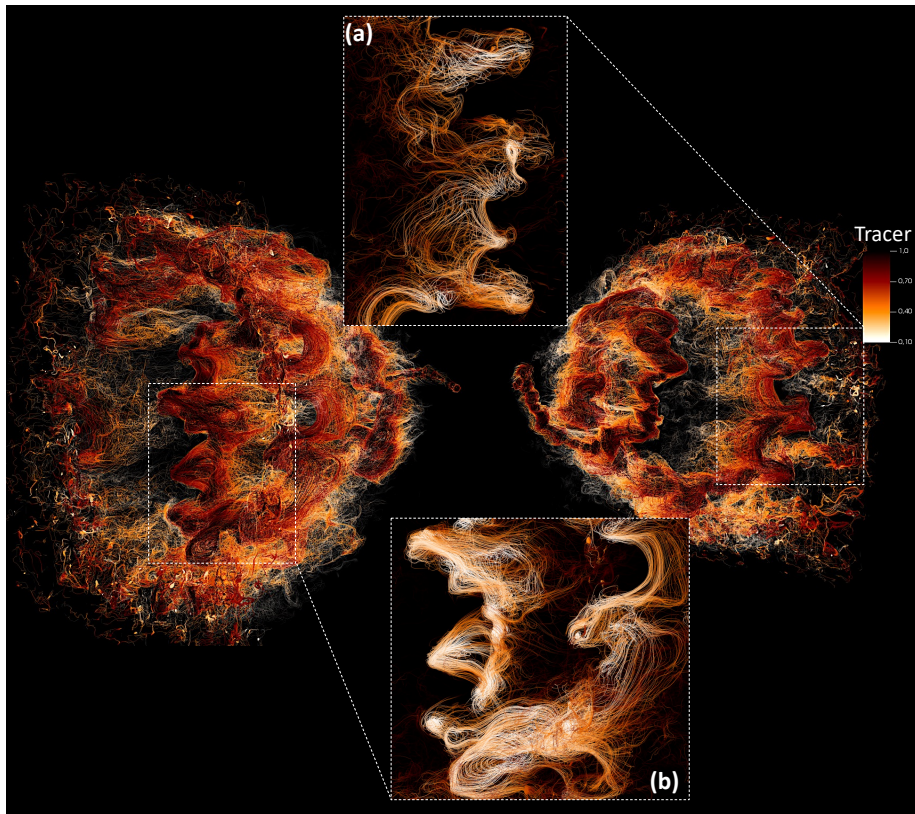


Figure 6.12 Integrated magnetic field lines for RUN II simulation, where the colour map represents the tracer function. Inset plots show the magnetic field in the blobs, where colour map is inverted to highlight the magnetic field in the jet plasma. Inset plots (a,b) show two regions where the interaction of discrete components breaks the homogeneity of the toroidal magnetic field.

the y-axis of the plane of the sky is shown in Fig. 6.14, where all curves have been smoothed with a gaussian filter. These curves are compared with the polarisation data of Miller-Jones et al. 2008, represented with black squares on each panel. Although in the case of continuous injection the magnetic field angle follows the trace curve (as already inferred from Fig. 6.11), the amplitude of the oscillation is lower. We propose that these could be related with the intrinsic toroidal configuration of the field in the simulations, which could lead to a certain degree of vector cancellation when integrating along the line of sight.

To quantify statistically the alignment of the magnetic field with respect to the jet locus or the local velocity vector, we determined the Pearson product-moment correlation coefficients between those quantities. This yields  $C_f^B \sim 0.81$ ,

$C_V^B \sim 0.07$  in RUN I, and  $C_f^B \sim 0.15$ ,  $C_V^B \sim 0.67$  in RUN II, where  $C_f^B$  is the correlation coefficient between the trace and the magnetic field and  $C_V^B$  is the correlation coefficient between the velocity and the magnetic field. This result suggests that in case of continuous injection the magnetic field is aligned with the projected kinematic trace, while in the case of colliding bullets, the magnetic field tends to follow the local velocity direction (specially after 1 precession period), in promising agreement with the results by Miller-Jones et al. 2008.

## 6.4 Conclusions

In this chapter of the thesis, I present the preliminary results of a project performed within the Spanish Supercomputing Network (*Red Espanola de Supercomputacion*), where we have developed large-scale simulations of the precessing jets in the microquasar SS 433, including for the first time the dynamical evolution of magnetic fields and the apparent knotty jet morphology observed with VLBI. Our simulations were performed in a stretched grid that extends up to  $(0.2 \text{ pc})^3$ , where the inner  $(0.07 \text{ pc})^3$  are covered with uniform cells with high resolution (i.e. 10 cells/ $R_j$ ). In this work, we followed a strategy based on performing two running simulations (plus a third one), where the aim of the former is to establish a shocked cavity in the uniform part of the grid that is later used to initialise the main simulation.

After our preliminary analysis, we found two relevant arguments that support the existence of discrete components in the arcsec precessing jets, as previously suggested by Miller-Jones et al. 2008: first, if blobs have a velocity scatter –that seems reasonable according to past observations of the source– their interaction lead to compact elongated structures which are less prone to the development of instabilities than the continuous stream. These larger blobs, which do not suffer significant deceleration in the simulated scales, can propagate more easily to larger distances. Secondly, by post-processing algorithms, we showed that the existence of colliding knots produce a component of the magnetic field which is aligned with the local velocity vector, in contrast to the continuous stream where the initial toroidal field follows the jet kinematic trace. Moreover, we also tried to address the existence of URFs in the system, but the parameter space of this simulation was not appropriate to reproduce the expected observational results. In Chapter 7, I will briefly describe the roadmap we will follow in the future to improve and extend the simulations presented in this chapter to assess the complex multi-scale dynamics of the outflows in SS 433.

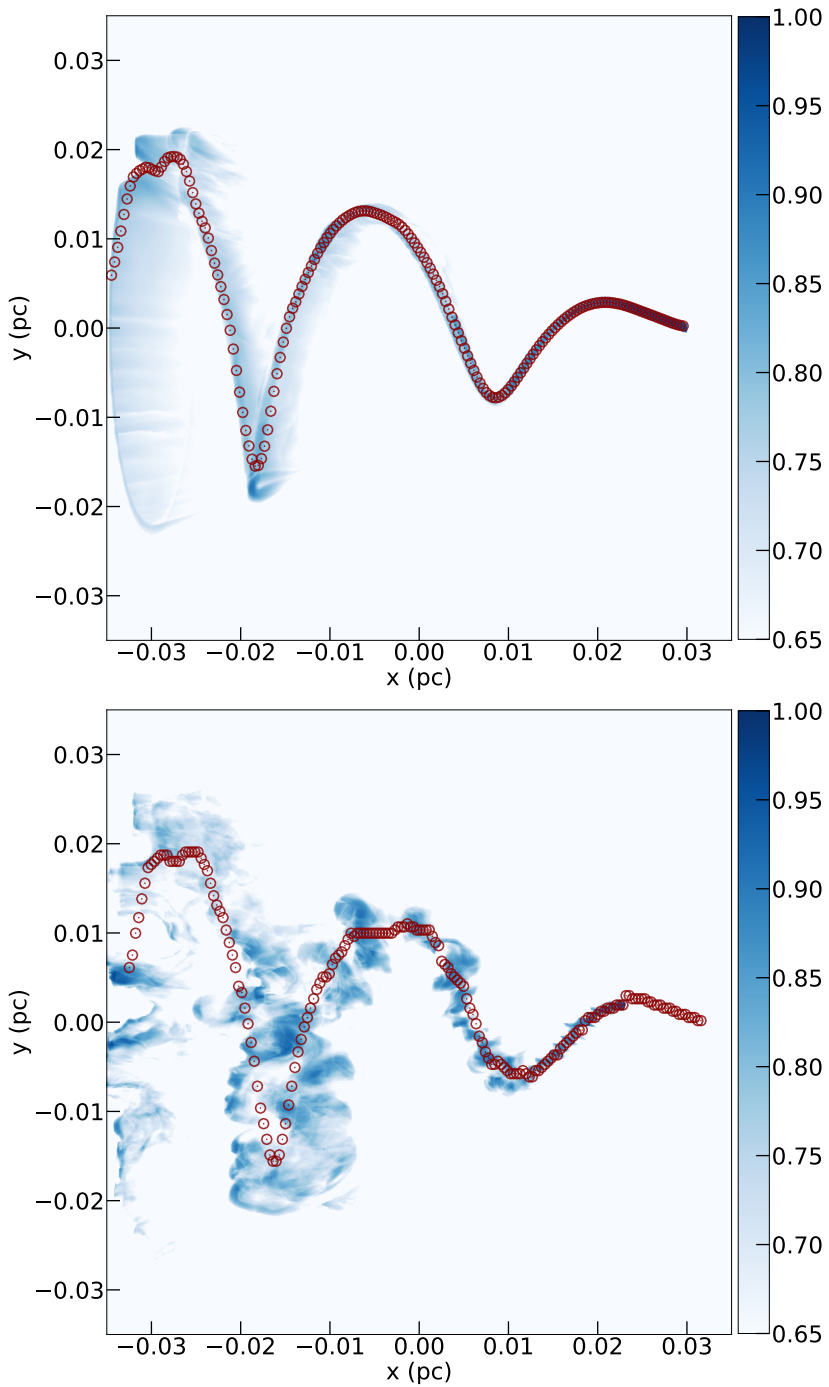


Figure 6.13 Tracer function integrated along the line of sight for RUN I (top) and RUN II (bottom) simulations. Red points represent the location of the extracted kinematic locus.

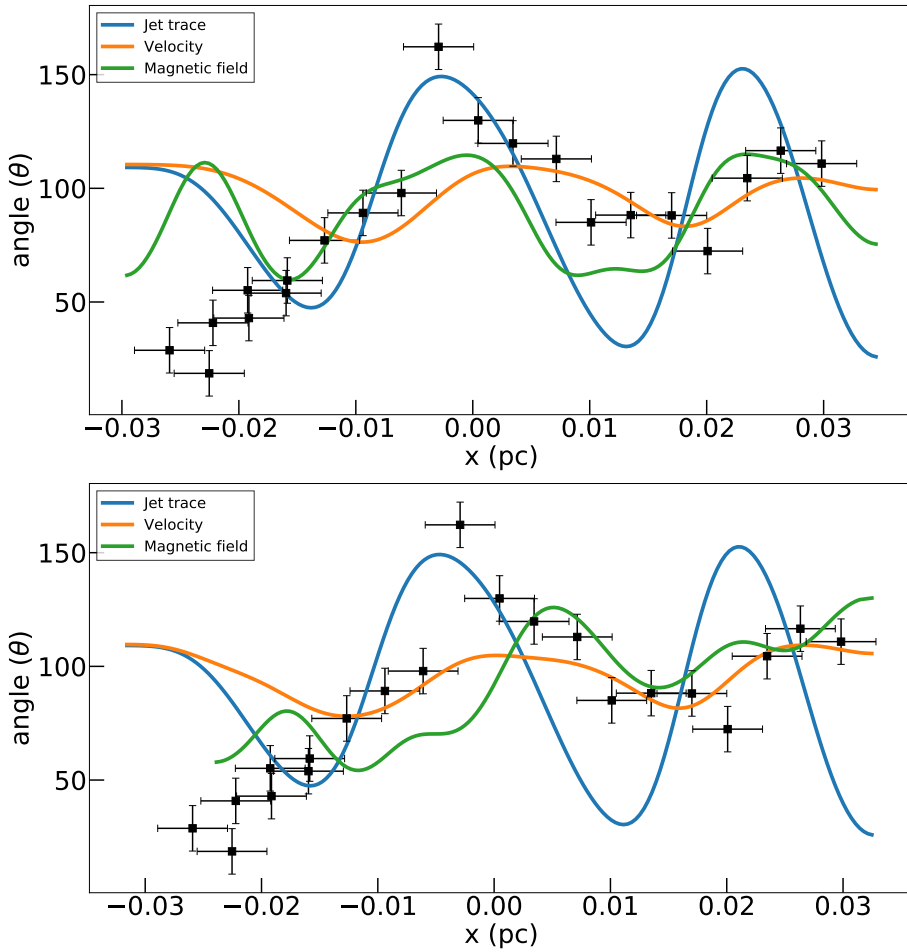


Figure 6.14 Angle of the extracted kinematic locus (blue), jet velocity (orange) and magnetic field (blue) with respect to the y-axis in the plane of the sky for RUN I (top) and RUN II (bottom). Black squares represent the polarisation data from Miller-Jones et al. 2008.

# Chapter 7

## Summary and future work

---

This chapter (Sec. 7.3) reproduces an extract of the following publication: *Numerical simulations of relativistic jets*. M. Perucho and **J. Lopez-Miralles**. *Journal of Plasma Physics*, 89(5), October 2023. DOI: 10.1017/S0022377823000892. *Reproduced with permission.*

---

On this second Part of the thesis, I have presented the first bunch of simulations we performed with our new code LÓSTREGO in the context of jet propagation in binary systems. These two chapters can be summarised as follows:

On **Chapter 5** (originally published in López-Miralles et al. 2022), I studied the interaction of jets in high-mass X-ray binaries (HMXBs) with the strong winds driven by the hot companion star in the vicinity of the compact object (CO), a fundamental process to understand the jet dynamics, non-thermal emission and long-term stability. In particular, I studied the dynamical role of weak and moderate-to-strong toroidal magnetic fields during the first hundreds of seconds of jet propagation, focusing on the magnetised flow dynamics and the mechanisms of energy conversion. Using the LÓSTREGO code, I performed the first three-dimensional (3D) relativistic magnetohydrodynamics (RMHD) numerical simulations of relativistic magnetised jets propagating through the clumpy stellar wind in a HMXB. The overall morphology and dynamics of weakly magnetised jet models is similar to previous hydrodynamical simulations, where

the jet head generates a strong shock in the ambient medium and the initial over-pressure with respect to the stellar wind drives one – or more – recollimation shocks. In the time scales of our simulations, these jets are ballistic and seem to be more stable against internal instabilities than jets with the same power in the absence of magnetic fields. However, moderate-to-strong toroidal magnetic fields favour the development of current-driven instabilities and the disruption of the jet within the binary. A detailed analysis of the energy distribution in the relativistic outflow and the ambient medium reveals that both magnetic and internal energies can contribute to the effective acceleration of the jet. These simulations also certify that the jet feedback into the ambient medium is highly dependent on the jet energy distribution at injection, where hotter, more dilute and/or more magnetised jets are more efficient, as anticipated by feedback studies in the case of jets in active galaxies.

On **Chapter 6**, I presented the results of a project that I developed within the Spanish Supercomputing Network (*Red Espanola de Supercomputación*), where we performed the most detailed large-scale 3D numerical simulations of the SS 433 precessing jets at the scale of the sub-parsec, including for the first time the dynamical evolution of the jet magnetic fields. The physical processes that govern the jet dynamics at this scale are essential, not only for understanding the observed optical, radio and X-ray emission, but also for explaining the astonishing SS 433-W50 large-scale source morphology. In this work, I explored how a precessing jet based on the physical parameters of SS 433 with an initial toroidal magnetic field configuration can develop a poloidal component –aligned with the local velocity vector in the plane of the sky– after the first precession cycle, and specifically, the role of discrete plasmon collisions into this process. I also addressed the effect of these interactions on the overall morphology, deceleration and the long-term jet stability, which are also needed for improving our understanding of particle acceleration and high-energy emission beyond the sub-parsec, in the SS 433/W50 lobes. Overall, our results suggest that the observed characteristics of the source are compatible with the existence of discrete structures, rather than with jets based on a continuous flow.

In the present chapter, I resume ongoing and future applications of the LÓSTREGO code in the context of relativistic jet simulations:

## 7.1 The binary scale

The stellar wind parameters employed on Chapter 5 are a reasonable assumption for an OB-type star. This means that the setup is appropriate to reproduce the black hole binary Cygnus X-1 (Cyg X-1), but it is less accurate when approaching, for example, Cygnus X-3 (Cyg X-3; see also Chapter 1.6). In the latter, the strong winds driven by the Wolf-Rayet (WR) star –which are denser and faster than in Cyg X-1– may have a larger impact on the jet dynamics, which can also be affected by the short orbital separation ( $2 - 3 \times 10^{11}$  cm), or even by the photon field of the star ( $L_{WR} \sim 4 - 6 \times 10^{38}$  erg/s). However, this type of simulations, which are also more demanding from the numerical point of view, have not been addressed in the literature even with hydrodynamical codes.

Thus, a first step forward in the simulations presented in Chapter 5 consists on changing the conditions of the stellar wind to reproduce the environment of a WR star. In particular, I plan to address the spectral transitions from/to the so-called hypersoft state – in which the radio and hard X-ray fluxes are found at their lowest levels (or non detected at all) – during an outburst, which contrary to other X-ray binaries (XRBs), are observed during the transitions from the soft to the hard state [Koljonen et al. 2010]. By analysing spectral and timing properties of the source multi-wavelength observations, Koljonen et al. 2018 proposed a model where systems with stronger winds should indeed develop powerful radio episodes at the transition from the soft to the the hard state. During this transition, the outflow acts against the powerful stellar wind in the system –which had time to refill the region during the hypersoft state– and evacuates a shocked cavity, while during the transition from the hard to the soft state the transient jet [see e.g. Miller-Jones et al. 2004] expand more freely within the existing cocoon and collide with the steady –possibly slower– jet in the hard state (Fig. 7.1). To test this model, I will perform a 3D RMHD simulation of a relativistic jet propagating in a stretched grid similar to the one employed in Chapter 6 (a uniform grid with high resolution plus an extended stretched grid), initially filled by the WR stellar wind (i.e. the soft to hard transition during an outburst). Once the jet head arrives to the extended mesh, we will modulate the Lorentz factor of the jet at injection to trigger internal shocks, reproducing the intermittent emission during the hard to soft state transition. A post-process step should be performed to calculate the expected radio emission in the two proposed scenarios (see e.g. Appendix A).

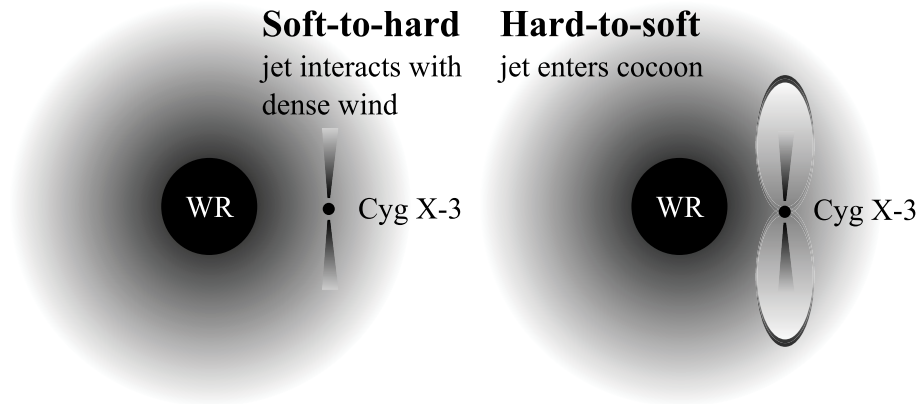


Figure 7.1 Cartoon of the jet-wind interaction for Cyg X-3. Reproduced with permission from Koljonen et al. 2018 (Fig. 13), ©ESO.

## 7.2 Beyond the binary scale

**Orbital motion and magnetic fields** As introduced in Chapter 1, Barkov and Bosch-Ramon 2022 performed long-term 3D relativistic hydrodynamics (RHD) simulations – using the `PLUTO` code – of jet propagation within a HMXB system considering the combined effect of the stellar wind and the orbital motion (with orbital parameters compatible with both an XRB as Cyg X-1 or Cyg X-3). In that study, they found that the moderate bending produced by the lateral impact of the wind, together with the orbital effect, leads to relativistic jet precession and flow disruption in scales  $\sim 1$  AU (even for jets with power  $\sim 10^{37}$  erg/s). Therefore, a next step forward in this analysis consists on including the dynamical evolution of magnetic fields in this kind of simulations using the `LÓSTREGO` code. Although we do not expect that the magnetic field is dynamically relevant at these scales, in Chapter 5 we showed that even weak magnetic fields can affect the development of instabilities [see also Massaglia et al. 2022, for the case of extragalactic jets], and furthermore, the field configuration beyond the interaction region can be relevant to understand the jet emission at these scales. This setup, however, should be treated carefully, since changing the injection point at the boundary could lead to non-physical solutions of the fields (i.e. non-zero divergence) in the first cells of the grid. These simulations will be performed in collaboration with Prof. Valentí Bosch-Ramon (University of Barcelona).

**Jet inflated bubbles** One application of the hydrogen ionisation module described in Appendix A in the context of microquasars is the study of jet-interstellar medium (ISM) interactions, where the system Cyg X-1 is possibly the most representative example. In this system, the powerful jets driven by the source are thought to inflate a bubble in the surrounding medium [Gallo et al. 2005, Russell et al. 2007], where the shocked heated ISM is observed through thermal Bremsstrahlung radiation from radio to optical wavelengths (see also Chapter 1.6). The study of this interaction (for example, in Gallo et al. 2005) revealed a larger jet power than that inferred from direct observations of the compact jet in the core. This could suggest, for example, the presence of a large amount of cold protons in the outflowing plasma [Heinz 2006]. We will then simulate the interaction of the jet with the ISM – which will be characterised based on observational data of the binary field – and perform a bunch of simulations varying the jet total power and composition in order to constrain these parameters. This can be done, for example, studying the accuracy by which the simulation reproduces the observed shell morphology of the source.

## 7.3 Kink instabilities and non-thermal emission

### 7.3.1 Improving magnetic field visualisation

The dynamics of Jet C in Chapter 5 is particularly interesting from several points of view. The jet evolution during the interaction with the stellar wind is significantly different with respect to a hydrodynamical jet with the same total power: whereas a powerful hydrodynamical jet evolves without losing collimation, the magnetised jet is prone to the development of current-driven instability pinching and kink modes triggered by overpressure and the toroidal field. Therefore, the jet shows a chain of recollimation shocks within the binary scale, followed by the development of a strong kink that spreads the jet momentum throughout a larger area and decelerates its advance (see e.g. Fig. 7.2, showing the jet core in the simulation). The magnetic field structure is toroidal from injection to the development of the kink, while it becomes highly entangled near the head, filling the cavity.

In Fig. 7.3 we present the resulting configuration of the magnetic field in this simulation by focusing on the field lines. This plot shows relevant information about the field structure in the jet spine, which was hidden by the mixed plasma in the cocoon in our representation in Fig. 5.11 of Chapter 5. Since the magnetic

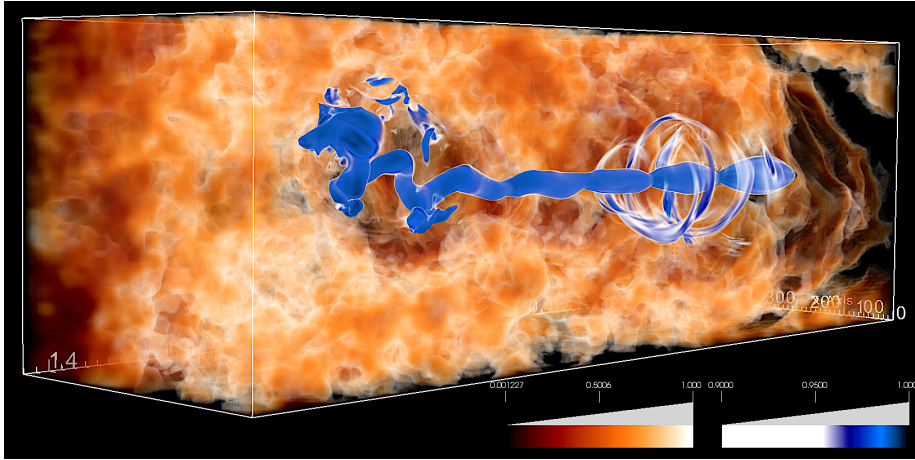


Figure 7.2 3D rendering visualisation of the jet core ( $f > 0.9$ ) propagating through the clumpy stellar wind. Originally published in Perucho and López-Miralles 2023.

field within the cocoon is low compared to that in the jet, we have applied a linear transparency to the field lines, weighted by the field vector module. In the mid-low part of the jet, the magnetic field preserves the toroidal structure of injection, which is reinforced at the recollimation shocks, as expected. The jet tracer 3D render (Fig. 7.2), which is limited to  $f > 0.9$  to highlight the jet core, shows a pinched morphology and a set of annulus of jet plasma surrounding the core, which are deposited in the cavity due to the jet dynamics during the first stages of propagation. This morphology is very particular and could give rise to different emission patterns that deserve to be studied in detail, but this is out of the scope of this thesis. In the mid-upper part of the simulation, both the new representation of the field and the tracer function allow us to distinguish a well-resolved precessing morphology, triggered by the development of a kink instability. The inset plot of Fig. 7.3 zooms in the jet head, showing that the field is highly reinforced at the elbow of the twisted trace, which is also directly impacting the shocked environment formed by the stellar wind.

### 7.3.2 Magnetic dissipation in ideal RMHD simulations

Further analysis will be required to investigate the consequences of this precessing morphology on the jet dynamics (within and beyond the binary), on the one hand, and its implications in terms of non-thermal emission, on the other. These kinks could contribute to the observed signatures of precessing jets that have been resolved at radio wavelengths for different XRBs with jet-like structures.

The most relevant example of jet precession is the well-known microquasar SS 433, but there are many other examples [see e.g., Mioduszewski et al. 2001, Massi, Ros, and Zimmermann 2012, Miller-Jones et al. 2019, Luque-Escamilla, Martí, and Martínez-Aroza 2020]. The origin of precession in microquasars is still debated for most of these sources. Although the classical theoretical models tend to explain precession by invoking relativistic effects of the inner disc [i.e., Lense-thirring precession, Liska et al. 2018, Motta et al. 2018] or the coupled effect of stellar winds and orbital motion [Barkov and Bosch-Ramon 2022], our simulation shows that current-driven instabilities can also trigger helical patterns during the jet-wind interaction, although the periods associated with this kind of precession should be accurately related. For example, current-driven instabilities have been suggested to explain the large-scale morphology of the jet structures observed in GRS 1758–258 [Luque-Escamilla, Martí, and Martínez-Aroza 2020].

This simulated jet thus represents an extraordinary candidate to produce high-energy radiation in microquasars, since energy dissipation may not only occur at the several reconfinement shocks where particles can be accelerated, but also in a kink instability that could lead to kink-driven magnetic reconnection processes further out from the injection base [see e.g., Bodo, Tavecchio, and Sironi 2021, Bodo et al. 2022]. The characterisation of the periodic behaviour of these processes (i.e., shocks and kink-driven precession) can be also relevant to interpret the rapid X-ray variability observed in some XRBs/microquasars. Therefore, future work will include consideration of those dissipative processes in the acceleration of non-thermal particles and the triggering of high-energy radiative output. Although magnetic reconnection is not reproduced in ideal RMHD codes like ours [see e.g., Mattia et al. 2023, for a recent example of a resistive RMHD jet simulation], numerical methods as those presented in Bodo, Tavecchio, and Sironi 2021 will allow us to characterise the formation of current-sheets and magnetic dissipation regions into our simulation. We expect that the combination of such analysis with numerical simulations as those presented in this thesis, will provide new insights into the physical processes that lead to non-thermal emission in microquasar jets.

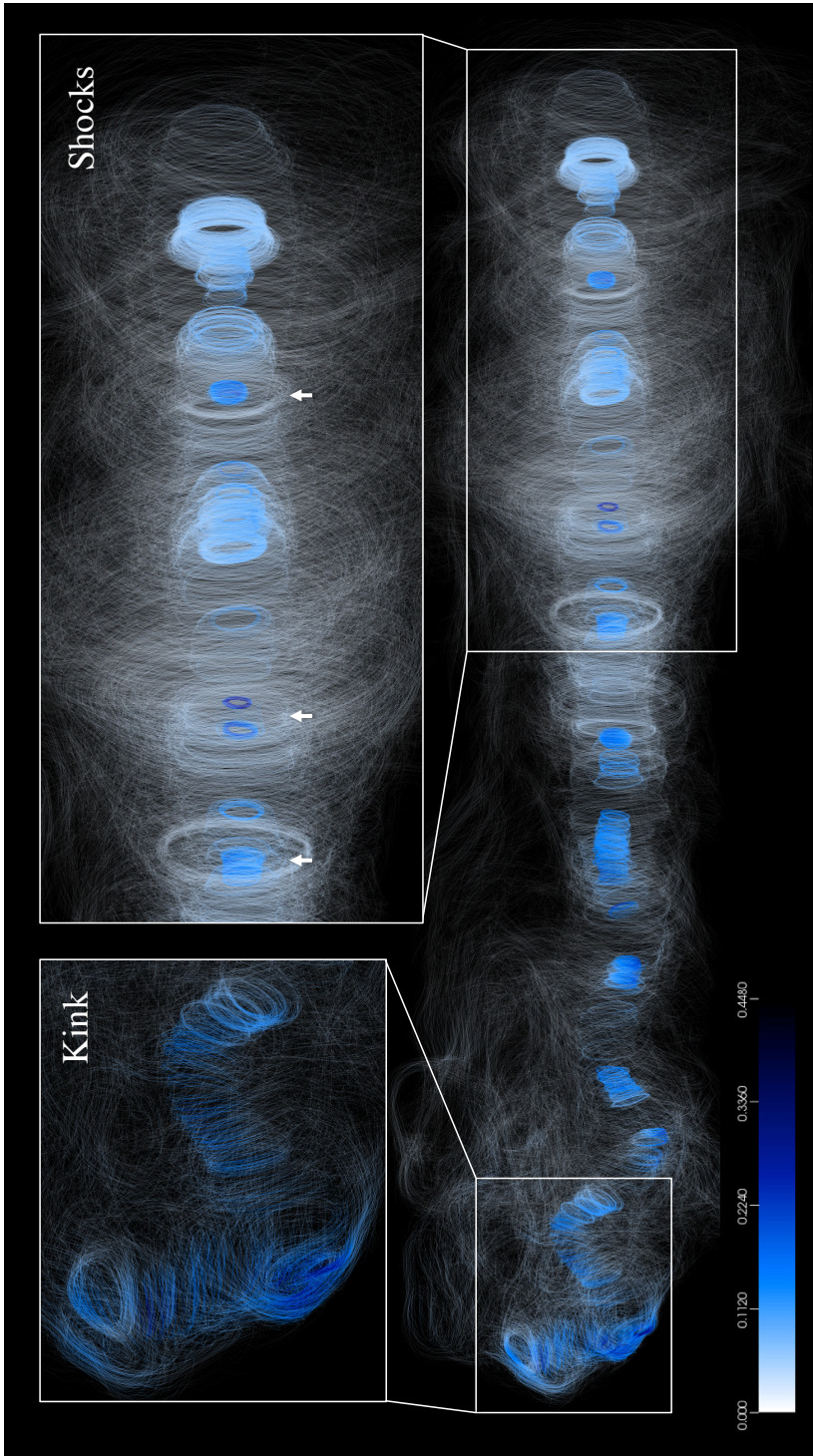


Figure 7.3 Magnetic field lines integrated in the 3D volume, where the colour map represents the magnetic field vector module. The transparency of the lines is inversely proportional to the vector module to highlight the jet skeleton. Inset plots zoomed in the recollimation shock region (right) and the twisted trace triggered by the kink instability in Perucho and López-Miralles 2023.

## 7.4 SS 433 jet simulations

**Variability and Ultra Relativistic Flows** In Chapter 6, I showed a simulation that aimed to assess the propagation of an underlying flow within the helix path created by the precessing jets in SS 433 (i.e. RUN III in the chapter nomenclature), as suggested by Migliari et al. 2005 to explain the rapid variability observed by Chandra. Nevertheless, the parameters of the Ultra Relativistic Flow (URF; i.e.  $V_j = 0.75 c$  and  $\rho \sim 2\rho_0$ ), which were arbitrarily chosen for the simulation, were not sufficient for the URF to collide with blobs ejected in the previous cycle. As I stated in Chapter 6, apart from showing the field configuration in the homogeneous blobs (which was interesting for the sake of completeness), we only discussed the results of the simulation to present a future line of work. We can then take advantage of the information provided by the failed RUN to perform a new simulation modifying the properties of the underlying outflow, for example, by increasing the velocity, density or even the magnetic field (although we do not expect a dynamically relevant magnetic field at the scale of the sub-parsec, the physical properties of the URF are unknown).

**Jet formation and Ultra-luminous X-ray sources** In a nutshell, three important questions remain unclear about jet formation in SS 433: (1) the fundamental nature of the jet (formation mechanism, composition, etc.) and its collimation agent, (2) the origin of jet precession at  $P \sim 162$  d and (3) the jet speed at  $V \sim 0.26 c$ , constant along more than 40 years of continuous monitoring of the source. In Marshall, Heinz, and Schulz 2014, the authors proposed two main jet formation models in SS 433 (see Fig. 7.4). In the first one (left panel), the supercritical accretion rate leads to a very thick accretion flow. The jet, however, is misaligned with respect to the accretion plane, and precesses at  $\theta \sim 20^\circ$  with respect to the disc axis, plowing through the thick disc. The jet, which could be leptonic and highly relativistic very close to the CO, is decelerated –and possibly mass-loaded– within the disc up to the observed velocity (i.e.  $V \sim 0.26 c$ ), and X-ray emission is only visible on the exit [e.g. Marshall et al. 2013]. In this model, radiation can also be channeled through the disc funnel by radiation pressure (as in the numerical simulations presented by Sądowski and Narayan 2015), and interact with the collimated jet at larger distances (see also Chapter 10). In the second model (right panel), the jet is instead aligned with the BH rotation axis, but if a thin tilted disc extends outwards, the interaction of the jet with the powerful winds driven from the outer disc (by radiation pressure) could also lead to jet bending and forced precession. Therefore, in order to study these

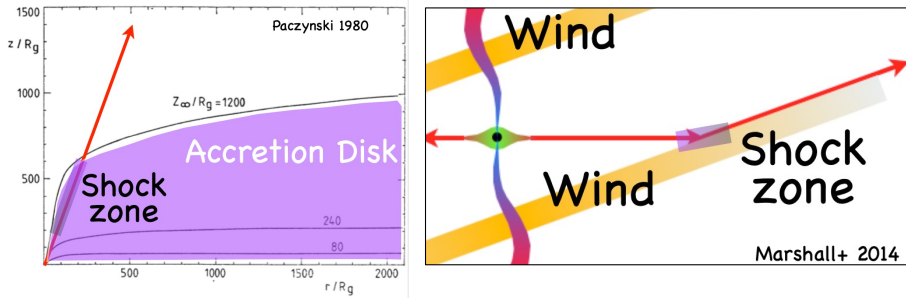


Figure 7.4 Scheme of two different models for jet formation and early propagation: jet precession within a thick disc (left) and forced precession due to the lateral impact of the external disc (right). Reproduced from Marshall, Heinz, and Schulz 2014.

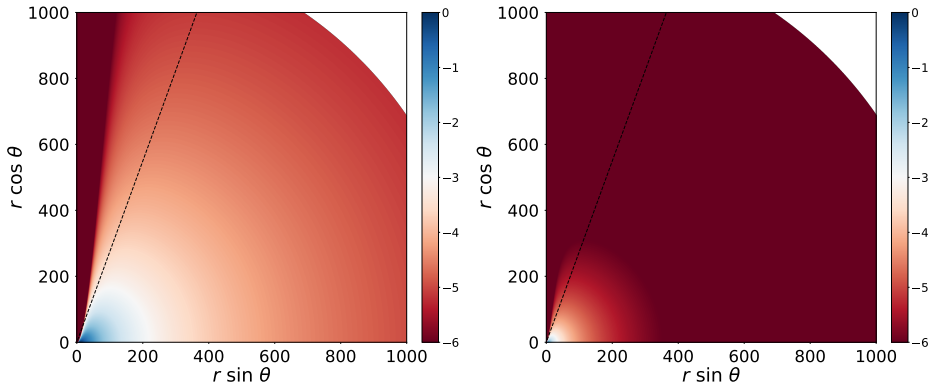


Figure 7.5 Logarithmic density in the vertical plane for a thick disc in a Schwarzschild (left) and Kerr (spin  $a=0.99$ ; right) metric. Courtesy of Dr. S. Gimeno-Soler (University of Aveiro).

scenarios with numerical simulations, the radiation module of LÓSTREGO –that allows to couple the plasma with an external photon field– is highly desirable. The first model also requires a thick disc solution (including radiation) to be used as initial conditions in the grid (Fig. 7.5), while for the second model I will follow a setup similar to Plewa et al. 1997. The interaction of jets with the accretion winds (as inferred by NuSTAR in Middleton et al. 2021) can be also addressed with future numerical simulations, since the role of these winds in the the jet propagation and the extended emission is also unclear. We will perform this study in collaboration with Herman Marshall (MIT Kavli Institute) and as part of a Chandra observation proposal, by which we aim to prove the ULX nature of the system (see Chapter 10).

## 7.5 Beyond microquasars: AGN jet simulations

On Appendix A, I present different projects in which I have participated during the thesis in the field of AGN relativistic jet simulations, where LÓSTREGO represents an optimal tool for a myriad of possible applications:

**Ring/arc structures in Hercules A** In Perucho et al. 2023, we presented a 3D RHD simulation that reproduces the large-scale morphology of the peculiar radio galaxy Hercules A. Nevertheless, one morphological feature that was not captured by the simulations –at least, as resolved extended structures– are the ring/arc-like features observed in the radio images (see discussion in Appendix A of the thesis and Timmerman et al. 2022). Since the characteristic time of the simulation differs from that of the real source, it is difficult to conclude if these features are not present in our solution, or should these type of structures develop in a later stage of the jet-lobe evolution. Nevertheless, the role of magnetic fields in the internal lobe structure must be addressed with a dedicated study, for which we will repeat the simulations in Perucho et al. 2023 with the LÓSTREGO code. Magnetic energy flux will then be injected in equipartition with the internal energy flux, and different field configurations (toroidal vs. non-toroidal, see Chapter 4) will be also tested in the setup.

**Long-term evolution of jets and feedback** We plan to assess the role of relativistic outflows in the evolution of their host galaxies and clusters, which is a key process in the shaping of these cosmological structures. In this respect, the combination of radiation dynamics with magnetohydrodynamical simulations (see Chapter 3) could allow us to tackle both quasar mode and radio mode feedback scenarios in this type of galaxies. On their own, magnetohydrodynamic simulations of jets can also contribute to improve our understanding of the jet-intergalactic medium interactions and explain the origin of the filaments and complex structures revealed, for example, by MeerKat [e.g., Ramatsoku et al. 2020, see Fig. 7.6].

**Instabilities** The development of instabilities in relativistic plasmas is a relevant process to understand jet properties and their remarkable stability, which allow them to propagate up to very large distances. This would be an academic approach to plasma physics, following a similar strategy to e.g., Perucho et al. 2004, Perucho, Martí, and Hanasz 2004, Perucho, Martí, and Hanasz 2005, Perucho and Martí 2007.

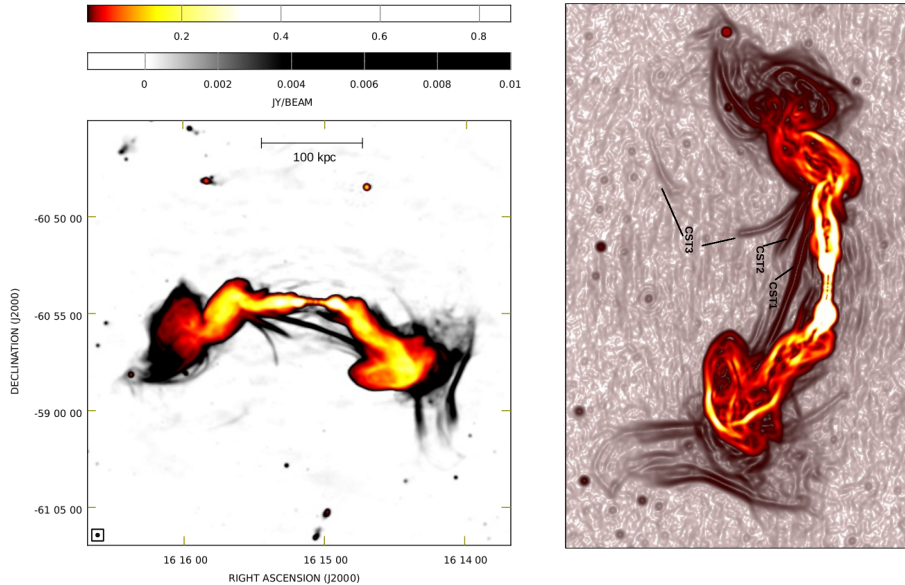


Figure 7.6 Left: Radio continuum emission from ESO137-006 detected by MeerKAT at 1030MHz. Right: Gradient image (Sobel convolution kernel) with the three most prominent collimated synchrotron threads labelled. Reproduced with permission from Ramatsoku et al. 2020 (Fig. 1 and Fig. 2), ©ESO.

**Jet physics at sub-parsec and parsec-scale** At these scales, space and global VLBI observations reveal complex dynamics and structures that are advected from the jet forming regions. Relatively straightforward improvements of the code would increase the amount of scenarios that the code could probe in the future. Among these, we can study, for example, the propagation of injected perturbations through a jet to be compared with observations such as those obtained for 3C 111 [Kadler et al. 2008, Beuchert et al. 2018, Schulz et al. 2020], jet collimation and acceleration [e.g. NGC 1052; Baczko et al. 2022, Fromm et al. 2019], or jet stability and generation of structures [e.g. 3C 273; Bruni et al. 2021]. In particular, in a recent paper submitted to *Astronomy & Astrophysics* (L. Ricci, M. Perucho, J. Lopez-Miralles et al., 2023), we developed 2D axisymmetric RMHD simulations to explore jet acceleration from sub-pc to pc scales. As initial conditions, we used previous observational constraints on jet properties derived by means of VLBI observations for a prototypical Fanaroff-Riley I radio galaxy, the source NGC 315 [Ricci et al. 2022], and analyse the contribution of both thermal (i.e. Bernoulli) and magnetic energies on the jet acceleration pattern. The results of this analysis, which are promising to understand jet acceleration in AGN jets, can be also extended to 3D using the LÓSTREGO code.

## Part III

# Observations and data analysis



# Rapid X-ray variability of the $\gamma$ -ray binary LS I +61°303

---

This chapter was originally published in **J. López-Miralles, S.E. Motta, S. Migliari, F. Jaron.** *Rapid X-ray variability of the gamma-ray binary LS I +61°303.* *Monthly Notices of the Royal Astronomical Society*, June 2023. DOI: [10.1093/mnras/stad1658](https://doi.org/10.1093/mnras/stad1658). *Reproduced with permission.*

---

## 8.1 Introduction

The high-mass X-ray binary LS I +61°303 consists of a compact object (CO) with an eccentric orbit ( $e \approx 0.7$ ) around a rapidly rotating B0 Ve type star [Casares et al. 2005], whose orbital period is  $P_1 = 26.496 \pm 0.0028$  days [Gregory 2002]. The nature of the CO in LS I +61°303 is still unclear. Since optical observations are not accurate enough to place strong constraints on the mass function of the object, which is in this case affected by large statistical uncertainties [Casares et al. 2005], some authors argue that the central engine of the binary is a stellar-mass black hole [BH; see e.g., Punsly 1999, Massi, Migliari, and Chernyakova 2017], while others suggest that the system contains a neutron star [NS; see e.g., Maraschi and Treves 1981, Torres et al. 2012].

LS I +61°303 has been detected in a wide range of wavelengths, from radio [i.e., non-thermal synchrotron, see e.g., Gregory and Taylor 1978] to X-rays [see

e.g., Bignami et al. 1981], as well as at high-energies, at GeV [Abdo et al. 2009], and very high-energies, at TeV [Albert et al. 2006]. It is therefore one of the very few  $\gamma$ -ray emitting binaries [see e.g., Mirabel 2007, Chernyakova and Malyshev 2020, and references therein], together with other canonical systems as LS 5039, HESS J0632+057 or 1FGL J1018.6-5856.

In the X-ray energy range, LS I +61°303 is a weak source, with an average luminosity of  $L_x \sim 10^{33}$  erg/s [Bignami et al. 1981]. The Rossi X-ray Timing Explorer (RXTE) satellite [Paredes et al. 1997, Harrison et al. 2000, Greiner and Rau 2001, Leahy 2001, Smith et al. 2009, Torres et al. 2010, Li et al. 2011], as well as instruments on other missions, such as Swift-XRT [Esposito et al. 2007] or INTEGRAL-IBIS/ISGRI [Ubertini et al. 2009, Zhang et al. 2010], allowed to perform long-term X-ray monitoring of LS I +61°303, while soft X-ray pointed observations performed by XMM-Newton [Sidoli et al. 2006], Chandra [Paredes et al. 2007, Kargaltsev et al. 2014], ASCA [Leahy, Harrison, and Yoshida 1997], ROSAT [Taylor et al. 1996] and Einstein [Bignami et al. 1981] were in general too short to cover a full single orbit. In 1996, the source was intensively observed by RXTE for one entire orbital cycle [Harrison et al. 2000]. Other authors [Greiner and Rau 2001, Neronov and Chernyakova 2007] analyzed the same data set and found that the energy spectrum could be fitted properly by a simple, relatively hard, absorbed power law, suggesting an underlying non-thermal X-ray emission mechanism. Smith et al. 2009 analysed five months of RXTE Proportional Counter Array (PCA) observations and found that the light-curve showed a two-peak profile in the 2-10 keV band, where the flux and the photon index were anti-correlated. Similar results were previously reported by Paredes et al. 1997, but using RXTE/ASM data. Later on, Torres et al. 2010 and Li et al. 2011 considered respectively 35 and 42 full cycles of the source orbital motion. They showed that the orbital profile was not stable (meaning that the phase of the light-curve peak varied over time) and reported a strong anti-correlation between the X-ray flux and the source photon index. Together with the X-ray flux modulation, at radio wavelengths LS I +61°303 shows periodic radio outbursts [Gregory, Peracaula, and Taylor 1999], whose phase was also reported to vary periodically with the same period as the X-ray peak [Gregory, Peracaula, and Taylor 1999, Jaron and Massi 2013]. More recently, Massi et al. [2020] also performed a campaign of simultaneous multi-wavelength observations of the system along one single orbit, confirming not only the predicted double-peak light-curve, but also that X-ray dips were coincident with radio and  $\gamma$ -ray peaks.

### 8.1.1 High-energy emission models

There are two main competing scenarios to explain the multi-wavelength observations of LS I +61°303, with a special focus on the origin of its non-thermal emission (see Fig. 8.1): accretion onto a CO and jet ejection (i.e., a NS or BH microquasar, as first proposed by Taylor and Gregory 1982), or the interaction of a pulsar with the wind of the companion star [first proposed by Maraschi and Treves 1981].

#### 8.1.1.1 Microquasar model

In the microquasar model [see e.g., Bosch-Ramon et al. 2006], high-energy emission can be produced in jet recollimation shocks that form when the jet crosses the stellar wind of the companion [Perucho and Bosch-Ramon 2008, Perucho, Bosch-Ramon, and Khangulyan 2010], or even in a chain of these type of shocks [López-Miralles et al. 2022, see also Chapter 5 of this thesis], that could lead to efficient particle acceleration [Rieger, Bosch-Ramon, and Duffy 2007] and synchrotron non-thermal emission, inverse Compton and even proton-proton collisions. In this model, the resolved radio structures and the flat radio spectrum shown, for example, by Massi, Ros, and Zimmermann 2012 and Zimmermann, Fuhrmann, and Massi 2015, can be interpreted as radio emitting relativistic jets. Several Very Long Baseline Interferometry (VLBI) images [Hjellming and Johnston 1988, Massi et al. 2004, Dhawan, Mioduszewski, and Rupen 2006, Massi, Ros, and Zimmermann 2012, Wu et al. 2018] also show that the jet-like morphology changes from one-sided to double-sided, compatible with variable Doppler (de)boosting due to changes in the jet orientation with respect to the line of sight. The main drawback of this model is that it has not been possible to confirm any direct proof of accretion in LS I +61°303, like a disk black-body component in the energy spectrum or a cutoff power-law spectrum in the high-energy band.

#### 8.1.1.2 Pulsar wind model

By contrast, Dubus 2006 and Dhawan, Mioduszewski, and Rupen 2006 interpreted the one-sided radio jet of LS I +61°303 as the cometary tail resulting from the interaction between a pulsar wind and the companion wind, in analogy with the system PSR B1259–63 [Wang, Johnston, and Manchester 2004] that hosts a fast-rotating non-accreting NS with strong magnetic fields. The hypothesis that LS I +61°303 contains a NS with strong magnetic fields was also proposed by Torres et al. 2012, who reported on a Swift-BAT detection of a short burst that

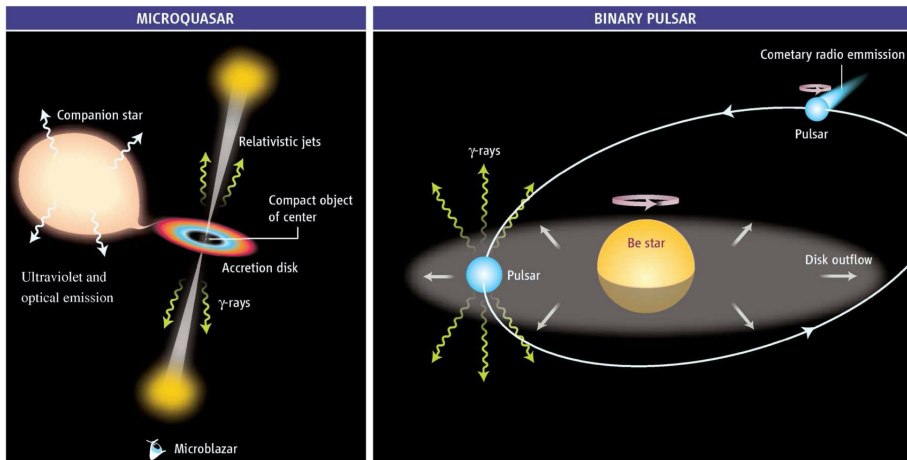


Figure 8.1 Microquasar (left) and pulsar wind (right) models for very energetic gamma-ray binaries. From Mirabel 2006. Reprinted with permission from AAAS.

resembles those generally labelled as magnetar-like events. More recently, Weng et al. 2022 found transient radio pulsations of  $P \sim 296$  ms using observations from the Five-Hundred-meter Aperture Spherical radio telescope. However, these pulses seem to be faster than the typical spin period of a magnetar (which usually ranges in the order of several seconds) and were not present in three out of four observations of the source.

### 8.1.2 Source periodicities

Apart from the source orbital period ( $P_1$ ), LS I +61°303 shows other periodicities. Massi, Ros, and Zimmermann 2012 first estimated with radio astrometry a precession period of the radio structure of 27-28 days. Timing analysis of long-term radio flux data from several archives resulted in the detection of a signal with period  $\sim 26.9$  d [Massi and Jaron 2013, Massi and Torricelli-Ciamponi 2016, Jaron et al. 2018], which is close to the orbital period but still significantly different, and which is in agreement with the previously estimated precession period of the putative jet [Massi, Ros, and Zimmermann 2012]. Analysis of the VLBI astrometry has revealed that the core indeed traces an ellipse with a period of  $P_2 = 26.926 \pm 0.005$  d [Wu et al. 2018]. The same precession period has also been detected at X-rays [D’Ài et al. 2016] and  $\gamma$ -rays [Jaron et al. 2018, and references therein].

The simplest explanation is that the observed flux density from a relativistic jet is the product of an intrinsically variable jet and Doppler boosting towards

the observer [Massi and Torricelli-Ciamponi 2014]. The radio outburst also exhibits a long-term periodic modulation of  $P_{\text{long}} = 1667 \pm 8$  days [Gregory 2002], possibly due to the beat of the two close periods,  $P_1$  and  $P_2$ . Using 6.7 years of data from the Green Bank Interferometer (GBI), Massi and Jaron 2013 suggested that the beating between  $P_1$  and  $P_2$  also leads to a new apparent periodicity,  $P_{\text{av}} = 26.70 \pm 0.05$  days, which is modulated by  $P_{\text{beat}} = 1667 \pm 393$  days and that is not directly detected in the periodograms (but see also Massi and Jaron 2013 and Ray et al. 1997).

### 8.1.3 Objectives and organisation

In this chapter, I analyse the whole archival RXTE/PCA data of LS I +61°303. The main objective of the work is to present a complete study of the X-ray spectral and fast time variability of the source over the years of exposure, by means of phase-resolved spectral and timing analysis for enhanced count statistics.

The chapter is organised as follows: In Sec. 8.2 I describe the RXTE/PCA observations that I use in this work and the methodology I follow to split the dataset into three independent sub-intervals. I also describe the phase-resolved analysis and the techniques employed to produce phase-folded light curves and phase-averaged energy spectra and power density spectra (PDS) for different phase bins. In Sec. 8.3 I discuss the main results of the analysis and I compare the work with previous results in the X-ray wavelength. Finally, in Sec. 8.4 I summarise the main results and I draw the most relevant conclusions.

## 8.2 Observations and data analysis

We analysed all the available LS I +61°303 X-ray observations performed with the PCA instrument [Jahoda et al. 2006] on-board the RXTE satellite. This data set comprises 527 observations covering a broad time interval that extends from 01-03-1996 to 29-12-2011<sup>1</sup>, providing a total exposure of over 850 ks. A light-curve of the source (in units of counts/s) including all the observations that we considered is shown in Fig. 8.2 (top, see Sec. 8.2.2.1 for details on the light-curve extraction).

---

<sup>1</sup>After a first inspection of the archive, we discarded some observations because of very short exposures or lack of data. The ObsId of these observations are: 10172-08-01-00, 93100-01-33-00, 95102-01-54-00 and 96102-01-17-00.

### 8.2.1 RXTE/PCA periodicity

In order to confirm if the periods introduced in Sec. 8.1 are also intrinsic periodicities of our X-ray dataset (for the sake of correctness, we should not accept a priori that radio and X-rays show exactly the same orbital modulation), we first produced a Lomb-Scargle (LS) periodogram [Lomb 1976, Scargle 1989], which is suitable for detecting and characterising periodic signals in unevenly sampled data. Figure 8.2 (middle) shows the periodogram (LS Power vs. period) for the data set (dark blue crosses) and for the window function (red crosses). The latter is computed to determine what features are intrinsic to the data, and what are instead an artefact introduced by the characteristics of the window (i.e. the data sampling). The minimum frequency sampled by the LS periodogram is  $f_{\min} = 1/(t_{\max} - t_{\min}) = 2 \times 10^{-9}$  Hz (which corresponds to  $P \approx 5781$  days) and the maximum frequency is  $f_{\max} = 3.18 \times 10^{-6}$  Hz (which corresponds to  $P \approx 3.6$  days). The frequency resolution is  $\Delta f = 4 f_{\min}$  (i.e., we use an oversampling factor of 4). The LS periodogram shows a narrow peak that we fitted with a Gaussian function as shown in the inset plot in Fig. 8.2 (middle). The central period of the Gaussian curve is  $P = 26.65 \pm 0.28$  days, where the error corresponds with the Gaussian full width at half maximum.

The LS periodogram is optimised to identify sinusoidal-shaped periodic signals. Essentially, the LS method fits a sinusoidal model to the underlying data at each frequency, with a larger power reflecting a better fit. However, for some signals, the assumption of stationary sinusoidal models could lead to inaccurate results, besides the limitation in frequency resolution imposed by the data time coverage. Thus, to confirm the period found in the LS periodogram of Fig. 8.2 (middle), we repeated the analysis using two complementary statistical methods: (1) the Phase Dispersion Minimization (PDM) method<sup>2</sup> [Stellingwerf 1978, Fig. 8.2 (bottom)] and (2) amplitude maximisation with a sinusoidal fit, which is not shown in Fig. 8.2. The first technique finds periodic variations by minimising the dispersion of the folded dataset and it is commonly used to analyse time series with gaps, non-sinusoidal variations, poor time coverage or when the Fourier techniques lead to wrong solutions. For this particular case, we used 10 phase bins with 5 phase-shifted sets of bins (dark blue line) and with no phase covers (red line), for comparison. In both cases, the results obtained are very similar. A Gaussian fit over the phase-shifted data yields  $P = 26.63 \pm 0.26$  days, in good agreement with the LS period. In the second complementary method, we directly searched for the best sinusoidal fit parameters of the phase-folded

<sup>2</sup><https://pyastronomy.readthedocs.io/en/latest/pyTimingDoc/pyPDMDoc/pdm.html>

light curve modulation in the period range 26.0 – 28.0 days, using 400 fit trials. Considering the following sinusoid,  $y = a_0 + a_1 \sin(a_2 t + a_3)$ , the period that maximises  $|a_1/a_0|$  represents the best possible data modulation. In this case, the peak of the Gaussian fit yields a central period  $P = 26.62 \pm 0.30$  days, in good agreement with our two previous estimations.

## 8.2.2 Data analysis

We aim to track any possible variation of the spectral and timing features of the source over 15 years, and hence we phase-folded the observations with a given X-ray period to increase the signal-to-noise (S/N) ratio of each phase bin. Assuming no relevant variations occur at a particular phase, this method allows us to obtain averaged phase resolved energy spectra and PDS with enhanced statistics.

We divided our data set into three intervals, intended to maintain a good S/N ratio while we avoid the smearing of any possible long-term variability. We considered the following subsets: Interval I, that includes all the March 1996 observations (identified with proposal number 10172), and Intervals II and III, each including about half of the remaining observations (covering more than five years in the time range from 13-10-2006 to 29-12-2011). The number of observations in each interval, the time covered and the total exposure are listed in Table 8.1.

The phase associated to any given periodicity  $P$  is given by:

$$\phi = \frac{T_{\text{REF}} + T - T_0}{P} - \text{int} \left[ \frac{T_{\text{REF}} + T - T_0}{P} \right], \quad (8.1)$$

where  $T_0 = 43366.275$  MJD is the time of the first radio detection of the source,  $T_{\text{REF}} = 49353.00069657407$  MJD is the RXTE reference epoch and  $T$  is the spacecraft clock reading (including clock corrections).

Data filtering was performed with the standard criteria typically applied to RXTE/PCA<sup>3</sup>, while data analysis was carried out using HEASoft 6.28. For light-curve extraction (Sec. 8.2.2.1) and spectral fitting (Sec. 8.2.2.3), only data from the Proportional Counter Unit (PCU)-2 was used for the analysis. This is commonly done as the PCU-2 is the only detector that always kept on along the entire duration of the RXTE mission.

---

<sup>3</sup>[https://heasarc.gsfc.nasa.gov/docs/xte/recipes/cook\\_book.html](https://heasarc.gsfc.nasa.gov/docs/xte/recipes/cook_book.html)

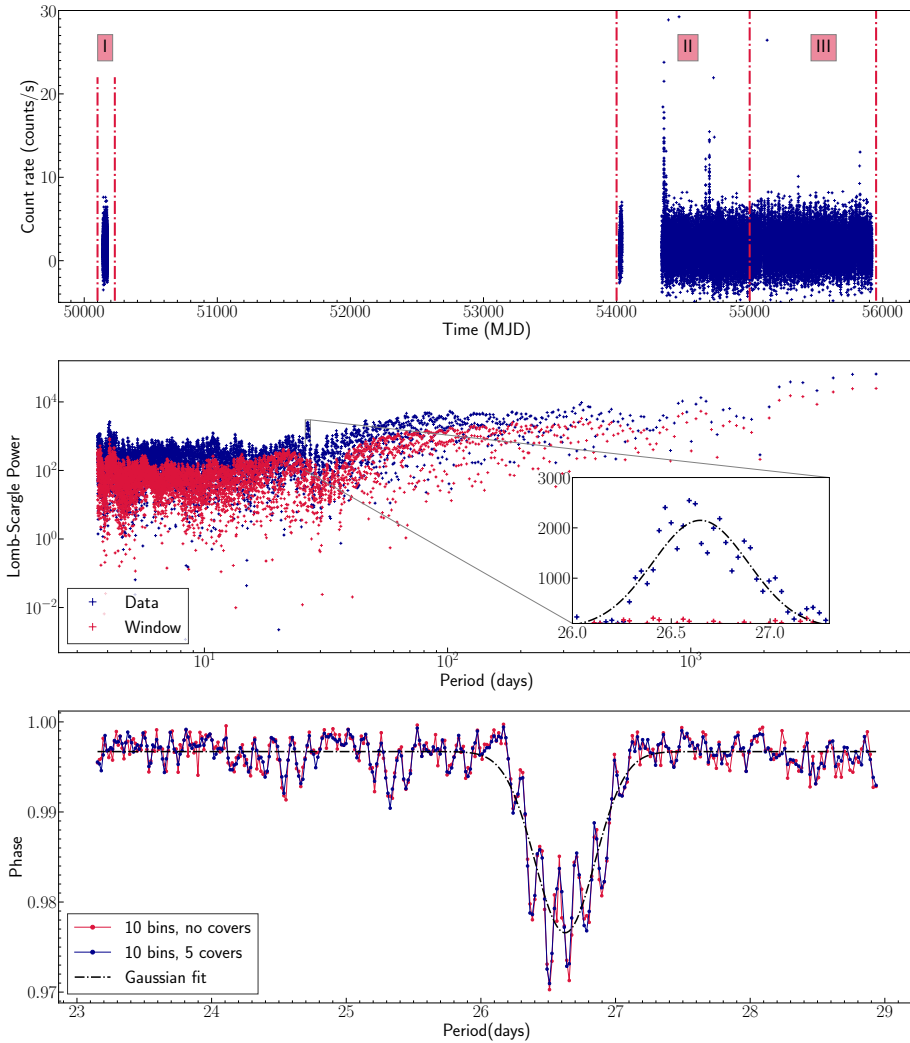


Figure 8.2 Top: Total light curve with vertical red dash-dot lines showing the start and the end of our three subintervals. Middle: Lomb-Scargle periodogram. The LS periodogram shows both the transform of RXTE observations (blue crosses) and the window function (red crosses). The inset plot shows a zoom of the periodic signal, where a Gaussian fit of the peak yields  $P = 26.65 \pm 0.28$  days. Bottom: Phase Dispersion Minimization analysis using 10 phase bins with 5 phase-shifted set of bins (red dot line) and with no phase cover (blue dot line). The peak of the Gaussian fit yields  $P = 26.63 \pm 0.26$  days.

Table 8.1 Main parameters of the three subsets of observations considered in this work. The number of observations of the 1996 campaign is much lower than Interval II and Interval III, but the total exposure of the subset is comparable within a factor.

Subset	Number of observations	Start date	End date	Exposure
Interval I	12	01-03-96	30-03-96	106 ks
Interval II	255	13-10-06	11-06-09	397 ks
Interval III	254	14-06-09	29-12-11	360 ks

### 8.2.2.1 Light curves

For each of the three sub-intervals in Tab. 8.1, we produced a phase-folded light curve using Standard 2 type data, which is characterised by low time resolution (16 s) and moderate energy resolution ( $< 18\%$  at 6 keV, with 129 energy channels covering the nominal energy range 2-120 keV). We selected canonical Good Time Intervals (GTIs) by choosing the times when the source elevation was  $>10^\circ$  and the pointing offset was  $<0.02^\circ$ . We estimated the background using PCABACKEST v3.12a and the most recent background file available on the HEASARC website for faint sources <sup>4</sup>. Source and background light curves were then extracted using the FTOOL [Blackburn 1995] software package utility SAEXTRACT by selecting channels in the absolute range 4-128 (see the discussion in Sec. 8.2.2.2 about low energy channels). We estimated the background-subtracted light curve for each observation using the FTOOL routine LCMATH. Barycentric corrections were applied using the routine BARYCORR and the ephemeris file JPLEPH.430, which contains the most up-to-date solutions as of the writing of this chapter. To fold the light curve in phase, we calculated the phase for each point in the curve using the period we measured in Sec. 8.2.1. For the sake of consistency, and given the uncertainties of our statistical methods, hereinafter we consider  $P = 26.6$  days. We have checked that no significant differences in the phase modulation appears when considering instead the orbital period,  $P_1$ . This procedure was then repeated for all the observations in the subset to produce one single unbinned phase-folded light curve for the entire duration of the interval, as shown in the three panels of Fig. 8.3. Then, we divided the data into 10 phase bins of width 0.1 (i.e., 2.66 days/bin), and we estimated the mean count rate in each of them. Outlier points (i.e., detections where the count rate exceeded more than five times the mean of the light curve) were removed before rebinning the light curve in phase, since these might affect the source phase modulation (see, for example, Fig. 2 in Li et al. 2011). These outlying points correspond to short flares that were previously identified by other authors [see e.g., Smith et al.

<sup>4</sup>pca\_bkgd\_cmfaintl7\_eMv20151128.mdl

2009, Li et al. 2011]. Figure 8.3 shows the location of these flares, besides other random outliers (red points), for each of the three sub-intervals that we analysed in this work. Apart from the big flares of Interval II grouped in the 0.0-0.3 and 0.7-1.0 phase bins, the light curves also show a few, likely instrumental, smaller deviations that do not appear to be preferentially observed at any particular phase.

### 8.2.2.2 Power density spectra

We used RXTE Good Xenon data mode, which are science event format files characterised by very high time ( $\sim 0.95 \mu\text{s}$ ) and energy resolution (256-channel pass band with energy resolution  $< 18\%$  at 6 keV). The Good Xenon configurations use two Event Analyzers (EA) simultaneously to provide detailed spectral and temporal information about every event that survives background rejection. Each EA creates matched pairs of files that we merged with the Perl script MAKE\_SE, prioritising data with a readout time of 16 s over 2 s, depending on availability. We phase-folded all the observations in the data set (using the X-ray intrinsic period  $P = 26.6$  days), obtaining ten different phase bins as described in the previous section. For each of these bins, we produced a PDS using the custom GHATS package<sup>5</sup>. PDS were extracted only for energy channels in the range 8-255<sup>6</sup> ( $< 3.7$  keV). We avoided channels 1-7 because we found that its inclusion in the timing analysis produced artefacts in the PDS which we could not mitigate (i.e., PDS were distorted with undesirable drops near the Nyquist frequency). The effective area of the PCA is small at these energies, therefore the exclusion of events in these bands does not change significantly the amount of photons collected, especially after phase-folding. On the other hand, we also removed sharp drop outs from the data (that usually appear at the beginning or at the end of an observation), whose nature is instrumental and not related with the source. If present, the existence of instrumental drops can introduce artificial step features in the low-frequency noise. This task was performed by a specific selection of GTIs based on three fundamental steps: (1) first, we selected RXTE standard GTIs using MAKE TIME based on housekeeping information, by choosing the times when the source elevation was  $> 10^\circ$  and the pointing offset was  $< 0.02^\circ$ . (2) Secondly, we used a bi-weight algorithm<sup>7</sup> to detect and handle outliers, for which we considered a threshold of  $\pm 3.5\sigma_{\text{bi}}$ , where  $\sigma_{\text{bi}}$  is

<sup>5</sup>See [http://www.brera.inaf.it/utenti/belloni/GHATS\\_Package/Home.html](http://www.brera.inaf.it/utenti/belloni/GHATS_Package/Home.html).

<sup>6</sup>[https://heasarc.gsfc.nasa.gov/docs/xte/e-c\\_table.html](https://heasarc.gsfc.nasa.gov/docs/xte/e-c_table.html)

<sup>7</sup>The bi-weight algorithm calculates the centre and dispersion of a distribution using bisquare weighting.

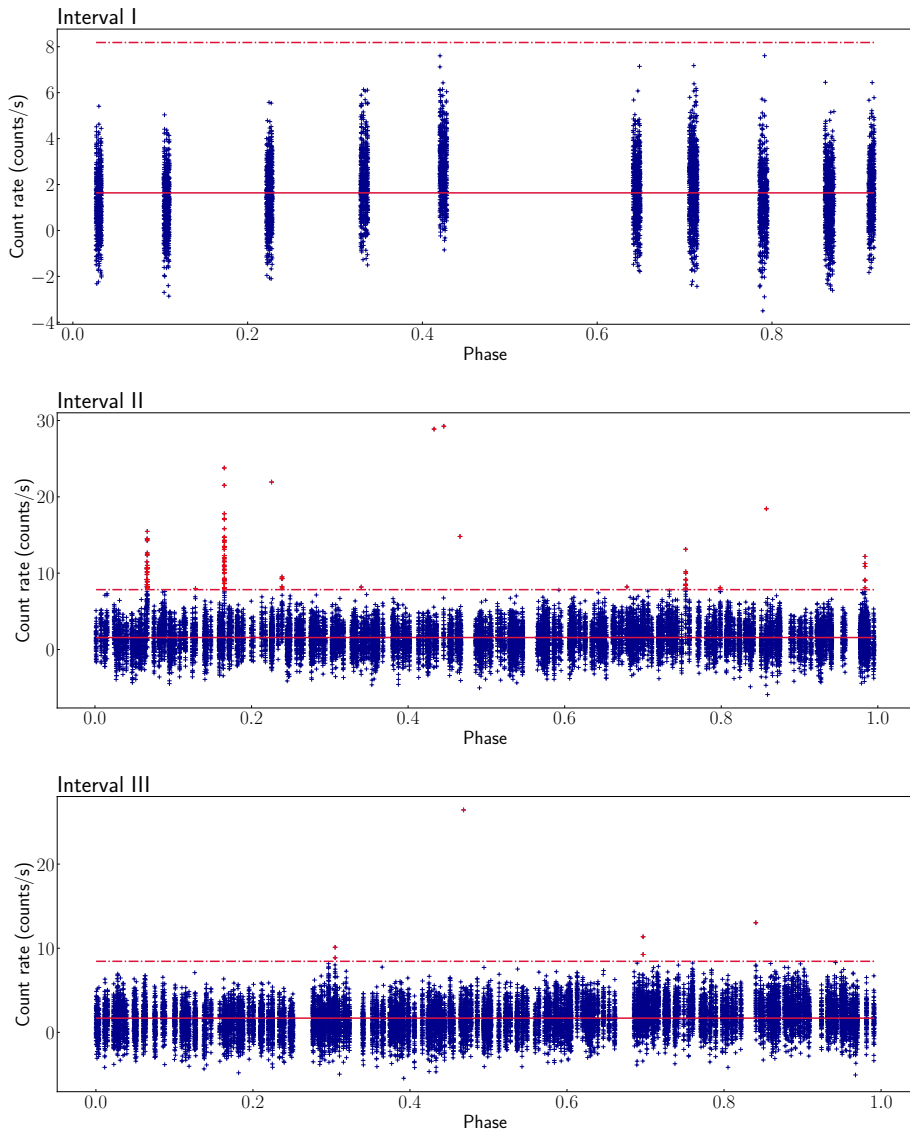


Figure 8.3 Unbinned phase-folded lightcurve for Interval I (top), Interval II (middle) and Interval III (bottom). The mean count rate of each interval is represented with a red solid line. Detections above the red dashed-dot line (which is placed at five times the average count rate) are not considered for light curve rebinning. These points could be either real events associated to the source flaring activity (e.g., the big flares of Interval II) or non-physical instrumental features that do not show any hint of phase dependency.

the bi-weight standard deviation. When an outlier is detected, we remove an interval of  $\pm 16$  s around the outlier point. Intervals with a time length lower than the previous threshold of 16 s were automatically discarded. (3) Finally, we used the FTOOLS utility FTMGTIME to merge by intersection the GTI files obtained in the two previous steps.

All event files and GTIs were barycenter corrected with the FTOOL utility FXBARY, but no deadtime corrections nor background subtractions were performed before creating the PDS due to the very low count rate. Using Fast Fourier Transform techniques [van der Klis 1989], we rebinned the data in time to obtain a Nyquist frequency of 4096 Hz and we produced PDS for continuous 256-s-long data segments (leading to a frequency resolution of  $1/256$  s  $\approx$  0.004 Hz). For each phase bin, we averaged all the PDS normalised according to Leahy et al. 1983 and subtracted the Poisson noise spectrum following Zhang et al. 1995. Finally, we estimated the PDS root mean squared deviation (rms) in a low frequency (0.006 – 0.1 Hz) and a high frequency (0.1 – 512 Hz) band as a function of phase, in order to investigate the variability of the emission. Background count rate was estimated from the background light curve (see the details on Sec. 8.2.2.1); for those phase bins which contained only one observation, the mean background was calculated as the mean count rate of the background light curve. For bins including more than one observation, we first calculated the mean of each individual observation and then, after checking that no large differences existed in the average background rates from individual observations, we computed the average and standard deviation of the bin.

The objective of this analysis is to search for timing features in the data (i.e., broad-band red noise components, quasi-periodic oscillations (QPOs), etc), for which we aim to maximise the S/N ratio. Therefore, for this section, we only consider –and thus we only show in the thesis– the PDS calculated with the whole set of observations. The rms, however, is splitted in the three subintervals of Table 8.1 for the sake of completeness.

### 8.2.2.3 Spectral fitting

We calculated source and background spectra for each individual observation using the FTOOLS utility SAEXTRACT using Standard 2 data, applying the same GTIs described in Sec. 8.2.2.2. Dead time corrections were applied using the standard RXTE procedures<sup>8</sup> v11.7.1 and we averaged the source and background spectra in each of the ten phase bins using the FORTRAN wrapper ADDSPEC

<sup>8</sup>[https://heasarc.gsfc.nasa.gov/docs/xte/recipes/cook\\_book.html](https://heasarc.gsfc.nasa.gov/docs/xte/recipes/cook_book.html)

v1.4.0 to obtain one source and one background averaged spectrum per bin. Then, we fitted the background-subtracted spectra between 4 and 30 keV in XSPEC v12.11.1 [Arnaud 1996] using three model components: the interstellar photoelectric absorption (TBABS), one power-law (POWER) to fit the source signal at low energies and a second power-law (POWER) to fit the galactic ridge emission, which is present in all energy spectra dominating the emission above  $\sim 20$  keV [Revnivtsev, Vikhlinin, and Sazonov 2007]. The absorption coefficient  $N_H = 7.8 \times 10^{21} \text{ cm}^{-2}$  and the photon index of the second power-law  $\Gamma = 0.0$  were frozen before fitting the model to the spectra. As in the previous section, we only show the averaged energy spectra obtained using the whole set of observations, although the photon index is also calculated in the three sub-intervals defined in Tab. 8.1.

### 8.2.3 Results

The main results of our data analysis are shown in Fig. 8.4 for Interval I (blue circles), Interval II (green squares), Interval III (red up-triangles), and the total dataset (grey upside-down triangles), which is also shown for the sake of comparison.

Figure 8.4 (a) shows the light curve in units of counts/s as a function of phase (with respect to the measured period), where error bars include both the Poisson error and a 2% systematic uncertainty to account for the low number statistics. We note that Interval I shows a gap at phase 0.5 – 0.6 because there is no data in the archive for this particular bin. All light curves show a clear modulation which is consistent with the orbital periodicity, with the count rate reaching its minimum in the bin 0.1 – 0.2 for Interval I ( $1.124 \pm 0.045$  counts/s) and Interval III ( $1.149 \pm 0.023$  counts/s), and in the bin 0.4 – 0.5 for Interval II ( $1.182 \pm 0.025$  counts/s). Interval I shows a maximum in the bin 0.4 – 0.5 ( $2.741 \pm 0.068$  counts/s), which is shifted in phase to bin 0.7 – 0.8 for Interval II ( $2.021 \pm 0.031$  counts/s) and Interval III ( $2.437 \pm 0.032$  counts/s). For each of these intervals, we fitted a constant and a single or double sinusoidal function, where the best fit parameters are given in Tab. 8.2. The two-wave sinusoidal function aims to test statistically the accretion models that predict a two-peak light-curve, which in this case is more apparent for Interval I and Interval II. In all three cases, statistics improve significantly by fitting the light-curve with the sum of two sinusoids, but the goodness of fit is only statistically acceptable for the double sinusoidal function in Interval III.

Table 8.2 Best fit parameters of the sinusoid functions used in Fig. 8.4 (a), where  $H$  is the vertical shift,  $|a|$  is the wave amplitude,  $\omega$  is the angular frequency and  $\phi$  is the phase. Sub-indices 1,2 refer to the single and double sinusoids used in the analysis, respectively. Last column shows the  $\chi^2_{\nu}$  for the constant fit.

Sinusoids	Fit parameters								$\chi^2_{\nu}$ (dof)	$\chi^2_{\nu}$ (dof) -const.
	$H$	$a_1$	$w_1$	$\phi_1$	$a_2$	$w_2$	$\phi_2$	$\chi^2_{\nu}$ (dof)		
Interval I (1)	1.74	-0.57	6.52	1.37	-	-	-	21.55(16)	50.97(19)	
Interval I (2)	1.74	-0.60	6.29	1.56	-0.33	12.43	-0.88	10.10(13)	-	
Interval II (1)	1.52	0.17	6.86	2.21	-	-	-	26.85(16)	29.95(19)	
Interval II (2)	1.53	0.26	12.62	-7.52	0.16	6.39	-3.57	3.05(13)	-	
Interval III (1)	1.68	0.63	6.13	3.12	-	-	-	9.80(16)	125.96(19)	
Interval III (2)	1.68	0.64	6.25	3.00	0.16	12.44	-8.58	0.87(13)	-	

Figure 8.4 (b) shows the rms measured for every phase bin as described in Sec. 8.2.2.2. Although we calculated the rms in two frequency ranges (0.006 – 0.1 Hz and 0.1 – 521 Hz), we only report the low-frequency segment since the high-frequency rms is massively dominated by the instrumental noise of the detectors. There are hints for rms phase dependency in the three intervals, where the rms maximum always appears in the bin 0.0 – 0.1. We note, however, that the overall rms of Interval III is considerably lower than in the other two intervals. Indeed, in Fig. 8.4 (b) Interval III rms is displayed multiplied by a factor 5 to facilitate the inspection of the curve as compared with the other two intervals. We could not identify a clear reason why the variability in this interval is overall significantly lower than in the others, although we speculate that this behaviour could be attributed to the degradation of the instruments over time. Overall, the bumps in the rms seems to occur near the minimum of the X-ray flux (or light curve count rate), although the large uncertainties prevent us to firmly establish the presence of any statistically significant correlation with phase. A constant fit gives in this case  $\chi^2_{\nu} = 1.62(19)$  for Interval I,  $\chi^2_{\nu} = 2.35(19)$  for Interval II and  $\chi^2_{\nu} = 2.49(19)$  for Interval III. This means that, at least for Interval I (where error bars are larger), the low-frequency rms is statistically compatible with a constant, but Interval II and Interval III show weak variability. In order to investigate the goodness of the correlation between the X-ray flux and the rms, we have estimated the Spearman’s rank correlation coefficient [Zwillinger and Kokoska 2000], using data from all intervals together. The test

yields  $\rho = -0.4$ , which indicates a weak negative correlation, but it can be increased up to  $\rho = -0.6$  considering only data from Interval I (which is however affected by larger uncertainties).

The X-ray flux (in units of  $\text{erg}/\text{cm}^2/\text{s}$ ), which has been extracted in the energy range 4.0–10.0 keV assuming an error of 10% to be conservative with the response of the instrument, is shown in Fig. 8.4 (c). As expected, the modulation of the flux is consistent with the count rate modulation seen in Fig. 8.4 (a) for all intervals. The flux shows a minimum in the bin 0.1–0.2 ( $0.59 \pm 0.06 \times 10^{-11}$   $\text{erg}/\text{cm}^2/\text{s}$ ) and 0.8–0.9 ( $0.58 \pm 0.06 \times 10^{-11}$   $\text{erg}/\text{cm}^2/\text{s}$ ) for Interval I, in the bin 0.4–0.5 for Interval II ( $0.66 \pm 0.07 \times 10^{-11}$   $\text{erg}/\text{cm}^2/\text{s}$ ), and in the bin 0.1–0.2 for Interval III ( $0.68 \pm 0.07 \times 10^{-11}$   $\text{erg}/\text{cm}^2/\text{s}$ ). The maximum flux occurs at 0.4–0.5 for Interval I ( $1.46 \pm 0.015 \times 10^{-11}$   $\text{erg}/\text{cm}^2/\text{s}$ ), at 0.7–0.8 for Interval II ( $1.11 \pm 0.11 \times 10^{-11}$   $\text{erg}/\text{cm}^2/\text{s}$ ), and at 0.8–0.9 for Interval III ( $1.34 \pm 0.13 \times 10^{-11}$   $\text{erg}/\text{cm}^2/\text{s}$ ). As in Fig. 8.4 (a), there is a second peak at bin 0.9–1.0 for Interval I ( $0.96 \pm 0.10 \times 10^{-11}$   $\text{erg}/\text{cm}^2/\text{s}$ ) and at bin 0.1–0.2 for Interval II ( $0.93 \pm 0.09 \times 10^{-11}$   $\text{erg}/\text{cm}^2/\text{s}$ ), which provides more significance to the two-peak light-curve modulation.

Figure 8.4 (d) shows the evolution of the source photon index as a function of phase. The photon index is anti-correlated with respect to both the count rate and the X-ray flux, being maximum near the first and last bins for our three intervals. This anti-correlation becomes evident when the photon index is plotted as a function of the flux, as shown in Fig. 8.5. In order to investigate the goodness of this correlation, we have also estimated the Spearman’s rank correlation coefficient, using data from all intervals together. The test yields  $\rho = -0.87$ , which indicates a strong anti-correlation. The linear fits to the data have slopes  $-1 \pm 0.3$  ( $\chi^2/\text{dof}=6.21/7$ ) for Interval I,  $-0.81 \pm 0.3$  ( $\chi^2/\text{dof}=3.85/8$ ) for Interval II and  $-0.59 \pm 0.2$  ( $\chi^2/\text{dof}=7.85/8$ ) for Interval III, such that the slope experiences a smooth flattening from the former to the latter interval.

In Fig. 8.6, we show a collection of PDS for the ten phase bins calculated with the entire data set. Save for low-frequency red noise below 0.1 Hz, there are no statistically significant features in any of the PDS we extracted (i.e., other types of broad-band noise or QPOs). There is only a weak narrow feature that looks more prominent in the bin  $\phi = 0.7–0.8$ , at  $f \sim 0.08$  Hz. However, a Lorentzian fit of the feature gives no statistical significance ( $\sim 2\sigma$ ).

A collection of energy spectra, also for the entire set of observations, is given in Fig. 8.7. In the plots, we have represented the two power-law components (black dashed line) and the combined statistical model (red solid line). In

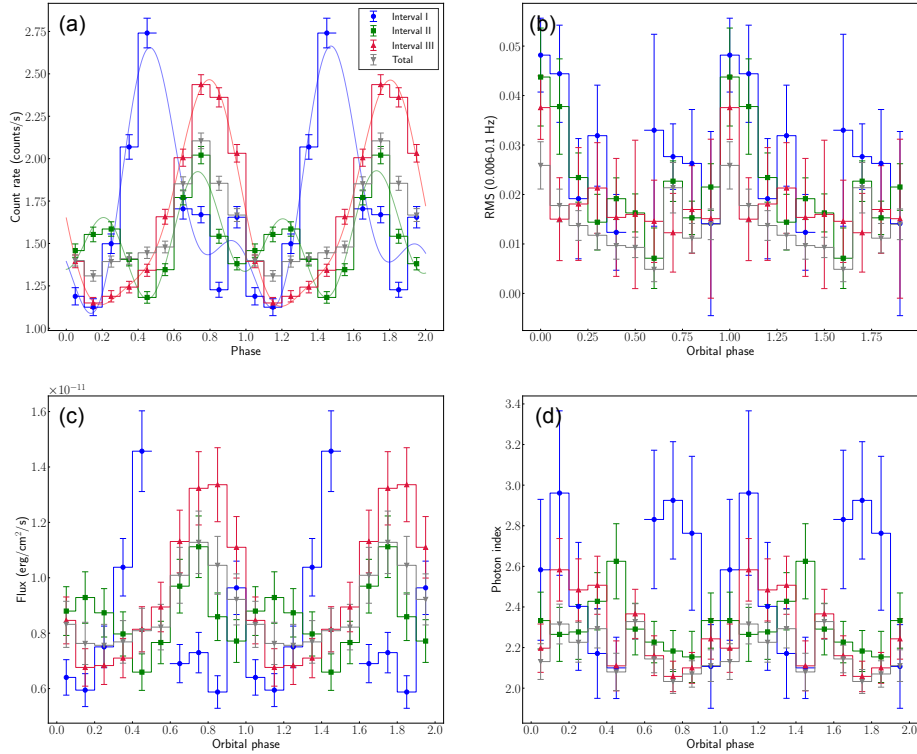


Figure 8.4 RXTE/PCA data vs. phase: (a) light curve count rate (counts/s) over-plotted with the best sinusoidal fitting shown in Tab. 8.2, (b) low frequency rms (0.006-0.01 Hz). In Interval III, the rms is multiplied by a correcting factor of 5 (c) 4-10 keV flux ( $\text{erg}/\text{cm}^2/\text{s}$ ), (d) photon index. There is a gap in Interval I because of lack of data in the phase bin 0.5 – 0.6.

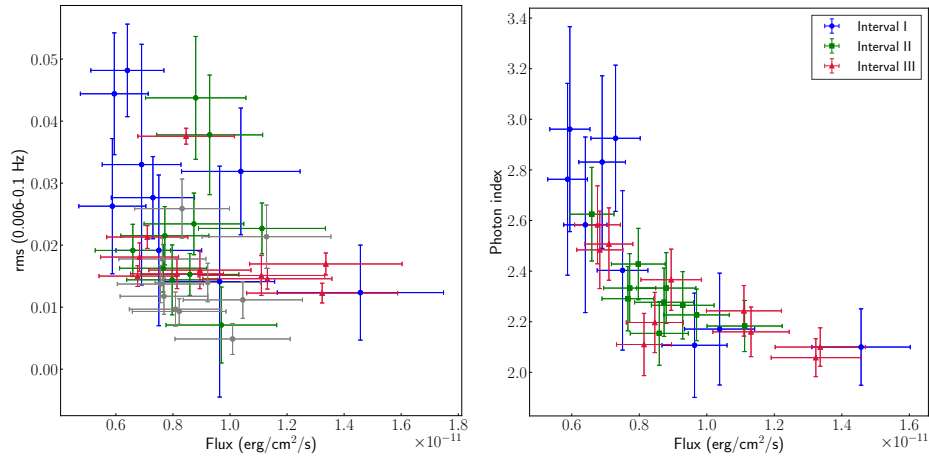


Figure 8.5 Left: Fractional rms in 0.006 – 0.1 Hz vs. 4-10 keV flux. Right: Photon index vs. 4-10 keV flux, where data shows a negative strong correlation.

general, energy spectra pertaining to different phase bins do not show significant variations.

### 8.3 Discussion

The  $\gamma$ -ray binary LS I +61°303 has been extensively studied at different wavelengths since its discovery more than sixty years ago. However, the nature of the CO and the reasons for its peculiar behavior, unique among other galactic binaries, are still debated.

In this work, we have analysed all the available RXTE/PCA X-ray data of LS I +61°303, i.e. over 500 individual observations taken between 1996 and 2011, in order to investigate the spectral and fast time variability of the binary. Since LS I +61°303 is a faint source that shows a clear phase modulation, we performed a phase-resolved analysis folding on its intrinsic period to calculate averaged energy spectra and PDS with enhanced S/N. For the sake of full consistency, we measured the periodicity in the RXTE/PCA data in order to avoid biases by adopting previous estimates of the period obtained in other energy bands, or by other instruments in X-rays. Since significant time variations in the X-ray modulation have been reported in previous studies [see e.g., Torres et al. 2010, Li et al. 2011], our analysis was performed considering three different intervals (see Tab. 8.1). The number of divisions, and thus the time length of each interval, aims to blur any possible trend in the data, but keeping an acceptable S/N for the analysis, as explained in Sec. 8.2 of this chapter.

The results of the three timing methods described in Sec. 8.2.1 are shown in Tab. 8.3, together with a list of periodicities found in the literature, at different wavelengths and within the time interval 26-27 days. For each value, we report the energy band, instrument and statistical method used to determine the period. Even though the results of Torres et al. 2010 using RXTE/PCA data (i.e.,  $P = 26.68 \pm 0.58$  days) and Ray et al. 1997 based on GBI radio observations (i.e.,  $P = 26.69 \pm 0.02$  days) are the closest to our central period, all the results reported in Tab. 8.3 are compatible with our measurements within  $1\sigma$ , so we cannot exclude that our period is respectively higher or lower than the well-defined orbital [Gregory 2002] and precession periods [Wu et al. 2018]. Nevertheless, we note that despite the high frequency resolution of our dataset, the LS periodogram does not show a double peak distribution as found in radio [see e.g., Massi and Jaron 2013] or in hard X-rays from Swift/BAT survey data [D’Aì et al. 2016].

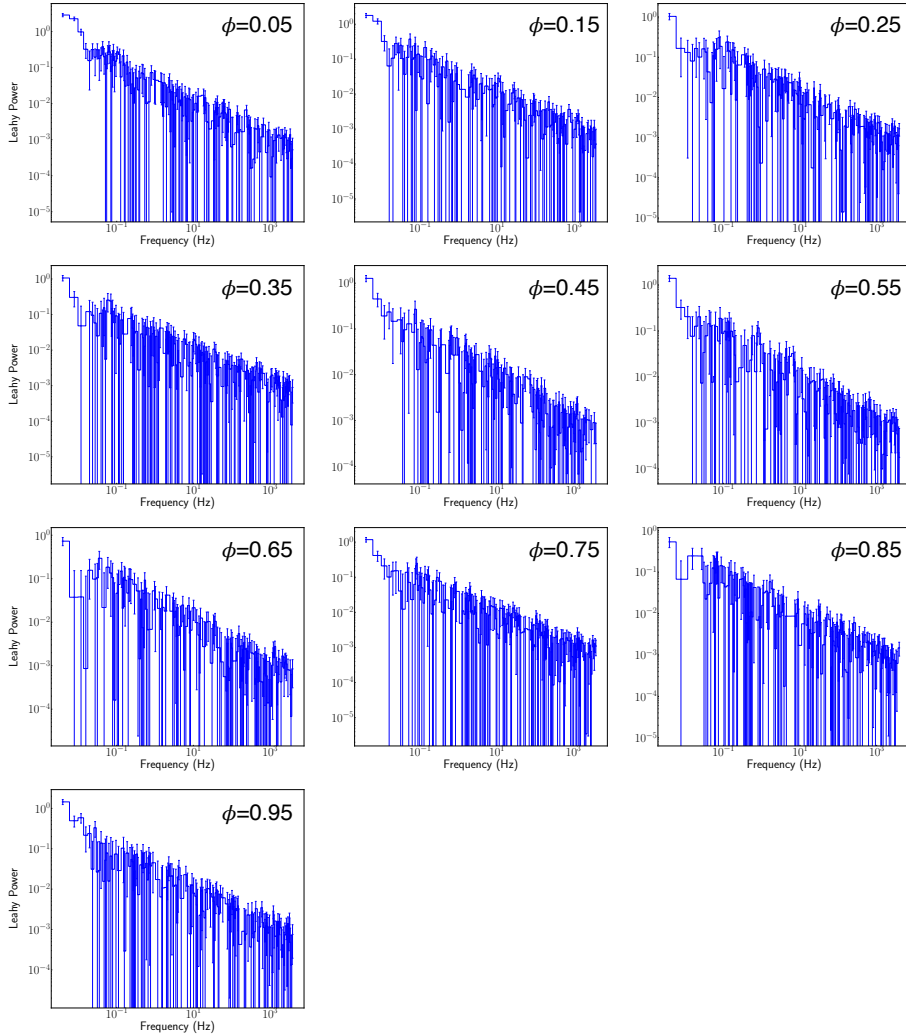


Figure 8.6 Leahy normalized Poisson noise-subtracted PDS averaged on ten phase bins using the entire X-ray dataset. The signal from the source is significant only below 0.1 Hz, above which all PDS are dominated by the instrumental noise.

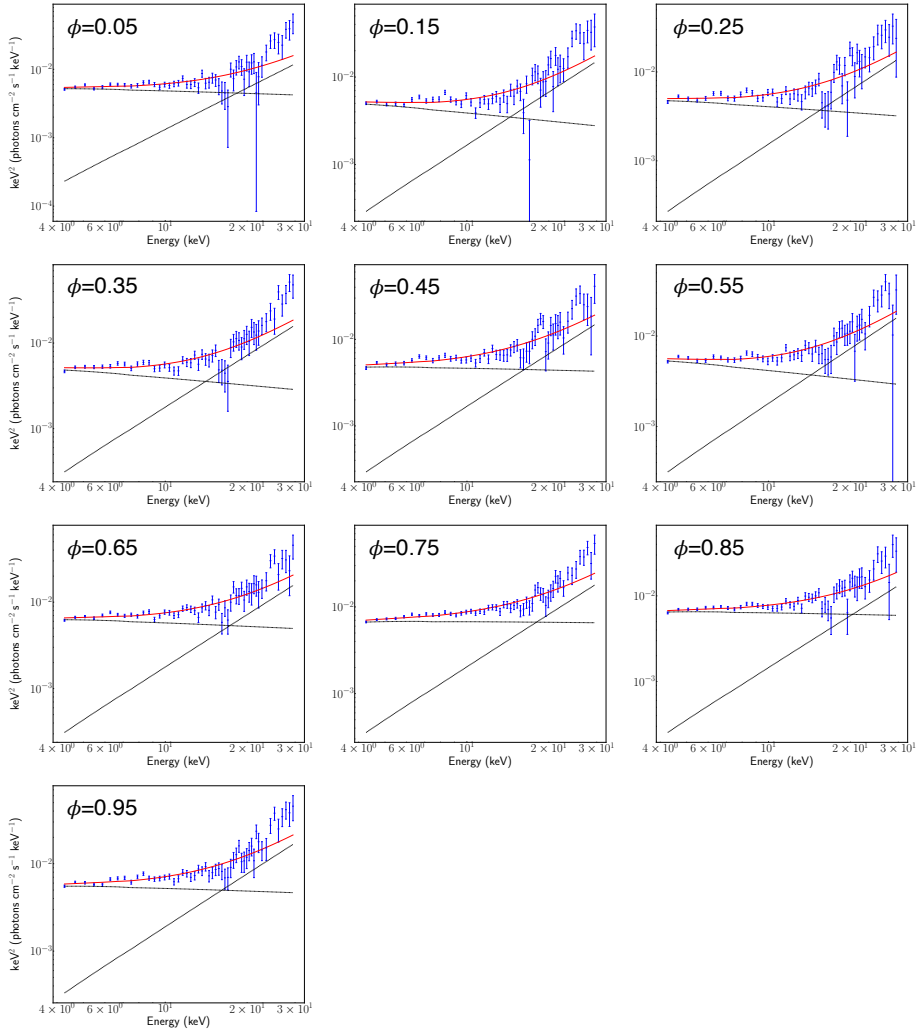


Figure 8.7 Energy spectra averaged on ten phase bins using the entire X-ray dataset. The statistical model (solid red line) results from the combination of three model components: the interstellar photoelectric absorption and two power-laws (dashed black lines).

Table 8.3 Summary of LS I +61°303 periodicities found in the literature in the range 26-27 days for different instruments and energy wavelengths. For each result, we show the statistical method by which the periodicity was calculated.

Reference	Period (days)	Error	Energy band	Instrument	Statistical method
This work	<b>26.65</b>	$\pm 0.28$	<b>X-ray</b>	<b>RXTE/PCA</b>	<b>LS Periodogram</b>
	<b>26.63</b>	$\pm 0.26$	<b>X-ray</b>	<b>RXTE/PCA</b>	<b>PDM</b>
	<b>26.62</b>	$\pm 0.30$	<b>X-ray</b>	<b>RXTE/PCA</b>	<b>Sinusoidal fit</b>
Jaron et al. 2018	26.45	$\pm 0.05$	$\gamma$ -ray	Fermi-LAT	LS Periodogram
Leahy 2001	26.99	$\pm 0.05$	$\gamma$ -ray	Fermi-LAT	LS Periodogram
Torres et al. 2010	26.42	$\pm 0.05$	X-ray	RXTE/ASM	Epoch folding
D’Ai et al. 2016	26.68	$\pm 0.58$	X-ray	RXTE/PCA	Power spectrum
	26.47	$\pm 0.10$	X-ray	Swift/BAT	LS Periodogram
	26.93	$\pm 0.10$	X-ray	Swift/BAT	LS Periodogram
Ray et al. 1997	26.69	$\pm 0.02$	Radio	GBI	Linear fitting
Gregory 2002	26.496	$\pm 0.0028$	Radio	GBI	Gregory-Loredo Bayesian
Massi and Jaron 2013	26.70	$\pm 0.05$	Radio	GBI	(Aparent)
Massi and Torricelli-Ciamponi 2016	26.496	$\pm 0.013$	Radio	GBI	LS Periodogram
	26.935	$\pm 0.013$	Radio	GBI	LS Periodogram
Wu et al. 2018	26.926	$\pm 0.005$	Radio	VLBA	Pattern alignment
Zamanov et al. 2013	26.502	$\pm 0.007$	Optical H $\alpha$	RCC/Coude	PDM/CLEAN

One interesting outcome of our analysis, shown in Fig. 8.4, is that the light curve peak is phase shifted ( $\Delta\Phi \sim 0.3$ ) from Interval I to Interval II/Interval III. As expected, the same behaviour is seen both in the light-curve and in the flux. This is consistent with the fact that the X-ray light-curve modulation changes with time, as previously reported by other authors [Torres et al. 2010, Li et al. 2011]. Using radio data, Gregory 2002 also reported a super-orbital period in the radio band,  $P_{\text{long}} = 1667 \pm 8$  days [see also Jaron 2021, for a discussion of this long-term modulation across the electromagnetic spectrum]. Li et al. 2011 could not detect such modulation in the system flux history, but Li et al. 2012 found evidence for the existence of this period using the longest RXTE/PCA continuous monitoring of LS I +61°303. Thus, since we do not apply any specific correction, it is plausible that the underlying long-term periodicity –if really present in the X-ray data– phase-shifts the peak of the light curve from Interval I to Interval II, inasmuch as there is a time gap of 10 years between both intervals. Although the study of the super-orbital period is beyond the scope of the thesis, the LS periodogram does not show any signal at that period, likely because our dataset is not long enough to properly sample such a long-term periodicity using Fourier techniques. Moreover, we have checked that no significant super-orbital phase modulation appears when folding the light-curve with this long period using the same methodology described in Sec. 8.2.2.1

Regarding phase modulation, theory and numerical modelling predicts two main peaks in the accretion rate of LS I +61°303 [Bosch-Ramon et al. 2006, Romero et al. 2007], each of which should be followed (assuming the microquasar model) by an ejection of particles in the form of a jet that will emit non-thermal synchrotron radiation. According to the statistical models shown in Tab. 8.2, all intervals are better approximated by a sum of two sinusoids. This is especially relevant for Interval II (where the amplitude of the main peak at phase  $\theta = 0.7$  is lower than in the other two intervals), while in Interval I the secondary peak at  $\theta = 0.95$  is narrower. In this case, the relevance of the secondary peak is supported by a flux local maximum (Fig. 8.4, c) together with a deep of the photon index (Fig. 8.4, d). Moreover, the phase shift between the primary and secondary peak is similar for Interval I and for Interval II,  $\sim 0.5$ . In the X-ray energy range, the light-curve displayed in Fig. 2 of Smith et al. 2009 using RXTE/PCA data (taken every other day between 2007 August 28 and 2008 February 2, so it is enclosed in our Interval II) shows a similar phase modulation and a similar ratio between the amplitude of the two accretion peaks. Nevertheless, the authors concluded that there was no statistically strong detection of modulation of the flux with the orbital phase. Later, Torres et al.

2010 showed that the two-peak structure evolves into a more clearly visible, single-peaked light curve analysing individual six month periods that partly covered our Intervals II and III. This is also consistent with the fact that the secondary peak is only marginally detected in the light-curve of Interval III. Massi et al. 2020 also found the two-peak light curve analysing Swift-XRT, XMM-Newton and NuSTAR data taken on July 2017, showing that radio and  $\gamma$ -ray peaks are coincident with X-ray dips as expected for emitting ejections depleting the X-ray emitting flow. Therefore, RXTE/PCA observations confirm the two-peak light-curve predicted by previous accretion models for LS I +61°303. However, our results suggest that either this behaviour is a transient feature of the source, or the amplitude of the secondary peak varies with time.

We also confirm the findings of Li et al. 2011, who reported that an anti-correlation between the flux and the spectral index is an orbit-associated effect, and that this correlation holds in time in a rather stable way. The slopes we found for our three intervals are steeper than the ones reported in Li et al. 2011. A plausible explanation for such distinction, besides the differences in the dataset, resides in the different spectral models that we used in this work; we fitted the energy spectra between 4 and 30 keV with a combination of two power laws, while Li et al. 2011 only consider the 3-10 keV energy range.

Following the approach we described in Sec. 8.2.2.2, we performed the timing analysis of the entire LS I +61°303 RXTE/PCA data in a phase-resolved manner, producing average PDS for a set of ten bins, in order to investigate the presence of timing features in the PDS and, particularly, its possible connection with the source periodicity. We did not split the dataset in the three intervals described above in an attempt to improve the (limited) S/N in the PDS. The recent discovery of transient radio pulsations by Weng et al. 2022 implied the possibility of the detection of pulsations or quasi-periodic modulations in the X-ray lightcurves. Nevertheless, despite the high-resolution provided by the RXTE/PCA Good Xenon data, the PDS shown in Fig. 8.6 do not exhibit any statistically significant coherent pulsation, QPO nor other type of broad-band component, aside from a very weak red noise component at low frequencies. The absence of timing features in the PDS is consistent with previous studies [see e.g., Rea et al. 2010, a 95 ks Chandra observation, using the ACIS-S camera in continuous clocking mode].

According to the literature, there are three potentially interesting characteristic frequencies to search for timing signals: (I) Weng et al. 2022 reported the existence of transient radio pulsation from the direction of LS I +61°303 with frequency  $f = 3.715$  Hz (i.e.,  $P = 269.15508 \pm 0.00016$  ms), with a significance

$> 20\sigma$ . This is the first statistically significant evidence of pulsations from the source at any frequency. (II) During a RXTE monitoring of LS I +61°303 and by a spectral analysis of a period of strong variability, Ray and Jacob M. Hartman 2008 suggested the existence of a strong red-noise component and an apparent QPO at  $f = 2$  Hz [see also, Massi and Zimmermann 2010]. Indeed, Smith et al. 2009 and Li et al. 2011 presented a detailed timing analysis of the LS I +61°303 main flares, showing that one of them seemed to reveal a tentative QPO at  $f \sim 2$  Hz. Nevertheless, the authors concluded that the feature was not statistically significant. (III)  $P_{\text{spin}} \sim 11$  s ( $f \sim 0.09$  Hz), which is the frequency of the neutron star predicted by the Corbet diagram [Zamanov et al. 2013] and that seems to be valid for wind-fed sources.

Given the detection of a pulsation reported in Weng et al. 2022, we investigated the PDS feature which is visible in phase  $\phi = 0.7$ , at frequency  $0.08 - 0.09$  Hz (Fig. 8.6). The fitting of the PDS does not return any significant narrow component ( $< 2\sigma$ ), and therefore we conclude that this feature is possibly the result of statistical fluctuations.

The rms shows a moderate modulation with the phase, especially for Interval I and Interval II. In Interval III, the rms also shows a tentative phase modulation, but the profile is severely flattened with respect to the first two intervals. As we show in Fig. 8.4, the rms maxima coincides with the dips of X-ray flux (and count rate), which is maximum in the first phase bin for all intervals, and interestingly, in those bins that gather the largest flares of the source (see Fig. 8.3). However, the possibility that the rms is modulated by the presence of flares seems unlikely, since as described in Sec. 8.2.2.2 outliers are removed by a specific GTI selection. Our results show that the rms tend to decrease when the flux increases and *vice-versa*, which is typical of accreting systems such as low-mass X-ray binaries (LMXBs), where higher fluxes corresponds to lower variability levels due to the increased contribution of non-variable photons from the optically thick, geometrically thin accretion disc. However, increased fluxes also correspond to softer spectra in such systems. But in the case of LS I +61°303, save perhaps for Interval I, higher fluxes correspond to harder spectra (i.e., lower photon index). This behaviour does not necessarily exclude the possibility of an accretion disk around LS I +61°303, but suggests that – if present – the disc around the CO in LS I +61°303 must have peculiar properties that make it different from the discs usually observed in LMXBs (e.g., it is particularly small compared to the size of the system, and possibly warped).

## 8.4 Summary and conclusions

We have analysed all the archival RXTE/PCA X-ray data of LS I +61°303, taken between 1996 and 2011, in order to investigate the rapid X-ray time variability of the source. Using the intrinsic period found by timing techniques, we performed the phase-resolved analysis of the data, obtaining a set of phase-bin-averaged energy spectra and PDS. In the following, we summarise our main conclusions:

- We have searched for the RXTE/PCA intrinsic period using three independent timing techniques: (1) the LS periodogram, (2) the PDM method and (3) amplitude maximisation with sinusoid fitting in the time domain. All three methods yielded a period  $P \approx 26.6 \pm 0.3$  days, compatible within  $\sim 1\sigma$  with either the orbital period and the precession period. Thus, this dataset does not allow us to distinguish between them. This result is consistent with previous estimations using RXTE/PCA data.
- The phase-averaged PDS do not show any statistically significant periodic or aperiodic signal, aside from a weak red noise component at low frequencies. The amplitude of such noise component shows a moderate phase dependence, although no strong correlation along all phases could be found. Our results also show that the rms tends to decrease when the flux increases, something which is typical of accreting binary systems. Moreover, in agreement with previous studies, the flux is anti-correlated with the photon index, meaning that higher values of rms are also related with softer spectra. This may indicate the presence of a small accretion disc in the system.
- The data show a clear phase modulation. A significant phase shift between the X-ray flux peak of Interval I and Intervals II/III is evident. Such a shift could be possibly explained as an effect of a super-orbital periodicity, which might also underlay the data, albeit not shown in the periodograms.
- At least in one of the data intervals that we considered for the analysis we find a well-resolved two-peak phase-folded light-curve. The absence of a second peak in Interval III suggests that this feature is either transient or variable, which at times might cause smearing in the light-curve.
- Our timing analysis does not shed light on the nature of the system, nor on the type of CO that powers the binary. Therefore, further observations of LS I +61°303 in the X-ray energy range are required to investigate the source behaviour in deeper detail.

# Timing analysis of Scorpius X-1 with NICER data

## 9.1 Introduction

Neutron Star Low-mass X-ray binaries (NS LMXBs) are stellar binary systems in which the compact object (CO; i.e., the accretor) is a NS orbiting a low-mass companion (i.e., the donor). Based on their spectral and timing properties, they are classified in two main categories: Z-type sources and atoll-type sources [Hasinger and van der Klis 1989], where the nomenclature refers to the characteristic shape that NS LMXBs trace in the X-ray colour-colour diagram (CD). In particular, Z-type sources are the most luminous, which are believed to accrete near or at the Eddington rate. In the CD, they trace a characteristic Z-like shape where we can distinguish three separate branches: the horizontal branch (HB), the normal branch (NB) and the flaring branch (FB), named from top to bottom according to the position in the diagram. A hard apex (HA) separates the HB and the NB, and a soft apex (SA) separates the NB and the FB. These branches represent specific accretion states of the system, where these sources show rapid transitions from different phases in very short time [Muñoz-Darias et al. 2014]. Moreover, all known Z-type NS LMXBs are persistent radio emitting sources, where radio luminosity also varies as a function of the state in the CD [Penninx et al. 1988, Hjellming et al. 1990a]. This variability is thought to be physically related with changes in the accretion flow, exhibiting a disc-jet coupling behaviour similar to LMXBs hosting a stellar-mass black hole [BH; Migliari and

Fender 2006]. The power density spectrum (PDS) of Z-type NSs also changes from one accretion state to another [i.e., Méndez and van der Klis 1999], showing different type of quasi-periodic oscillations (QPOs) that can be classified in two main categories: kHz QPOs, detected isolated or in pairs above 500 Hz [i.e., van der Klis 1989], and low-frequency QPOs, usually appearing below  $\sim 50$  Hz. The latter are further divided in three different types, depending on the branch of the CD where they are detected: horizontal branch oscillations (HBOs), normal branch oscillations (NBOs) and flaring branch oscillations [FBOs; van der Klis 1989]. These are typically referred, respectively, as the NS equivalent of type C, type B and type A QPOs found in BH systems [e.g., Ingram and Motta 2019].

The X-ray binary (XRB) Scorpius X-1 (hereinafter, Sco X-1) is one of the most studied XRBs since its discovery in 1962 [Giacconi et al. 1962], and the brightest extrasolar X-ray source in the sky, located at a distance of  $2.8 \pm 0.3$  kpc [Bradshaw, Fomalont, and Geldzahler 1999] in the constellation of Scorpius. It is classified as a LMXB with an orbital period of 18.9 h [Gottlieb, Wright, and Liller 1975], containing a later than K4 spectral type companion star ( $0.28M_{\odot} < M < 0.70M_{\odot}$ ) and a weakly magnetised NS with mass  $< 1.73 M_{\odot}$  [Mata Sanchez et al. 2015]. Regarding the spectral properties of the binary, it is one of the few known examples of Z-type sources (together with GX 349+2, GX 340+0, GX 17+2, GX 5-1, Cyg X-2 and the peculiar system Cir X-1), showing extended radio luminous ejecta [i.e., radio lobes; Fomalont, Geldzahler, and Bradshaw 2001a].

During the last decades, extensive X-ray observations of Sco X-1 with different instruments –mainly the European X-ray Observatory Satellite (EXOSAT) and the Rossi X-ray Timing Explorer (RXTE)– have explored the timing properties of the source and the transition of different types of low frequency QPOs along the three spectral states [see e.g., Titarchuk, Seifina, and Shrader 2014, and references therein]. Using EXOSAT observations, Middleditch and Priedhorsky 1986 first discovered a  $\sim 6$  Hz QPO while the source was quiescent. Priedhorsky et al. 1986 later proved that the QPO was anti-correlated with intensity, while during an active state the QPO frequency varied from 10 to 20 Hz, exhibiting a positive correlation. In particular, the transition between an active (FB) and a quiescent state was characterised by variations in the QPO frequency between 6 and 16 Hz on very short time scales, with no intensity correlation [van der Klis et al. 1987]. Based on previous findings, Dieters and van der Klis 2000 also investigated all power spectral properties of low-frequency QPOs and noise components as a function of the position in the CD. They also found an abrupt increase of the QPO frequency from 6 to 10 Hz, the so-called rapid

excursions near the SA in the hardness–intensity diagram (HID), along with grand transitions from 8 Hz to 21 Hz when the object goes from the lower FB to the upper FB. Similarly, but using RXTE data, van der Klis et al. 1996 reported the discovery of  $\sim 45$  Hz QPOs, which were most prominent in the NB, and (sub)millisecond oscillations (the so-called kHz QPOs) that correlate with the frequency of the well-known 6–20 Hz QPOs in the NB/FB. Casella, Belloni, and Stella 2006 also reported the first resolved rapid transition from a FBO to a NBO and showed a monotonic (smooth) increase of the QPO centroid frequency from 4.5–7 Hz (at the NB) to 6–25 Hz (at the FB).

Sco X-1 has been largely studied at different wavelengths. In the radio band, Fomalont, Geldzahler, and Bradshaw 2001a showed that the radio structure of Sco X-1 is composed by a radio core and two symmetric radio lobes. In Fomalont, Geldzahler, and Bradshaw 2001b, the authors reported for the first time the existence of ultra-relativistic outflows (URFs) in the system, inferred by correlating X-ray flares in the core with subsequent radio flares in the approaching and receding lobes. These new type of fast flows, whose origin and physical properties are still unclear, have been also observed in two more XRBs, namely Cir X-1 (Fender, Belloni, and Gallo 2004, Tudose et al. 2008, but see also Miller-Jones et al. 2012) and SS 433 [Migliari et al. 2005], where URFs were proposed as an explanation of the rapid variability observed by Chandra on the extended X-ray emission [but see also Miller-Jones et al. 2008]. More recently, Motta and Fender 2019 reanalysed RXTE data of Sco X-1 and suggested that these type of outflows were related with the appearance of a particular class of QPO in the PDS, while radio emitting outflows seemed to be associated with flat-top broad-band noise components. In particular, the authors found evidence that URFs ejections occur when both the NBO and HBO were present in the X-ray power spectrum. This indicated that the ejection of URFs might be connected with specific changes in the accretion flow, but due to the low number of these events, new X-ray observations are strongly needed to confirm this result.

From 21 to 25 February 2019, an extensive multi-wavelength campaign was organised to monitor Sco X-1 with different instruments, providing the largest simultaneous coverage at all possible wavelengths with radio (VLBI and VLA), optical/IR (SALT, VLT, NOT and TNG), X-ray (NICER, Chandra, XMM-Newton) and  $\gamma$ -ray (INTEGRAL) observations (see Fig. 9.1). In the X-ray energy range, the large collecting area of the NICER observatory [Gendreau, Arzoumanian, and Okajima 2012], together with its ability to properly handle the high count rates of the source, provided the highest quality data of the X-ray instruments involved in the campaign.

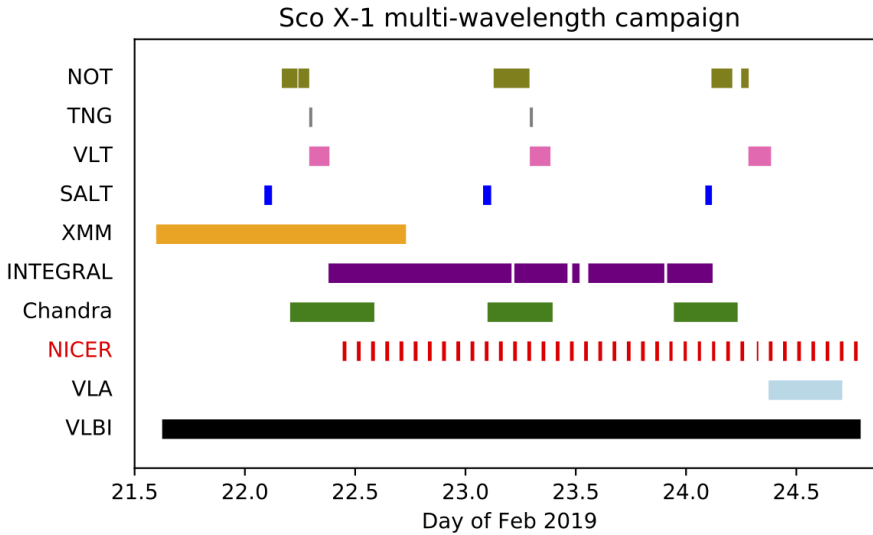


Figure 9.1 Coverage by NICER together with other telescopes/instruments at different wavelengths involved in the massive campaign to monitor Sco X-1 in 2019. Credit: NASA.

In this chapter of the thesis, I present an analysis of the timing properties of Sco X-1 using NICER observations performed in the February 2019 multi-wavelength campaign. I will mainly focus on the different type of LF QPOs that appear in the dataset, specially how the characteristics of these QPOs (specially the central frequency) change along the position in the HID. This constitutes the first comprehensive analysis of Sco X-1 based on NICER X-ray observations.

The chapter is organised as follows: In Sec. 9.2 we describe the NICER observations and the methodology we follow to produce a light-curve, the HID and the (dynamical) PDS. In Sec. 9.3, we present the main results of the timing analysis. Finally, in Sec. 9.4, we discuss our results, we present our preliminary conclusions and we establish the basis for extending our analysis in future work.

## 9.2 Observations and data analysis

### 9.2.1 MAXI

We first produced a light-curve and a HID using MAXI data taken from 01-02-2019 to 31-03-2019, using the MAXI/GSC on-demand web interface<sup>1</sup> [Matsuoka et al. 2009]. We analyse data extracted within a circular region of  $1.6^\circ$  radius

<sup>1</sup><http://maxi.riken.jp/mxondem/>

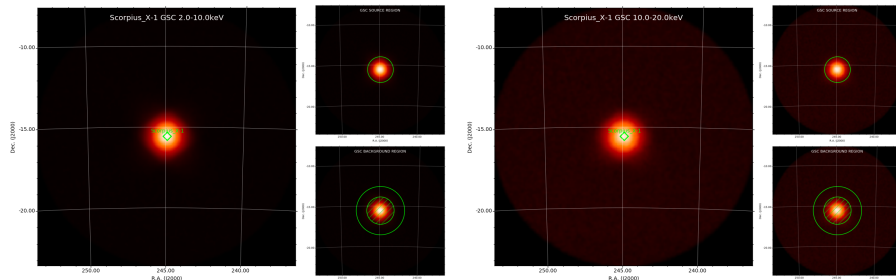


Figure 9.2 GSC 2-10 keV (left) and 10-20 keV (right) MAXI images of Sco X-1.

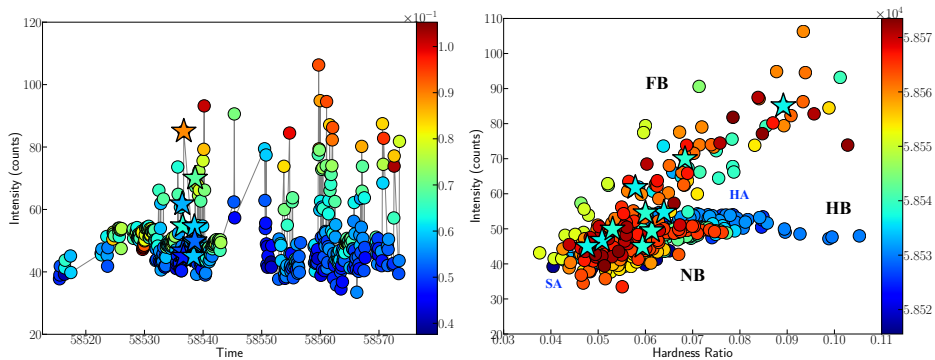


Figure 9.3 Light-curve (left) and HID (right) of Sco X-1 using MAXI data taken from 01-02-2019 to 31-03-2019 with a time resolution of 0.04 days. The light-curve is coloured by the  $HR=B/A$  and the HID by the exposure time. Data taken from 22-02-210 and 24-02-2019 is represented with star markers. The location of the three branches (HB, NB, FB) and their transitions (HA, SA) are overlaid on the plot.

around the source position (244.979455, -15.640283), where background region was extracted in a concentric ring with outer radius of  $3^\circ$  (see Fig. 9.2). The bin size is 1 hour (i.e., 0.04 days). In order to calculate a hardness ratio (HR), light-curves were extracted in two energy bands: 2-10 keV (A) and 10-20 keV (B).

Figure 9.3 shows the light-curve coloured by HR (A+B, in units of counts; top) and the HID coloured by time (B/A vs. A+B; bottom). Data taken simultaneously to NICER during the multi-wavelength campaign (from 22 February 2019 to 24 February 2019) is represented with star markers. The three branches of the Z-track are indicated on the plot, showing that data taken with MAXI simultaneously to NICER is mainly located in the NB, near the SA. Two main incursions into the FB (one up to  $HR \sim 0.09$ ) are observed in the light-curve and in the HID.

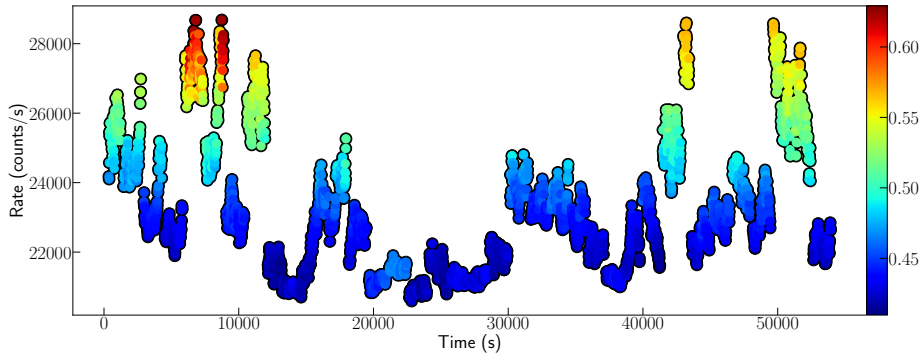


Figure 9.4 Light-curve (in units of counts/s) for the entire dataset, including the three individual NICER observations. Color scale represents the hardness ratio, defined as  $HR=B/A+C/A$ .

## 9.2.2 NICER

The NICER dataset is composed by three different observations identified with proposal number 110803010 (Obs 1), 1108030111 (Obs 2) and 1108030112 (Obs 3). For each observation, we used the unfiltered merged Measurement/Power Unit (MPU) Science data (available in the path `/xti/event_cl/`) and performed the standard cleaning using the task `NICERCLEAN` (Heasoft v6.28). As in Chapter 8, data analysis (including light-curve and PDS extraction) was performed using the General High-energy Aperiodic Timing Software (GHATS)<sup>2</sup>.

### 9.2.2.1 Light-curve and Hardness-Intensity diagram

We produced a light-curve (Fig. 9.4) and a HID (Fig. 9.5) employing 13s-long time bins from the three NICER observations. We extracted the count rate in the energy bands  $A = [500 - 2000]$  eV,  $B = [2000 - 10000]$  eV and  $C = [10000 - 15000]$  eV, and we defined the HR as  $HR=B/A + C/A$ . In Fig. 9.4, the light-curve is displayed coloured by the HR, and we removed time gaps from the data, as well as instrumental drops at the beginning of each segment. As in the case of Fig. 9.3, the HID — for the entire dataset (top) and for each individual observation (bottom) — was produced by plotting the HR vs. the intensity (i.e., the accumulated count rate in the three energy bands, i.e.,  $A+B+C$ ), where colormap sets the total exposure time for the three observations.

<sup>2</sup>See [http://www.brera.inaf.it/utenti/belloni/GHATS\\_Package/Home.html](http://www.brera.inaf.it/utenti/belloni/GHATS_Package/Home.html).

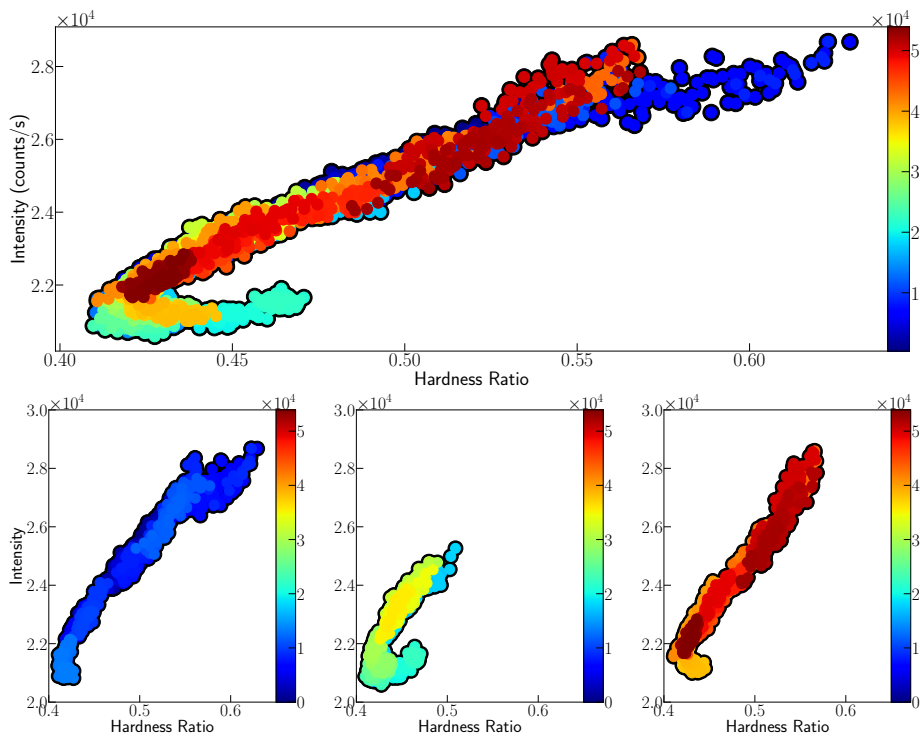


Figure 9.5 Hardness-Intensity diagram for the entire dataset (top) and for each individual observation (bottom): Obs 1 (left), Obs 2 (middle) and Obs 3 (right). Color scale represents the exposure time.

### 9.2.2.2 Power Density Spectra

We rebinned the NICER high-resolution Science mode data in time ( $\times 10^4$ ) to obtain a Nyquist frequency of 1250 Hz. Using Fast Fourier Transform (FFT) techniques [van der Klis 1989], we produced PDS for continuous 13s-long intervals and we averaged them to obtain a PDS for the whole dataset (including the three observations). Figure 9.6 shows this PDS in the traditional  $\nu, P_\nu$  representation, where we applied the Leahy normalisation [Leahy et al. 1983] and we subtracted the contribution of the Poisson noise. We fitted the PDS with the XSPEC package using a one-to-one energy-frequency conversion and a unity response matrix to allow us to fit a power versus frequency spectrum as if it was a flux versus energy spectrum. Along this work, we consider a multi-Lorentzian model plus a power law component to take into account the contribution of the Poisson noise [see e.g., Belloni, Psaltis, and van der Klis 2002].

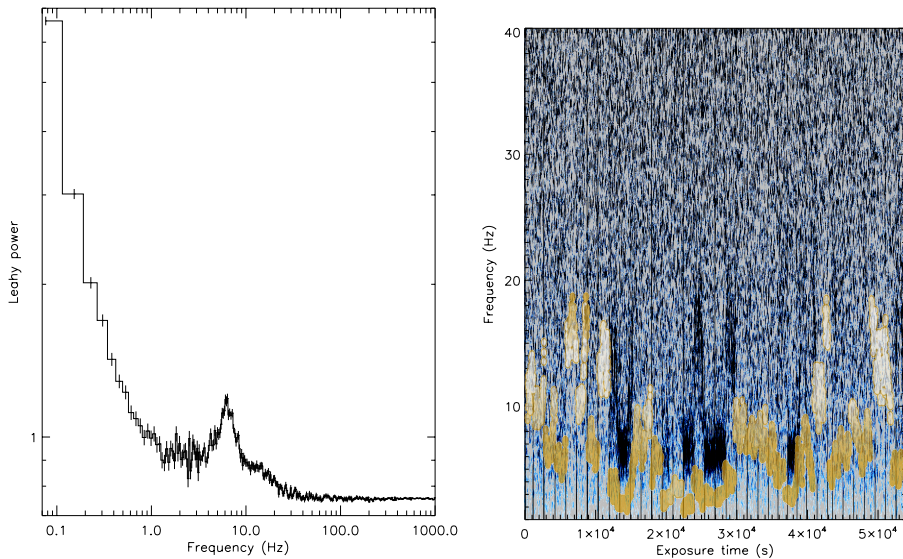


Figure 9.6 Power density spectra (left) and dynamical power density spectra (right) for the entire NICER dataset, including Obs 1, Obs 2 and Obs 3. The light-curve of the source has been rescaled and over-plotted with gold contours for the sake of comparison.

To show how the PDS changes with time, in the right panel of Fig. 9.6 we also show a dynamical PDS (i.e.,  $P_\nu$  in the time vs. frequency plane), which reveals the occasional presence of strong variability around 6 Hz (dark blue), but also weaker variability in the 6-20 Hz frequency range (light blue), which seems to be connected with the strongest signal of the source. In order to search for fainter and/or short-lived timing features, for each of the three NICER observations we divided the dataset in continuous shorter segments, based on the location of the light-curve gaps. For each of these segments, we produced a collection of PDS which result from averaging 30 consecutive 13s-long bins (i.e., 390 s), covering the total time length of the three observations. Before averaging, PDS sets containing less than 15 bins were automatically discarded. For this part of the analysis, we also removed photons in the energy range 0-750 eV in order to increase the variability of the averaged PDS.

### 9.3 Results

The light-curve shown in Fig. 9.3 (left) reveals that the source experiences frequent flaring activity along the two months of MAXI continuous monitoring, where the HID (right) shows the characteristic pattern of a NS Z-source, with a

FB, a NB and a HB (from top to bottom). In both panels, star markers represent data collected simultaneously to NICER, from 58536.4 to 58538.7 MJD. This small subset of points ( $\sim 1$  hr time bins) shows two distinct important incursions into the FB, the first one at 58536.7 MJD and the second one at 58538.6 MJD. However, the information provided by the light-curve in this time range is very limited, since no MAXI observations are available from 58536.7 to 58538.4 MJD.

The NICER light-curve of Fig. 9.4 shows these two big flares with much more resolution. Even in a flaring state, the source is very variable, showing back and forth rapid transitions along the FB (Fig. 9.5). It is also interesting to note that, despite that the main flares show approximately the same count rate ( $\sim 28000$  counts/s), the HR is higher during the first incursion. In the HID, this manifests as a fork shape in the top of the FB, with a harder –and longer– branch corresponding to the first burst, and a softer branch corresponding to the second. In the case of NICER data, the NB is generally not well resolved, and the HA can only be slightly deduced at the time of Obs 2 (bottom panel, central plot).

The PDS shown in the left panel of Fig. 9.6 is dominated by a  $\sim 6$  Hz strong QPO, showing a low-frequency red noise component below 1 Hz and flat-top noise above this frequency (aside from the QPO). We fitted the PDS with a five-Lorentzian model plus a power-law component to account for the contribution of the Poisson noise. Using this model, the central frequency of the QPO yields  $6.35 \pm 0.06$  Hz ( $\chi^2_{\nu} = 281/266$ ). This QPO is responsible for the strongest variability shown by the dynamical PDS (Fig. 9.6, right panel; dark blue), where we have rescaled and overlaid on the background the light-curve of Fig. 9.4 (gold contours). This brings to light that the strongest variability appears when the source is quiet (near the light-curve minima at  $2.0 \times 10^4$  counts/s), while rapid (and fainter) variability up to 20 Hz precedes/follows the flaring state ( $\gtrsim 2.2 \times 10^4$  counts/s).

In order to characterise these transitions along the HID, in the rest of the section I will report the results of the analysis described in Sec. 9.2, where we have computed averaged PDS every  $\sim 400$  s for the three NICER observations. Each of these PDS are fitted with a multi-Lorentzian+power-law statistical model in XSPEC, revealing a rich variety of timing features. To identify a QPO, we follow the convention of considering narrow features ( $Q > 2$ ) with sufficient statistical significance ( $> 3\sigma$ ), although a few exceptions of this rule are also accepted by establishing a new definition. On the one hand, when the Q-factor is  $Q \leq 2$ , QPOs are referred as *blurred* features. On the other hand, when the

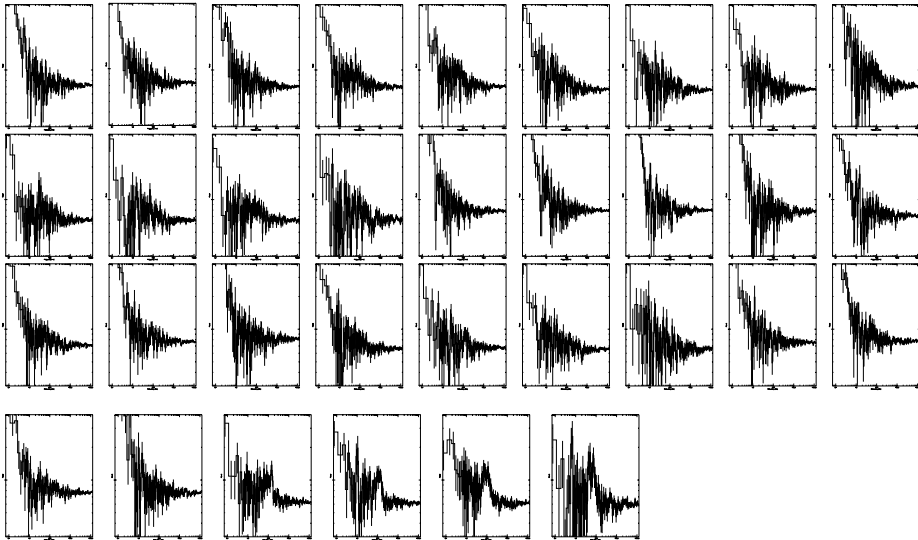
statistical significance is  $\leq 3\sigma$ , QPOs are referred as *faint* ( $2.5\sigma - 3\sigma$ ) or *hint* ( $< 2.5\sigma$ ) features.

### 9.3.1 Obs 1 (110803010)

Figure 9.7 shows the averaged PDS extracted every  $\sim 400$  s for Obs 1 (top panel), together with a dynamical PDS and a total averaged PDS for the whole length of the observation (bottom panel). All PDS were fitted in XSPEC, following the procedure described in Sec. 9.2, and we identified timing features according to the Q-factor and its statistical significance, as mentioned above. This information is gathered in Tab. 9.1, where each PDS is characterised with a unique ID that identifies the PDS number, the light-curve segment and the position of the PDS in the segment, in this order. The table also shows the start time of the bin in MJD, the specific timing events detected in the PDS, the central frequency of the LF QPOs and the location of the bins in the HID. Since in these observations the FB is by far the longest branch, in order to follow the evolution of the source in this state we divided the FB in three different frames: low FB, mid FB and high FB. Although the subset of bins that defines each PDS is generally not sparse in the HID, sometimes this division is ambiguous, for which we also consider two intermediate states: mid-low FB and mid-high FB. The characteristics of the QPOs found in this analysis (central frequency, Q-factor and significance) are displayed on Tab. 9.2.

In this first observation, the source spends most of the time in the FB, showing several transitions from the low FB to the high FB. As it is evident from the dynamical PDS of Fig. 9.7, no relevant aperiodic variability is expected during this state, and PDS are dominated by a broad-band noise component. Only one PDS (220601) shows a significant –according to our previous definition– FBO centred at 12.35 Hz, while the source was in the low FB. The strongest signal is concentrated on segment #08 (58536.961 MJD), when the source moves from the FB towards the SA. This transition is characterised by the presence of a rather blurred FBO and a NBO, which is however not well resolved in any of the PDS we have inspected. In 320803, there is a hint of an HBO at  $\sim 48$  Hz ( $Q > 14$ ), which has however very low statistical significance ( $\sim 1.75\sigma$ ). Apart from the expected LF QPOs near the SA, in three PDS located along the FB (i.e., 010001, 070202, 280703) we found a very narrow feature at  $\sim 40$  Hz. This feature is statistically significant for 010001 and 070202 ( $> 3\sigma$ ), and faint in 280703 ( $\sim 2.5\sigma$ ).

### Power Density Spectra



### Dynamical+Total Power Density Spectrum

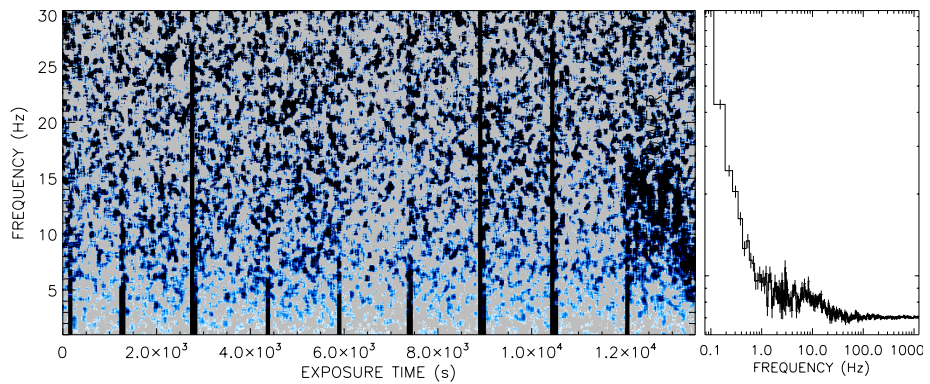


Figure 9.7 Top: PDS averaged every 390 s (i.e., 30 bins of 13 s.). Time goes from left to right and from top to bottom. Bottom: Dynamical+Total PDS of Obs 110803010. Black vertical lines show the location of time gaps.

Table 9.1 Main timing features found in the PDS shown in Fig. 9.7.

<b>Id</b>	<b>Start time (MJD)</b>	<b>Timing event</b>	<b>NBO (Hz)</b>	<b>FBO (Hz)</b>	<b>HBO (Hz)</b>	<b>HID</b>
000000	58536.450	Broad-band noise	-	-	-	FB (mid)
010001	58536.454	QPO	-	-	-	FB (mid)
020100	58536.510	Broad-band noise	-	-	-	FB (mid)
030101	58536.514	Broad-band noise	-	-	-	FB (mid)
040102	58536.519	Broad-band noise	-	-	-	FB (mid)
050200	58536.574	Broad-band noise	-	-	-	FB (low)
060201	58536.578	Broad-band noise	-	-	-	FB (low)
070202	58536.583	QPO	-	-	-	FB (low)
080203	58536.587	Broad-band noise	-	-	-	FB (mid)
090300	58536.638	Broad-band noise	-	-	-	FB (low)
100301	58536.643	Broad-band noise	-	-	-	FB (low)
110302	58536.647	Broad-band noise	-	-	-	FB (low)
120303	58536.652	Broad-band noise	-	-	-	FB (low)
130400	58536.703	Broad-band noise	-	-	-	FB (high)
140401	58536.707	Broad-band noise	-	-	-	FB (high)
150402	58536.712	Broad-band noise	-	-	-	FB (high)
160403	58536.716	Broad-band noise	-	-	-	FB (high)
170500	58536.767	Broad-band noise	-	-	-	FB (mid)
180501	58536.772	Broad-band noise	-	-	-	FB (mid)
190502	58536.776	Broad-band noise	-	-	-	FB (mid-high)
200503	58536.781	Broad-band noise	-	-	-	FB (high)
210600	58536.831	Broad-band noise	-	-	-	FB (low)
220601	58536.836	FBO	-	$12.35^{+0.69}_{-0.66}$	-	FB (low)
230602	58536.840	Broad-band noise	-	-	-	FB (low)
240603	58536.845	Broad-band noise	-	-	-	FB (low)
250700	58536.896	Broad-band noise	-	-	-	FB (mid-high)
260701	58536.900	Broad-band noise	-	-	-	FB (mid-high)

270702	58536.905	Broad-band noise	-	-	-	-	-	-	-	-	-	-	-	-	FB (mid-high)
280703	58536.909	QPO (hint)	-	-	-	-	-	-	-	-	-	-	-	-	FB (mid-high)
290800	58536.961	FBO (faint) + NBO (very blurred)	8.61 <sup>+1.21</sup> <sub>-0.98</sub>	-	-	-	14.59 <sup>+0.26</sup> <sub>-0.25</sub>	-	-	-	-	-	-	-	FB/SA
300801	58536.965	FBO (blurred)	-	-	-	-	11.82 <sup>+0.48</sup> <sub>-0.50</sub>	-	-	-	-	-	-	-	FB/SA
310802	58536.970	FBO (blurred)	-	-	-	-	9.77 <sup>+0.49</sup> <sub>-0.29</sub>	-	-	-	-	-	-	-	FB/SA
320803	58536.974	FBO + NBO (hint) + HBO (hint)	4.54 <sup>+0.14</sup> <sub>-0.19</sub>	-	-	-	7.46 <sup>+0.29</sup> <sub>-0.27</sub>	48.46 <sup>+2.89</sup> <sub>-1.51</sub>	-	-	-	-	-	-	NB/SA

Table 9.2 Centroid frequency, Q-factor and significance ( $\sigma$ ) of the QPOs found in Tab. 9.1.

Id	NBO			FBO			HBO			Other QPO		
	Freq. (Hz)	Q factor	$\sigma$	Freq. (Hz)	Q factor	$\sigma$	Freq. (Hz)	Q factor	$\sigma$	Freq. (Hz)	Q factor	$\sigma$
010001	-	-	-	-	-	-	-	-	-	38.23 <sup>+0.33</sup> <sub>-0.89</sub>	38.23*	3.30
070202	-	-	-	-	-	-	-	-	-	34.85 <sup>+0.83</sup> <sub>-0.29</sub>	34.85*	3.17
220601	-	-	-	12.35 <sup>+0.70</sup> <sub>-0.66</sub>	3.18	3.36	-	-	-	-	-	-
280703	-	-	-	-	-	-	-	-	-	49.11 <sup>+0.89</sup> <sub>-0.60</sub>	24.56*	2.43
290800	8.61 <sup>+1.21</sup> <sub>-0.98</sub>	0.9	3.81	14.59 <sup>+0.26</sup> <sub>-0.25</sub>	7.01	2.89	-	-	-	-	-	-
300801	-	-	-	11.82 <sup>+0.48</sup> <sub>-0.50</sub>	1.56	9.75	-	-	-	-	-	-
310802	-	-	-	9.77 <sup>+0.49</sup> <sub>-0.49</sub>	1.10	11	-	-	-	-	-	-
320803	4.54 <sup>+0.14</sup> <sub>-0.19</sub>	6.22	2.67	7.46 <sup>+0.29</sup> <sub>-0.27</sub>	2.87	4.58	48.46 <sup>+2.89</sup> <sub>-1.51</sub>	14.21	1.75	-	-	-

\* The width of the QPO is not well constraint and we froze it before fitting.

### 9.3.2 Obs 2 (110803011)

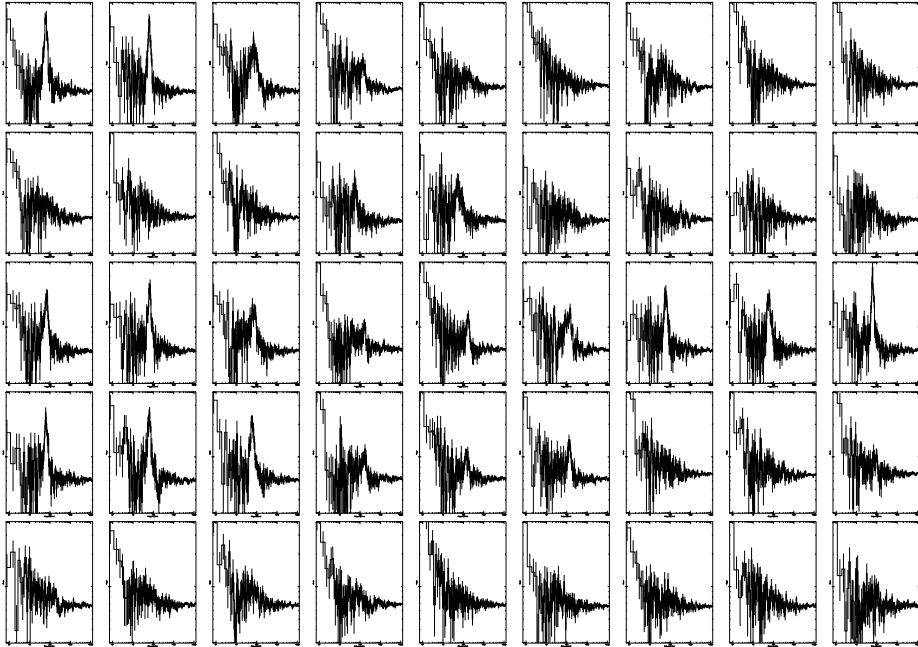
Figure 9.8 shows the averaged PDS extracted every  $\sim 400$  s for Obs 2 (top panel), together with the dynamical PDS and the total averaged PDS for the whole length of the observation (bottom panel). Timing events for the whole bunch of PDS are gathered in Tab. 9.3, and the characteristics of the detected QPOs are displayed in Tab 9.4. We note that no high FB states appear in the HID column of Tab. 9.3, since we established an *ad hoc* definition based on the total HID, where the FB is larger.

This NICER observation is by far the richest regarding its timing properties, where approximately half of the PDS show some kind of QPO-like feature. In this case, we can consider two main incursions into the FB, one in segment #01 (58537.09 MJD) and the other in segment #10 (58537.669). There is also a fast transition into the low-FB in segment #07 (58537.476 MJD), where the dynamical PDS shows rapid back and forth variability in the frequency range 6-20 Hz. The three PDS of segment #00 (from 58537.026 to 58537.035 MJD) are dominated by a strong NBO ( $> 13\sigma$ ), that shifts slightly in frequency from 6.34 Hz (000000) to 7.68 Hz (020002) as the source moves from the NB towards the SA.

The first incursion into the FB is marked by the presence of an FBO in the first PDS of segment #01 (13.5 Hz), which results from the shift of the NBO towards higher frequencies. In the FB, PDS usually display a broad-band noise component with no aperiodic features. On segment #04 (58537.283 MJD), the source comes back to the NB, where NBOs reappear. As the HR increases and the source moves towards the HA, the NBO smears in the noise. On segment #05, the source remains in the HB, where we could resolve an isolated HBO at  $33.66_{-0.76}^{+0.71}$  Hz ( $Q\sim 9$  and  $3.7\sigma$ ), which is the only example of this type of QPO that we could detect in the whole NICER dataset.

When the source moves again towards the SA, the NBO reappears together with hints of HBO-like features at higher frequencies (in PDS 180600 and 190601). In segments #07-09, the source shows a rapid incursion into the low FB that triggers an FBO in the frequency range 14-17 Hz, that turns back into a strong NBO when the source returns to NB. From segment #10 onwards, the source moves into the FB and the FBO is detected again in the PDS, even when the source is in the mid-low FB state (see PDS 361200). In this observation, there is only one hint of a narrow QPO-like feature in the FB (441402) centred at  $\sim 29$  Hz, which nevertheless has low statistical significance ( $\sim 1.7\sigma$ ).

## Power Density Spectra



## Dynamical+Total Power Density Spectrum

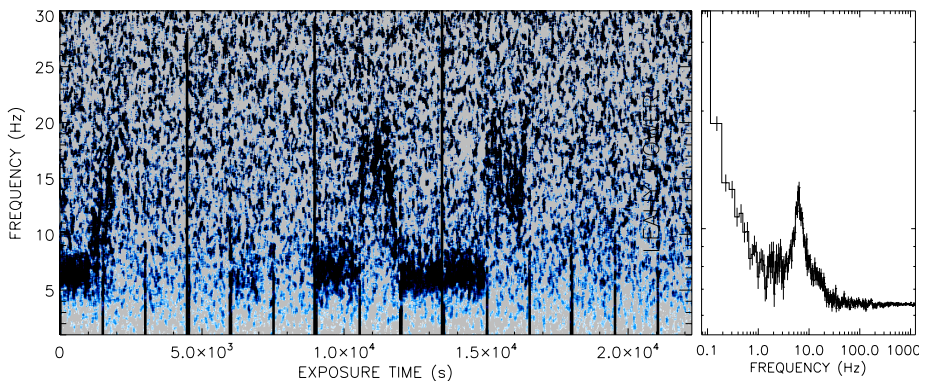


Figure 9.8 Top: PDS averaged every 390 s (i.e., 30 bins of 13 s.) in Obs 110803011. Time goes from left to right and from top to bottom. Bottom: Dynamical+Total PDS. Black vertical lines show the location of time gaps.

Table 9.3 Main timing features found in the PDS shown in Fig. 9.8.

<b>Id</b>	<b>Start time (MJD)</b>	<b>Timing event</b>	<b>NBO (Hz)</b>	<b>FBO (Hz)</b>	<b>HBO (Hz)</b>	<b>HID</b>
000000	58537.026	NBO	$6.34^{+0.08}_{-0.08}$	-	-	NB
010001	58537.030	NBO	$6.40^{+0.08}_{-0.08}$	-	-	NB
020002	58537.035	NBO (blurred)	$7.68^{+0.30}_{-0.30}$	-	-	NB/SA
030100	58537.090	FBO (blurred)	-	$13.53^{+0.70}_{-0.87}$	-	FB (low)
040101	58537.095	Broad-band noise	-	-	-	FB (low-mid)
050102	58537.099	Broad-band noise	-	-	-	FB (mid)
060200	58537.154	Broad-band noise	-	-	-	FB (low-mid)
070201	58537.159	Broad-band noise	-	-	-	FB (mid)
080202	58537.163	Broad-band noise	-	-	-	FB (mid)
090300	58537.219	Broad-band noise	-	-	-	FB (low-mid)
100301	58537.223	Broad-band noise	-	-	-	FB (low-mid)
110302	58537.228	Broad-band noise	-	-	-	FB (low-mid)
120400	58537.283	NBO	$5.85^{+0.22}_{-0.21}$	-	-	NB
130401	58537.288	NBO (very blurred)	$5.84^{+0.38}_{-0.34}$	-	-	NB
140402	58537.292	Broad-band noise	-	-	-	NB/HA
150500	58537.348	HBO	-	-	$33.66^{+0.71}_{-0.76}$	HB
160501	58537.352	Broad-band noise	-	-	-	HB
170502	58537.357	Broad-band noise	-	-	-	HB
180600	58537.412	NBO + HBO	$6.80^{+0.14}_{-0.14}$	-	-	HB
190601	58537.416	NBO + HBO (hint)	$6.68^{+0.10}_{-0.10}$	-	$19.48^{+0.81}_{-1.17}$	NB/SA
200602	58537.421	NBO (blurred)	$7.32^{+0.26}_{-0.27}$	-	$30.55^{+5.23}_{-4.26}$	NB/SA
210700	58537.476	FBO + NBO (hint)	$6.92^{+2.54}_{-1.78}$	$16.60^{+0.46}_{-0.35}$	-	NB/SA
220701	58537.481	FBO	-	$17.06^{+0.33}_{-0.33}$	-	FB (low)
230702	58537.485	FBO + NBO (hint)	$9.97^{+2.02}_{-1.29}$	$14.81^{+0.33}_{-0.55}$	-	FB (low)
240800	58537.541	NBO	$6.27^{+0.12}_{-0.12}$	-	-	FB/SA
250801	58537.545	NBO	$6.13^{+0.14}_{-0.14}$	-	-	NB/SA
260802	58537.550	NBO	$6.25^{+0.07}_{-0.07}$	-	-	NB

270900	58537.605	NBO	$6.47^{+0.11}_{-0.10}$	-	-	NB
280901	58537.609	NBO	$6.43^{+0.09}_{-0.09}$	-	-	NB/SA
290902	58537.614	NBO	$6.20^{+0.13}_{-0.13}$	-	-	NB/SA
301000	58537.669	FBO (blurred)	-	$16.15^{+0.64}_{-0.66}$	-	FB (low)
311001	58537.674	FBO (blurred)	-	$14.25^{+0.65}_{-0.60}$	-	FB (low)
321002	58537.678	FBO	-	$13.62^{+0.31}_{-0.32}$	-	FB (low)
331100	58537.734	Broad-band noise	-	-	-	FB (mid)
341101	58537.738	Broad-band noise	-	-	-	FB (mid)
351102	58537.743	Broad-band noise	-	-	-	FB (mid)
361200	58537.799	FBO	-	$15.85^{+1.65}_{-1.62}$	-	FB (low-mid)
371201	58537.803	Broad-band noise	-	-	-	FB (low-mid)
381202	58537.808	Broad-band noise	-	-	-	FB (mid)
391300	58537.863	Broad-band noise	-	-	-	FB (mid)
401301	58537.867	Broad-band noise	-	-	-	FB (mid)
411302	58537.872	Broad-band noise	-	-	-	FB (low-mid)
421400	58537.927	Broad-band noise	-	-	-	FB (low-mid)
431401	58537.932	Broad-band noise	-	-	-	FB (low-mid)
441402	58537.936	QPO (hint)	-	-	-	FB (low-mid)



Id	NBO			FBO			HBO			Other QPO		
	Freq. (Hz)	Q factor	$\sigma$	Freq. (Hz)	Q factor	$\sigma$	Freq. (Hz)	Q factor	$\sigma$	Freq. (Hz)	Q factor	$\sigma$
250801	$6.13^{+0.14}_{-0.14}$	2.48	11.21	-	-	-	-	-	-	-	-	-
260802	$6.25^{+0.07}_{-0.07}$	4.83	14.22	-	-	-	-	-	-	-	-	-
270900	$6.47^{+0.11}_{-0.10}$	2.98	13.22	-	-	-	-	-	-	-	-	-
280901	$6.43^{+0.09}_{-0.09}$	2.94	13.91	-	-	-	-	-	-	-	-	-
290902	$6.20^{+0.13}_{-0.13}$	2.52	12.89	-	-	-	-	-	-	-	-	-
301000	-	-	-	$16.15^{+0.64}_{-0.66}$	1.99	9.37	-	-	-	-	-	-
311001	-	-	-	$14.25^{+0.65}_{-0.60}$	1.91	7.20	-	-	-	-	-	-
321002	-	-	-	$13.62^{+0.31}_{-0.32}$	12.29	10.29	-	-	-	-	-	-
361200	-	-	-	$15.85^{+1.65}_{-1.62}$	2.06	4.21	-	-	-	-	-	-
441402	-	-	-	-	-	-	-	-	-	$29.43^{+0.77}_{-0.77}$	$14.72^*$	1.68

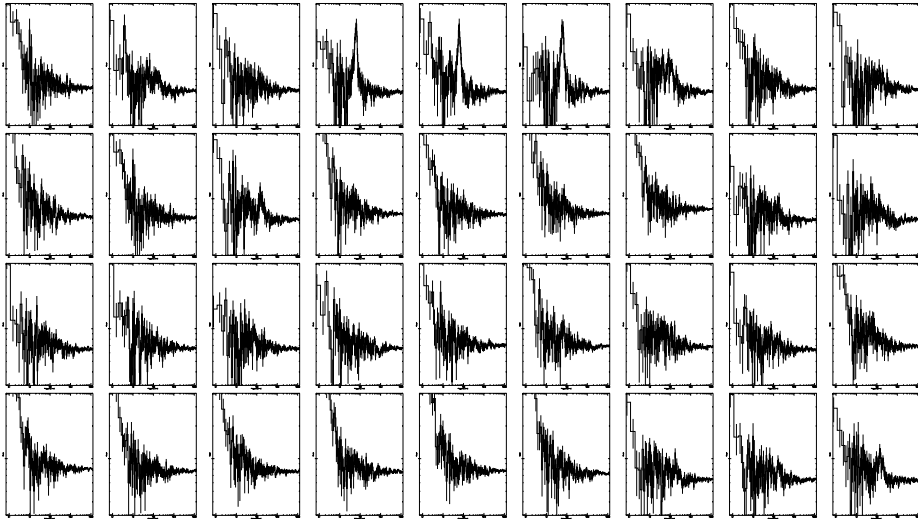
\* The width of the QPO is not well constrained and we froze it before fitting.

### 9.3.3 Obs 3 (110803012)

Figure 9.9 shows the averaged PDS extracted every  $\sim 400$  s for Obs 3 (top panel), together with a dynamical PDS and a total averaged PDS for the whole length of the observation (bottom panel). Timing events for the whole bunch of PDS are gathered in Tab. 9.5, and the characteristics of the detected QPOs are displayed in Tab. 9.6, as in the the other two intervals.

As in Obs 1, the source spends most of the time in a flaring state, showing two main incursions into the NB: the first one at 58538 MJD (segment #01) and the second one at the end of the observation, at 58538.8 MJD (segment #12). In the former, 3 PDS show strong NBOs at  $\sim 6.2$  Hz (i.e., 030100, 040101, 050102), where the first two of them also show hints of HBO-like features above 20 Hz ( $< 2.5\sigma$ ). In PDS 060200, a blurred FBO ( $Q=1.1$ ) at  $\sim 10$  Hz marks the transition from the NB to the FB, as also shown in segment #02 of the dynamical PDS. During the transitions within the FB, PDS are dominated by broad-band noise, and we only detected 3 FBO features, where one is blurred (110302), one is faint (160600) and one is statistically significant (230801). We also point out an almost significant detection in PDS 311100 ( $\sim 2.92\sigma$ ), which is compatible with a blurred FBO. The last three PDS (i.e., 341200, 351201, 361202) represent the second transition to the NB. These are characterised by blurred FBOs ( $>14$  Hz) and one single resolved NBO ( $\sim 6.51$  Hz) in PDS 351201. Narrow QPOs are present in three PDS (i.e., 000000, 103001, 351201), all of them above 60 Hz.

### Power Density Spectra



### Dynamical+Total Power Density Spectrum

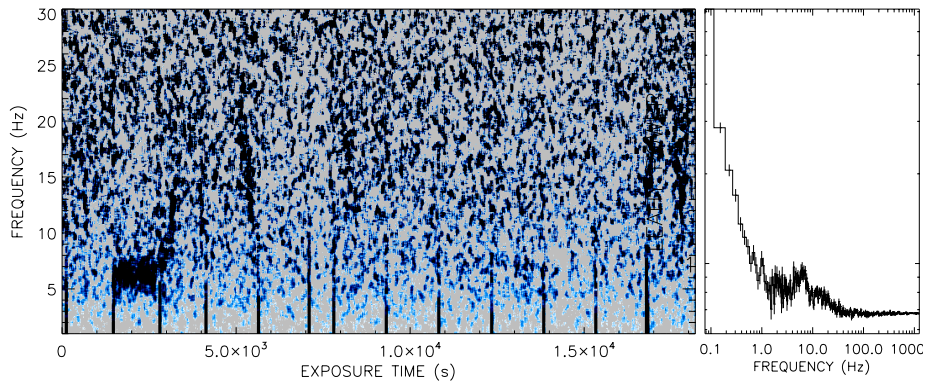


Figure 9.9 Top: PDS averaged every 390 s (i.e., 30 bins of 13 s.) in Obs 110803012. Time goes from left to right and from top to bottom. Bottom: Dynamical+Total PDS. Black vertical lines show the location of time gaps.

Table 9.5 Main timing features found in the PDS shown in Fig. 9.9.

<b>Id</b>	<b>Start time (MJD)</b>	<b>Timing event</b>	<b>NBO (Hz)</b>	<b>FBO (Hz)</b>	<b>HBO (Hz)</b>	<b>HID</b>
000000	58537.991	QPO (faint)	-	-	-	FB (low)
010001	58537.995	Broad-band noise	-	-	-	FB (low)
020002	58538.000	Broad-band noise	-	-	-	FB (low)
030100	58538.055	NBO + HBO (hint)	$6.30^{+0.08}_{-0.09}$	-	$25.31^{+2.12}_{-1.92}$	NB/SA
040101	58538.060	NBO + HBO (hint)	$6.18^{+0.09}_{-0.09}$	-	$22.86^{+0.55}_{-0.21}$	NB
050102	58538.064	NBO	$6.20^{+0.10}_{-0.10}$	-	-	NB
060200	58538.120	FBO (blurred) + NBO (hint)	$4.19^{+0.19}_{-0.26}$	$9.97^{+0.68}_{-0.71}$	-	FB/SA
070201	58538.124	Broad-band noise	-	-	-	FB (low)
080201	58538.129	Broad-band noise	-	-	-	FB (low)
090300	58538.184	Broad-band noise	-	-	-	FB (low-mid)
100301	58538.189	QPO (faint)	-	-	-	FB (low)
110302	58538.193	FBO (blurred)	-	$16.30^{+0.72}_{-0.67}$	-	FB (low)
120400	58538.249	Broad-band noise	-	-	-	FB (mid)
130401	58538.253	Broad-band noise	-	-	-	FB (mid)
140402	58538.258	Broad-band noise	-	-	-	FB (mid)
150500	58538.324	Broad-band noise	-	-	-	FB (high)
160600	58538.377	FBO (faint)	-	$17.42^{+0.93}_{-2.34}$	-	FB/SA
170601	58538.382	Broad-band noise	-	-	-	FB (low)
180602	58538.386	Broad-band noise	-	-	-	FB (low)
190700	58538.442	Broad-band noise	-	-	-	FB (low)
200701	58538.446	Broad-band noise	-	-	-	FB (low)
210702	58538.451	Broad-band noise	-	-	-	FB (low)
220800	58538.506	Broad-band noise	-	-	-	FB (mid)
230801	58538.511	FBO	-	$6.82^{+0.32}_{-0.36}$	-	FB (mid)
240802	58538.515	Broad-band noise	-	-	-	FB (low-mid)
250900	58538.571	Broad-band noise	-	-	-	FB (low)
260901	58538.57	Broad-band noise	-	-	-	FB (low)

270902	58538.580	Broad-band noise	-	-	FB (low-mid)
281000	58538.635	Broad-band noise	-	-	FB (high)
291001	58538.640	Broad-band noise	-	-	FB (mid-high)
301002	58538.644	Broad-band noise	-	-	FB (mid-high)
311100	58538.699	FBO (hint, blurred)	-	$6.37^{+0.86}_{-0.83}$	FB (mid-high)
321101	58538.704	Broad-band noise	-	-	FB (mid-high)
331102	58538.708	Broad-band noise	-	-	FB (mid)
341200	58538.764	FBO (blurred)	-	$17.86^{+1.04}_{-1.53}$	FB (low)
351201	58538.768	NBO + FBO + QPO (faint)	$6.51^{+0.20}_{-0.19}$	$17.82^{+1.05}_{-0.80}$	FB (low)
361202	58538.773	FBO (very blurred)	-	$14.63^{+0.79}_{-0.68}$	FB/SA

Table 9.6 Centroid frequency, Q-factor and significance ( $\sigma$ ) of the QPOs found in Tab. 9.5.

Id	NBO			FBO			HBO			Other QPO		
	Freq. (Hz)	Q factor	$\sigma$	Freq. (Hz)	Q factor	$\sigma$	Freq. (Hz)	Q factor	$\sigma$	Freq. (Hz)	Q factor	$\sigma$
000000	-	-	-	-	-	-	-	-	-	87.56 <sup>+0.65</sup> <sub>-0.50</sub>	43.78*	3.06
030100	6.30 <sup>+0.08</sup> <sub>-0.09</sub>	3.64	13.10	-	-	-	25.31 <sup>+2.12</sup> <sub>-1.92</sub>	7.42	1.61	-	-	-
040101	6.18 <sup>+0.09</sup> <sub>-0.09</sub>	3.57	12.13	-	-	-	22.86 <sup>+0.55</sup> <sub>-0.21</sub>	228.6	2.29	-	-	-
050102	6.20 <sup>+0.10</sup> <sub>-0.10</sub>	3.35	12.63	-	-	-	-	-	-	-	-	-
060200	4.19 <sup>+0.19</sup> <sub>-0.26</sub>	5.30	1.97	9.97 <sup>+0.68</sup> <sub>-0.71</sub>	1.10	3.19	-	-	-	-	-	-
100301	-	-	-	-	-	-	-	-	-	66.11 <sup>+1.14</sup> <sub>-0.50</sub>	33.06*	3.72
110302	-	-	-	16.30 <sup>+0.72</sup> <sub>-0.67</sub>	1.62	7.88	-	-	-	-	-	-
160600	-	-	-	17.42 <sup>+0.93</sup> <sub>-2.34</sub>	2.15	2.92	-	-	-	-	-	-
230801	-	-	-	6.82 <sup>+0.32</sup> <sub>-0.36</sub>	3.13	3.70	-	-	-	-	-	-
311100	-	-	-	6.37 <sup>+0.86</sup> <sub>-0.83</sub>	1.60	2.92	-	-	-	-	-	-
341200	-	-	-	17.86 <sup>+1.04</sup> <sub>-1.53</sub>	1.76	4.13	-	-	-	-	-	-
351201	6.51 <sup>+0.20</sup> <sub>-0.19</sub>	8.04	3.06	17.82 <sup>+1.05</sup> <sub>-0.80</sub>	2.72	4.07	-	-	-	73.10 <sup>+0.63</sup> <sub>-1.42</sub>	36.55*	2.42
361202	-	-	-	14.63 <sup>+0.79</sup> <sub>-0.68</sub>	1.34	8.89	-	-	-	-	-	-

\* The width of the QPO is not well constraint and we froze it before fitting.

## 9.4 Discussion and ongoing work

In this chapter, we performed the first analysis of the NS LMXB Sco X-1 based on NICER X-ray observations. This monitoring is part of a large multi-wavelength campaign performed during almost four days in February 2019, where thanks to the large collecting area of the instrument and the possibility to process the high count rates of the source, NICER provided the highest quality data among all the X-ray instruments. Using the GHATS software package, we extracted a light-curve and a HID to characterise the spectral states of the source during these observations. Then, we employed timing techniques to obtain a collection of PDS to detect the rapid aperiodic variability of the source (i.e., the QPOs), and to follow the evolution of the features in time and along the different spectral states that Sco X-1 traces in the HID.

Considering the 3 NICER observations that we analysed in the work (i.e. 110803010, 110803011, 110803012), we fitted a total number of 115 PDS, which were averaged every  $\sim 400$  s (in 30 contiguous 13-s-long bins). The results of the fitting were reported on Sec. 9.3, where we observed a rich variety of LF QPOs: 19 PDS contain NBOs (plus 4 faint detections), 18 PDS show FBOs (plus 3 faint detections) and 2 PDS show HBO-like signals (plus 4 faint features). This means that approximately half of the PDS we inspected show some kind of quasi-periodic structure, while the rest are dominated by broad-band noise components. We also observe two distinct types of QPOs that are more difficult to classify according to the above categories, which are rare features that appear in the flaring state (with no obvious preferential location in the FB). These are the 4 QPOs detected in the frequency range 20 – 30 Hz in Obs 1 and Obs 2 (where 2 of them are statistically significant) and the 3 QPOs found in the range 65 – 85 Hz in Obs 3 (where also 2 of them are statistically significant).

The overall behaviour of the source is consistent with previous studies. Given the similarities of our approach with the analysis performed by Motta and Fender 2019 using archival RXTE data, for the sake of comparison I will mainly focus on the results of their analysis, also because that work is the more recent timing survey of Sco X-1 based on RXTE.

PDS in the NB are dominated by strong NBOs at  $\sim 6$  Hz (see Obs 2 and Obs 3), while all of them show a broad-band noise component along the FB. The transition from the NB to the FB along the SA is marked by the shift of the NBO towards higher frequencies, while as shown in Obs 2 the NBO also disappears as the source moves towards the HA (140402). In the NB, NBOs appear isolated with only a few exceptions, where HBO-like QPOs manifest at

higher frequencies, above 20 Hz (PDS 180600 and 190601 in Obs 2; PDS 030100 and 040101 in Obs 3). These timing events are especially relevant in this context, since as suggested by Motta and Fender 2019, their existence –when observed together with NBOs– could be tentatively related with the ejection of URFs. Among these 4 detections, only 1 is statistically significant (i.e. PDS 180600). The fact that the existence of simultaneous NBO+HBO are rare features in our PDS bunch is not surprising, especially if one assumes that, due to the soft response of the instrument, HBOs are harder to detect with the NICER observatory with respect to RXTE. On the other hand, since we have detected at least 1 significant HBO (simultaneously to an NBO) at  $\sim 34$  Hz, we accept that any aperiodic feature in this frequency range could be relevant, albeit not formally statistically significant. We also discovered one isolated HBO, which was not reported by Motta and Fender 2019, although were previously detected in the RXTE data (Motta et al., in preparation).

In Motta and Fender 2019, all HBOs show approximately the same central frequency ( $\sim 45$  Hz), while in our case they are more sparse at lower frequencies, ranging from 20 to 35 Hz. Due to this fact, we question whether these features (specially the ones at the lowest frequencies, i.e.  $\sim 20$  Hz) could represent a sub-harmonic of the HBO, which would be in this case smeared in the noise of the PDS. However, since these QPOs are transient and usually short-lived, it is also possible that the characteristic frequency of the QPO varies over time in a wider frequency range.

The nature of the narrow QPOs detected in the FB is unclear, since these features show similar properties to HBOs, but appear in a completely different spectral state compared to standard HBOs. Indeed, a similar type of QPOs have been observed in the soft state of BH systems, the so-called type-C QPOs in the soft state [see e.g. Motta et al. 2012, Franchini, Motta, and Lodato 2017, who suggested that these QPO are triggered in the inner edge of the accretion flow]. In these papers, the central frequency is typically below 20 Hz, although at least two systems show type-C soft QPOs at higher frequencies ( $\sim 30$  Hz, see Tab. 1 in Franchini, Motta, and Lodato 2017). Assuming that our QPOs are the NS equivalent of these features, it is not surprising that in NSs they could be displayed at higher frequencies, as NS sources are less massive than BH binaries. It could also be possible that the two populations of QPOs that we observed are indeed harmonically related, but due to the low number of events this suggestion is only tentative.

Another feature that deserves more attention is the FBO observed in PDS 230801 of Obs 3, which also manifest –but very blurred– on PDS 311000. We

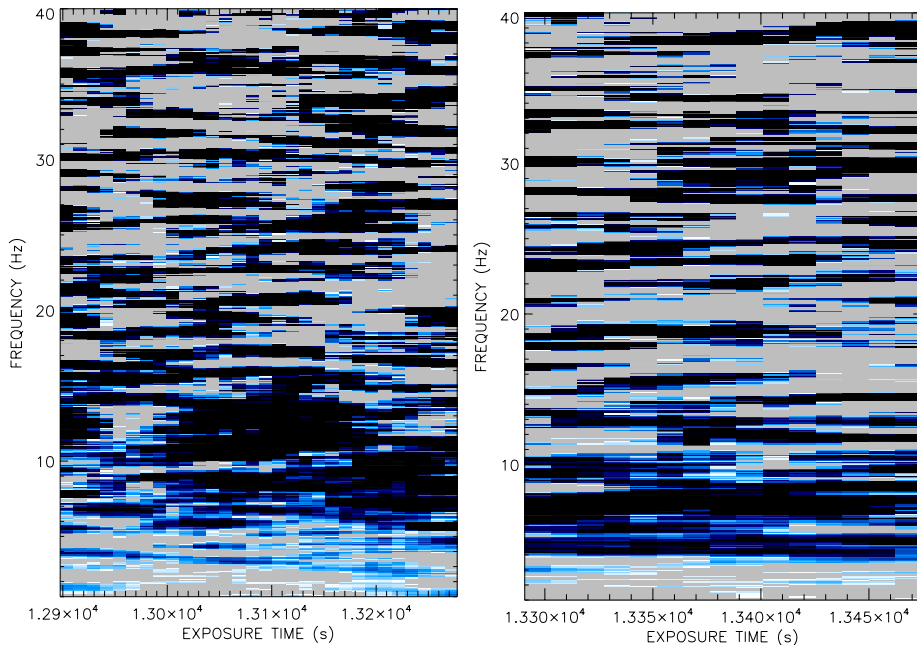


Figure 9.10 Dynamical PDS corresponding to PDS 310802 and PDS 320803 of Obs 1.

classified this QPO as an FBO because it is located in the mid-high FB, but its central frequency at  $\sim 6$  Hz is by contrast more compatible with an NBO. In these 2 time bins, the dynamical PDS does not show any compatible signal at this frequency, revealing that these QPOs are transient events, possibly experiencing very fast variability. The possibility that the source makes a rapid incursion in the NB in a time scale much shorter than the typical length of the bin must be explored in the future.

In Obs 1, the transition from the FB to the NB at 58536.091 MJD is characterised by the rapid shift in frequency of an FBO, from  $\sim 15$  Hz to  $\sim 8$  Hz, which also produces a blurred shape of the FBOs in the PDS. There is nothing unusual in this type of transitions, which have been observed in the literature since the past century [see e.g. Priedhorsky et al. 1986]. However, a deeper inspection of the dynamical PDS of these 2 bins reveals a more complex behaviour, since as shown in Fig. 9.10, the 2 QPOs in the PDS seem to be present at the same time. This could suggest, at least for some spectral transitions, that the NBO and the FBO may be related in a different way, as the two QPOs can be sometimes observed together rather than evolving one into the other.

This chapter of the thesis presents a preliminary analysis of the NICER monitoring of the source Sco X-1. Given the complexity of the timing analysis and the rich phenomenology of Sco X-1, in this work I have focused on the properties of LF QPOs. Nevertheless, this study can be extended in different ways. A revised version of the analysis incorporating these improvements will be presented elsewhere in the future:

- Although I have not fitted any QPO above 100 Hz, some of the PDS presented in this chapter show hints of faint features in this frequency range, sometimes above  $\sim 500$  Hz. The existence of kHz QPOs in Sco X-1 is not surprising, since these have been previously detected in RXTE data [see e.g., van der Klis et al. 1997, Motta and Fender 2019]. However, given the proximity of the Nyquist frequency to the region of interest (which in this case is  $\sim 1000$  Hz), the analysis performed in this work is not optimal for searching QPOs at such high frequencies. This will require a dedicated procedure, where a new set of PDS will be produced by (1) increasing the Nyquist frequency of the PDS (i.e., reducing the rebinning in the time domain prior to FFTs) and (2) applying a linear rebinning in frequency instead of a logarithmic one.
- I will also improve the definition of the spectral states in the HID. In this chapter, these states have been defined qualitatively, but a better description should be adopted in the future. This can be done, for example, by placing the HID in a numerical grid, allowing to assign an integer number to each location in the branch.
- In parallel, I will collaborate with Joe Bright (University of Oxford) and Sara E. Motta (INAF) to analyse the radio data taken during the multi-wavelength campaign of February 2019, specially the VLBI observations. This analysis will be essential to deepen into the connection between accretion states and the formation of URFs, following the work by Motta and Fender 2019. Time intervals where the PDS displays a simultaneous NBO+HBO –although usually not significant– are specially relevant to this objective.

# Chapter 10

## Summary and future work

On this last Part of the thesis, I have presented two projects that I performed in the field of X-ray data analysis, following the first contribution I have resumed on Appendix B. These two chapters can be summarised as follows:

On **Chapter 8** (originally published in López-Miralles et al. 2023), I have analysed the system LS I +61°303, which is a  $\gamma$ -ray binary that has been widely monitored since its discovery more than sixty years ago. Nevertheless, despite all the multi-wavelength observations that have been performed, the nature of the compact object, as well as the properties of the system, are still largely debated. Aimed at investigating the rapid X-ray variability of LS I +61°303, I have analysed all the archival Rossi X-ray Timing Explorer/Proportional Counter Array (RXTE/PCA) data of the source, which was taken between 1996 and 2011. A preliminary timing analysis based on different statistical methods, i.e., (i) Lomb-Scargle periodogram, (ii) Phase Dispersion Minimisation, and (iii) folding and amplitude maximisation, yields a periodicity of  $P \sim 26.6 \pm 0.3$  days, which is statistically compatible with other similar periodicities reported in the literature by other authors. This result does not allow us to distinguish the two radio periodicities traditionally related with the orbital period ( $P \sim 26.499 \pm 0.0028$  days) or the jet precession ( $P \sim 26.926 \pm 0.005$  days), assuming the microquasar model for the latter one. Using the resolved period, I performed a data phase-resolved analysis to produce a set of phase-bin-averaged energy spectra and Power Density Spectra (PDS) with enhanced statistics and signal-to-noise ratio with respect to the original data. The results of the analysis show that the PDS are dominated by weak read noise below 0.1 Hz, and show no signal above this frequency. The

amplitude of the noise varies mildly with the phase, and shows a maximum that coincides with a dip of the X-ray flux and a softer photon index. However, no statistically periodic or aperiodic timing feature could be found in the RX-TE/PCA data of LS I +61°303.

On **Chapter 9**, I present the first analysis of the neutron star (NS) low-mass X-ray binary (LMXB) Scorpius X-1 (Sco X-1) based on NICER X-ray observations, a detector aboard the International Space Station. These observations were performed from 21 to 25 February 2019 as part of a big campaign to monitor Sco X-1 with different instruments, providing the largest simultaneous coverage of the source at all possible wavelengths with radio, optical/IR, X-ray and  $\gamma$ -ray observations. In the X-ray energy range, the large collecting area of the NICER observatory, together with its ability to properly handle the high count rates of the source, provided the highest quality data of the X-ray instruments involved in the campaign. Using three NICER observations of Sco X-1, I performed an extensive timing analysis to characterise the quasi-periodic oscillations (QPOs) that underlaid in the light-curve, specially the evolution of these features with respect to the spectral states of the source, that I characterised in a Hardness-Intensity Diagram. The results of the analysis are compared with previous findings in the X-ray energy band.

In the following, I briefly summarise different lines of work based on ongoing collaborations to extend the work presented on this Part of the thesis.

## 10.1 Multi-wavelength campaign of Sco X-1

The timing analysis shown in Chapter 9 revealed the presence of different type of QPOs in the Sco X-1 NICER dataset, compatible in the vast majority with QPOs found in previous RXTE surveys. In Motta and Fender 2019, some of these features have been related with the existence of underlying ultra relativistic flows (URFs), inferred by correlating X-ray flares in the core with radio flares in the extended lobes. In particular, a tentative correlation between the accretion flow and the ejection of URFs was suggested, since these seem to be launched when both a normal branch oscillation (NBO) and an horizontal branch oscillation (HBO) are present in the PDS.

Although due to the response of the instruments HBOs are harder to detect with NICER, our data analysis showed small hints for their existence, both isolated or in combination with strong NBOs. To assess the possible relation

of these features with the source radio flares, I will collaborate with Joe Bright (University of Oxford) and Sara E. Motta (INAF-Osservatorio Astronomico di Brera) to analyse the radio data taken during the multi-wavelength campaign, specially the VLBI observations. This analysis will be essential to understand the connection between accretion states and the formation of URFs, following the work by Motta and Fender 2019. In parallel, I will also explore Chandra and XMM-Newton data, although in this case observations might be corrupted by undesirable instrumental issues (e.g., pile-up effects).

Moreover, as already mentioned in Chapter 9, I will complete the timing analysis of NICER data by addressing the existence of kHz QPOs in the PDS, since these have been previously resolved by RXTE [see e.g., van der Klis et al. 1997, Motta and Fender 2019]. Indeed, some of the PDS I have inspected show faint features above 500 Hz which could be compatible with a kHz QPO, but a dedicated study should be performed to prove their existence in the NICER data. With this aim, I will first increase the Nyquist frequency in all the PDS I showed in Chapter 9, and then, to highlight high-frequency features, I will apply a linear frequency rebinning instead of a logarithmic one (as we did so far in the PDS shown in Part III of the thesis).

## 10.2 Chandra proposals

I am co-investigator of two Chandra proposals: one that have been accepted for Cycle 24 [Marshall 2022] and one that have been submitted for Cycle 25 (in collaboration with R. di Stefano).

**SS 433 as an ULX** The first of them, titled *A test to establish that SS 433 is an Ultraluminous X-ray source*, aims to demonstrate that the microquasar SS 433 is the first galactic Ultra-luminous X-ray source (ULX), following the hypothesis by King et al. 2001 who suggested that ULXs in nearby galaxies are linked to microquasars with the supposition that their X-ray emission is restricted to a small cone angle aligned to the line of sight. SS 433 shows extended arc-sec scale X-ray jets, and there have been proposed several models to explain this emission; for example, one model assumes reheating due to internal shocks as faster blobs overtakes slower material ejected at almost the same precession phase. An alternative hypothesis is that SS 433's extended X-ray emission is actually reflected core emission as observed at arc-second scales in Seyfert-2 galaxies. In that case, this extended emission may provide a solid measurement of axially beamed radiation from the core and demonstrate the link to ULXs.

Using new Chandra observations, we will perform a variability test that could discriminate between these two models. But, for testing the reflection scenario, a deliberately planned program of monitoring both the core flux and the extended flux over a characteristic variability time scale of weeks to months is required. This model has a very specific prediction that intensity and structural variations should correlate with the variability of the beamed core flux. Furthermore, the extent of the illumination along the jet's apparent spiral pattern should be directly related to the radiation beam pattern. By observing variations of the core X-ray emission over a span of a few months, we can test whether the extended emission responds with the appropriate light travel time delay and that the illuminated region evolves around the jet spiral pattern. Furthermore, the delays will generally have opposite signs on the two sides of the core. Thus, observing such delay differences would be a definite signature of the ULX model.

In particular, we will measure secular changes in the intensity and spatial structure of the SS 433 extended outflows, which is separable from the core only using Chandra angular resolution. To track variations, we will image SS 433 every week for 12 weeks to cover half of a precession cycle of 162 days (the total requested exposure is 120 ks). Moreover, while the reflected light in the Chandra HRC band will be dominated by the 1-3 keV range, high energy photons actually dominate the luminous power (after correcting for absorption along the line of sight). Thus, we will also monitor SS 433 with Swift XRT observations at a 3 day cadence supplemented with monthly Swift BAT averages to measure the spectral power out to 30 keV. We will also support these observations by several 25-30 ks Chandra HETGS exposures at regular intervals in order to validate the core spectral model.

**Dips and blips in Chandra archive** The second proposal, titled *Dips and blips: facilitating the archival discovery of planetary transits, binary self-lensing, and other short-duration X-ray phenomena*, is an archival project that aims to explore all bright X-ray sources listed in the Chandra Source Catalog in order to search for and study X-ray events of short duration. These short duration events provide unique and valuable information about astrophysical systems and the processes occurring within them, as planetary transits, other short transits caused by small objects (e.g., brown dwarfs, white-dwarfs, small stars, etc), dips caused by clouds of gas and dust, or irregularities in the accretion disc. Blips, or short-duration flux enhancements, are also important, including accretion variations and/or explosions (e.g., type I X-ray bursts in NSs). A remarkable example of this type of events is the discovery of a potential extragalactic

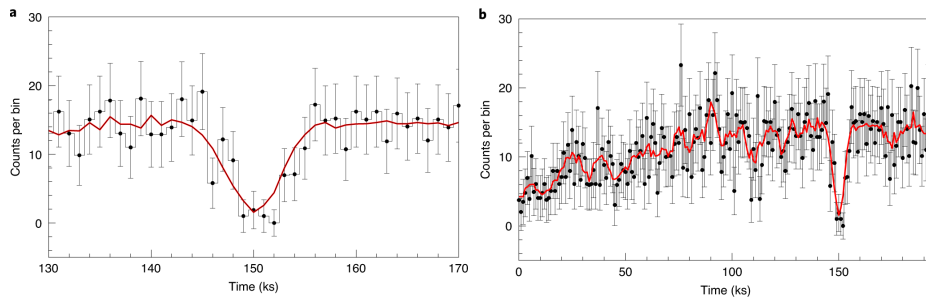


Figure 10.1 Background subtracted X-ray light-curves defined by data points for Chandra ObsID 13814. Reproduced with permission from Di Stefano et al. 2021 (Fig 1).

planetary transient in the X-ray binary M51-ULS-1 (located in the galaxy M51), where the eclipser is most likely a Saturn size planet [Fig. 10.1; Di Stefano et al. 2021].

The research plan of the archival proposal is divided in two parts: (1) we will conduct searches for short events within each X-ray light curve by applying both classical algorithms and machine learning techniques, and (2) we will make preliminary classifications of all significant short-term deviations from baseline. To do so, we will use all available Chandra data, cross-match with catalogs across wavebands, and test simple models of dips and blips. The primary output of this project will be a complete catalog of events. This catalog will be an useful resource for the X-ray community to identify and study eclipses, short accretion-related dips, and other dips associated with planetary transits, as well as short X-ray flares of all types, including X-ray bursts due to nuclear burning on NSs. This archival project is expected to uncover roughly 3000-5000 interesting candidates for future research. We will create and publish a catalog of Chandra-Discovered Short-Duration X-Ray Events, which will be included in the VizieR database. We will also document our software and place it in readily accessible repositories, such as Github. These resources will allow researchers to conduct groundbreaking investigations on a wealth of phenomena that produce short duration X-ray events, selecting individual events or categories of events for detailed studies that can reveal the nature of exciting and diverse processes.

### 10.3 GRS 1747-312: a third body system?

In collaboration with Prof. Rosanne di Stefano and her group of the Astronomy Department at Harvard University, we are analysing the system GRS 1747-312, a bright NS LMXB located in the globular cluster Terzan 6 (at a distance of

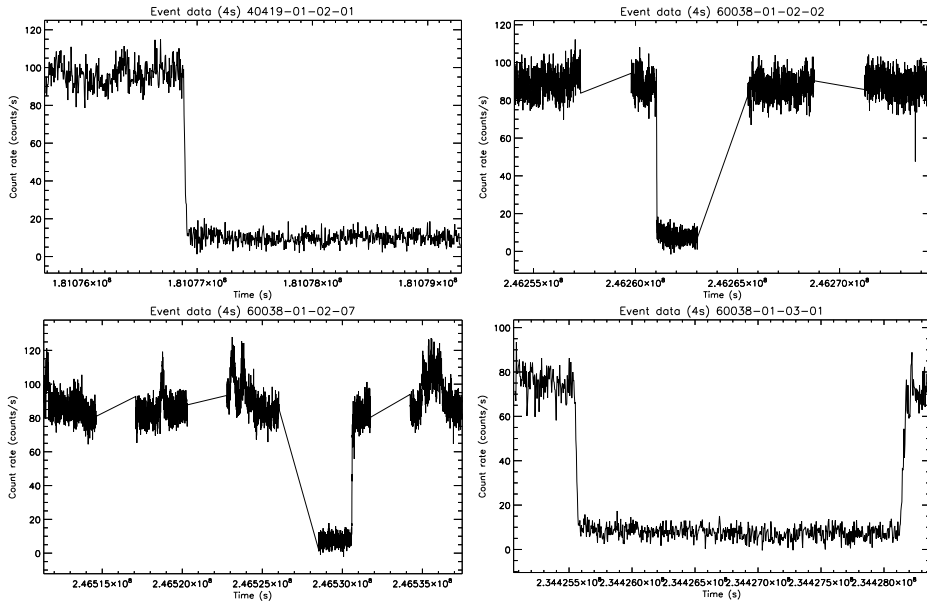


Figure 10.2 RXTE light-curves (time vs. count rate) with a time resolution of 4 s for observations 40419-01-02-01, 60038-01-02-02, 60038-01-02-07 and 60038-01-03-01. A standard  $\sim 2$  ks eclipse is shown in all these light-curves.

$\sim 9.5$  kpc from the Earth). This system shows quasi-periodic outbursts every  $\sim 4.5$  months, where periodic eclipses are also expected to occur [in't Zand et al. 2003], although these have been elusive in the quiescent state. Using Chandra observations of the source performed in June 2019 and April, June, and August of 2021, we are analysing an eclipse-like event that occurred while the source was quiescent, which is of longer duration (twice the standard eclipse duration of  $\sim 2$  ks) and whose timing does not fit the ephemeris of the companion star. Given all of these characteristics, this could suggest that GRS 1747-312 is a triple system where eclipses could be associated with the motion of (at least) two separate bodies. To support the Chandra observations, aimed at confirming the multi-body model in the X-ray historical data, I have analysed all the archival RXTE data of GRS 1747-312 ( $\sim 200$  observations) and extracted light curves with high resolution (i.e., event mode data, see Fig. 10.2), for which I used a modified version of the pipeline developed for Chapter 8. After a first inspection of the results, all detected eclipses in the RXTE data are, however, compatible with the standard timing and ephemeris of the source.

Part IV

Appendices



In this appendix, I present the contribution I made in a series of publications that I have co-authored, both in the field of relativistic jet simulations (Appendix A) and X-ray timing analysis (Appendix B). This extends, respectively, the results presented in Part II and Part III of the thesis.

- In **Appendix A**, I present a collection of papers where I have been involved developing and/or post-processing numerical simulations of relativistic outflows in the context of Active Galactic Nuclei, using the code RATPENAT. Although this type of scenario is beyond the scope of the thesis, in Chapter 7 I pointed out an ongoing line of work where we plan to extend our code LÓSTREGO for extra-galactic applications, following the research lines of our group. In this manner, the work presented below, as well as other simulations that I will not resume in this appendix, are the starting point towards constructing more realistic setups, including for example the dynamical evolution of magnetic fields, or the the interaction of plasma with radiation. The contributions revisited in this chapter are the following:

1. **Jet propagation through inhomogeneous media and shock ionisation** (originally published in Perucho et al. 2021), where I present numerical simulations of relativistic outflows propagating through the inner host galaxy, including for the first time atomic and ionised hydrogen and the cooling effects of ionisation. Moreover, as a particular application of this new version of the code RATEPNAT, I summarise the results of a three-dimensional relativistic hydrodynamics simulation we performed to support the discovery by *RadioAstron* of a mini-cocoon-like structure around the restarted jet in the radio galaxy 3C 84 [originally published in Savolainen et al. 2023].
2. **The large scale morphology of Hercules A** (originally published in Perucho et al. 2023), where we performed and post-processed global three-dimensional relativistic hydrodynamics simulations aimed at reproducing the peculiar large-scale morphology of the radio galaxy Hercules A.

- In **Appendix B** (originally published in Marino et al. 2020), we applied for the first time the Internal Shocks model to characterise the multi-wavelength spectrum of the neutron star low-mass X-ray binary 4U 0614+091, allowing to change the jet geometry from a conical to non-conical flow. This is the first attempt to apply this kind of study in the context of a X-ray binary hosting a neutron star.



# AGN jet simulations

## A.1 Jet propagation through inhomogeneous media and shock ionisation

---

This chapter was originally published in *Jet propagation through inhomogeneous media and shock ionisation*. M. Perucho, **J. López-Miralles**, V. Reynaldi and A. Labiano. *Astronomische Nachrichten*, November 2021. DOI: [10.1002/asna.20210051](https://doi.org/10.1002/asna.20210051). Reproduced with permission.

This chapter also reproduces an extract of the following publications: [1] *Numerical simulations of relativistic jets*. M. Perucho and **J. López-Miralles**. *Journal of Plasma Physics*, 89(5), October 2023. DOI: [10.1017/S0022377823000892](https://doi.org/10.1017/S0022377823000892). [2] *RadioAstron discovery of a mini-cocoon around the restarted parsec-scale jet in 3C 84*. T. Savolainen et al. (including **J. López-Miralles**). *Astronomy & Astrophysics*, Volume 676, id.A114, 28 pp. August 2023. DOI: [10.1051/0004-6361/202142594](https://doi.org/10.1051/0004-6361/202142594). Reproduced with permission.

---

### A.1.1 Introduction

Jets are triggered around supermassive black holes (BHs) in Active Galactic Nuclei (AGN) via the extraction of rotational energy from the BH-accretion disc system that sits at the core of those galaxies [Blandford and Znajek 1977, The Event Horizon Telescope Collaboration 2019]. Jets become relativistic and

super(magneto)sonic beyond the acceleration region, thus triggering shocks in the galactic interstellar medium (ISM) during the first stages of propagation through the host galaxy.

The role of shocks is certainly relevant for the subsequent evolution of the host galaxy. On the one hand, shocks heat and ionise the ISM, providing it with momentum and triggering outflows of ISM gas [e.g., Morganti et al. 2016, Morganti and Oosterloo 2018, Schulz et al. 2021, and references therein]. These outflows could eventually extract large amounts of ISM gas from the galaxy, with the consequent quenching of star formation [see, e.g., Perucho, Quilis, and Martí 2011, Perucho et al. 2014b]. On the other hand, there is debate about the possibility that the compression induced by shocks could cause a burst of star formation, although heated up ISM would increase the turbulence in its molecular gas, which would prevent the collapse of the star forming cloud [see the discussion in, e.g. Wagner, Bicknell, and Umemura 2012].

During the last years, a number of numerical simulations have tackled the evolution of jets through the two-phase, inhomogeneous media expected within the inner kiloparsecs of host galaxies [Wagner and Bicknell 2011, Wagner, Bicknell, and Umemura 2012, Mukherjee et al. 2016, Bicknell et al. 2018, Zovaro et al. 2019]. These works have shown that jet evolution can be strongly modified by the presence of local, dense inhomogeneities and that these are shocked and destroyed by jets in time-scales that could allow star formation. Although the physical conditions of shocked clouds are complex and more detailed, specific studies should be performed.

In this work, we have presented our first simulations to study the role of jets within their host galaxies. The novelty of these numerical experiments is the addition of atomic hydrogen as a species to our simulations, along with the effects of cooling and recombination of hydrogen in terms of radiative losses.

### A.1.2 First simulations with ionisation

With the aim to run numerical simulations that account for ionisation of hydrogen, we have modified the code RATPENAT [Perucho et al. 2010, Perucho, Martí, and Quilis 2019] to include atomic hydrogen and ionisation terms from Vaidya et al. 2015. We have chosen to implement the non-equilibrium conditions, because of the low densities in both AGN jets and the ISM. Therefore, ionisation plays a role as a source of 1) energetic losses, which means a source term to include the collisional ionisation cooling and the radiative recombination in the energy conservation equation, and 2) the particle number densities, i.e., it appears as

a source term in the conservation equation of the different species. We have kept the Sygne equation of state (EoS) for the jet flow, composed of pairs with high internal energies. The selection of the EoS for each cell is based on the presence or not of atomic hydrogen. In contrast to the work by Vaidya et al. 2015, we have not included neither atomic helium nor molecular hydrogen in this first step of our project. The energy density of the gas is thus determined by the translational energy of hydrogen alone [see Vaidya et al. 2015] and the thermodynamical relations become trivial.

Despite the lack of analytic solutions for relativistic shock propagation in combination with hydrogen ionisation (Vaidya et al. 2015 limit their work to classical flows), we have run a number of tests that have been successfully passed by the code, and compare well with those presented in Vaidya et al. 2015. The tests performed will be shown elsewhere in the future.

The simulations were run in 512 cores at Tirant, the local supercomputer at the Universitat de València. The grid size is  $512 \times 512 \times 512$  cells, with a resolution of 6 cells/ $R_j$ , and  $R_j = 6$  pc at injection. This means that the simulation follows the jet evolution along 512 pc, from the point where the jet radius is the selected one (i.e.,  $\sim 60$  pc from the active nucleus).

The initial three-dimensional (3D) density distribution was set by means of the PyFC fractal code [Wagner and Bicknell 2011]. This algorithm implements an iterative process such that density inhomogeneities follow a log-normal single-point statistics in space (with parameters  $\mu = 1.0, \sigma^2 = 5.0$ ). The fractal structure of the scalar field is achieved multiplying the Fourier-transformed distribution by a Kolmogorov power-law with spectral index  $\beta = -5/3$ . The scale of the largest cloud in the box is approximately 16 pc, which corresponds to a minimum sampling wave-number,  $k_{\min} = 17$ . The medium is set in pressure equilibrium to a given value ( $P_{\text{ISM}} = 3.4 \times 10^{-10} - 3.4 \times 10^{-11}$  erg cm $^{-3}$ ), depending on the mean ambient density, by adapting temperatures. Once temperatures are fixed, we use Saha equilibrium equations to set an initial value for hydrogen density. The medium is obviously out from the equilibrium required by Saha, and is thus dynamic, in the sense that the hydrogen density changes with time due to cooling. The numerical box is assumed to be optically thin, so all the energy lost via cooling is radiated away.

We have run three numerical simulations: J46a, J46b and J44a. Simulations J46 share the same jet properties and gas distribution, but the ISM mean density is scaled up by an order of magnitude in simulation J46b with respect to J46a. Simulation J44a shares the ambient medium properties with J46a, but the jet injected in J44a is two orders of magnitude lower in power with respect to J46a.

The jets are all purely leptonic at injection. A tracer function  $f$  has been set to  $f = 1$  at the densest and coldest regions and  $f = 0$  for the rest of the grid, with the aim to track the original material in ISM clouds. Left panel of Fig. A.1 shows 3D contours of atomic hydrogen density in the grid prior to jet injection. As in the rest of the thesis, we have used LLNL VisIt [Childs, H. et al. 2012] to produce the figures.

### A.1.3 Preliminary results and first conclusions

Right panel of Fig. A.1 shows, for the last snapshot of simulation J46b, the projected 3D distribution of pressure contours (red and dark blue) indicating the position of the bow-shock and hot-spot; a leptonic fraction contour (orange) indicating the jet surface; a tracer contour (pink) indicating the location of material originally sitting in the densest and coldest regions that has been shock-ionised; and contours showing the atomic hydrogen density in two different sets: the blueish contours indicate hydrogen outside the bow shock, whereas the green/yellow contours indicate hydrogen inside the red surface. Altogether, the image shows how the inhomogeneous density of the ISM forces an irregular structure in the bow-shock. The distortion and expansion that the passage of the shock and, mainly, close passage by the jet, force in the cloud material, as shown by the pink spots at the centre of the image, are remarkable. Images not shown here provide evidence of strong mixing and chaotic motions inside the shocked region, causing an efficient mixing between the original cloud gas and the dilute, hotter ISM. The original gas inside the clouds is thus scattered through larger volumes, as revealed by the image.

The jet in simulation J46a crossed the grid in  $\sim 5100$  years, which implies an advance velocity of  $\simeq 0.3c$ . In the case of J46b, the simulation time is  $\sim 6700$  years (advance speed  $\simeq 0.25c$ ), whereas in the case of J44a (not shown), it is  $\sim 9000$  years (advance speed  $\simeq 0.18c$ ). These advance velocities are just slightly above those observed by Owsianik and Conway 1998, Polatidis and Conway 2003 for Compact Symmetric Objects, probably due to the dilute media used in these initial simulations.

All the green/yellow spots lie close to the bow-shock discontinuity, showing that all the atomic hydrogen gets completely ionised as the shock crosses the cloud. This result has been confirmed by histograms (not shown here) of the number of cells with atomic hydrogen embedded inside a given pressure. These histograms show that the cells containing atomic hydrogen rapidly tend to zero with increasing pressure, close to the isobaric surface shown in red in the image,

as temperatures reach  $10^4 - 10^5$  K. The same behaviour found in J46a is seen in both J46b and J44a: atomic hydrogen seems to be ionised as the shock crosses the clouds.

The temperatures measured inside the shocked regions are extremely high ( $\sim 10^{10} - 10^{11}$  K), which makes it impossible for the ionised gas to cool and recombine within the simulation time-scales. The heating is due to both the shock and mixing with shocked jet material, and the high temperatures in the relatively dilute space between cold clouds (as forced by the large span of ISM density values and the imposed pressure equilibrium in the ambient medium). These initially already high temperatures get increased by the shock, and facilitate reaching the observed values within the shocked region via mixing.

We have computed histograms of transversal and longitudinal velocities (with respect to the jet direction) in cells inside the shocked region. The count was weighted with density in order to focus on the cells with larger densities (and original cloud material). The results –not shown in the thesis– show that, in J46b, where the jet propagates through a denser medium, the most common velocities are  $\leq 5000$  km/s (also in the case of J44a), with the largest bins indicating velocities up to  $\sim 10^{2-3}$  km/s, whereas a significant number of cells reach up to  $10^4$  km/s in J46a. The longitudinal velocity distributions also show the trend towards narrower wings (smaller velocities) in J46b and J44a. The axial velocity distributions show fairly symmetric profiles around zero, which implies that the shocked ISM is involved in both forward motions and backflow towards the galactic nucleus, probably when mixed with the shocked jet gas. Altogether, this reveals chaotic motions, which translates in an ideal scenario for turbulence.

These results show that, in the lower velocity limit, our simulations are capable of reproducing the observed kinematics in Compact Steep Spectrum (CSS) sources such as those reported in Labiano, A. et al. 2005 and Reynaldi and Feinstein 2016 through ionised gas observations. Furthermore, the structure and distribution of the ionised clouds (pink contours in Fig. A.1) is consistent with the ionised fast clouds observed in CSS [see also e.g., Shih, Stockton, and Kewley 2013, Holt et al. 2011, O’Dea et al. 2002]. A refinement on both the ISM initial conditions and jet properties are mandatory in order to reach the velocity ranges with which the ionised gas is observed in CSS sources.

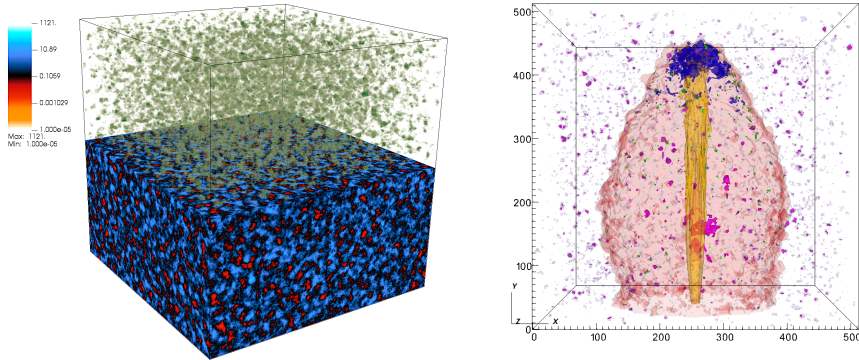


Figure A.1 Left: Initial setup, including a slice of density (bottom) and atomic hydrogen clouds. Right: Last frame of simulation J46b, within a 512 pc side box. Pressure contours are red at the bow-shock ( $P = 10^{-4} c^2$ ), and dark blue at the hot-spot ( $P = 6 \times 10^{-3} c^2$ ); leptonic fraction contour is orange ( $x_e = 0.5$ ); tracer contour is pink ( $f = 0.5$ ), and those showing the atomic hydrogen density inside and outside the bow shock, are green/yellow ( $n_H = 0.1$  and  $n_H = 1 \text{ cm}^{-3}$ ) and purple ( $10 \text{ cm}^{-3}$ ), respectively.

#### A.1.4 Improving the first simulations

As a step forward in this project, we have now improved the set up, using realistic ambient/cloud densities and temperatures. In these simulations, a purely leptonic ( $e^-/e^+$ ) jet is injected into an inhomogeneous medium composed of a mixture of clouds that host atomic hydrogen, at temperatures  $\sim 100 \text{ K}$  and maximum number density  $n \sim 10^9 \text{ m}^{-3}$ , and an ionised medium with  $T \sim 10^6 \text{ K}$  and  $n \sim 10^5 \text{ m}^{-3}$ . The numerical box reproduces the inner 500 pc in the host galaxy, with the jet injected as a boundary condition at a certain distance from the forming region with relativistic velocity  $0.98 c$ , density  $\rho_j = 1.67 \times 10^{-26} \text{ kg/m}^3$ , and a very high specific internal energy  $\varepsilon \sim 10^3 c^2$  to simulate the high pressure expected in this region (the simulation does not include a magnetic field so this approach could only account for a magnetic pressure generated by a disordered field configuration). In the simulations, the ambient medium also has a transversal velocity of 100 km/s to emulate the rotation around the galactic nucleus.

Altogether, the parameter range in the simulations spans throughout more than eight orders of magnitude in density and pressure, which makes the simulation extremely challenging. Moreover, time-step limiters need to be included to allow for the short hydrogen recombination rates in cold regions or ionisation in shocked cells. The simulation uses two EoS: relativistic [Synge 1957] and non-relativistic [see Vaidya et al. 2015] ideal gas. The criterion to choose between

them is based on the cell composition, namely, on the fact that neutral hydrogen is present or not.

The top panels of Fig. A.2 show cuts of rest-mass density (left, in code units  $\rho_a = 10^7 m_p/m^3$ , with an upper limit to the colour scale set at  $10^8 m_p/m^3$ , where  $m_p$  is the proton mass), pressure (centre, in code units  $\rho_a c^2 = 1.5 \times 10^{-3} \text{ Pa}$ , with a lower limit set at  $1.5 \times 10^{-8} \text{ Pa}$ ), and velocity field (right, in code units  $c$ , limited at  $10^{-5} c$ ) at the last snapshot obtained for the simulation, which is still being run, at  $t = 460 \text{ yr}$  after injection. These plots reveal a complex shock structure around the jet as forced by the strong inhomogeneity in density found in the ambient medium. The shocked region is also highly inhomogeneous in density, revealing the richness in the interaction between the jet and the ISM shocked gas. The high sound speed contributes to homogenise pressure within the shocked region with the exception of some knots of denser (ambient) gas, and the jet's hot-spot. Finally, the velocity field shows a wide range of values, from  $10^{-4}$  to  $0.1 c$ . Obviously, the smaller velocities correspond to the denser regions (see the comparison with the density panel). Although there are regions with values that can fall to several tens of km/s (blue colour within the shocked area,  $\sim 10^{-4} c$ ), the dominating blue-white transition implies typical velocities of the order of hundreds to a thousand km/s. These values are in agreement with the typical ones measured from line emission in jetted active galaxies [see e.g., Morganti and Oosterloo 2018, Schulz et al. 2021].

The bottom left panel in Fig. A.2 shows a limited box centred in the region occupied by the jet structure with a rendering of a tracer that indicates the regions where originally dense, cloud, atomic gas can be found. From the image, it is evident that this gas is fixed in clouds outside the shocked volume, but it is completely disrupted and mixed by the shock, and appears concentrated towards the shock region. Finally, the bottom right panel displays, for the same box, a collection of isosurfaces of pressure (red) to highlight the shock wave ( $7 \times 10^{-7} \rho_a c^2 \simeq 10^{-10} \text{ Pa}$ ), leptonic number ( $\rho_{e^-/e^+}/\rho$  at  $10^{-3}$ , as compared to  $\simeq 5.4 \times 10^{-4}$  for  $e^-/p$  gas) to show the jet and still lepton dominated, unmixed, regions, atomic hydrogen density outside the shock (orange, for  $10^8 m_p/m^3$ ) to show the cloud distribution, and inside the shock (bluish, for  $10^5 m_p/m^3$ ) to show hints of atomic hydrogen within the shocked cavity. The low density (bluish) hydrogen density contours follow clearly the shock surface and thus reveal a very fast and complete ionisation of the atomic gas. Therefore, we observe that the shocked gas is completely ionised, so despite our simulation recovers the observed velocities, as stated above, it shows that the shocks produced by powerful jets ionise atomic (and therefore molecular) gas very rapidly and

this forbids line detection, unlike observations clearly reveal. The origin of this discrepancy probably lies in the fact that observed lines correspond to radio sources more evolved than our simulation at the current position (several kpc vs 200 pc) and that post-shock temperatures (typically  $10^6 - 10^7$  K) are too high to allow for recombination of shock-ionised hydrogen within the simulated time. Nevertheless, we observe white spotted areas in the cuts (top left panel) which imply densities between  $10^7$  and  $10^8$   $m_p/m^3$  and this could translate in cooling times of  $\sim 10^{3-4} - 10^{4-5}$  yr for gas between solar and 0 metallicity at the aforementioned temperatures [Dopita and Sutherland 2003]. Although the simulations are limited to pairs, and atomic+ionised hydrogen in the composition of the gas, they show that the conditions for line emission with the observed velocities could be recovered once the jet has evolved for, at least, twice the simulated time so far. Therefore our simulations represent a promising first step in the understanding of ISM dynamics driven by jet injection in the host galaxies.

### A.1.5 A particular scenario: the restarted jet in 3C 84

In Savolainen et al. 2023, we present *RadioAstron* space-based very long baseline interferometry (VLBI) observations of the nearby radio galaxy 3C 84 (NGC 1275) at the centre of the Perseus cluster. The observations were carried out on September 21-22, 2013 and involved a global array of 24 ground radio telescopes observing at 5 GHz and 22 GHz, together with the Space Radio Telescope. Furthermore, the Very Long Baseline Array (VLBA) and the phased Very Large Array (VLA) observed the source quasi-simultaneously at 15 GHz and 43 GHz. The space-VLBI images reveal a previously unseen sub-structure inside the compact 1 pc long jet that was ejected about ten years earlier (see Fig. A.3). In the 5 GHz image, we detected, for the first time, low-intensity emission from a cocoon-like structure around the restarted jet. Our results suggest that the increased power of the young jet is inflating a bubble of hot plasma as it carves its way through the ambient medium of the central region of the galaxy. About half of the energy delivered by the jet is dumped into the mini-cocoon and the quasi-spherical shape of the bubble suggests that this energy may be transferred to a significantly larger volume of the ISM than what would be accomplished by the well-collimated jet on its own. The pressure of the hot mini-cocoon also provides a natural explanation for the almost cylindrical jet profile seen in the 22 GHz *RadioAstron* image.

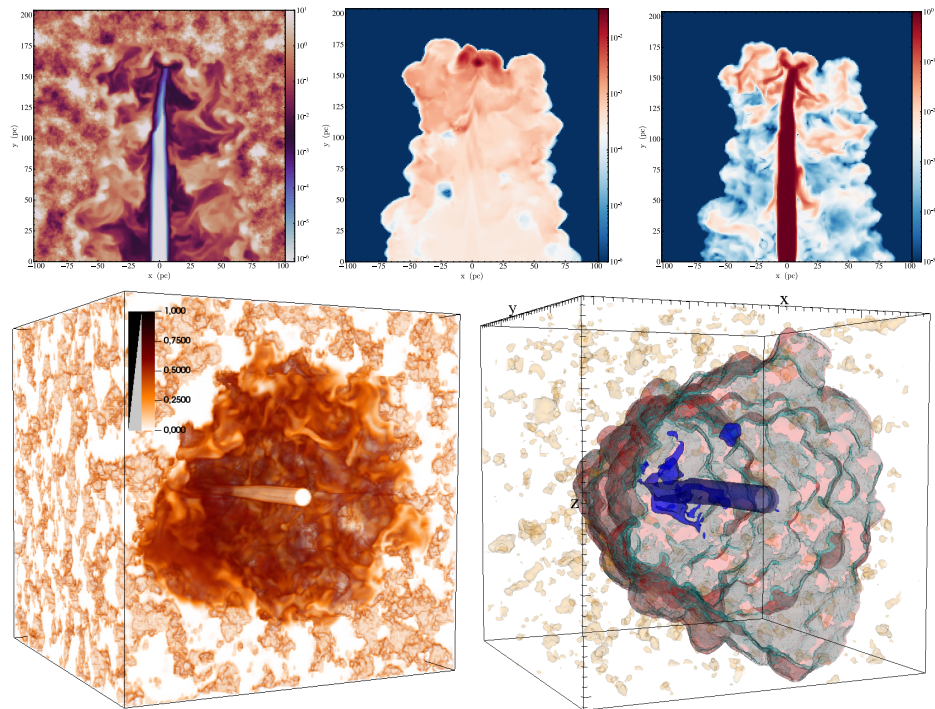


Figure A.2 Top panels: Cuts of rest-mass density (left, in code units  $\rho_a = 10^7 m_p/m^3$ , where  $m_p$  is the proton mass), pressure (centre, in code units  $\rho_a c^2 = 1.5 \times 10^{-3}$  Pa), and velocity field (right, in code units  $c$ ) at  $t = 460$  yr after injection. Bottom left: Tracer rendering showing the locations with originally dense, cloud, atomic gas. Bottom right: isosurfaces of pressure (red,  $\simeq 10^{-10}$  Pa), leptonic number ( $\rho_{e^-}/\rho_{e^+} = 10^{-3}$ ), atomic hydrogen density outside the shock (orange,  $10^8 m_p/m^3$ ), and inside the shock (bluish,  $10^5 m_p/m^3$ ).

### A.1.5.1 Numerical simulations

In order to support the *RadioAstron* observations presented in the paper, we run a numerical simulation employing the new version of the code RATPENAT that I briefly introduced in this chapter [see also Perucho et al. 2021], including a module of hydrogen ionisation and recombination physics [based on Vaidya et al. 2015]. This simulation was run during  $\sim 36$  hours in 1024 cores, at *Tirant*, the local supercomputer at the University of València. The jet is injected in the grid with a radius of 0.07 pc, velocity  $v_j = 0.98 c$ , and temperature  $2.4 \times 10^{10}$  K (jet specific enthalpy is  $h_j = 12 c^2$ ), which results in a kinetic power  $L_j = 3 \times 10^{44}$  erg s $^{-1}$ . The grid is set up with an inhomogeneous ambient medium with mean density of  $15 m_p \text{ cm}^{-3}$ , with a density distribution ranging from  $3000 m_p \text{ cm}^{-3}$  to  $0.01 m_p \text{ cm}^{-3}$ , and temperatures ranging from 1000 K to  $4 \times 10^8$  K. To define the initial density distribution, we used the publicly

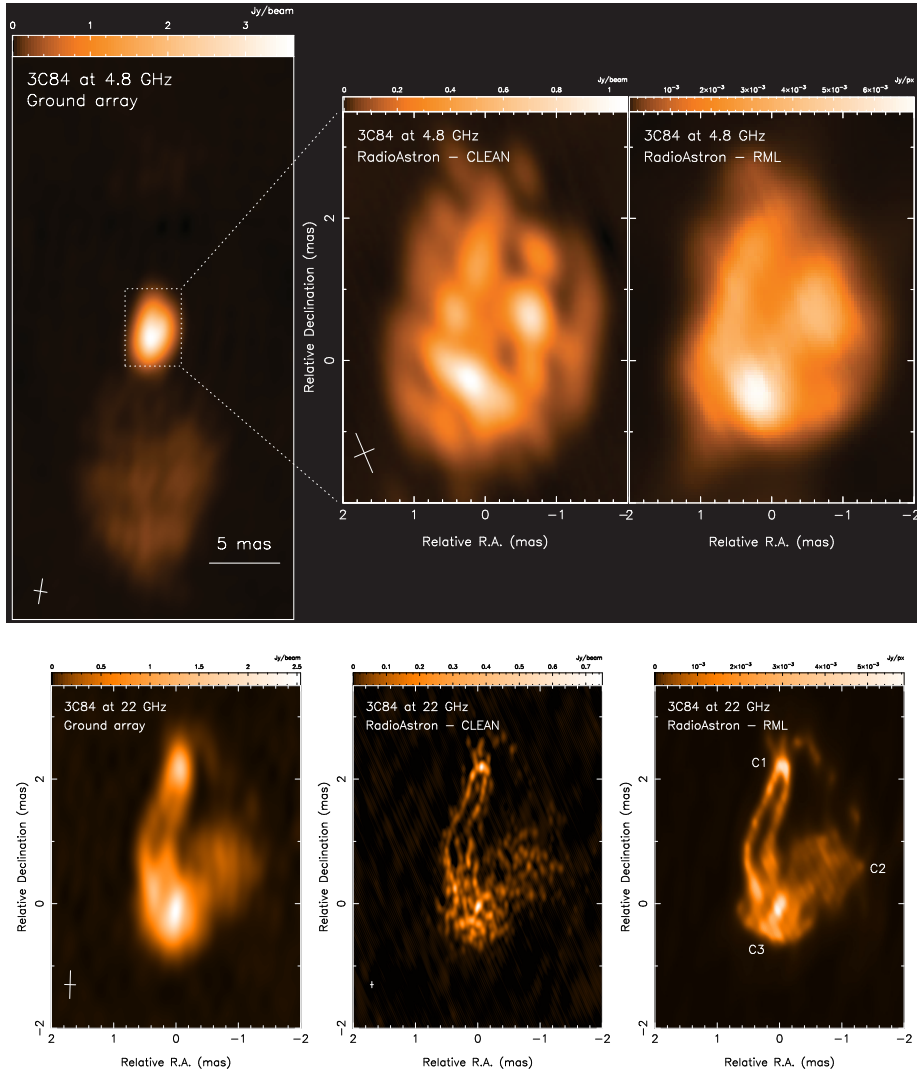


Figure A.3 Ground-based and space-based VLBI images of 3C 84 at 5 GHz (top) and at 22 GHz (bottom).

available PyFC code [Wagner and Bicknell 2011], a package which is useful to represent a dense, inhomogeneous component embedded in a smooth background. The distribution of clouds is set up by an iterative process following the work on terrestrial clouds in Lewis and Austin 2002. The 3D scalar field follows a log-normal single-point statistics in cartesian space and the fractal distribution is established by Fourier transforming and multiplying the cube by a Kolmogorov power-law with spectral index  $\beta = -5/3$ . The mean ( $\mu$ ) of the parent distribution

is 1.0 and the variance  $\sigma^2 = 5.0$  [Wagner and Bicknell 2011]. The dimensions of the numerical box are  $512^3$  cells, with a resolution of 5.8 mpc/cell (resulting in a resolution of 12 cells/ $R_j$ ), so the box covers the inner 3 pc of evolution of the relativistic, electron-positron jet propagation. Based on the computational box dimensions, we set a minimum sampling wave-number  $k_{\min} = 17$ , such that the scale of the largest fractal structure in the cube (i.e., the cloud size) is approximately 0.1 pc.

Figure A.4 shows the results of the simulation, for which we have used the approximate parameters derived for the jet in 3C 84 in this paper. The images show the initial jet expansion and a transition to nearly cylindrical geometry caused by the jet's cocoon pressure. Because these represent the initial stages of evolution, the jet head is close enough to the injection point that the jet has not covered enough distance to recollimate in a conical shock. Following the jet evolution would allow us to see how, as the jet head evolves to larger distances, a recollimation shock would be formed due to the collimating effect — already observed in the simulations — of the cocoon [this has been observed in previous simulations of jet evolution, see e.g., Perucho and Martí 2007]. This is precisely the structure observed in the jet of 3C 84, which shows no bright features from initial expansion until the hotspot.

Interestingly, the plots also show, not only the aforementioned qualitative morphological resemblance, but also that the hottest regions in the jet are the shear layer, where dissipation takes place, and the hotspot itself. The dissipation of the kinetic energy due to the friction between different velocity layers, or the development of instabilities that play this same role can create a layer of hot gas where particles are accelerated [e.g., Rieger 2019, and references therein]. In the case of 3C 84, energy dissipation at the jet boundaries could well be produced by shear, as it is the case in the simulation (the generation and effects of shear-layers have been recently reported for the case of the radio galaxy 3C 111 [Beuchert et al. 2018, Schulz et al. 2020]). The bow shock (external contours) shows a granular structure produced by the interaction of the jet with the colder, denser clouds.

The main difference between the simulation and the observed jet is the bend observed in 3C 84 close to the hot-spot. The jet shows no signs of instability development before this bend, which would correspond to an already nonlinear amplitude. Another option would be jet precession, which, considering that jet propagation is basically ballistic, could also be excluded as the cause of the bend because there is no continuous change in direction either. Finally, the presence of a local, relatively large-scale inhomogeneity in the density distribution could

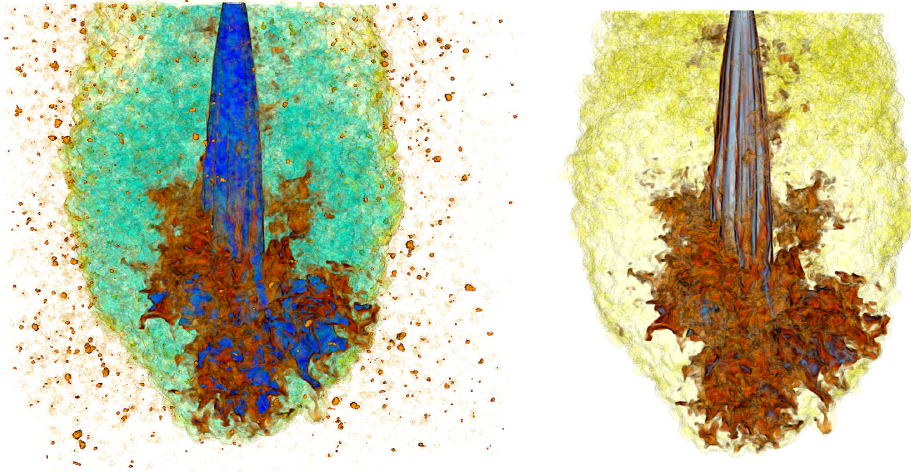


Figure A.4 Snapshots of a simulation of a relativistic, electron-positron jet propagating through a dilute ambient medium, as expected to be the case for the re-started jet in 3C 84. The left panel shows a 3D render of the leptonic mass fraction (which identifies the jet), three temperature contours ( $2.5 \times 10^8$  K in faint yellow,  $2.1 \times 10^{10}$  K in faint blue and  $1.8 \times 10^{12}$  K in dark blue), and atomic hydrogen density (brown clumps). The right panel shows a 3D render of the leptonic mass fraction and a pressure contour (faint yellow), to show the position of the jet bow shock.

trigger a differential cocoon pressure on both sides of the jet, forcing it to change direction. The fact that the lobe seems to develop in the direction of the bend favours this interpretation. The reason is that the lobe plasma will preferentially move towards the lower pressure regions. Interestingly, Kino et al. 2021 reach the same conclusion based on 43 GHz VLBI monitoring during 2016–2020 which shows  $\sim 1$  yr long frustration of the hot spot motion in 2017 and a subsequent breakout.

### A.1.5.2 Jet feedback

It is well established that fully developed, large-scale jets of massive radio galaxies can heat the intergalactic or intracluster medium suppressing the cooling flows and controlling the growth of the massive galaxies [McNamara and Nulsen 2007, McNamara and Nulsen 2012]. There is good evidence that this *radio mode* or *maintenance mode* feedback mechanism is at work also in the Perseus Cluster and generations of outbursts from 3C 84 have inflated multiple X-ray cavities in this cluster [Boehringer et al. 1993, Fabian et al. 2000, Fabian et al. 2003]. A more recent idea is that the jet, especially a young, confined jet, could be an important feedback mechanism also *inside* the host galaxy, heating gas and driving molecular outflows [e.g., Morganti, Tadhunter, and Oosterloo 2005,

Morganti et al. 2013, Wagner, Bicknell, and Umemura 2012]. One of the central problems of the latter type of feedback has been how well-collimated jets can affect the entire volume of the bulge, i.e., how the jet couples to the ISM and how it can deposit energy and momentum relatively isotropically. There are several mechanisms that can play a role here, which will be discussed below.

First of all, jets are light and overpressured; they can inflate a highly overpressured cocoon that expands quasi-isotropically. We can now, for the first time, see evidence for this in sub-pc scales. The mini-cocoon expands at a transverse velocity of  $\sim 0.1c$  and its aspect ratio is about 1.4, hence the cocoon can process a significantly larger volume of the ISM than the collimated jet alone. However, the transverse expansion speed of the cocoon will decrease as the cocoon pressure decreases over time and this will increase the aspect ratio – for the southern mini-lobe, created by the previous activity period, the aspect ratio is about 2. The results shown in the paper indicate that the jet can dump about half of its energy in the mini-cocoon.

In a series of numerical simulations, first 2D axisymmetric [Perucho, Quilis, and Martí 2011, Perucho et al. 2014b], and later 3D simulations [Perucho, Martí, and Quilis 2019, Perucho et al. 2021], the authors have shown that collimated, relativistic jets can deposit a large fraction (up to 80 – 90%) of their energy into heating and displacing the ambient medium both in the galactic halos and intergalactic medium. In Perucho et al. 2017 the authors gave an explanation to this efficiency, on the basis of the aforementioned jet collimation and relativistic nature of AGN jets. In this work, they studied the ratio of the cavity (cocoon) pressure to the maximum cavity pressure defined as

$$p_{c,\max} = \frac{L_j \Delta t}{V_c}, \quad (\text{A.1})$$

where  $V_c$  is the cavity volume and it is implicitly assumed that all the injected energy is transferred to the cocoon to drive the shock [Begelman and Cioffi 1989]. Perucho et al. 2017 found that in the relativistic simulations  $p_c/p_{c,\max} \simeq 0.4$  throughout the whole propagation phase. Taking this ratio and assuming  $\theta = 18^\circ$ ,  $P_j \simeq p_c V_c / (0.4 \Delta t) \gtrsim 2 \times 10^{43} (1+k)^{4/7} \text{ erg s}^{-1}$  (see details in Savolainen et al. 2023). This lower limit for  $P_j$  matches the lower limit calculated in Sec. 4.1.2 of Savolainen et al. 2023 and it is a factor of two smaller than the lower limit calculated in Sec. 4.2.1 of Savolainen et al. 2023. This is consistent with a large proportion of the energy transfer from the jet taking place through a strong shock with the ambient medium, which, according to the cited works, could be assigned to its collimation and relativistic nature.

Numerical simulations of jet propagation using a multi-phase description of the ambient medium have also shown that the jets couple strongly to a *clumpy* ISM e.g., Wagner and Bicknell 2011, Wagner, Bicknell, and Umemura 2012, Mukherjee et al. 2018, and the work described in the previous section. When a jet in these simulations struggles through a dense cluster of gas clouds of various sizes, it is deflected and the flow is channelled to many different directions in the porous ISM. According to the simulations by Wagner, Bicknell, and Umemura 2012 these channel flows provide an efficient means of energy transfer from the jet to the ISM with up to 40% of the jet energy being deposited to the cold and warm gas. The earlier works by Nagai et al. 2017, Kino et al. 2018, and Kino et al. 2021 indicate that the restarted jet in 3C 84 is likely moving through a clumpy, multi-phase medium and this mechanism can be also, at least partly, responsible for creating the cocoon bubble. The interaction between the jet and a dense gas clump is also the most likely explanation for the molecular outflow found by Nagai et al. 2019.

Finally, yet another effect that can increase the volume of the ISM that a jet can have an impact on, is the wobbling or precession of the jet. If the jet direction changes significantly with time, it naturally interacts with a larger volume of ambient gas. The 3C 84 has clearly ejected sub-pc scale jets in different directions over the past 30 years as can be seen by comparing VLBI observations made in the 1990s to the jet direction visible in the 22 GHz *RadioAstron* image. In the 43 GHz VLBA images of Dhawan, Kellermann, and Romney 1998 made in 1995–1996, the sub-pc jet points to southwest, to the direction of the current feature C2; in 2013, the jet was pointing to south-southeast.

It is quite possible that all three mechanisms — an overpressured cocoon, interaction with a clumpy ISM, and changes in the jet direction — work at the same time in 3C 84 helping to transfer energy and momentum from the jet to the ISM.

---

## A.2 The large scale morphology of Hercules A

---

This chapter was originally published in *On the large scale morphology of Hercules A: destabilized hot jets?*. M. Perucho, **J. Lopez-Miralles**, N. Gizani, Jose Maria Marti, B. Boccardi. *Monthly Notices of the Royal Astronomical Society*, Volume 523, Issue 3, August 2023, Pages 3583–3594. DOI: 10.1093/mnras/stad1640. *Reproduced with permission.*

---

### A.2.1 Introduction

Extragalactic jets are formed at the surroundings of supermassive BHs in AGN by means of magneto-hydrodynamical processes that extract rotational energy from the BH [Blandford and Znajek 1977]. The jets are thought to be accelerated along the collimating region by the toroidal magnetic field [see e.g. Vlahakis and Königl 2004, Komissarov et al. 2007], and by the conversion of internal into kinetic energy (through the Bernoulli process) at jet expansions [see e.g. Perucho and Martí 2007]. Expansion and acceleration cause a drop in the intensity of the jet's magnetic field and thermal pressure, which leads to outflows being kinetically dominated unless dissipative processes [instabilities, shocks, interactions... see e.g., Perucho 2019, for a review] take over. The large scale morphology of jets is therefore a consequence of the evolution of the flowing plasma along its propagation.

Fanaroff and Riley 1974 showed the existence of a morphological dichotomy of radio galaxies, with Fanaroff-Riley type I (FRI) being brighter at their centres and becoming dimmer and more symmetric in brightness towards the outer regions, and Fanaroff-Riley type II (FR II) being, in contrast, brighter at their extremes, namely, at the sites of interaction with the interstellar or the warm-hot intergalactic medium (ISM/WHIM). The dichotomy was associated to jet power, with FR II radio galaxies corresponding to the more powerful jets [e.g., Ghisellini and Celotti 2001]. Nevertheless, this classification, albeit very useful as an initial grouping, has been shown to simplify in excess the complexity of radio source morphologies. Recent observational works have shown that the relation between power and morphology is unclear, mainly at intermediate and low jet powers, with some low power jets showing FR II morphology, or equal power jets showing different morphologies [see, e.g. Vardoulaki et al. 2021, Mingo et al. 2019, Mingo et al. 2022].

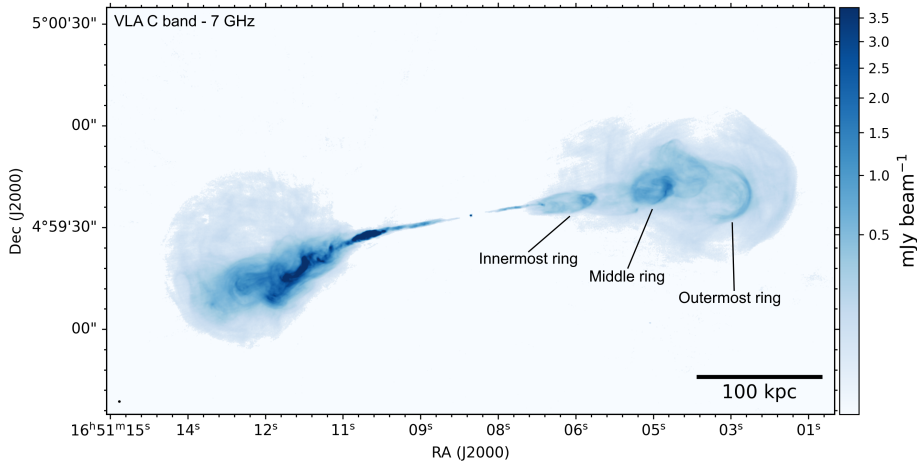


Figure A.5 Radio image of Hercules A constructed from the VLA C band at 7 GHz. Reproduced with permission from Timmerman et al. 2022.

The radio galaxy Hercules A is a good example of this complexity: on the one hand, its relatively powerful jets would be expected to develop typical FRII morphologies, but, on the other hand, they exhibit no hotspots at their limbs, and the jets seem to transit from a collimated regime into a disruptive process. The images of this source obtained with different arrays [Sadun and Morrison 2002, Gizani and Leahy 2003, Timmerman et al. 2022] show the development of a kink prior to jet disruption. Beyond these disruptive points, at  $\sim 100$  kpc [as derived from VLA and LOFAR observations, e.g., Kassim et al. 1993, Gizani and Leahy 2003, Timmerman et al. 2022, –it is noteworthy that this coincides with the cluster density core radius], the jets inflate large, quasi-spherical lobes that resemble those found in FRII radio sources and are surrounded by bow shocks [Nulsen et al. 2005], albeit missing the bright interaction sites, or hotspots (see also Fig. A.5). These lobes show, furthermore, notorious arc-shaped filaments. Finally, the western jet/lobe show bow-shock structures that could be triggered with the propagation front of enhanced injection. In summary, the detailed imaging of this source reveals the large level of complexity required to interpret it.

The jet formation and acceleration paradigm establishes that the jet energy flux is dominated by the magnetic and/or internal energy contributions at injection and it becomes kinetically dominated after becoming superfast magnetosonic [see e.g., Komissarov 2012]. Entrainment contributes to mass-loading and the correspondent relative increase of kinetic+rest mass energy flux in the flow

[Anglés-Castillo et al. 2021]. Moreover, jet propagation through a decreasing density ambient medium facilitates head acceleration [e.g., Perucho, Martí, and Quilis 2019] and also the gain of flow inertia, which contributes to further jet stability, by increasing the relativistic density relative to the ambient medium [the cocoon expands faster and its density falls faster, too, see e.g., Perucho 2012]. The role of jet inertia in the growth rates of Kelvin-Helmholtz instability (KHI) modes in relativistic flows was discussed in detail in Perucho, Martí, and Hanasz 2005, both for symmetric (pinching) and antisymmetric (helical) modes.

Numerical simulations of extragalactic jets have been traditionally aimed to either reproduce the morphologies of powerful FR II jets [e.g., Martí et al. 1997, Komissarov and Falle 1998, Aloy et al. 1999, Scheck et al. 2002, Mignone et al. 2010, Massaglia et al. 2016, English, Hardcastle, and Krause 2016, Mukherjee et al. 2020, Seo, Kang, and Ryu 2021, Perucho, Quilis, and Martí 2011, Perucho et al. 2014a, Perucho, Martí, and Quilis 2019, Perucho, Martí, and Quilis 2022], or low-power, FR I jets [e.g. Perucho and Martí 2007, Rossi et al. 2008, Perucho et al. 2014a, Massaglia et al. 2016, Massaglia et al. 2019, Massaglia et al. 2022]. Few works have tried to address the complex morphology of Hercules A-like sources. Nakamura et al. 2008 simulated the jets in this source as *magnetic towers*, obtaining one of the closest approaches to this source found in the literature. However, the simulations show jets that are much wider than the observed ones, relative to the lobe size obtained. Furthermore, inherent to the magnetic tower model is the assumption of a Poynting-flux dominated flow, while there are serious doubts about magnetic energy dominating the jet energy flux at these scales [see e.g. Begelman, Blandford, and Rees 1984, Vlahakis and Königl 2004, Croston et al. 2005, Komissarov et al. 2007]. Hence, the question remains about how to produce the morphologies seen in the Hercules A jets with non-magnetically dominated flows. Saxton, Bicknell, and Sutherland 2002 studied the generation of rings in the western lobe of this source via non-relativistic, hydrodynamical simulations. The authors suggested that these rings could be triggered by shocks propagating through the lobes of the disrupted jet and the presence of strong recollimation shocks as the origin of jet disruption and transition to turbulence. However, as we will discuss in this appendix, a non-relativistic, axisymmetric approach is probably insufficient to reproduce and interpret correctly the morphology of the lobes in Hercules A.

As previously noted, jet disruption by helical instability modes or kinks seems to happen at around the distance at which the cluster density profile starts to fall, after which the quasi-spherical lobes develop. This sphericity is a signature of pressure-driven expansion, which could be favoured by the jets being initially

hot [Perucho et al. 2017]. It is very important to remark that when we refer to a *hot* jet, it is not only that its sound speed is large, and its Mach number is thus small, but to the fact that its specific internal energy is relativistic.

In this appendix, we try to explain the generation of large scale diffuse lobe morphologies similar to those observed in Hercules A from a purely relativistic hydrodynamics (RHD) approach, using our code RATPENAT [Perucho et al. 2010]. Therefore, an attempt to reproduce internal lobe features (rings/arcs) in detail is out of the scope of this work. Interestingly, though, our simulations also reveal a possible physical mechanism responsible for the formation of the observed arcs in Hercules A. From our results, we suggest that these features could be the consequence of the development of (helical) instability-triggered shocks. Future work will revisit this scenario with relativistic magnetohydrodynamics (RMHD) simulations using the code LÓSTREGO [López-Miralles et al. 2022, López-Miralles, Martí, and Perucho 2023]. As a warning note, we point out that it is not the aim of this chapter to reproduce the exact morphology of the source, which would require not only a detailed knowledge of the jet injection conditions, including the jet power, rest-mass density and velocity, specific internal energy, and the structure of the magnetic field, but also of the environment prior to jet injection. It would be therefore reckless to approach the problem with this aim. Alternatively, we adopt a qualitative approach, which allows us to discard some scenarios and to put the focus on particular jet/ambient medium configurations to explain both jet disruption and lobe inflation.

We have run numerical simulations of jets with a set of parameters that are based on two different hypothesis about the origin of the observed morphology. In particular, the two possibilities considered are: 1) a kinetically dominated jet, with a periodic variation in injection power, and 2) an internal-energy dominated jet, prone to the development of instabilities and disruption. In the first case, the lobes would be inflated by the shocked jet plasma injected prior to the drop in jet power, whereas in the second this task would be done by the continuously injected, high-pressure plasma going through the disruption point. We show that a jet with a large internal energy (with a possibly contribution of magnetic energy) can produce a qualitatively similar morphology to that in Hercules A, avoiding the assumption of Poynting-flux dominated, force-free jets at kpc scales, not favoured by current models of jet acceleration [Komissarov 2012] and evolution [Perucho 2019]. Owing to the large computational cost of 3D numerical simulations, we are forced to run only a few runs, focusing on fitted density/pressure profile of the cluster from observational results [Gizani and Leahy 2004] and basic estimates on the jet properties [Gizani and Leahy 2003].

A broad sweep in parameter space is prohibitive in 3D simulations like the ones we present here, which require between  $5 \times 10^5$  and  $10^6$  hours of calculation in supercomputing resources.

The structure of the chapter is the following: Section A.2.2 is devoted to the description of the simulation setup; in Section A.2.3 we describe our results, and in sections A.2.4 and A.2.5 we discuss those results and present our conclusions, respectively.

## A.2.2 Numerical simulations

We have used the code RATPENAT running in the supercomputing resources at the University of València. This code solves the RHD equations in conservation form, using high-resolution-shock-capturing methods [see Perucho et al. 2010]. The code is a hybrid parallel code – message passing interface/MPI + OpenMP – that is optimised for the use of supercomputers with a shared/distributed memory structure. The simulations have been run in 256 to 1024 cores at Tirant (*Servei d'Informàtica de la Universitat de València*). We have used LLNL VisIt [Childs, H. et al. 2012] to generate the figures for this work.

We also introduced a source term in the energy equation to account for thermal cooling in a simplified way [Perucho, Bosch-Ramon, and Barkov 2017, Perucho, Martí, and Quilis 2022]. The cooling term  $\Lambda$  (cgs units; considering hydrogen ions only) is taken as in the approximation given in Myasnikov, Zhekov, and Belov 1998:

$$\Lambda = n_e n_H \times \begin{cases} 7 \times 10^{-27} T, & 10^4 \leq T \leq 10^5 \\ 7 \times 10^{-19} T^{-0.6}, & 10^5 \leq T \leq 4 \times 10^7 \\ 3 \times 10^{-27} T^{0.5}, & T \geq 4 \times 10^7 \end{cases}$$

where  $T$  is the gas temperature and  $n_e$  and  $n_H$  are the electron and hydrogen ion number densities. Whereas  $n_e = \rho_e/m_e$  with  $\rho_e$  the electron mass density and  $m_e$  the electron mass, for purely ionised hydrogen,  $n_H = \rho_p/m_p$  with  $\rho_p$  the proton mass density and  $m_p$  the proton mass. Electron and proton mass densities are computed with the Sygne EoS, implemented as described in Appendix A of Perucho and Martí 2007, which allows us to describe our system as a mixture of relativistic (electron, proton and positron) ideal gases. We therefore implicitly assume thermodynamical equilibrium at each cell.

### A.2.2.1 The ambient medium

The numerical box used in the simulations defines a cube with sides of 256 or 512 kpc, with the jet injected from the centre of one of its faces as a boundary condition. The jet injection point is taken to be at  $\sim 10$  kpc from the active nucleus, as fixed by the distribution of the ambient medium (see below). The jet radius at injection is taken as  $R_j = 1$  kpc. The ambient medium is given by a density profile that corresponds to that estimated for Hercules A [see e.g., Gizani and Leahy 2004]. We model it as a hot medium dominated by ionised hydrogen (electron-proton gas) with the following profile

$$n_{\text{ext}} = n_c \left( 1 + \left( \frac{r}{r_c} \right)^2 \right)^{-3\beta_{\text{atm},c}/2}, \quad (\text{A.2})$$

where  $r$  is the radial spherical coordinate. Here, we have used  $n_c = 0.01 \text{ cm}^{-3}$ ,  $r_c = 120$  kpc, and  $\beta_{\text{atm},c} = 2.22$ . The temperature  $T_{\text{ext}}$  is set constant to  $4.9 \times 10^7$  K. The pressure is then derived from

$$p_{\text{ext}} = \frac{k_B T_{\text{ext}}}{\mu X} n_{\text{ext}}, \quad (\text{A.3})$$

where  $\mu$  is the mass per particle in atomic mass units ( $\mu = 0.5$  here),  $X$  is the abundance of hydrogen per mass unit, which is set to 1, and  $k_B$  is the Boltzmann's constant. The chosen profiles for the density and temperature define a dilute and hot ambient medium. Whereas this can be the result of the passage of the jets (which sweep and heat the original ambient medium as they propagate), the lack of hotspots and strong bow shocks around the radio source at the simulated scales, along with the long lifetimes estimated for the source would suggest that the ambient medium has got enough time to recover its original distribution ( $t_{\text{jet}} > t_G$ , the dynamical time of the gravitational pull from the host galaxy). Nevertheless, it is impossible to know the initial distribution of the WHIM prior to the injection of the radio galaxy.

### A.2.2.2 Kinetically dominated jets

The jet power, in the absence of a dynamically relevant magnetic field, is given by  $L_j = \rho(hW - 1)Wc^2vA_j$ , with  $\rho$  the rest mass density,  $h$  the specific enthalpy,  $v$  the jet flow speed and  $W$  the corresponding Lorentz factor,  $A_j$  the jet area at injection, and the subtraction in the bracket removes the contribution of the rest-mass energy of the particles. The specific enthalpy is related with the

specific internal energy  $\varepsilon$  through  $h = 1 + \Gamma\varepsilon/c^2$ , where  $\Gamma$  is the adiabatic index provided by the EoS.

As pointed out in Perucho et al. 2017, the amount of internal energy transported by the jet affects the lobe pressure, and it is precisely when  $\varepsilon \gg c^2$  that the jet energy flux is dominated by internal energy. On the contrary, when  $\varepsilon \sim c^2$  or smaller, the jet is dominated by kinetic energy.

The injection power of the kinetically dominated jet is  $L_j = 2 \times 10^{46}$  erg/s, within the estimated range of jet power for the source [Saxton, Bicknell, and Sutherland 2002]. The jet was injected into the ambient medium grid (a numerical box with  $512^3$  cells, covering a physical region of  $(256 \text{ kpc})^3$ ) as kinetically dominated, with velocity  $v = 0.92c$  and rest mass density  $10^{-4}$  times that of the ambient medium at injection, i.e.,  $\rho_j = 1.67 \times 10^{-30} \text{ g/cm}^3$ . The leptonic contribution to the total density is taken to be of the 80%. By doing this we account for possible entrainment of protons along the initial kiloparsecs of evolution, as expected from, at least, jet/star interactions [see e.g., Anglés-Castillo et al. 2021]. The jet specific internal energy is  $\varepsilon = 1.15c^2$ , which makes the jet also thermodynamically relativistic, but still dominated by kinetic energy. The adiabatic exponent of the flow at injection is  $\Gamma = 1.39$ . The classical Mach number of the jet at injection is thus 1.88, whereas the relativistic Mach number is 4.8.

In this first set-up, we fixed constant injection up to  $t \simeq 19 \text{ Myr}$ , which is the time at which the bow shock has crossed the density core,  $z_{\text{BS}} \simeq 125 \text{ kpc}$ . After that point, three different simulations were run as a continuation of the initial one: 1) uninterrupted, constant injection, 2) a gradual switch off of injection after  $t_c$ , and 3) periodical modulation of the injection velocity between  $0.83c$  (dropping jet power to  $L_j = 4 \times 10^{45}$  erg/s) and  $0.92c$ , with a periodicity of  $10 \text{ Myr}$ . This period was chosen following the hypothesis that the observed arcs in Hercules A are triggered by patterns, which could propagate at smaller velocities than the jet flow and turn into shocks when moving through the slower lobe plasma [see e.g., Perucho, Martí, and Hanasz 2005, for a discussion on instability generated shocks]. In addition, we chose velocity values for the modulated injection that resulted in jet powers between the limits estimated by Saxton, Bicknell, and Sutherland 2002 ( $2 \times 10^{45} - 2 \times 10^{46}$  erg/s). We want to stress that the introduction of such modulation was mainly aimed to increase the internal energy of the flow and not to produce the observed arcs.

In all these simulations we introduced a helical perturbation pattern in velocity [see Eq. 13 in Perucho, Martí, and Quilis 2019] with different periodicities ranging from  $\sim 4 \times 10^4$  to  $\sim 2 \times 10^6$  yr. The total amplitude given to these

helical motions is  $2.5 \times 10^{-4}$  of the injection velocity. These helical patterns allow us to break symmetries and trigger KHI helical modes if the flow is prone to their development [see e.g., Perucho et al. 2006].

### A.2.2.3 Internal energy dominated jet

In the case of the internal energy dominated outflow, jet injection velocity is  $v_j = 0.92 c$  –with the helical injection pattern mentioned above–, the gas rest-mass density ratio with the ambient medium is  $10^{-7}$ , i.e.,  $\rho_j = 1.67 \times 10^{-33} \text{ g/cm}^3$ , with the same composition as the kinetically dominated jet (80% of the mass as electrons and positrons, and 20% as protons); the jet specific internal energy is  $\varepsilon = 404 c^2$ , and the adiabatic exponent is  $\Gamma = 1.33$ . The total jet power is, in this case,  $L_j = 4 \times 10^{45} \text{ erg/s}$ , within the estimated range of jet power for the source [Saxton, Bicknell, and Sutherland 2002]. This simulation was run in a numerical box with  $1024^3$  cells, with physical dimensions of  $(512 \text{ kpc})^3$ .

## A.2.3 Results

### A.2.3.1 Kinetically dominated jets

Figure A.6 shows cuts of density, pressure and velocity module squared, for the aforementioned simulations 1, 2 and 3, at the last snapshots. Constant injection –case 1, top panels– produces a very different lobe morphology to that observed in Hercules A, and very similar to the typical structures obtained in long-term numerical simulations of powerful, kinetically dominated jets [e.g., Martí et al. 1997, Komissarov and Falle 1998, Aloy et al. 1999, Scheck et al. 2002, Mignone et al. 2010, Massaglia et al. 2016, English, Hardcastle, and Krause 2016, Mukherjee et al. 2020, Seo, Kang, and Ryu 2021, Perucho, Quilis, and Martí 2011, Perucho et al. 2014a, Perucho, Martí, and Quilis 2019, Perucho, Martí, and Quilis 2022]. Although the jet shows periodical expansions and recollimations, visible in the pressure map, the jet disruption is clearly caused by helical distortions of the jet, as seen in the density, left panel. The gradual switch off –case 2, central panels– produces a detached lobe, but this lobe does not develop a spherical shape ( $\sim 100 \text{ kpc}$  and  $\sim 50 \text{ kpc}$  in the axial and transversal directions, respectively), unlike the observed lobes in Hercules A. Furthermore, the jet is not observed to enter the lobes as it happens in the VLA images of the source.

The third simulation –bottom panels in Fig. A.6– involves a periodical modulation of injection power without completely switching it off. At the last snapshot, the jet power is close to its minimum, with  $v_j \simeq 0.83 c$ . This set

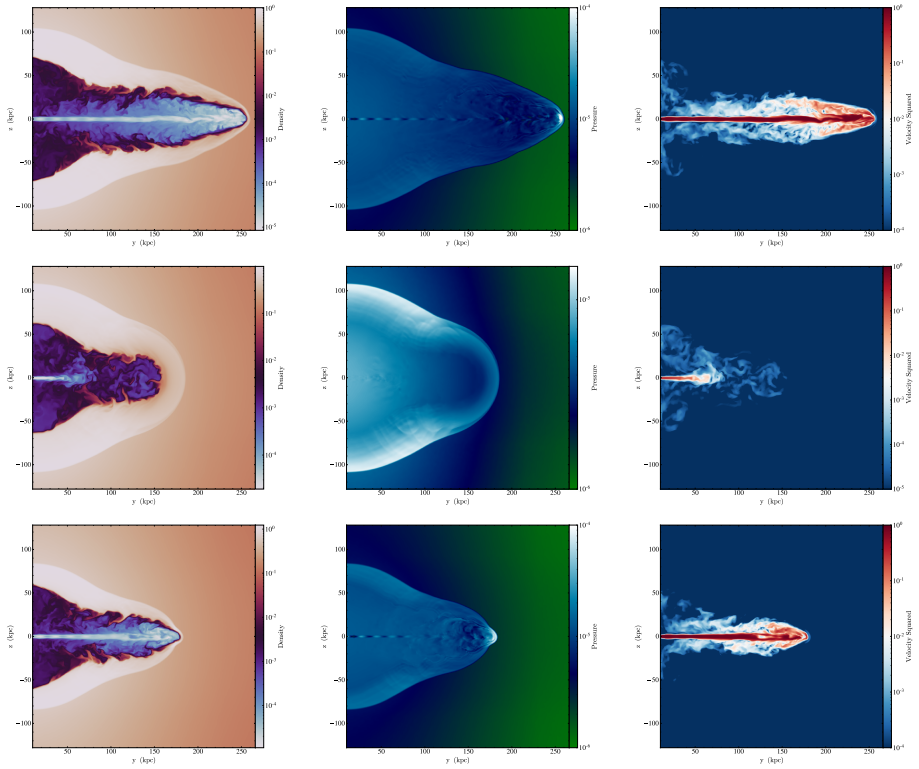


Figure A.6 Rest-mass density (left panels), pressure (central panels) and velocity module squared (right panels) cuts for the three kinetically dominated jets at the last snapshots ( $t \simeq 41, 43,$  and  $30$  Myr, respectively). The top row shows case 1, constant injection, the central row shows case 2, with a gradual switch off, and the bottom panel shows case 3, with modulated injection. Units are:  $\rho_a$  for density,  $\rho_a c^2$  for pressure, and  $c$  for velocity.

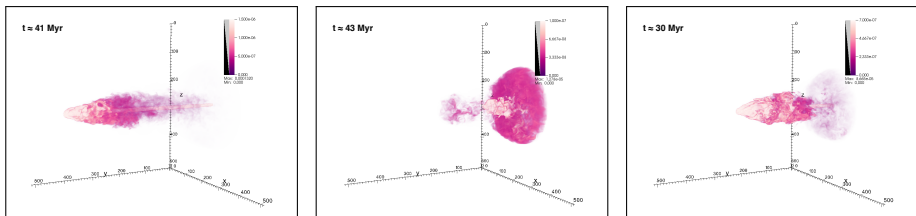


Figure A.7 Pressure (weighted with tracer) renderings of the numerical box for the three kinetically dominated jets, cases 1 to 3 from left to right. We apply limits to the range of values in the box, which permits to visualise the regions of interest –jets and lobes. The axes indicate cell numbers.

up develops turbulent, inhomogeneous lobes. The resulting structure shows a pinching structure in the jet and strong irregularities caused by the interaction between the different enhanced injection epochs. However, no strong internal shocks are observed, which could be explained by the smoothness of the change in jet power. Timmerman et al. 2022 have concluded that the periodicity in the jet activity could probably be more than an order of magnitude shorter than the one we have used. Such a short period could result in a more continuous jet-lobe structure, and generate the bow shock structures observed in the western jet, if the changes are significant enough along the activity cycle. Perhaps, a more abrupt change would facilitate shock formation and the generation of arcs, but the morphology obtained from this simulation seems to be far away from the observed radio source. New simulations should be run to test this scenario properly for the case of hot jets, as we show in the next sections. This is however, out of the scope of the work, which is focused on the generation of the peculiar large scale, jet-lobe morphology of Hercules A.

Figure A.7 shows renderings of pressure weighted with tracer for the three cases, for the same snapshots shown in Fig. A.6. These images highlight the high energy density regions, i.e., those associated to the jet or shocked jet gas, expected to have higher synchrotron emissivity. Altogether, these simulations show that kinetically dominated jets tend to form elongated lobes, even if jet injection is modulated or interrupted [as shown in previous work, Perucho et al. 2014b], or fail to reproduce the observed jet-lobe connection (i.e., case 2).

### A.2.3.2 Internal energy dominated jet

Figure A.8 shows cuts of rest-mass density, pressure and velocity module squared at different times along the simulation. Although along the initial stages of the evolution (two upper rows) the structure generated by the jet resembles that seen for case 3 in Fig. A.6, once the jet head reaches distances over 100 kpc, the terminal shock detaches from the bow-shock and starts feeding a lobe with low-density, high-energy density, shocked gas. This hot gas drives the expansion of the radio source by means of its high pressure. The high sound speed in this region isotropizes pressure and the bow shock becomes quasi-spherical (this can be better seen in Fig. A.9). Thus, the lobes also tend to achieve this shape, in contrast with the elongated lobes obtained in the kinetically dominated simulations.

Figure A.9 displays renderings of pressure and axial velocity distributions at the end of this simulation, i.e., after  $\sim 152$  Myr. At this time, the front shock is

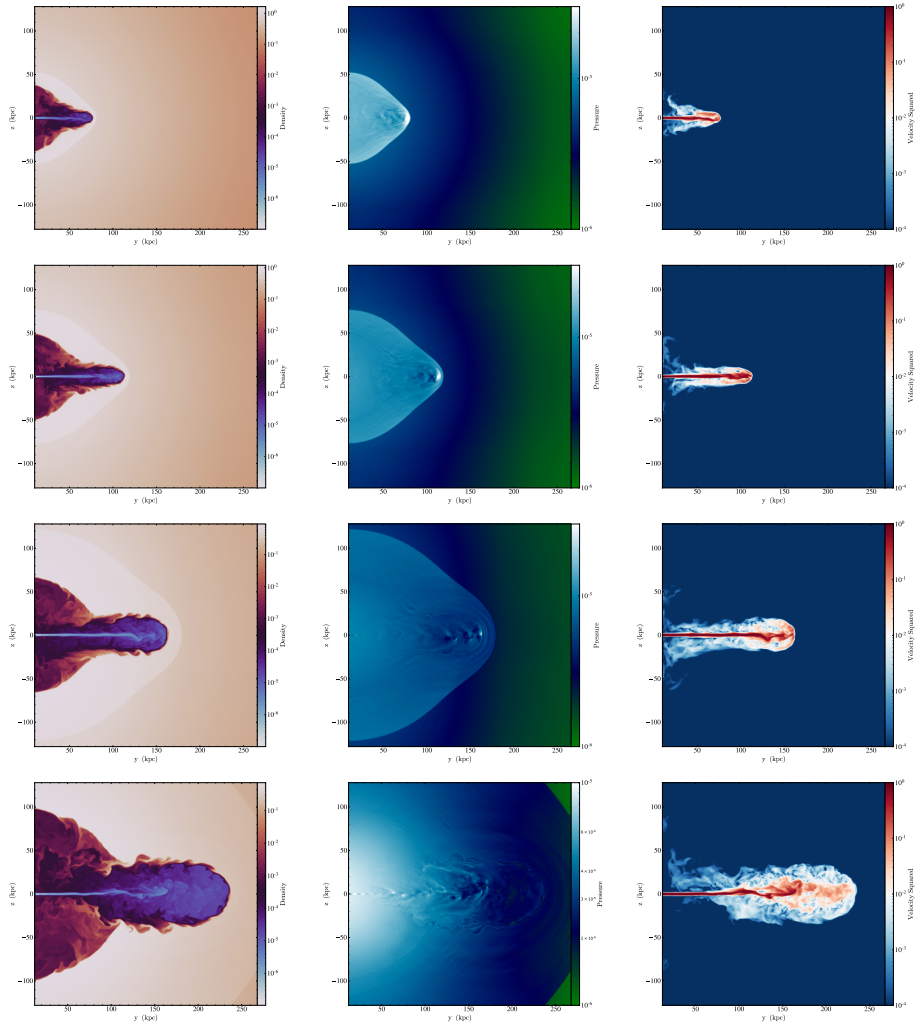


Figure A.8 Rest-mass density (left panels), pressure (central panels) and velocity module squared (right panels) cuts for the internal energy dominated jet at times 21 (first row), 36 (second), 67 (third), and 152 Myr (fourth). Units are:  $\rho_a$  for density,  $\rho_a c^2$  for pressure, and  $c$  for velocity.

at 280 kpc.<sup>1</sup> The purple scale shows the rendering of pressure distribution in code units ( $\rho_a c^2$ , with  $\rho_a$  the ISM density at injection, i.e.,  $1.67 \times 10^{-26}$  g/cm<sup>3</sup>). The image captures the mild shock around the jet, with an almost spherical

<sup>1</sup>The advance velocity of the shock ranges from  $\sim 0.015 c$  at the beginning of the simulation to  $\sim 5 \times 10^{-3} c$  at the end.

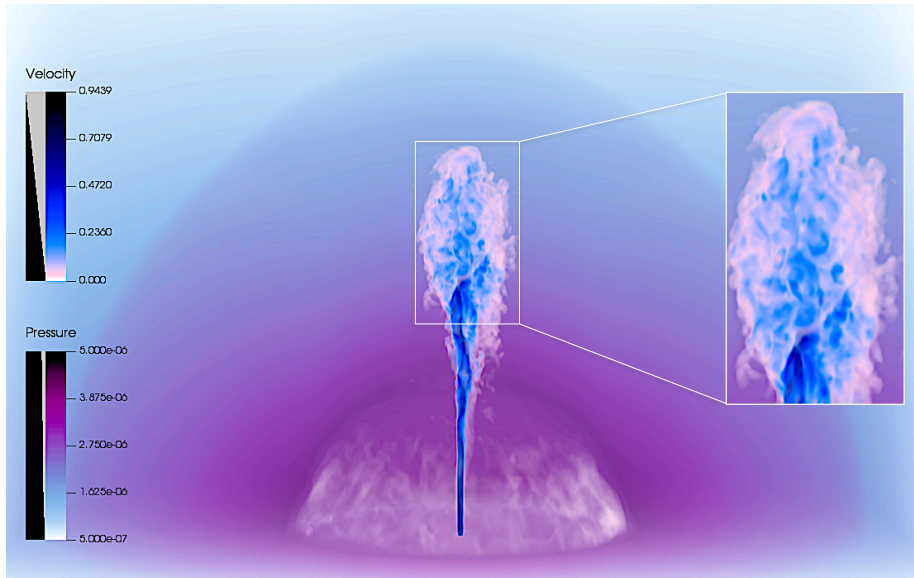


Figure A.9 Pressure (purple scale) and velocity (blue scale, only positive values) rendering of the numerical box, highlighting the ambient medium and bow-shock, and the jet flow, respectively, at  $t \simeq 152$  Myr. The spatial scale covers  $\simeq 300$  kpc along the vertical axis and 512 kpc along the horizontal axes. The inset shows a zoom of the positive axial velocity in the lobe. Units are:  $\rho_a c^2$  for pressure, and  $c$  for velocity.

shape, sweeping the smooth ambient medium distribution. The simulation had to be stopped at this point to avoid the bow-shock crossing the grid boundary.

The blue scale in Fig. A.9 shows the axial velocity distribution –limited to positive values–, which reveals the inner jet structure, the lobes, and the hot bubble of shocked jet material accumulated by the host galaxy gravitational potential.<sup>2</sup> The jet shows a kinked morphology due to the development of KHI modes, excited by the helical motions set up as injection boundary conditions. The growth of these modes is faster in hot flows [e.g., Perucho, Martí, and Hanasz 2005], and they trigger oscillations in the physical variables of the jet [e.g., Hardee 2000]. Indeed, the image shows the oscillations in axial jet velocity, which end up with the disruption of the flow at  $\sim 70$  kpc from injection, i.e.,  $\sim 80$  kpc from the galactic nucleus.

<sup>2</sup>The dynamical time scale estimated for the gravitational field,  $t_d \sim 1/\sqrt{G\rho_{\text{DM}}}$  (with  $G$  the gravitational constant and  $\rho_{\text{DM}}$  the central density of the dark matter halo deduced from the hydrostatic equilibrium condition), is  $\simeq 180$  Myr. Although the simulation time is slightly shorter ( $\simeq 150$  Myr), the blackflow velocities found in the lobes accelerate the fall of the shocked jet gas towards the galactic core and the formation of the observed spherical distribution [see also Perucho et al. 2014a].

The simulated jet does not show expansions and recollimations before the kinks become non-linear, in agreement with the observations of the jets in Hercules A previous to disruption [O’Dea et al. 2013], and in contrast to other simulations of low-power, hot relativistic jets [Perucho and Martí 2007] or non-relativistic, low Mach number jets [Saxton, Bicknell, and Sutherland 2002]. It is worth to mention that the Mach discs reported to be responsible for jet disruption in those works are common in axisymmetric simulations because of the imposed symmetry. This kind of structures are hardly found in 3D simulations. The reason is the high cocoon pressure, which keeps the jet collimated and prevents its fast expansion. As shown by Perucho et al. 2017, the lobe pressure correlates with the flux of available (i.e., internal plus kinetic) energy transported by the jet. In the case of the present simulation, the internal energy of the jet at injection, together with the large scale density/pressure core helps to keep the jet collimated.

The disruption point of the jet stands in the region 100 – 150 kpc since the jet head reaches  $\sim 100$  kpc (at  $t \approx 36$  My), and oscillates back and forth throughout the rest of the simulation ( $t \approx 152$  My) (note that disruption is farther from injection in the third row of Fig. A.8 than in the fourth,  $\simeq 80$  Myr later). This fact indicates that disruption is caused by the development of helical instabilities and that the precise point at which it takes place may change slightly due to changes in local conditions. However, as far as conditions remain unchanged at injection, it is difficult to foresee a dramatic change in the jet stability conditions. Therefore, we can conclude that the final snapshot of the simulation is not a transitory phase. Injection conditions should be changed in order to see changes in the whole jet/lobe structure, which would, furthermore, require times of the order of the simulated one,  $\sim 100$  Myr.

Figure A.10 shows a rendering of pressure (weighted by tracer, in units of  $\rho_a c^2$ ) to be compared with Fig. A.7 for kinetically dominated jets. The image is a mirrored composition of the simulated jet, which has been rotated to a viewing angle of  $45^\circ$  counterclockwise (around a vertical axis) to show two perspectives of the 3D structure. There is an evident difference with the kinetically dominated jets in terms of lobe shape, which is more spherical in this simulation. The image reveals the kink of the jet before disruption inside the lobes, and their turbulent internal appearance. The kinks and disruption region show high values of internal energy as a consequence of the dissipation of kinetic energy.

Figure A.11 shows projected pseudo-synchrotron emissivity images for the jet at its last snapshot at  $50^\circ$  (eastern lobe; left) and  $130^\circ$  (western lobe; right) viewing angles, in arbitrary units, following the results from radio and X-ray



Figure A.10 Pressure weighted by tracer rendering of the numerical box. The simulated jet has been mirrored to emulate a double sided jet and show a different perspective of the source.

observations [e.g., Gizani and Leahy 2003]. The expression used to compute the emissivity at a given frequency is the same as that used by Hardee 2003 [see also Clarke, Norman, and Burns 1989]:

$$\epsilon_\nu \propto n^{1-2\alpha} p^{2\alpha} (B \sin \theta_B)^{1+\alpha} D^{2+\alpha}, \quad (\text{A.4})$$

where  $n$  is the lepton number density,  $p$  is pressure,  $B$  is the assumed magnetic field strength in the comoving frame, taken to be proportional to  $\sqrt{p}$ ,  $\theta_B$  is the angle between the field lines and the viewing angle (also in the comoving frame) assumed to be a constant,  $D$  is the Doppler factor, and  $\alpha$  is the spectral index (defined as  $S_\nu \propto \nu^{-\alpha}$ ). The spectral index has been defined as a linear function of the jet gas tracer  $f$ ,  $\alpha = 0.6 + 0.9(1 - f)$ , to obtain values from 0.6 (in the jets) to 1.5 [in the lobes; Gizani and Leahy 2003, Gizani, Cohen, and Kassim 2005, Timmerman et al. 2022]. The Doppler factor has been computed using only the axial velocity component. The image shows that the simulated lobes extend up to  $\simeq 175$  kpc in projection, whereas the jets in Hercules A reach  $\simeq 260$  kpc, which explains that the lobes in Hercules A are more inflated. The advance velocity of the radio structure along the jet axis falls rapidly after disruption and as the jet expands. Thus, it is reasonable to expect a slow evolution of the lobes towards a spherical shape within the remaining  $\simeq 80 - 90$  kpc that the simulation would need to reach the actual size of Hercules A.<sup>3</sup>

Despite the simplifications, the images show interesting features, namely, bright jets that develop helical patterns and disrupt into the lobes, and arcs (e.g., at  $\simeq 120$  kpc in the western jet) that are produced by the disruption of

<sup>3</sup>Reaching these scales would imply an amount of computing time far beyond the one used for this work.

the jet when the helical instability achieves large amplitude and forces parts of the jet to generate shocks into its environment. This effect was also observed in numerical simulations that tackled the development of KHI in relativistic flows [Perucho, Martí, and Hanasz 2005]. The possibility that the arcs could be helical features observed in projection was actually suggested by Gizani and Leahy 2003. Keeping in mind that our simulation did not reach the extension of Hercules A, perhaps the simulation shows the beginning of the formation of those arcs as instability-generated shocks. Therefore, it would be necessary to continue the simulation to make a better comparison. Interestingly, the hints of arc-like structures are mainly observed in the right panel (western jet). All other things being equal (these images are produced from a single simulated jet), this difference is caused by the viewing angle: Doppler boosting makes the eastern jet brighter and reduces the contrast that allows the arc-shaped structure to be enhanced in the western jet.

Finally, we can also compare the lobe pressure at the end of the simulation with the estimated one in Gizani and Leahy 2004 for the lobes in Hercules A, as a test for the validity of our approach. In the simulations, we find  $P_l \simeq 10^{-10}$  dyn/cm<sup>2</sup>, as compared to  $P_l \simeq 2 - 3 \times 10^{-11}$  dyn/cm<sup>2</sup> from observations. Taking into account the aforementioned difference in size and that the cocoon pressure evolves with distance as  $d^{-0.9}$  [a fit obtained in Perucho, Martí, and Quilis 2019], the difference in lobe pressures could be reduced from a factor 3-5 to a factor 2-3. This discrepancy is possibly due to the large injection power [see Perucho et al. 2017] used in the simulation with respect to the expected current jet power in Hercules A (see also the discussion below).

## A.2.4 Discussion

### A.2.4.1 Global morphology

The sphericity of the lobes (accentuated by the perspective) is a sign of a pressure-driven isotropic expansion of the lobes. It has been suggested that the lobes are fed by a possibly intermittent jet [e.g., Timmerman et al. 2022] with a periodicity of the order of factor  $10^5$  yr [within a long activity burst of  $\simeq 60$  Myr, Nulsen et al. 2005]. The jet shows continuous emission from the source to the disruption point, implying that the activity periods must be long enough to allow the plasma to reach  $\sim 100$  kpc. According to the authors, for an estimated velocity of  $0.8c$ , this implies a minimum activity time of  $4 \times 10^5$  yr. If this is correct, our simulations (which do not consider such a short periodicity) would then represent the continuous injection of the mean properties of the

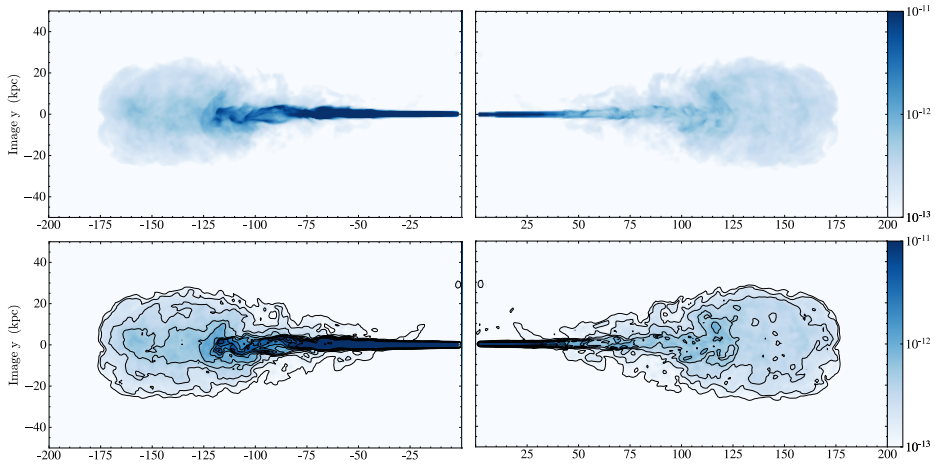


Figure A.11 Pseudo-synchrotron emissivity images, in arbitrary units, for the jet at its last snapshot, projected at  $50^\circ$  (left) and  $130^\circ$  (right) viewing angles.

jet, i.e., the long activity burst. Nevertheless, this is irrelevant for the main point revealed in this work: the global morphology can be recovered by jets dominated by internal energy flux, and not by those kinetically dominated. It is possible, though, that such a fast periodicity triggers internal shocks in the jets that dissipate kinetic energy along the jet channel, heating the flow as it evolves, relaxing the requirement of a very large internal energy from injection that we have considered in our simulation.

The idea behind the setup of the simulations was actually to provide a plausible explanation to the overall morphology of the radio galaxy Hercules A, which does not fit into the classical FRI/FRII classification. The initial hypothesis was inspired by the sphericity of the lobes plus the fact that the lobe expansion takes place beyond the density/pressure fall of the ambient medium profiles. Also the results obtained in a series of numerical and theoretical works on jet evolution [Perucho, Quilis, and Martí 2011, Perucho et al. 2014b, Perucho et al. 2017] showed that the morphology of the lobes depends on whether the jet energy flux is dominated by the kinetic energy (mass of the particles) or by the internal energy. In the first case the inertia of the flow tend to give rise to elongated structures. In the second case, the expansion of the lobes, driven by their high pressure, is isotropic. Furthermore, it was concluded that this second option is limited to relativistically hot jets, in which the internal energy budget is large enough to dominate, or at the least, compete, with the kinetic energy flux. Therefore, this effect cannot be studied with non-relativistic simulations [Saxton, Bicknell, and Sutherland 2002].

The setup was thought to keep jet collimation by means of environment pressure, at the same time as developing unstable (helical) KHI modes that trigger disruption; all these requirements are fulfilled by a (slowly expanding) relativistically hot jet. Those properties produce a high pressure lobe, as expected from previous theoretical work [Perucho et al. 2017], and keep the jet confined. In addition, the lack of significant jet expansion [see e.g., Hardee 1982, showing that jet expansion decelerates the growth of instability amplitudes] together with the high internal energy of the flow [Perucho, Martí, and Hanasz 2005] cause a relatively faster development of the KHI modes. As a result, the simulated jet evolution shows a global jet and lobe morphology that are similar to the observed eastern jet/lobe system, in terms of development of unstable kink patterns, jet disruption within the lobes, the lack of hotspots, and a more realistic jet-to-lobe width ratio [ $\sim 2.7 \times 10^{-2}$  in the source, Gizani and Leahy 2003, versus  $\sim 4.5 \times 10^{-2}$  in the simulation, see Fig. A.11] between the jet and the lobe at the current simulated size. All in all, the basic morphological and dynamical properties of the jets and lobes of Hercules A (kink unstable jets, quasi-spherical lobes, lack of hotspots, right jet-to-lobe width ratio) are reproduced by a relativistic jet with high internal energy.

Massaglia et al. 2016 have shown that low power jets ( $L_j \leq 10^{43}$  erg/s) can result in a similar morphology, mainly due to the dissipation of kinetic energy at disruption. Yates-Jones, Shabala, and Krause 2021 have also obtained similar structures for jets injected with an opening angle into the grid. However, the jet-lobe structure is not expected for more powerful jets with small opening angles, like the one we simulate.

Taking into account that kinetically dominated jets generate elongated lobes [see Perucho et al. 2014b, for a comparison between large scale morphology of cold and hot flows], our work shows evidence favouring that the jets in Hercules A are not kinetically dominated at large scales, but by internal energy. As noted in the introduction of this chapter, we have not included magnetic fields in our simulations. However, the isotropic expansion of the lobes requires the contribution of the magnetic field to be mainly in the form of pressure, i.e., requires the magnetic field to be disordered. Gizani and Leahy 2003 showed that the magnetic field is aligned with the lobe surfaces [see also Guidetti et al. 2011]. However, the lobes seem to be less polarised towards the central regions, which could be an indication of a disordered field, consistently with the turbulent character of the flow within the lobes. The contribution of such a magnetic field to the simulations would have not changed the obtained morphology. However, the role of a dynamically relevant toroidal field in the jet remains a plausible

option to explain the development of the kink instability that finally disrupts the jet,<sup>4</sup> which should be explored by means of RMHD simulations, and will be left for future work. This, again, would not change our conclusion, since the field would become disordered beyond the disruption point, which is supported by the turbulent dynamics of the region and the relative depolarisation observed at the lobe central regions [Gizani and Leahy 2003].

A last point about the jets in Hercules A concerns the origin of structures seen inside the western lobe and whether they are associated with the disruption of the jet. Comparing with pseudo-synchrotron images from their numerical simulations, Saxton, Bicknell, and Sutherland 2002 interpret these structures as rings associated to nearly annular shocks propagating through the backflow surrounding the jet. However, on the one hand, the ring-like structures seen in the pseudo-synchrotron images are probably an artifact produced by the imposed axisymmetry, as also observed in Scheck et al. 2002 for completely different simulations and setups. On the other hand, the detailed imaging of the source [e.g., Gizani and Leahy 2003, Timmerman et al. 2022] reveals that the jet propagates inside the first expansion region [structure E in Gizani and Leahy 2003]. Moreover, if interpreted as a jet expansion, it would imply a sudden change in jet-to-lobe pressure ratio that is difficult to explain taking into account the expected pressure homogeneity in radio lobes favoured by large values of the sound speed. This argues against jet expansion as the mechanism to produce the elongated arc-shaped structure E. We suggest that it could be associated with a bow-shock triggered by changes in the injection power, in agreement with Gizani and Leahy 2003 and Timmerman et al. 2022, or with instability patterns frozen in the disrupted structure, as suggested by our simulations (see Fig. A.11), or with a combination of both. Similar structures observed downstream [structures D, C, B and A in the western jet; Gizani and Leahy 2003] could also be interpreted in this way. Furthermore, the jet itself does not show evidence of expansion/recollimation before the appearance of the innermost ring [O’Dea et al. 2013, Timmerman et al. 2022], as expected if disruption would be caused by this process.

Altogether, we understand that the jets keep collimation until the disruption point [features W4 and E7 in the western and eastern jet, respectively, Gizani and Leahy 2003] and therefore it cannot be caused by the arcs/rings and thus we can discard jet pinching as its trigger. Specific simulations using modulated

---

<sup>4</sup>The presence of a toroidal field could, on the one hand, relax the high values of the internal energy flux in the jet and, on the other, trigger the development of current-driven instability modes.

injection and/or different instability modes should be run to try to reproduce those remarkable features; what our work shows is that the base set up to do this would necessarily imply a non-kinetically dominated flow.

#### A.2.4.2 A hot jet

Our interpretation of the nature of the jets in Hercules A poses the question about the reason why the jets do not become completely kinetically dominated while keeping collimation at kiloparsec scales, as in the case of FR II jets, or show fast expansion due to mass-load and deceleration, as in the case of FR I jets, but remain hot, become disrupted, and generate bright lobes without hotspots.

The internal shocks produced by a relatively short-period variability in jet injection conditions [Gizani and Leahy 2003, Timmerman et al. 2022] and the growth of the instability itself are effective agents in heating the jet plasma. The large size of the galactic core contributes to keeping a large lobe pressure that favours jet collimation, too, preventing the adiabatic cooling of the flow.

The radius of the core of the density profile in this source is estimated to be  $r_c = 120$  kpc, much larger than those of the galactic and group cores 1.2 kpc and 52 kpc, respectively, that we have used in previous simulations of long-term jet evolution [Perucho et al. 2014b, Perucho, Martí, and Quilis 2019, Perucho, Martí, and Quilis 2022]. Furthermore, the ambient pressure fall beyond  $\sim 100$  kpc can also facilitate the fast lobe expansion in Hercules A at these scales. Our simulations seem to confirm this, thus pointing towards an active role of the ambient medium, together with the intrinsic jet properties, in shaping the global morphology of the radio source.

It has also been shown that even a relatively mild toroidal field can favour jet collimation [e.g., López-Miralles et al. 2022]. By avoiding jet expansion, and therefore, the conversion of the stored internal energy into kinetic energy, the field contributes to keep a relatively high internal energy density. A test to probe the relative relevance of each of the plausible main actors leading to the observed global morphology in Hercules A (jet internal energy, magnetic field and ambient pressure profile) is left as future work.

#### A.2.4.3 A HEG to LEG transition?

Finally, it is interesting to relate the large-scale properties of the jet to the properties of the accretion disc in Hercules A. In particular, the high values of internal energy that seem to explain their global morphology according to our results, thus linking the jet properties at formation with their final fate.

Boccardi et al. 2021 investigated the relation between the accretion mode and the properties of the jet collimation region, by considering a sample of nearby sources classified as high- or low-excitation galaxies (HEGs or LEGs). The nuclei in the former class are thought to harbour standard accretion discs fuelled by cold gas, whereas those in the latter are instead powered by radiatively inefficient, hot accretion flows [Heckman and Best 2014, and references therein]. The authors suggested that jets in LEGs are mainly composed of a narrow relativistic hot spine anchored in the surroundings of the black hole ergosphere, while HEGs generate wider jets, likely due to the formation of an extended disc wind shielding the inner spine. Such winds may significantly contribute to the jet stability and result in the development of a kinetically dominated jet with an FRII morphology, as observed in the vast majority of HEGs. On the contrary, jets in LEGs would lack such mass-loaded, high-inertia, stabilising shear layer, which prevents them from becoming kinetically-dominated and often results in the formation of an FRI morphology. Hercules A presents a low-luminosity nucleus, and is optically classified as LEG [Buttiglione et al. 2010]. In the scenario discussed above, we could thus speculate that this source forms a hot relativistic jet which, however, remains well collimated due to its peculiar ambient density/pressure profile, as explained before.

While we have provided here a qualitative interpretation of the radio source properties in relation to the nucleus and the environment, it is necessary to note that a more complete description can be obtained by taking into account the complexity of the source evolution, in particular the evolution of nuclear properties. Our simulation of an internal energy dominated jet shows that the bow shock has propagated  $\simeq 280$  kpc in  $\simeq 150$  Myr. This long evolution time suggests that the jet could have initially propagated to a large distance while being more powerful and probably kinetically dominated [see e.g. Perucho, Martí, and Quilis 2019, Perucho, Martí, and Quilis 2022], and has later transitioned to a low-power regime due to a slow switching-off of the nucleus.

Such a past, quasar-like activity is consistent with the analysis of the cavities and shock front observed in X-rays [Nulsen et al. 2005]. Actually, these authors provide an age estimate for the activity burst of 60 Myr in which the size reached by the lobes is  $\simeq 350$  kpc. This is a 25% larger than the size reached by our simulation in a 40% of the simulated time, revealing a clear dynamical contradiction. The authors obtain an estimated jet power of  $10^{46}$  erg/s, i.e., a factor 2.5 larger than the one we have used in our simulation, which is consistent with the faster expansion given by their model. Therefore, either the model used by Nulsen et al. 2005 to estimate the source age fails to recover the detailed

propagation dynamics, or indeed a quasar-like activity allowing for fast initial expansion is needed to reconcile both results. This mismatch can be explained by a slow transition in the accretion mode from efficient (HEG regime giving rise to the large scale structure) to inefficient (current LEG phase), probably caused by the depletion of the gas fueling galactic activity. The existence of this transition is in fact supported by the mismatch between the nuclear properties and the large scale structure of the source, as indicated by optical and radio data [Buttiglione et al. 2010, Wu et al. 2020].

### A.2.5 Conclusions

We present a numerical simulation that succeeds in reproducing the global morphology of Hercules A-like jets, following an *a priori* hypothesis. The basic ideas behind the simulation are that 1) the spherical morphology of the lobes is pressure-driven, so the jet must be dominated by thermal (and perhaps magnetic) pressure, 2) the high lobe pressure keeps the jet collimated up to  $\sim 100$  kpc, where it expands in the rapidly falling pressure/density WHIM, 3) the pressure in the lobe keeps high values due to the high internal energy flux through the jet and the opposition of the large ambient core, 4) the faster growth of KHI modes in hot flows favours jet disruption and the generation of the observed turbulent lobes, and 5) the observed arcs inside the lobes could be produced by non-linear amplitude helical instability modes, which are the responsible for jet disruption at  $\sim 100 - 150$  kpc.

We also speculate with the possibility that Hercules A has transited from a HEG to a LEG, which could explain the large size of the radio galaxy, achieved by a powerful, probably kinetically dominated jet expected from HEGs, and the currently observed structure, which would imply a hot outflow like the one presented here. This interpretation would be in agreement with the implications of recent observational work on the properties of HEGs and LEGs, in terms of their size and the properties of the accretion flow from which they emerge [Boccardi et al. 2021].

Our hypothesis has proven valid to reproduce the large scale structure of the radio galaxy Hercules A. Future work could be aimed to study the role of the magnetic field in this process, the possible transition phase and to confirm whether the generation of arcs can be fully explained by instability-induced shocks or whether periodicity in jet injection power is required.



# Appendix **B**

## X-ray timing

---

This chapter summarises the following publication: *Testing jet geometries and disc-jet coupling in the neutron star LMXB 4U 0614+091 with the internal shocks model*. A. Marino, J. Malzac, M. Del Santo, S. Migliari, R. Belmont, T. Di salvo, D. M. Russell, **J. López-Miralles**, M. Perucho, A. D’Ai, R. Iaria, L. Burderi. *Monthly Notices of the Royal Astronomical Society*. Volume 498, Issue 3, November 2020. DOI: 10.1093/mnras/staa2570. Reproduced with permission.

---

### **B.1 Testing jet geometries and disc-jet coupling in LMXB 4U 0614+091**

In this appendix, I summarise a contribution in a paper that aims to apply the so-called internal shocks model for the first time to a neutron star (NS) low-mass X-ray binary (LMXB), namely 4U 0614+091. This model, which assumes that the fluctuations in the velocity of the ejecta along the jet are driven by fluctuations in the accretion flow, has been successfully applied in the context of black hole (BH) LMXBs to reproduce the flat radio-to-mid infrared (IR) spectra, but never in the context of NSs. The code that has been used in the paper allows to change the geometry of the jet (i.e., conical vs. non-conical geometry) and to choose a specific power spectral density (PDS) to shed light on the possibility that jets in NSs and BHs could have different geometries or coupling properties with the accretion disc.

### B.1.1 Introduction

In contrast to relativistic jets in active galaxies, in binary systems outflows are not usually observed as extended structures, but inferred from a radio-to-mid-IR flat (or slightly inverted) spectrum (see Chapter 1.2.3). This spectrum is characterised by a jet break, where emission goes from optically thick (at the jet base) to optically thin, and at lower frequencies by a continuum, which results from the superposition of self-absorbed synchrotron radiation emitted from different regions in the jet flow. However, as jets propagate away from the binary centre, the magnetic field decays and particles lose energy, so one would expect to observe an effective inverted radio spectrum, and not a flat one. Traditionally, this has been explained relying on the existence of a mechanism of energy replenishment of the relativistic plasma that compensates the adiabatic losses due to jet expansion [Blandford and Königl 1979].

Although the specific mechanisms that provide this source of energy are still debated, (1) magnetic reconnection [Sobacchi and Lyubarsky 2020], (2) acceleration in shear flows [Rieger and Duffy 2019] or (3) internal shocks [Malzac 2013] seem plausible scenarios. This last model (the so-called Internal Shocks model, or ISHEM), which consider that the conversion of kinetic energy into thermal energy occur by collisions of jet portions ejected with different bulk velocities, have been successfully applied to reproduce the spectral energy distribution (SED) of BH X-ray binaries (XRBs), as long as the fluctuations in the Lorentz factor match the fluctuations in the accretion flow [Malzac 2014]. Nevertheless, this model has not been applied before in the context of NS XRBs.

The objective of the paper is thus to reproduce the entire SED of a NS LMXB using the ISHEM. For this, we chose the source 4U 0614+091 (a brief description of the system has been provided in Chapter 1.6.2 of this thesis), for which a multi-wavelength observational campaign –from radio (VLA) to X-rays (RXTE, XRT/Swift)– has been performed between October 30 and November 4 2006. In the paper, we reproduced the spectral modelling of the dataset first performed by Migliari et al. 2010, except the optical-UV data (SMARTS-UVOT) that was re-analysed for this work.

To apply the internal shocks model, we employed an updated version of the so-called ISHEM code [i.e., Drappeau et al. 2015]. This code aims to describe the jet component of the SED based on how energy is dissipated along the jet. In a nutshell, dissipation depends mainly on two parameters: (1) the velocity of jet expansion, which depends on the jet geometry, and (2) the variability of the fluctuations, which are related with the accretion flow variability (assuming

a disc-jet coupling scenario). In this new version of the code, the jet geometry (conical vs. non-conical) is controlled with a geometrical parameter  $\xi$  ( $r \propto z^\xi$ , where  $\xi = 1$  describes a conical geometry while  $\xi < 1$  describes a parabolic flow), while a PDS is used as a proxy for the Lorentz factor fluctuations [Drappeau et al. 2015, Malzac et al. 2018].

### B.1.2 Contribution

As introduced in the previous section, the ISHEM model depends on three fundamental ingredients: (1) a multi-wavelength SED, (2) a X-ray PDS, which is used as a tracer of the accretion flow variability and (3) a synthetic SED, which is calculated on the basis of the aforementioned PDS to be compared with the real SED of the source.

As part of a research residence at the European Space and Astronomy Center of the European Space Agency (April-May 2019), I worked on the timing analysis of 4U 0614+091 to provide the ISHEM code with the required PDS, based on X-ray observations taken during the multi-wavelength campaign of 2006. To perform the analysis, we used RXTE/PCA data taken on 2006 October 30 (ObsID 92411-01-06-07). Data was in the event mode configuration with a time resolution of  $\sim 125 \mu\text{s}$ , such that the Nyquist frequency is 4096 Hz. Using Fast Fourier Transform techniques [van der Klis 1989], we obtained PDS for continuous 128s-long time intervals covering a total time length of 2048 s. These PDS were averaged to obtain one single PDS, from which we subtracted the Poisson noise power, derived in the frequency range between 1536 and 2048 Hz [Zhang et al. 1995]. No deadtime corrections nor background subtraction were performed before creating the PDS.

The resulting PDS (in the traditional  $\nu \times P_\nu$  representation) is shown in Fig. B.1, where we applied the Leahy normalisation [Leahy et al. 1983] before converting the PDS to squared fractional root mean square (rms). Following the arguments given in Chapter 1.3.3, we fitted the PDS with a model consisting on the sum of two Lorentzians: one broad Lorentzian to fit the low-frequency noise and one narrow Lorentzian to fit the kHz quasi-periodic oscillation (QPO). The fitting results are shown in Tab. B.1, where we found  $\chi_\nu(\text{dof}) = 1.49(126)$ . As shown in the paper, the output of the ISHEM code is not sensitive to the high-frequency QPO, obtaining similar results using only one-single Lorentzian component. This can be explained considering that the origin of the QPO is related to orbital motion in the accretion flow that will hardly produce a modulation in the Lorentz factor that could be transmitted to the jet.

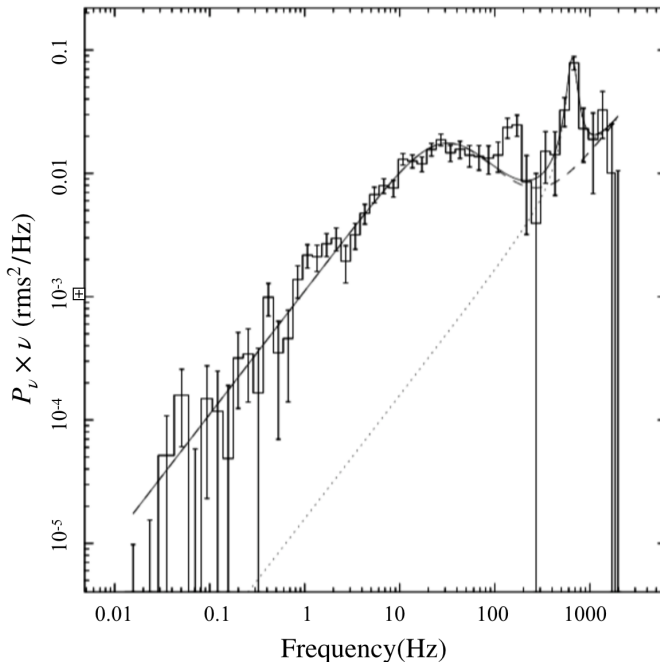


Figure B.1 PDS in the normalised power ( $P_\nu$ ) times frequency ( $\nu$ ) representation. Reproduced with permission from Marino et al. 2020.

### B.1.3 Results and conclusions

Figure B.2 shows the source SED, together with the best-fit model for different jet geometries and disc variability configurations. The optical-to-X-ray data (i.e., the accretion disc contribution) is fitted with an irradiated plus Comptonization plus black-body disc model, while the radio-to-IR data (i.e., the relativistic jet component) is simulated with the ISHEM code. Regarding the radio-to-IR component, only two ISHEM configurations resulted in an acceptable fit: (1) a paraboloidal jet ( $\xi < 1$ ) together with the X-ray PDS as a tracer of the disc variability, and (2) a conical geometry ( $\xi = 1$ ) but with a flicker noise PDS ( $P(f) \propto 1/f$ ), assuming in this case that the observed X-ray variability does not reproduce the fluctuations in the jet Lorentz factor.

On the one hand, the fact that a paraboloidal jet geometry gives a better fit than a strictly conical flow is not surprising, since the conical shape is only an approximation of the real jet geometry. Close to the compact object jets are expected to have a certain degree of collimation, which can be provided either by a toroidal magnetic field component [e.g., Begelman 1995] or by the external

Table B.1 Fit results of the PDS described with a sum of two Lorentzians, each of them given by  $P(\nu) = r^2/\pi [\Delta^2 + (\nu - \nu_0)^2]$ , with  $r$  the integrated *rms* over the full range of frequencies  $-\infty$  to  $+\infty$ ,  $\Delta$  the Full Width Half Maximum of the Lorentzian and  $\nu_0$  its central frequency. Values in round parentheses were kept frozen during the fit. Quoted errors reflect 68% confidence levels. Reproduced with permission from Marino et al. 2020.

Lorentzian Component	$\nu_0$	$\Delta$	$r$
1	(0)	$62.0 \pm 5.0$	$0.106^{+0.003}_{-0.006}$
2	$650^{+30}_{-24}$	$<250$	$0.030^{+0.010}_{-0.008}$
$\chi^2_{\nu}(\text{d.o.f.}) = 1.49(126)$			

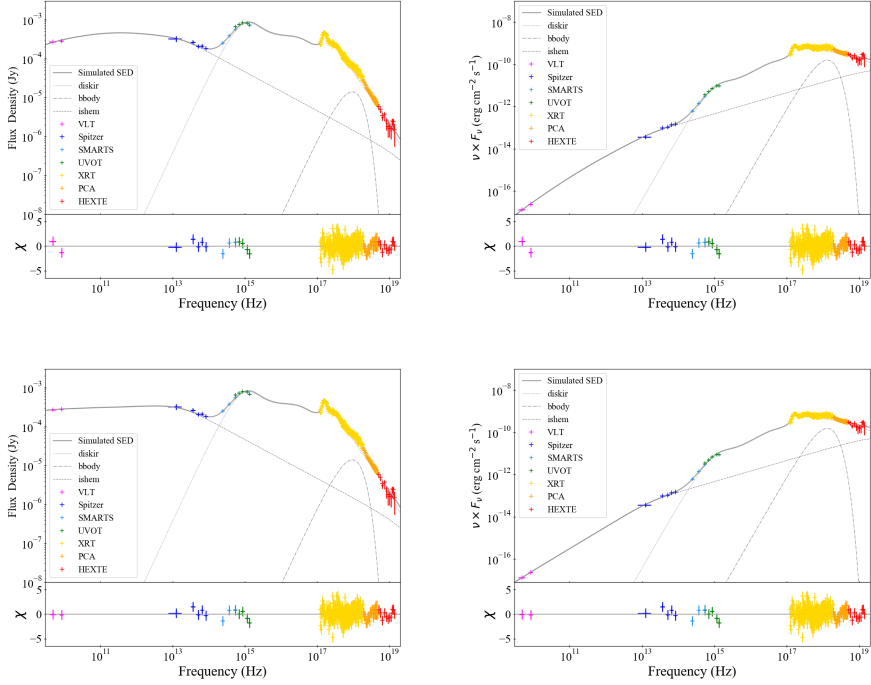


Figure B.2 Best-fit unabsorbed SED compared with the whole multi-wavelength dataset available for 4U 0614+091, in both Flux Density (*Left*) and  $\nu \times F_{\nu}$  (*Right*) representation. The optical-to-X-ray data set has been analysed with an irradiated disk + black-body model, while the radio-to-IR data set was modelled with ISHEM. In this plot we show both best-fit ISHEM models found in this paper: on *Top* the model built with the X-ray PDS and corresponding to a non-conical geometry ( $\zeta = 0.6$ ) and on (*bottom*) the model corresponding to a flicker noise PDS in conical geometry. Reproduced with permission from Marino et al. 2020.

medium [e.g., Asada and Nakamura 2012]. However, the fact that BH jets in XRBs can be properly fitted with a conical geometry does not necessarily imply that this is the real geometry of the jet, so dedicated simulations of paraboloidal jets in BH systems are also strongly needed.

On the other hand, it is interesting to pay attention to the second scenario, in which the source X-ray variability (represented with the X-ray PDS) is not a good proxy of the Lorentz factor fluctuations in the ejecta. In this case, the dissipation pattern is not related with the timing properties of the X-ray emission, but with a flicker noise component. For NS XRBs, it is possible that the NS surface might play a role, since in this case the variability of the emission might not be transmitted to the jet, breaking the connection with the X-ray PDS. Moreover, even the jet launching mechanism can be different in systems hosting NSs with respect to BHs, but statistics is very limited by the low number of systems that have been analysed up to now with the ISHEM model. Indeed, we cannot even assume that the breaking of the variability correlation can be generalised, for example, to other NS systems in the hard state.

Therefore, the main conclusion of the paper is that the compatibility between the real and simulated SED depends significantly on the jet geometry. In particular, a highly paraboloidal geometry together with the X-ray PDS results in an acceptable fit, while for a conical geometry a good fit can only be found with a flicker-noise PDS, in contrast to BH XRBs where the conical geometry worked correctly. This suggests, but only tentatively, that for NS LMXS the PDS is not a good tracer for the accretion flow variability.

# Bibliography

- [1] A. A. Abdo et al. “Fermi LAT Observations of LS I +61°303: First Detection of an Orbital Modulation in GeV Gamma Rays.” In: *Astrophys. J. Lett.* 701.2 (Aug. 2009), pp. L123–L128. DOI: [10.1088/0004-637X/701/2/L123](https://doi.org/10.1088/0004-637X/701/2/L123). arXiv: [0907.4307](https://arxiv.org/abs/0907.4307) [[astro-ph.HE](#)].
- [2] G. O. Abell and B. Margon. “A kinematic model for SS433.” In: *Nature* 279.5715 (June 1979), pp. 701–703. DOI: [10.1038/279701a0](https://doi.org/10.1038/279701a0).
- [3] A. U. Abeysekara et al. “Very-high-energy particle acceleration powered by the jets of the microquasar SS 433.” In: *Nature* 562.7725 (Oct. 2018), pp. 82–85. DOI: [10.1038/s41586-018-0565-5](https://doi.org/10.1038/s41586-018-0565-5).
- [4] S. Adrián-Martínez et al. “A search for time dependent neutrino emission from microquasars with the ANTARES telescope.” In: *Journal of High Energy Astrophysics* 3 (Sept. 2014), pp. 9–17. DOI: [10.1016/j.jheap.2014.06.002](https://doi.org/10.1016/j.jheap.2014.06.002). arXiv: [1402.1600](https://arxiv.org/abs/1402.1600) [[astro-ph.HE](#)].
- [5] F. Aharonian et al. “Discovery of Very High Energy Gamma Rays Associated with an X-ray Binary.” In: *Science* 309.5735 (July 2005), pp. 746–749. DOI: [10.1126/science.1113764](https://doi.org/10.1126/science.1113764). arXiv: [astro-ph/0508298](https://arxiv.org/abs/astro-ph/0508298) [[astro-ph](#)].
- [6] J. Albert et al. “Variable Very-High-Energy Gamma-Ray Emission from the Microquasar LS I +61 303.” In: *Science* 312.5781 (June 2006), pp. 1771–1773. DOI: [10.1126/science.1128177](https://doi.org/10.1126/science.1128177). arXiv: [astro-ph/0605549](https://arxiv.org/abs/astro-ph/0605549) [[astro-ph](#)].
- [7] J. Albert et al. “Very High Energy Gamma-Ray Radiation from the Stellar Mass Black Hole Binary Cygnus X-1.” In: *Astrophys. J. Lett.* 665.1 (Aug. 2007), pp. L51–L54. DOI: [10.1086/521145](https://doi.org/10.1086/521145). arXiv: [0706.1505](https://arxiv.org/abs/0706.1505) [[astro-ph](#)].
- [8] M. A. Aloy et al. “High-Resolution Three-dimensional Simulations of Relativistic Jets.” In: *Astrophys. J. Lett.* 523.2 (Oct. 1999), pp. L125–L128. DOI: [10.1086/312266](https://doi.org/10.1086/312266). arXiv: [astro-ph/9906428](https://arxiv.org/abs/astro-ph/9906428) [[astro-ph](#)].
- [9] M. A. Aloy and L. Rezzolla. “A Powerful Hydrodynamic Booster for Relativistic Jets.” In: *Astrophys. J. Lett.* 640.2 (Apr. 2006), pp. L115–L118. DOI: [10.1086/503608](https://doi.org/10.1086/503608). arXiv: [astro-ph/0602437](https://arxiv.org/abs/astro-ph/0602437) [[astro-ph](#)].
- [10] D. Altamirano et al. “X-Ray Time Variability Across the Atoll Source States of 4U 1636-53.” In: *Astrophys. J.* 685.1 (Sept. 2008), pp. 436–450. DOI: [10.1086/590897](https://doi.org/10.1086/590897). arXiv: [0806.0962](https://arxiv.org/abs/0806.0962) [[astro-ph](#)].

- [11] A. Anglés-Castillo et al. “On the deceleration of Fanaroff-Riley Class I jets: mass loading of magnetized jets by stellar winds.” In: *Mon. Not. R. Astron. Soc.* 500.1 (Jan. 2021), pp. 1512–1530. DOI: [10.1093/mnras/staa3291](https://doi.org/10.1093/mnras/staa3291). arXiv: [2010.10234](https://arxiv.org/abs/2010.10234) [[astro-ph.HE](#)].
- [12] A. M. Anile. *Relativistic fluids and magneto-fluids : with applications in astrophysics and plasma physics*. 1989.
- [13] L. Antón et al. “Relativistic Magnetohydrodynamics: Renormalized Eigenvectors and Full Wave Decomposition Riemann Solver.” In: *Astrophys. J. Suppl. Ser.* 188.1 (May 2010), pp. 1–31. DOI: [10.1088/0067-0049/188/1/1](https://doi.org/10.1088/0067-0049/188/1/1). arXiv: [0912.4692](https://arxiv.org/abs/0912.4692) [[astro-ph.IM](#)].
- [14] K. A. Arnaud. “XSPEC: The First Ten Years.” In: *Astronomical Data Analysis Software and Systems V*. Ed. by G. H. Jacoby and J. Barnes. Vol. 101. Astronomical Society of the Pacific Conference Series. Jan. 1996, p. 17.
- [15] K. Asada and M. Nakamura. “The Structure of the M87 Jet: A Transition from Parabolic to Conical Streamlines.” In: *Astrophys. J. Lett.* 745.2, L28 (Feb. 2012), p. L28. DOI: [10.1088/2041-8205/745/2/L28](https://doi.org/10.1088/2041-8205/745/2/L28). arXiv: [1110.1793](https://arxiv.org/abs/1110.1793) [[astro-ph.HE](#)].
- [16] E. Audit et al. “A radiation-hydrodynamics scheme valid from the transport to the diffusion limit.” In: *arXiv e-prints*, astro-ph/0206281 (June 2002), astro-ph/0206281. arXiv: [astro-ph/0206281](https://arxiv.org/abs/astro-ph/0206281) [[astro-ph](#)].
- [17] A. Avakyan et al. “XRBcats: Galactic Low Mass X-ray Binary Catalogue.” In: *arXiv e-prints*, arXiv:2303.16168 (Mar. 2023), arXiv:2303.16168. DOI: [10.48550/arXiv.2303.16168](https://doi.org/10.48550/arXiv.2303.16168). arXiv: [2303.16168](https://arxiv.org/abs/2303.16168) [[astro-ph.HE](#)].
- [18] A. K. Baczko et al. “Ambilateral collimation study of the twin-jets in NGC 1052.” In: *Astron. Astrophys.* 658, A119 (Feb. 2022), A119. DOI: [10.1051/0004-6361/202141897](https://doi.org/10.1051/0004-6361/202141897). arXiv: [2111.09850](https://arxiv.org/abs/2111.09850) [[astro-ph.HE](#)].
- [19] S. A. Balbus and J. F. Hawley. “A Powerful Local Shear Instability in Weakly Magnetized Disks. I. Linear Analysis.” In: *Astrophys. J.* 376 (July 1991), p. 214. DOI: [10.1086/170270](https://doi.org/10.1086/170270).
- [20] D. Balsara. “Total Variation Diminishing Scheme for Relativistic Magnetohydrodynamics.” In: *Astrophys. J. Suppl. Ser.* 132.1 (Jan. 2001), pp. 83–101. DOI: [10.1086/318941](https://doi.org/10.1086/318941).
- [21] D. S. Balsara. “Higher-order accurate space-time schemes for computational astrophysics—Part I: finite volume methods.” In: *Living Reviews in Computational Astrophysics* 3.1, 2 (Dec. 2017), p. 2. DOI: [10.1007/s41115-017-0002-8](https://doi.org/10.1007/s41115-017-0002-8). arXiv: [1703.01241](https://arxiv.org/abs/1703.01241) [[astro-ph.IM](#)].
- [22] D. S. Balsara and D. S. Spicer. “A Staggered Mesh Algorithm Using High Order Godunov Fluxes to Ensure Solenoidal Magnetic Fields in Magnetohydrodynamic Simulations.” In: *Journal of Computational Physics* 149.2 (Mar. 1999), pp. 270–292. DOI: [10.1006/jcph.1998.6153](https://doi.org/10.1006/jcph.1998.6153).
- [23] M. V. Barkov and V. Bosch-Ramon. “Relativistic hydrodynamical simulations of the effects of the stellar wind and the orbit on high-mass microquasar jets.” In: *Mon. Not. R. Astron. Soc.* 510.3 (Mar. 2022), pp. 3479–3494. DOI: [10.1093/mnras/stab3609](https://doi.org/10.1093/mnras/stab3609). arXiv: [2112.04202](https://arxiv.org/abs/2112.04202) [[astro-ph.HE](#)].

- [24] M. V. Barkov and V. Bosch-Ramon. “The Major Role of Eccentricity in the Evolution of Colliding Pulsar-Stellar Winds.” In: *Universe* 7.8 (July 2021), p. 277. DOI: [10.3390/universe7080277](https://doi.org/10.3390/universe7080277). arXiv: [2204.07494](https://arxiv.org/abs/2204.07494) [[astro-ph.HE](#)].
- [25] M. V. Barkov, E. Kalinin, and M. Lyutikov. “3D RMHD simulations of the Gamma-ray binaries.” In: *arXiv e-prints*, arXiv:2211.12053 (Nov. 2022), arXiv:2211.12053. DOI: [10.48550/arXiv.2211.12053](https://doi.org/10.48550/arXiv.2211.12053). arXiv: [2211.12053](https://arxiv.org/abs/2211.12053) [[astro-ph.HE](#)].
- [26] M. V. Barkov and M. Lyutikov. “On the nature of radio filaments near the Galactic Centre.” In: *Mon. Not. R. Astron. Soc.* 489.1 (Oct. 2019), pp. L28–L31. DOI: [10.1093/mnras/slz124](https://doi.org/10.1093/mnras/slz124). arXiv: [1905.13103](https://arxiv.org/abs/1905.13103) [[astro-ph.HE](#)].
- [27] M. V. Barkov, M. Lyutikov, and D. Khangulyan. “3D dynamics and morphology of bow-shock pulsar wind nebulae.” In: *Mon. Not. R. Astron. Soc.* 484.4 (Apr. 2019), pp. 4760–4784. DOI: [10.1093/mnras/stz213](https://doi.org/10.1093/mnras/stz213). arXiv: [1804.07327](https://arxiv.org/abs/1804.07327) [[astro-ph.HE](#)].
- [28] T. Bassi et al. “The long outburst of the black hole transient GRS 1716-249 observed in the X-ray and radio band.” In: *Mon. Not. R. Astron. Soc.* 482.2 (Jan. 2019), pp. 1587–1601. DOI: [10.1093/mnras/sty2739](https://doi.org/10.1093/mnras/sty2739). arXiv: [1810.03914](https://arxiv.org/abs/1810.03914) [[astro-ph.HE](#)].
- [29] W. Becker et al. *Neutron stars and pulsars*. Vol. 357. Springer, 2009.
- [30] K. Beckwith and J. M. Stone. “A Second-order Godunov Method for Multi-dimensional Relativistic Magnetohydrodynamics.” In: *Astrophys. J. Suppl. Ser.* 193.1, 6 (Mar. 2011), p. 6. DOI: [10.1088/0067-0049/193/1/6](https://doi.org/10.1088/0067-0049/193/1/6). arXiv: [1101.3573](https://arxiv.org/abs/1101.3573) [[astro-ph.HE](#)].
- [31] M. C. Begelman, A. R. King, and J. E. Pringle. “The nature of SS433 and the ultraluminous X-ray sources.” In: *Mon. Not. R. Astron. Soc.* 370.1 (July 2006), pp. 399–404. DOI: [10.1111/j.1365-2966.2006.10469.x](https://doi.org/10.1111/j.1365-2966.2006.10469.x). arXiv: [astro-ph/0604497](https://arxiv.org/abs/astro-ph/0604497) [[astro-ph](#)].
- [32] M. C. Begelman, C. F. McKee, and G. A. Shields. “Compton heated winds and coronae above accretion disks. I. Dynamics.” In: *Astrophys. J.* 271 (Aug. 1983), pp. 70–88. DOI: [10.1086/161178](https://doi.org/10.1086/161178).
- [33] M. C. Begelman. “The Acceleration and Collimation of Jets.” In: *Proceedings of the National Academy of Science* 92.25 (Dec. 1995), pp. 11442–11446. DOI: [10.1073/pnas.92.25.11442](https://doi.org/10.1073/pnas.92.25.11442).
- [34] M. C. Begelman, R. D. Blandford, and M. J. Rees. “Theory of extragalactic radio sources.” In: *Reviews of Modern Physics* 56.2 (Apr. 1984), pp. 255–351. DOI: [10.1103/RevModPhys.56.255](https://doi.org/10.1103/RevModPhys.56.255).
- [35] M. C. Begelman and D. F. Cioffi. “Overpressured Cocoons in Extragalactic Radio Sources.” In: *Astrophys. J. Lett.* 345 (Oct. 1989), p. L21. DOI: [10.1086/185542](https://doi.org/10.1086/185542).
- [36] T. M. Belloni and D. Altamirano. “High-frequency quasi-periodic oscillations from GRS 1915+105.” In: *Mon. Not. R. Astron. Soc.* 432.1 (June 2013), pp. 10–18. DOI: [10.1093/mnras/stt500](https://doi.org/10.1093/mnras/stt500). arXiv: [1303.4551](https://arxiv.org/abs/1303.4551) [[astro-ph.HE](#)].

- [37] T. Belloni, D. Psaltis, and M. van der Klis. “A Unified Description of the Timing Features of Accreting X-Ray Binaries.” In: *Astrophys. J.* 572.1 (June 2002), pp. 392–406. DOI: [10.1086/340290](https://doi.org/10.1086/340290). arXiv: [astro-ph/0202213](https://arxiv.org/abs/astro-ph/0202213) [[astro-ph](#)].
- [38] T. M. Belloni. “X-ray emission from black-hole and neutron-star binaries.” In: *arXiv e-prints*, arXiv:1803.03641 (Mar. 2018), arXiv:1803.03641. DOI: [10.48550/arXiv.1803.03641](https://doi.org/10.48550/arXiv.1803.03641). arXiv: [1803.03641](https://arxiv.org/abs/1803.03641) [[astro-ph.HE](#)].
- [39] T. M. Belloni and S. E. Motta. “Transient Black Hole Binaries.” In: *Astrophysics of Black Holes: From Fundamental Aspects to Latest Developments*. Ed. by C. Bambi. Vol. 440. 2016, p. 61. DOI: [10.1007/978-3-662-52859-4\\_2](https://doi.org/10.1007/978-3-662-52859-4_2).
- [40] V. S. Beskin, N. L. Zakamska, and H. Sol. “Radiation drag effects on magnetically dominated outflows around compact objects.” In: *Monthly Notices of the Royal Astronomical Society* 347.2 (Jan. 2004), pp. 587–600. ISSN: 0035-8711. DOI: [10.1111/j.1365-2966.2004.07229.x](https://doi.org/10.1111/j.1365-2966.2004.07229.x). URL: <https://doi.org/10.1111/j.1365-2966.2004.07229.x>.
- [41] T. Beuchert et al. “VLBA polarimetric monitoring of 3C 111.” In: *Astron. Astrophys.* 610, A32 (Feb. 2018), A32. DOI: [10.1051/0004-6361/201731952](https://doi.org/10.1051/0004-6361/201731952). arXiv: [1711.01593](https://arxiv.org/abs/1711.01593) [[astro-ph.GA](#)].
- [42] G. V. Bicknell et al. “Relativistic jet feedback - II. Relationship to gigahertz peak spectrum and compact steep spectrum radio galaxies.” In: *Mon. Not. R. Astron. Soc.* 475.3 (Apr. 2018), pp. 3493–3501. arXiv: [1801.06518](https://arxiv.org/abs/1801.06518) [[astro-ph.GA](#)].
- [43] G. F. Bignami et al. “Einstein X-ray identification of the variable radio star LS I +61 303.” In: *Astrophys. J. Lett.* 247 (July 1981), pp. L85–L88. DOI: [10.1086/183595](https://doi.org/10.1086/183595).
- [44] J. K. Blackburn. “FTOOLS: A FITS Data Processing and Analysis Software Package.” In: *Astronomical Data Analysis Software and Systems IV*. Ed. by R. A. Shaw, H. E. Payne, and J. J. E. Hayes. Vol. 77. Astronomical Society of the Pacific Conference Series. Jan. 1995, p. 367.
- [45] R. D. Blandford and A. Königl. “Relativistic jets as compact radio sources.” In: *Astrophys. J.* 232 (Aug. 1979), pp. 34–48. DOI: [10.1086/157262](https://doi.org/10.1086/157262).
- [46] R. D. Blandford and D. G. Payne. “Hydromagnetic flows from accretion disks and the production of radio jets.” In: *Mon. Not. R. Astron. Soc.* 199 (June 1982), pp. 883–903. DOI: [10.1093/mnras/199.4.883](https://doi.org/10.1093/mnras/199.4.883).
- [47] R. D. Blandford and R. L. Znajek. “Electromagnetic extraction of energy from Kerr black holes.” In: *Mon. Not. R. Astron. Soc.* 179 (May 1977), pp. 433–456. DOI: [10.1093/mnras/179.3.433](https://doi.org/10.1093/mnras/179.3.433).
- [48] K. M. Blundell and M. G. Bowler. “Symmetry in the Changing Jets of SS 433 and Its True Distance from Us.” In: *Astrophys. J. Lett.* 616.2 (Dec. 2004), pp. L159–L162. DOI: [10.1086/426542](https://doi.org/10.1086/426542). arXiv: [astro-ph/0410456](https://arxiv.org/abs/astro-ph/0410456) [[astro-ph](#)].
- [49] K. M. Blundell, M. G. Bowler, and L. Schmidtbreich. “SS 433: Observation of the Circumbinary Disk and Extraction of the System Mass.” In: *Astrophys. J. Lett.* 678.1 (May 2008), p. L47. DOI: [10.1086/588027](https://doi.org/10.1086/588027).

- [50] B. Boccardi et al. “Jet collimation in NGC 315 and other nearby AGN.” In: *Astron. Astrophys.* 647, A67 (Mar. 2021), A67. DOI: [10.1051/0004-6361/202039612](https://doi.org/10.1051/0004-6361/202039612). arXiv: [2012.14831](https://arxiv.org/abs/2012.14831) [[astro-ph.HE](#)].
- [51] G. Bodo, F. Tavecchio, and L. Sironi. “Kink-driven magnetic reconnection in relativistic jets: consequences for X-ray polarimetry of BL Lacs.” In: *MNRAS* 501.2 (Feb. 2021), pp. 2836–2847. DOI: [10.1093/mnras/staa3620](https://doi.org/10.1093/mnras/staa3620). arXiv: [2006.14976](https://arxiv.org/abs/2006.14976) [[astro-ph.HE](#)].
- [52] G. Bodo et al. “Current-driven kink instabilities in relativistic jets: dissipation properties.” In: *MNRAS* 510.2 (Feb. 2022), pp. 2391–2406. DOI: [10.1093/mnras/stab3492](https://doi.org/10.1093/mnras/stab3492). arXiv: [2111.14575](https://arxiv.org/abs/2111.14575) [[astro-ph.HE](#)].
- [53] G. Bodo et al. “Kelvin-Helmholtz instability of hydrodynamic supersonic jets.” In: *Astron. Astrophys.* 283 (Mar. 1994), pp. 655–676.
- [54] H. Boehringer et al. “A ROSAT HRI study of the interaction of the X-ray emitting gas and radio lobes of NGC 1275.” In: *Mon. Not. R. Astron. Soc.* 264 (Oct. 1993), pp. L25–L28. DOI: [10.1093/mnras/264.1.L25](https://doi.org/10.1093/mnras/264.1.L25).
- [55] S. V. Bogovalov et al. “Modelling interaction of relativistic and non-relativistic winds in binary system PSR B1259-63/SS2883 - I. Hydrodynamical limit.” In: *Mon. Not. R. Astron. Soc.* 387.1 (June 2008), pp. 63–72. DOI: [10.1111/j.1365-2966.2008.13226.x](https://doi.org/10.1111/j.1365-2966.2008.13226.x). arXiv: [0710.1961](https://arxiv.org/abs/0710.1961) [[astro-ph](#)].
- [56] S. V. Bogovalov et al. “Modelling the interaction between relativistic and non-relativistic winds in binary pulsar systems: strong magnetization of the pulsar wind.” In: *Mon. Not. R. Astron. Soc.* 490.3 (Dec. 2019), pp. 3601–3607. DOI: [10.1093/mnras/stz2815](https://doi.org/10.1093/mnras/stz2815). arXiv: [1911.07441](https://arxiv.org/abs/1911.07441) [[astro-ph.HE](#)].
- [57] S. V. Bogovalov et al. “Modelling the interaction between relativistic and non-relativistic winds in the binary system PSR B1259-63/SS2883-II. Impact of the magnetization and anisotropy of the pulsar wind.” In: *Mon. Not. R. Astron. Soc.* 419.4 (Feb. 2012), pp. 3426–3432. DOI: [10.1111/j.1365-2966.2011.19983.x](https://doi.org/10.1111/j.1365-2966.2011.19983.x). arXiv: [1107.4831](https://arxiv.org/abs/1107.4831) [[astro-ph.HE](#)].
- [58] S. Boldyrev, J. C. Perez, and V. Zhdankin. “Residual energy in MHD turbulence and in the solar wind.” In: *AIP Conference Proceedings* 1436.1 (May 2012), pp. 18–23. ISSN: 0094-243X. DOI: [10.1063/1.4723584](https://doi.org/10.1063/1.4723584). eprint: [https://pubs.aip.org/aip/acp/article-pdf/1436/1/18/11719431/18\\_online.pdf](https://pubs.aip.org/aip/acp/article-pdf/1436/1/18/11719431/18_online.pdf). URL: <https://doi.org/10.1063/1.4723584>.
- [59] P. Bordas et al. “Detection of Persistent Gamma-Ray Emission Toward SS433/W50.” In: *Astrophys. J. Lett.* 807.1, L8 (July 2015), p. L8. DOI: [10.1088/2041-8205/807/1/L8](https://doi.org/10.1088/2041-8205/807/1/L8). arXiv: [1411.7413](https://arxiv.org/abs/1411.7413) [[astro-ph.HE](#)].
- [60] P. Bordas et al. “Non-thermal emission from microquasar/ISM interaction.” In: *Astron. Astrophys.* 497.2 (Apr. 2009), pp. 325–334. DOI: [10.1051/0004-6361/200810781](https://doi.org/10.1051/0004-6361/200810781). arXiv: [0903.3293](https://arxiv.org/abs/0903.3293) [[astro-ph.GA](#)].
- [61] V. Bosch-Ramon. “Fermi I particle acceleration in converging flows mediated by magnetic reconnection.” In: *Astron. Astrophys.* 542, A125 (June 2012), A125. DOI: [10.1051/0004-6361/201219231](https://doi.org/10.1051/0004-6361/201219231). arXiv: [1205.3450](https://arxiv.org/abs/1205.3450) [[astro-ph.HE](#)].

- [62] V. Bosch-Ramon and M. V. Barkov. “Large-scale flow dynamics and radiation in pulsar  $\gamma$ -ray binaries.” In: *Astron. Astrophys.* 535, A20 (Nov. 2011), A20. DOI: [10.1051/0004-6361/201117235](https://doi.org/10.1051/0004-6361/201117235). arXiv: [1105.6236](https://arxiv.org/abs/1105.6236) [[astro-ph.HE](#)].
- [63] V. Bosch-Ramon and M. V. Barkov. “The effects of the stellar wind and orbital motion on the jets of high-mass microquasars.” In: *Astron. Astrophys.* 590, A119 (May 2016), A119. DOI: [10.1051/0004-6361/201628564](https://doi.org/10.1051/0004-6361/201628564). arXiv: [1604.06360](https://arxiv.org/abs/1604.06360) [[astro-ph.HE](#)].
- [64] V. Bosch-Ramon, M. V. Barkov, and M. Perucho. “Orbital evolution of colliding star and pulsar winds in 2D and 3D: effects of dimensionality, EoS, resolution, and grid size.” In: *Astron. Astrophys.* 577, A89 (May 2015), A89. DOI: [10.1051/0004-6361/201425228](https://doi.org/10.1051/0004-6361/201425228). arXiv: [1411.7892](https://arxiv.org/abs/1411.7892) [[astro-ph.HE](#)].
- [65] V. Bosch-Ramon, M. Perucho, and P. Bordas. “The termination region of high-mass microquasar jets.” In: *Astron. Astrophys.* 528, A89 (Apr. 2011), A89. DOI: [10.1051/0004-6361/201016364](https://doi.org/10.1051/0004-6361/201016364). arXiv: [1101.5049](https://arxiv.org/abs/1101.5049) [[astro-ph.HE](#)].
- [66] V. Bosch-Ramon and F. M. Rieger. “Exploring Particle Acceleration in Gamma-Ray Binaries.” In: *Astroparticle*. Aug. 2012, pp. 219–225. DOI: [10.1142/9789814405072\\_0033](https://doi.org/10.1142/9789814405072_0033). arXiv: [1110.1534](https://arxiv.org/abs/1110.1534) [[astro-ph.HE](#)].
- [67] V. Bosch-Ramon et al. “Simulations of stellar/pulsar-wind interaction along one full orbit.” In: *Astron. Astrophys.* 544, A59 (Aug. 2012), A59. DOI: [10.1051/0004-6361/201219251](https://doi.org/10.1051/0004-6361/201219251). arXiv: [1203.5528](https://arxiv.org/abs/1203.5528) [[astro-ph.HE](#)].
- [68] V. Bosch-Ramon et al. “The radio to TeV orbital variability of the microquasar LS I +61 303.” In: *Astron. Astrophys.* 459.2 (Nov. 2006), pp. L25–L28. DOI: [10.1051/0004-6361:20065830](https://doi.org/10.1051/0004-6361:20065830).
- [69] V. Bosch-Ramon and D. Khangulyan. “Understanding the Very-High Emission from Microquasars.” In: *International Journal of Modern Physics D* 18.3 (Jan. 2009), pp. 347–387. DOI: [10.1142/S0218271809014601](https://doi.org/10.1142/S0218271809014601). arXiv: [0805.4123](https://arxiv.org/abs/0805.4123) [[astro-ph](#)].
- [70] V. Bosch-Ramon, D. Khangulyan, and F. Aharonian. “Interactions between jets and massive stars in microquasars.” In: *Microquasars and Beyond*. Jan. 2008, 70, p. 70. DOI: [10.22323/1.062.0070](https://doi.org/10.22323/1.062.0070).
- [71] V. Bosch-Ramon et al. “HESS J0632+057: hydrodynamics and non-thermal emission.” In: *Mon. Not. R. Astron. Soc.* 471.1 (Oct. 2017), pp. L150–L154. DOI: [10.1093/mnrasl/slx124](https://doi.org/10.1093/mnrasl/slx124). arXiv: [1708.00066](https://arxiv.org/abs/1708.00066) [[astro-ph.HE](#)].
- [72] T. A. Bowen et al. “Impact of Residual Energy on Solar Wind Turbulent Spectra.” In: *Astrophys. J.* 865.1, 45 (Sept. 2018), p. 45. DOI: [10.3847/1538-4357/aad95b](https://doi.org/10.3847/1538-4357/aad95b). arXiv: [1805.02739](https://arxiv.org/abs/1805.02739) [[astro-ph.SR](#)].
- [73] M. G. Bowler. “SS 433: Two robust determinations fix the mass ratio.” In: *Astron. Astrophys.* 619, L4 (Nov. 2018), p. L4. DOI: [10.1051/0004-6361/201834121](https://doi.org/10.1051/0004-6361/201834121).
- [74] M. G. Bowler and R. Keppens. “W 50 and SS 433.” In: *Astron. Astrophys.* 617, A29 (Sept. 2018), A29. DOI: [10.1051/0004-6361/201732488](https://doi.org/10.1051/0004-6361/201732488). arXiv: [1805.10094](https://arxiv.org/abs/1805.10094) [[astro-ph.GA](#)].

- [75] S. Bowyer et al. “Cosmic X-ray Sources.” In: *Science* 147.3656 (Jan. 1965), pp. 394–398. DOI: [10.1126/science.147.3656.394](https://doi.org/10.1126/science.147.3656.394).
- [76] J. U. Brackbill and D. C. Barnes. “The Effect of Nonzero  $\nabla \cdot \mathbf{B}$  on the numerical solution of the magnetohydrodynamic equations.” In: *Journal of Computational Physics* 35.3 (May 1980), pp. 426–430. DOI: [10.1016/0021-9991\(80\)90079-0](https://doi.org/10.1016/0021-9991(80)90079-0).
- [77] C. F. Bradshaw, E. B. Fomalont, and B. J. Geldzahler. “High-Resolution Parallax Measurements of Scorpius X-1.” In: *Astrophys. J. Lett.* 512.2 (Feb. 1999), pp. L121–L124. DOI: [10.1086/311889](https://doi.org/10.1086/311889).
- [78] C. F. Bradshaw, B. J. Geldzahler, and E. B. Fomalont. “The X-Ray Spectral Changes of Scorpius X-1.” In: *Astrophys. J.* 592.1 (July 2003), pp. 486–497. DOI: [10.1086/375577](https://doi.org/10.1086/375577).
- [79] H. V. Bradt, R. E. Rothschild, and J. H. Swank. “X-ray timing explorer mission.” In: 97.1 (Jan. 1993), pp. 355–360.
- [80] W. Brinkmann et al. “The X-ray emission of SS 433.” In: *Astron. Astrophys.* 241 (Jan. 1991), p. 112.
- [81] M. Brio and C. C. Wu. “An Upwind Differencing Scheme for the Equations of Ideal Magnetohydrodynamics.” In: *Journal of Computational Physics* 75.2 (Apr. 1988), pp. 400–422. DOI: [10.1016/0021-9991\(88\)90120-9](https://doi.org/10.1016/0021-9991(88)90120-9).
- [82] O. Bromberg and A. Tchekhovskoy. “Relativistic MHD simulations of core-collapse GRB jets: 3D instabilities and magnetic dissipation.” In: *Mon. Not. R. Astron. Soc.* 456.2 (Feb. 2016), pp. 1739–1760. DOI: [10.1093/mnras/stv2591](https://doi.org/10.1093/mnras/stv2591). arXiv: [1508.02721](https://arxiv.org/abs/1508.02721) [[astro-ph.HE](#)].
- [83] G. Bruni et al. “RadioAstron reveals a spine-sheath jet structure in 3C 273.” In: *Astron. Astrophys.* 654, A27 (Oct. 2021), A27. DOI: [10.1051/0004-6361/202039423](https://doi.org/10.1051/0004-6361/202039423). arXiv: [2101.07324](https://arxiv.org/abs/2101.07324) [[astro-ph.GA](#)].
- [84] N. Bucciantini and L. Del Zanna. “A fully covariant mean-field dynamo closure for numerical 3 + 1 resistive GRMHD.” In: *Mon. Not. R. Astron. Soc.* 428.1 (Jan. 2013), pp. 71–85. DOI: [10.1093/mnras/sts005](https://doi.org/10.1093/mnras/sts005). arXiv: [1205.2951](https://arxiv.org/abs/1205.2951) [[astro-ph.HE](#)].
- [85] J. R. Buchler and W. R. Yueh. “Compton scattering opacities in a partially degenerate electron plasma at high temperatures.” In: *Astrophys. J.* 210 (Dec. 1976), pp. 440–446. DOI: [10.1086/154847](https://doi.org/10.1086/154847).
- [86] A. Burrows, D. Radice, and D. Vartanyan. “Three-dimensional supernova explosion simulations of 9-, 10-, 11-, 12-, and 13- $M_{\odot}$  stars.” In: *Mon. Not. R. Astron. Soc.* 485.3 (May 2019), pp. 3153–3168. DOI: [10.1093/mnras/stz543](https://doi.org/10.1093/mnras/stz543). arXiv: [1902.00547](https://arxiv.org/abs/1902.00547) [[astro-ph.SR](#)].
- [87] Y. M. Butt, T. J. Maccarone, and N. Prantzos. “Jet-induced Nucleosynthesis in Misaligned Microquasars.” In: *Astrophys. J.* 587.2 (Apr. 2003), pp. 748–753. DOI: [10.1086/368301](https://doi.org/10.1086/368301). arXiv: [astro-ph/0208370](https://arxiv.org/abs/astro-ph/0208370) [[astro-ph](#)].
- [88] S. Buttiglione et al. “An optical spectroscopic survey of the 3CR sample of radio galaxies with  $z < 0.3$ . II. Spectroscopic classes and accretion modes in radio-loud AGN.” In: *Astron. Astrophys.* 509, A6 (Jan. 2010), A6. DOI: [10.1051/0004-6361/200913290](https://doi.org/10.1051/0004-6361/200913290). arXiv: [0911.0536](https://arxiv.org/abs/0911.0536) [[astro-ph.CO](#)].
- [89] I. Caballero and J. Wilms. “X-ray pulsars: a review.” In: 83 (Jan. 2012), p. 230. DOI: [10.48550/arXiv.1206.3124](https://doi.org/10.48550/arXiv.1206.3124). arXiv: [1206.3124](https://arxiv.org/abs/1206.3124) [[astro-ph.HE](#)].

- [90] P. Cargo and G. Gallice. “Roe Matrices for Ideal MHD and Systematic Construction of Roe Matrices for Systems of Conservation Laws.” In: *Journal of Computational Physics* 136.2 (Sept. 1997), pp. 446–466. DOI: [10.1006/jcph.1997.5773](https://doi.org/10.1006/jcph.1997.5773).
- [91] J. Casares et al. “Orbital parameters of the microquasar LS I +61 303.” In: *Mon. Not. R. Astron. Soc.* 360.3 (July 2005), pp. 1105–1109. DOI: [10.1111/j.1365-2966.2005.09106.x](https://doi.org/10.1111/j.1365-2966.2005.09106.x). arXiv: [astro-ph/0504332](https://arxiv.org/abs/astro-ph/0504332) [[astro-ph](#)].
- [92] P. Casella, T. Belloni, and L. Stella. “A continuous flaring- to normal-branch transition in <ASTROBJ>Scorpius X-1</ASTROBJ>.” In: *Astron. Astrophys.* 446.2 (Feb. 2006), pp. 579–582. DOI: [10.1051/0004-6361:20052912](https://doi.org/10.1051/0004-6361:20052912). arXiv: [astro-ph/0506483](https://arxiv.org/abs/astro-ph/0506483) [[astro-ph](#)].
- [93] J. P. Cassinelli et al. “The Effects of Clumps in Explaining X-Ray Emission Lines from Hot Stars.” In: *Astrophys. J.* 683.2 (Aug. 2008), pp. 1052–1062. DOI: [10.1086/589760](https://doi.org/10.1086/589760). arXiv: [0804.4680](https://arxiv.org/abs/0804.4680) [[astro-ph](#)].
- [94] M. Castro, J. Gallardo, and A. Marquina. “A Class of Incomplete Riemann Solvers Based on Uniform Rational Approximations to the Absolute Value Function.” In: *Journal of Scientific Computing* 60 (Aug. 2014), pp. 363–389. DOI: [10.1007/s10915-013-9800-2](https://doi.org/10.1007/s10915-013-9800-2).
- [95] M. J. Castro, J. M. Gallardo, and A. Marquina. “Jacobian-free approximate solvers for hyperbolic systems: Application to relativistic magneto-hydrodynamics.” In: *Computer Physics Communications* 219 (Oct. 2017), pp. 108–120. DOI: [10.1016/j.cpc.2017.05.013](https://doi.org/10.1016/j.cpc.2017.05.013).
- [96] M. J. Castro, J. M. Gallardo, and A. Marquina. “Approximate Osher–Solomon schemes for hyperbolic systems.” In: *Applied Mathematics and Computation* 272 (2016). Recent Advances in Numerical Methods for Hyperbolic Partial Differential Equations, pp. 347–368. ISSN: 0096-3003. DOI: <https://doi.org/10.1016/j.amc.2015.06.104>.
- [97] M. J. Castro Díaz and E. Fernández-Nieto. “A Class of Computationally Fast First Order Finite Volume Solvers: PVM Methods.” In: *SIAM Journal on Scientific Computing* 34.4 (2012), A2173–A2196. DOI: [10.1137/100795280](https://doi.org/10.1137/100795280). eprint: <https://doi.org/10.1137/100795280>. URL: <https://doi.org/10.1137/100795280>.
- [98] A. J. Castro-Tirado et al. “Discovery and Observations by WATCH of the X-Ray Transient GRS 1915+105.” In: *Astrophys. J. Suppl. Ser.* 92 (June 1994), p. 469. DOI: [10.1086/191998](https://doi.org/10.1086/191998).
- [99] S. Chakravorty et al. “Absorption lines from magnetically driven winds in X-ray binaries.” In: *Astron. Astrophys.* 589, A119 (May 2016), A119. DOI: [10.1051/0004-6361/201527163](https://doi.org/10.1051/0004-6361/201527163). arXiv: [1512.09149](https://arxiv.org/abs/1512.09149) [[astro-ph.HE](#)].
- [100] A. Charlet et al. “Effects of radiative losses on the relativistic jets of high-mass microquasars.” In: *Astron. Astrophys.* 658, A100 (Feb. 2022), A100. DOI: [10.1051/0004-6361/202141730](https://doi.org/10.1051/0004-6361/202141730). arXiv: [2110.08116](https://arxiv.org/abs/2110.08116) [[astro-ph.HE](#)].
- [101] C. H. K. Chen et al. “Residual Energy Spectrum of Solar Wind Turbulence.” In: *Astrophys. J.* 770.2, 125 (June 2013), p. 125. DOI: [10.1088/0004-637X/770/2/125](https://doi.org/10.1088/0004-637X/770/2/125). arXiv: [1304.7818](https://arxiv.org/abs/1304.7818) [[physics.space-ph](#)].

- [102] A. M. Cherepashchuk, K. A. Postnov, and A. A. Belinski. “On masses of the components in SS433.” In: *Mon. Not. R. Astron. Soc.* 479.4 (Oct. 2018), pp. 4844–4848. DOI: [10.1093/mnras/sty1853](https://doi.org/10.1093/mnras/sty1853). arXiv: [1807.02626](https://arxiv.org/abs/1807.02626) [[astro-ph.HE](#)].
- [103] M. Chernyakova and D. Malyshev. “Gamma-ray binaries.” In: *Multifrequency Behaviour of High Energy Cosmic Sources - XIII. 3-8 June 2019. Palermo*. Dec. 2020, 45, p. 45. arXiv: [2006.03615](https://arxiv.org/abs/2006.03615) [[astro-ph.HE](#)].
- [104] Childs, H. et al. “High Performance Visualization—Enabling Extreme-Scale Scientific Insight.” In: *Proceedings of SciDAC 2011* (2012).
- [105] E. Choi and P. J. Wiita. “A Multidimensional Relativistic Hydrodynamic Code with a General Equation of State.” In: *Astrophys. J. Suppl. Ser.* 191.1 (Nov. 2010), pp. 113–123. DOI: [10.1088/0067-0049/191/1/113](https://doi.org/10.1088/0067-0049/191/1/113). arXiv: [1009.3774](https://arxiv.org/abs/1009.3774) [[astro-ph.HE](#)].
- [106] M. J. Church, A. Gibiec, and M. Bałucińska-Church. “The nature of the island and banana states in atoll sources and a unified model for low-mass X-ray binaries.” In: *Mon. Not. R. Astron. Soc.* 438.4 (Mar. 2014), pp. 2784–2797. DOI: [10.1093/mnras/stt2364](https://doi.org/10.1093/mnras/stt2364). arXiv: [1312.1823](https://arxiv.org/abs/1312.1823) [[astro-ph.HE](#)].
- [107] D. A. Clarke, M. L. Norman, and J. O. Burns. “Numerical Observations of a Simulated Jet with a Passive Helical Magnetic Field.” In: *ApJ* 342 (July 1989), p. 700. DOI: [10.1086/167631](https://doi.org/10.1086/167631).
- [108] S. Corbel and R. P. Fender. “Near-Infrared Synchrotron Emission from the Compact Jet of GX 339-4.” In: *Astrophys. J. Lett.* 573.1 (July 2002), pp. L35–L39. DOI: [10.1086/341870](https://doi.org/10.1086/341870). arXiv: [astro-ph/0205402](https://arxiv.org/abs/astro-ph/0205402) [[astro-ph](#)].
- [109] S. Corbel et al. “Radio/X-ray correlation in the low/hard state of GX 339-4.” In: *Astron. Astrophys.* 400 (Mar. 2003), pp. 1007–1012. DOI: [10.1051/0004-6361:20030090](https://doi.org/10.1051/0004-6361:20030090). arXiv: [astro-ph/0301436](https://arxiv.org/abs/astro-ph/0301436) [[astro-ph](#)].
- [110] F. Cordier, P. Degond, and A. Kumbaro. “Phase Appearance or Disappearance in Two-Phase Flows.” In: *J Sci Comput* 58 (2014), 115–148. DOI: [10.1007/s10915-013-9725-9](https://doi.org/10.1007/s10915-013-9725-9).
- [111] M. Coriat et al. “Radiatively efficient accreting black holes in the hard state: the case study of H1743-322.” In: *Mon. Not. R. Astron. Soc.* 414.1 (June 2011), pp. 677–690. DOI: [10.1111/j.1365-2966.2011.18433.x](https://doi.org/10.1111/j.1365-2966.2011.18433.x). arXiv: [1101.5159](https://arxiv.org/abs/1101.5159) [[astro-ph.HE](#)].
- [112] J. H. Croston et al. “An X-Ray Study of Magnetic Field Strengths and Particle Content in the Lobes of FR II Radio Sources.” In: *Astrophys. J.* 626.2 (June 2005), pp. 733–747. DOI: [10.1086/430170](https://doi.org/10.1086/430170). arXiv: [astro-ph/0503203](https://arxiv.org/abs/astro-ph/0503203) [[astro-ph](#)].
- [113] A. Cruz-Osorio et al. “State-of-the-art energetic and morphological modelling of the launching site of the M87 jet.” In: *Nature Astronomy* (Nov. 2021). DOI: [10.1038/s41550-021-01506-w](https://doi.org/10.1038/s41550-021-01506-w). arXiv: [2111.02517](https://arxiv.org/abs/2111.02517) [[astro-ph.HE](#)].
- [114] A. D’Ài et al. “Temporal features of LS I +61°303 in hard X-rays from the Swift/BAT survey data.” In: *Mon. Not. R. Astron. Soc.* 456.2 (Feb. 2016), pp. 1955–1959. DOI: [10.1093/mnras/stv2716](https://doi.org/10.1093/mnras/stv2716). arXiv: [1601.03260](https://arxiv.org/abs/1601.03260) [[astro-ph.HE](#)].

- [115] E. M. de Gouveia Dal Pino, P. P. Piovezan, and L. H. S. Kadowaki. “The role of magnetic reconnection on jet/accretion disk systems.” In: *Astron. Astrophys.* 518, A5 (July 2010), A5. DOI: [10.1051/0004-6361/200913462](https://doi.org/10.1051/0004-6361/200913462). arXiv: [1005.3067](https://arxiv.org/abs/1005.3067) [[astro-ph.HE](#)].
- [116] V. M. de la Cita et al. “Gamma rays from clumpy wind-jet interactions in high-mass microquasars.” In: *Astron. Astrophys.* 604, A39 (July 2017), A39. DOI: [10.1051/0004-6361/201630060](https://doi.org/10.1051/0004-6361/201630060). arXiv: [1701.05028](https://arxiv.org/abs/1701.05028) [[astro-ph.HE](#)].
- [117] A. Dedner et al. “Hyperbolic Divergence Cleaning for the MHD Equations.” In: *Journal of Computational Physics* 175.2 (Jan. 2002), pp. 645–673. DOI: [10.1006/jcph.2001.6961](https://doi.org/10.1006/jcph.2001.6961).
- [118] L. Del Zanna and N. Bucciantini. “An efficient shock-capturing central-type scheme for multidimensional relativistic flows. I. Hydrodynamics.” In: *Astron. Astrophys.* 390 (Aug. 2002), pp. 1177–1186. DOI: [10.1051/0004-6361:20020776](https://doi.org/10.1051/0004-6361:20020776). arXiv: [astro-ph/0205290](https://arxiv.org/abs/astro-ph/0205290) [[astro-ph](#)].
- [119] L. Del Zanna, N. Bucciantini, and P. Londrillo. “An efficient shock-capturing central-type scheme for multidimensional relativistic flows. II. Magnetohydrodynamics.” In: *Astron. Astrophys.* 400 (Mar. 2003), pp. 397–413. DOI: [10.1051/0004-6361:20021641](https://doi.org/10.1051/0004-6361:20021641). arXiv: [astro-ph/0210618](https://arxiv.org/abs/astro-ph/0210618) [[astro-ph](#)].
- [120] L. Del Zanna et al. “ECHO: a Eulerian conservative high-order scheme for general relativistic magnetohydrodynamics and magnetodynamics.” In: *Astron. Astrophys.* 473.1 (Oct. 2007), pp. 11–30. DOI: [10.1051/0004-6361:20077093](https://doi.org/10.1051/0004-6361:20077093). arXiv: [0704.3206](https://arxiv.org/abs/0704.3206) [[astro-ph](#)].
- [121] V. Dhawan, K. I. Kellermann, and J. D. Romney. “Kinematics of the Nucleus of NGC 1275 (3C 84).” In: *Astrophys. J. Lett.* 498 (May 1998), pp. L111–L114. DOI: [10.1086/311313](https://doi.org/10.1086/311313).
- [122] V. Dhawan, I. F. Mirabel, and L. F. Rodríguez. “AU-Scale Synchrotron Jets and Superluminal Ejecta in GRS 1915+105.” In: *Astrophys. J.* 543.1 (Nov. 2000), pp. 373–385. DOI: [10.1086/317088](https://doi.org/10.1086/317088). arXiv: [astro-ph/0006086](https://arxiv.org/abs/astro-ph/0006086) [[astro-ph](#)].
- [123] V. Dhawan, A. Mioduszewski, and M. Rupen. “LS I +61 303 is a Be-Pulsar binary, not a Microquasar.” In: *VI Microquasar Workshop: Microquasars and Beyond*. Jan. 2006, 52.1, p. 52.1.
- [124] R. Di Stefano et al. “A possible planet candidate in an external galaxy detected through X-ray transit.” In: *Nature Astronomy* 5 (Oct. 2021), pp. 1297–1307. DOI: [10.1038/s41550-021-01495-w](https://doi.org/10.1038/s41550-021-01495-w).
- [125] M. Díaz Trigo and L. Boirin. “Accretion disc atmospheres and winds in low-mass X-ray binaries.” In: *Astronomische Nachrichten* 337.4-5 (May 2016), p. 368. DOI: [10.1002/asna.201612315](https://doi.org/10.1002/asna.201612315). arXiv: [1510.03576](https://arxiv.org/abs/1510.03576) [[astro-ph.HE](#)].
- [126] M. Díaz Trigo et al. “Baryons in the relativistic jets of the stellar-mass black-hole candidate 4U1630-47.” In: *Nature* 504.7479 (Dec. 2013), pp. 260–262. DOI: [10.1038/nature12672](https://doi.org/10.1038/nature12672). arXiv: [1311.5080](https://arxiv.org/abs/1311.5080) [[astro-ph.HE](#)].
- [127] S. W. Dieters and M. van der Klis. “The timing properties of Sco X-1 along its Z track with EXOSAT.” In: *Mon. Not. R. Astron. Soc.* 311.1 (Jan. 2000), pp. 201–224. DOI: [10.1046/j.1365-8711.2000.03050.x](https://doi.org/10.1046/j.1365-8711.2000.03050.x). arXiv: [astro-ph/9909472](https://arxiv.org/abs/astro-ph/9909472) [[astro-ph](#)].

- [128] S. D’Odorico et al. “Evidence that the compact object in SS433 is a neutron star and not a black hole.” In: *Nature* 353.6342 (Sept. 1991), pp. 329–331. DOI: [10.1038/353329a0](https://doi.org/10.1038/353329a0).
- [129] A. Dolezal and S. S. M. Wong. “Relativistic Hydrodynamics and Essentially Non-oscillatory Shock Capturing Schemes.” In: *Journal of Computational Physics* 120.2 (Sept. 1995), pp. 266–277. DOI: [10.1006/jcph.1995.1164](https://doi.org/10.1006/jcph.1995.1164).
- [130] M. A. Dopita and R. S. Sutherland. *Astrophysics of the diffuse universe*. 2003. DOI: [10.1007/978-3-662-05866-4](https://doi.org/10.1007/978-3-662-05866-4).
- [131] S. Dorfman et al. “Generation of residual energy by many interacting Alfvén waves.” In: *AGU Fall Meeting Abstracts*. Vol. 2021. Dec. 2021, SH54B-05, SH54B-05.
- [132] S. Drappeau et al. “Internal shocks driven by accretion flow variability in the compact jet of the black hole binary GX 339-4.” In: *Mon. Not. R. Astron. Soc.* 447.4 (Mar. 2015), pp. 3832–3839. DOI: [10.1093/mnras/stu2711](https://doi.org/10.1093/mnras/stu2711). arXiv: [1412.5819](https://arxiv.org/abs/1412.5819) [[astro-ph.HE](#)].
- [133] M. R. Dubal. “Numerical simulations of special relativistic, magnetic gas flows.” In: *Computer Physics Communications* 64.2 (May 1991), pp. 221–234. DOI: [10.1016/0010-4655\(91\)90033-H](https://doi.org/10.1016/0010-4655(91)90033-H).
- [134] G. Dubus. “Gamma-ray binaries: pulsars in disguise?” In: *Astron. Astrophys.* 456.3 (Sept. 2006), pp. 801–817. DOI: [10.1051/0004-6361:20054779](https://doi.org/10.1051/0004-6361:20054779). arXiv: [astro-ph/0605287](https://arxiv.org/abs/astro-ph/0605287) [[astro-ph](#)].
- [135] G. Dubus. “Gamma-ray binaries and related systems.” In: 21, 64 (Aug. 2013), p. 64. DOI: [10.1007/s00159-013-0064-5](https://doi.org/10.1007/s00159-013-0064-5). arXiv: [1307.7083](https://arxiv.org/abs/1307.7083) [[astro-ph.HE](#)].
- [136] S. S. Eikenberry et al. “Twenty Years of Timing SS 433.” In: *Astrophys. J.* 561.2 (Nov. 2001), pp. 1027–1033. DOI: [10.1086/323380](https://doi.org/10.1086/323380). arXiv: [astro-ph/0107296](https://arxiv.org/abs/astro-ph/0107296) [[astro-ph](#)].
- [137] M. Elvis et al. “Discovery of powerful transient X-ray source A0620-00 with Ariel V Sky Survey Experiment.” In: *Nature* 257.5528 (Oct. 1975), pp. 656–657. DOI: [10.1038/257656a0](https://doi.org/10.1038/257656a0).
- [138] W. English, M. J. Hardcastle, and M. G. H. Krause. “Numerical modelling of the lobes of radio galaxies in cluster environments - III. Powerful relativistic and non-relativistic jets.” In: *Mon. Not. R. Astron. Soc.* 461.2 (Sept. 2016), pp. 2025–2043. DOI: [10.1093/mnras/stw1407](https://doi.org/10.1093/mnras/stw1407). arXiv: [1606.03374](https://arxiv.org/abs/1606.03374) [[astro-ph.HE](#)].
- [139] A. A. Esin, J. E. McClintock, and R. Narayan. “Advection-Dominated Accretion and the Spectral States of Black Hole X-Ray Binaries: Application to Nova Muscae 1991.” In: *Astrophys. J.* 489.2 (Nov. 1997), pp. 865–889. DOI: [10.1086/304829](https://doi.org/10.1086/304829). arXiv: [astro-ph/9705237](https://arxiv.org/abs/astro-ph/9705237) [[astro-ph](#)].
- [140] P. Esposito et al. “Swift/XRT monitoring of five orbital cycles of LS I +61° 303.” In: *Astron. Astrophys.* 474.2 (Nov. 2007), pp. 575–578. DOI: [10.1051/0004-6361:20078334](https://doi.org/10.1051/0004-6361:20078334). arXiv: [0708.3330](https://arxiv.org/abs/0708.3330) [[astro-ph](#)].
- [141] C. R. Evans and J. F. Hawley. “Simulation of Magnetohydrodynamic Flows: A Constrained Transport Model.” In: *Astrophys. J.* 332 (Sept. 1988), p. 659. DOI: [10.1086/166684](https://doi.org/10.1086/166684).

- [142] Event Horizon Telescope Collaboration et al. “First M87 Event Horizon Telescope Results. I. The Shadow of the Supermassive Black Hole.” In: *Astrophys. J. Lett.* 875.1, L1 (Apr. 2019), p. L1. DOI: [10.3847/2041-8213/ab0ec7](https://doi.org/10.3847/2041-8213/ab0ec7). arXiv: [1906.11238](https://arxiv.org/abs/1906.11238) [[astro-ph.GA](#)].
- [143] A. C. Fabian. “SS 433 : a freely precessing neutron star ?” In: *Mon. Not. R. Astron. Soc.* 192 (July 1980), 11P–14. DOI: [10.1093/mnras/192.1.11P](https://doi.org/10.1093/mnras/192.1.11P).
- [144] A. C. Fabian et al. “A deep Chandra observation of the Perseus cluster: shocks and ripples.” In: *Mon. Not. R. Astron. Soc.* 344.3 (Sept. 2003), pp. L43–L47. DOI: [10.1046/j.1365-8711.2003.06902.x](https://doi.org/10.1046/j.1365-8711.2003.06902.x). arXiv: [astro-ph/0306036](https://arxiv.org/abs/astro-ph/0306036) [[astro-ph](#)].
- [145] A. C. Fabian et al. “Chandra imaging of the complex X-ray core of the Perseus cluster.” In: *Mon. Not. R. Astron. Soc.* 318.4 (Nov. 2000), pp. L65–L68. DOI: [10.1046/j.1365-8711.2000.03904.x](https://doi.org/10.1046/j.1365-8711.2000.03904.x). arXiv: [astro-ph/0007456](https://arxiv.org/abs/astro-ph/0007456) [[astro-ph](#)].
- [146] A. C. Fabian et al. “X-ray fluorescence from the inner disc in Cygnus X-1.” In: *Mon. Not. R. Astron. Soc.* 238 (May 1989), pp. 729–736. DOI: [10.1093/mnras/238.3.729](https://doi.org/10.1093/mnras/238.3.729).
- [147] S. Fabrika. “The jets and supercritical accretion disk in SS433.” In: 12 (Jan. 2004), pp. 1–152. arXiv: [astro-ph/0603390](https://arxiv.org/abs/astro-ph/0603390) [[astro-ph](#)].
- [148] H. Falcke and P. L. Biermann. “Galactic jet sources and the AGN connection.” In: *Astron. Astrophys.* 308 (Apr. 1996), pp. 321–329. DOI: [10.48550/arXiv.astro-ph/9506138](https://doi.org/10.48550/arXiv.astro-ph/9506138). arXiv: [astro-ph/9506138](https://arxiv.org/abs/astro-ph/9506138) [[astro-ph](#)].
- [149] B. L. Fanaroff and J. M. Riley. “The morphology of extragalactic radio sources of high and low luminosity.” In: *Mon. Not. R. Astron. Soc.* 167 (May 1974), 31P–36P. DOI: [10.1093/mnras/167.1.31P](https://doi.org/10.1093/mnras/167.1.31P).
- [150] K. Fang, E. Charles, and R. D. Blandford. “GeV–TeV Counterparts of SS 433/W50 from Fermi-LAT and HAWC Observations.” In: *Astrophys. J. Lett.* 889.1, L5 (Jan. 2020), p. L5. DOI: [10.3847/2041-8213/ab62b8](https://doi.org/10.3847/2041-8213/ab62b8). arXiv: [2001.03599](https://arxiv.org/abs/2001.03599) [[astro-ph.HE](#)].
- [151] B. D. Farris et al. “Relativistic radiation magnetohydrodynamics in dynamical spacetimes: Numerical methods and tests.” In: *Phys. Rev. D* 78.2, 024023 (July 2008), p. 024023. DOI: [10.1103/PhysRevD.78.024023](https://doi.org/10.1103/PhysRevD.78.024023). arXiv: [0802.3210](https://arxiv.org/abs/0802.3210) [[astro-ph](#)].
- [152] C.-A. Faucher-Giguère and E. Quataert. “The physics of galactic winds driven by active galactic nuclei.” In: *Mon. Not. R. Astron. Soc.* 425.1 (Sept. 2012), pp. 605–622. DOI: [10.1111/j.1365-2966.2012.21512.x](https://doi.org/10.1111/j.1365-2966.2012.21512.x). arXiv: [1204.2547](https://arxiv.org/abs/1204.2547) [[astro-ph.CO](#)].
- [153] R. P. Fender, T. M. Belloni, and E. Gallo. “Towards a unified model for black hole X-ray binary jets.” In: *Mon. Not. R. Astron. Soc.* 355.4 (Dec. 2004), pp. 1105–1118. DOI: [10.1111/j.1365-2966.2004.08384.x](https://doi.org/10.1111/j.1365-2966.2004.08384.x). arXiv: [astro-ph/0409360](https://arxiv.org/abs/astro-ph/0409360) [[astro-ph](#)].
- [154] R. P. Fender et al. “Comprehensive coverage of particle acceleration and kinetic feedback from the stellar mass black hole V404 Cygni.” In: *Mon. Not. R. Astron. Soc.* 518.1 (Jan. 2023), pp. 1243–1259. DOI: [10.1093/mnras/stac1836](https://doi.org/10.1093/mnras/stac1836). arXiv: [2206.09831](https://arxiv.org/abs/2206.09831) [[astro-ph.HE](#)].

- [155] R. P. Fender et al. “MERLIN observations of relativistic ejections from GRS 1915+105.” In: *Mon. Not. R. Astron. Soc.* 304.4 (Apr. 1999), pp. 865–876. DOI: [10.1046/j.1365-8711.1999.02364.x](https://doi.org/10.1046/j.1365-8711.1999.02364.x). arXiv: [astro-ph/9812150](https://arxiv.org/abs/astro-ph/9812150) [[astro-ph](#)].
- [156] R. P. Fender et al. “The very flat radio-millimetre spectrum of Cygnus X-1.” In: *Mon. Not. R. Astron. Soc.* 312.4 (Mar. 2000), pp. 853–858. DOI: [10.1046/j.1365-8711.2000.03219.x](https://doi.org/10.1046/j.1365-8711.2000.03219.x). arXiv: [astro-ph/9910184](https://arxiv.org/abs/astro-ph/9910184) [[astro-ph](#)].
- [157] R. Fender. “Jets from X-ray binaries.” In: *Compact stellar X-ray sources*. Vol. 39. 2006, pp. 381–419. DOI: [10.48550/arXiv.astro-ph/0303339](https://doi.org/10.48550/arXiv.astro-ph/0303339).
- [158] R. Fender et al. “An ultra-relativistic outflow from a neutron star accreting gas from a companion.” In: *Nature* 427.6971 (Jan. 2004), pp. 222–224. DOI: [10.1038/nature02137](https://doi.org/10.1038/nature02137). arXiv: [astro-ph/0401290](https://arxiv.org/abs/astro-ph/0401290) [[astro-ph](#)].
- [159] R. Fender et al. “An Asymmetric Arcsecond Radio Jet from Circinus X-1.” In: *Astrophys. J. Lett.* 506.2 (Oct. 1998), pp. L121–L125. DOI: [10.1086/311660](https://doi.org/10.1086/311660). arXiv: [astro-ph/9808251](https://arxiv.org/abs/astro-ph/9808251) [[astro-ph](#)].
- [160] Fermi LAT Collaboration et al. “Modulated High-Energy Gamma-Ray Emission from the Microquasar Cygnus X-3.” In: *Science* 326.5959 (Dec. 2009), p. 1512. DOI: [10.1126/science.1182174](https://doi.org/10.1126/science.1182174).
- [161] J. Ferreira et al. “A unified accretion-ejection paradigm for black hole X-ray binaries. I. The dynamical constituents.” In: *Astron. Astrophys.* 447.3 (Mar. 2006), pp. 813–825. DOI: [10.1051/0004-6361:20052689](https://doi.org/10.1051/0004-6361:20052689). arXiv: [astro-ph/0511123](https://arxiv.org/abs/astro-ph/0511123) [[astro-ph](#)].
- [162] E. B. Fomalont, B. J. Geldzahler, and C. F. Bradshaw. “Scorpius X-1: Energy Transfer from the Core to the Radio Lobes.” In: *Astrophys. J. Lett.* 553.1 (May 2001), pp. L27–L30. DOI: [10.1086/320490](https://doi.org/10.1086/320490). arXiv: [astro-ph/0104325](https://arxiv.org/abs/astro-ph/0104325) [[astro-ph](#)].
- [163] E. B. Fomalont, B. J. Geldzahler, and C. F. Bradshaw. “Scorpius X-1: The Evolution and Nature of the Twin Compact Radio Lobes.” In: *Astrophys. J.* 558.1 (Sept. 2001), pp. 283–301. DOI: [10.1086/322479](https://doi.org/10.1086/322479). arXiv: [astro-ph/0104372](https://arxiv.org/abs/astro-ph/0104372) [[astro-ph](#)].
- [164] W. Forman et al. “The fourth Uhuru catalog of X-ray sources.” In: *Astrophys. J. Suppl. Ser.* 38 (Dec. 1978), pp. 357–412. DOI: [10.1086/190561](https://doi.org/10.1086/190561).
- [165] F. Foucart et al. “Post-merger evolution of a neutron star-black hole binary with neutrino transport.” In: *Phys. Rev. D* 91.12, 124021 (June 2015), p. 124021. DOI: [10.1103/PhysRevD.91.124021](https://doi.org/10.1103/PhysRevD.91.124021). arXiv: [1502.04146](https://arxiv.org/abs/1502.04146) [[astro-ph.HE](#)].
- [166] P. C. Fragile, A. Olejar, and P. Anninos. “Numerical Simulations of Optically Thick Accretion onto a Black Hole. II. Rotating Flow.” In: *Astrophys. J.* 796.1, 22 (Nov. 2014), p. 22. DOI: [10.1088/0004-637X/796/1/22](https://doi.org/10.1088/0004-637X/796/1/22). arXiv: [1408.4460](https://arxiv.org/abs/1408.4460) [[astro-ph.IM](#)].
- [167] P. C. Fragile et al. “Numerical Simulations of Optically Thick Accretion onto a Black Hole. I. Spherical Case.” In: *Astrophys. J. Suppl. Ser.* 201.2, 9 (Aug. 2012), p. 9. DOI: [10.1088/0067-0049/201/2/9](https://doi.org/10.1088/0067-0049/201/2/9). arXiv: [1204.5538](https://arxiv.org/abs/1204.5538) [[astro-ph.IM](#)].

- [168] A. Franchini, S. E. Motta, and G. Lodato. “Constraining black hole spins with low-frequency quasi-periodic oscillations in soft states.” In: *Mon. Not. R. Astron. Soc.* 467.1 (May 2017), pp. 145–154. DOI: [10.1093/mnras/stw3363](https://doi.org/10.1093/mnras/stw3363). arXiv: [1701.01760](https://arxiv.org/abs/1701.01760) [[astro-ph.HE](#)].
- [169] C. M. Fromm et al. “Using evolutionary algorithms to model relativistic jets. Application to NGC 1052.” In: *Astron. Astrophys.* 629, A4 (Sept. 2019), A4. DOI: [10.1051/0004-6361/201834724](https://doi.org/10.1051/0004-6361/201834724). arXiv: [1904.00106](https://arxiv.org/abs/1904.00106) [[astro-ph.HE](#)].
- [170] C. Fromm et al. “Radiative Signatures of Parsec-Scale Magnetised Jets.” In: *Galaxies* 5.4 (Nov. 2017), p. 73. DOI: [10.3390/galaxies5040073](https://doi.org/10.3390/galaxies5040073).
- [171] A. Fuentes et al. “Magnetized relativistic jets and helical magnetic fields. II. Radiation.” In: *Astron. Astrophys.* 650, A61 (June 2021), A61. DOI: [10.1051/0004-6361/202140659](https://doi.org/10.1051/0004-6361/202140659).
- [172] A. Fuentes et al. “Total and Linearly Polarized Synchrotron Emission from Overpressured Magnetized Relativistic Jets.” In: *Astrophys. J.* 860.2, 121 (June 2018), p. 121. DOI: [10.3847/1538-4357/aac091](https://doi.org/10.3847/1538-4357/aac091). arXiv: [1804.01928](https://arxiv.org/abs/1804.01928) [[astro-ph.HE](#)].
- [173] F. Gagliardi et al. “The international race towards Exascale in Europe.” In: *CCF Transactions on High Performance Computing* 1.1 (2019), pp. 3–13. DOI: [10.1007/s42514-019-00002-y](https://doi.org/10.1007/s42514-019-00002-y). URL: <https://doi.org/10.1007/s42514-019-00002-y>.
- [174] E. Gallo et al. “The radio/X-ray domain of black hole X-ray binaries at the lowest radio luminosities.” In: *Mon. Not. R. Astron. Soc.* 445.1 (Nov. 2014), pp. 290–300. DOI: [10.1093/mnras/stu1599](https://doi.org/10.1093/mnras/stu1599). arXiv: [1408.3130](https://arxiv.org/abs/1408.3130) [[astro-ph.HE](#)].
- [175] E. Gallo, N. Degenaar, and J. van den Eijnden. “Hard state neutron star and black hole X-ray binaries in the radio:X-ray luminosity plane.” In: *Mon. Not. R. Astron. Soc.* 478.1 (July 2018), pp. L132–L136. DOI: [10.1093/mnrasl/sly083](https://doi.org/10.1093/mnrasl/sly083). arXiv: [1805.01905](https://arxiv.org/abs/1805.01905) [[astro-ph.HE](#)].
- [176] E. Gallo, B. P. Miller, and R. Fender. “Assessing luminosity correlations via cluster analysis: evidence for dual tracks in the radio/X-ray domain of black hole X-ray binaries.” In: *Mon. Not. R. Astron. Soc.* 423.1 (June 2012), pp. 590–599. DOI: [10.1111/j.1365-2966.2012.20899.x](https://doi.org/10.1111/j.1365-2966.2012.20899.x). arXiv: [1203.4263](https://arxiv.org/abs/1203.4263) [[astro-ph.HE](#)].
- [177] E. Gallo et al. “A dark jet dominates the power output of the stellar black hole Cygnus X-1.” In: *Nature* 436.7052 (Aug. 2005), pp. 819–821. DOI: [10.1038/nature03879](https://doi.org/10.1038/nature03879). arXiv: [astro-ph/0508228](https://arxiv.org/abs/astro-ph/0508228) [[astro-ph](#)].
- [178] D. K. Galloway et al. “Thermonuclear (Type I) X-Ray Bursts Observed by the Rossi X-Ray Timing Explorer.” In: *Astrophys. J. Suppl. Ser.* 179.2 (Dec. 2008), pp. 360–422. DOI: [10.1086/592044](https://doi.org/10.1086/592044). arXiv: [astro-ph/0608259](https://arxiv.org/abs/astro-ph/0608259) [[astro-ph](#)].
- [179] P. Gandhi et al. “Frontiers in accretion physics at high X-ray spectral resolution.” In: *Nature Astronomy* 6 (Dec. 2022), pp. 1364–1375. DOI: [10.1038/s41550-022-01857-y](https://doi.org/10.1038/s41550-022-01857-y).

- [180] T. A. Gardiner and J. M. Stone. “An unsplit Godunov method for ideal MHD via constrained transport.” In: *Journal of Computational Physics* 205.2 (May 2005), pp. 509–539. DOI: [10.1016/j.jcp.2004.11.016](https://doi.org/10.1016/j.jcp.2004.11.016). arXiv: [astro-ph/0501557](https://arxiv.org/abs/astro-ph/0501557) [[astro-ph](#)].
- [181] K. C. Gendreau, Z. Arzoumanian, and T. Okajima. “The Neutron star Interior Composition Explorer (NICER): an Explorer mission of opportunity for soft x-ray timing spectroscopy.” In: *Space Telescopes and Instrumentation 2012: Ultraviolet to Gamma Ray*. Ed. by T. Takahashi, S. S. Murray, and J.-W. A. den Herder. Vol. 8443. Society of Photo-Optical Instrumentation Engineers (SPIE) Conference Series. Sept. 2012, 844313, p. 844313. DOI: [10.1117/12.926396](https://doi.org/10.1117/12.926396).
- [182] K. C. Gendreau et al. “The Neutron star Interior Composition Explorer (NICER): design and development.” In: *Space Telescopes and Instrumentation 2016: Ultraviolet to Gamma Ray*. Ed. by J.-W. A. den Herder, T. Takahashi, and M. Bautz. Vol. 9905. Society of Photo-Optical Instrumentation Engineers (SPIE) Conference Series. July 2016, 99051H, 99051H. DOI: [10.1117/12.2231304](https://doi.org/10.1117/12.2231304).
- [183] G. Ghisellini and A. Celotti. “The dividing line between FR I and FR II radio-galaxies.” In: *Astron. Astrophys.* 379 (Nov. 2001), pp. L1–L4. DOI: [10.1051/0004-6361:20011338](https://doi.org/10.1051/0004-6361:20011338). arXiv: [astro-ph/0106570](https://arxiv.org/abs/astro-ph/0106570) [[astro-ph](#)].
- [184] G. Ghisellini et al. “The power of relativistic jets is larger than the luminosity of their accretion disks.” In: *Nature* 515.7527 (Nov. 2014), pp. 376–378. DOI: [10.1038/nature13856](https://doi.org/10.1038/nature13856). arXiv: [1411.5368](https://arxiv.org/abs/1411.5368) [[astro-ph.HE](#)].
- [185] R. Giacconi et al. “Evidence for x Rays From Sources Outside the Solar System.” In: *Phys. Rev. Lett.* 9.11 (Dec. 1962), pp. 439–443. DOI: [10.1103/PhysRevLett.9.439](https://doi.org/10.1103/PhysRevLett.9.439).
- [186] B. Giacomazzo and L. Rezzolla. “The exact solution of the Riemann problem in relativistic magnetohydrodynamics.” In: *Journal of Fluid Mechanics* 562 (Sept. 2006), pp. 223–259. DOI: [10.1017/S0022112006001145](https://doi.org/10.1017/S0022112006001145). arXiv: [gr-qc/0507102](https://arxiv.org/abs/gr-qc/0507102) [[gr-qc](#)].
- [187] B. Giacomazzo and L. Rezzolla. “WhiskyMHD: a new numerical code for general relativistic magnetohydrodynamics.” In: *Classical and Quantum Gravity* 24.12 (June 2007), S235–S258. DOI: [10.1088/0264-9381/24/12/S16](https://doi.org/10.1088/0264-9381/24/12/S16). arXiv: [gr-qc/0701109](https://arxiv.org/abs/gr-qc/0701109) [[gr-qc](#)].
- [188] M. Gierliński and A. A. Zdziarski. “Discovery of powerful millisecond flares from Cygnus X-1.” In: *Mon. Not. R. Astron. Soc.* 343.3 (Aug. 2003), pp. L84–L88. DOI: [10.1046/j.1365-8711.2003.06890.x](https://doi.org/10.1046/j.1365-8711.2003.06890.x). arXiv: [astro-ph/0303508](https://arxiv.org/abs/astro-ph/0303508) [[astro-ph](#)].
- [189] D. R. Gies and C. T. Bolton. “The Optical Spectrum of HDE 226868=Cygnus X-1. II. Spectrophotometry and Mass Estimates.” In: *Astrophys. J.* 304 (May 1986), p. 371. DOI: [10.1086/164171](https://doi.org/10.1086/164171).
- [190] F. Giovannelli. “Cataclysmic Variables: A Review.” In: *Chinese Journal of Astronomy and Astrophysics Supplement* 8 (Oct. 2008), pp. 237–258.
- [191] N. A. B. Gizani, A. Cohen, and N. E. Kassim. “First results of the 74-MHz Very Large Array-Pie Town link. Hercules A at low frequencies.” In: *Mon. Not. R. Astron. Soc.* 358.3 (Apr. 2005), pp. 1061–1068. DOI: [10.1111/j.1365-2966.2005.08849.x](https://doi.org/10.1111/j.1365-2966.2005.08849.x). arXiv: [astro-ph/0501470](https://arxiv.org/abs/astro-ph/0501470) [[astro-ph](#)].

- [192] N. A. B. Gizani and J. P. Leahy. “A multiband study of Hercules A - I. ROSAT observations of the intracluster medium.” In: *Mon. Not. R. Astron. Soc.* 350.3 (May 2004), pp. 865–878. DOI: [10.1111/j.1365-2966.2004.07685.x](https://doi.org/10.1111/j.1365-2966.2004.07685.x). arXiv: [astro-ph/0402072](https://arxiv.org/abs/astro-ph/0402072) [[astro-ph](#)].
- [193] N. A. B. Gizani and J. P. Leahy. “A multiband study of Hercules A - II. Multifrequency Very Large Array imaging.” In: *Mon. Not. R. Astron. Soc.* 342.2 (June 2003), pp. 399–421. DOI: [10.1046/j.1365-8711.2003.06469.x](https://doi.org/10.1046/j.1365-8711.2003.06469.x). arXiv: [astro-ph/0305600](https://arxiv.org/abs/astro-ph/0305600) [[astro-ph](#)].
- [194] M. González, E. Audit, and P. Huynh. “HERACLES: a three-dimensional radiation hydrodynamics code.” In: *Astron. Astrophys.* 464.2 (Mar. 2007), pp. 429–435. DOI: [10.1051/0004-6361:20065486](https://doi.org/10.1051/0004-6361:20065486).
- [195] P. T. Goodall, F. Alouani-Bibi, and K. M. Blundell. “When microquasar jets and supernova collide: hydrodynamically simulating the SS 433-W 50 interaction.” In: *Mon. Not. R. Astron. Soc.* 414.4 (July 2011), pp. 2838–2859. DOI: [10.1111/j.1365-2966.2011.18388.x](https://doi.org/10.1111/j.1365-2966.2011.18388.x). arXiv: [1101.3486](https://arxiv.org/abs/1101.3486) [[astro-ph.SR](#)].
- [196] E. W. Gottlieb, E. L. Wright, and W. Liller. “Optical studies of UHURU sources. XI. A probable period for Scorpius X-1 = V818 Scorpil.” In: *Astrophys. J. Lett.* 195 (Jan. 1975), pp. L33–L35. DOI: [10.1086/181703](https://doi.org/10.1086/181703).
- [197] K. N. Gourgouliatos and S. S. Komissarov. “Reconfinement and loss of stability in jets from active galactic nuclei.” In: *Nature Astronomy* 2 (Dec. 2018), pp. 167–171. DOI: [10.1038/s41550-017-0338-3](https://doi.org/10.1038/s41550-017-0338-3). arXiv: [1806.05683](https://arxiv.org/abs/1806.05683) [[astro-ph.HE](#)].
- [198] K. N. Gourgouliatos and S. S. Komissarov. “Relativistic centrifugal instability.” In: *Mon. Not. R. Astron. Soc.* 475.1 (Mar. 2018), pp. L125–L129. DOI: [10.1093/mnrasl/sly016](https://doi.org/10.1093/mnrasl/sly016). arXiv: [1710.01345](https://arxiv.org/abs/1710.01345) [[astro-ph.HE](#)].
- [199] P. C. Gregory. “Bayesian Analysis of Radio Observations of the Be X-Ray Binary LS I +61°303.” In: *Astrophys. J.* 575.1 (Aug. 2002), pp. 427–434. DOI: [10.1086/341257](https://doi.org/10.1086/341257).
- [200] P. C. Gregory, M. Peracaula, and A. R. Taylor. “Bayesian Periodic Signal Detection. II. Discovery of Periodic Phase Modulation in LS I +61°303 Radio Outbursts.” In: *Astrophys. J.* 520.1 (July 1999), pp. 376–390. DOI: [10.1086/307432](https://doi.org/10.1086/307432).
- [201] P. C. Gregory and A. R. Taylor. “New highly variable radio source, possible counterpart of  $\gamma$ -ray source CG135+1.” In: *Nature* 272.5655 (Apr. 1978), pp. 704–706. DOI: [10.1038/272704a0](https://doi.org/10.1038/272704a0).
- [202] P. C. Gregory et al. “Discovery of Giant Radio Outburst from Cygnus X-3.” In: *Nature* 239.5373 (Oct. 1972), pp. 440–443. DOI: [10.1038/239440a0](https://doi.org/10.1038/239440a0).
- [203] J. Greiner and A. Rau. “The X-ray spectrum of LSI+61° 303.” In: *Astron. Astrophys.* 375 (Aug. 2001), pp. 145–148. DOI: [10.1051/0004-6361:20010826](https://doi.org/10.1051/0004-6361:20010826). arXiv: [astro-ph/0105304](https://arxiv.org/abs/astro-ph/0105304) [[astro-ph](#)].
- [204] P. Grete, F. W. Glines, and B. W. O’Shea. “K-Athena: a performance portable structured grid finite volume magnetohydrodynamics code.” In: *IEEE Transactions on Parallel and Distributed Systems* 32.1 (Jan. 2021), pp. 85–907. DOI: [10.1109/TPDS.2020.3010016](https://doi.org/10.1109/TPDS.2020.3010016). arXiv: [1905.04341](https://arxiv.org/abs/1905.04341) [[cs.DC](#)].

- [205] V. Grinberg et al. “Cyg X-1 transiting into the hard state.” In: *The Astronomer’s Telegram* 7316 (Mar. 2015), p. 1.
- [206] V. Grinberg et al. “Cygnus X-1 entered the soft state.” In: *The Astronomer’s Telegram* 3616 (Aug. 2011), p. 1.
- [207] X. Guan, H. Li, and S. Li. “Relativistic MHD Simulations of Poynting Flux-driven Jets.” In: *Astrophys. J.* 781.1, 48 (Jan. 2014), p. 48. DOI: [10.1088/0004-637X/781/1/48](https://doi.org/10.1088/0004-637X/781/1/48). arXiv: [1312.0661](https://arxiv.org/abs/1312.0661) [[astro-ph.HE](#)].
- [208] D. Guidetti et al. “Ordered magnetic fields around radio galaxies: evidence for interaction with the environment.” In: *Mon. Not. R. Astron. Soc.* 413.4 (June 2011), pp. 2525–2544. DOI: [10.1111/j.1365-2966.2011.18321.x](https://doi.org/10.1111/j.1365-2966.2011.18321.x). arXiv: [1101.1807](https://arxiv.org/abs/1101.1807) [[astro-ph.CO](#)].
- [209] P. E. Hardee. “Helical and pinching instability of supersonic expanding jets in extragalactic radio sources.” In: *Astrophys. J.* 257 (June 1982), pp. 509–526. DOI: [10.1086/160008](https://doi.org/10.1086/160008).
- [210] P. E. Hardee. “Modeling Helical Structures in Relativistic Jets.” In: *ApJ* 597.2 (Nov. 2003), pp. 798–808. DOI: [10.1086/381223](https://doi.org/10.1086/381223). arXiv: [astro-ph/0307400](https://arxiv.org/abs/astro-ph/0307400) [[astro-ph](#)].
- [211] P. E. Hardee. “On Three-dimensional Structures in Relativistic Hydrodynamic Jets.” In: *Astrophys. J.* 533.1 (Apr. 2000), pp. 176–193. DOI: [10.1086/308656](https://doi.org/10.1086/308656).
- [212] F. A. Harrison et al. “Simultaneous X-Ray and Radio Monitoring of the Unusual Binary LS I +61°303: Measurements of the Light Curve and High-Energy Spectrum.” In: *Astrophys. J.* 528.1 (Jan. 2000), pp. 454–461. DOI: [10.1086/308157](https://doi.org/10.1086/308157). arXiv: [astro-ph/9908076](https://arxiv.org/abs/astro-ph/9908076) [[astro-ph](#)].
- [213] A. Harten, P. Lax, and B. van Leer. “On Upstream Differencing and Godunov-Type Schemes for Hyperbolic Conservation Laws.” In: *SIAM Rev* 25 (Jan. 1983), pp. 35–61.
- [214] R. C. Hartman et al. “The Third EGRET Catalog of High-Energy Gamma-Ray Sources.” In: *Astrophys. J. Suppl. Ser.* 123.1 (July 1999), pp. 79–202. DOI: [10.1086/313231](https://doi.org/10.1086/313231).
- [215] G. Hasinger and M. van der Klis. “Two patterns of correlated X-ray timing and spectral behaviour in low-mass X-ray binaries.” In: *Astron. Astrophys.* 225 (Nov. 1989), pp. 79–96.
- [216] K. Hayashi et al. “General-relativistic neutrino-radiation magnetohydrodynamic simulation of seconds-long black hole-neutron star mergers.” In: *Phys. Rev. D* 106.2, 023008 (July 2022), p. 023008. DOI: [10.1103/PhysRevD.106.023008](https://doi.org/10.1103/PhysRevD.106.023008).
- [217] J. C. Hayes and M. L. Norman. “Beyond Flux-limited Diffusion: Parallel Algorithms for Multidimensional Radiation Hydrodynamics.” In: *Astrophys. J. Suppl. Ser.* 147.1 (July 2003), pp. 197–220. DOI: [10.1086/374658](https://doi.org/10.1086/374658). arXiv: [astro-ph/0207260](https://arxiv.org/abs/astro-ph/0207260) [[astro-ph](#)].
- [218] A. F. Heavens, K. R. Ballard, and J. G. Kirk. “Relativistic particles in SS 433.” In: *Mon. Not. R. Astron. Soc.* 244 (June 1990), p. 474.

- [219] T. M. Heckman and P. N. Best. “The Coevolution of Galaxies and Supermassive Black Holes: Insights from Surveys of the Contemporary Universe.” In: *Annu. Rev. Astron. Astrophys.* 52 (Aug. 2014), pp. 589–660. DOI: [10.1146/annurev-astro-081913-035722](https://doi.org/10.1146/annurev-astro-081913-035722). arXiv: [1403.4620](https://arxiv.org/abs/1403.4620) [[astro-ph.GA](#)].
- [220] S. Heinz. “Composition, Collimation, Contamination: The Jet of Cygnus X-1.” In: *Astrophys. J.* 636.1 (Jan. 2006), pp. 316–322. DOI: [10.1086/497954](https://doi.org/10.1086/497954). arXiv: [astro-ph/0509777](https://arxiv.org/abs/astro-ph/0509777) [[astro-ph](#)].
- [221] S. Heinz and R. Sunyaev. “Cosmic rays from microquasars: A narrow component to the CR spectrum?” In: *Astron. Astrophys.* 390 (Aug. 2002), pp. 751–766. DOI: [10.1051/0004-6361:20020615](https://doi.org/10.1051/0004-6361:20020615). arXiv: [astro-ph/0204183](https://arxiv.org/abs/astro-ph/0204183) [[astro-ph](#)].
- [222] S. Heinz et al. “Evidence of a Parsec-Scale X-Ray Jet from the Accreting Neutron Star Circinus X-1.” In: *Astrophys. J. Lett.* 663.2 (July 2007), pp. L93–L96. DOI: [10.1086/519950](https://doi.org/10.1086/519950). arXiv: [0706.3881](https://arxiv.org/abs/0706.3881) [[astro-ph](#)].
- [223] S. Heinz et al. “The Youngest Known X-Ray Binary: Circinus X-1 and Its Natal Supernova Remnant.” In: *Astrophys. J.* 779.2, 171 (Dec. 2013), p. 171. DOI: [10.1088/0004-637X/779/2/171](https://doi.org/10.1088/0004-637X/779/2/171). arXiv: [1312.0632](https://arxiv.org/abs/1312.0632) [[astro-ph.HE](#)].
- [224] T. C. Hillwig et al. “Identification of the Mass Donor Star’s Spectrum in SS 433.” In: *Astrophys. J.* 615.1 (Nov. 2004), pp. 422–431. DOI: [10.1086/423927](https://doi.org/10.1086/423927). arXiv: [astro-ph/0403634](https://arxiv.org/abs/astro-ph/0403634) [[astro-ph](#)].
- [225] R. M. Hjellming and K. J. Johnston. “An analysis of the proper motions of SS 433 radio jets.” In: *Astrophys. J. Lett.* 246 (June 1981), pp. L141–L145. DOI: [10.1086/183571](https://doi.org/10.1086/183571).
- [226] R. M. Hjellming and K. J. Johnston. “Radio Emission from Conical Jets Associated with X-Ray Binaries.” In: *Astrophys. J.* 328 (May 1988), p. 600. DOI: [10.1086/166318](https://doi.org/10.1086/166318).
- [227] R. M. Hjellming and C. M. Wade. “Radio Spectrum of Cygnus X-1.” In: *Nature* 234.5325 (Nov. 1971), p. 138. DOI: [10.1038/234138a0](https://doi.org/10.1038/234138a0).
- [228] R. M. Hjellming and C. M. Wade. “The Radio Sources Associated with Scorpius X-1.” In: *Astrophys. J. Lett.* 164 (Feb. 1971), p. L1. DOI: [10.1086/180680](https://doi.org/10.1086/180680).
- [229] R. M. Hjellming et al. “Radio and X-Ray States in the X-Ray Binary Scorpius X-1.” In: *Astrophys. J.* 365 (Dec. 1990), p. 681. DOI: [10.1086/169522](https://doi.org/10.1086/169522).
- [230] R. M. Hjellming et al. “Radio observations of the X-ray binary Cygnus X-2.” In: *Astron. Astrophys.* 235 (Aug. 1990), p. 147.
- [231] J. Holt et al. “The impact of the warm outflow in the young (GPS) radio source and ULIRG PKS 1345+12 (4C 12.50).” In: *Mon. Not. R. Astron. Soc.* 410.3 (Jan. 2011), pp. 1527–1536. arXiv: [1008.2846](https://arxiv.org/abs/1008.2846) [[astro-ph.CO](#)].
- [232] W. G. Horner. “A New Method of Solving Numerical Equations of All Orders, by Continuous Approximation.” In: *Philosophical Transactions of the Royal Society of London Series I* 109 (Jan. 1819), pp. 308–335.

- [233] G. G. Howes and K. D. Nielson. “Alfvén wave collisions, the fundamental building block of plasma turbulence. I. Asymptotic solution.” In: *Physics of Plasmas* 20.7, 072302 (July 2013), p. 072302. DOI: [10.1063/1.4812805](https://doi.org/10.1063/1.4812805). arXiv: [1306.1455](https://arxiv.org/abs/1306.1455) [[astro-ph.SR](#)].
- [234] C. Huete and M. Vera. “D’Yakov-Kontorovich instability in planar reactive shocks.” In: *Journal of Fluid Mechanics* 879 (Nov. 2019), pp. 54–84. DOI: [10.1017/jfm.2019.689](https://doi.org/10.1017/jfm.2019.689).
- [235] A. R. Ingram and S. E. Motta. “A review of quasi-periodic oscillations from black hole X-ray binaries: Observation and theory.” In: 85, 101524 (Sept. 2019), p. 101524. DOI: [10.1016/j.newar.2020.101524](https://doi.org/10.1016/j.newar.2020.101524). arXiv: [2001.08758](https://arxiv.org/abs/2001.08758) [[astro-ph.HE](#)].
- [236] J. J. M. in’t Zand et al. “Bursts, eclipses, dips and a refined position for the luminous low-mass X-ray binary in the globular cluster Terzan 6.” In: *Astron. Astrophys.* 406 (July 2003), pp. 233–243. DOI: [10.1051/0004-6361:20030681](https://doi.org/10.1051/0004-6361:20030681). arXiv: [astro-ph/0302417](https://arxiv.org/abs/astro-ph/0302417) [[astro-ph](#)].
- [237] M. R. Izquierdo et al. “Global high-order numerical schemes for the time evolution of the general relativistic radiation magneto-hydrodynamics equations.” In: *arXiv e-prints*, arXiv:2211.00027 (Oct. 2022), arXiv:2211.00027. DOI: [10.48550/arXiv.2211.00027](https://doi.org/10.48550/arXiv.2211.00027). arXiv: [2211.00027](https://arxiv.org/abs/2211.00027) [[gr-qc](#)].
- [238] K. Jahoda et al. “Calibration of the Rossi X-Ray Timing Explorer Proportional Counter Array.” In: *Astrophys. J. Suppl. Ser.* 163.2 (Apr. 2006), pp. 401–423. DOI: [10.1086/500659](https://doi.org/10.1086/500659). arXiv: [astro-ph/0511531](https://arxiv.org/abs/astro-ph/0511531) [[astro-ph](#)].
- [239] F. Jansen et al. “XMM-Newton observatory. I. The spacecraft and operations.” In: *Astron. Astrophys.* 365 (Jan. 2001), pp. L1–L6. DOI: [10.1051/0004-6361:20000036](https://doi.org/10.1051/0004-6361:20000036).
- [240] M. Janssen et al. “Event Horizon Telescope observations of the jet launching and collimation in Centaurus A.” In: *Nature Astronomy* (July 2021). DOI: [10.1038/s41550-021-01417-w](https://doi.org/10.1038/s41550-021-01417-w).
- [241] F. Jaron and M. Massi. “Prediction of the radio outbursts of LS I + 61°303.” In: *Astron. Astrophys.* 559, A129 (Nov. 2013), A129. DOI: [10.1051/0004-6361/201322557](https://doi.org/10.1051/0004-6361/201322557).
- [242] F. Jaron. “A Precessing Jet Scenario for the Multi-Wavelength Long-Term Modulation of LS I +61°303.” In: *Universe* 7.7 (July 2021), p. 245. DOI: [10.3390/universe7070245](https://doi.org/10.3390/universe7070245). arXiv: [2107.09610](https://arxiv.org/abs/2107.09610) [[astro-ph.HE](#)].
- [243] F. Jaron et al. “Simultaneous long-term monitoring of LS I +61°303 by OVRO and Fermi-LAT.” In: *Mon. Not. R. Astron. Soc.* 478.1 (July 2018), pp. 440–447. DOI: [10.1093/mnras/sty1037](https://doi.org/10.1093/mnras/sty1037). arXiv: [1804.07692](https://arxiv.org/abs/1804.07692) [[astro-ph.HE](#)].
- [244] Y.-F. Jiang, J. M. Stone, and S. W. Davis. “A Godunov Method for Multidimensional Radiation Magnetohydrodynamics Based on a Variable Eddington Tensor.” In: *Astrophys. J. Suppl. Ser.* 199.1, 14 (Mar. 2012), p. 14. DOI: [10.1088/0067-0049/199/1/14](https://doi.org/10.1088/0067-0049/199/1/14). arXiv: [1201.2223](https://arxiv.org/abs/1201.2223) [[astro-ph.HE](#)].
- [245] P. G. Jonker, M. van der Klis, and R. Wijnands. “A Persistent  $\sim 1$  Hz Quasi-periodic Oscillation in the Dipping Low-Mass X-Ray Binary 4U 1323–62.” In: *Astrophys. J. Lett.* 511.1 (Jan. 1999), pp. L41–L44. DOI: [10.1086/311840](https://doi.org/10.1086/311840). arXiv: [astro-ph/9811404](https://arxiv.org/abs/astro-ph/9811404) [[astro-ph](#)].

- [246] A. M. Juett, D. Psaltis, and D. Chakrabarty. “Ultracompact X-Ray Binaries with Neon-rich Degenerate Donors.” In: *Astrophys. J. Lett.* 560.1 (Oct. 2001), pp. L59–L63. DOI: [10.1086/324225](https://doi.org/10.1086/324225). arXiv: [astro-ph/0108102](https://arxiv.org/abs/astro-ph/0108102) [[astro-ph](#)].
- [247] P. Kaaret et al. “X-Ray Emission from the Jets of XTE J1550-564.” In: *Astrophys. J.* 582.2 (Jan. 2003), pp. 945–953. DOI: [10.1086/344540](https://doi.org/10.1086/344540). arXiv: [astro-ph/0210401](https://arxiv.org/abs/astro-ph/0210401) [[astro-ph](#)].
- [248] M. Kadler et al. “The Trails of Superluminal Jet Components in 3C 111.” In: *Astrophys. J.* 680.2 (June 2008), pp. 867–884. DOI: [10.1086/529539](https://doi.org/10.1086/529539). arXiv: [0801.0617](https://arxiv.org/abs/0801.0617) [[astro-ph](#)].
- [249] C. R. Kaiser, R. Sunyaev, and H. C. Spruit. “Internal shock model for microquasars.” In: *Astron. Astrophys.* 356 (Apr. 2000), pp. 975–988. DOI: [10.48550/arXiv.astro-ph/0001501](https://doi.org/10.48550/arXiv.astro-ph/0001501). arXiv: [astro-ph/0001501](https://arxiv.org/abs/astro-ph/0001501) [[astro-ph](#)].
- [250] E. Kalemci et al. “Complete Multiwavelength Evolution of Galactic Black Hole Transients during Outburst Decay. I. Conditions for “Compact” Jet Formation.” In: *Astrophys. J.* 779.2, 95 (Dec. 2013), p. 95. DOI: [10.1088/0004-637X/779/2/95](https://doi.org/10.1088/0004-637X/779/2/95). arXiv: [1310.5482](https://arxiv.org/abs/1310.5482) [[astro-ph.HE](#)].
- [251] E. Kalemci et al. “Multiwavelength observations of the black hole transient Swift J1745-26 during the outburst decay.” In: *Mon. Not. R. Astron. Soc.* 445.2 (Dec. 2014), pp. 1288–1298. DOI: [10.1093/mnras/stu1851](https://doi.org/10.1093/mnras/stu1851). arXiv: [1409.1932](https://arxiv.org/abs/1409.1932) [[astro-ph.HE](#)].
- [252] O. Kargaltsev et al. “Chandra imaging of gamma-ray binaries.” In: *Astronomische Nachrichten* 335.3 (Mar. 2014), pp. 301–306. DOI: [10.1002/asna.201312036](https://doi.org/10.1002/asna.201312036). arXiv: [1310.1392](https://arxiv.org/abs/1310.1392) [[astro-ph.HE](#)].
- [253] N. E. Kassim et al. “Subarcminute Resolution Imaging of Radio Sources at 74 MHz With the Very Large Array.” In: *Astrophys. J.* 106 (Dec. 1993), p. 2218. DOI: [10.1086/116795](https://doi.org/10.1086/116795).
- [254] E. Kefala and V. Bosch-Ramon. “Modeling the effects of clumpy winds in the high-energy light curves of  $\gamma$ -ray binaries.” In: *Astron. Astrophys.* 669, A21 (Jan. 2023), A21. DOI: [10.1051/0004-6361/202244531](https://doi.org/10.1051/0004-6361/202244531). arXiv: [2210.16102](https://arxiv.org/abs/2210.16102) [[astro-ph.HE](#)].
- [255] R. Keppens et al. “Extragalactic jets with helical magnetic fields: relativistic MHD simulations.” In: *Astron. Astrophys.* 486.3 (Aug. 2008), pp. 663–678. DOI: [10.1051/0004-6361:20079174](https://doi.org/10.1051/0004-6361:20079174). arXiv: [0802.2034](https://arxiv.org/abs/0802.2034) [[astro-ph](#)].
- [256] I. Khabibullin and S. Sazonov. “Is SS 433 a misaligned ultraluminous X-ray source? Constraints from its reflected signal in the Galactic plane.” In: *Mon. Not. R. Astron. Soc.* 457.4 (Apr. 2016), pp. 3963–3974. DOI: [10.1093/mnras/stw266](https://doi.org/10.1093/mnras/stw266). arXiv: [1512.02616](https://arxiv.org/abs/1512.02616) [[astro-ph.HE](#)].
- [257] D. Khangulyan and F. Aharonian. “On the formation of energy spectra of synchrotron X-rays and inverse Compton  $\gamma$ -rays in binary systems with luminous optical stars.” In: *High Energy Gamma-Ray Astronomy*. Ed. by F. A. Aharonian, H. J. Völk, and D. Horns. Vol. 745. American Institute of Physics Conference Series. Feb. 2005, pp. 359–364. DOI: [10.1063/1.1878430](https://doi.org/10.1063/1.1878430). arXiv: [astro-ph/0503499](https://arxiv.org/abs/astro-ph/0503499) [[astro-ph](#)].
- [258] J.-Y. Kim et al. “Event Horizon Telescope imaging of the archetypal blazar 3C 279 at an extreme 20 microarcsecond resolution.” In: *Astron. Astrophys.* 640, A69 (Aug. 2020), A69. DOI: [10.1051/0004-6361/202037493](https://doi.org/10.1051/0004-6361/202037493).

- [259] A. R. King et al. “Ultraluminous X-Ray Sources in External Galaxies.” In: *Astrophys. J. Lett.* 552.2 (May 2001), pp. L109–L112. DOI: [10.1086/320343](https://doi.org/10.1086/320343). arXiv: [astro-ph/0104333](https://arxiv.org/abs/astro-ph/0104333) [[astro-ph](#)].
- [260] M. Kino et al. “Evidence of Jet-Clump Interaction: A Flip of the Radio Jet Head of 3C 84.” In: *Astrophys. J.* 864.2, 118 (Sept. 2018), p. 118. DOI: [10.3847/1538-4357/aad6e3](https://doi.org/10.3847/1538-4357/aad6e3). arXiv: [1808.08855](https://arxiv.org/abs/1808.08855) [[astro-ph.HE](#)].
- [261] M. Kino et al. “Morphological Transition of the Compact Radio Lobe in 3C 84 via the Strong Jet–Cloud Collision.” In: *Astrophys. J.* 920.1 (2021), p. L24. DOI: [10.3847/2041-8213/ac24fa](https://doi.org/10.3847/2041-8213/ac24fa). URL: <https://doi.org/10.3847/2041-8213/ac24fa>.
- [262] S. Kitamoto et al. “GS2023+338: a new class of X-ray transient source?” In: *Nature* 342.6249 (Nov. 1989), pp. 518–520. DOI: [10.1038/342518a0](https://doi.org/10.1038/342518a0).
- [263] M. Klein-Wolt et al. “Hard X-ray states and radio emission in GRS 1915+105.” In: *Mon. Not. R. Astron. Soc.* 331.3 (Apr. 2002), pp. 745–764. DOI: [10.1046/j.1365-8711.2002.05223.x](https://doi.org/10.1046/j.1365-8711.2002.05223.x). arXiv: [astro-ph/0112044](https://arxiv.org/abs/astro-ph/0112044) [[astro-ph](#)].
- [264] K. I. I. Koljonen et al. “The hardness-intensity diagram of Cygnus X-3: revisiting the radio/X-ray states.” In: *Mon. Not. R. Astron. Soc.* 406.1 (July 2010), pp. 307–319. DOI: [10.1111/j.1365-2966.2010.16722.x](https://doi.org/10.1111/j.1365-2966.2010.16722.x). arXiv: [1003.4351](https://arxiv.org/abs/1003.4351) [[astro-ph.HE](#)].
- [265] K. I. I. Koljonen et al. “The hypersoft state of Cygnus X-3. A key to jet quenching in X-ray binaries?” In: *Astron. Astrophys.* 612, A27 (Apr. 2018), A27. DOI: [10.1051/0004-6361/201732284](https://doi.org/10.1051/0004-6361/201732284). arXiv: [1712.07933](https://arxiv.org/abs/1712.07933) [[astro-ph.HE](#)].
- [266] S. S. Komissarov. “A Godunov-type scheme for relativistic magnetohydrodynamics.” In: *Mon. Not. R. Astron. Soc.* 303.2 (Feb. 1999), pp. 343–366. DOI: [10.1046/j.1365-8711.1999.02244.x](https://doi.org/10.1046/j.1365-8711.1999.02244.x).
- [267] S. S. Komissarov. “Magnetic acceleration of relativistic jets.” In: 82 (Jan. 2011), p. 95. arXiv: [1006.2242](https://arxiv.org/abs/1006.2242) [[astro-ph.HE](#)].
- [268] S. S. Komissarov. “Numerical simulations of relativistic magnetized jets.” In: *Mon. Not. R. Astron. Soc.* 308.4 (Oct. 1999), pp. 1069–1076. DOI: [10.1046/j.1365-8711.1999.02783.x](https://doi.org/10.1046/j.1365-8711.1999.02783.x).
- [269] S. S. Komissarov and S. A. E. G. Falle. “The large-scale structure of FR-II radio sources.” In: *Mon. Not. R. Astron. Soc.* 297.4 (July 1998), pp. 1087–1108. DOI: [10.1046/j.1365-8711.1998.01547.x](https://doi.org/10.1046/j.1365-8711.1998.01547.x).
- [270] S. Komissarov. “Central Engines: Acceleration, Collimation and Confinement of Jets.” In: *Relativistic Jets from Active Galactic Nuclei*. 2012, pp. 81–114. DOI: [10.1002/9783527641741.ch4](https://doi.org/10.1002/9783527641741.ch4).
- [271] S. S. Komissarov, O. Porth, and M. Lyutikov. “Stationary relativistic jets.” In: *Computational Astrophysics and Cosmology* 2, 9 (Nov. 2015), p. 9. DOI: [10.1186/s40668-015-0013-y](https://doi.org/10.1186/s40668-015-0013-y). arXiv: [1504.07534](https://arxiv.org/abs/1504.07534) [[astro-ph.HE](#)].
- [272] S. S. Komissarov et al. “Magnetic acceleration of relativistic active galactic nucleus jets.” In: *Mon. Not. R. Astron. Soc.* 380.1 (Sept. 2007), pp. 51–70. DOI: [10.1111/j.1365-2966.2007.12050.x](https://doi.org/10.1111/j.1365-2966.2007.12050.x). arXiv: [astro-ph/0703146](https://arxiv.org/abs/astro-ph/0703146) [[astro-ph](#)].

- [273] T. Kotani et al. “ASCA Observations of the Absorption Line Features from the Superluminal Jet Source GRS 1915+105.” In: *Astrophys. J.* 539.1 (Aug. 2000), pp. 413–423. DOI: [10.1086/309200](https://doi.org/10.1086/309200). arXiv: [astro-ph/0003237](https://arxiv.org/abs/astro-ph/0003237) [[astro-ph](#)].
- [274] J. Kristian et al. “On the Optical Identification of Cygnus X-1.” In: *Astrophys. J. Lett.* 168 (Sept. 1971), p. L91. DOI: [10.1086/180790](https://doi.org/10.1086/180790).
- [275] J. H. Krolik et al. “Future Simulations of Tidal Disruption Events.” In: 216.5, 88 (July 2020), p. 88. DOI: [10.1007/s11214-020-00680-z](https://doi.org/10.1007/s11214-020-00680-z). arXiv: [2006.03693](https://arxiv.org/abs/2006.03693) [[astro-ph.HE](#)].
- [276] J. Krtićka. “Mass loss in main-sequence B stars.” In: *Astron. Astrophys.* 564, A70 (Apr. 2014), A70. DOI: [10.1051/0004-6361/201321980](https://doi.org/10.1051/0004-6361/201321980). arXiv: [1401.5511](https://arxiv.org/abs/1401.5511) [[astro-ph.SR](#)].
- [277] E. Kuulkers and M. van der Klis. “Detection of 26Hz quasi-periodic oscillations in the flaring branch of CygnusX-2.” In: *Astron. Astrophys.* 303 (Nov. 1995), p. 801.
- [278] E. Kuulkers et al. “What ignites on the neutron star of 4U 0614+091?” In: *Astron. Astrophys.* 514, A65 (May 2010), A65. DOI: [10.1051/0004-6361/200913210](https://doi.org/10.1051/0004-6361/200913210). arXiv: [0909.3391](https://arxiv.org/abs/0909.3391) [[astro-ph.HE](#)].
- [279] N. D. Kylafis et al. “Formation and destruction of jets in X-ray binaries.” In: *Astron. Astrophys.* 538, A5 (Feb. 2012), A5. DOI: [10.1051/0004-6361/201117052](https://doi.org/10.1051/0004-6361/201117052).
- [280] Labiano, A. et al. “HST/STIS low dispersion spectroscopy of three Compact Steep Spectrum sources. Evidence for jet-cloud interaction.” In: *Astron. Astrophys.* 436 (June 2005), pp. 493–501. eprint: [astro-ph/0504330](https://arxiv.org/abs/astro-ph/0504330).
- [281] D. A. Leahy. “The gamma-ray source LSI +61deg303. I. RXTE/ASM observations.” In: *Astron. Astrophys.* 380 (Dec. 2001), pp. 516–519. DOI: [10.1051/0004-6361:20011390](https://doi.org/10.1051/0004-6361:20011390).
- [282] D. A. Leahy et al. “On searches for pulsed emission with application to four globular cluster X-ray sources : NGC 1851, 6441, 6624 and 6712.” In: *Astrophys. J.* 266 (Mar. 1983), pp. 160–170. DOI: [10.1086/160766](https://doi.org/10.1086/160766).
- [283] D. A. Leahy, F. A. Harrison, and A. Yoshida. “The ASCA X-Ray Spectrum of the Unusual Binary LSI +61°303.” In: *Astrophys. J.* 475.2 (Feb. 1997), pp. 823–828. DOI: [10.1086/303557](https://doi.org/10.1086/303557).
- [284] B. van Leer. “Towards the Ultimate Conservative Difference Scheme. II. Monotonicity and Conservation Combined in a Second-order Scheme.” In: *Journal of Computational Physics* 14 (Mar. 1974), pp. 361–370. DOI: [10.1016/0021-9991\(74\)90019-9](https://doi.org/10.1016/0021-9991(74)90019-9).
- [285] T. Leismann et al. “Relativistic MHD simulations of extragalactic jets.” In: *Astron. Astrophys.* 436.2 (June 2005), pp. 503–526. DOI: [10.1051/0004-6361:20042520](https://doi.org/10.1051/0004-6361:20042520).
- [286] C. D. Levermore. “Relating Eddington factors to flux limiters.” In: 31.2 (Feb. 1984), pp. 149–160. DOI: [10.1016/0022-4073\(84\)90112-2](https://doi.org/10.1016/0022-4073(84)90112-2).
- [287] C. D. Levermore and G. C. Pomraning. “A flux-limited diffusion theory.” In: *Astrophys. J.* 248 (Aug. 1981), pp. 321–334. DOI: [10.1086/159157](https://doi.org/10.1086/159157).

- [288] G. M. Lewis and P. H. Austin. In: *11th Conference on Atmospheric Radiation, American Meteorological Society Conference Series*. Ed. by G. Smith and J. Brodie. 2002, pp. 123–126.
- [289] J. Li et al. “Gamma-ray heartbeat powered by the microquasar SS 433.” In: *Nature Astronomy* 4 (Jan. 2020), pp. 1177–1184. DOI: [10.1038/s41550-020-1164-6](https://doi.org/10.1038/s41550-020-1164-6). arXiv: [2008.10523](https://arxiv.org/abs/2008.10523) [[astro-ph.HE](#)].
- [290] J. Li et al. “Long-term X-Ray Monitoring of LS I +61°303: Analysis of Spectral Variability and Flares.” In: *Astrophys. J.* 733.2, 89 (June 2011), p. 89. DOI: [10.1088/0004-637X/733/2/89](https://doi.org/10.1088/0004-637X/733/2/89). arXiv: [1103.4205](https://arxiv.org/abs/1103.4205) [[astro-ph.HE](#)].
- [291] J. Li et al. “Unveiling the Super-orbital Modulation of LS I +61°303 in X-Rays.” In: *Astrophys. J. Lett.* 744.1, L13 (Jan. 2012), p. L13. DOI: [10.1088/2041-8205/744/1/L13](https://doi.org/10.1088/2041-8205/744/1/L13). arXiv: [1111.7068](https://arxiv.org/abs/1111.7068) [[astro-ph.HE](#)].
- [292] J.-T. Li. “The New Progress on the Research of SS433.” In: *Progress in Astronomy* 25.1 (Mar. 2007), pp. 45–57.
- [293] K. R. Lind et al. “Numerical Simulations of Magnetized Jets.” In: *Astrophys. J.* 344 (Sept. 1989), p. 89. DOI: [10.1086/167779](https://doi.org/10.1086/167779).
- [294] J. C. Ling et al. “The states of Cygnus X-1.” In: *Astrophys. J.* 275 (Dec. 1983), pp. 307–315. DOI: [10.1086/161534](https://doi.org/10.1086/161534).
- [295] M. Liska et al. “Formation of precessing jets by tilted black hole discs in 3D general relativistic MHD simulations.” In: *Mon. Not. R. Astron. Soc.* 474.1 (Feb. 2018), pp. L81–L85. DOI: [10.1093/mnrasl/slx174](https://doi.org/10.1093/mnrasl/slx174). arXiv: [1707.06619](https://arxiv.org/abs/1707.06619) [[astro-ph.HE](#)].
- [296] M. T. P. Liska et al. “H-AMR: A New GPU-accelerated GRMHD Code for Exascale Computing with 3D Adaptive Mesh Refinement and Local Adaptive Time Stepping.” In: *Astrophys. J. Suppl. Ser.* 263.2, 26 (Dec. 2022), p. 26. DOI: [10.3847/1538-4365/ac9966](https://doi.org/10.3847/1538-4365/ac9966). arXiv: [1912.10192](https://arxiv.org/abs/1912.10192) [[astro-ph.HE](#)].
- [297] Q. Z. Liu, J. van Paradijs, and E. P. J. van den Heuvel. “A catalogue of low-mass X-ray binaries in the Galaxy, LMC, and SMC (Fourth edition).” In: *Astron. Astrophys.* 469.2 (July 2007), pp. 807–810. DOI: [10.1051/0004-6361:20077303](https://doi.org/10.1051/0004-6361:20077303). arXiv: [0707.0544](https://arxiv.org/abs/0707.0544) [[astro-ph](#)].
- [298] Q. Z. Liu, J. van Paradijs, and E. P. J. van den Heuvel. “Catalogue of high-mass X-ray binaries in the Galaxy (4th edition).” In: *Astron. Astrophys.* 455.3 (Sept. 2006), pp. 1165–1168. DOI: [10.1051/0004-6361:20064987](https://doi.org/10.1051/0004-6361:20064987). arXiv: [0707.0549](https://arxiv.org/abs/0707.0549) [[astro-ph](#)].
- [299] Q. Z. Liu, J. van Paradijs, and E. P. J. van den Heuvel. “High-mass X-ray binaries in the Magellanic Clouds.” In: *Astron. Astrophys.* 442.3 (Nov. 2005), pp. 1135–1138. DOI: [10.1051/0004-6361:20053718](https://doi.org/10.1051/0004-6361:20053718).
- [300] M. Livio, G. I. Ogilvie, and J. E. Pringle. “Extracting Energy from Black Holes: The Relative Importance of the Blandford-Znajek Mechanism.” In: *Astrophys. J.* 512.1 (Feb. 1999), pp. 100–104. DOI: [10.1086/306777](https://doi.org/10.1086/306777). arXiv: [astro-ph/9809093](https://arxiv.org/abs/astro-ph/9809093) [[astro-ph](#)].
- [301] N. R. Lomb. “Least-Squares Frequency Analysis of Unequally Spaced Data.” In: 39.2 (Feb. 1976), pp. 447–462. DOI: [10.1007/BF00648343](https://doi.org/10.1007/BF00648343).

- [302] P. Londrillo and L. Del Zanna. “High-Order Upwind Schemes for Multidimensional Magnetohydrodynamics.” In: *Astrophys. J.* 530.1 (Feb. 2000), pp. 508–524. DOI: [10.1086/308344](https://doi.org/10.1086/308344). arXiv: [astro-ph/9910086](https://arxiv.org/abs/astro-ph/9910086) [[astro-ph](#)].
- [303] J. López-Miralles et al. “3D RMHD simulations of jet-wind interactions in high-mass X-ray binaries.” In: *Astron. Astrophys.* 661, A117 (May 2022), A117. DOI: [10.1051/0004-6361/202142968](https://doi.org/10.1051/0004-6361/202142968). arXiv: [2202.11119](https://arxiv.org/abs/2202.11119) [[astro-ph.HE](#)].
- [304] J. López-Miralles et al. “Rapid X-ray variability of the gamma-ray binary LS I +61°303.” In: *Mon. Not. R. Astron. Soc.* 523.3 (Aug. 2023), pp. 4282–4293. DOI: [10.1093/mnras/stad1658](https://doi.org/10.1093/mnras/stad1658). arXiv: [2305.18580](https://arxiv.org/abs/2305.18580) [[astro-ph.HE](#)].
- [305] J. López-Miralles, J. M. Martí, and M. Perucho. “On the application of Jacobian-free Riemann solvers for relativistic radiation magnetohydrodynamics under M1 closure.” In: *Computer Physics Communications* 284, 108630 (Mar. 2023), p. 108630. DOI: [10.1016/j.cpc.2022.108630](https://doi.org/10.1016/j.cpc.2022.108630). arXiv: [2212.00370](https://arxiv.org/abs/2212.00370) [[astro-ph.HE](#)].
- [306] F. D. Lora-Clavijo, A. Cruz-Osorio, and F. S. Guzmán. “CAFE: A New Relativistic MHD Code.” In: *Astrophys. J. Suppl. Ser.* 218.2, 24 (June 2015), p. 24. DOI: [10.1088/0067-0049/218/2/24](https://doi.org/10.1088/0067-0049/218/2/24). arXiv: [1408.5846](https://arxiv.org/abs/1408.5846) [[gr-qc](#)].
- [307] P. L. Luque-Escamilla, J. Martí, and J. Martínez-Aroza. “Effects of precession versus instabilities on the jets of GRS 1758-258.” In: *Astron. Astrophys.* 643, A150 (Nov. 2020), A150. DOI: [10.1051/0004-6361/202038290](https://doi.org/10.1051/0004-6361/202038290). arXiv: [2010.11729](https://arxiv.org/abs/2010.11729) [[astro-ph.HE](#)].
- [308] T. J. Maccarone and P. S. Coppi. “Spectral fits to the 1999 Aql X-1 outburst data.” In: *Astron. Astrophys.* 399 (Mar. 2003), pp. 1151–1157. DOI: [10.1051/0004-6361:20021881](https://doi.org/10.1051/0004-6361:20021881). arXiv: [astro-ph/0301091](https://arxiv.org/abs/astro-ph/0301091) [[astro-ph](#)].
- [309] J. F. Mahlmann et al. “Electromagnetic Fireworks: Fast Radio Bursts from Rapid Reconnection in the Compressed Magnetar Wind.” In: *Astrophys. J. Lett.* 932.2, L20 (June 2022), p. L20. DOI: [10.3847/2041-8213/ac7156](https://doi.org/10.3847/2041-8213/ac7156). arXiv: [2203.04320](https://arxiv.org/abs/2203.04320) [[astro-ph.HE](#)].
- [310] J. Malzac. “Internal shocks at the origin of the flat spectral energy distribution of compact jets.” In: *Mon. Not. R. Astron. Soc.* 429 (Feb. 2013), pp. L20–L24. DOI: [10.1093/mnras/sls017](https://doi.org/10.1093/mnras/sls017). arXiv: [1210.4308](https://arxiv.org/abs/1210.4308) [[astro-ph.HE](#)].
- [311] J. Malzac. “The spectral energy distribution of compact jets powered by internal shocks.” In: *Mon. Not. R. Astron. Soc.* 443.1 (Sept. 2014), pp. 299–317. DOI: [10.1093/mnras/stu1144](https://doi.org/10.1093/mnras/stu1144). arXiv: [1406.2208](https://arxiv.org/abs/1406.2208) [[astro-ph.HE](#)].
- [312] J. Malzac et al. “A jet model for the fast IR variability of the black hole X-ray binary GX 339-4.” In: *Mon. Not. R. Astron. Soc.* 480.2 (Oct. 2018), pp. 2054–2071. DOI: [10.1093/mnras/sty2006](https://doi.org/10.1093/mnras/sty2006). arXiv: [1807.09835](https://arxiv.org/abs/1807.09835) [[astro-ph.HE](#)].
- [313] L. Maraschi and A. Treves. “A model for LS I +61 303.” In: *Mon. Not. R. Astron. Soc.* 194 (Jan. 1981), 1P–5. DOI: [10.1093/mnras/194.1.1P](https://doi.org/10.1093/mnras/194.1.1P).
- [314] B. Margon et al. “The bizarre spectrum of SS 433.” In: *Astrophys. J. Lett.* 230 (May 1979), pp. L41–L45. DOI: [10.1086/182958](https://doi.org/10.1086/182958).

- [315] B. Margon. “Observations of SS 433.” In: *Annu. Rev. Astron. Astrophys.* 22 (Jan. 1984), pp. 507–536. DOI: [10.1146/annurev.aa.22.090184.002451](https://doi.org/10.1146/annurev.aa.22.090184.002451).
- [316] A. Marino et al. “Testing jet geometries and disc-jet coupling in the neutron star LMXB 4U 0614 + 091 with the internal shocks model.” In: *Mon. Not. R. Astron. Soc.* 498.3 (Nov. 2020), pp. 3351–3367. DOI: [10.1093/mnras/staa2570](https://doi.org/10.1093/mnras/staa2570). arXiv: [2008.04710](https://arxiv.org/abs/2008.04710) [astro-ph.HE].
- [317] S. Markoff, H. Falcke, and R. Fender. “A jet model for the broadband spectrum of XTE J1118+480. Synchrotron emission from radio to X-rays in the Low/Hard spectral state.” In: *Astron. Astrophys.* 372 (June 2001), pp. L25–L28. DOI: [10.1051/0004-6361/20010420](https://doi.org/10.1051/0004-6361/20010420). arXiv: [astro-ph/0010560](https://arxiv.org/abs/astro-ph/0010560) [astro-ph].
- [318] S. Markoff, M. A. Nowak, and J. Wilms. “Going with the Flow: Can the Base of Jets Subsume the Role of Compact Accretion Disk Coronae?” In: *Astrophys. J.* 635.2 (Dec. 2005), pp. 1203–1216. DOI: [10.1086/497628](https://doi.org/10.1086/497628). arXiv: [astro-ph/0509028](https://arxiv.org/abs/astro-ph/0509028) [astro-ph].
- [319] S. Markoff et al. “Modeling the X-ray contribution of XRB jets.” In: 47.6-7 (Oct. 2003), pp. 491–493. DOI: [10.1016/S1387-6473\(03\)00078-2](https://doi.org/10.1016/S1387-6473(03)00078-2). arXiv: [astro-ph/0301479](https://arxiv.org/abs/astro-ph/0301479) [astro-ph].
- [320] A. Marquina. “Local Piecewise Hyperbolic Reconstruction of Numerical Fluxes for Nonlinear Scalar Conservation Laws.” In: *SIAM Journal on Scientific Computing* 15.4 (1994), pp. 892–915. DOI: [10.1137/0915054](https://doi.org/10.1137/0915054). eprint: <https://doi.org/10.1137/0915054>. URL: <https://doi.org/10.1137/0915054>.
- [321] H. Marshall. *A Test to Establish that SS 433 is an Ultraluminous X-ray Source*. Chandra Proposal ID #24400466. Sept. 2022.
- [322] H. L. Marshall, C. R. Canizares, and N. S. Schulz. “The High-Resolution X-Ray Spectrum of SS 433 Using the Chandra HETGS.” In: *Astrophys. J.* 564.2 (Jan. 2002), pp. 941–952. DOI: [10.1086/324398](https://doi.org/10.1086/324398). arXiv: [astro-ph/0108206](https://arxiv.org/abs/astro-ph/0108206) [astro-ph].
- [323] H. L. Marshall, S. Heinz, and N. S. Schulz. “Formation and Evolution of the SS 433 Jets.” In: *American Astronomical Society Meeting Abstracts #223*. Vol. 223. American Astronomical Society Meeting Abstracts. Jan. 2014, 323.07, p. 323.07.
- [324] H. L. Marshall et al. “Multiwavelength Observations of the SS 433 Jets.” In: *Astrophys. J.* 775.1, 75 (Sept. 2013), p. 75. DOI: [10.1088/0004-637X/775/1/75](https://doi.org/10.1088/0004-637X/775/1/75). arXiv: [1307.8427](https://arxiv.org/abs/1307.8427) [astro-ph.HE].
- [325] J. Martí, J. M. Paredes, and M. Peracaula. “Development of a two-sided relativistic jet in Cygnus X-3.” In: *Astron. Astrophys.* 375 (Aug. 2001), pp. 476–484. DOI: [10.1051/0004-6361/20010907](https://doi.org/10.1051/0004-6361/20010907).
- [326] J. M. Martí, M. Perucho, and J. L. Gómez. “The Internal Structure of overpressured, Magnetized, Relativistic Jets.” In: *Astrophys. J.* 831.2, 163 (Nov. 2016), p. 163. DOI: [10.3847/0004-637X/831/2/163](https://doi.org/10.3847/0004-637X/831/2/163). arXiv: [1609.00593](https://arxiv.org/abs/1609.00593) [astro-ph.HE].
- [327] J. M. Martí et al. “Morphology and Dynamics of Relativistic Jets.” In: *Astrophys. J.* 479.1 (Apr. 1997), pp. 151–163. DOI: [10.1086/303842](https://doi.org/10.1086/303842).

- [328] J.-M. Martí. “Numerical Simulations of Jets from Active Galactic Nuclei.” In: *Galaxies* 7.1 (Jan. 2019), p. 24. DOI: [10.3390/galaxies7010024](https://doi.org/10.3390/galaxies7010024).
- [329] J.-M. Martí. “On the correction of conserved variables for numerical RMHD with staggered constrained transport.” In: *Computer Physics Communications* 191 (June 2015), pp. 100–105. DOI: [10.1016/j.cpc.2015.02.004](https://doi.org/10.1016/j.cpc.2015.02.004). arXiv: [1501.02697](https://arxiv.org/abs/1501.02697) [[astro-ph.IM](#)].
- [330] J.-M. Martí. “The structure of steady, relativistic, magnetized jets with rotation.” In: *Mon. Not. R. Astron. Soc.* 452.3 (Sept. 2015), pp. 3106–3123. DOI: [10.1093/mnras/stv1524](https://doi.org/10.1093/mnras/stv1524). arXiv: [1506.06519](https://arxiv.org/abs/1506.06519) [[astro-ph.IM](#)].
- [331] J. M. Martí and E. Müller. “Grid-based Methods in Relativistic Hydrodynamics and Magnetohydrodynamics.” In: *Living Reviews in Computational Astrophysics* 1.1, 3 (Dec. 2015), p. 3. DOI: [10.1007/lrca-2015-3](https://doi.org/10.1007/lrca-2015-3).
- [332] J. Martí et al. “A galactic microquasar mimicking winged radio galaxies.” In: *Nature Communications* 8, 1757 (Nov. 2017), p. 1757. DOI: [10.1038/s41467-017-01976-5](https://doi.org/10.1038/s41467-017-01976-5).
- [333] J. Martí et al. “Real-time evolution of a large-scale relativistic jet.” In: *Astron. Astrophys.* 578, L11 (June 2015), p. L11. DOI: [10.1051/0004-6361/201526355](https://doi.org/10.1051/0004-6361/201526355). arXiv: [1505.07641](https://arxiv.org/abs/1505.07641) [[astro-ph.HE](#)].
- [334] S. Massaglia et al. “Making Fanaroff-Riley I radio sources. III. The effects of the magnetic field on relativistic jets’ propagation and source morphologies.” In: *Astron. Astrophys.* 659, A139 (Mar. 2022), A139. DOI: [10.1051/0004-6361/202038724](https://doi.org/10.1051/0004-6361/202038724). arXiv: [2112.06827](https://arxiv.org/abs/2112.06827) [[astro-ph.HE](#)].
- [335] S. Massaglia et al. “Making Faranoff-Riley I radio sources. I. Numerical hydrodynamic 3D simulations of low-power jets.” In: *Astron. Astrophys.* 596, A12 (Nov. 2016), A12. DOI: [10.1051/0004-6361/201629375](https://doi.org/10.1051/0004-6361/201629375). arXiv: [1609.02497](https://arxiv.org/abs/1609.02497) [[astro-ph.HE](#)].
- [336] S. Massaglia et al. “Making Faranoff-Riley I radio sources. II. The effects of jet magnetization.” In: *Astron. Astrophys.* 621, A132 (Jan. 2019), A132. DOI: [10.1051/0004-6361/201834512](https://doi.org/10.1051/0004-6361/201834512). arXiv: [1812.00657](https://arxiv.org/abs/1812.00657) [[astro-ph.HE](#)].
- [337] M. Massi and F. Jaron. “Long-term periodicity in LS I +61°303 as beat frequency between orbital and precessional rate.” In: *Astron. Astrophys.* 554, A105 (June 2013), A105. DOI: [10.1051/0004-6361/201219685](https://doi.org/10.1051/0004-6361/201219685). arXiv: [1303.2007](https://arxiv.org/abs/1303.2007) [[astro-ph.HE](#)].
- [338] M. Massi, S. Migliari, and M. Chernyakova. “The black hole candidate LS I +61°0303.” In: *Mon. Not. R. Astron. Soc.* 468.3 (July 2017), pp. 3689–3693. DOI: [10.1093/mnras/stx778](https://doi.org/10.1093/mnras/stx778). arXiv: [1704.01335](https://arxiv.org/abs/1704.01335) [[astro-ph.HE](#)].
- [339] M. Massi, E. Ros, and L. Zimmermann. “VLBA images of the precessing jet of LS I +61°303.” In: *Astron. Astrophys.* 540, A142 (Apr. 2012), A142. DOI: [10.1051/0004-6361/201118088](https://doi.org/10.1051/0004-6361/201118088). arXiv: [1203.4621](https://arxiv.org/abs/1203.4621) [[astro-ph.HE](#)].
- [340] M. Massi and G. Torricelli-Ciamponi. “Intrinsic physical properties and Doppler boosting effects in LS I +61°303.” In: *Astron. Astrophys.* 564, A23 (Apr. 2014), A23. DOI: [10.1051/0004-6361/201322760](https://doi.org/10.1051/0004-6361/201322760). arXiv: [1402.3983](https://arxiv.org/abs/1402.3983) [[astro-ph.HE](#)].
- [341] M. Massi and G. Torricelli-Ciamponi. “Origin of the long-term modulation of radio emission of LS I +61°303.” In: *Astron. Astrophys.* 585, A123 (Jan. 2016), A123. DOI: [10.1051/0004-6361/201526938](https://doi.org/10.1051/0004-6361/201526938). arXiv: [1511.05621](https://arxiv.org/abs/1511.05621) [[astro-ph.HE](#)].

- [342] M. Massi and L. Zimmermann. “Feasibility study of Lense-Thirring precession in LS I +61°303.” In: *Astron. Astrophys.* 515, A82 (June 2010), A82. DOI: [10.1051/0004-6361/200913787](https://doi.org/10.1051/0004-6361/200913787). arXiv: [1003.3693](https://arxiv.org/abs/1003.3693) [[astro-ph.HE](#)].
- [343] M. Massi et al. “Evidence for periodic accretion-ejection in LS I +61°303.” In: *Mon. Not. R. Astron. Soc.* 498.3 (Nov. 2020), pp. 3592–3600. DOI: [10.1093/mnras/staa2623](https://doi.org/10.1093/mnras/staa2623). arXiv: [2010.08598](https://arxiv.org/abs/2010.08598) [[astro-ph.HE](#)].
- [344] M. Massi et al. “Hints for a fast precessing relativistic radio jet in LS I +61°303.” In: *Astron. Astrophys.* 414 (Jan. 2004), pp. L1–L4. DOI: [10.1051/0004-6361:20031760](https://doi.org/10.1051/0004-6361:20031760). arXiv: [astro-ph/0312091](https://arxiv.org/abs/astro-ph/0312091) [[astro-ph](#)].
- [345] D. Mata Sanchez et al. “Mass constraints to Sco X-1 from Bowen fluorescence and deep near-infrared spectroscopy.” In: *Mon. Not. R. Astron. Soc.* 449 (Apr. 2015), pp. L1–L5. DOI: [10.1093/mnrasl/slv002](https://doi.org/10.1093/mnrasl/slv002). arXiv: [1501.02269](https://arxiv.org/abs/1501.02269) [[astro-ph.HE](#)].
- [346] M. Matsuoka et al. “The MAXI Mission on the ISS: Science and Instruments for Monitoring All-Sky X-Ray Images.” In: *Publ. Astron. Soc. Jpn* 61 (Oct. 2009), p. 999. DOI: [10.1093/pasj/61.5.999](https://doi.org/10.1093/pasj/61.5.999). arXiv: [0906.0631](https://arxiv.org/abs/0906.0631) [[astro-ph.IM](#)].
- [347] G. Mattia et al. “Resistive relativistic MHD simulations of astrophysical jets.” In: *arXiv e-prints*, arXiv:2308.09477 (Aug. 2023), arXiv:2308.09477. DOI: [10.48550/arXiv.2308.09477](https://doi.org/10.48550/arXiv.2308.09477). arXiv: [2308.09477](https://arxiv.org/abs/2308.09477) [[astro-ph.HE](#)].
- [348] J. E. McClintock and R. A. Remillard. “The Black Hole Binary A0620-00.” In: *Astrophys. J.* 308 (Sept. 1986), p. 110. DOI: [10.1086/164482](https://doi.org/10.1086/164482).
- [349] J. C. McKinney and R. D. Blandford. “Stability of relativistic jets from rotating, accreting black holes via fully three-dimensional magnetohydrodynamic simulations.” In: *Mon. Not. R. Astron. Soc.* 394.1 (Mar. 2009), pp. L126–L130. DOI: [10.1111/j.1745-3933.2009.00625.x](https://doi.org/10.1111/j.1745-3933.2009.00625.x). arXiv: [0812.1060](https://arxiv.org/abs/0812.1060) [[astro-ph](#)].
- [350] J. C. McKinney, A. Tchekhovskoy, and R. D. Blandford. “General relativistic magnetohydrodynamic simulations of magnetically choked accretion flows around black holes.” In: *Mon. Not. R. Astron. Soc.* 423.4 (July 2012), pp. 3083–3117. DOI: [10.1111/j.1365-2966.2012.21074.x](https://doi.org/10.1111/j.1365-2966.2012.21074.x). arXiv: [1201.4163](https://arxiv.org/abs/1201.4163) [[astro-ph.HE](#)].
- [351] J. C. McKinney et al. “Three-dimensional general relativistic radiation magnetohydrodynamical simulation of super-Eddington accretion, using a new code HARMRAD with M1 closure.” In: *Mon. Not. R. Astron. Soc.* 441.4 (July 2014), pp. 3177–3208. DOI: [10.1093/mnras/stu762](https://doi.org/10.1093/mnras/stu762). arXiv: [1312.6127](https://arxiv.org/abs/1312.6127) [[astro-ph.CO](#)].
- [352] B. R. McNamara and P. E. J. Nulsen. “Heating Hot Atmospheres with Active Galactic Nuclei.” In: *Annu. Rev. Astron. Astrophys.* 45.1 (Sept. 2007), pp. 117–175. DOI: [10.1146/annurev.astro.45.051806.110625](https://doi.org/10.1146/annurev.astro.45.051806.110625). arXiv: [0709.2152](https://arxiv.org/abs/0709.2152) [[astro-ph](#)].
- [353] B. R. McNamara and P. E. J. Nulsen. “Mechanical feedback from active galactic nuclei in galaxies, groups and clusters.” In: *New Journal of Physics* 14.5, 055023 (May 2012), p. 055023. DOI: [10.1088/1367-2630/14/5/055023](https://doi.org/10.1088/1367-2630/14/5/055023). arXiv: [1204.0006](https://arxiv.org/abs/1204.0006) [[astro-ph.CO](#)].

- [354] D. L. Meier. “The Association of Jet Production with Geometrically Thick Accretion Flows and Black Hole Rotation.” In: *Astrophys. J. Lett.* 548.1 (Feb. 2001), pp. L9–L12. DOI: [10.1086/318921](https://doi.org/10.1086/318921). arXiv: [astro-ph/0010231](https://arxiv.org/abs/astro-ph/0010231) [[astro-ph](#)].
- [355] D. L. Meier, S. Koide, and Y. Uchida. “Magnetohydrodynamic Production of Relativistic Jets.” In: *Science* 291.5501 (Jan. 2001), pp. 84–92. DOI: [10.1126/science.291.5501.84](https://doi.org/10.1126/science.291.5501.84).
- [356] J. D. Melon Fuksman and A. Mignone. “A Radiative Transfer Module for Relativistic Magnetohydrodynamics in the PLUTO Code.” In: *Astrophys. J. Suppl. Ser.* 242.2, 20 (June 2019), p. 20. DOI: [10.3847/1538-4365/ab18ff](https://doi.org/10.3847/1538-4365/ab18ff). arXiv: [1903.10456](https://arxiv.org/abs/1903.10456) [[astro-ph.IM](#)].
- [357] M. Méndez and M. van der Klis. “Precise Measurements of the Kilohertz Quasi-periodic Oscillations in 4U 1728-34.” In: *Astrophys. J. Lett.* 517.1 (May 1999), pp. L51–L54. DOI: [10.1086/312025](https://doi.org/10.1086/312025). arXiv: [astro-ph/9903303](https://arxiv.org/abs/astro-ph/9903303) [[astro-ph](#)].
- [358] M. Méndez et al. “Coupling between the accreting corona and the relativistic jet in the microquasar GRS 1915+105.” In: *Nature Astronomy* 6 (Mar. 2022), pp. 577–583. DOI: [10.1038/s41550-022-01617-y](https://doi.org/10.1038/s41550-022-01617-y). arXiv: [2203.02963](https://arxiv.org/abs/2203.02963) [[astro-ph.HE](#)].
- [359] A. Merloni, S. Heinz, and T. di Matteo. “A Fundamental Plane of black hole activity.” In: *Mon. Not. R. Astron. Soc.* 345.4 (Nov. 2003), pp. 1057–1076. DOI: [10.1046/j.1365-2966.2003.07017.x](https://doi.org/10.1046/j.1365-2966.2003.07017.x). arXiv: [astro-ph/0305261](https://arxiv.org/abs/astro-ph/0305261) [[astro-ph](#)].
- [360] P. Mészáros. “Gamma-ray bursts.” In: *Reports on Progress in Physics* 69.8 (Aug. 2006), pp. 2259–2321. DOI: [10.1088/0034-4885/69/8/R01](https://doi.org/10.1088/0034-4885/69/8/R01). arXiv: [astro-ph/0605208](https://arxiv.org/abs/astro-ph/0605208) [[astro-ph](#)].
- [361] J. Middleditch and W. C. Priedhorsky. “Discovery of Rapid Quasi-periodic Oscillations in Scorpius X-1.” In: *Astrophys. J.* 306 (July 1986), p. 230. DOI: [10.1086/164335](https://doi.org/10.1086/164335).
- [362] M. J. Middleton et al. “NuSTAR reveals the hidden nature of SS433.” In: *Mon. Not. R. Astron. Soc.* 506.1 (Sept. 2021), pp. 1045–1058. DOI: [10.1093/mnras/stab1280](https://doi.org/10.1093/mnras/stab1280). arXiv: [1810.10518](https://arxiv.org/abs/1810.10518) [[astro-ph.HE](#)].
- [363] S. Migliari and R. P. Fender. “Jets in neutron star X-ray binaries: a comparison with black holes.” In: *Mon. Not. R. Astron. Soc.* 366.1 (Feb. 2006), pp. 79–91. DOI: [10.1111/j.1365-2966.2005.09777.x](https://doi.org/10.1111/j.1365-2966.2005.09777.x). arXiv: [astro-ph/0510698](https://arxiv.org/abs/astro-ph/0510698) [[astro-ph](#)].
- [364] S. Migliari, J. C. A. Miller-Jones, and D. M. Russell. “The influence of spin on jet power in neutron star X-ray binaries.” In: *Mon. Not. R. Astron. Soc.* 415.3 (Aug. 2011), pp. 2407–2416. DOI: [10.1111/j.1365-2966.2011.18868.x](https://doi.org/10.1111/j.1365-2966.2011.18868.x). arXiv: [1104.1115](https://arxiv.org/abs/1104.1115) [[astro-ph.HE](#)].
- [365] S. Migliari et al. “Disc-jet coupling in an atoll-type neutron star X-ray binary: 4U 1728-34 (GX 354-0).” In: *Mon. Not. R. Astron. Soc.* 342.4 (July 2003), pp. L67–L71. DOI: [10.1046/j.1365-8711.2003.06795.x](https://doi.org/10.1046/j.1365-8711.2003.06795.x). arXiv: [astro-ph/0305221](https://arxiv.org/abs/astro-ph/0305221) [[astro-ph](#)].
- [366] S. Migliari et al. “Disc-jet coupling in atoll-type neutron star X-ray binaries.” In: *Nuclear Physics B Proceedings Supplements* 132 (June 2004), pp. 628–631. DOI: [10.1016/j.nuclphysbps.2004.04.109](https://doi.org/10.1016/j.nuclphysbps.2004.04.109).

- [367] S. Migliari et al. “Rapid variability of the arcsec-scale X-ray jets of SS 433.” In: *Mon. Not. R. Astron. Soc.* 358.3 (Apr. 2005), pp. 860–868. DOI: [10.1111/j.1365-2966.2005.08791.x](https://doi.org/10.1111/j.1365-2966.2005.08791.x). arXiv: [astro-ph/0501097](https://arxiv.org/abs/astro-ph/0501097) [[astro-ph](#)].
- [368] S. Migliari et al. “The Complete Spectrum of the Neutron Star X-ray Binary 4U 0614+091.” In: *Astrophys. J.* 710.1 (Feb. 2010), pp. 117–124. DOI: [10.1088/0004-637X/710/1/117](https://doi.org/10.1088/0004-637X/710/1/117). arXiv: [0912.1139](https://arxiv.org/abs/0912.1139) [[astro-ph.HE](#)].
- [369] S. Migliari, R. Fender, and M. Méndez. “Iron Emission Lines from Extended X-ray Jets in SS 433: Reheating of Atomic Nuclei.” In: *Science* 297.5587 (Sept. 2002), pp. 1673–1676. DOI: [10.1126/science.1073660](https://doi.org/10.1126/science.1073660). arXiv: [astro-ph/0209131](https://arxiv.org/abs/astro-ph/0209131) [[astro-ph](#)].
- [370] A. Mignone and G. Bodo. “An HLLC Riemann solver for relativistic flows – II. Magnetohydrodynamics.” In: *Monthly Notices of the Royal Astronomical Society* 368.3 (Apr. 2006), pp. 1040–1054. ISSN: 0035-8711. DOI: [10.1111/j.1365-2966.2006.10162.x](https://doi.org/10.1111/j.1365-2966.2006.10162.x). eprint: <https://academic.oup.com/mnras/article-pdf/368/3/1040/18664367/mnras0368-1040.pdf>. URL: <https://doi.org/10.1111/j.1365-2966.2006.10162.x>.
- [371] A. Mignone and L. Del Zanna. “Systematic construction of upwind constrained transport schemes for MHD.” In: *Journal of Computational Physics* 424, 109748 (Jan. 2021), p. 109748. DOI: [10.1016/j.jcp.2020.109748](https://doi.org/10.1016/j.jcp.2020.109748). arXiv: [2004.10542](https://arxiv.org/abs/2004.10542) [[physics.comp-ph](#)].
- [372] A. Mignone and J. C. McKinney. “Equation of state in relativistic magnetohydrodynamics: variable versus constant adiabatic index.” In: *Mon. Not. R. Astron. Soc.* 378.3 (July 2007), pp. 1118–1130. DOI: [10.1111/j.1365-2966.2007.11849.x](https://doi.org/10.1111/j.1365-2966.2007.11849.x). arXiv: [0704.1679](https://arxiv.org/abs/0704.1679) [[astro-ph](#)].
- [373] A. Mignone, M. Ugliano, and G. Bodo. “A five-wave Harten-Lax-van Leer Riemann solver for relativistic magnetohydrodynamics.” In: *Mon. Not. R. Astron. Soc.* 393.4 (Mar. 2009), pp. 1141–1156. DOI: [10.1111/j.1365-2966.2008.14221.x](https://doi.org/10.1111/j.1365-2966.2008.14221.x). arXiv: [0811.1483](https://arxiv.org/abs/0811.1483) [[astro-ph](#)].
- [374] A. Mignone et al. “High-resolution 3D relativistic MHD simulations of jets.” In: *Mon. Not. R. Astron. Soc.* 402.1 (Feb. 2010), pp. 7–12. DOI: [10.1111/j.1365-2966.2009.15642.x](https://doi.org/10.1111/j.1365-2966.2009.15642.x). arXiv: [0908.4523](https://arxiv.org/abs/0908.4523) [[astro-ph.CO](#)].
- [375] A. Mignone et al. “PLUTO: A Numerical Code for Computational Astrophysics.” In: *Astrophys. J. Suppl. Ser.* 170.1 (May 2007), pp. 228–242. DOI: [10.1086/513316](https://doi.org/10.1086/513316). arXiv: [astro-ph/0701854](https://arxiv.org/abs/astro-ph/0701854) [[astro-ph](#)].
- [376] A. Mignone et al. “The PLUTO Code for Adaptive Mesh Computations in Astrophysical Fluid Dynamics.” In: *Astrophys. J. Suppl. Ser.* 198.1, 7 (Jan. 2012), p. 7. DOI: [10.1088/0067-0049/198/1/7](https://doi.org/10.1088/0067-0049/198/1/7). arXiv: [1110.0740](https://arxiv.org/abs/1110.0740) [[astro-ph.HE](#)].
- [377] A. Mignone, S. Massaglia, and G. Bodo. “Relativistic MHD Simulations of Jets with Toroidal Magnetic Fields.” In: 121.1-4 (Nov. 2005), pp. 21–31. DOI: [10.1007/s11214-006-3588-4](https://doi.org/10.1007/s11214-006-3588-4). arXiv: [astro-ph/0511769](https://arxiv.org/abs/astro-ph/0511769) [[astro-ph](#)].
- [378] D. Mihalas and B. W. Mihalas. *Foundations of radiation hydrodynamics*. 1984.
- [379] J. C. A. Miller-Jones et al. “Coupled Radio and X-Ray Emission and Evidence for Discrete Ejecta in the Jets of SS 433.” In: *Astrophys. J.* 682.2 (Aug. 2008), pp. 1141–1151. DOI: [10.1086/589144](https://doi.org/10.1086/589144). arXiv: [0804.1337](https://arxiv.org/abs/0804.1337) [[astro-ph](#)].

- [380] J. C. A. Miller-Jones et al. “Evolution of the Radio-X-ray Coupling Throughout an Entire Outburst of Aquila X-1.” In: *Astrophys. J. Lett.* 716.2 (June 2010), pp. L109–L114. DOI: [10.1088/2041-8205/716/2/L109](https://doi.org/10.1088/2041-8205/716/2/L109). arXiv: [1005.3066](https://arxiv.org/abs/1005.3066) [astro-ph.HE].
- [381] J. C. A. Miller-Jones et al. “The first resolved imaging of milliarcsecond-scale jets in Circinus X-1.” In: *Mon. Not. R. Astron. Soc.* 419.1 (Jan. 2012), pp. L49–L53. DOI: [10.1111/j.1745-3933.2011.01176.x](https://doi.org/10.1111/j.1745-3933.2011.01176.x). arXiv: [1110.3996](https://arxiv.org/abs/1110.3996) [astro-ph.HE].
- [382] J. C. A. Miller-Jones et al. “A rapidly changing jet orientation in the stellar-mass black-hole system V404 Cygni.” In: *Nature* 569.7756 (Apr. 2019), pp. 374–377. DOI: [10.1038/s41586-019-1152-0](https://doi.org/10.1038/s41586-019-1152-0). arXiv: [1906.05400](https://arxiv.org/abs/1906.05400) [astro-ph.HE].
- [383] J. C. A. Miller-Jones et al. “Cygnus X-1 contains a 21-solar mass black hole—Implications for massive star winds.” In: *Science* 371.6533 (Mar. 2021), pp. 1046–1049. DOI: [10.1126/science.abb3363](https://doi.org/10.1126/science.abb3363). arXiv: [2102.09091](https://arxiv.org/abs/2102.09091) [astro-ph.HE].
- [384] J. C. A. Miller-Jones et al. “Time-sequenced Multi-Radio Frequency Observations of Cygnus X-3 in Flare.” In: *Astrophys. J.* 600.1 (Jan. 2004), pp. 368–389. DOI: [10.1086/379706](https://doi.org/10.1086/379706). arXiv: [astro-ph/0311277](https://arxiv.org/abs/astro-ph/0311277) [astro-ph].
- [385] G. N. Minerbo. “Maximum entropy Eddington factors.” In: 20.6 (Jan. 1978), pp. 541–545. DOI: [10.1016/0022-4073\(78\)90024-9](https://doi.org/10.1016/0022-4073(78)90024-9).
- [386] S. Mineshige and K. Ohsuga. “Supercritical accretion and ULXs - what can we achieve?” In: *Astronomische Nachrichten* 332.4 (May 2011), p. 402. DOI: [10.1002/asna.201011509](https://doi.org/10.1002/asna.201011509).
- [387] B. Mingo et al. “Accretion mode versus radio morphology in the LOFAR Deep Fields.” In: *Mon. Not. R. Astron. Soc.* 511.3 (Apr. 2022), pp. 3250–3271. DOI: [10.1093/mnras/stac140](https://doi.org/10.1093/mnras/stac140). arXiv: [2201.04433](https://arxiv.org/abs/2201.04433) [astro-ph.GA].
- [388] B. Mingo et al. “Revisiting the Fanaroff-Riley dichotomy and radio-galaxy morphology with the LOFAR Two-Metre Sky Survey (LoTSS).” In: *Mon. Not. R. Astron. Soc.* 488.2 (Sept. 2019), pp. 2701–2721. DOI: [10.1093/mnras/stz1901](https://doi.org/10.1093/mnras/stz1901). arXiv: [1907.03726](https://arxiv.org/abs/1907.03726) [astro-ph.GA].
- [389] F. Miniati and P. Colella. “A modified higher order Godunov’s scheme for stiff source conservative hydrodynamics.” In: *Journal of Computational Physics* 224.2 (June 2007), pp. 519–538. DOI: [10.1016/j.jcp.2006.10.008](https://doi.org/10.1016/j.jcp.2006.10.008). arXiv: [astro-ph/0601519](https://arxiv.org/abs/astro-ph/0601519) [astro-ph].
- [390] A. J. Mioduszewski et al. “A Summer of SS433: Forty Days of VLBA Imaging.” In: *AAS/High Energy Astrophysics Division #8*. Vol. 8. AAS/High Energy Astrophysics Division. Aug. 2004, 29.03, p. 29.03.
- [391] A. J. Mioduszewski et al. “A One-sided Highly Relativistic Jet from Cygnus X-3.” In: *Astrophys. J.* 553.2 (June 2001), pp. 766–775. DOI: [10.1086/320965](https://doi.org/10.1086/320965). arXiv: [astro-ph/0102018](https://arxiv.org/abs/astro-ph/0102018) [astro-ph].
- [392] I. F. Mirabel. “Gamma-ray binaries.” In: 309.1-4 (June 2007), pp. 267–270. DOI: [10.1007/s10509-007-9459-y](https://doi.org/10.1007/s10509-007-9459-y). arXiv: [astro-ph/0610707](https://arxiv.org/abs/astro-ph/0610707) [astro-ph].
- [393] I. F. Mirabel. “Very energetic gamma-rays from microquasars and binary pulsars.” In: *Science* 312 (June 2006), p. 1759. DOI: [10.1126/science.1129815](https://doi.org/10.1126/science.1129815). arXiv: [astro-ph/0606393](https://arxiv.org/abs/astro-ph/0606393) [astro-ph].

- [394] I. F. Mirabel and L. F. Rodríguez. “A superluminal source in the Galaxy.” In: *Nature* 371.6492 (Sept. 1994), pp. 46–48. DOI: [10.1038/371046a0](https://doi.org/10.1038/371046a0).
- [395] I. F. Mirabel and L. F. Rodríguez. “Sources of Relativistic Jets in the Galaxy.” In: *Annu. Rev. Astron. Astrophys.* 37 (Jan. 1999), pp. 409–443. DOI: [10.1146/annurev.astro.37.1.409](https://doi.org/10.1146/annurev.astro.37.1.409). arXiv: [astro-ph/9902062](https://arxiv.org/abs/astro-ph/9902062) [[astro-ph](#)].
- [396] S. Miyamoto et al. “Large Hysteretic Behavior of Stellar Black Hole Candidate X-Ray Binaries.” In: *Astrophys. J. Lett.* 442 (Mar. 1995), p. L13. DOI: [10.1086/187804](https://doi.org/10.1086/187804).
- [397] Y. Mizuno, P. Hardee, and K.-I. Nishikawa. “Three-dimensional Relativistic Magnetohydrodynamic Simulations of Magnetized Spine-Sheath Relativistic Jets.” In: *Astrophys. J.* 662.2 (June 2007), pp. 835–850. DOI: [10.1086/518106](https://doi.org/10.1086/518106). arXiv: [astro-ph/0703190](https://arxiv.org/abs/astro-ph/0703190) [[astro-ph](#)].
- [398] A. F. J. Moffat. “Observational overview of clumping in hot stellar winds.” In: *Clumping in Hot-Star Winds*. Ed. by W.-R. Hamann, A. Feldmeier, and L. M. Oskinova. Apr. 2008, p. 17.
- [399] E. Molina and V. Bosch-Ramon. “Nonthermal emission from high-mass microquasar jets affected by orbital motion.” In: *Astron. Astrophys.* 618, A146 (Oct. 2018), A146. DOI: [10.1051/0004-6361/201833681](https://doi.org/10.1051/0004-6361/201833681). arXiv: [1808.02260](https://arxiv.org/abs/1808.02260) [[astro-ph.HE](#)].
- [400] E. Molina, S. del Palacio, and V. Bosch-Ramon. “A model for high-mass microquasar jets under the influence of a strong stellar wind.” In: *Astron. Astrophys.* 629, A129 (Sept. 2019), A129. DOI: [10.1051/0004-6361/201935960](https://doi.org/10.1051/0004-6361/201935960). arXiv: [1908.10131](https://arxiv.org/abs/1908.10131) [[astro-ph.HE](#)].
- [401] R. Monceau-Baroux et al. “Relativistic 3D precessing jet simulations for the X-ray binary SS433.” In: *Astron. Astrophys.* 561, A30 (Jan. 2014), A30. DOI: [10.1051/0004-6361/201322682](https://doi.org/10.1051/0004-6361/201322682). arXiv: [1311.7593](https://arxiv.org/abs/1311.7593) [[astro-ph.HE](#)].
- [402] R. Monceau-Baroux et al. “The SS433 jet from subparsec to parsec scales.” In: *Astron. Astrophys.* 574, A143 (Feb. 2015), A143. DOI: [10.1051/0004-6361/201425015](https://doi.org/10.1051/0004-6361/201425015).
- [403] E. H. Morgan, R. A. Remillard, and J. Greiner. “RXTE Observations of QPOs in the Black Hole Candidate GRS 1915+105.” In: *Astrophys. J.* 482.2 (June 1997), pp. 993–1010. DOI: [10.1086/304191](https://doi.org/10.1086/304191).
- [404] R. Morganti, C. N. Tadhunter, and T. A. Oosterloo. “Fast neutral outflows in powerful radio galaxies: a major source of feedback in massive galaxies.” In: *Astron. Astrophys.* 444.1 (Dec. 2005), pp. L9–L13. DOI: [10.1051/0004-6361:200500197](https://doi.org/10.1051/0004-6361:200500197). arXiv: [astro-ph/0510263](https://arxiv.org/abs/astro-ph/0510263) [[astro-ph](#)].
- [405] R. Morganti and T. Oosterloo. “The interstellar and circumnuclear medium of active nuclei traced by H i 21 cm absorption.” In: 26.1, 4 (July 2018), p. 4. arXiv: [1807.01475](https://arxiv.org/abs/1807.01475) [[astro-ph.GA](#)].
- [406] R. Morganti et al. “Another piece of the puzzle: The fast H I outflow in Mrk 231.” In: *Astron. Astrophys.* 593, A30 (Sept. 2016), A30. arXiv: [1606.01640](https://arxiv.org/abs/1606.01640) [[astro-ph.GA](#)].
- [407] R. Morganti et al. “Radio Jets Clearing the Way Through a Galaxy: Watching Feedback in Action.” In: *Science* 341.6150 (Sept. 2013), pp. 1082–1085. DOI: [10.1126/science.1240436](https://doi.org/10.1126/science.1240436). arXiv: [1309.1240](https://arxiv.org/abs/1309.1240) [[astro-ph.CO](#)].

- [408] S. Motta et al. “Discovery of two simultaneous non-harmonically related quasi-periodic oscillations in the 2005 outburst of the black hole binary GRO J1655-40.” In: *Mon. Not. R. Astron. Soc.* 427.1 (Nov. 2012), pp. 595–606. DOI: [10.1111/j.1365-2966.2012.22037.x](https://doi.org/10.1111/j.1365-2966.2012.22037.x). arXiv: [1209.0327](https://arxiv.org/abs/1209.0327) [[astro-ph.HE](#)].
- [409] S. E. Motta and R. P. Fender. “A connection between accretion states and the formation of ultrarelativistic outflows in a neutron star X-ray binary.” In: *Mon. Not. R. Astron. Soc.* 483.3 (Mar. 2019), pp. 3686–3699. DOI: [10.1093/mnras/sty3331](https://doi.org/10.1093/mnras/sty3331). arXiv: [1812.04867](https://arxiv.org/abs/1812.04867) [[astro-ph.HE](#)].
- [410] S. E. Motta et al. “Links between quasi-periodic oscillations and accretion states in neutron star low-mass X-ray binaries.” In: *Mon. Not. R. Astron. Soc.* 468.2 (June 2017), pp. 2311–2324. DOI: [10.1093/mnras/stx570](https://doi.org/10.1093/mnras/stx570). arXiv: [1703.01263](https://arxiv.org/abs/1703.01263) [[astro-ph.HE](#)].
- [411] S. E. Motta et al. “On the different flavours of Lense-Thirring precession around accreting stellar mass black holes.” In: *MNRAS* 473.1 (Jan. 2018), pp. 431–439. DOI: [10.1093/mnras/stx2358](https://doi.org/10.1093/mnras/stx2358). arXiv: [1709.02608](https://arxiv.org/abs/1709.02608) [[astro-ph.HE](#)].
- [412] S. E. Motta et al. “Precise mass and spin measurements for a stellar-mass black hole through X-ray timing: the case of GRO J1655-40.” In: *Mon. Not. R. Astron. Soc.* 437.3 (Jan. 2014), pp. 2554–2565. DOI: [10.1093/mnras/stt2068](https://doi.org/10.1093/mnras/stt2068). arXiv: [1309.3652](https://arxiv.org/abs/1309.3652) [[astro-ph.HE](#)].
- [413] I. Moya-Torregrosa et al. “Magnetized relativistic jets and helical magnetic fields. I. Dynamics.” In: *Astron. Astrophys.* 650, A60 (June 2021), A60. DOI: [10.1051/0004-6361/202037898](https://doi.org/10.1051/0004-6361/202037898).
- [414] T. Muñoz-Darias et al. “Black hole-like hysteresis and accretion states in neutron star low-mass X-ray binaries.” In: *Mon. Not. R. Astron. Soc.* 443.4 (Oct. 2014), pp. 3270–3283. DOI: [10.1093/mnras/stu1334](https://doi.org/10.1093/mnras/stu1334). arXiv: [1407.1318](https://arxiv.org/abs/1407.1318) [[astro-ph.HE](#)].
- [415] L. E. Muijres et al. “Predictions for mass-loss rates and terminal wind velocities of massive O-type stars.” In: *Astron. Astrophys.* 537, A37 (Jan. 2012), A37. DOI: [10.1051/0004-6361/201015818](https://doi.org/10.1051/0004-6361/201015818). arXiv: [1112.0944](https://arxiv.org/abs/1112.0944) [[astro-ph.SR](#)].
- [416] D. Mukherjee et al. “Relativistic jet feedback - III. Feedback on gas discs.” In: *Mon. Not. R. Astron. Soc.* 479.4 (Oct. 2018), pp. 5544–5566. DOI: [10.1093/mnras/sty1776](https://doi.org/10.1093/mnras/sty1776). arXiv: [1803.08305](https://arxiv.org/abs/1803.08305) [[astro-ph.HE](#)].
- [417] D. Mukherjee et al. “Relativistic jet feedback in high-redshift galaxies - I. Dynamics.” In: *Mon. Not. R. Astron. Soc.* 461.1 (Sept. 2016), pp. 967–983. arXiv: [1606.01143](https://arxiv.org/abs/1606.01143) [[astro-ph.HE](#)].
- [418] D. Mukherjee et al. “Simulating the dynamics and non-thermal emission of relativistic magnetized jets I. Dynamics.” In: *Mon. Not. R. Astron. Soc.* 499.1 (Nov. 2020), pp. 681–701. DOI: [10.1093/mnras/staa2934](https://doi.org/10.1093/mnras/staa2934). arXiv: [2009.10475](https://arxiv.org/abs/2009.10475) [[astro-ph.HE](#)].
- [419] E. Muller and W. Brinkmann. “Numerical Simulations of the Precessing Jets of SS433.” In: *Highly Energetic Physical Processes and Mechanisms for Emission from Astrophysical Plasmas*. Ed. by P. C. H. Martens, S. Tsuruta, and M. A. Weber. Vol. 195. May 2000, p. 415.

- [420] P. Murdin, D. H. Clark, and P. G. Martin. “The optical spectrum of SS 433.” In: *Mon. Not. R. Astron. Soc.* 193 (Oct. 1980), pp. 135–151. DOI: [10.1093/mnras/193.1.135](https://doi.org/10.1093/mnras/193.1.135).
- [421] A. V. Myasnikov, S. A. Zhekov, and N. A. Belov. “Radiative steady-state colliding stellar wind models: are they correct?” In: *Mon. Not. R. Astron. Soc.* 298.4 (Aug. 1998), pp. 1021–1029. DOI: [10.1046/j.1365-8711.1998.01666.x](https://doi.org/10.1046/j.1365-8711.1998.01666.x).
- [422] H. Nagai et al. “Enhanced Polarized Emission from the One-parsec-scale Hotspot of 3C 84 as a Result of the Interaction with the Clumpy Ambient Medium.” In: *Astrophys. J.* 849.1, 52 (Nov. 2017), p. 52. DOI: [10.3847/1538-4357/aa8e43](https://doi.org/10.3847/1538-4357/aa8e43). arXiv: [1709.06708](https://arxiv.org/abs/1709.06708) [[astro-ph.HE](#)].
- [423] H. Nagai et al. “The ALMA Discovery of the Rotating Disk and Fast Outflow of Cold Molecular Gas in NGC 1275.” In: *Astrophys. J.* 883.2, 193 (Oct. 2019), p. 193. DOI: [10.3847/1538-4357/ab3e6e](https://doi.org/10.3847/1538-4357/ab3e6e). arXiv: [1905.06017](https://arxiv.org/abs/1905.06017) [[astro-ph.GA](#)].
- [424] M. Nakamura et al. “A Numerical Model of Hercules A by Magnetic Tower: Jet/Lobe Transition, Wiggling, and the Magnetic Field Distribution.” In: *Astrophys. J.* 686.2 (Oct. 2008), pp. 843–850. DOI: [10.1086/591222](https://doi.org/10.1086/591222). arXiv: [0806.4150](https://arxiv.org/abs/0806.4150) [[astro-ph](#)].
- [425] A. Neronov and M. Chernyakova. “Compactified pulsar wind nebula model of gamma-ray loud binary LSI +61 303.” In: *arXiv e-prints*, astro-ph/0701144 (Jan. 2007), astro-ph/0701144. arXiv: [astro-ph/0701144](https://arxiv.org/abs/astro-ph/0701144) [[astro-ph](#)].
- [426] M. Neumann et al. “XRBCats: Galactic High Mass X-ray Binary Catalogue.” In: *arXiv e-prints*, arXiv:2303.16137 (Mar. 2023), arXiv:2303.16137. DOI: [10.48550/arXiv.2303.16137](https://doi.org/10.48550/arXiv.2303.16137). arXiv: [2303.16137](https://arxiv.org/abs/2303.16137) [[astro-ph.HE](#)].
- [427] J. Nickolls et al. “Scalable Parallel Programming with CUDA.” In: *ACM SIGGRAPH 2008 Classes*. SIGGRAPH '08. Los Angeles, California: Association for Computing Machinery, 2008. ISBN: 9781450378451. DOI: [10.1145/1401132.1401152](https://doi.org/10.1145/1401132.1401152). URL: <https://doi.org/10.1145/1401132.1401152>.
- [428] W. Noh. “Errors for calculations of strong shocks using an artificial viscosity and an artificial heat flux.” In: *Journal of Computational Physics* 72.1 (1987), pp. 78–120. ISSN: 0021-9991. DOI: [https://doi.org/10.1016/0021-9991\(87\)90074-X](https://doi.org/10.1016/0021-9991(87)90074-X). URL: <https://www.sciencedirect.com/science/article/pii/002199918790074X>.
- [429] P. E. J. Nulsen et al. “The Powerful Outburst in Hercules A.” In: *Astrophys. J. Lett.* 625.1 (May 2005), pp. L9–L12. DOI: [10.1086/430945](https://doi.org/10.1086/430945). arXiv: [astro-ph/0504350](https://arxiv.org/abs/astro-ph/0504350) [[astro-ph](#)].
- [430] M. Obergaulinger, O. Just, and M. A. Aloy. “Core collapse with magnetic fields and rotation.” In: *Journal of Physics G Nuclear Physics* 45.8 (Aug. 2018), p. 084001. DOI: [10.1088/1361-6471/aac982](https://doi.org/10.1088/1361-6471/aac982). arXiv: [1806.00393](https://arxiv.org/abs/1806.00393) [[astro-ph.HE](#)].
- [431] C. P. O’Dea et al. “Hubble Space Telescope Observations of Dusty Filaments in Hercules A: Evidence for Entrainment.” In: *Astrophys. J.* 771.1, 38 (July 2013), p. 38. DOI: [10.1088/0004-637X/771/1/38](https://doi.org/10.1088/0004-637X/771/1/38). arXiv: [1305.4935](https://arxiv.org/abs/1305.4935) [[astro-ph.CO](#)].

- [432] C. P. O’Dea et al. “Hubble Space Telescope STIS Observations of the Kinematics of Emission-Line Nebulae in Three Compact Steep-Spectrum Radio Sources.” In: *Astrophys. J.* 123.5 (May 2002), pp. 2333–2351.
- [433] T. Ohmura et al. “Continuous Jets and Backflow Models for the Formation of W50/SS 433 in Magnetohydrodynamics Simulations.” In: *Astrophys. J.* 910.2, 149 (Apr. 2021), p. 149. DOI: [10.3847/1538-4357/abe5a1](https://doi.org/10.3847/1538-4357/abe5a1). arXiv: [2102.06728](https://arxiv.org/abs/2102.06728) [[astro-ph.HE](#)].
- [434] K. Ohsuga and S. Mineshige. “Global Structure of Three Distinct Accretion Flows and Outflows around Black Holes from Two-dimensional Radiation-magnetohydrodynamic Simulations.” In: *Astrophys. J.* 736.1, 2 (July 2011), p. 2. DOI: [10.1088/0004-637X/736/1/2](https://doi.org/10.1088/0004-637X/736/1/2). arXiv: [1105.5474](https://arxiv.org/abs/1105.5474) [[astro-ph.HE](#)].
- [435] K. Ohsuga et al. “Global Radiation-Magnetohydrodynamic Simulations of Black-Hole Accretion Flow and Outflow: Unified Model of Three States.” In: *Publ. Astron. Soc. Jpn* 61.3 (June 2009), pp. L7–L11. DOI: [10.1093/pasj/61.3.L7](https://doi.org/10.1093/pasj/61.3.L7). arXiv: [0903.5364](https://arxiv.org/abs/0903.5364) [[astro-ph.HE](#)].
- [436] K. Ohsuga et al. “Supercritical Accretion Flows around Black Holes: Two-dimensional, Radiation Pressure-dominated Disks with Photon Trapping.” In: *Astrophys. J.* 628.1 (July 2005), pp. 368–381. DOI: [10.1086/430728](https://doi.org/10.1086/430728). arXiv: [astro-ph/0504168](https://arxiv.org/abs/astro-ph/0504168) [[astro-ph](#)].
- [437] A. T. Okazaki et al. “Hydrodynamic Interaction between the Be Star and the Pulsar in the TeV Binary PSR B1259-63/LS 2883.” In: *Publ. Astron. Soc. Jpn* 63 (Aug. 2011), p. 893. DOI: [10.1093/pasj/63.4.893](https://doi.org/10.1093/pasj/63.4.893). arXiv: [1105.1481](https://arxiv.org/abs/1105.1481) [[astro-ph.HE](#)].
- [438] T. Okuda, G. V. Lipunova, and D. Molteni. “The jets and disc of SS 433 at super-Eddington luminosities.” In: *Mon. Not. R. Astron. Soc.* 398.4 (Oct. 2009), pp. 1668–1677. DOI: [10.1111/j.1365-2966.2009.15169.x](https://doi.org/10.1111/j.1365-2966.2009.15169.x). arXiv: [0906.3308](https://arxiv.org/abs/0906.3308) [[astro-ph.HE](#)].
- [439] T. Okuda et al. “Black hole accretion discs and jets at super-Eddington luminosity.” In: *Mon. Not. R. Astron. Soc.* 357.1 (Feb. 2005), pp. 295–303. DOI: [10.1111/j.1365-2966.2005.08647.x](https://doi.org/10.1111/j.1365-2966.2005.08647.x). arXiv: [astro-ph/0411743](https://arxiv.org/abs/astro-ph/0411743) [[astro-ph](#)].
- [440] T. Oosterbroek et al. “Circinus X-1 revisited: fast-timing properties in relation to spectral state.” In: *Astron. Astrophys.* 297 (May 1995), pp. 141–158.
- [441] S. A. Orszag and C. M. Tang. “Small-scale structure of two-dimensional magnetohydrodynamic turbulence.” In: *Journal of Fluid Mechanics* 90 (Jan. 1979), pp. 129–143. DOI: [10.1017/S002211207900210X](https://doi.org/10.1017/S002211207900210X).
- [442] S. Osher and F. Solomon. “Upwind difference schemes for hyperbolic systems of conservation laws.” In: *Mathematics of computation* 38.158 (1982), pp. 339–374.
- [443] I. Owsianik and J. E. Conway. “First detection of hotspot advance in a Compact Symmetric Object. Evidence for a class of very young extragalactic radio sources.” In: *Astron. Astrophys.* 337 (Sept. 1998), pp. 69–79. arXiv: [astro-ph/9712062](https://arxiv.org/abs/astro-ph/9712062) [[astro-ph](#)].

- [444] Z. Paragi et al. “The inner radio jet region and the complex environment of SS433.” In: *Astron. Astrophys.* 348 (Aug. 1999), pp. 910–916. arXiv: [astro-ph/9907169](https://arxiv.org/abs/astro-ph/9907169) [[astro-ph](#)].
- [445] J. M. Paredes and J. Martí. “Microquasars in the galaxy.” In: *Contributions to Science 2.3* (Jan. 2003), pp. 303–314.
- [446] J. M. Paredes et al. “Evidence of X-ray periodicity in LSI+61 303.” In: *Astron. Astrophys.* 320 (Apr. 1997), pp. L25–L28.
- [447] J. M. Paredes et al. “Chandra Observations of the Gamma-Ray Binary LSI I +61 303: Extended X-Ray Structure?” In: *Astrophys. J. Lett.* 664.1 (July 2007), pp. L39–L42. DOI: [10.1086/520674](https://doi.org/10.1086/520674). arXiv: [0706.0877](https://arxiv.org/abs/0706.0877) [[astro-ph](#)].
- [448] J. M. Paredes et al. “Discovery of a High-Energy Gamma-Ray-Emitting Persistent Microquasar.” In: *Science* 288.5475 (June 2000), pp. 2340–2342. DOI: [10.1126/science.288.5475.2340](https://doi.org/10.1126/science.288.5475.2340). arXiv: [astro-ph/0102235](https://arxiv.org/abs/astro-ph/0102235) [[astro-ph](#)].
- [449] L. Pareschi and G. Russo. “Implicit-explicit runge-kutta schemes and applications to hyperbolic systems with relaxation.” In: *Journal of Scientific Computing* 25.1 (2005), pp. 129–155. DOI: [10.1007/BF02728986](https://doi.org/10.1007/BF02728986). URL: <https://doi.org/10.1007/BF02728986>.
- [450] M.-G. Park. “Equations of general relativistic radiation hydrodynamics from a tensor formalism.” In: *Mon. Not. R. Astron. Soc.* 367.4 (Apr. 2006), pp. 1739–1745. DOI: [10.1111/j.1365-2966.2006.10081.x](https://doi.org/10.1111/j.1365-2966.2006.10081.x). arXiv: [astro-ph/0601635](https://arxiv.org/abs/astro-ph/0601635) [[astro-ph](#)].
- [451] A. Patruno and A. L. Watts. “Accreting Millisecond X-ray Pulsars.” In: *Timing Neutron Stars: Pulsations, Oscillations and Explosions*. Ed. by T. M. Belloni, M. Méndez, and C. Zhang. Vol. 461. Astrophysics and Space Science Library. Jan. 2021, pp. 143–208. DOI: [10.1007/978-3-662-62110-3\\_4](https://doi.org/10.1007/978-3-662-62110-3_4). arXiv: [1206.2727](https://arxiv.org/abs/1206.2727) [[astro-ph.HE](#)].
- [452] A. Pavan et al. “Short gamma-ray burst jet propagation in binary neutron star merger environments.” In: *Mon. Not. R. Astron. Soc.* 506.3 (Sept. 2021), pp. 3483–3498. DOI: [10.1093/mnras/stab1810](https://doi.org/10.1093/mnras/stab1810). arXiv: [2104.12410](https://arxiv.org/abs/2104.12410) [[astro-ph.HE](#)].
- [453] W. Penninx et al. “A connection between the X-ray spectral branches and the radio brightness in GX17 + 2.” In: *Nature* 336.6195 (Nov. 1988), pp. 146–148. DOI: [10.1038/336146a0](https://doi.org/10.1038/336146a0).
- [454] M. Perucho and V. Bosch-Ramon. “3D simulations of microquasar jets in clumpy stellar winds.” In: *Astron. Astrophys.* 539, A57 (Mar. 2012), A57. DOI: [10.1051/0004-6361/201118262](https://doi.org/10.1051/0004-6361/201118262). arXiv: [1112.2520](https://arxiv.org/abs/1112.2520) [[astro-ph.HE](#)].
- [455] M. Perucho and V. Bosch-Ramon. “On the interaction of microquasar jets with stellar winds.” In: *Astron. Astrophys.* 482.3 (May 2008), pp. 917–927. DOI: [10.1051/0004-6361:20078929](https://doi.org/10.1051/0004-6361:20078929). arXiv: [0802.1134](https://arxiv.org/abs/0802.1134) [[astro-ph](#)].
- [456] M. Perucho, V. Bosch-Ramon, and M. V. Barkov. “Impact of red giant/AGB winds on active galactic nucleus jet propagation.” In: *Astron. Astrophys.* 606, A40 (Oct. 2017), A40. DOI: [10.1051/0004-6361/201630117](https://doi.org/10.1051/0004-6361/201630117). arXiv: [1706.06301](https://arxiv.org/abs/1706.06301) [[astro-ph.HE](#)].

- [457] M. Perucho, V. Bosch-Ramon, and D. Khangulyan. “3D simulations of wind-jet interaction in massive X-ray binaries.” In: *Astron. Astrophys.* 512, L4 (Mar. 2010), p. L4. DOI: [10.1051/0004-6361/201014241](https://doi.org/10.1051/0004-6361/201014241). arXiv: [1002.4562](https://arxiv.org/abs/1002.4562) [[astro-ph.HE](#)].
- [458] M. Perucho and J. M. Martí. “A numerical simulation of the evolution and fate of a Fanaroff-Riley type I jet. The case of 3C 31.” In: *Mon. Not. R. Astron. Soc.* 382.2 (Dec. 2007), pp. 526–542. DOI: [10.1111/j.1365-2966.2007.12454.x](https://doi.org/10.1111/j.1365-2966.2007.12454.x). arXiv: [0709.1784](https://arxiv.org/abs/0709.1784) [[astro-ph](#)].
- [459] M. Perucho, J. M. Martí, and M. Hanasz. “Nonlinear stability of relativistic sheared planar jets.” In: *Astron. Astrophys.* 443.3 (Dec. 2005), pp. 863–881. DOI: [10.1051/0004-6361:20053115](https://doi.org/10.1051/0004-6361:20053115). arXiv: [astro-ph/0510426](https://arxiv.org/abs/astro-ph/0510426) [[astro-ph](#)].
- [460] M. Perucho, J. M. Martí, and M. Hanasz. “Stability of hydrodynamical relativistic planar jets. II. Long-term nonlinear evolution.” In: *Astron. Astrophys.* 427 (Nov. 2004), pp. 431–444. DOI: [10.1051/0004-6361:20040350](https://doi.org/10.1051/0004-6361:20040350). arXiv: [astro-ph/0407574](https://arxiv.org/abs/astro-ph/0407574) [[astro-ph](#)].
- [461] M. Perucho et al. “On the deceleration of Fanaroff-Riley Class I jets: mass loading by stellar winds.” In: *Mon. Not. R. Astron. Soc.* 441.2 (June 2014), pp. 1488–1503. DOI: [10.1093/mnras/stu676](https://doi.org/10.1093/mnras/stu676). arXiv: [1404.1209](https://arxiv.org/abs/1404.1209) [[astro-ph.HE](#)].
- [462] M. Perucho et al. “Stability of hydrodynamical relativistic planar jets. I. Linear evolution and saturation of Kelvin-Helmholtz modes.” In: *Astron. Astrophys.* 427 (Nov. 2004), pp. 415–429. DOI: [10.1051/0004-6361:20040349](https://doi.org/10.1051/0004-6361:20040349). arXiv: [astro-ph/0407548](https://arxiv.org/abs/astro-ph/0407548) [[astro-ph](#)].
- [463] M. Perucho et al. “Stability of three-dimensional relativistic jets: implications for jet collimation.” In: *Astron. Astrophys.* 519, A41 (Sept. 2010), A41. DOI: [10.1051/0004-6361/200913012](https://doi.org/10.1051/0004-6361/200913012). arXiv: [1005.4332](https://arxiv.org/abs/1005.4332) [[astro-ph.HE](#)].
- [464] M. Perucho et al. “The role of Kelvin-Helmholtz instability in the internal structure of relativistic outflows. The case of the jet in 3C 273.” In: *Astron. Astrophys.* 456.2 (Sept. 2006), pp. 493–504. DOI: [10.1051/0004-6361:20065310](https://doi.org/10.1051/0004-6361:20065310). arXiv: [astro-ph/0606109](https://arxiv.org/abs/astro-ph/0606109) [[astro-ph](#)].
- [465] M. Perucho. “Dissipative Processes and Their Role in the Evolution of Radio Galaxies.” In: *Galaxies* 7.3 (July 2019), p. 70. DOI: [10.3390/galaxies7030070](https://doi.org/10.3390/galaxies7030070). arXiv: [1907.13599](https://arxiv.org/abs/1907.13599) [[astro-ph.HE](#)].
- [466] M. Perucho. “Jet Stability, Dynamics and Energy Transport.” In: *International Journal of Modern Physics Conference Series*. Vol. 8. International Journal of Modern Physics Conference Series. Jan. 2012, pp. 241–252. DOI: [10.1142/S2010194512004667](https://doi.org/10.1142/S2010194512004667). arXiv: [1109.2403](https://arxiv.org/abs/1109.2403) [[astro-ph.CO](#)].
- [467] M. Perucho and J. López-Miralles. “Numerical simulations of relativistic jets.” In: *Journal of Plasma Physics* 89.5 (2023), p. 915890501. DOI: [10.1017/S0022377823000892](https://doi.org/10.1017/S0022377823000892).
- [468] M. Perucho, J.-M. Martí, and V. Quilis. “Long-term FR II jet evolution: clues from three-dimensional simulations.” In: *Mon. Not. R. Astron. Soc.* 482.3 (Jan. 2019), pp. 3718–3735. DOI: [10.1093/mnras/sty2912](https://doi.org/10.1093/mnras/sty2912). arXiv: [1810.10968](https://arxiv.org/abs/1810.10968) [[astro-ph.GA](#)].

- [469] M. Perucho, J.-M. Martí, and V. Quilis. “Long-term FR II jet evolution in dense environments.” In: *Mon. Not. R. Astron. Soc.* 510.2 (Feb. 2022), pp. 2084–2096. DOI: [10.1093/mnras/stab3560](https://doi.org/10.1093/mnras/stab3560). arXiv: [2112.02978](https://arxiv.org/abs/2112.02978) [[astro-ph.HE](#)].
- [470] M. Perucho, V. Quilis, and J.-M. Martí. “Intracluster Medium Reheating by Relativistic Jets.” In: *Astrophys. J.* 743.1, 42 (Dec. 2011), p. 42. DOI: [10.1088/0004-637X/743/1/42](https://doi.org/10.1088/0004-637X/743/1/42). arXiv: [1107.5484](https://arxiv.org/abs/1107.5484) [[astro-ph.CO](#)].
- [471] M. Perucho et al. “Jet propagation through inhomogeneous media and shock ionization.” In: *Astronomische Nachrichten* 342.1171 (Nov. 2021), pp. 1171–1175. DOI: [10.1002/asna.20210051](https://doi.org/10.1002/asna.20210051). arXiv: [2109.15234](https://arxiv.org/abs/2109.15234) [[astro-ph.HE](#)].
- [472] M. Perucho et al. “Large-scale jets from active galactic nuclei as a source of intracluster medium heating: cavities and shocks.” In: *Mon. Not. R. Astron. Soc.* 445.2 (Dec. 2014), pp. 1462–1481. DOI: [10.1093/mnras/stu1828](https://doi.org/10.1093/mnras/stu1828). arXiv: [1409.3335](https://arxiv.org/abs/1409.3335) [[astro-ph.HE](#)].
- [473] M. Perucho et al. “On the large scale morphology of Hercules A: destabilized hot jets?” In: *Mon. Not. R. Astron. Soc.* 523.3 (Aug. 2023), pp. 3583–3594. DOI: [10.1093/mnras/stad1640](https://doi.org/10.1093/mnras/stad1640). arXiv: [2305.14060](https://arxiv.org/abs/2305.14060) [[astro-ph.HE](#)].
- [474] M. Perucho et al. “Radio mode feedback: Does relativity matter?” In: *Mon. Not. R. Astron. Soc.* 471.1 (Oct. 2017), pp. L120–L124. DOI: [10.1093/mnrasl/slx115](https://doi.org/10.1093/mnrasl/slx115). arXiv: [1707.05794](https://arxiv.org/abs/1707.05794) [[astro-ph.HE](#)].
- [475] S. Piraino et al. “BeppoSAX observations of the atoll X-ray binary 4U 0614+091.” In: *Astron. Astrophys.* 349 (Sept. 1999), pp. L77–L81. DOI: [10.48550/arXiv.astro-ph/9910115](https://doi.org/10.48550/arXiv.astro-ph/9910115). arXiv: [astro-ph/9910115](https://arxiv.org/abs/astro-ph/9910115) [[astro-ph](#)].
- [476] T. Plewa et al. “Bending Relativistic Jets in AGNs.” In: *Relativistic Jets in AGNs*. Ed. by M. Ostrowski et al. Jan. 1997, pp. 104–109. DOI: [10.48550/arXiv.astro-ph/9706124](https://doi.org/10.48550/arXiv.astro-ph/9706124). arXiv: [astro-ph/9706124](https://arxiv.org/abs/astro-ph/9706124) [[astro-ph](#)].
- [477] A. G. Polatidis and J. E. Conway. “Proper Motions in Compact Symmetric Objects.” In: 20.1 (Jan. 2003), pp. 69–74. arXiv: [astro-ph/0212122](https://arxiv.org/abs/astro-ph/0212122) [[astro-ph](#)].
- [478] G. Ponti, T. Muñoz-Darias, and R. P. Fender. “A connection between accretion state and Fe K absorption in an accreting neutron star: black hole-like soft-state winds?” In: *Mon. Not. R. Astron. Soc.* 444.2 (Oct. 2014), pp. 1829–1834. DOI: [10.1093/mnras/stu1742](https://doi.org/10.1093/mnras/stu1742). arXiv: [1407.4468](https://arxiv.org/abs/1407.4468) [[astro-ph.HE](#)].
- [479] O. Porth. “Three-dimensional structure of relativistic jet formation.” In: *Mon. Not. R. Astron. Soc.* 429.3 (Mar. 2013), pp. 2482–2492. DOI: [10.1093/mnras/sts519](https://doi.org/10.1093/mnras/sts519). arXiv: [1212.0676](https://arxiv.org/abs/1212.0676) [[astro-ph.HE](#)].
- [480] O. Porth, S. S. Komissarov, and R. Keppens. “Three-dimensional magnetohydrodynamic simulations of the Crab nebula.” In: *Mon. Not. R. Astron. Soc.* 438.1 (Feb. 2014), pp. 278–306. DOI: [10.1093/mnras/stt2176](https://doi.org/10.1093/mnras/stt2176). arXiv: [1310.2531](https://arxiv.org/abs/1310.2531) [[astro-ph.HE](#)].
- [481] K. G. Powell. *Approximate Riemann solver for magnetohydrodynamics (that works in more than one dimension)*. Unknown. Mar. 1994.
- [482] W. Priedhorsky et al. “Bimodal Quasi-oscillatory and Spectral Behavior in Scorpius X-1.” In: *Astrophys. J. Lett.* 306 (July 1986), p. L91. DOI: [10.1086/184712](https://doi.org/10.1086/184712).

- [483] D. Proga and T. R. Kallman. “On the Role of the Ultraviolet and X-Ray Radiation in Driving a Disk Wind in X-Ray Binaries.” In: *Astrophys. J.* 565.1 (Jan. 2002), pp. 455–470. DOI: [10.1086/324534](https://doi.org/10.1086/324534). arXiv: [astro-ph/0109064](https://arxiv.org/abs/astro-ph/0109064) [[astro-ph](#)].
- [484] D. Psaltis, T. Belloni, and M. van der Klis. “Correlations in Quasi-periodic Oscillation and Noise Frequencies among Neutron Star and Black Hole X-Ray Binaries.” In: *Astrophys. J.* 520.1 (July 1999), pp. 262–270. DOI: [10.1086/307436](https://doi.org/10.1086/307436). arXiv: [astro-ph/9902130](https://arxiv.org/abs/astro-ph/9902130) [[astro-ph](#)].
- [485] B. Punsly and F. V. Coroniti. “Ergosphere-driven Winds.” In: *Astrophys. J.* 354 (May 1990), p. 583. DOI: [10.1086/168717](https://doi.org/10.1086/168717).
- [486] B. Punsly. “A Magnetized Black Hole Model of LS I +61<sup>deg</sup>303.” In: *Astrophys. J.* 519.1 (July 1999), pp. 336–344. DOI: [10.1086/307341](https://doi.org/10.1086/307341).
- [487] J. J. Quirk. “A contribution to the great Riemann solver debate.” In: *International Journal for Numerical Methods in Fluids* 18.6 (Mar. 1994), pp. 555–574. DOI: [10.1002/fld.1650180603](https://doi.org/10.1002/fld.1650180603).
- [488] D. Radice et al. “A new moment-based general-relativistic neutrino-radiation transport code: Methods and first applications to neutron star mergers.” In: *Mon. Not. R. Astron. Soc.* 512.1 (May 2022), pp. 1499–1521. DOI: [10.1093/mnras/stac589](https://doi.org/10.1093/mnras/stac589). arXiv: [2111.14858](https://arxiv.org/abs/2111.14858) [[astro-ph.HE](#)].
- [489] M. Ramatsoku et al. “Collimated synchrotron threads linking the radio lobes of ESO 137-006.” In: *Astron. Astrophys.* 636, L1 (Apr. 2020), p. L1. DOI: [10.1051/0004-6361/202037800](https://doi.org/10.1051/0004-6361/202037800). arXiv: [2004.03203](https://arxiv.org/abs/2004.03203) [[astro-ph.GA](#)].
- [490] C. Ramos Almeida and C. Ricci. “Nuclear obscuration in active galactic nuclei.” In: *Nature Astronomy* 1 (Oct. 2017), pp. 679–689. DOI: [10.1038/s41550-017-0232-z](https://doi.org/10.1038/s41550-017-0232-z). arXiv: [1709.00019](https://arxiv.org/abs/1709.00019) [[astro-ph.GA](#)].
- [491] P. S. Ray et al. “Long-Term Flux Monitoring of LSI +61°303 at 2.25 and 8.3 GHz.” In: *Astrophys. J.* 491.1 (Dec. 1997), pp. 381–387. DOI: [10.1086/304923](https://doi.org/10.1086/304923). arXiv: [astro-ph/9710033](https://arxiv.org/abs/astro-ph/9710033) [[astro-ph](#)].
- [492] P. S. Ray and J. M. Jacob M. Hartman. “Unusual X-ray Activity from LS I +61 303 on 2008 August 21.” In: *The Astronomer’s Telegram* 1730 (Sept. 2008), p. 1.
- [493] S. Raychaudhuri, M. K. Vyas, and I. Chattopadhyay. “Simulations of radiation-driven winds from Keplerian discs.” In: *Mon. Not. R. Astron. Soc.* 501.4 (Mar. 2021), pp. 4850–4860. DOI: [10.1093/mnras/staa3920](https://doi.org/10.1093/mnras/staa3920). arXiv: [2012.08886](https://arxiv.org/abs/2012.08886) [[astro-ph.HE](#)].
- [494] N. Rea et al. “Deep Chandra observations of TeV binaries - I. LSI+61°303.” In: *Mon. Not. R. Astron. Soc.* 405.4 (July 2010), pp. 2206–2214. DOI: [10.1111/j.1365-2966.2010.16642.x](https://doi.org/10.1111/j.1365-2966.2010.16642.x). arXiv: [1002.2223](https://arxiv.org/abs/1002.2223) [[astro-ph.HE](#)].
- [495] M. J. Reid et al. “A Parallax Distance to the Microquasar GRS 1915+105 and a Revised Estimate of its Black Hole Mass.” In: *Astrophys. J.* 796.1, 2 (Nov. 2014), p. 2. DOI: [10.1088/0004-637X/796/1/2](https://doi.org/10.1088/0004-637X/796/1/2). arXiv: [1409.2453](https://arxiv.org/abs/1409.2453) [[astro-ph.GA](#)].
- [496] T. Rembiasz et al. “On the Measurements of Numerical Viscosity and Resistivity in Eulerian MHD Codes.” In: *Astrophys. J. Suppl. Ser.* 230.2, 18 (June 2017), p. 18. DOI: [10.3847/1538-4365/aa6254](https://doi.org/10.3847/1538-4365/aa6254). arXiv: [1611.05858](https://arxiv.org/abs/1611.05858) [[astro-ph.IM](#)].

- [497] M. Revnivtsev, A. Vikhlinin, and S. Sazonov. “Resolving the Galactic ridge X-ray background.” In: *Astron. Astrophys.* 473.3 (Oct. 2007), pp. 857–862. DOI: [10.1051/0004-6361:20066850](https://doi.org/10.1051/0004-6361:20066850). arXiv: [astro-ph/0611952](https://arxiv.org/abs/astro-ph/0611952) [[astro-ph](#)].
- [498] V. Reynaldi and C. Feinstein. “The fingerprints of photoionization and shock-ionization in two CSS sources.” In: *Mon. Not. R. Astron. Soc.* 455.2 (Jan. 2016), p. 2242. arXiv: [1510.06979](https://arxiv.org/abs/1510.06979) [[astro-ph.GA](#)].
- [499] L. Rezzolla and O. Zanotti. *Relativistic Hydrodynamics*. 2013.
- [500] L. Ricci et al. “Exploring the disk-jet connection in NGC 315.” In: *Astron. Astrophys.* 664, A166 (Aug. 2022), A166. DOI: [10.1051/0004-6361/202243958](https://doi.org/10.1051/0004-6361/202243958). arXiv: [2206.12193](https://arxiv.org/abs/2206.12193) [[astro-ph.HE](#)].
- [501] G. A. Richter. “V404 Cyg - a Further Outburst in 1956.” In: *Information Bulletin on Variable Stars* 3362 (Aug. 1989), p. 1.
- [502] F. M. Rieger. “An Introduction to Particle Acceleration in Shearing Flows.” In: *Galaxies* 7.3 (Sept. 2019), p. 78. DOI: [10.3390/galaxies7030078](https://doi.org/10.3390/galaxies7030078). arXiv: [1909.07237](https://arxiv.org/abs/1909.07237) [[astro-ph.HE](#)].
- [503] F. M. Rieger, V. Bosch-Ramon, and P. Duffy. “Fermi acceleration in astrophysical jets.” In: 309.1-4 (June 2007), pp. 119–125. DOI: [10.1007/s10509-007-9466-z](https://doi.org/10.1007/s10509-007-9466-z). arXiv: [astro-ph/0610141](https://arxiv.org/abs/astro-ph/0610141) [[astro-ph](#)].
- [504] F. M. Rieger and P. Duffy. “Particle Acceleration in Shearing Flows: Efficiencies and Limits.” In: *Astrophys. J. Lett.* 886.2, L26 (Dec. 2019), p. L26. DOI: [10.3847/2041-8213/ab563f](https://doi.org/10.3847/2041-8213/ab563f). arXiv: [1911.05348](https://arxiv.org/abs/1911.05348) [[astro-ph.HE](#)].
- [505] B. Ripperda et al. “Weak Alfvénic turbulence in relativistic plasmas. Part 2. current sheets and dissipation.” In: *Journal of Plasma Physics* 87.5, 905870512 (Oct. 2021), p. 905870512. DOI: [10.1017/S0022377821000957](https://doi.org/10.1017/S0022377821000957). arXiv: [2105.01145](https://arxiv.org/abs/2105.01145) [[astro-ph.HE](#)].
- [506] F. J. Rivera-Paleo and F. S. Guzmán. “CAFE-R: A Code That Solves the Special Relativistic Radiation Hydrodynamics Equations.” In: *Astrophys. J. Suppl. Ser.* 241.2, 28 (Apr. 2019), p. 28. DOI: [10.3847/1538-4365/ab0d8c](https://doi.org/10.3847/1538-4365/ab0d8c). arXiv: [1903.04994](https://arxiv.org/abs/1903.04994) [[astro-ph.HE](#)].
- [507] F. J. Rivera-Paleo and F. S. Guzmán. “Evolution of jets driven by relativistic radiation hydrodynamics as long and low-luminosity GRBs.” In: *Mon. Not. R. Astron. Soc.* 479.2 (Sept. 2018), pp. 2796–2809. DOI: [10.1093/mnras/sty1603](https://doi.org/10.1093/mnras/sty1603). arXiv: [1710.09480](https://arxiv.org/abs/1710.09480) [[astro-ph.HE](#)].
- [508] F. J. Rivera-Paleo and F. S. Guzmán. “Modelling long GRBs using a single shock with relativistic radiation hydrodynamics.” In: *Mon. Not. R. Astron. Soc.* 459.3 (July 2016), pp. 2777–2786. DOI: [10.1093/mnras/stw830](https://doi.org/10.1093/mnras/stw830). arXiv: [1604.03457](https://arxiv.org/abs/1604.03457) [[astro-ph.HE](#)].
- [509] F. J. Rivera-Paleo et al. “Classifying initial conditions of long GRBs modeled with relativistic radiation hydrodynamics.” In: *Phys. Rev. D* 95.12, 123005 (June 2017), p. 123005. DOI: [10.1103/PhysRevD.95.123005](https://doi.org/10.1103/PhysRevD.95.123005). arXiv: [1705.08995](https://arxiv.org/abs/1705.08995) [[astro-ph.IM](#)].
- [510] D. H. Roberts et al. “Structure and Magnetic Fields in the Precessing Jet System SS 433. I. Multifrequency Imaging from 1998.” In: *Astrophys. J.* 676.1 (Mar. 2008), pp. 584–593. DOI: [10.1086/527544](https://doi.org/10.1086/527544). arXiv: [0712.2005](https://arxiv.org/abs/0712.2005) [[astro-ph](#)].

- [511] J. Rodriguez et al. “Correlated optical, X-ray, and  $\gamma$ -ray flaring activity seen with INTEGRAL during the 2015 outburst of V404 Cygni.” In: *Astron. Astrophys.* 581, L9 (Sept. 2015), p. L9. DOI: [10.1051/0004-6361/201527043](https://doi.org/10.1051/0004-6361/201527043). arXiv: [1507.06659](https://arxiv.org/abs/1507.06659) [[astro-ph.HE](#)].
- [512] L. F. Rodriguez, I. F. Mirabel, and J. Martí. “The Radio Counterpart of the Hard X-Ray Source GRS 1758-258.” In: *Astrophys. J. Lett.* 401 (Dec. 1992), p. L15. DOI: [10.1086/186659](https://doi.org/10.1086/186659).
- [513] P. L. Roe. “Characteristic-based schemes for the euler equations.” In: *Annual Review of Fluid Mechanics* 18 (Jan. 1986), pp. 337–365. DOI: [10.1146/annurev.fl.18.010186.002005](https://doi.org/10.1146/annurev.fl.18.010186.002005).
- [514] P. L. Roe. “Discrete Models for the Numerical Analysis of Time-Dependent Multidimensional Gas Dynamics.” In: *Journal of Computational Physics* 63.2 (Apr. 1986), pp. 458–476. DOI: [10.1016/0021-9991\(86\)90204-4](https://doi.org/10.1016/0021-9991(86)90204-4).
- [515] G. E. Romero. “Hadronic models of high-energy radiation from microquasars: recent developments.” In: *Microquasars and Beyond*. Jan. 2008, 20, p. 20. DOI: [10.22323/1.062.0020](https://doi.org/10.22323/1.062.0020).
- [516] G. E. Romero and M. Orellana. “Gamma-ray and neutrino emission from misaligned microquasars.” In: *Astron. Astrophys.* 439.1 (Aug. 2005), pp. 237–244. DOI: [10.1051/0004-6361:20052664](https://doi.org/10.1051/0004-6361:20052664). arXiv: [astro-ph/0505287](https://arxiv.org/abs/astro-ph/0505287) [[astro-ph](#)].
- [517] G. E. Romero et al. “Accretion vs. colliding wind models for the gamma-ray binary LS I +61 303: an assessment.” In: *Astron. Astrophys.* 474.1 (Oct. 2007), pp. 15–22. DOI: [10.1051/0004-6361:20078035](https://doi.org/10.1051/0004-6361:20078035). arXiv: [0706.1320](https://arxiv.org/abs/0706.1320) [[astro-ph](#)].
- [518] G. E. Romero et al. “Hadronic gamma-ray emission from windy microquasars.” In: *Astron. Astrophys.* 410 (Oct. 2003), pp. L1–L4. DOI: [10.1051/0004-6361:20031314-1](https://doi.org/10.1051/0004-6361:20031314-1). arXiv: [astro-ph/0309123](https://arxiv.org/abs/astro-ph/0309123) [[astro-ph](#)].
- [519] P. Rossi et al. “Formation of dynamical structures in relativistic jets: the FRI case.” In: *Astron. Astrophys.* 488.3 (Sept. 2008), pp. 795–806. DOI: [10.1051/0004-6361:200809687](https://doi.org/10.1051/0004-6361:200809687). arXiv: [0806.1648](https://arxiv.org/abs/0806.1648) [[astro-ph](#)].
- [520] M. C. Runacres and S. P. Owocki. “The outer evolution of instability-generated structure in radiatively driven stellar winds.” In: *Astron. Astrophys.* 381 (Jan. 2002), pp. 1015–1025. DOI: [10.1051/0004-6361:20011526](https://doi.org/10.1051/0004-6361:20011526).
- [521] D. M. Russell et al. “The jet-powered optical nebula of Cygnus X-1.” In: *Mon. Not. R. Astron. Soc.* 376.3 (Apr. 2007), pp. 1341–1349. DOI: [10.1111/j.1365-2966.2007.11539.x](https://doi.org/10.1111/j.1365-2966.2007.11539.x). arXiv: [astro-ph/0701645](https://arxiv.org/abs/astro-ph/0701645) [[astro-ph](#)].
- [522] T. D. Russell et al. “Radio monitoring of the hard state jets in the 2011 outburst of MAXI J1836-194.” In: *Mon. Not. R. Astron. Soc.* 450.2 (June 2015), pp. 1745–1759. DOI: [10.1093/mnras/stv723](https://doi.org/10.1093/mnras/stv723). arXiv: [1503.08634](https://arxiv.org/abs/1503.08634) [[astro-ph.HE](#)].
- [523] D. Ryu et al. “A Divergence-free Upwind Code for Multidimensional Magnetohydrodynamic Flows.” In: *Astrophys. J.* 509.1 (Dec. 1998), pp. 244–255. DOI: [10.1086/306481](https://doi.org/10.1086/306481). arXiv: [astro-ph/9807228](https://arxiv.org/abs/astro-ph/9807228) [[astro-ph](#)].
- [524] A. C. Sadun and P. Morrison. “Hercules A (3C 348): Phenomenology of an Unusual Active Galactic Nucleus.” In: *Astrophys. J.* 123.5 (May 2002), pp. 2312–2320. DOI: [10.1086/339829](https://doi.org/10.1086/339829).

- [525] S. Safi-Harb and H. Ögelman. “ROSAT and ASCA Observations of W50 Associated with the Peculiar Source SS 433.” In: *Astrophys. J.* 483.2 (July 1997), pp. 868–881. DOI: [10.1086/304274](https://doi.org/10.1086/304274).
- [526] S. Safi-Harb and R. Petre. “Rossi X-Ray Timing Explorer Observations of the Eastern Lobe of W50 Associated with SS 433.” In: *Astrophys. J.* 512.2 (Feb. 1999), pp. 784–792. DOI: [10.1086/306803](https://doi.org/10.1086/306803).
- [527] S. Safi-Harb et al. “Hard X-Ray Emission from the Eastern Jet of SS 433 Powering the W50 “Manatee” Nebula: Evidence for Particle Reacceleration.” In: *Astrophys. J.* 935.2, 163 (Aug. 2022), p. 163. DOI: [10.3847/1538-4357/ac7c05](https://doi.org/10.3847/1538-4357/ac7c05). arXiv: [2207.00573](https://arxiv.org/abs/2207.00573) [[astro-ph.HE](#)].
- [528] P. Saikia et al. “Lorentz Factors of Compact Jets in Black Hole X-Ray Binaries.” In: *Astrophys. J.* 887.1, 21 (Dec. 2019), p. 21. DOI: [10.3847/1538-4357/ab4a09](https://doi.org/10.3847/1538-4357/ab4a09). arXiv: [1910.01151](https://arxiv.org/abs/1910.01151) [[astro-ph.HE](#)].
- [529] A. Savitzky and M. J. E. Golay. “Smoothing and differentiation of data by simplified least squares procedures.” In: *Analytical Chemistry* 36 (Jan. 1964), pp. 1627–1639. DOI: [10.1021/ac60214a047](https://doi.org/10.1021/ac60214a047).
- [530] T. Savolainen et al. “RadioAstron discovery of a mini-cocoon around the restarted parsec-scale jet in 3C 84.” In: *Astron. Astrophys.* 676, A114 (Aug. 2023), A114. DOI: [10.1051/0004-6361/202142594](https://doi.org/10.1051/0004-6361/202142594). arXiv: [2111.04481](https://arxiv.org/abs/2111.04481) [[astro-ph.HE](#)].
- [531] C. J. Saxton, G. V. Bicknell, and R. S. Sutherland. “Production of Ringlike Structure in the Cocoon of Hercules A.” In: *Astrophys. J.* 579.1 (Nov. 2002), pp. 176–187. DOI: [10.1086/342679](https://doi.org/10.1086/342679). arXiv: [astro-ph/0204475](https://arxiv.org/abs/astro-ph/0204475) [[astro-ph](#)].
- [532] J. D. Scargle. “Studies in Astronomical Time Series Analysis. III. Fourier Transforms, Autocorrelation Functions, and Cross-Correlation Functions of Unevenly Spaced Data.” In: *Astrophys. J.* 343 (Aug. 1989), p. 874. DOI: [10.1086/167757](https://doi.org/10.1086/167757).
- [533] L. Scheck et al. “Does the plasma composition affect the long-term evolution of relativistic jets?” In: *Mon. Not. R. Astron. Soc.* 331.3 (Apr. 2002), pp. 615–634. DOI: [10.1046/j.1365-8711.2002.05210.x](https://doi.org/10.1046/j.1365-8711.2002.05210.x). arXiv: [astro-ph/0111369](https://arxiv.org/abs/astro-ph/0111369) [[astro-ph](#)].
- [534] R. Schulz et al. “Parsec-scale HI outflows in powerful radio galaxies.” In: *Astron. Astrophys.* 647, A63 (Mar. 2021), A63. arXiv: [2010.05996](https://arxiv.org/abs/2010.05996) [[astro-ph.GA](#)].
- [535] R. Schulz et al. “Sub-millisecond imaging of a bright flare and ejection event in the extragalactic jet 3C 111.” In: *Astron. Astrophys.* 644, A85 (Dec. 2020), A85. DOI: [10.1051/0004-6361/202037737](https://doi.org/10.1051/0004-6361/202037737). arXiv: [2009.01294](https://arxiv.org/abs/2009.01294) [[astro-ph.HE](#)].
- [536] M. Sekora and J. Stone. “A Higher Order Godunov Method for Radiation Hydrodynamics: Radiation Subsystem.” In: *arXiv e-prints*, arXiv:0910.1372 (Oct. 2009), arXiv:0910.1372. arXiv: [0910.1372](https://arxiv.org/abs/0910.1372) [[math.NA](#)].
- [537] J. Seo, H. Kang, and D. Ryu. “A Simulation Study of Ultra-relativistic Jets. II. Structures and Dynamics of FR-II Jets.” In: *Astrophys. J.* 920.2, 144 (Oct. 2021), p. 144. DOI: [10.3847/1538-4357/ac19b4](https://doi.org/10.3847/1538-4357/ac19b4). arXiv: [2106.04100](https://arxiv.org/abs/2106.04100) [[astro-ph.HE](#)].

- [538] T. Shahbaz et al. “Time-Resolved Optical Photometry of the Ultra-compact Binary 4U 0614+091.” In: 120.870 (Aug. 2008), p. 848. DOI: [10.1086/590505](https://doi.org/10.1086/590505). arXiv: [0806.1419](https://arxiv.org/abs/0806.1419) [[astro-ph](#)].
- [539] N. I. Shakura and R. A. Sunyaev. “A theory of the instability of disk accretion on to black holes and the variability of binary X-ray sources, galactic nuclei and quasars.” In: *Mon. Not. R. Astron. Soc.* 175 (June 1976), pp. 613–632. DOI: [10.1093/mnras/175.3.613](https://doi.org/10.1093/mnras/175.3.613).
- [540] N. I. Shakura and R. A. Sunyaev. “Black holes in binary systems. Observational appearance.” In: *Astron. Astrophys.* 24 (Jan. 1973), pp. 337–355.
- [541] J. V. Shebalin, W. H. Matthaeus, and D. Montgomery. “Anisotropy in MHD turbulence due to a mean magnetic field.” In: *Journal of Plasma Physics* 29.3 (June 1983), pp. 525–547. DOI: [10.1017/S002237780000933](https://doi.org/10.1017/S002237780000933).
- [542] M. Shibata, S. Fujibayashi, and Y. Sekiguchi. “Long-term evolution of a merger-remnant neutron star in general relativistic magnetohydrodynamics: Effect of magnetic winding” In: *Phys. Rev. D* 103.4, 043022 (Feb. 2021), p. 043022. DOI: [10.1103/PhysRevD.103.043022](https://doi.org/10.1103/PhysRevD.103.043022). arXiv: [2102.01346](https://arxiv.org/abs/2102.01346) [[astro-ph.HE](#)].
- [543] H.-Y. Shih, A. Stockton, and L. Kewley. “Ionized Outflows from Compact Steep Spectrum Sources.” In: *Astrophys. J.* 772.2, 138 (2013), p. 138. arXiv: [1306.5237](https://arxiv.org/abs/1306.5237) [[astro-ph.CO](#)].
- [544] H. L. Shipman. “The Implausible History of Triple Star Models for Cygnus X-1: Evidence for a Black Hole.” In: 16 (Feb. 1975), p. 9.
- [545] R. E. Shirey, H. V. Bradt, and A. M. Levine. “The Complete “Z” Track of Circinus X-1.” In: *Astrophys. J.* 517.1 (May 1999), pp. 472–487. DOI: [10.1086/307188](https://doi.org/10.1086/307188). arXiv: [astro-ph/9901003](https://arxiv.org/abs/astro-ph/9901003) [[astro-ph](#)].
- [546] R. E. Shirey et al. “Quasi-periodic Oscillations Associated with Spectral Branches in Rossi X-Ray Timing Explorer Observations of Circinus X-1.” In: *Astrophys. J.* 506.1 (Oct. 1998), pp. 374–383. DOI: [10.1086/306247](https://doi.org/10.1086/306247). arXiv: [astro-ph/9803278](https://arxiv.org/abs/astro-ph/9803278) [[astro-ph](#)].
- [547] I. S. Shklovsky. “On the Nature of the Source of X-Ray Emission of Sco XR-1.” In: *Astrophys. J. Lett.* 148 (Apr. 1967), p. L1. DOI: [10.1086/180001](https://doi.org/10.1086/180001).
- [548] C.-W. Shu and S. Osher. “Efficient Implementation of Essentially Non-oscillatory Shock-Capturing Schemes, II.” In: *Journal of Computational Physics* 83.1 (July 1989), pp. 32–78. DOI: [10.1016/0021-9991\(89\)90222-2](https://doi.org/10.1016/0021-9991(89)90222-2).
- [549] L. Sidoli et al. “XMM-Newton observation of a spectral state transition in the peculiar radio/X-ray/ $\gamma$ -ray source LS I +61 303.” In: *Astron. Astrophys.* 459.3 (Dec. 2006), pp. 901–907. DOI: [10.1051/0004-6361:20065933](https://doi.org/10.1051/0004-6361:20065933). arXiv: [astro-ph/0606722](https://arxiv.org/abs/astro-ph/0606722) [[astro-ph](#)].
- [550] M. Sikora et al. “Radiation drag in relativistic active galactic nucleus jets.” In: *Mon. Not. R. Astron. Soc.* 280.3 (June 1996), pp. 781–796. DOI: [10.1093/mnras/280.3.781](https://doi.org/10.1093/mnras/280.3.781).
- [551] A. Sądowski and R. Narayan. “Powerful radiative jets in supercritical accretion discs around non-spinning black holes.” In: *Mon. Not. R. Astron. Soc.* 453.3 (Nov. 2015), pp. 3213–3221. DOI: [10.1093/mnras/stv1802](https://doi.org/10.1093/mnras/stv1802). arXiv: [1503.00654](https://arxiv.org/abs/1503.00654) [[astro-ph.HE](#)].

- [552] A. Sądowski et al. “Semi-implicit scheme for treating radiation under M1 closure in general relativistic conservative fluid dynamics codes.” In: *Mon. Not. R. Astron. Soc.* 429.4 (Mar. 2013), pp. 3533–3550. DOI: [10.1093/mnras/sts632](https://doi.org/10.1093/mnras/sts632). arXiv: [1212.5050](https://arxiv.org/abs/1212.5050) [[astro-ph.HE](#)].
- [553] M. A. Skinner and E. C. Ostriker. “A Two-moment Radiation Hydrodynamics Module in Athena Using a Time-explicit Godunov Method.” In: *Astrophys. J. Suppl. Ser.* 206.2, 21 (June 2013), p. 21. DOI: [10.1088/0067-0049/206/2/21](https://doi.org/10.1088/0067-0049/206/2/21). arXiv: [1306.0010](https://arxiv.org/abs/1306.0010) [[astro-ph.IM](#)].
- [554] A. Smith et al. “Long-Term X-Ray Monitoring of the TeV Binary LS I +61 303 With the Rossi X-Ray Timing Explorer.” In: *Astrophys. J.* 693.2 (Mar. 2009), pp. 1621–1627. DOI: [10.1088/0004-637X/693/2/1621](https://doi.org/10.1088/0004-637X/693/2/1621). arXiv: [0809.4254](https://arxiv.org/abs/0809.4254) [[astro-ph](#)].
- [555] E. Sobacchi and Y. E. Lyubarsky. “Magnetic energy dissipation and origin of non-thermal spectra in radiatively efficient relativistic sources.” In: *Mon. Not. R. Astron. Soc.* 491.3 (Jan. 2020), pp. 3900–3907. DOI: [10.1093/mnras/stz3313](https://doi.org/10.1093/mnras/stz3313). arXiv: [1911.11570](https://arxiv.org/abs/1911.11570) [[astro-ph.HE](#)].
- [556] H. Sol, G. Pelletier, and E. Asseo. “Two-flow model for extragalactic radio jets.” In: *Mon. Not. R. Astron. Soc.* 237 (Mar. 1989), pp. 411–429. DOI: [10.1093/mnras/237.2.411](https://doi.org/10.1093/mnras/237.2.411).
- [557] P. Soleri et al. “Linking jet emission and X-ray properties in the peculiar neutron star X-ray binary Circinus X-1.” In: *Mon. Not. R. Astron. Soc.* 399.1 (Oct. 2009), pp. 453–464. DOI: [10.1111/j.1365-2966.2009.15297.x](https://doi.org/10.1111/j.1365-2966.2009.15297.x). arXiv: [0906.4280](https://arxiv.org/abs/0906.4280) [[astro-ph.HE](#)].
- [558] R. E. Spencer. “A radio jet in SS433.” In: *Nature* 282.5738 (Nov. 1979), pp. 483–484. DOI: [10.1038/282483a0](https://doi.org/10.1038/282483a0).
- [559] R. E. Spencer. “Flux density and structure variations in SS 433.” In: *Mon. Not. R. Astron. Soc.* 209 (Aug. 1984), pp. 869–879. DOI: [10.1093/mnras/209.4.869](https://doi.org/10.1093/mnras/209.4.869).
- [560] D. Steeghs and J. Casares. “The Mass Donor of Scorpius X-1 Revealed.” In: *Astrophys. J.* 568.1 (Mar. 2002), pp. 273–278. DOI: [10.1086/339224](https://doi.org/10.1086/339224). arXiv: [astro-ph/0107343](https://arxiv.org/abs/astro-ph/0107343) [[astro-ph](#)].
- [561] L. Stella and M. Vietri. “Lense-Thirring Precession and Quasi-periodic Oscillations in Low-Mass X-Ray Binaries.” In: *Astrophys. J. Lett.* 492.1 (Jan. 1998), pp. L59–L62. DOI: [10.1086/311075](https://doi.org/10.1086/311075). arXiv: [astro-ph/9709085](https://arxiv.org/abs/astro-ph/9709085) [[astro-ph](#)].
- [562] R. F. Stellingwerf. “Period determination using phase dispersion minimization.” In: *Astrophys. J.* 224 (Sept. 1978), pp. 953–960. DOI: [10.1086/156444](https://doi.org/10.1086/156444).
- [563] A. M. Stirling et al. “A relativistic jet from Cygnus X-1 in the low/hard X-ray state.” In: *Mon. Not. R. Astron. Soc.* 327.4 (Nov. 2001), pp. 1273–1278. DOI: [10.1046/j.1365-8711.2001.04821.x](https://doi.org/10.1046/j.1365-8711.2001.04821.x). arXiv: [astro-ph/0107192](https://arxiv.org/abs/astro-ph/0107192) [[astro-ph](#)].
- [564] A. M. Stirling et al. “Polarization and kinematic studies of SS 433 indicate a continuous and decelerating jet.” In: *Mon. Not. R. Astron. Soc.* 354.4 (Nov. 2004), pp. 1239–1254. DOI: [10.1111/j.1365-2966.2004.08285.x](https://doi.org/10.1111/j.1365-2966.2004.08285.x).

- [565] A. M. Stirling et al. “Radio-emitting component kinematics in SS433.” In: *Mon. Not. R. Astron. Soc.* 337.2 (Dec. 2002), pp. 657–665. DOI: [10.1046/j.1365-8711.2002.05944.x](https://doi.org/10.1046/j.1365-8711.2002.05944.x).
- [566] J. M. Stone and M. Edelman. “The Corrugation Instability in Slow Magnetosonic Shock Waves.” In: *Astrophys. J.* 454 (Nov. 1995), p. 182. DOI: [10.1086/176476](https://doi.org/10.1086/176476).
- [567] J. M. Stone, D. Mihalas, and M. L. Norman. “ZEUS-2D: A Radiation Magnetohydrodynamics Code for Astrophysical Flows in Two Space Dimensions. III. The Radiation Hydrodynamic Algorithms and Tests.” In: *Astrophys. J. Suppl. Ser.* 80 (June 1992), p. 819. DOI: [10.1086/191682](https://doi.org/10.1086/191682).
- [568] S. Subramanian et al. “Techniques, Tricks and Algorithms for Efficient GPU-Based Processing of Higher Order Hyperbolic PDEs.” In: *arXiv e-prints*, arXiv:2211.13295 (Nov. 2022), arXiv:2211.13295. DOI: [10.48550/arXiv.2211.13295](https://doi.org/10.48550/arXiv.2211.13295). arXiv: [2211.13295](https://arxiv.org/abs/2211.13295) [math.NA].
- [569] R. Sunyaev et al. “Two hard X-ray sources in 100 square degrees around the Galactic Center.” In: *Astron. Astrophys.* 247 (July 1991), pp. L29–L32.
- [570] A. Suresh and H. T. Huynh. “Accurate Monotonicity-Preserving Schemes with Runge Kutta Time Stepping.” In: *Journal of Computational Physics* 136.1 (Sept. 1997), pp. 83–99. DOI: [10.1006/jcph.1997.5745](https://doi.org/10.1006/jcph.1997.5745).
- [571] J. Synge. *The Relativistic Gas*. North-Holland publishing Company, 1957.
- [572] H. R. Takahashi and Y. Masada. “Stability of MRI-turbulent Accretion Disks.” In: *Astrophys. J.* 727.2, 106 (Feb. 2011), p. 106. DOI: [10.1088/0004-637X/727/2/106](https://doi.org/10.1088/0004-637X/727/2/106). arXiv: [1011.4643](https://arxiv.org/abs/1011.4643) [astro-ph.HE].
- [573] H. R. Takahashi and K. Ohsuga. “A Numerical Treatment of Anisotropic Radiation Fields Coupled with Relativistic Resistive Magnetofluids.” In: *Astrophys. J.* 772.2, 127 (Aug. 2013), p. 127. DOI: [10.1088/0004-637X/772/2/127](https://doi.org/10.1088/0004-637X/772/2/127). arXiv: [1306.0049](https://arxiv.org/abs/1306.0049) [astro-ph.HE].
- [574] H. R. Takahashi et al. “Explicit-Implicit Scheme for Relativistic Radiation Hydrodynamics.” In: *Astrophys. J.* 764.2, 122 (Feb. 2013), p. 122. DOI: [10.1088/0004-637X/764/2/122](https://doi.org/10.1088/0004-637X/764/2/122). arXiv: [1212.4910](https://arxiv.org/abs/1212.4910) [astro-ph.HE].
- [575] S. Takeuchi, K. Ohsuga, and S. Mineshige. “A Novel Jet Model: Magnetically Collimated, Radiation-Pressure Driven Jet.” In: *Publ. Astron. Soc. Jpn* 62 (Oct. 2010), pp. L43–47. DOI: [10.1093/pasj/62.5.L43](https://doi.org/10.1093/pasj/62.5.L43). arXiv: [1009.0161](https://arxiv.org/abs/1009.0161) [astro-ph.HE].
- [576] M. Tavani et al. “The Variable Gamma-Ray Source 2CG 135+01.” In: *Astrophys. J. Lett.* 497.2 (Apr. 1998), pp. L89–L91. DOI: [10.1086/311281](https://doi.org/10.1086/311281).
- [577] A. R. Taylor and P. C. Gregory. “Periodic radio emission from LS I + 61 303.” In: *Astrophys. J.* 255 (Apr. 1982), pp. 210–216. DOI: [10.1086/159819](https://doi.org/10.1086/159819).
- [578] A. R. Taylor et al. “An X-ray outburst. from the radio emitting X-ray binary LSI+61 303.” In: *Astron. Astrophys.* 305 (Jan. 1996), p. 817.
- [579] A. Tchekhovskoy and O. Bromberg. “Three-dimensional relativistic MHD simulations of active galactic nuclei jets: magnetic kink instability and Fanaroff-Riley dichotomy.” In: *Mon. Not. R. Astron. Soc.* 461.1 (Sept. 2016), pp. L46–L50. DOI: [10.1093/mnras/slw064](https://doi.org/10.1093/mnras/slw064). arXiv: [1512.04526](https://arxiv.org/abs/1512.04526) [astro-ph.HE].

- [580] A. Tchekhovskoy, R. Narayan, and J. C. McKinney. “Efficient generation of jets from magnetically arrested accretion on a rapidly spinning black hole.” In: *Mon. Not. R. Astron. Soc.* 418.1 (Nov. 2011), pp. L79–L83. DOI: [10.1111/j.1745-3933.2011.01147.x](https://doi.org/10.1111/j.1745-3933.2011.01147.x). arXiv: [1108.0412](https://arxiv.org/abs/1108.0412) [[astro-ph.HE](#)].
- [581] J. M. TenBerge et al. “Weak Alfvénic turbulence in relativistic plasmas. Part 1. Dynamical equations and basic dynamics of interacting resonant triads.” In: *Journal of Plasma Physics* 87.6, 905870614 (Dec. 2021), p. 905870614. DOI: [10.1017/S002237782100115X](https://doi.org/10.1017/S002237782100115X). arXiv: [2105.01146](https://arxiv.org/abs/2105.01146) [[astro-ph.HE](#)].
- [582] A. J. Tetarenko et al. “Disc-jet coupling in the Terzan 5 neutron star X-ray binary EXO 1745-248.” In: *Mon. Not. R. Astron. Soc.* 460.1 (July 2016), pp. 345–355. DOI: [10.1093/mnras/stw1013](https://doi.org/10.1093/mnras/stw1013). arXiv: [1604.07752](https://arxiv.org/abs/1604.07752) [[astro-ph.HE](#)].
- [583] A. J. Tetarenko et al. “Extreme jet ejections from the black hole X-ray binary V404 Cygni.” In: *Mon. Not. R. Astron. Soc.* 469.3 (Aug. 2017), pp. 3141–3162. DOI: [10.1093/mnras/stx1048](https://doi.org/10.1093/mnras/stx1048). arXiv: [1704.08726](https://arxiv.org/abs/1704.08726) [[astro-ph.HE](#)].
- [584] A. J. Tetarenko et al. “Measuring fundamental jet properties with multi-wavelength fast timing of the black hole X-ray binary MAXI J1820+070.” In: *Mon. Not. R. Astron. Soc.* 504.3 (July 2021), pp. 3862–3883. DOI: [10.1093/mnras/stab820](https://doi.org/10.1093/mnras/stab820). arXiv: [2103.09318](https://arxiv.org/abs/2103.09318) [[astro-ph.HE](#)].
- [585] The Event Horizon Telescope Collaboration. “First M87 Event Horizon Telescope Results. I. The Shadow of the Supermassive Black Hole.” In: *Astrophys. J. Lett.* 875.1, L1 (2019), p. L1. arXiv: [1906.11238](https://arxiv.org/abs/1906.11238) [[astro-ph.GA](#)].
- [586] K. S. Thorne. “Disk-Accretion onto a Black Hole. II. Evolution of the Hole.” In: *Astrophys. J.* 191 (July 1974), pp. 507–520. DOI: [10.1086/152991](https://doi.org/10.1086/152991).
- [587] K. Thornton et al. “Energy Input and Mass Redistribution by Supernovae in the Interstellar Medium.” In: *Astrophys. J.* 500.1 (June 1998), pp. 95–119. DOI: [10.1086/305704](https://doi.org/10.1086/305704). arXiv: [astro-ph/9706175](https://arxiv.org/abs/astro-ph/9706175) [[astro-ph](#)].
- [588] R. Timmerman et al. “Origin of the ring structures in Hercules A. Sub-arcsecond 144 MHz to 7 GHz observations.” In: *Astron. Astrophys.* 658, A5 (Feb. 2022), A5. DOI: [10.1051/0004-6361/202140880](https://doi.org/10.1051/0004-6361/202140880). arXiv: [2108.07287](https://arxiv.org/abs/2108.07287) [[astro-ph.GA](#)].
- [589] S. J. Tingay et al. “Relativistic motion in a nearby bright X-ray source.” In: *Nature* 374.6518 (Mar. 1995), pp. 141–143. DOI: [10.1038/374141a0](https://doi.org/10.1038/374141a0).
- [590] L. Titarchuk, E. Seifina, and C. Shrader. “X-Ray Spectral and Timing Behavior of Scorpius X-1. Spectral Hardening during the Flaring Branch.” In: *Astrophys. J.* 789.2, 98 (July 2014), p. 98. DOI: [10.1088/0004-637X/789/2/98](https://doi.org/10.1088/0004-637X/789/2/98). arXiv: [1405.6375](https://arxiv.org/abs/1405.6375) [[astro-ph.SR](#)].
- [591] A. Tolstov et al. “Shock Wave Structure in Astrophysical Flows with an Account of Photon Transfer.” In: *Astrophys. J.* 811.1, 47 (Sept. 2015), p. 47. DOI: [10.1088/0004-637X/811/1/47](https://doi.org/10.1088/0004-637X/811/1/47). arXiv: [1412.1434](https://arxiv.org/abs/1412.1434) [[astro-ph.HE](#)].
- [592] E. F. Toro. *Riemann solvers and numerical methods for fluid dynamics: a practical introduction*. Springer Science & Business Media, 2013.

- [593] D. F. Torres, G. E. Romero, and F. Mirabel. “Neutrinos from Microquasars.” In: *Chinese Journal of Astronomy and Astrophysics Supplement* 5 (June 2005), pp. 183–188. DOI: [10.1088/1009-9271/5/S1/133](https://doi.org/10.1088/1009-9271/5/S1/133). arXiv: [astro-ph/0407494](https://arxiv.org/abs/astro-ph/0407494) [[astro-ph](#)].
- [594] D. F. Torres et al. “A Magnetar-like Event from LS I +61°303 and Its Nature as a Gamma-Ray Binary.” In: *Astrophys. J.* 744.2, 106 (Jan. 2012), p. 106. DOI: [10.1088/0004-637X/744/2/106](https://doi.org/10.1088/0004-637X/744/2/106). arXiv: [1109.5008](https://arxiv.org/abs/1109.5008) [[astro-ph.HE](#)].
- [595] D. F. Torres et al. “Variability in the Orbital Profiles of the X-ray Emission of the  $\gamma$ -ray Binary LS I +61° 303.” In: *Astrophys. J. Lett.* 719.1 (Aug. 2010), pp. L104–L108. DOI: [10.1088/2041-8205/719/1/L104](https://doi.org/10.1088/2041-8205/719/1/L104). arXiv: [1007.2272](https://arxiv.org/abs/1007.2272) [[astro-ph.HE](#)].
- [596] M. Torrilhon. “Krylov–Riemann Solver for Large Hyperbolic Systems of Conservation Laws.” In: *SIAM Journal on Scientific Computing* 34.4 (2012), A2072–A2091. DOI: [10.1137/110840832](https://doi.org/10.1137/110840832). eprint: [https://doi.org/10.1137/110840832](https://doi.org/https://doi.org/10.1137/110840832). URL: <https://doi.org/10.1137/110840832>.
- [597] G. Tóth. “The  $\nabla \cdot \mathbf{B}=0$  Constraint in Shock-Capturing Magnetohydrodynamics Codes.” In: *Journal of Computational Physics* 161.2 (July 2000), pp. 605–652. DOI: [10.1006/jcph.2000.6519](https://doi.org/10.1006/jcph.2000.6519).
- [598] V. Tudose et al. “A decade of radio imaging the relativistic outflow in the peculiar X-ray binary CircinusX-1.” In: *Mon. Not. R. Astron. Soc.* 390.1 (Oct. 2008), pp. 447–464. DOI: [10.1111/j.1365-2966.2008.13788.x](https://doi.org/10.1111/j.1365-2966.2008.13788.x). arXiv: [0807.5108](https://arxiv.org/abs/0807.5108) [[astro-ph](#)].
- [599] P. Ubertini et al. “The Fermi/LAT Sky as Seen by INTEGRAL/IBIS.” In: *Astrophys. J. Lett.* 706.1 (Nov. 2009), pp. L7–L11. DOI: [10.1088/0004-637X/706/1/L7](https://doi.org/10.1088/0004-637X/706/1/L7). arXiv: [0910.1738](https://arxiv.org/abs/0910.1738) [[astro-ph.HE](#)].
- [600] Y. Ueda et al. “Detection of Absorption-Line Features in the X-Ray Spectra of the Galactic Superluminal Source GRO J1655-40.” In: *Astrophys. J.* 492.2 (Jan. 1998), pp. 782–787. DOI: [10.1086/305063](https://doi.org/10.1086/305063).
- [601] B. Vaidya et al. “Astrophysical fluid simulations of thermally ideal gases with non-constant adiabatic index: numerical implementation.” In: *Astron. Astrophys.* 580, A110 (Aug. 2015), A110. DOI: [10.1051/0004-6361/201526247](https://doi.org/10.1051/0004-6361/201526247). arXiv: [1506.01562](https://arxiv.org/abs/1506.01562) [[astro-ph.IM](#)].
- [602] J. van den Eijnden et al. “An evolving jet from a strongly magnetized accreting X-ray pulsar.” In: *Nature* 562.7726 (Sept. 2018), pp. 233–235. DOI: [10.1038/s41586-018-0524-1](https://doi.org/10.1038/s41586-018-0524-1). arXiv: [1809.10204](https://arxiv.org/abs/1809.10204) [[astro-ph.HE](#)].
- [603] M. van der Klis. “Overview of QPOs in neutron-star low-mass X-ray binaries.” In: *Advances in Space Research* 38.12 (Jan. 2006), pp. 2675–2679. DOI: [10.1016/j.asr.2005.11.026](https://doi.org/10.1016/j.asr.2005.11.026).
- [604] M. van der Klis. “Quasi-periodic oscillations and noise in low-mass X-ray binaries.” In: *Annu. Rev. Astron. Astrophys.* 27 (Jan. 1989), pp. 517–553. DOI: [10.1146/annurev.aa.27.090189.002505](https://doi.org/10.1146/annurev.aa.27.090189.002505).
- [605] M. van der Klis et al. “Discovery of Submillisecond Quasi-periodic Oscillations in the X-Ray Flux of Scorpius X-1.” In: *Astrophys. J. Lett.* 469 (Sept. 1996), p. L1. DOI: [10.1086/310251](https://doi.org/10.1086/310251). arXiv: [astro-ph/9607047](https://arxiv.org/abs/astro-ph/9607047) [[astro-ph](#)].

- [606] M. van der Klis et al. “Intensity and Source State Dependence of the Quasi-periodic Oscillations in Scorpius X-1.” In: *Astrophys. J.* 316 (May 1987), p. 411. DOI: [10.1086/165210](https://doi.org/10.1086/165210).
- [607] M. van der Klis et al. “Kilohertz Quasi-Periodic Oscillation Peak Separation Is Not Constant in Scorpius X-1.” In: *Astrophys. J. Lett.* 481.2 (June 1997), pp. L97–L100. DOI: [10.1086/310656](https://doi.org/10.1086/310656). arXiv: [astro-ph/9703025](https://arxiv.org/abs/astro-ph/9703025) [[astro-ph](#)].
- [608] H. van der Laan. “A Model for Variable Extragalactic Radio Sources.” In: *Nature* 211.5054 (Sept. 1966), pp. 1131–1133. DOI: [10.1038/2111131a0](https://doi.org/10.1038/2111131a0).
- [609] M. H. van Kerkwijk et al. “The Wolf-Rayet counterpart of Cygnus X-3.” In: *Astron. Astrophys.* 314 (Oct. 1996), pp. 521–540. DOI: [10.48550/arXiv.astro-ph/9604100](https://doi.org/10.48550/arXiv.astro-ph/9604100). arXiv: [astro-ph/9604100](https://arxiv.org/abs/astro-ph/9604100) [[astro-ph](#)].
- [610] B. van Leer. “Towards the Ultimate Conservation Difference Scheme. II. Monotonicity and Conservation Combined in a Second-Order Scheme.” In: *Journal of Computational Physics* 14.4 (Mar. 1974), pp. 361–370. DOI: [10.1016/0021-9991\(74\)90019-9](https://doi.org/10.1016/0021-9991(74)90019-9).
- [611] B. van Leer. “Towards the Ultimate Conservative Difference Scheme. IV. A New Approach to Numerical Convection.” In: *Journal of Computational Physics* 23 (Mar. 1977), p. 276. DOI: [10.1016/0021-9991\(77\)90095-X](https://doi.org/10.1016/0021-9991(77)90095-X).
- [612] M. H. P. M. van Putten. “A numerical implementation of MHD in divergence form.” In: *Journal of Computational Physics* 105.2 (Apr. 1993), pp. 339–353. DOI: [10.1006/jcph.1993.1080](https://doi.org/10.1006/jcph.1993.1080).
- [613] E. Vardoulaki et al. “FR-type radio sources at 3 GHz VLA-COSMOS: Relation to physical properties and large-scale environment.” In: *Astron. Astrophys.* 648, A102 (Apr. 2021), A102. DOI: [10.1051/0004-6361/202039488](https://doi.org/10.1051/0004-6361/202039488). arXiv: [2009.10721](https://arxiv.org/abs/2009.10721) [[astro-ph.GA](#)].
- [614] P. F. Velázquez and A. C. Raga. “A numerical simulation of the W 50-SS 433 system.” In: *Astron. Astrophys.* 362 (Oct. 2000), pp. 780–785.
- [615] A. Veledina et al. “Astronomical puzzle Cyg X-3 is a hidden Galactic ultraluminous X-ray source.” In: *arXiv e-prints*, arXiv:2303.01174 (Mar. 2023), arXiv:2303.01174. DOI: [10.48550/arXiv.2303.01174](https://doi.org/10.48550/arXiv.2303.01174). arXiv: [2303.01174](https://arxiv.org/abs/2303.01174) [[astro-ph.HE](#)].
- [616] J. L. Verniero, G. G. Howes, and K. G. Klein. “Nonlinear energy transfer and current sheet development in localized Alfvén wavepacket collisions in the strong turbulence limit.” In: *Journal of Plasma Physics* 84.1, 905840103 (Feb. 2018), p. 905840103. DOI: [10.1017/S0022377817001003](https://doi.org/10.1017/S0022377817001003). arXiv: [1705.07046](https://arxiv.org/abs/1705.07046) [[physics.plasm-ph](#)].
- [617] M. Vigelius et al. “Three-dimensional hydrodynamic simulations of asymmetric pulsar wind bow shocks.” In: *Mon. Not. R. Astron. Soc.* 374.3 (Jan. 2007), pp. 793–808. DOI: [10.1111/j.1365-2966.2006.11193.x](https://doi.org/10.1111/j.1365-2966.2006.11193.x). arXiv: [astro-ph/0610454](https://arxiv.org/abs/astro-ph/0610454) [[astro-ph](#)].
- [618] O. Vilhu et al. “Wind suppression by X-rays in Cygnus X-3.” In: *Astron. Astrophys.* 649, A176 (May 2021), A176. DOI: [10.1051/0004-6361/202140620](https://doi.org/10.1051/0004-6361/202140620). arXiv: [2104.02305](https://arxiv.org/abs/2104.02305) [[astro-ph.HE](#)].
- [619] N. Vlahakis. “The Efficiency of the Magnetic Acceleration in Relativistic Jets.” In: 293.1 (Sept. 2004), pp. 67–74. DOI: [10.1023/B:ASTR.0000044653.77654.fb](https://doi.org/10.1023/B:ASTR.0000044653.77654.fb). arXiv: [astro-ph/0401105](https://arxiv.org/abs/astro-ph/0401105) [[astro-ph](#)].

- [620] N. Vlahakis and A. Königl. “Magnetic Driving of Relativistic Outflows in Active Galactic Nuclei. I. Interpretation of Parsec-Scale Accelerations.” In: *Astrophys. J.* 605.2 (Apr. 2004), pp. 656–661. DOI: [10.1086/382670](https://doi.org/10.1086/382670). arXiv: [astro-ph/0310747](https://arxiv.org/abs/astro-ph/0310747) [[astro-ph](#)].
- [621] A. Y. Wagner and G. V. Bicknell. “Relativistic Jet Feedback in Evolving Galaxies.” In: *Astrophys. J.* 728.1, 29 (Feb. 2011), p. 29. DOI: [10.1088/0004-637X/728/1/29](https://doi.org/10.1088/0004-637X/728/1/29). arXiv: [1012.1092](https://arxiv.org/abs/1012.1092) [[astro-ph.CO](#)].
- [622] A. Y. Wagner, G. V. Bicknell, and M. Umemura. “Driving Outflows with Relativistic Jets and the Dependence of Active Galactic Nucleus Feedback Efficiency on Interstellar Medium Inhomogeneity.” In: *Astrophys. J.* 757.2, 136 (Oct. 2012), p. 136. DOI: [10.1088/0004-637X/757/2/136](https://doi.org/10.1088/0004-637X/757/2/136). arXiv: [1205.0542](https://arxiv.org/abs/1205.0542) [[astro-ph.CO](#)].
- [623] E. B. Waltman et al. “Quenched Radio Emission in Cygnus X-3.” In: *Astrophys. J.* 112 (Dec. 1996), p. 2690. DOI: [10.1086/118213](https://doi.org/10.1086/118213).
- [624] N. Wang, S. Johnston, and R. N. Manchester. “13 years of timing of PSR B1259-63.” In: *Mon. Not. R. Astron. Soc.* 351.2 (June 2004), pp. 599–606. DOI: [10.1111/j.1365-2966.2004.07806.x](https://doi.org/10.1111/j.1365-2966.2004.07806.x). arXiv: [astro-ph/0403612](https://arxiv.org/abs/astro-ph/0403612) [[astro-ph](#)].
- [625] P. Wang, T. Abel, and W. Zhang. “Relativistic Hydrodynamic Flows Using Spatial and Temporal Adaptive Structured Mesh Refinement.” In: *Astrophys. J. Suppl. Ser.* 176.2 (June 2008), pp. 467–483. DOI: [10.1086/529434](https://doi.org/10.1086/529434). arXiv: [astro-ph/0703742](https://arxiv.org/abs/astro-ph/0703742) [[astro-ph](#)].
- [626] L. R. Weih et al. “Beyond moments: relativistic lattice Boltzmann methods for radiative transport in computational astrophysics.” In: *Mon. Not. R. Astron. Soc.* 498.3 (Nov. 2020), pp. 3374–3394. DOI: [10.1093/mnras/staa2575](https://doi.org/10.1093/mnras/staa2575). arXiv: [2007.05718](https://arxiv.org/abs/2007.05718) [[physics.comp-ph](#)].
- [627] L. R. Weih, H. Olivares, and L. Rezzolla. “Two-moment scheme for general-relativistic radiation hydrodynamics: a systematic description and new applications.” In: *Mon. Not. R. Astron. Soc.* 495.2 (June 2020), pp. 2285–2304. DOI: [10.1093/mnras/staa1297](https://doi.org/10.1093/mnras/staa1297). arXiv: [2003.13580](https://arxiv.org/abs/2003.13580) [[gr-qc](#)].
- [628] M. C. Weisskopf et al. “Chandra X-ray Observatory (CXO): overview.” In: *X-Ray Optics, Instruments, and Missions III*. Ed. by J. E. Truemper and B. Aschenbach. Vol. 4012. Society of Photo-Optical Instrumentation Engineers (SPIE) Conference Series. July 2000, pp. 2–16. DOI: [10.1117/12.391545](https://doi.org/10.1117/12.391545). arXiv: [astro-ph/0004127](https://arxiv.org/abs/astro-ph/0004127) [[astro-ph](#)].
- [629] S.-S. Weng et al. “Radio pulsations from a neutron star within the gamma-ray binary LS I +61° 303.” In: *Nature Astronomy* (Mar. 2022). DOI: [10.1038/s41550-022-01630-1](https://doi.org/10.1038/s41550-022-01630-1). arXiv: [2203.09423](https://arxiv.org/abs/2203.09423) [[astro-ph.HE](#)].
- [630] J. A. J. Whelan et al. “The optical and radio counterpart of Circinus X-1 (3U 1516-56).” In: *Mon. Not. R. Astron. Soc.* 181 (Nov. 1977), pp. 259–271. DOI: [10.1093/mnras/181.2.259](https://doi.org/10.1093/mnras/181.2.259).
- [631] C. J. White et al. “An Extension of the Athena++ Code Framework for Radiation-Magnetohydrodynamics in General Relativity Using a Finite-Solid-Angle Discretization.” In: *arXiv e-prints*, arXiv:2302.04283 (Feb. 2023), arXiv:2302.04283. DOI: [10.48550/arXiv.2302.04283](https://doi.org/10.48550/arXiv.2302.04283). arXiv: [2302.04283](https://arxiv.org/abs/2302.04283) [[astro-ph.HE](#)].

- [632] R. Wijnands, J. Homan, and M. van der Klis. “The Complex Phase-Lag Behavior of the 3-12 HZ Quasi-Periodic Oscillations during the Very High State of XTE J1550-564.” In: *Astrophys. J. Lett.* 526.1 (Nov. 1999), pp. L33–L36. DOI: [10.1086/312365](https://doi.org/10.1086/312365). arXiv: [astro-ph/9909515](https://arxiv.org/abs/astro-ph/9909515) [[astro-ph](#)].
- [633] H. Wolter. “Spiegelsysteme streifenden Einfalls als abbildende Optiken für Röntgenstrahlen.” In: *Annalen der Physik* 445.1 (Jan. 1952), pp. 94–114. DOI: [10.1002/andp.19524450108](https://doi.org/10.1002/andp.19524450108).
- [634] A. J. Wright and I. Hawke. “Resistive and Multi-fluid RMHD on Graphics Processing Units.” In: *Astrophys. J. Suppl. Ser.* 240.1, 8 (Jan. 2019), p. 8. DOI: [10.3847/1538-4365/aaf1b0](https://doi.org/10.3847/1538-4365/aaf1b0). arXiv: [1808.09721](https://arxiv.org/abs/1808.09721) [[physics.comp-ph](#)].
- [635] L.-H. Wu et al. “The dying accretion and jet in a powerful radio galaxy of Hercules A.” In: *Research in Astronomy and Astrophysics* 20.8, 122 (Aug. 2020), p. 122. DOI: [10.1088/1674-4527/20/8/122](https://doi.org/10.1088/1674-4527/20/8/122).
- [636] Y. W. Wu et al. “Revisiting LS I +61°303 with VLBI astrometry.” In: *Mon. Not. R. Astron. Soc.* 474.3 (Mar. 2018), pp. 4245–4253. DOI: [10.1093/mnras/stx3003](https://doi.org/10.1093/mnras/stx3003). arXiv: [1711.07598](https://arxiv.org/abs/1711.07598) [[astro-ph.GA](#)].
- [637] P. M. Yates-Jones, S. S. Shabala, and M. G. H. Krause. “Dynamics of relativistic radio jets in asymmetric environments.” In: *Mon. Not. R. Astron. Soc.* 508.4 (Dec. 2021), pp. 5239–5250. DOI: [10.1093/mnras/stab2917](https://doi.org/10.1093/mnras/stab2917). arXiv: [2110.03162](https://arxiv.org/abs/2110.03162) [[astro-ph.HE](#)].
- [638] D. Yoon and S. Heinz. “Global Simulations of the Interaction of Microquasar Jets with a Stellar Wind in High-mass X-ray Binaries.” In: *Astrophys. J.* 801.1, 55 (Mar. 2015), p. 55. DOI: [10.1088/0004-637X/801/1/55](https://doi.org/10.1088/0004-637X/801/1/55). arXiv: [1501.03827](https://arxiv.org/abs/1501.03827) [[astro-ph.HE](#)].
- [639] D. Yoon et al. “Jet Trails and Mach Cones: The Interaction of Microquasars with the Interstellar Medium.” In: *Astrophys. J.* 742.1, 25 (Nov. 2011), p. 25. DOI: [10.1088/0004-637X/742/1/25](https://doi.org/10.1088/0004-637X/742/1/25). arXiv: [1108.4058](https://arxiv.org/abs/1108.4058) [[astro-ph.HE](#)].
- [640] D. Yoon, A. A. Zdziarski, and S. Heinz. “Formation of recollimation shocks in jets of high-mass X-ray binaries.” In: *Mon. Not. R. Astron. Soc.* 456.4 (Mar. 2016), pp. 3638–3644. DOI: [10.1093/mnras/stv2954](https://doi.org/10.1093/mnras/stv2954). arXiv: [1508.04539](https://arxiv.org/abs/1508.04539) [[astro-ph.HE](#)].
- [641] R. Zamanov et al. “H $\alpha$  observations of the  $\gamma$ -ray-emitting Be/X-ray binary LSI+61°303: orbital modulation, disk truncation, and long-term variability.” In: *Astron. Astrophys.* 559, A87 (Nov. 2013), A87. DOI: [10.1051/0004-6361/201321991](https://doi.org/10.1051/0004-6361/201321991). arXiv: [1309.3947](https://arxiv.org/abs/1309.3947) [[astro-ph.SR](#)].
- [642] R. Zanin et al. “Gamma rays detected from Cygnus X-1 with likely jet origin.” In: *Astron. Astrophys.* 596, A55 (Nov. 2016), A55. DOI: [10.1051/0004-6361/201628917](https://doi.org/10.1051/0004-6361/201628917). arXiv: [1605.05914](https://arxiv.org/abs/1605.05914) [[astro-ph.HE](#)].
- [643] O. Zanotti et al. “General relativistic radiation hydrodynamics of accretion flows - I. Bondi-Hoyle accretion.” In: *Mon. Not. R. Astron. Soc.* 417.4 (Nov. 2011), pp. 2899–2915. DOI: [10.1111/j.1365-2966.2011.19451.x](https://doi.org/10.1111/j.1365-2966.2011.19451.x). arXiv: [1105.5615](https://arxiv.org/abs/1105.5615) [[astro-ph.HE](#)].
- [644] J. Zavala et al. “Three-dimensional hydrodynamical simulations of the large-scale structure of W50-SS433.” In: *Mon. Not. R. Astron. Soc.* 387.2 (June 2008), pp. 839–844. DOI: [10.1111/j.1365-2966.2008.13281.x](https://doi.org/10.1111/j.1365-2966.2008.13281.x).

- [645] S. Zhang et al. “Long-term monitoring of LS I +61°303 with INTEGRAL.” In: *Mon. Not. R. Astron. Soc.* 408.1 (Oct. 2010), pp. 642–646. DOI: [10.1111/j.1365-2966.2010.17152.x](https://doi.org/10.1111/j.1365-2966.2010.17152.x). arXiv: [1006.1427](https://arxiv.org/abs/1006.1427) [[astro-ph.HE](#)].
- [646] W. Zhang et al. “Dead-Time Modifications to Fast Fourier Transform Power Spectra.” In: *Astrophys. J.* 449 (Aug. 1995), p. 930. DOI: [10.1086/176111](https://doi.org/10.1086/176111).
- [647] L. Zimmermann, L. Fuhrmann, and M. Massi. “The broad-band radio spectrum of LS I +61°303 in outburst.” In: *Astron. Astrophys.* 580, L2 (Aug. 2015), p. L2. DOI: [10.1051/0004-6361/201425545](https://doi.org/10.1051/0004-6361/201425545). arXiv: [1507.00859](https://arxiv.org/abs/1507.00859) [[astro-ph.HE](#)].
- [648] H. R. M. Zovaro et al. “Searching for signs of jet-driven negative feedback in the nearby radio galaxy UGC 05771.” In: *Mon. Not. R. Astron. Soc.* 489.4 (Nov. 2019), pp. 4944–4961. arXiv: [1909.00144](https://arxiv.org/abs/1909.00144) [[astro-ph.GA](#)].
- [649] D. Zwillinger and S. Kokoska. “CRC Standard Probability and Statistics Tables and Formulae.” In: (Jan. 2000).